Thermodynamic study of the in-vessel corium - Application to the corium/concrete interaction

Andrea Quaini

▶ **To cite this version:**

Andrea Quaini. Thermodynamic study of the in-vessel corium - Application to the corium/concrete interaction. Materials. Université Grenoble Alpes, 2015. English. NNT : 2015GREAI061 . tel-01311262

HAL Id: tel-01311262
https://theses.hal.science/tel-01311262

Submitted on 4 May 2016

HAL is a multi-disciplinary open access archive for the deposit and dissemination of scientific research documents, whether they are published or not. The documents may come from teaching and research institutions in France or abroad, or from public or private research centers.

L'archive ouverte pluridisciplinaire **HAL**, est destinée au dépôt et à la diffusion de documents scientifiques de niveau recherche, publiés ou non, émanant des établissements d'enseignement et de recherche français ou étrangers, des laboratoires publics ou privés.

UNIVERSITÉ GRENOBLE ALPES

THÈSE

Pour obtenir le grade de

DOCTEUR DE L'UNIVERSITÉ GRENOBLE ALPES

Spécialité : **Matériaux, Mécanique, Génie civil, Electrochimie**

Arrêté ministériel : le 6 janvier 2005 - 7 août 2006

Présentée par

Andrea QUAINI

Thèse dirigée par **Fiqiri HODAJ** et
codirigée par **Christine GUÉNEAU** et **Stéphane GOSSÉ**

préparée au sein du **Laboratoire de Modélisation, de Thermodynamique et de Thermochimie du CEA Saclay** et au **Laboratoire SIMAP**
dans **l'École Doctorale IMEP-2**

Étude thermodynamique du corium en cuve - Application à l'interaction corium/béton

Thèse soutenue publiquement le 03 Novembre 2015,
devant le jury composé de :

Prof. Hans Juergen SEIFERT
Directeur de Recherche au KIT de Karlsruhe, Rapporteur
Dr. Daniel NEUVILLE
Directeur de Recherche à l'IPGP de Paris, Rapporteur
Dr. Bengt HALLSTEDT
Chercheur au RWTH de l'Université d'Aachen, Examinateur
Dr. Marc BARRACHIN
Ingénieur chercheur à l'IRSN, Examinateur
Dr. Dario MANARA
Chercheur au JRC-ITU, Invité
Dr. Christine GUÉNEAU
Ingénieur chercheur au CEA, Examinateur
Dr. Stéphane GOSSÉ
Ingénieur chercheur au CEA, Examinateur
Prof. Fiqiri HODAJ
Professeur à Grenoble INP, Directeur de thèse
Prof. Rudy KONINGS
Directeur de Recherche au JRC-ITU, Président du jury

In this house we obey the laws of thermodynamics!
H.J.S.

Acknowledgments

The work presented in this manuscript was performed to obtain the PhD diploma at the Grenoble INP under the direction of Prof. Fiqiri Hodaj. This work has been carried out at the Laboratoire de Modélisation, de Thermodynamique et de Thermochimie (LM2T), CEA Saclay. I would like to thank the Heads of this laboratory: Jean-Luis Fleche and Clara Desgranges. I would also like to thank Philippe Prené and Fabrice Legendre, Heads of the SCCME Unit at the CEA Saclay.

I wish to thank all the members of my PhD thesis jury, in particular my committee members, Prof. Hans Jürgen Seifert and Dr. Daniel Neuville, for the brilliant comments and questions during the defence.

During the past three years I had the opportunity to work with wonderful people. I warmly thank my supervisors, Stéphane Gossé and Christine Guéneau for their continuous support and the fruitful scientific discussion. They introduced me to CALPHAD and they have taught me a lot on material science!

I would also like to thank Thierry Alpettaz and Eric Lizon a Lugrin for their precious help during the design of the ATTILHA setup. Their enormous technical backgrounds have been essential for the success in the development of this novel experimental setup.

During my thesis I had also the chance to perform experiments at the JRC-ITU under the supervision of my friend Dario Manara: thank you for having willingly transmitted me your knowledge on laser heating technique and material science. I also thank the TALISMAn project committee for funding these activities at the JRC-ITU.

I also thank all the people who contributed with their work to this thesis: Didier Bossu, Pierre-François Giroux, Sylvie Poissonnet, Patrick Bonnaillie, Michel Tabarant, Emmanuelle Brackx, Fabrice Gamboa and Laurent Risser.

A special thanks to my parents, for their continuous support during my studies.

I would also thank all my friends for providing me support and friendship! In particular, Tia, Fede and Andre… far away but so close!

The last part of this section is dedicated to my Crapin, Irene. You have been the person who supported me the most all along the past three years, during my good and bad times. You always have had faith in me, even when I didn't. I thank you deeply for staying by my side during the most difficult moments of this adventure called PhD. Without you, this wouldn't have been possible.

Étude thermodynamique du corium en cuve – Application à l'interaction corium/béton

Résumé :
Lors d'un accident grave dans un réacteur nucléaire à eau pressurisée, le combustible nucléaire va réagir avec le gaines en Zircaloy, les absorbants neutroniques et les structures métalliques environnantes pour former un mélange partiellement ou complètement fondu. Ce cœur fondu peut ensuite interagir avec la cuve en acier du réacteur pour former un mélange appelé corium en cuve. Par la suite, le corium peut percer la cuve et venir se déverser sur le radier en béton en-dessous du réacteur. En fonction du scénario considéré, le corium qui va réagir avec le béton peut être constitué soit d'une seule phase liquide oxyde ou de deux liquides, métallique et oxyde. L'objectif de la thèse est l'étude de la thermodynamique du corium en cuve, prototypique U-Pu-Zr-Fe-O. L'approche utilisée est basée sur la méthode CALPHAD, qui permet de développer un modèle thermodynamique sur ce système complexe à partir de données expérimentales thermodynamiques et de diagramme de phases. Des traitements thermiques sur le système O-U-Zr ont permis de mesurer deux conodes dans la lacune de miscibilité à l'état liquide à 2567 K. De plus, des températures de liquidus ont été mesurées sur trois échantillons riches en Zr, en utilisant le montage de chauffage laser de l'ITU. Par la même méthode, des températures de solidus ont été obtenues sur le système UO_2-PuO_2-ZrO_2. L'influence de l'atmosphère réductrice ou oxydante sur le comportement à la fusion de ce système a été étudiée pour la première fois. Les résultats montrent que la stœchiométrie en oxygène de ces oxydes dépend fortement du potentiel d'oxygène et de la composition en métal des échantillons. La lacune de miscibilité à l'état liquide a également été mise en évidence dans un échantillon U-O-Zr-Fe. L'ensemble de ces nouvelles données expérimentales avec celles de la littérature a permis de développer le modèle sur le système U-Pu-Zr-Fe-O. Pour tous les échantillons, des calculs de chemin de solidification avec ce modèle ont servi à interpréter les microstructures de solidification observées. Un bon accord est obtenu entre les calculs et les résultats expérimentaux. Des traitements thermiques sur deux échantillons de corium hors cuve ont permis de montrer l'influence de la composition du béton sur la nature des phases liquides formées à haute température. Les microstructures de solidification ont été interprétées à l'aide de calculs avec la base de données TAF-ID. En parallèle, un nouveau montage expérimental appelé ATTILHA, utilisant la lévitation aérodynamique et le chauffage laser, a été conçu et développé pour mesurer des données de diagramme de phase à haute température. Ce montage a été validé avec des systèmes oxydes bien connus. De plus, cette méthode a permis d'observer in-situ à l'aide de la caméra infra-rouge la formation de la lacune de miscibilité à l'état liquide dans le système O-Fe-Zr lors de l'oxydation d'une bille d'alliage Fe-Zr. La prochaine étape du développement est la nucléarisation du montage pour effectuer des mesures sur des échantillons contenant de l'uranium. La mise en place d'une caméra ultra rapide (5000 Hz) pour l'étude de propriétés thermo-physiques de mélanges de corium en cuve et hors cuve est également envisagée. La synergie entre le développement de ces outils expérimentaux et de calcul devrait permettre d'améliorer la description thermodynamique du corium et des codes de calcul sur les accidents graves utilisant ces données thermodynamiques.

Mots clés :

Thermodynamique, Système U-Pu-Zr-Fe-O, CALPHAD, Chauffage laser, Interaction corium/béton

Thermodynamic study on the in-vessel corium – Application to the corium/concrete interaction

Abstract :
During a severe accident in a pressurised water reactor, the nuclear fuel can interact with the Zircaloy cladding, the neutronic absorber and the surrounding metallic structure forming a partially or completely molten mixture. The molten core can then interact with the reactor steel vessel forming a mixture called in-vessel corium. In the worst case, this mixture can pierce the vessel and pour onto the concrete underneath the reactor, leading the formation of the ex-vessel corium. Furthermore, depending on the considered scenario, the corium can be formed by a liquid phase or by two liquids, one metallic the other oxide. The objective of this thesis is the investigation of the thermodynamics of the prototypic in-vessel corium U-Pu-Zr-Fe-O. The approach used during the thesis is based on the CALPHAD method, which allows to obtain a thermodynamic model for this complex system starting from phase diagram and thermodynamic data. Heat treatments performed on the O-U-Zr system allowed to measure two tie-lines in the miscibility gap in the liquid phase at 2567 K. Furthermore, the liquidus temperatures of three Zr-enriched samples have been obtained by laser heating in collaboration with ITU. With the same laser heating technique, solidus temperatures have been obtained on the UO_2-PuO_2-ZrO_2 system. The influence of the reducing or oxidising on the melting behaviour of this system has been studied for the first time. The results show that the oxygen stoichiometry of these oxides strongly depends on the oxygen potential and on the metal composition of the samples. The miscibility gap in the liquid phase of the U-Zr-Fe-O system has been also observed. The whole set of experimental results with the literature data allowed to develop the thermodynamic model of the U-Pu-Zr-Fe-O system. Solidification path calculations have been performed for all the investigated samples to interpret the microstructures of the solidified samples. A good accordance has been obtained between calculation and experimental results. Heat treatments on two ex-vessel corium samples showed the influence of the concrete composition on the nature of the liquid phases formed at high temperature. The observed microstructures have been interpreted by means of calculation performed with the TAF-ID database. In parallel, a novel experimental setup named ATTILHA based on aerodynamic levitation and laser heating has been conceived and developed to obtain high temperature phase diagram data. This setup has been validated on well-known oxide systems. Furthermore, this technique allowed to observe in-situ, by using an infrared camera, the formation of a miscibility gap in the liquid phase of the O-Fe-Zr system by oxidation of a Fe-Zr sample. The next step of the development will be the nuclearization of the apparatus to investigate U-containing samples. The implementation of a very fast visible camera (5000 Hz) to investigate the thermo-physical properties of in-vessel and ex-vessel corium mixtures is also underway. The synergy between the development of experimental and calculation tools will allow to improve the thermodynamic description of the corium and the severe accident code using thermodynamic input data.

Keywords :

Thermodynamics, U-Pu-Zr-Fe-O system, CALPHAD, Laser heating, Corium/concrete interaction

Contents

1 Introduction and Context 13
1.1 Severe accident in LWR- -The INES scale 14
1.1.1 Three Mile Island unit 2 – TMI-2 (1979) 15
1.1.2 Fukushima Daiichi (2011) 16
1.1.3 Consideration on severe accidents – EPR design 17
1.2 PWR core degradation phenomena 18
1.2.1 In-vessel corium retention 19
1.2.2 Ex-vessel corium retention 22
1.3 Concluding remarks 23
1.4 References 25

2 Critical review of literature data 27
2.1 Thermodynamic and phase data on in-vessel corium systems 27
2.1.1 O-U-Zr system 27
2.1.2 UO_2-ZrO_2 system 33
2.1.3 O-Fe-U system 37
2.1.4 O-Fe-Zr system 39
2.1.5 O-Pu-Zr system 41
2.1.6 O-Fe-U-Zr system 42
2.1.7 O-Pu-U-Zr system 43
2.1.8 Summary 44
2.2 Molten Corium-Concrete interaction large scale experiments 44
2.2.1 Degradation of fuel bundles and in-vessel retention 45
2.2.2 Fission products release 46
2.2.3 Molten corium-water interaction 46
2.2.4 Molten corium-concrete interaction MCCI 48
2.2.5 The PLINIUS facility 49
2.2.6 Summary 53
2.3 Conclusions 54
2.4 References 55

3 Thermodynamics of the in-vessel corium: experimental study 59
3.1 Methodology 59
3.2 Experimental study 60
3.2.1 O-U-Zr system 61
3.2.1.1 Heat treatments 61
3.2.1.3 Laser heating experiments 76
3.2.2 O-Fe-Zr system 86
3.2.3 UO_2-PuO_2-ZrO_2 system 87
3.2.3.1 Sample preparation and characterisation 88
3.2.3.2 Laser heating results 89
3.2.3.3 Discussion 92
3.2.3.4 Summary 96

3.3 Conclusions....97
3.4 References....99

4 Thermodynamics of the in-vessel corium: modelling and calculations....103
4.1 Thermodynamic modelling....104
4.1.1 O-U-Zr system....104
4.1.1.1 UO_2-ZrO_2 system....104
4.1.1.2 O-U-Zr isothermal sections at high temperatures (2273, 2567 and 3223 K)....105
4.1.1.3 O-U-Zr isothermal sections at low temperatures (1373 and 1673 K)....111
4.1.1.4 Summary....115
4.1.2 O-Fe-Zr system....115
4.1.2.1 ZrO_2-FeO section....116
4.1.2.2 ZrO_2-Fe_2O_3 section....116
4.1.2.3 O-Fe-Zr isothermal section at 1473 K....117
4.1.2.4 Calculated O-Fe-Zr isothermal sections....118
4.1.2.5 Summary....118
4.1.3 O-Fe-U....119
4.1.3.1 UO_2-$FeO_{1.1}$ section....120
4.1.3.2 Calculated O-Fe-U isothermal sections....121
4.1.3.3 Summary....121
4.1.4 O-Pu-U-Zr system....122
4.1.4.1 PuO_2-ZrO_2 system....122
4.1.4.2 UO_2-PuO_2-ZrO_2 system....123
4.2 Solidification path calculations....124
4.2.1 O-U-Zr samples....124
4.2.1.1 Sample OUZr_1....124
4.2.1.2 Sample OUZr_3....127
4.2.1.3 Sample OUZr_7....130
4.2.1.4 Summary....131
4.2.2 Laser heating results on the UO_2-PuO_2-ZrO_2 system....132
4.2.2.1 Solidification path of sample U48P3Z49....133
4.2.2.2 Solidification path of sample P50Z50....134
4.2.2.3 Solidus and liquidus surfaces calculation....135
4.2.2.4 Structural analysis on as-synthetized samples....136
4.2.2.5 Structural analysis after melting....140
4.2.2.6 Summary....140
4.2.3 In-vessel corium investigation....141
4.2.3.1 Oxide liquid (Liquid 2)....142
4.2.3.2 Metallic liquid (Liquid 1)....145
4.2.3.3 Summary....148
4.3 Conclusions....148
4.4 References....149

5 Experimental and calculation results on ex-vessel corium 153
5.1 Experimental results.....153
5.1.1 Sample preparation and characterisation.....154
5.1.2 CORIUM_1 154
5.1.3 CORIUM_2 156
5.1.4 Summary.....161
5.2 Solidification path calculations.....161
5.2.1 TAF-ID database.....161
5.2.2 Results.....162
5.2.2.1 CORIUM_1 162
5.2.2.2 CORIUM_2 164
5.3 Conclusions.....166
5.4 References.....167

6 ATTILHA experimental setup 170
6.1 Apparatus description 170
6.1.1 Bi-chromatic pyrometer.....170
6.1.2 HgCdTe detector 172
6.1.3 Infrared camera.....174
6.1.3.1 Calibration of the infrared camera.....174
6.1.3.2 Infrared images processing.....176
6.2 Validation of the experimental setup 177
6.2.1 Al_2O_3.....178
6.2.2 Al_2O_3-ZrO_2 182
6.2.3 Exploration of the liquid miscibility gap in O-Fe-Zr ..188
6.3 Conclusions and perspectives 193
6.4 References.....194

Conclusions and perspectives.....195

Appendix A 199
Appendix B.....211
Appendix C 221
Appendix D 231
Appendix E.....239
Appendix F.....241
Résumé 249

Chapter 1 – Introduction and Context

The 435 operating nuclear reactors represent 11 % of the world electricity production [1]. These nuclear power plants are competitive thanks to their low operational costs. Moreover, since the fuel represents only a small fraction of the nuclear electricity cost, fluctuations of the uranium price barely affect the competitive position of the nuclear option. From the environmental point of view, the nuclear option is considered as a low-emission CO_2 alternative. In this framework, the nuclear security is of paramount importance, especially considering the potential effects of a severe accident.

During the nominal operation of a Light Water Reactor (LWR), the radioactive products (nuclear fuel, fission products, transuranium elements) are separated from the environment by three barriers: the fuel cladding, the primary circuit and the containment reactor vessel (Figure 1).

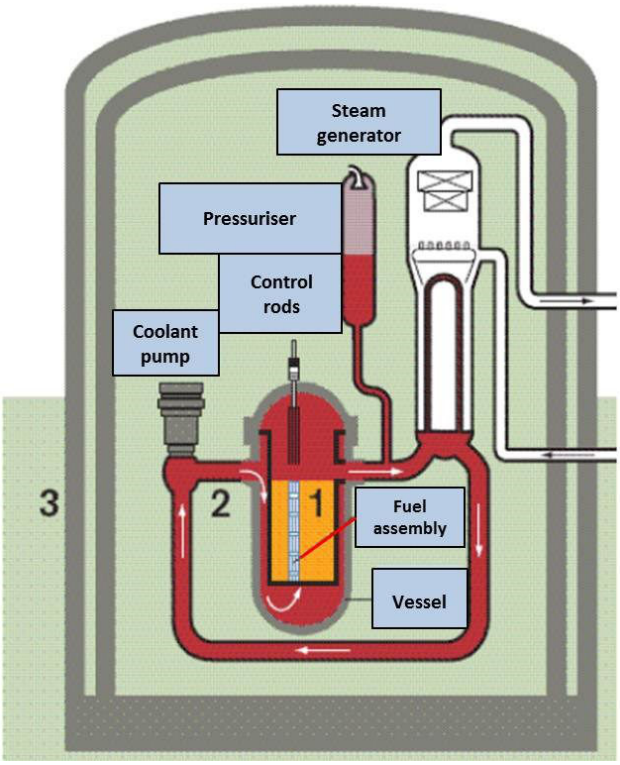

Figure 1: Scheme of a Pressurised Water Reactor (PWR). The numerical labels remind the three radiological barriers: (1) fuel cladding, (2) primary circuit and (3) containment reactor vessel

A nuclear accident may be defined as the non-intentional event that significantly reduces, under the accepted design level, the integrity of one or more barriers. This kind of situations does not necessarily imply a danger and it can be corrected before start again the normal operation of the reactor. However, an accident may turn into a severe accident if the implemented corrections are not sufficient to re-establish the nominal functioning conditions of the Nuclear Power Plant (NPP). For example, if the residual heat of decay produced by the reactor core (even in condition of reactor shut-down) is not removed by the reactor coolant, the temperature of the fuel assembly can rapidly increase.

Generally, during the nominal functioning of a Pressurised Water Reactor (PWR), the temperature at the centre of the fuel pin does not exceed 1373 K. If the cooling system fails, the heat produced by the radioactive decay is uniformly redistributed in the fuel pin leading to

a rise of its superficial temperature. As a direct consequence, the temperature of the fuel cladding may pass from 573 K to 973-1073 K in few seconds.

1.1 Severe accidents in LWR - The INES scale

A severe accident may be originated by internal or external causes. The internal events may be malfunctioning, plant ruptures or mistakes of the operators, whilst the external events are mostly of natural origin (earthquakes, tornados, flooding) but they can also be plane crashes, missiles attacks or flammable gas explosions. The International Nuclear and Radiological Event Scale INES [2] is a tool for a rapid communication between media, population and the nuclear community on the safety significance of events concerning nuclear installations. The INES classifies these out-of-nominal functioning events in seven categories. In Figure 2 the INES is reported.

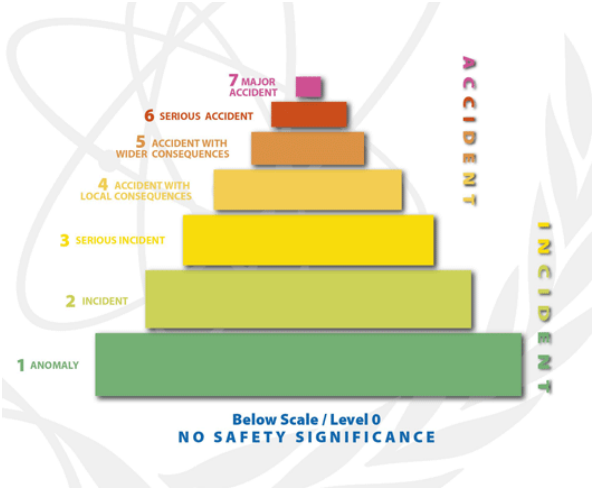

Figure 2: The International Nuclear and Radiological Event Scale [2]
Each step is separated by an order of magnitude from the previous and following in terms of its effect.
In the history of nuclear energy, some events occurred with different levels of gravity. A list of the most severe accidents is reported in Table 1.

Event	Reactor design	Description	INES level
Windscale, UK (1957)	B-Reactor, AGR	Pile 1 caught fire leading to the spread of a considerable quantity of fission products, especially iodine-131, in the environment.	5
Three Mile Island, USA (1979)	PWR	Partial melt-down of the reactor core	5
Chernobyl, URSS (1986)	RBMK	Partial destruction of the nuclear core. Large degradation of the nuclear fuel. Large release of radioactive materials in the environment due to a graphite fire.	7
Fukushima, Japan (2011)	BWR	Meltdown of the units 1, 2 and 3 cores of the NPP. Considerable release of radioactive material in the sea and in the surrounding of the NPP	7

Table 1: INES level of the most severe accidents in nuclear installations.
AGR=Advanced Gas Reactor; PWR=Pressurised Water Reactor;
RBMK=Reaktor Bolshoy Moshchnosti Kanalnyy (High Power Channel-type Reactor);
BWR=Boiling Water Reactor; NPP=Nuclear Power Plant

The Three Mile Island accident (Table 1) led to severe damages to the reactor but to a limited radioactive release in the environment (1% of the background radiation dose). Windscale caused a relevant release of radioactive material leading the authorities to partially set up the emergency plan to limit the effects on the population health.

During the Chernobyl and Fukushima accidents, a more critical situation was faced. In the case of the Chernobyl accident the core was destroyed and the radioactive materials were spread in the air reaching most of the radioactivity monitoring stations in Europe. It is estimated that 3.5 % of the fuel was ejected from the reactor. All the radioactive noble gases, 33 % of the core inventory of caesium and 50 % of iodine-131 were released as well [3]. The most recent severe accident occurred the 11th March, 2011 at the Fukushima Daiichi nuclear power plant. Three of the four units at the Fukushima Daiichi NPP experienced core melt-down and release of radioactive materials.

In the following a brief description of the progression of the Three Miles Island and Fukushima accidents will be given. These severe accidents are of particular interest for the present study because represent two accidental scenarios occurred in LWRs. Even if the Chernobyl accident can be considered as the most serious, its progression will not be reported. In fact, the accidental phenomenology is different compared with the LWRs' one. A detailed description of the accidental progression of Chernobyl accident can be found elsewhere [3].

1.1.1 Three Mile Island unit 2 – TMI-2 (1979)

The Three Mile Island NPP consists of 2 units equipped with PWRs. The reactor of the unit 2 had a thermal power of 2272 MW_{th} and an electrical power of 880 MW_e.

The unit 2 (TMI-2) was operating at 97% of the nominal maximum power when the accident happened. During maintenance operations performed some days before, the valves of the Automatic Feedwater System (AFS) were closed. This system allows removing the heat of decay from the reactor in the case of an emergency shut-down of the reactor. At 4:00 am on 28th March the feedwater flow to the steam generator was lost (event that can occur 2 to 3 times per year in a plant such as TMI-2 [3]). Because of the sudden loss of the heat removal, the pressure began to rise in the primary system up to 163.8 bars. The Pilot Operator Relief Valve (PORV) on the pressuriser opened and the reactor was shut down inserting the control rods. At 153 bars the PORV failed to close leading the system pressure continue dropping. The high pressure Emergency Core Cooling System (ECCS) automatically turned on when the pressure reached 111.8 bars. After a short time the operator thought that the primary system was full of water and to prevent the overfilling of the vessel he turned the ECCS off. This procedure led the remaining water in the reactor to evaporate: the core was in direct contact with water vapour leading to a dramatic overheating of the fuel. The cladding started a strong exothermic oxidation reaction that caused a rapid rise in temperature. Without any active cooling system the fuel melted and reacted first with the partially oxidised Zircaloy cladding. At the same time the metallic structures inside the reactor vessel (mechanical supports, fuel assembly grids, instrumentation, control rods) started to melt. The mixture of the molten fuel+cladding system and the metallic structure lead to the formation of the so-called ***in-vessel corium***. Due to the damage at the fuel cladding a significant fraction of the gaseous fission products were released. The operators started again the ECCS and the cooling of the reactor finally continued. The final configuration of the reactor after the accident is reported in Figure 3.

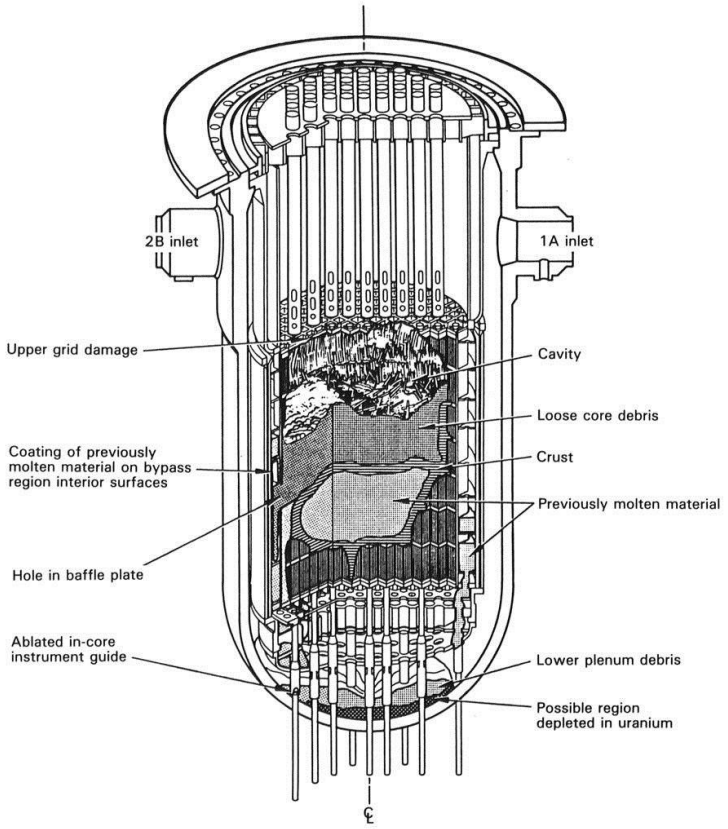

Figure 3: Final configuration of the TMI-2 reactor vessel and damaged core after the accident as reported by Broughton et al. [4]

Broughton et al. [4] estimated that about 45 % of the core mass was melted after the accident. It may be noted that from the protection of the public point of view, the safety systems worked very well. In fact, only a small fraction of the radioactive materials was released in the environment. In this case, the retention of the in-vessel corium mixture by the reactor vessel resulted efficient.

1.1.2 Fukushima Daiichi (2011)

A 9.0 magnitude earthquake with an epicentre in the ocean off the coast of Sanriku (Japan) occurred at 2:46 pm on March 11th, 2011. The control rods of all the operating units (units 1, 2 and 3 were operating whilst unit 4 was undergoing regular inspection) at the Daiichi NPP were automatically inserted and the reactors tripped. Due to the loss of electrical power, the emergency diesel generators automatically started and the reactors cooling begun. As a result of the tsunami that hit the Fukushima Daiichi NPP at 3:35 pm pumps and outdoor equipment for releasing the heat from the reactors to the sea were irreparably damaged and almost the entire nuclear installation was flooded. Furthermore, all the emergency diesel generators and the DC batteries were lost. In these conditions the residual heat of decay could not be removed from the reactor cores. The general outline of the accident evolution [5] is reported in Figure 4.

The sequence of events that led to the severe accident in unit 1 can be applied to unit 2 and 3. The timing at which the cooling systems were lost is however delayed from unit to unit. In the following a more detailed sequence of events will be given for unit 1 accident.

In unit 1, the water in the reactor vessel evaporated leaving part of the fuel bundles directly exposed to water vapour. Due to the elevated temperature of the fuel rods, the Zircaloy cladding reacted with the water vapour forming large amounts of hydrogen. The fuel itself

was damaged because of the high temperature reached at that time. The primary containment vessel was damaged as well. Hydrogen and radioactive materials leaked in the reactor building and gathered in its upper part. At 3:36 pm on 12th March the accumulated hydrogen ignited leading to an explosion. The gaseous and volatile fission products were thus released in the atmosphere. The reactor core experienced a meltdown forming a molten corium: it firstly accumulated at the bottom of the containment steel vessel, and then it pierced the vessel pouring on the underneath concrete. The so-called ***molten core/concrete interaction (MCCI)*** took place. The molten in-vessel corium start to ablate the concrete pit: the interaction at high temperature between in-vessel corium and the decomposition products of concrete led to the formation of a complex mixture called ***ex-vessel corium***.

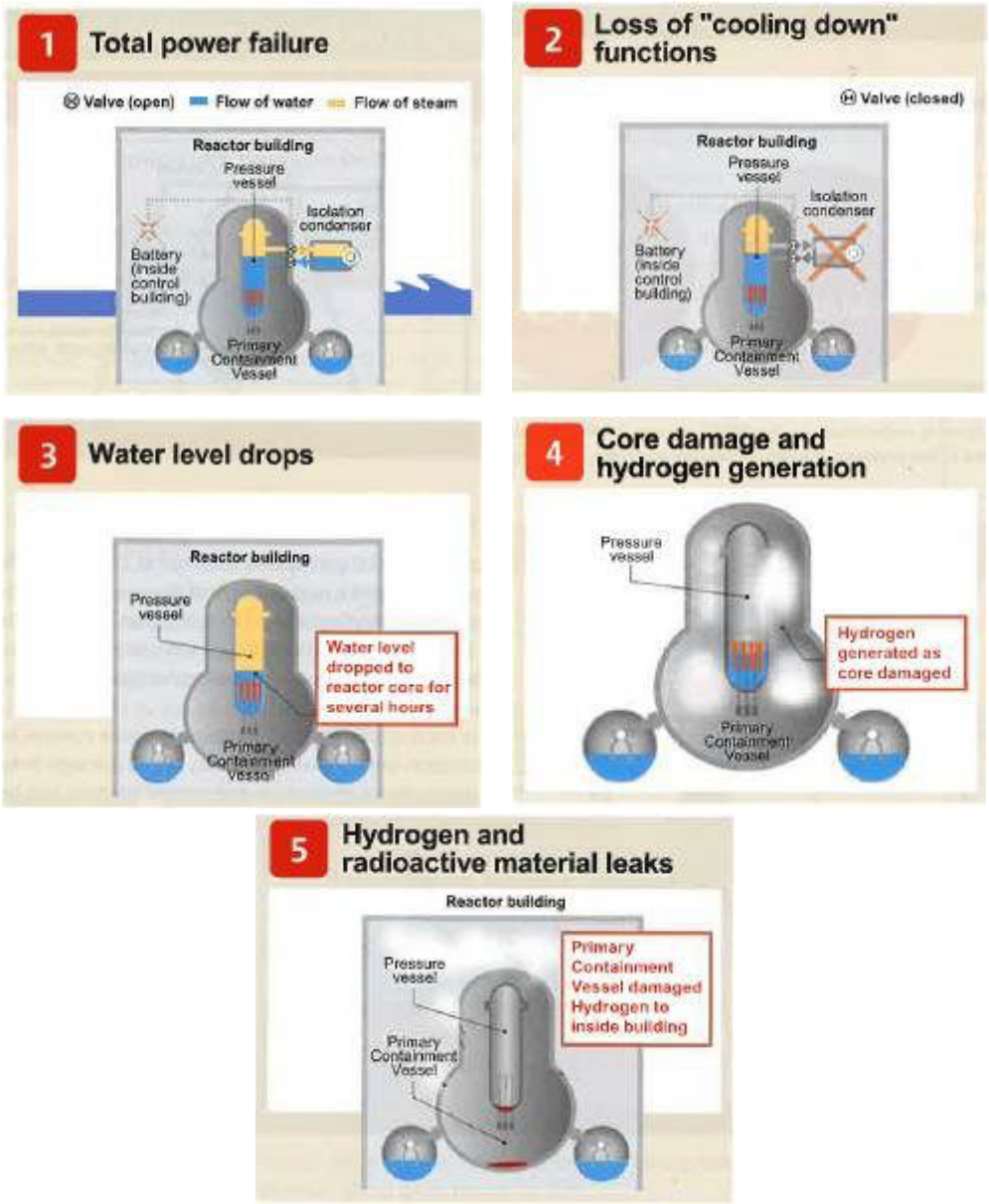

Figure 4: Outline of the accident evolution at Fukushima Daiichi units 1, 2 and 3 [5]. The reported sequence is simplified and considers only the main events that lead to the severe accident

1.1.3 Considerations on severe accidents - Defence in depth and EPR design

The Three Mile Island and the Chernobyl severe accidents stimulated the nuclear community and the nuclear security agencies reconsidering the approach for the design of new nuclear

reactors. The defence in depth philosophy is the result of a change in the nuclear installation design strategy. Defence in depth means preparing countermeasures corresponding to the various stages of an accident. In other words, if the first security action fails to stop the accident, a second action is put in place to prevent a further progression of the accident.

The design of the European Pressurised Reactor (EPR, 1600 MW_e) is based on the defence in depth concept. The corresponding French security requirement is that there must be *"no need for emergency evacuation outside the immediate vicinity of the plant, only limited sheltering, and no long-term restrictions in the consumption of food even in the case of a core melt accident"* [6].

In the EPR concept, all the critical load situations in the reactor containment must be either "practically eliminated", or avoided by specific design. In particular, these situations include:

- High pressure core melting
- Hydrogen detonation
- Steam explosion
- Penetration of the containment basement by the molten core.

The schematic representation of the EPR design is reported in Figure 5.

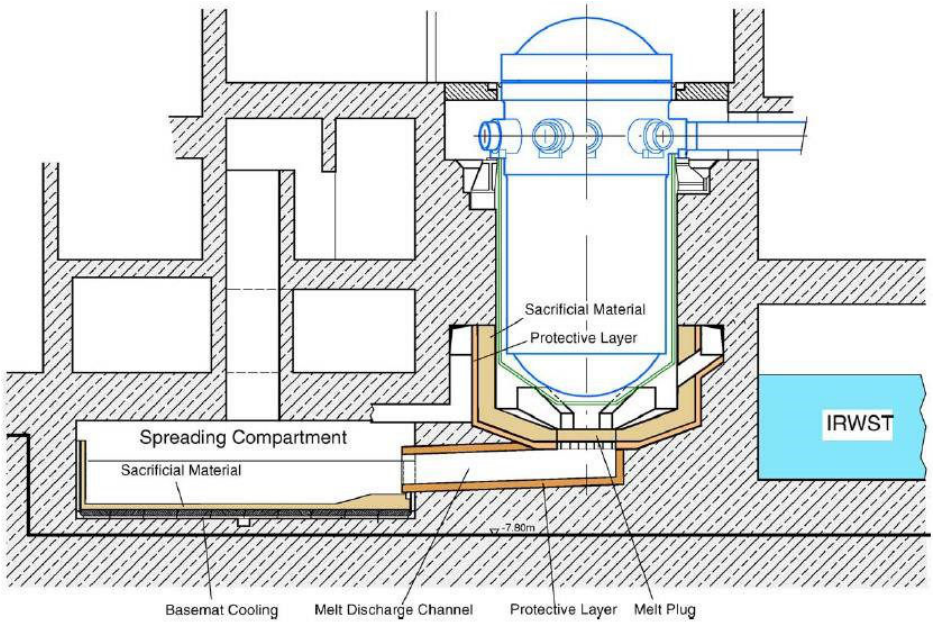

Figure 5: EPR design [6]. IRWST=Internal Refueling Water Storage Tank

The core catcher is placed in a lateral spreading compartment, therefore a physical and functional separation exist between the core catcher and the concrete reactor pit. The reactor pit consists of a 0.5 m thick layer of sacrificial concrete backed up by a cylindrical shielding consisting of refractory materials. This design allows a complete accumulation of the molten in-vessel corium before spreading.

1.2 PWR core degradation phenomena

As already seen in the previous sections, the loss of cooling of a PWR leads to core overheating due to the residual heat of decay. If this event is prolonged an accidental scenario occurs (Figure 6) [7].

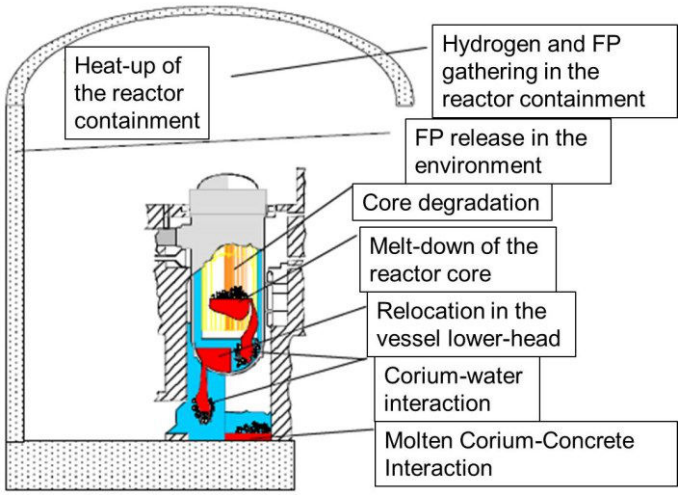

Figure 6: Scheme of the main events occurring during a severe accident [7]

1.2.1 In-vessel corium retention

The description of the progression of a severe accident is paramount to be able to mitigate its consequences and possibly to terminate it. In this framework, the physicochemical behaviour of the reactor core materials under accident condition is capital. During the severe accident progression, the temperature inside the reactor may reach extreme values (2700-3200 K): this temperature rise leads to complex interactions between the fuel, the cladding, the control rods, etc. Hofmann [8] reported a straightforward representation of the in-vessel core degradation phenomena with increasing temperature (Figure 7).

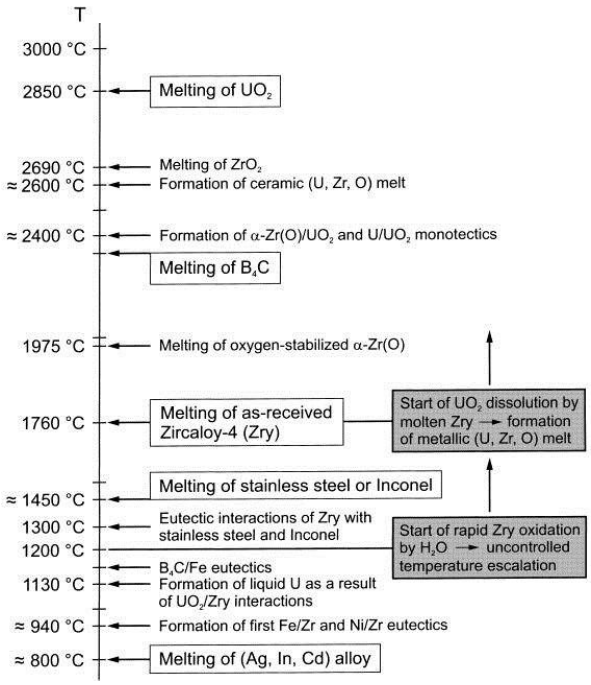

Figure 7: Melting and chemical interaction temperatures leading to liquid phases formation during a severe accident in a LWR [8]

A crucial point is shown in this clear-cut scheme: the nuclear fuel (as a first approximation one may assume a UO_2-fuel) can be already dissolved by molten Zircaloy at 1000 K below its melting point. In fact, the uncontrolled temperature rise of the Zircaloy cladding due to oxidation by H_2O leads first to the melting of the cladding and then to the dissolution of UO_2

leading to the formation of a (U,Zr,O) melt: then the relocation of the fuel may take place already below 2273 K.

Since the end of the 70's numerous studies have been performed on the chemical interaction between fuel and its cladding [9–13]. Several tests were performed between 1173 K and 1973 K. Hofmann and Politis [9] reported annealing test results showing the formation of different layers due to the direct UO_2-Zircaloy interaction. Figure 8 shows a diffusion couple profile obtained at 1673 K.

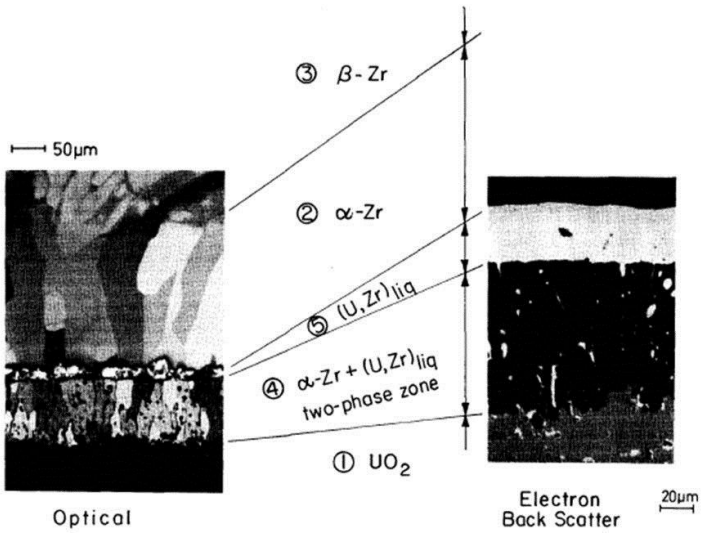

Figure 8: Sequence of layers obtained during diffusion couple test UO_2-Zircaloy under oxidising atmosphere (T=1673 K). It may be noted that a liquid phase is formed

During the UO_2-Zircaloy interaction, a progressive reduction of the fuel was observed, leading to the formation of oxidised form of zirconium, namely α-Zr(O) at the UO_2-Zircaloy interface and ZrO_2 at the Zircaloy-oxidising atmosphere interface. The formation of these phases leads to the embrittlement of the fuel cladding and to the loss of its mechanical stability. However, as long as the ZrO_2 layer remains intact, the relocation of the molten materials is prevented. If mitigation actions are not effective at this stage, the dissolution of ZrO_2 and UO_2 by molten Zircaloy may take place (M.S. Veshchunov, 1994) leading to the loss of the first radiological barrier.

Starting from 1473 K the Inconel spacer grid and the control rods stainless steel (ss-316 18 wt% Ni, 8 wt% Cr) cladding melt due to chemical interactions. Direct contact with Zircaloy may drive liquefaction well below this temperature [14]. During the interaction with the control rods, the absorbers (silver, cadmium and indium) may further lower the liquefaction temperature resulting in an even lower UO_2 dissolution temperature. In these conditions, the relocation of a metallic and a ceramic melts, the ***in-vessel corium***, in the lower-head of the reactor vessel happens as a direct consequence of these high temperature interactions. In the 3rd Generation LWR, the in-vessel retention is the chosen strategy: the reactor steel vessel is thus externally water-cooled to limit thermal creep.

Because of the existence of a miscibility gap in the liquid phase of the in-vessel corium system [15], inside the reactor a metallic and an oxidic melts stratify (Figure 9a). The density difference drives this phenomenon, leading the heavier oxidic melt to the bottom of the lower-head, and the metallic melt above the ceramic melt. Depending on the degree of oxidation of zirconium, the U/Zr ratio and on the amount of molten steel in the in-vessel corium, a heavy metal layer may relocate underneath the oxidic melt [15], as shown in Figure 9b.

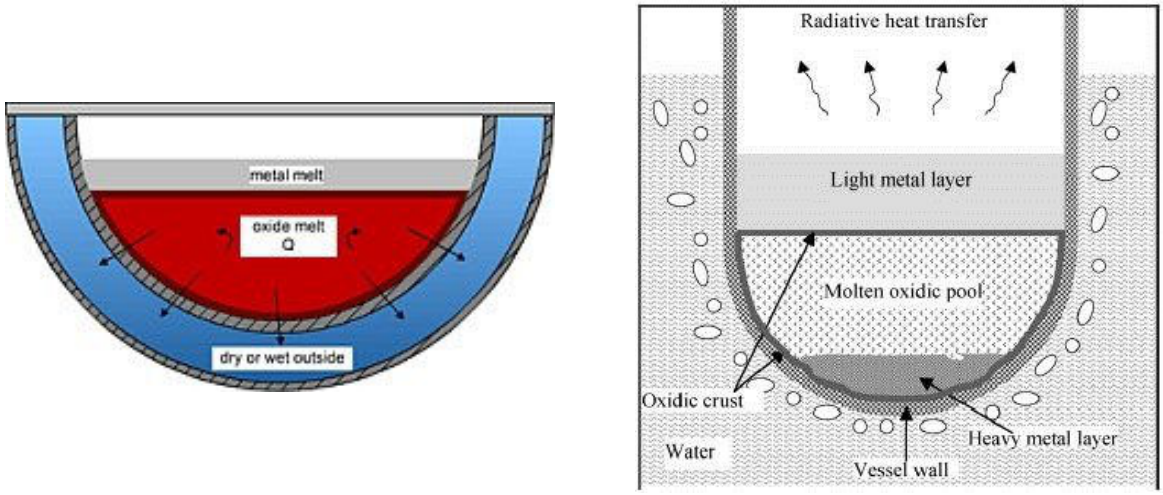

a) b)

Figure 9: Possible in-vessel corium configuration in the case of an in-vessel relocation strategy. a) oxidic melt underneath the metallic melt; b) heavy metal melt formation under the oxidic pool [15]

Since liquid metal has a low emissivity, the radiative heat transfer from the metal is limited. The main part of the heat release occurs at the molten metallic layer/steel vessel interface. If the thickness of the upper metallic layer is excessively reduced, the so-called ***focusing effect*** may take place. In this situation, the heat flux from the liquid metal to the steel vessel is important and it may lead to the vessel breach (if this heat flux is greater than the Critical Heat Flux, CHF=1.5 MWm^{-2} in the reported scenario). Seiler et al. considered the ***U-Zr-Fe-O*** system as a first approximation in-vessel corium. The authors showed that depending on the amount of dissolved iron an inversion of the melts density may be observed (Figure 10).

The intersection between the oxidic phase density and the metallic phase density in Figure 10 gives the maximum amount of steel (iron simulates steel behaviour) that stratify under the oxidic pool. For example, for an in-vessel corium with 30 % of oxidised zirconium (C30 in Figure 10), the metallic phase is heavier than the oxidic phase until 25 tons of dissolved iron. This means that a considerable amount of steel may stratify under the oxidic pool. It may be also noted that the density of the oxidic phase is practically not affected by the iron addition suggesting that the solubility of iron in the oxidic phase is limited.

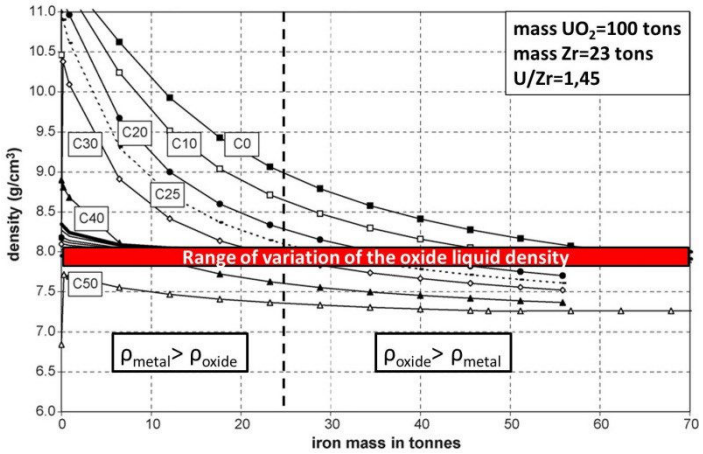

Figure 10: Evolution of the density of oxidic (red line) and metallic (black lines with different amount of initial oxidised zirconium) melts as a function of the amount of dissolved iron [15]

These calculations were performed by coupling thermochemical data with thermal and thermo-hydraulics data. **The uncertainties related to the chemical composition of the metallic and oxidic phases affect the density results and therefore affects also the**

maximum mass of steel that can stratify underneath the oxidic pool. The coupling with thermo-hydraulics allowed to determine the minimum amount of steel needed to maintain the heat flux under the CHF (in the reported scenario the calculated minimum mass of steel is 80 tons). A better thermodynamic description of the in-vessel corium system is thus needed in order to improve the simulation accuracy.

Once the second radiological barrier is lost, the relocated molten material can interact with the vessel containment structures: the ***ex-vessel stage*** of the severe accident starts. During the Three Mile Island accident the in-vessel retention worked, preventing the direct interaction between the molten corium and the concrete. On the other hand, during the Fukushima Daiichi accident the reactor vessel failed, leading the molten corium contacts the concrete.

1.2.2 Ex-vessel corium retention

The ex-vessel relocation of the molten core material is the last retention option for 2nd and 3rd Generation nuclear reactor before a significant release of radioactive materials in the environment. In the case of the EPR configuration, the in-vessel retention is only temporary. It was chosen instead ex-vessel retention in a dedicated lateral core catcher [6].

When the molten core pours on the containment concrete the so-called ***Molten Corium-Concrete Interaction (MCCI)*** will start. The molten corium at about 2673 K starts interacting with the concrete. At the beginning, the MCCI is controlled by the melt overheat that heats the concrete. CO_2 and steam are released and concrete starts to melt. The released gases may then move within the corium oxidising zirconium and steel. Afterwards the decay heat becomes the main source of heat. If the ex-vessel retention actions work, the radioactive materials stay inside the reactor containment, preventing a massive release in the environment. From the chemical point of view, all the components of the concrete (mainly CaO, SiO_2, Al_2O_3, MgO, H_2O, CO_2) are added to the already complex in-vessel system. The ***ex-vessel corium*** may then be defined as a metallic/oxidic mixture within the in-vessel corium+concrete system. As a first approximation the ***U-Zr-Fe-Ca-Si-O*** system can be considered as a representative ex-vessel corium.

High temperature concrete decomposition, gas bubbles agitation, formation of several phases, oxidation of metals, ablation process are only a part of the phenomena observed during MCCI. The whole comprehension of MCCI depends on a multitude of parameters: the design of the reactor containment and the mitigation actions applied during the severe accident may reduce the effect of an ex-vessel relocation of the molten core. In the same way, the knowledge of the physicochemical properties of in-vessel corium, concrete and ex-vessel corium can help the reactor designers to use the appropriate materials during the project realisation. In fact, **thermodynamic and thermochemical data are fundamental for severe accident codes** as TOLBIAC-ICB [16], ASTEC [17], MAAP [18] and MELCOR [19]. The coupling of thermodynamics with thermo-hydraulics based software, allows describing the thermo-physical properties of molten corium both during in-vessel and ex-vessel retention. The presence of a miscibility gap in the liquid phase of the corium system plays a crucial role for the simulation of the accidental scenario: thermo-hydraulics has to face two liquids (in addition to water) with different density and viscosity. Furthermore, the residual heat of decay that drives the accident progression is not homogeneously distributed within the oxide and the metallic liquids. The oxide liquid has a larger solubility for the fission products and the radioactive actinides. This fact has to be taken into account during a severe accident simulation and during the design of the reactor.

1.3 Concluding remarks

The comprehension of the phenomena occurring during a severe accident is paramount for the design of new reactors and to find more efficient mitigation actions. Since the beginning of the civil nuclear industry, several experimental programs have been performed to investigate all these phenomena. The physicochemical properties of the in-vessel materials were studied as well as the complex phenomena involved during MCCI.

The main objective of this thesis is contributing to the thermodynamic description of the physicochemical interactions occurring during a severe accident. As already introduced, the ***real corium system is extremely complex*** and difficult to describe because it includes a large number of chemical elements. In this framework a simplified version of the in-vessel and ex-vessel systems are considered. Since in some cases the UO_2-based fuel can be replaced by a $(Pu,U)O_2$-based fuel, the so-called MOx, the ***U-Pu-Zr-Fe-O*** system will be considered as the prototypic in-vessel corium, neglecting as a first approximation fission products and additional elements contained in the metallic structures inside the vessel (e.g., nickel, chromium, niobium …). Notwithstanding the high item importance of this system for the severe accident comprehension, a lack of data exists on its high temperature behaviour. In particular, the experimental needs on the sub-systems are:

- O-U-Zr: extension of the miscibility gap in the liquid phase and liquidus transition in the Zr-rich side of the ternary phase diagram
- O-Fe-Zr: lack of experimental data within the ternary phase diagram
- O-Fe-U: lack of experimental data within the ternary phase diagram
- Pu-containing systems: lack of experimental data mainly due to difficulties related to the handling Pu-containing samples

In this framework, during the present study new experimental results on the ***O-U-Zr, Fe-Zr-O, Pu-Zr-O, U-Zr-Fe-O*** and ***U-Pu-Zr-O*** systems were obtained. Those results have been used for the ***thermodynamic reassessment*** of the in-vessel corium prototype system using the CALPHAD method [20,21].

For the ex-vessel corium description, the concrete will be considered as an oxide mixture (without taking into account H_2O and CO_2 since these compounds have already been released due to high temperatures): the prototypic concrete will be simulated by the ***Al_2O_3-CaO-SiO_2*** system. Therefore, the final prototypic ex-vessel corium will be the ***U-Pu-Zr-Fe-Al-Ca-Si-O*** system.

In the second chapter, the critical review on the existing literature on prototypic in-vessel corium sub-systems is reported. The selection of significant experimental allows the re-assessment of the thermodynamic model of the in-vessel corium system. Furthermore, a selection of large scale experiment results will be given.

The third chapter reports the experimental investigation on interesting in-vessel corium sub-systems. This new set of data will be used for the thermodynamic modelling as well. The fourth chapter contains the thermodynamic modelling on the prototypic in-vessel corium. The reassessed model will be discussed in detail. The last part of the fourth chapter is dedicated to solidification path calculations to better interpret the current experimental results.
Chapter five represents an exploring approach to investigate two complex prototypic ex-vessel corium samples. Solidification path calculations will be used to test the validity of the current model coupled with the TAF-ID database.

In Chapter six, the novel experimental setup – ATTILHA – will be presented. The first results on well-known system as well as the future perspectives for this device will be discussed.

The general conclusions of this thesis, the impact of the present work and the perspectives for future investigations will be finally presented in the last Chapter.

1.4 References

[1] *Electricity Information*. Paris: OECD/IEA, 2014.

[2] *INES The International Nuclear and Radiological Event Scale User's Manual*. Vienna: OECD/NEA IAEA, 2008.

[3] J. R. Lamarsh and A. J. Baratta, Book, *Introduction to Nuclear Energy*. 2012.

[4] J. M. Broughton, P. Kuan, D. A. Petti, and E. L. Tolman, "A SCENARIO OF THE THREE MILE ISLAND UNIT 2 ACCIDENT," *Nucl. Saf.*, vol. 87, pp. 34–53, 1989.

[5] "The Development of and Lessons from the Fukushima Daiichi Nuclear Accident," TEPCO report 2013.

[6] M. Fischer, "The severe accident mitigation concept and the design measures for core melt retention of the European Pressurized Reactor (EPR)," *Nucl. Eng. Des.*, vol. 230, pp. 169–180, 2004.

[7] C. Journeau, "Contribution des Essais en Matériaux Prototypiques sur la Plate-Forme PLINIUS à l'Etude des Accidents Graves de Réacteurs Nucléaires," HDR Thesis, 2008.

[8] P. Hofmann, "Current knowledge on core degradation phenomena, a review," *J. Nucl. Mater.*, vol. 270, no. 1-2, pp. 194-211, 1999.

[9] P. Hofmann and C. Politis, "The kinetics of the uranium dioxide—Zircaloy reactions at high temperatures," *J. Nucl. Mater.*, vol. 83, no. 2-3, pp. 375-397, 1979.

[10] D. R. Olander, "The UO_2-Zircaloy chemical interaction," *J. Nucl. Mater.*, vol. 115, pp. 271–285, 1983.

[11] P. Hofmann and D. Kerwin-Peck, "UO_2/Zircaloy-4 chemical interactions from 1000 to 1700°C under isothermal and transient temperature conditions," *J. Nucl. Mater.*, vol. 124, pp. 80-105, 1984.

[12] W. Dienst and P. Hofmann, "Chemical Interations between UO_2 and Zircaloy-4 from 1000 to 2000 ^{o}C," *Nucl. Technol.*, vol. 65, pp. 109–124, 1984.

[13] P. Nikolopoulos, P. Hofmann, and D. Kerwin-Peck, "Determination of the interfacial energy and work of adhesion in the UO_2/Zircaloy-4 diffusion couple," *J. Nucl. Mater.*, vol. 124, pp. 106–113, 1984.

[14] P. Hofmann, S. Hagen, V. Noack, G. Schanz, and L. Sepold, "Chemical-physical behavior of light water reactor core components tested under severe accident conditions in the CORA facility," *Nucl. Technol.*, vol. 118, pp. 200–224, 1997.

[15] J. M. Seiler, B. Tourniaire, F. Defoort, and K. Froment, "Consequences of material effects on in-vessel retention," *Nucl. Eng. Des.*, vol. 237, pp. 1752–1758, 2007.

[16] B. Spindler, B. Tourniaire, and J. M. Seiler, “Simulation of MCCI with TOLBIAC-ICB code based on the phase segregation model,” *Nucl. Eng. Des.*, vol. 236, pp. 2264–2270, 2006.

[17] J. P. Van Dorsselaere, C. Seropian, P. Chatelard, F. Jacq, J. Fleurot, P. Giordano, N. Reinke, B. Schwinges, H. J. Allelein, and W. Luther, “THE ASTEC INTEGRAL CODE FOR SEVERE ACCIDENT SIMULATION.”

[18] “Modular Accident Analysis Program User’s Manual,” 1994.

[19] “MELTCOR Computer Code Manuals,” 1995.

[20] N. Saunders and A. Miodokwin, Book, *CALPHAD - Calculation of Phase Diagrams, A Comprehensive Guide*. 1998.

[21] H. Lukas, S. Fries, and B. Sundman, Book, *Computational Thermodynamics - The Calphad Method*. 2007.

Chapter 2 – Critical review of literature data

During the last six decades numerous research groups investigated the high temperature behaviour of the chemical systems involved during a severe accident in a PWR. Above 1300 K the interaction between the UO_2-based nuclear fuel and the Zircaloy cladding may lead to the formation of a liquid phase and to the loss of the first radioactive barrier. In this framework, the ternary O-U-Zr system has been studied with particular interest. The molten O-U-Zr mixture may then interact with the metallic structures inside the reactor (stainless steel coming from the control rods cladding and Inconel spacer grids) and finally with the reactor steel vessel, leading to the formation of the so-called ***in-vessel corium***. As a first approximation the U-Zr-Fe-O system may be considered as the simulant for the in-vessel corium behaviour. In order to deduce the thermodynamic properties of the U-Zr-Fe-O system, the three ternary subsystems may be considered. In this framework, the U-Fe-O and Zr-Fe-O systems are of significant interest. Plutonium may be added to the in-vessel corium composition if MOx fuels are considered leading to the more complex ***U-Pu-Zr-Fe-O*** system.

In the following a critical review of the thermodynamic and phase diagram data for the ternary O-U-Zr, U-Fe-O, O-Fe-Zr systems, and the quaternary U-Zr-Fe-O and U-Pu-Zr-O systems will be given. The data will be chronologically listed. This review allowed the **selection of the experimental data** that have been used during the reassessment of the thermodynamic model of the simplified in-vessel corium system (U-Pu-Zr-Fe-O).

In the case of reactor vessel mechanical failure, the molten in-vessel corium directly contacts the concrete of the reactor containment leading to the formation of the complex ***ex-vessel corium system***. The composition of the concrete used for the reactor containment is not a constant parameter; ideally for each nuclear power plant one should refer to the specific concrete composition. In order to simplify and generalise the study, the water and CO_2 contributions are neglected (at the severe accident temperature one may consider that water and CO_2 are not present anymore in the ex-vessel corium mixture). Considering only the main constituent of the concrete, the ***Al_2O_3-CaO-SiO_2*** can be taken as the representative system. In the present work, the will not be further investigated, considering satisfactory the thermodynamic model described in the TAF-ID thermodynamic database [1].

The second part of the chapter is dedicated to the accidental scenario phenomenology. The main phenomena occurring during the first in-vessel retention and then during the Molten Corium – Concrete Interaction (MCCI) are described and a selection of large scale experiments will be given. It might be noted that a limited number of data are available on the thermochemistry of the MCCI.

2.1 Thermodynamic and phase diagram data on in-vessel corium systems

In this section the existing literature on the systems investigated during this work will be presented. The thermodynamic and phase diagram data of the ternary O-U-Zr, U-Fe-O, O-Fe-Zr and Pu-Zr-O systems as well as of quaternary U-Zr-Fe-O and Pu-U-Zr-O systems are reported.

2.1.1 O-U-Zr system

Saller et al. performed the first investigation of the phase stability relations in the O-U-Zr system in 1955 [2]. The authors investigated 20 samples on the UO_2-Zr section by heat

treatments and proposed three tentative sections at 810 K, 977 K and 1373 K. Juenke & White (1970) [3] investigated the interaction between UO_2 based fuel and the Zircaloy cladding. The UO_2-Zr pseudo-binary system was studied above 1900 K. A thermal arrest technique was used to explore the UO_2 rich region of the phase diagram, whilst annealing and quench tests were performed to identify the phases present at equilibrium at a given temperature. The heating method was not specified.

In the UO_2 rich region the authors expected to find liquidus and solidus lines because of the similarities with the U-UO_2 monotectic system. The samples were prepared placing metallic Zr in UO_2 crucibles, weighing about 34 g, and sealed under vacuum in tungsten crucibles.

For the quench tests the samples were firstly heated for 1.5 hours in the temperature range 1920 K – 2700 K and then quenched and analysed using metallography and X-ray diffraction.

With the obtained experimental points they established the high temperature region of the UO_2-rich zone (see Figure 1).

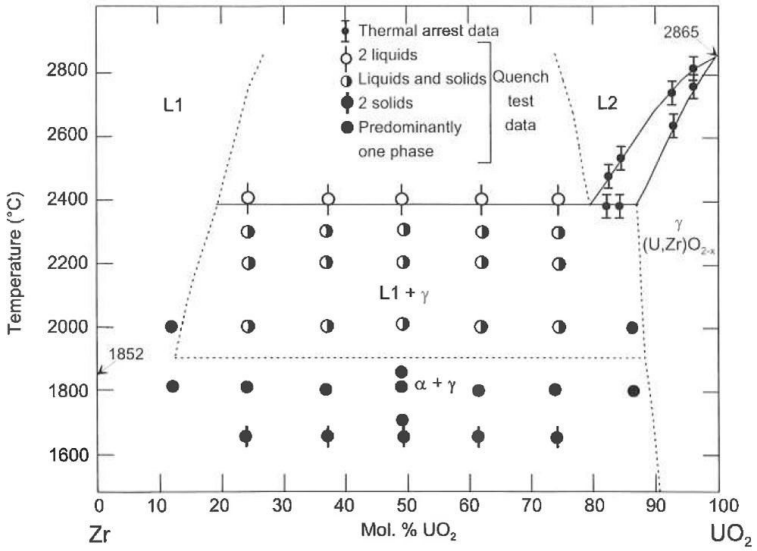

Figure 1: Tentative Zr-UO_2 phase diagram reported by Juenke & White [3]

Figure 1 shows the experimental results obtained by Juenke & White. Above 2673 K, the authors found a miscibility gap in the liquid phase: a metallic liquid L1 and an oxide liquid L2 were observed. The composition of the two liquids in equilibrium was not reported. The authors proposed a tentative phase diagram based on their results. The existence of a monotectic reaction at about 2673 K was argued on the basis of the similarities between the Zr-UO_2 system and the U-UO_2 system. However, from a thermodynamic point of view, the Zr-UO_2 system given in Figure 1 cannot be treated as a pseudo-binary system as it was interpreted by Juenke & White. This is due to the fact that this system contains a ternary monotectic reaction and thus the tie-lines correspond to the three-phase equilibrium [L1+L2+$(U,Zr)O_{2-x}$] from a triangle in the ternary O-U-Zr system. In fact, the degree of freedom (v) of this ternary monotectic reaction is equal to 1. Using the Gibbs' phase rule [4] the degree of freedom ν of a system, i.e., the number of independent variables necessary to fully define the state of the system, is given by:

$$\nu = C + 1 - \phi$$

where C is the number of components (C=3 in a ternary system), ϕ the number of phase in equilibrium (ϕ=3 for a monotectic reaction). Considering the pressure as a fixed intensive variable, in the present case one obtains:

$\nu = 3 + 1 - 3 = 1$.

Therefore, the temperature can vary across a ternary monotectic reaction. The experimental data obtained by Juenke & White can be considered reliable but are lacking of experimental details. **The reported results are selected for the thermodynamic modelling**.

Politis (1976) [5] investigated the UO_2-ZrO_2-U-Zr sub-system of the O-U-Zr system. The author performed heat treatments at 1273 K, 1773 K and 2273 K and metallographic analyses. He also studied the $ZrO_{0.51}$-UO_2 section by optical pyrometry. The author confirmed the presence of a miscibility gap in the liquid phase within the O-U-Zr ternary system above 2673 K (Figure 2b). The temperature of the eutectic reaction $[ZrO_{0.51}+(U,Zr)O_{2-x}] \rightarrow$ L was measured equal to 2073±20 K at 5 mol% UO_2. An inconsistency exists between the reported ternary isothermal section at 2273 K and the $ZrO_{0.51}$-UO_2 section (see Figures 2a and 2b): the liquidus line in the ternary section crosses the $ZrO_{0.51}$-UO_2 section at 14 mol% UO_2 whilst in the isopleth it is reported a value of 8 mol% UO_2. Furthermore, Politis did not reported the domain of existence of α-Zr(O) in the isothermal ternary diagram at 2273 K.

Note also that agreementing to Politis, the liquidus line in the isothermal ternary section at 2273 K crosses the Zr-UO_2 section at about 55 mol% UO_2 whilst in the Zr-UO_2 isopleth section given by Juenke & White, the UO_2-content of the liquidus line at the same temperature is situated at 15 mol% UO_2.

Skokan (1984) [6] investigated the inconsistency of Politis' work concerning the position of the liquidus line as well as the eutectic temperature. The author performed high temperature thermal analysis (DTA) and pyrometric measurement to investigate the liquidus curves between 1773 K and 2273 K. The samples were prepared starting from a mixture of UO_2, ZrO_2 and Zr powders. The post-experiment analyses were performed by means of X-ray diffraction and metallography.

First the author fixed the value of the oxygen concentration of α-Zr(O) at 30 at% ~ $ZrO_{0.43}$ (Politis reported 34 at% O ~ $ZrO_{0.51}$).

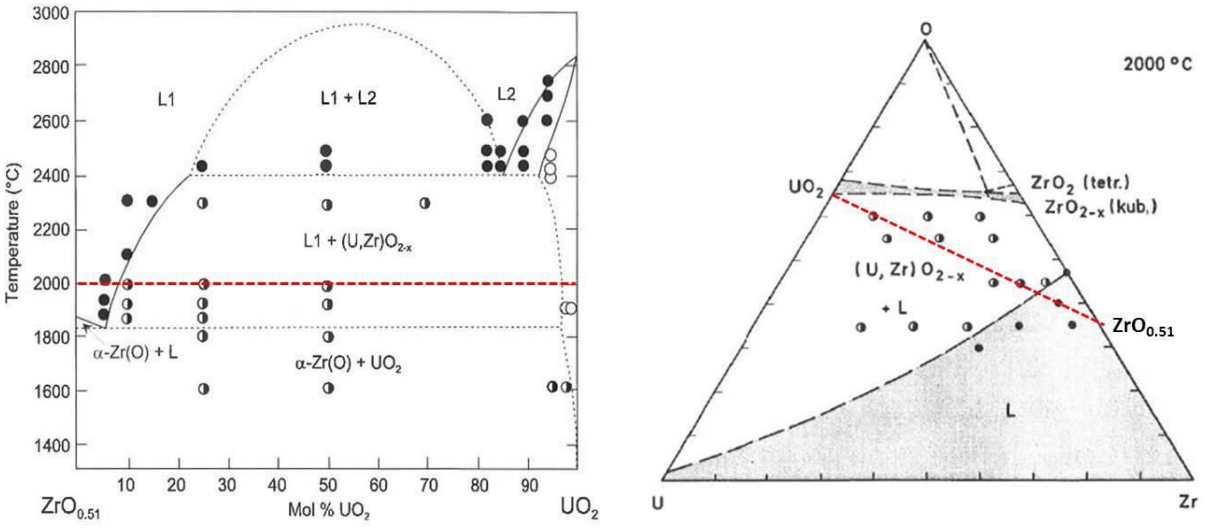

a) b)

Figure 2: Results reported by Politis [5]. a) $ZrO_{0.51}$-UO_2 section. b) Isothermal ternary section at 2273 K. ● = liquid; ○ = solid; ◑ solid+liquid

The measured eutectic temperature (2173 K) is 60 K higher than previous works [5]. The eutectic composition in the α-Zr(O)-UO_2 section lies at 15 mol% UO_2.

The maximum solubility of UO_2 across the α-Zr(O)-UO_2 section at 2273 K is 16 mol% UO_2, in agreement with Juenke & White. This value corroborates the results on the isothermal section reported by Politis, confirming the error in the isopleth section. Politis [5] and Skokan [6] reported an isothermal monotectic reaction lying in the $ZrO_{0.51}$-UO_2 section. As already pointed out for Juenke & White's work [3], the use of the term isothermal monotectic passing through a ternary system is not thermodynamically correct.

Yamanaka et al. investigated the isothermal section at 1773 K by heat treatment. The samples were then analysed by X-ray diffraction, metallography examination and scanning electron microscopy.

In a series of publications, Hayward & George (1994-1996) [7–10] studied the interaction between UO_2 and Zircaloy from 2273 K to 2773 K. In particular they focused their interest on the study of the solubility of unirradiated UO_2 in initially O-free Zircaloy and in Zircaloy with an initial 25 at% O content. A powder of Zircaloy was firstly placed inside a UO_2 crucible. Thus, the whole system underwent the scheduled heat treatment.The authors pointed out that the solubility of UO_2 in the liquid phase increases with temperature and decreases with the initial amount of oxygen in the Zircaloy cladding. Furthermore they observed the progressive shrinking of the two phase [$(U,Zr)O_2$+L] region in the ternary O-U-Zr system as soon as the temperature raises.

It may be noted in Figure 3 that **the authors did not find any miscibility gap in the liquid state** in disagreement with Politis [5] and Juenke & White [3].

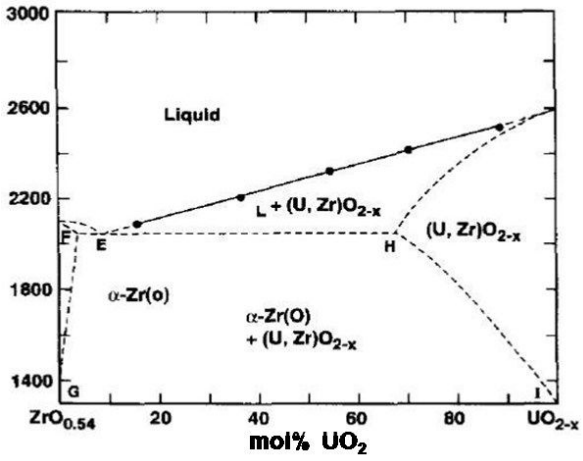

Figure 3: $ZrO_{0.54}$-UO_2 section reported by Hayward and George [9]

Note however that the isopleth section investigated by the authors is at the limit of the domain of existence of the miscibility gap: a slight change in the sample composition during the experiment (e.g., due to the vaporisation of UO that shifts the global composition of the sample towards the Zr-O side of the ternary diagram) could easily lead to a composition outside the immiscibility region. **None of the experimental results of Hayward & George will be considered for the thermodynamic modelling**.

One of the main objectives of the PhD thesis of Maurizi (1998) [11] was the determination of the liquidus line within the O-U-Zr system at 2273 K. For a ratio U/Zr=1.35, the author obtained an oxygen solubility in the ternary (U,Zr,O) liquid of 7±1 at% O, as reported in Figure 4.

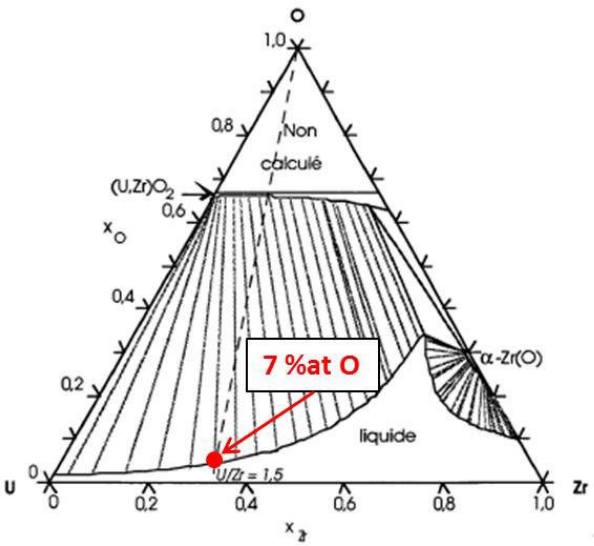

Figure 4: O-U-Zr isothermal section calculated at 2273 K [11]

The experimental result obtained at 2273 K allowed reassessing the liquidus line shape: the resulting oxygen solubility in the liquid phase is lower compared with the previous works of Politis [5] and Skokan [6]. The solubility data obtained by Maurizi **is retained for the thermodynamic reassessment**.

In the same period Guéneau et al. (1998) [12] obtained new experimental data on the miscibility gap in the liquid phase in the ternary O-U-Zr and in the binary U-UO_2 system. Recalling what previously showed by Juenke & White [3] and Politis [5], a wide miscibility gap in the liquid state exists in the ternary O-U-Zr system.

The authors used an electron bombardment system in order to melt and quench different samples. In particular, for the investigation of the O-U-Zr system they used two ternary alloys:

- (UO_2+Zr) mixture
- (U+ZrO_2) mixture

Concerning the binary U-UO_2 system, the investigations were conducted by placing a UO_2 pellet under an ingot of pure natural uranium. The post-melting analysis of the U-UO_2 sample showed a microstructure typical of two immiscible liquids. In Figure 5 the authors identified quenched droplets of oxide liquid L2 within a solidified U-rich metallic liquid L1.

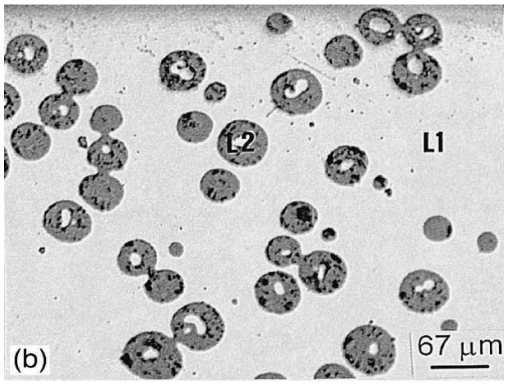

Figure 5: Back scattered electrons image showing the microstructure of the U-UO_2 quenched sample from T=3100 K. It may be noted the presence of quenched droplets of liquid L2 (oxidic) within the solidified liquid L1 (metallic) [12]

The post-melting analyses performed on the quenched U-ZrO_2 sample also revealed the presence of a miscibility gap in the ternary liquid.

Figure 6 reports a BSE image of the quenched U-ZrO_2 sample. A droplet of solidified oxide liquid is surrounded by quenched metallic liquid.

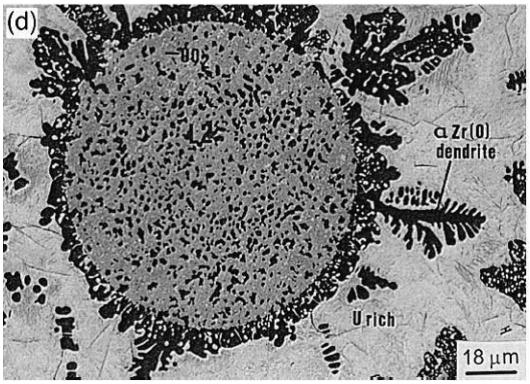

Figure 6: Backscattering electrons image of the U-ZrO_2 sample after quenching [12]

The authors employed their experimental results and other significant literature data [3] to redefine the thermodynamic description of the ternary O-U-Zr system. The interaction parameters are not reported in the paper. It may be pointed out that Guéneau et al. are the only authors reporting a tie-line for the miscibility gap in the ternary liquid phase. Even if affected by a significant uncertainty due to the high temperature reached during the experiment and the control of the cooling rate, this result is paramount because it allows a better shape of the immiscible region. **For this reason these tie-line data will be used for the thermodynamic assessment of the O-U-Zr system.**

Bakardjieva et al. (2008) [13] summarised the experimental and modelling results obtained on the system corium/concrete. Of particular interest are the results on the pseudo-binary Zr-UO_2 system. Using the laser heating technique [14], specimens in the UO_2-rich region were studied. The specimens were prepared pressing into pellets and sintering under inert atmosphere at 1973 K a mixture of UO_2 and ZrO_2 (or Zr) powders. The results confirm the presence of a miscibility gap in the liquid phase in the Zr-UO_2 section. Furthermore, the liquidus/solidus results obtained for the same section were in good agreement with the results of Juenke & White [3].

In the framework of the CORPHAD project (Phase Diagrams for Multicomponent Systems Containing Corium and Products of its Interaction with NPP Materials), the aim of which is the study of the major binary, ternary and quaternary systems involved during a severe accident, some experimental results were obtained on the O-U-Zr system. In the MASCA (**MA**terial **SCA**ling) project tests [15], two immiscible liquids (one oxidic the other metallic) were observed studying the O-U-Zr system. The experimental results compared with calculation performed with GEMINI-2 software and NUCLEA database are shown in Table 1. It can be noted from Table 1 that a significant discrepancy exists between experimental data and calculations results on the oxygen and zirconium contents in the metallic liquid. The experimental miscibility gap appears to be significantly smaller than the calculated one. The calculations are based on the results of Guéneau et al. [12].

Composition, atomic fraction/ temperature, K	Composition of metallic liquid, at%						Composition of oxidic liquid, at%					
	Experiment			Calculation			Experiment			Calculation		
	U	Zr	O	U	Zr	O	U	Zr	O	U	Zr	O
$U_{0.325}Zr_{0.292}O_{0.383}$/ 2643	40.8	32.2	27.0	44.0	41.5	14.5	25.1	26.7	48.2	24.8	21.1	54.1
$U_{0.405}Zr_{0.270}O_{0.325}$/ 2753	53.1	29.3	17.6	49.8	36.8	13.4	27.6	23.2	49.2	30.3	16.2	53.5

Table 1: Comparison between experimental data and calculations (GEMINI2 + NUCLEA database) of coexisting liquids in the O-U-Zr ternary system [15]

These measured tie-lines compositions will not be used for the thermodynamic modelling; the authors argued that segregation phenomena occurred during the experiment, leading to the shift of the tie lines. A more detailed discussion on these experimental results will be given in Chapter 3.

Table 2 reports the O-U-Zr phase diagram data selected for the thermodynamic modelling. These data are used to reassess the ternary interaction parameters of the O-U-Zr system.

Authors	Type of data	T (K)	Comments
Juenke & White [3]	Phases equilibria Liquidus/solidus across the Zr-UO_2 section	2073-2673 K 2673-3140 K	 UO_2 side
Politis [5]	Phases equilibria	2000-3100 K	
Maurizi [11]	Solubility of oxygen in ternary (U,Zr,O) liquid	2273 K	U/Zr=1.35
Guéneau et al. [12]	Miscibility gap tie-line	3223 K	

Table 2: Phase diagram data retained for the thermodynamic modelling

It must be pointed out that most of the experimental data obtained within the O-U-Zr system concern the region close to the Zr-UO_2 section between 2000 and 2600 K due to the interest of the Zircaloy cladding-UO_2 fuel interaction during a severe accident. However, in order to have a straightforward description of the O-U-Zr thermodynamics, **new experimental data are needed, especially to better describe the shape of the miscibility gap in the liquid phase and the liquidus line in the oxygen-poor side of the ternary phase diagram**.

2.1.2 UO_2-ZrO_2 system

During the normal functioning of a PWR, inside the vessel, an oxidising environment is present. In the case of a severe accident it is thus frequently imposed that the corium pouring on the concrete underneath the damaged steel vessel should be completely oxidised. In this framework, the pseudo-binary UO_2-ZrO_2 system at high temperature is paramount. Several studies were performed on this system since the 1950's, showing rather important experimental constraints related to the control of the oxygen level during the tests.

Lambertson & Müller (1953) [16] heat-treated and quenched UO_2-ZrO_2 samples to determine the post-melting compositions by chemical analysis and XRD. The samples were firstly sintered at 1973 K under pure H_2. The experimental temperature was controlled by using thermocouples and optical pyrometers. The authors investigated the liquidus/solidus transitions. They reported a minimum in the liquidus/solidus lines at 2823 K at a composition of about 52.5 mol% ZrO_2. Since the reported liquidus temperatures are close to 2900 K, it can be concluded that the chemical homogenisation of the samples is achieved. **The liquidus data of Lambertson & Müller are selected for the thermodynamic modelling.**

Voronov et al. (1958) [17] fabricated UO_2-ZrO_2 samples starting from UO_2 and ZrO_2 powders. The powders were mixed in different compositions, pressed and sintered at 2573 K for 2 hours. After a heat treatment in a W-resistance oven under argon at different temperatures between 1679 K and 1950 K, the samples were quenched in water. **The retained solubility data obtained via XRD and dilatometry are reported in Table 3.**

T / K	1823	1921	1947	1947	1950	1843	1817	1679
x(ZrO_2) molar fraction	0.201	0.301	0.402	0.501	0.597	0.798	0.848	0.848

Table 3: Solubility data of tetragonal ZrO_2 in cubic UO_2 [17]

Cohen & Shaner (1963) [18] mixed pure oxide powders in order to obtain the desired compositions set. The dry powders were blended, compacted and calcinated at 1998 K in H_2 to form UO_2-ZrO_2 solid solution. In order to ensure the homogeneity of the samples, the briquettes were crushed and re-pressed into disks and finally sintered for 72-110 hours at 1998-2048 K. Afterwards, the samples were annealed above 1473 K and quenched at a rate of 300 K/s. Above 2173 K, the annealing was performed in an induction furnace with a cooling rate of 700 K/s; optical pyrometers were used for the temperature detection. The quenched samples were finally analysed by X-ray diffraction and metallographic technique. The authors confirmed the existence, through the entire UO_2-ZrO_2 phase diagram, of a continuous solid solution between 2573 K and 2823 K, with a face-centred-cubic crystal structure. A two phase region was detected in the ZrO_2-rich part of the phase diagram. The two phases in equilibrium were found to be face centred cubic (fcc) and face centred tetragonal and extent between 1933 K and 2573 K. The composition limits of this two-phase region at 1973 K are respectively 50 mol% UO_2 and 19 mol% UO_2. The reported UO_2-ZrO_2 phase diagram is shown in Figure 7.

The lower temperature measurements (1473 and 1673 K) show a large ZrO_2 solubility in cubic UO_2 and a large UO_2 solubility in tetragonal ZrO_2. Note that, since the low kinetics of the solid-solid reaction at low temperature, solubility limits measurements are challenging. Romberger et al. (1967) [20] measured the solubility limits from 873 K to 1403 K in the UO_2-ZrO_2 pseudo binary system. The authors mixed hyper-stoichiometric $UO_{2.012}$ with ZrO_2 to obtain three solid solutions respectively containing 19, 50 and 80 mol%UO_2. Afterwards the solvent LiF(66)-BeF_2(34) was added. After a heat treatment, the residual fluoride LiF-LiF_2 phases was removed by dissolution in an aqueous 0.02 M Na_2EDTA solution. **This technique allows an excellent homogenisation of the samples even at relativly low temperatures (T<1673 K)** [21]. **For this reason the low temperature solubility data of Romberger et al. are retained** for the thermodynamic modelling. **Due to kinetic limitations, the low temperature experimental data of Cohen & Shaner** [18]**, are discarded** but **their data obtained above 1673 K are retained**. The post-experiment analysis of Romberger et al. was performed by chemical analysis, X-ray diffraction and ceramographic investigation.

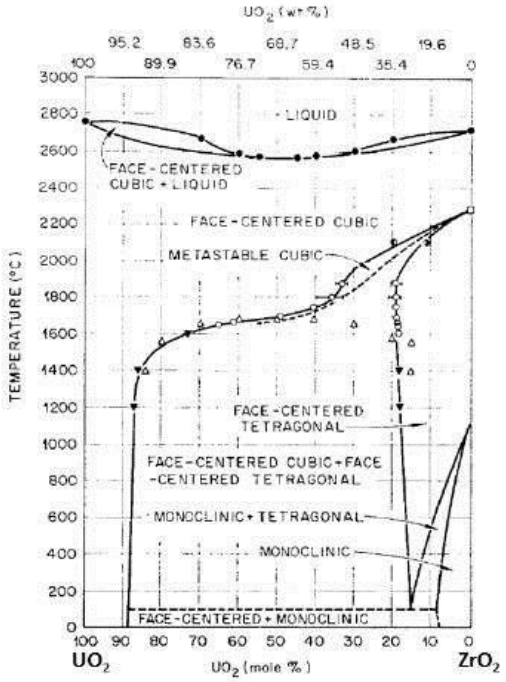

Figure 7: Tentative UO_2-ZrO_2 phase diagram reported by Cohen & Shaner [18]. The liquidus and solidus data are taken from [19], whilst the black and white triangles from [17]

The solubility of monoclinic ZrO_2 in cubic UO_2 was found to be approximately 0.35±0.15 mol% ZrO_2 between 873 K and 1404 K (significantly lower than values obtained by Cohen & Shaner [18]), whereas the solubility of UO_2 in monoclinic ZrO_2 was reported equal to 0.07 mol% UO_2 at 873 K and 0.2 mol% UO_2 at 1383±5 K.

Une & Oguma (1983) [22] measured the oxygen potential of the $U_{1-y}Zr_yO_{2+x}$ ($0.02<y<0.20$) solid solutions at 1773 K using equilibrium with $CO/CO_2/O_2$ mixtures. The $U_{1-y}Zr_yO_{2+x}$ samples were used for a thermogravimetric measurement for the oxygen potential determination coupled with XRD. Different levels of oxygen potential were imposed during the experiments by varying the CO/CO_2 ratio. The authors observed a linear decrease in the lattice parameter up to y=0.15 after 4 hours at 1773 K. This value is slightly lower than the value reported by Cohen & Shaner (y=0.18 at 1773 K).

Paschoal et al. (1987) [23] performed heat treatment at 1973 K for 100 hours in an Ar-8% H_2 atmosphere (oxygen partial pressure $<10^{-2}$ Pa). The maximum solubility of cubic UO_2 in tetragonal ZrO_2 at 1973 K was found to be 21 mol% UO_2, whereas the maximum solubility of ZrO_2 in UO_2 at the same temperature was 49 mol% UO_2. These values are in good agreement with those reported by Cohen & Shaner (see Figure 7) and **are retained for the thermodynamic modelling**.

The retained phase diagram data for the UO_2-ZrO_2 system are reported in Table 4.

Authors	Type of data	Experimental range
Lambertson [16]	Liquidus	0-100 mol% ZrO_2
Voronov et al. [17]	Solubility of UO_2 in ZrO_2	1679-1950 K
Cohen & Shaner [18]	Solubility of UO_2 in ZrO_2 and vice versa	1873-2549 K
Une & Oguma [22]	Solubility of ZrO_2 in UO_2	1773 K
Romberger et al. [20]	Low temperature solubility	873-1443 K
Paschoal et al. [23]	Solubility	1973 K

Table 4: Experimental data retained for the thermodynamic modelling of the UO_2-ZrO_2 pseudo-binary system

More recent studies focused on the measurement of the activities of UO_2 and ZrO_2 in gas mixtures in equilibrium with different solid UO_2-ZrO_2 mixtures and at different temperatures. Stolyarova et al. [24] used the Knudsen effusion high-temperature mass spectrometric method to study thermodynamic properties of the UO_2-ZrO_2 system between 2200 K and 2650 K. The samples were obtained by sintering and annealing UO_2 and ZrO_2 powders. The samples were finally crushed before experiments. The initial composition of the samples was confirmed using X-ray diffraction and spectro-chemical analysis. The activity of UO_2 and ZrO_2 were calculated comparing the corresponding partial pressures over the UO_2-ZrO_2 solid solution and over the pure oxides.

As the temperature increases from 2203 K to 2598 K the deviation from the ideal solution behaviour decreases as it may be seen in Figure 8.

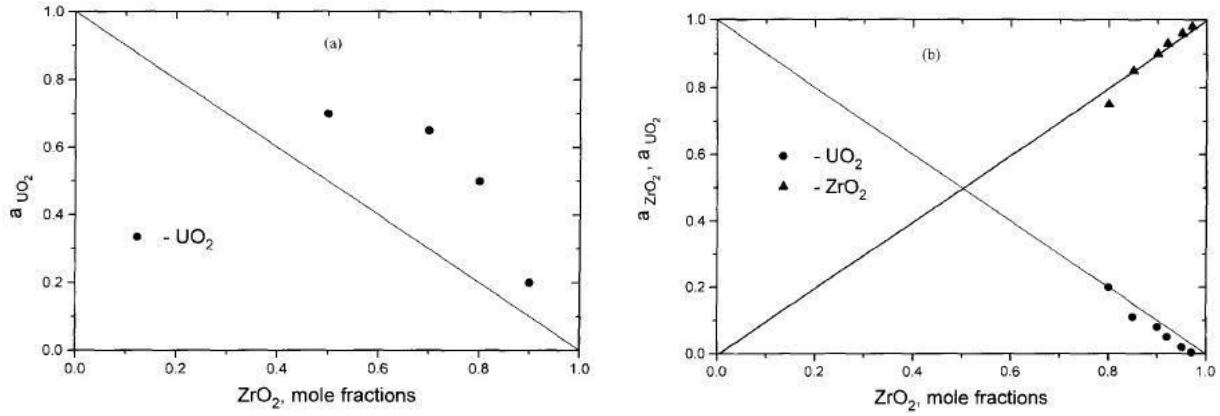

Figure 8: UO_2 (black circles) and ZrO_2 (black triangles) activities in the UO_2-ZrO_2 solid solution at a) 2203 K and b) 2598 K [24]

Baichi et al. [21] used a multiple Knudsen cell-mass spectrometric method to investigate the thermodynamic activity of UO_2 in the UO_2-ZrO_2 pseudo binary system. For this purpose the partial pressure of gaseous UO_2 in the range of 2000-2400 K was measured. The samples were prepared starting from the pure oxide powders. The mixture was then compacted and sintered at 1973 K for 96 hours in dry hydrogen.

A positive deviation from the ideality was observed at 2205 K (Figure 9a) as already observed in [24] (Figure 8). The UO_2-ZrO_2 solid solution becomes almost an ideal solution at 2498 K (Figure 9b).

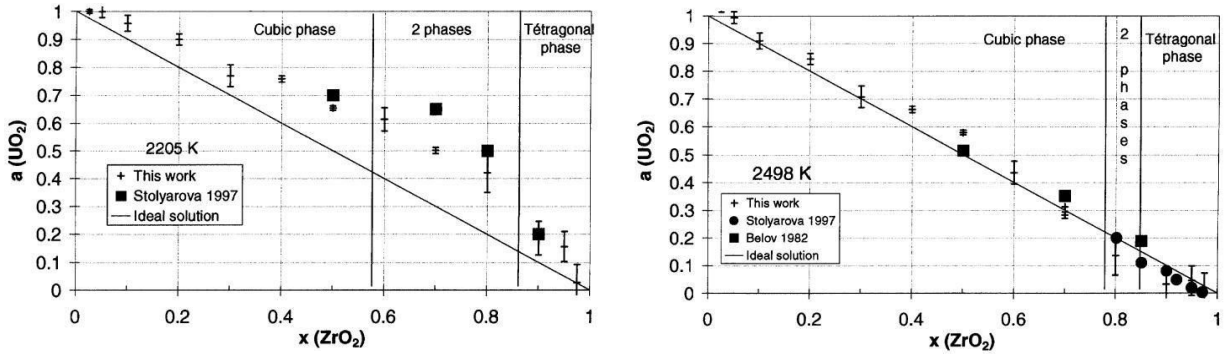

a) b)

Figure 9: Activity of UO_2 as a function of the molar fraction of ZrO_2 at (a) 2205 K and (b) 2498 K reported in [25]

The UO_2 activity data obtained by Baichi et al. are retained for the thermodynamic modelling of the UO_2-ZrO_2 system.

2.1.3 O-Fe-U system

The O-Fe-U system is of particular interest in the framework of severe accident studies. The molten mixture fuel+Zircaloy may interact with the surrounding metallic structure, leading to the formation of the in-vessel corium. The experimental investigation of this system is rather challenging. Both iron and uranium have multiple oxidation states depending on temperature, oxygen partial pressure and total pressure during the experiments. In addition, the vaporisation of iron makes more problematic the investigation of the aforementioned ternary system. The control of the composition of the samples under investigation is thus complicated. Therefore, an undoubted lack of experimental data exists for the present system. It may be noted that most of the reported experimental data concern the oxide region of the O-Fe-U ternary phase diagram: **the metallic side of the diagram is, as a matter of fact, experimentally unknown**.

Hofmann et al. [26] studied the U-Fe-O ternary interactions at 1273, 1773 and 2273 K in the framework of severe accident researches. Since UO_2 is the more stable oxide, it is in equilibrium with pure iron, iron oxides and metallic liquid. At 2273 K UO_2 is the only solid phase in the ternary phase diagram. Labroche [27] performed an experimental study at 1300 K in the U-Fe-O ternary system. The author identified the ternary $UFeO_4$ compound at 1300 K. A non-negligible solubility of iron has been observed in UO_{2+x}.

Evans and White (1964) [28] performed isobaric experiments on samples lying within the ternary diagram between 1573 and 1773 K. During the experiment, the samples were heated under different oxygen partial pressures (0.0088-0.21 atm) and the mass variation was measured by thermogravimetry. The authors highlighted the difficulties related to the numerous oxidation states of both uranium and iron. The variation of the oxygen partial pressure causes changes in the nature of both uranium and iron oxides. At atmospheric pressure (i.e., $p(O_2)$=0.21 atm) an eutectic transition Liq. → $[U_3O_{8(s.s.)}+Fe_2O_3]$ was observed at 1621 K at a composition of 66.4 mol% U_3O_8. At lower oxygen partial pressure ($p(O_2)$=0.070 atm) another transition was observed at 1633 K, that may be the transition Fe_2O_3→Fe_3O_4. At a $p(O_2)$=0.0058 atm the eutectic transition Liq. → $[UO_{2(s.s)}+Fe_3O_4]$ took place at 1623 K. Two ternary eutectic points were also observed in this system (Table 5).

Eutectic	Composition			Reaction	$p(O_2)$ / atm	Temperature / K
	at% U	at% Fe	at% O			
E1	14.65	20.75	64.6	L⇔U_3O_8+UO_2+Fe_3O_4	0.011	1599
E2	13.5	21.8	64.7	L⇔U_3O_8+Fe_2O_3+Fe_3O_4	0.028	1591

Table 5: Ternary eutectics measured by Evans and White [28]

Riley (1969) [29] investigated the UO_2-Fe_2O_3 system. The two end members show variations in composition with temperature and oxygen partial pressure. In air a eutectic transition was observed at 1533±10 K with a liquid composition of 70 wt% UO_{2+x}. If the oxygen potential was reduced enough for the formation of the U_4O_9 cubic phase, a miscibility gap in the liquid phase was observed. This paper lacks in experimental details and post-experiment analyses: **for this reason these experimental results will be not taken into account during the thermodynamic modelling**.

More recently Betcha et al. (2007) [30] performed a study on the oxide UO_2-FeO_{1+x} subsystem. Samples with a UO_2 concentration ranging from 3.9 to 67.5 mol% were used. The other end member of the investigated section was reported to be a non-stoichiometric FeO, with a composition $FeO_{1.062}$. The microstructure of the specimens was determined by SEM

and Energy Dispersive X-ray Spectral MicroAnalysis (EDXSMA). The phase transformations were observed using DTA, whereas the melting and crystallization were studied by DTA, Visual Polythermal Analysis (VPA) and Galakhov microfurnace, which allow a direct detection of a solid/liquid transition. The results obtained by the authors are shown in Figure 10.

As already pointed out, the control of the oxidation states of UO_2 and FeO_x is challenging. The authors argued their experimental data were obtained across the UO_2-$FeO_{1.062}$ section. **Even if a rather large uncertainty exists in the stoichiometry of FeO_{1+x}, it may be estimated lying between x=0 and x=0.1**. In another investigation on the UO_2-FeO_{1+x} system, the same research group [31] performed experiments with a FeO_{1+x} for which the closest composition to the stoichiometry (Fe_1O_1) was $FeO_{1.057}$. The authors reported a eutectic temperature of 1608±5 K at 4.0±0.1 mol% UO_2. The maximum solubility of FeO in UO_2 at the eutectic temperature was evaluated as 17.0±1.0 mol% UO_2.

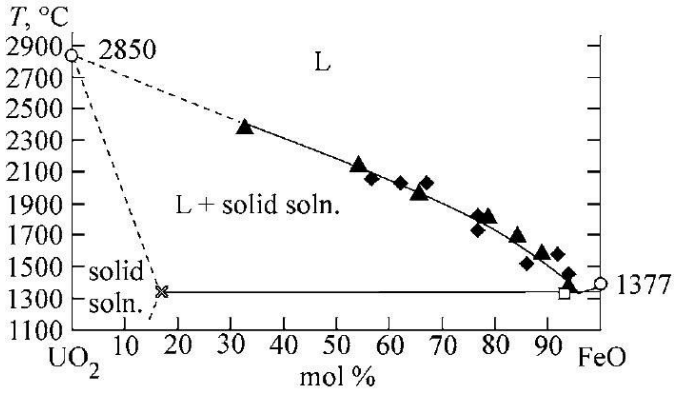

Figure 10: Tentative UO_2-FeO phase diagram. Triangles are data from VPA IMCC, rhombuses are data obtained by using the Galakhov microfurnace, squares are DTA data and crosses are results of IMCC/XMSA [30]

Petrov et al. [32] investigated the system UO_{2+x}-FeO_{1+x} using the cold crucible induction melting technique. Although this method allows very high temperature measurement, due to the dimensions of the samples, considerable temperature and composition gradients are inevitable (Figure 11).

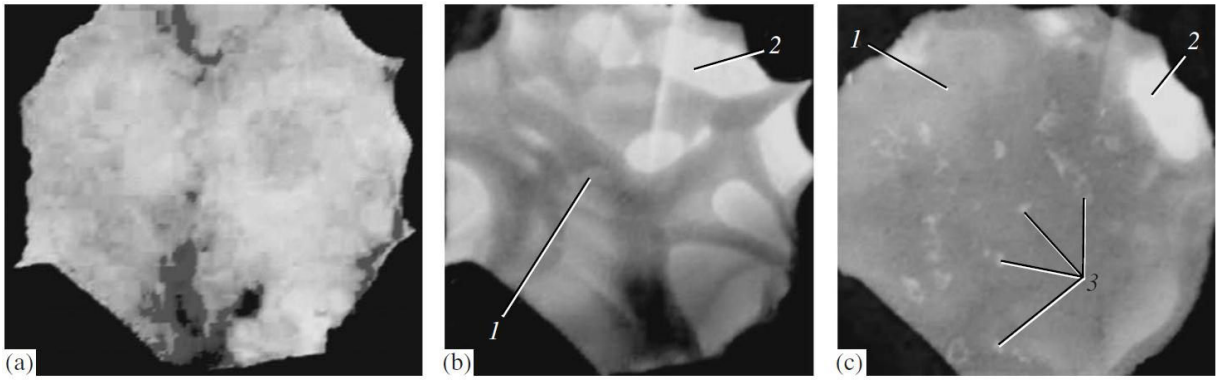

Figure 11: Image of the surface of the 50%UO_2-50%Fe_2O_3 melt observed by Petrov et al. (a) 10 s, (b) 49 min and (c) 69 min after the beginning of the melting. With the label (1) is reported the lighter liquid, with (2) the main molten material. The label (3) refers to the gas bubbles climbing through the light liquid layer

The oxide mixtures were heated 200-300 K above the liquidus temperature while the video recording was active. A sampling with a cold metal sampler allowed the quenching of the molten material in contact with the sampler itself. The rest of the molten bath was slowly

cooled and removed from the crucible. Finally the quenched rod and the cooled bath were analysed using SEM and X-ray powder diffraction.

In the 50%UO_2-50%Fe_2O_3 the presence of two liquids during the heating stage was observed (Figure 11). In both the quenched and the slowly cooled specimens five crystalline phases were observed: UO_2, $UO_{2.66}$, $FeO_{1.5}$, Fe_2O_3 and the compound $FeUO_4$ ($FeO•UO_3$). The authors argued that the coexistence of five crystalline phases was due to considerable oxygen partial pressure gradient**. For this reason these data cannot be retained for the thermodynamic modelling.**

Finally, as reported in [28] a transition from the [Fe_2O_3+melt] to [Fe_3O_4+melt] at about 1678 K was observed.

Due to intrinsic difficulties related to the control of the oxygen content, most of the authors who performed experiments on the O-Fe-U system reported large uncertainties on the sample compositions. Note however that Bechta et al. [30], [31] succeeds to maintain the investigated samples across the UO_2-FeO_x system. **Their data are retained for the thermodynamic modelling**.

2.1.4 O-Fe-Zr system

As for the U-Fe-O system, a lack of experimental data exists also for the O-Fe-Zr system. The affinity of zirconium for oxygen makes the control of the oxygen extremely difficult. Some studies were performed in the oxide zone of the ternary phase diagram. As for the O-Fe-U system, practically no experimental data are available in the oxygen-poor side of the ternary phase diagram.

Hofmann et al. [26] confirmed the existence of a Zr_2Fe phase at 1273 K (Figure 12).

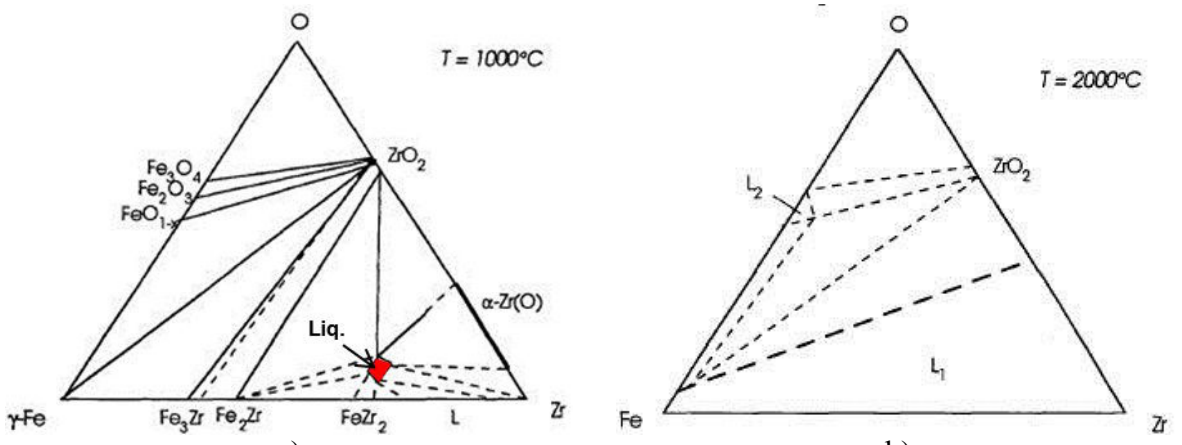

Figure 12: O-Fe-Zr phase diagram reported by Hofmann et al. [26]. a) 1273 K; b) 2273 K

The authors showed that at this temperature a liquid domain already exists close to the $FeZr_2$ composition range (see figure 12a). At 1773 K it extends towards the Zr_2Fe stability region up to 20 at% O. At 2273 K the liquid reaches 40 at% O in the Zr-rich side of the ternary diagram.

Jones et al. [33] reported a revised ZrO_2-Fe_3O_4 phase diagram traced starting from their own data obtained with the quenching method. The experiments were performed under air. The reported phase diagram is shown in Figure 13.

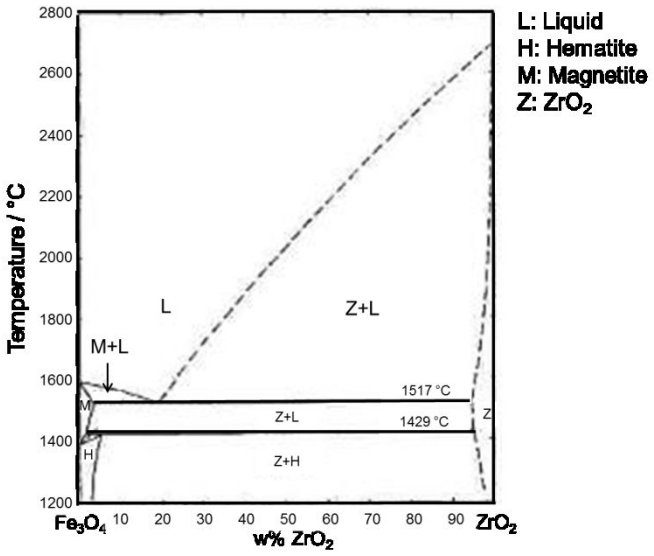

Figure 13: Tentative phase diagram of the Fe_3O_4-ZrO_2 section (T.S. Jones, 1967)

Kiminami (1987) [34] investigated the ZrO_2-FeO-Fe_2O_3 under air by thermogravimetry, obtaining solubility data of ZrO_2 in Fe_3O_4 and viceversa. Katsura et al. (1975) [35] determinated phase equilibria and measured the oxygen partial pressure in the FeO-Fe_2O_3-ZrO_2 system at 1473 K.

Petrov et al. (2002) [36] showed the presence of a miscibility gap along the ZrO_2-FeO_x section between 2143±30 and 2503±30 K in a concentration range from 34 to 82 wt% ZrO_2. For the investigation, the authors used a cold crucible induction melting technique. However, **the reported microstructure does not seem to correspond to two quenched immiscible liquids**.

Bechta et al. (2006) [37] investigated the ZrO_2-FeO system using the cold crucible induction melting technique, DTA and visual polythermal analysis (VPA) with Galakhov microfurnace. The experiments were performed under argon. It was reported a eutectic-type phase diagram, with the eutectic point located at 10.3±0.6 mol% ZrO_2 and 1605±5 K. The tentative phase diagram of the ZrO_2-FeO system obtained by the authors is reported in Figure 14.

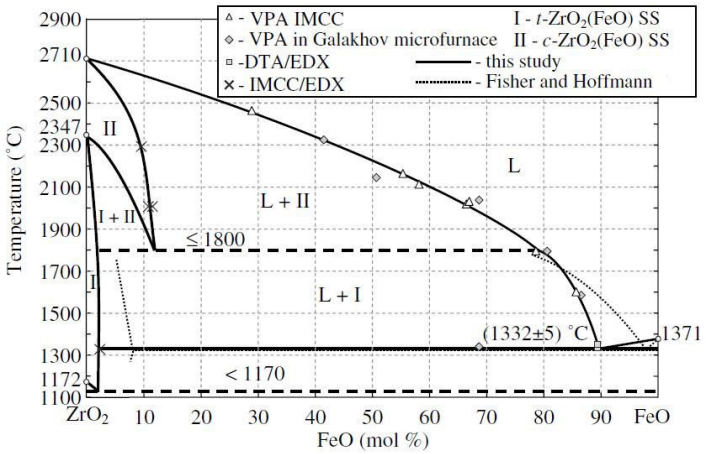

Figure 14: Tentative phase diagram of the ZrO_2-FeO system obtained in [37]

It may be noted that solubility of FeO in tetragonal and cubic ZrO_2 was observed. The reported results are retained for the thermodynamic modelling.

2.1.5 O-Pu-Zr system

Carroll (1963) [38] investigated the PuO_2-ZrO_2 system. He reported a tentative phase diagram reported in Figure 15. X-ray diffraction and metallographic techniques were used to explore the solid region. The samples were prepared starting from PuO_2 and ZrO_2 powders under helium atmosphere: given the fact that the chemical potential of oxygen in PuO_2 is relatively high, **the stoichiometry for these samples was probably not achieved**. Liquidus measurement was also performed along all the composition range by optical pyrometry. It may be pointed out that experimental details, especially concerning the post-examination analyses of the samples are missing.

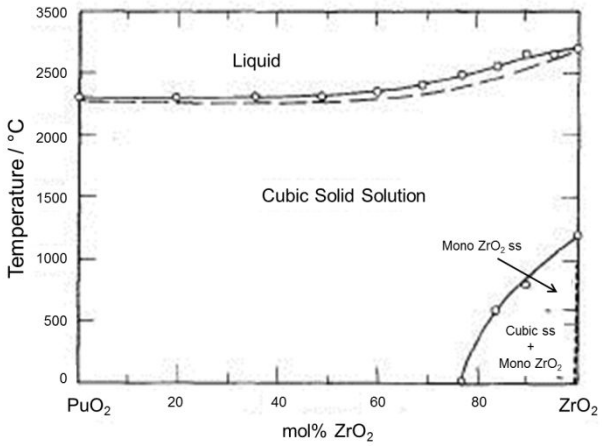

Figure 15: Tentative PuO_2-ZrO_2 phase diagram reported by Carroll [38]

It may be considered that the experimental data obtained by Carrol do not lie across the PuO_2-ZrO_2 section, but rather across a PuO_{2-x}-ZrO_{2-x} section.

Six year later, Mardon et al. (1969) [39] shed light on the effect of the experimental atmosphere on the behaviour of Pu-Zr-O samples. The samples were prepared by sintering at 1773 K in air or by arc melting. The arc melted samples underwent a vacuum-treatment at 2173 K to obtain reduced samples or rather a heat treatment at 1773 K in air to obtain oxidised samples.

The main features of the oxidised samples (i.e. lying on the PuO_2-ZrO_2 section) were a complete solubility between cubic PuO_2 and cubic ZrO_2 and a large solubility of tetragonal ZrO_2 in cubic PuO_2 (40 mol% ZrO_2 at 1773 K). A small solubility was observed between cubic PuO_2 and monoclinic ZrO_2. However the authors argued that the low temperature data in the PuO_2-ZrO_2 may be incorrect.

As far as the reduced samples are concerned (i.e. lying on the $PuO_{1.6}$-ZrO_{2-x} section) the solubility of $PuO_{1.6}$ in the monoclinic ZrO_{2-x} is lower than what observed for PuO_2.

The authors reported two tentative phase diagrams for the oxidised and reduce samples (Figure 16).

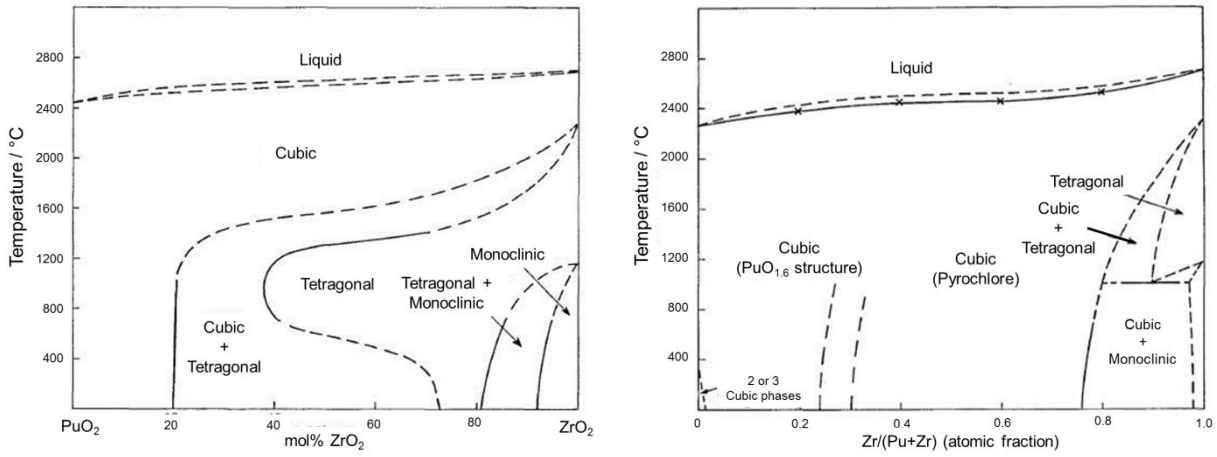

a) b)

Figure 16: Tentative phase diagrams reported by Mardon et al. [39]. a) PuO_2-ZrO_2 section; b) $PuO_{1.6}$-ZrO_{2-x} section

The authors performed a straightforward analysis on the influence of the experimental atmosphere on the samples oxygen content.

Albiol et al. (2002) [40] used a High Temperature X-Ray Diffractometer (HTXRD) to investigate the low PuO_2 side of the PuO_2-ZrO_2 section within the Pu-Zr-O system. The samples were calcined under argon at 1973 K for 13 hours, crushed and finally heat treated under argon for 22 hours. The authors performed a measurement under air and under argon on only one sample containing 90.8 mol% ZrO_2, and did not observe any difference between them. From their results, the authors concluded that all the samples were stoichiometric. Their experimental results are reported in Table 6.

	ZrO_2 (mol%)						
T (K)	77.2	81.7	88.9	90.8	94.4	96.9	97.7
1513							t
1473	c+t	c+t	c+t	c+t	c+t	c+t	m+t
1373	c+m (+t)	c+m (+t)	c+m (+t)	c+m (+t)	c+m (+t)	c+m (+t)	m (+t)
1273	c+m (+t)		c+m	c+m	c+m	c+m	c+m

Table 6: Experimental results obtained by Albiol et al. [40]. In the table are reported the observed phases at each heat-treatment temperature. c = cubic; m = monoclinic; t = tetragonal. The symbol (+t) means that the peaks of the monoclinic phase were decreasing in intensity, whilst the peaks corresponding to the tetragonal phase appeared

The authors inferred the stoichiometry of all the investigated samples by only testing the ZrO_2 richer part of the PuO_2-ZrO_2 system. However, as shown by Guéneau et al. [41] and Manara et al. [42] the presence of PuO_2 in the sample significantly influence its high temperature behaviour. The disappearance of the monoclinic phase was observed for samples with a composition ranging from 88.9 mol% to 96.9 mol% at 1463 K. The authors argued the existence of a eutectic reaction at 1463 K. The observation of traces of a tetragonal phase at 1373 K can be related to non-complete equilibrium conditions.

2.1.6 O-Fe-U-Zr system

This system is fundamental for in-vessel corium understanding. In fact it is the most common system used to simulate the more complex interactions between the molten core and the steel reactor vessel. Hofmann et al. [43] reported a straightforward O-Fe-U-Zr quaternary diagram at 2773 K (Figure 17).

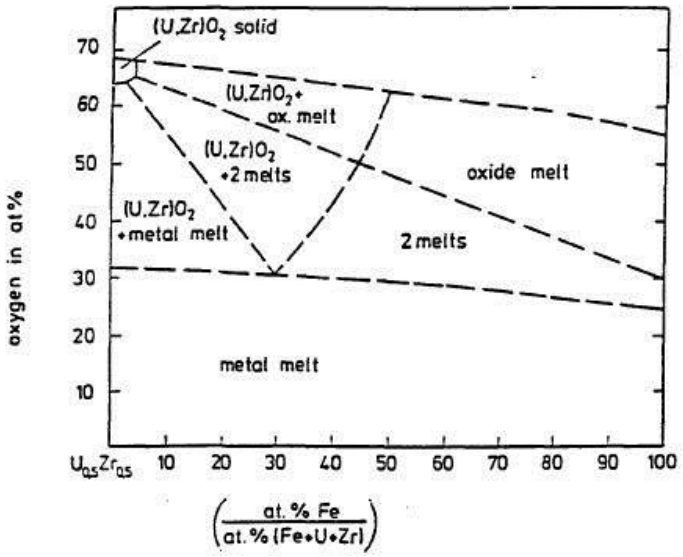

Figure 17: Phases in equilibrium at 2773 K in function of the oxygen and iron content [43]

Almjashev et al. [44] investigated the FeO_{1+x}-UO_{2+x}-ZrO_2 system with the aim of measure the pseudo-ternary eutectic temperature. They mixed in a cold crucible induction furnace Fe_2O_3, UO_2 and ZrO_2 (with HfO_2 impurities). The sample was heated up to 1800 K in air and then slowly cooled (data on the cooling rate are not given). The post-melting analyses were performed by means of SEM-EDS and XRD. The eutectic zone was determined by electron microscopy. A part of this zone was cut away from the sample and underwent a differential thermal analysis (DTA). The authors reported an eutectic temperature of 1596±7 K at a composition 67.4±1.0 $FeO_{1.5}$, 30.5±1.0 UO_{2+x}, 2.1±0.2 ZrO_2 (in molar percentage). The same group of research [45] confirmed that the eutectic transition in the oxide ternary system lies in the iron oxide-enriched region. The samples were fabricated with the same technique as in [44]. The ternary eutectic temperature of 1583 K was determined under neutral atmosphere. The measured eutectic composition is 91.8±0.5 mol%FeO_{1+x} - 3.8±0.3 mol%UO_2 - 4.4±0.4 mol%ZrO_2. In 2011 the authors published a review of their previous results [46]. Starting from FeO, Fe_2O_3, Fe, UO_2 and ZrO_2 the authors investigated the ternary eutectics of the FeO-UO_2-ZrO_2 system under argon and of the Fe_2O_3-U_3O_8-ZrO_2 system under air. Samples were prepared using cold crucible induction melting. After the melting the samples were analysed by XRD and SEM-EDX. The obtained results are reported in Table 7.

System	Eutectic composition, mol%			Eutectic temperature (K)
	FeO_x	UO_y	ZrO_2	
FeO-UO_2-ZrO_2	91.8	3.8	4.4	1583±5
Fe_2O_3-U_3O_8-ZrO_2	67.4	30.5	2.1	1596±7

Table 7: Experimental results on the FeO-UO_2-ZrO_2 and Fe_2O_3-U_3O_8-ZrO_2 systems

2.1.7 O-Pu-U-Zr system

Uchida et al. (2013) [47] performed a study on the melting behaviour of the ZrO_2-MOx system (MOx=(U,Pu)O_2). Samples were prepared mixing (U-4%Pu)O_2 and (U-8%Pu)O_2in mol% and metallic zirconium. The samples were then pressed into pellets and sintered at 1873 K for 2 hours in H_2/H_2O atmosphere. The pellets finally underwent an heat treatment at 1123 K for 5 hours under a controlled oxygen potential (i.e., $RT\ln(pO_2) = -400\,kJ/mol$) to keep the O/M=2.

The obtained experimental results are summarised in Table 8.

	%at metal content			Composition	u(T) = ± 35 K	
	Zr %at	U %at	Pu %at		T Solidus (K)	T Liquidus (K)
4% Pu-MOX	25	72	3	$(U_{24}Pu_1Zr_{8.33})O_2$	2929	2976
	50	48	2	$(U_{16}Pu_{0.67}Zr_{16.67})O_2$	2876	2901
	75	24	1	$(U_8Pu_{0.33}Zr_{25})O_2$	2873	2919
8% Pu-MOX	25	69	6	$(U_{23}Pu_2Zr_{8.33})O_2$	3008	3066
	50	46	4	$(U_{15.33}Pu_{1.33}Zr_{16.67})O_2$	2880	2911
	75	23	2	$(U_{7.67}Pu_{0.67}Zr_{25})O_2$	2873	2919

Table 8: experimental results obtained by Uchida et al. [47]. The reported solidus and liquidus temperatures have a related uncertainty u(T)=± 35 K

The reported experimental data are retained for the thermodynamic modelling of the PuO_2-UO_2-ZrO_2 system.

2.1.8 Summary

The first part of this chapter summarises the experimental studies performed on some interesting sub-systems of the prototypic in-vessel corium system (U-Pu-Zr-Fe-O).

The O-U-Zr system has been studied especially along the UO_2-Zr and UO_2-Zr(O) sections to better characterise the fuel-cladding behaviour in case of a severe accident. The UO_2-ZrO_2 pseudo-binary system has been widely studied leading to a rather complete experimental description. However, the oxygen-poor side of the O-U-Zr needs a deep experimental description in order to better describe the solubility limit of oxygen in the ternary liquid. Furthermore the miscibility gap in the liquid phase is still unknown, with only one reliable experimental tie-line obtained by Gueneau et al. [12].

A limited number of studies have been performed on the O-Fe-U and O-Fe-Zr systems. This is mainly due to experimental difficulties related to the control of the oxygen content. In fact, the oxygen-poor regions of the aforementioned ternary systems have not been investigated. In the same way, the quaternary O-Fe-U-Zr system has been only investigated in the oxygen-rich region.

The Pu-containing systems have been studied in the framework of MOx fuels use in PWR. Some innate experimental difficulties exist due to the radiotoxicity of plutonium. The oxide region of the O-Pu-Zr system has been studied. However, some doubts remain on the exact investigated isopleth sections (PuO_2-ZrO_2 or $PuO_{1.6}$-ZrO_{2-x}, see [39]). Only one experimental work was found on the PuO_2-UO_2-ZrO_2 system.

2.2 Molten Corium-Concrete interaction large scale experiments

In the case of the reactor vessel failure during a severe accident, the in-vessel corium – mainly composed of refractory materials (UO_2 and ZrO_2) and metals (Zr and Fe) – contacts the underneath concrete. In this situation the so-called Molten Core Concrete Interaction (MCCI) accidental scenario takes place involving a certain number of phenomena such as: high temperature concrete decomposition, heat transfer due to gas bubbles agitation, formation of several phases, oxidation of metals, etc.

Core degradation phenomena and MCCI phenomena have been widely studied in literature. The objective of these experiments was to identify the dominant phenomena occurring during

a severe accident. The main issue faced during the tests realisation was the choice of the materials employed during the experiment: from the radiological point of view, it is not possible to use the "real" molten corium. It was also shown that the thermophysical properties of UO_2 are rather unique: in order to simulate at best the accidental phenomena, **it is not possible to replace UO_2 with another component**. Prototypical UO_2-containing corium was then used for the severe accident progression investigation.

As already introduced in Chapter 1, a severe accident starts when the **fuel cladding is degraded** and then the first radiological barrier is lost. In parallel **Fission Products (FP) release** takes place. The **relocation of the molten core** in the lower head of the reactor vessel is the last step of the in-vessel retention. If the in-vessel retention fails the molten corium is ejected in the reactor containment: in this framework, the molten corium may firstly **interact with water** and with the **containment concrete.** In the EPR accidental scenario, the **spreading of molten mixture in a separate retention chamber** follows the interaction between the molten corium and the sacrificial concrete.

The main phenomena investigated can be summarised as follows:

- Core degradation phenomena
- Fission Products (FP) release
- Molten core relocation in the lower head of the reactor vessel
- In-vessel retention of the molten corium
- Molten corium-water interaction in the case of reactor vessel failure after a first attempt of external water cooling
- Spreading of the molten corium on the concrete. Molten Corium-Concrete Interaction (MCCI)
- Spreading of the molten corium-concrete mixture (ex-vessel corium) in the ex-vessel retention chamber (EPR configuration)

In the following, only the experiments where prototypic coria (UO_2-containing coria) were used will be summarised.

2.2.1 Degradation of fuel bundles and in-vessel retention phenomena

The CORA (Complex Out-of-pile Rode bundle Assembly) series of tests performed at the Forschungszentrum Karlruhe (FZK) investigated the fuel assembly degradation [48]. These tests showed that in a PWR the integrity of the fuel cladding might be lost at temperatures well below the temperature of fusion of Zircaloy. This is caused by eutectic reactions between the Zircaloy, stainless steel and Inconel spacer grids with neutronic absorber materials (Ag-Cd-In or B_4C). The experiments highlighted that the composition of the molten core varies in function of time and temperature. The oxidation of the Zircaloy cladding in contact with water leads to hydrogen formation and temperature rise during the accident. It was also shown that the absorber materials might separate from the fuel: for this reason the injection of borated water is needed to prevent the molten core re-criticality.

The RASPAV program [49] was devoted to the simulation of the behaviour of prototypic corium relocated inside the vessel. Mixtures of UO_2-ZrO_2-Zr with different level of zirconium oxidation were investigated. More recently the same experimental facility was used in the framework of the MASCA project [15]. The aim of this project was studying the impact of materials interactions on the stratification of the molten corium in close-to-thermal equilibrium conditions. It was shown that a configuration with a heavier metallic liquid under the oxidic liquid phase is possible in the case of a significant migration of uranium to the metallic phase. This is the condition that can lead to the already discussed **focusing effect**. Using again the RASPAV installation, the METCOR project [15] investigated the interaction between molten corium and steel. It was shown that the steel ablation front corresponds to the

propagation of an isothermal front at 1363 K (Figure 18), that is the eutectic temperature between the steel and the molten corium.

Figure 18: METCOR axial section of the sample after the corium-steel interaction [15]

The CORPHAD project [15] focused on the phase equilibrium in the U-Zr-Fe(Cr,Ni)-O system investigated by the MASCA project,. In particular the O-U-Zr, O-Fe-Zr and Fe-U-Zr-O systems were studied, showing the presence of a miscibility gap in the liquid phase. The reported experimental results may be found in Table 9.

		Metallic liquid				Oxidic liquid			
Sample	T (K)	U	Zr	Fe	O	U	Zr	Fe	O
$U_{0.325}Zr_{0.292}O_{0.383}$	2643	40.8	32.2	/	27.0	25.1	26.7	/	48.2
$U_{0.405}Zr_{0.270}O_{0.325}$	2753	53.1	29.3	/	17.6	27.1	23.2	/	49.2
$Zr_{0.505}Fe_{0.198}O_{0.297}$	2693	/	53.5	23.1	23.3	/	ND	48.5	2.7
$Zr_{0.464}Fe_{0.253}O_{0.283}$	2773	/	48.7	26.1	25.2	/	44.8	6.4	48.8
$U_{0.600}Zr_{0.400}Fe_{0.216}O_{0.144}$	2873	64.0	3.9	23.5	8.5	41.0	2.3	2.0	54.8

Table 9: Summary of the CORPHAD experimental results on the extension of the miscibility gap in the liquid phase of the O-U-Zr, O-Fe-Zr and U-Zr-Fe-O systems. ND=no data available

The validity of these results will be discussed more in detail in Chapter 4. As already introduced in the first part of this chapter, the authors argued that thermal gradients and segregation phenomena may have contributed to the final composition of the immiscible liquids.

2.2.2 Fission products release

The aim of the ACE/MACE tests [50], [51] performed at the Argonne National Laboratories was to study the fission products release during the interaction between molten corium and concrete. It was shown that the aerosols releases were essentially composed by decomposition products of concrete. The type of concrete employed (silica-rich or limestone-rich concrete) has an influence on the uranium release: namely with the limestone-rich concrete a larger amount of uranium was released.

2.2.3 Molten corium-water interaction

The investigation of melt coolability in the case of MCCI was the main purpose of the MACE program. The main objectives of the MACE program were:

- to get data on the heat transfer from the molten corium to the overlying water and underlying concrete;
- develop models describing the coolability process.

The MACE facility is reported in Figure 19.

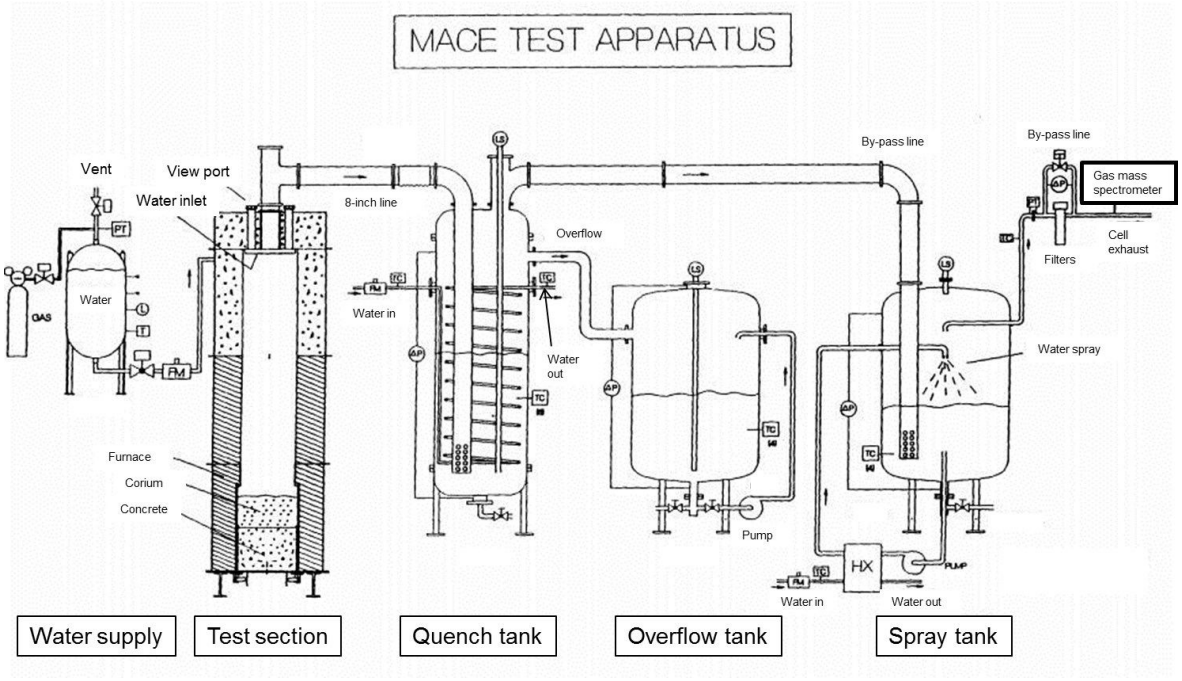

Figure 19: MACE test facility [50,51]

A prototypic corium composed by a (UO_2-ZrO_2-Zr) mixture was melted by a direct electric heating and then poured onto the prototypic concrete. Water is added when the molten corium started attacking concrete in order to simulate prototypic conditions obtained after the complete discharge of the corium due to vessel failure. The aims of the tests were to explore the benefits of massive addition of water in terms of quenching and stabilisation of the core melt, arresting the ablation of concrete and scrubbing of the fission products on the form of aerosols.

The COTELS project is a joint study between the NUPEC (Nuclear Power Engineering Corporation) and the National Nuclear Centre of the Republic of Kazakhstan. In this framework, several tests were performed to study the degradation phenomena occurring during MCCI. Scenarios with and without water addition were investigated. The molten corium (stainless steel or a mixture of UO_2-ZrO_2-Zr-stainless steel) was poured onto a 2D-concrete test section (Figure 20).

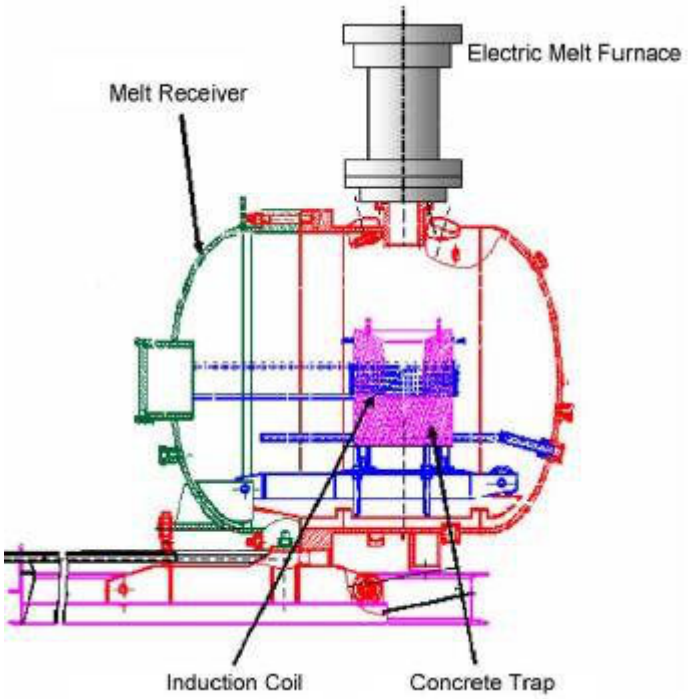

Figure 20: COTELS facility

The residual decay heat was simulated using induction heating. The dominant phenomenon driving the ablation process was the melting of aggregates. The water injection cooled down the sidewall of the concrete test section. The authors argued that water migrated within the degraded concrete sidewall leading thus to the cooling phenomenon.

KAERI (Korea Atomic Energy Research Institute) started the TROI (Test for Real cOrium Interaction with water) program with the aim to investigate the ex-vessel steam explosion scenario after the flooding of the reactor containment. Spontaneous explosions were observed with composition close to 50 mol% UO_2-50 mol% ZrO_2 where an azetropic reaction is expected.

Thanks to the experiments carried out at the KROTOS facility [52] the importance to use prototypic corium (i.e., containing UO_2) during MCCI simulation tests was highlighted. In fact, the authors showed that the behaviour of a UO_2-containing corium in contact with water is radically different from an Al_2O_3-based corium simulant.

2.2.4 Molten corium –concrete interaction MCCI

In the framework of the COMAS (COrium on MAterials Surfaces) project [53], the CARLA installation at Siempelkamp's Krefeld location was used for studying the ex-vessel core melt behaviour. The geometrical configuration of the experiment reproduces reduced scale EPR conditions. Two compositions representative of the EPR conditions were defined. The initial composition of the coria is reported in Table 10.

Wt%	UO_{2+x}	ZrO_2	FeO	Cr_2O_3	Fe	Zr
Corium R	29	12	18	2	39	/
Corium S	55	6	/	/	24.6	14

Table 10: Composition of coria R and S investigated during the COMAS experiments [53]. Corium R represents a more oxidized scenario

The spreading tests were performed on three substrates (concrete, ceramics and cast iron). The test on Corium R showed same spreading length for the three substrates. A clear separation

between the metallic and the oxide phases was observed during the spreading. It was observed that cast iron is an excellent substrate material thanks to its capacity for heat removal and its resistance during the substrate/corium interaction. The main parameters that influence the spreading process are the initial temperature, the oxide/metal phase ratio and the pouring rate of the corium.

At the Argonne National Laboratories a series of Core-Concrete Interaction tests were performed [54]. In particular the long term 2D core-concrete interaction under both dry and wet conditions was investigated. Two tests were conducted with siliceous concrete (CCI-1 and CCI-3) and the third with Limestone/Common Sand (LCS) concrete (CCI-2). It was shown that the long-term ablation behaviour was directly related to the concrete type. The formation of a crust was observed at the bottom of the concrete basement and on the sidewall for CCI-1 and CCI-2 tests, while CCI-3 test showed a crust formation only at the bottom of the basement. A quasi-isotropic ablation was observed for LCS concrete, whilst non-uniform ablation was observed in CCI-1 test. CCI-3 test showed symmetrical lateral ablation but anisotropic ablation (lateral ablation rate was significantly higher than observed in CCI-2 test). The observed difference in the ablation behaviour may be related to the initial gas content and chemical composition.

The HECLA [55] experiments investigated the ablation process of a metallic melt on a hematite-containing concrete. This type of concrete is used in EPR (European Pressurised Water Reactor) as sacrificial materials in the reactor pit. The metallic melt is heated by an induction furnace and poured onto the concrete test section. Experiments were also performed on ordinary siliceous concrete, in order to compare its ablation behaviour with the hematite-containing concrete. Only small differences were observed in the ablation process between siliceous and hematite-containing concrete.

2.2.5 The PLINIUS facility

The PLINIUS (Platform for Improvements in Nuclear Industry and Utility Safety) platform was developed at the CEA to better understand the phenomena occurring during a severe accident in a PWR. Four facilities are devoted to the study of the behaviour and to thermo-physical properties of corium:

- VULCANO (Versatile UO_2 Lab for Corium ANalysis and Observation). It is based on a plasma-arc rotating furnace able to melt up to 100 kg of oxides at 3000 K (Figure 21). This facility allows a large variety of experiments: corium solidification behaviour, corium pool thermohydraulics, long term corium/concrete interaction, spreading test with different types of coria and refractory substrate.
- COLIMA (COrium LIquid and MAterials). In this facility an induction heating can bring some kilograms of corium up to 3300 K under controlled atmosphere. It is mostly employed to study thermal exchanges and aerosol release.
- VITI (VIscosity Temperature Installation). It is used to perform viscosity and surface tension measurements by means of an aerodynamic levitation setup.
- KROTOS facility is dedicated to the steam explosions phenomena. The molten corium is dropped in water and it is observed by means of optical, thermal and pressure instrumentation.

In the framework of the current study on the MCCI, the VULCANO facility is of extreme interest, since it allows studying several aspects of a PWR severe accident.

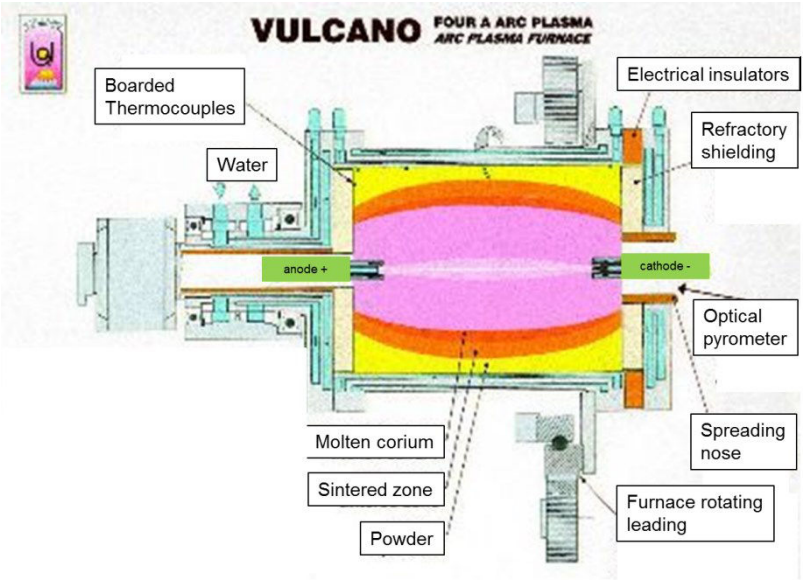

Figure 21: VULCANO furnace

EPR security design requires that in the case of a severe accident with a consequent melting of the core, the melt should spread on a large compartment underneath the vessel. This approach will allow minimising the thermal flux due to the residual radioactive decay heat. In this framework, spreading tests were needed and the VULCANO facility was used.

At the end of the melting, the furnace is tilted and the molten mixture pours onto the test substrate. The test substrates may be made of zirconia and magnesia bricks, depending on the test.

Journeau et al. [56] published the results of spreading tests results performed with different type of coria (initial compositions are reported in Table 11).

Component	HfO_2	UO_2	ZrO_2	SiO_2	Fe_3O_4	Fe_2O_3	CaO	Al_2O_3
VE-07	34.3	/	25.5	24.9	12.9	1.8	0.8	0.1
VE-U1	/	45.0	19.3	16.6	13.4	1.9	0.7	0.1

Table 11: Initial composition of the mixture of oxides in the VE-07 and VE-U1 spreading tests. The compositions are given in mass percentage. Corium VE-U1 composition is prototypical of corium discharge from the EPR reactor pit after the ablation of the ferrosiliceous concrete [56].

The post-test analyses highlighted the presence of several layers within the solidified material. Five layers were identified in VE-07 test, whilst only three layers were observed on test VE-U1. The authors ascribed these differences to the presence of UO_2 in the VE-U1 test. Within each layer, different phases were identified, leading to think that during cooling, important temperature gradients were present. Phases found within each layer of VE-07 and VE-U1 tests are reported in Table 12.

Layer	VE-07 analysis	VE-U1 analysis
5th layer: upper surface	$(Hf,Zr)O_2$ solid solution SiO_2 Fe_2O_3	/
4th layer	$(Hf,Zr)O_2$ solid solution SiO_2 Fe_2SiO_4 (fayalite)	$(U_{0.33}Zr_{0.47}Fe_{0.20})O_{1.83}$ $(U_{0.42}Zr_{0.55}Fe_{0.03})O_{1.83}$ SiO_2
3rd layer	Same as fourth layer	$(U_{0.78}Zr_{0.12}Fe_{0.10})O_{1.87}$ $(U_{0.26}Zr_{0.65}Fe_{0.09})O_{1.60}$ SiO_2 $Fe_{1.2}SiO_{3.56}$
2nd layer	$(Hf,Zr)O_2$ solid solution $(Hf,Zr)SiO_2$ solid solution SiO_2 Fe_2SiO_4 (fayalite)	$(U_{0.85}Zr_{0.11}Fe_{0.04})O_{1.69}$ $(U_{0.32}Zr_{0.82})SiO_{3.64}$ $(U_{0.13}Zr_{0.98})SiO_{3.75}$ UO_2 SiO_2 $Fe_{2.2}SiO_{3.76}$
1st layer	$(Hf,Zr)O_2$ solid solution $(Hf,Zr)SiO_2$ solid solution SiO_2 Fe_2O_3 and Fe_3O_4	/

Table 12: Phase distribution within the layer observed in the post-test analyses on VE-07 and VE-U1 spreading tests [56]. It may be noted that in VE-U1 test only three layers were identified

The presence of iron oxides at the bottom of layer 1 and at the top of layer 5 indicated that during spreading in the VE-07 test, the FeO is oxidised into Fe_2O_3 and Fe_3O_4 due the interaction between the corium and the oxidising atmosphere of the test. The observed microstructures highlights that important temperature gradients were present across the layers; the dendritic structure of the upper layer suggests that the cooling process was rather fast. The presence of $(A,Zr)SiO_4$ solid solution (A=Hf or U) in the first and second layers indicates that a rather slow cooling was undergone, at least below 2025 K. The transformation of $(A,Zr)O_2$ into $(A,Zr)SiO_4$, needs penetration of SiO_2 into the solid $(A,Zr)O_2$ at temperature lower than the decomposition temperature of $HfSiO_4$ (2023 K) or $ZrSiO_4$ (1949 K), which is a slow process.

In 2006 a test named VBS-U1 was performed at the VULCANO facility [57] (Figure 22). This test was aimed to the study of the interaction between molten corium and concrete, in particular, in the presence of a metallic layer (molten stainless steel).

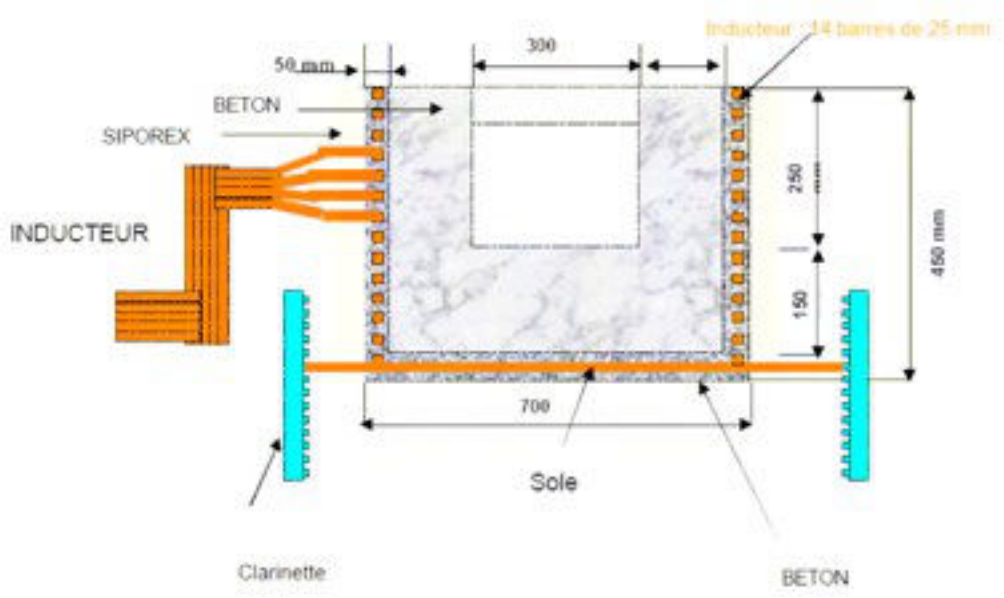

Figure 22: Concrete test section used during the MCCI VBS-U1 test [57]

The test section was a 600x300x400mm limestone-rich concrete block with a hemi cylindrical cavity of 300 mm in diameter and 250 mm height. The composition of the concrete was 25 SiO_2 - 41 CaO - 25 Al_2O_3 - 25 CO_2 - 3 H_2O (in weight percent). The corium was made of 15 kg of steel heated at 1973 K and of about 35 kg of oxides (70 % UO_2, 16 % ZrO_2 and 14 % sacrificial concrete) at 2273 K. Firstly the molten corium was poured in the concrete cavity, then the superheated steel at 1973 K was poured into the cavity as well. Four induction coils surrounded the section in order to provide sustained heating (see a sketch of the test section in Figure 22). Before the experiment pre-calculations with the TOLBIAC-ICB code were performed. Thanks to the calculations, the stratification time was estimate for a "thermodynamic equilibrium scenario" between the oxide and the metal phase and for an "out of thermodynamic equilibrium" scenario. During the test VBS-U1, a continuous flow of gases (mainly CO_2 and steam) and large flames were observed. Six volcanoes were found at the solidified pool surface (Figure 23).

Figure 23: One of the volcanoes found on the corium surface [57]

The test highlighted some differences compared with tests performed without a metal; a large void fraction was found within the solidified experimental section. Furthermore, more than 10 kg of initially metal materials was oxidised during the test probably by the combined action of CO_2, steam and the oxidising experimental atmosphere.

The concrete ablation shape during a severe accident was also investigated at the VULCANO facility [58]. Two oxide coria were tested on five concretes. The initial compositions of the molten coria and of the concretes are reported respectively in Table 13 and Table 14.

Wt%	UO_2	ZrO_2	SiO_2	Fe_2O_3	CaO
Corium 1	45	19	20	15	/
Corium 2	69	17	6	7	1

Table 13: initial composition of the molten coria [58]

Wt%	SiO_2	CaO	Al_2O_3	Fe_2O_3	MgO	CO_2	H_2O
Concrete C	29.6	49.2	3.9	2.1	0.9	/	10.7
Concrete E	45.5	12.7	3.3	32.9	0.3	1.4	3.7
Concrete F	63	16	5	/	/	9	3
Mortar F	58	18	5	1	0.5	7	7.5
Concrete G	26	42	2	/	/	25	4

Table 14: chemical composition of the concretes used during the MCCI tests. The Concrete E simulates the core catcher designed for the EPR reactor [58]

The authors showed that the ablation of concrete strongly depends on its initial composition. Silica-rich concrete exhibited anisotropic ablation: in general the sidewall ablation was twice faster and stronger than the vertical ablation. Limestone concrete showed a rather isotropic ablation instead. In order to understand the physical reason of this difference, the authors performed further tests. Their preliminary conclusions are that the composition of the molten corium pouring on the concrete does not seem to affect the ablation shape. It was however observed that while the limestone-based concrete was completely destroyed during the MCCI tests due to the decarbonation starting at 1000 K, it was possible to find unmolten siliceous gravel after the tests performed with siliceous concrete: this may affect the ablation shape. Furthermore, it was observed the formation of concrete-rich and concrete-poor liquids in presence of siliceous concrete. This may also be the cause of anisotropic ablation. Further investigations are needed to shed light on this paramount phenomenon.

2.2.6 Summary

The second section of this chapter reports a selection of large-scale severe accident experiments. Thanks to this experimental contribution, the driving phenomena can be identified.

During the in-vessel stage of the accident, the exothermic zirconium oxidation drives the rise in temperature that leads to the loss of the fuel cladding. The hydrogen production is also related to the Zircaloy oxidation. The miscibility gap in the liquid in-vessel corium system leads to the stratification of the corium inside the reactor vessel. Depending on the zirconium oxidation level, the U/Zr ratio and the amount of dissolved steel an inversion of the liquid density may cause the relocation of a heavy metallic layer below the oxidic pool, enhancing the focusing effect and the risk of the loss of the reactor vessel.

The ablation progress during the ex-vessel stage of the accident strongly depends on the initial composition of the concrete. Siliceous concrete showed an anisotropic progression of the ablation. Journeau et al. [58] argued that this phenomenon could be related to the presence of unmolten siliceous gravel or to the formation of two phases, one rich in concrete, and the other rich in corium elements. A strong oxidation of the metallic cast was observed during a metallic+oxidic corium/concrete interaction: the CO_2 and H_2O released from the concrete during the high temperature interaction with the corium oxidised the metallic cast as well as the oxidising experimental atmosphere.

2.3 Conclusions

The aim of this chapter is to gather the available experimental data obtained on the prototypic in-vessel corium system and its sub-systems. It can be concluded that:

- The available experimental data are not sufficient for a full thermodynamic description of the in-vessel corium. A lack of data exists especially on the extension of the miscibility gap in the liquid phase of the U-Zr-Fe-O system.
- The control of the oxygen content is challenging due to the high oxygen affinity of the main components of the corium (uranium, zirconium, iron).
- A thermodynamic description of the U-Pu-Zr-Fe-O prototypic in-vessel corium has never been published.
- The influence of plutonium in the case of a severe accident, especially in the case of the use of MOx fuel, is rather unknown.

The reported large-scale experiments investigated the phenomenological progression of a severe accident during the in-vessel and ex-vessel scenarios. The rare thermochemical data obtained during large scale experiments are affected by large uncertainties due to thermal and composition gradients. It can be concluded that:

- The severe accident phenomenology is extremely complex.

The thermodynamic description of the prototypic in-vessel corium and ex-vessel corium systems will contribute to the comprehension of accidental phenomena.

2.4 References

[1] TAF-ID, "www.oecd-nea.org/science/taf-id." .

[2] H. A. Saller, A. F. Rough, J. M. Fackelmann, A. A. Bauer, and J. R. Doig, "Phase relations in the uranium-zirconium-oxygen systems involving zirconium and uranium dioxide," Battelle Memorial Institute, Report no. BMI-1023, 1955.

[3] E. F. Juenke and J. F. White, "Physico-chemical studies of clad UO_2 under reactor accident conditions," General Electric Company, Report GEMP-731, 1970.

[4] A. Findlay, A. N. Campbell, and S. N. O, *The Phase Rule*, Dover Publ. 1961.

[5] C. Politis, "Untersuchungen im Dreistoffsystem Uran-Zirkon-Sauerstoff," Kernforschungszentrum Karlsruhe, Report no. KfK 2167, 1976.

[6] A. Skokan, "A High Temperature Phase Relation in the U-Zr-O system," in *5th International Meeting on Thermal Nuclear Reactor Safety*, 1984, pp. 1035–1041.

[7] P. J. Hayward and I. M. George, "Dissolution of UO_2 in molten Zircaloy-4 Part 1: Solubility from 2000 to 2200 ^{o}C," *J. Nucl. Mater.*, vol. 208, pp. 35–42, 1994.

[8] P. J. Hayward and I. M. George, "Dissolution of UO_2 in molten Zircaloy-4 Part 2: Phase evolution during dissolution and cooling," *J. Nucl. Mater.*, vol. 208, no. 43–52, 1994.

[9] P. J. Hayward and I. M. George, "Dissolution of UO_2 in molten Zircaloy-4 part 3: Solubility from 2000 to 2500°C," *J. Nucl. Mater.*, vol. 232, pp. 1-12, 1996.

[10] P. J. Hayward and I. M. George, "Dissolution of UO_2 in molten Zircaloy-4 Part 4: Phase evolution during dissolution and cooling of 2000 to 2500°C specimens," *J. Nucl. Mater.*, vol. 232, pp. 13-22, 1996.

[11] A. Maurizi, "Réactivité chimique a haute température dans le système (U,Zr,Fe,O) - contribution a l'étude de la zircone comme récuperatéur de 'corium,'", PhD Thesis, Univerisite Pierre et Marie Curie, 1996.

[12] C. Guéneau, V. Dauvois, P. Pérodeaud, C. Gonella, and O. Dugne, "Liquid immiscibility in a (O,U,Zr) model corium," *J. Nucl. Mater.*, vol. 254, no. 2–3, pp. 158–174, Apr. 1998.

[13] S. Bakardjieva, M. Barrachin, S. Bechta, D. Bottomley, L. Brissoneau, B. Cheynet, et al., "ERMSAR-2008," 2008.

[14] D. Manara, M. Sheindlin, W. Heinz, and C. Ronchi, "New techniques for high-temperature melting measurements in volatile refractory materials via laser surface heating," *Rev. Sci. Instrum.*, vol. 79, no. 2008, 2008.

[15] S. V. Bechta, V. S. Granovsky, V. B. Khabensky, V. V. Gusarov, V. I. Almiashev, L. P. Mezentseva, E. V. Krushinov, S. Y. Kotova, R. A. Kosarevsky, M. Barrachin, D. Bottomley, F. Fichot, and M. Fischer, "Corium phase equilibria based on MASCA, METCOR and CORPHAD results," *Nucl. Eng. Des.*, vol. 238, pp. 2761-2771, 2008.

[16] W. A. Lambertson and M. Mueller, "Uranium Oxide Phase Equilibria Systems: III, UO_2-ZrO_2," *J. Am. Ceram. Soc.*, vol. 36, pp. 365–368, 1953.

[17] N. M. Voronov, E. A. Voitekhova, and A. S. Danilin, “Phase Equilibrium Diagrams of the UO_2-ZrO_2 and ThO_2-ZrO_2 Systems,” in *Proc. 2nd Conf. Peaceful Uses of Atomic Energy*, 1958.

[18] I. Cohen and B. Shaner, “A metallographic and X-ray study of the UO_2-ZrO_2 system,” *J. Nucl. Mater.*, vol. 9, pp. 18–52, 1963.

[19] L. G. Wisnyi and S. W. Pijanowski, *The thermal stability of uranium dioxide*. Knolls Atomic Power Laboratory, General Electric Company, 1957.

[20] K. A. Romberger, C. F. Baes, and H. H. Stone, “Phase equilibrium studies in the UO_2-ZrO_2 system,” *J. Inorg. Nucl. Chem.*, vol. 29, pp. 1619–1630, 1967.

[21] M. Baïchi, “Contribution à l’étude du corium d’un réacteur nucléaire accidenté : aspects puissance résiduelle et thermodynamique des systèmes U-UO_2 et UO_2-ZrO_2,”, PhD Thesis, INP Grenoble, 2001.

[22] K. Une and M. Oguma, “Oxygen Potential of $U_{0.85}Zr_{0.15}O_{2+x}$ Solid Solutions at 1500°C,” *J. Am. Ceram. Soc.*, vol. 66, pp. c–179, 1983.

[23] J. O. Paschoal, H. Kleykamp, and F. Thummler, “Phase equilibria in the pseudoquaternary BaO-UO_2-ZrO_2-MoO_2 system,” *J. Nucl. Mater.*, vol. 151, pp. 10–21, 1987.

[24] V. Stolyarova, A. Shilov, and M. Shultz, “Thermodynamic properties of the UO_2-ZrO_2 system studied by the isothermal mass spectrometric vaporization method,” *J. Nucl. Mater*., vol. 247, pp. 41-45, 1997.

[25] M. Baïchi, C. Chatillon, and C. Guéneau, “Mass spectrometer study of the UO_2-ZrO_2 pseudo-binary system,” *J. Nucl. Mater.*, vol. 294, pp. 84–87, 2001.

[26] P. Hofmann, H. Holleck, C. Politis, and A. Skokan, “Konstitution und Reaktionsverhalten von LWR-Komponenten beim Coreschmelzen,” Kernforschungszentrum Karlsruhe, Report no. KfK 2242, 1976.

[27] D. Labroche, “Contribution à l’étude thermodynamique du système ternaire U-Fe-O,” PhD Thesis, INP Grenoble, 2000.

[28] W. D. J. Evans and J. White, “Equilibrium Relationships in the System UO_2-Fe_3O_4-O,” *Trans. Br. Ceram. Soc.*, vol. 63, no. 12, pp. 705–724, 1964.

[29] B. Riley, “The UO_2-Fe_2O_3 and PuO_2-Fe_2O_3 System in Air,” *Trans. Am. Nucl. Soc.*, vol. 12, pp. 543–544, 1969.

[30] S. V. Bechta, E. V. Krushinov, V. I. Almjashev, S. A. Vitol, L. P. Mezentseva, Y. B. Petrov, D. B. Lopukh, V. B. Khabensky, M. Barrachin, S. Hellmann, K. Froment, M. Fisher, W. Tromm, D. Bottomley, F. Defoort, and V. V. Gusarov, “Phase diagram of the UO_2-FeO_{1+x} system,” *J. Nucl. Mater.*, vol. 362, no. 1, pp. 46-52, 2007.

[31] S. Bechta, E. V. Krushinov, V. I. Almyashev, S. A. Vitol, L. Mezentseva, Y. B. Petrov, and E. Al., “Phase Transformation in the Binary Section of the UO_2-FeO-Fe System,” *Radiochemistry*, vol. 49, no. 1, pp. 20–24, 2007.

[32] Y. Petrov, Y. P. Udalov, J. Subrt, S. Bakardjieva, P. Sazavsky, M. Kiselova, P. Selucky, and E. Al., “Phase Equilibria during Crystallization of Melts in the Uranium Oxide-Iron Oxide system in Air,” *Glas. Phys. Chem.*, vol. 35, no. 3, pp. 298–307, 2009.

[33] T. S. Jones, S. Kimura, and A. Muan, "Phase Relation in the System FeO-Fe_2O_3-ZrO_2-SiO_2," *J. Am. Ceram. Soc.*, vol. 50, pp. 137–142, 1967.

[34] R. H. G. A. Kiminami, "Estudo do sistema ZrO_2-FeO-Fe_2O_3 através da termogravimetria à pressao parcial de oxygeno do ar e temperaturas de até 1500 ^oC," *Ceramica*, vol. 33, no. 213, pp. 207–210, 1987.

[35] T. Katsura, M. Wakihara, S.-I. Hara, and T. Sugihara, "Some Thermodynamic Properties in Spinel Solid Solutions with the Fe_3O_4 Component," *J. Solid State Chem.*, vol. 13, pp. 107–113, 1975.

[36] Y. B. Petrov, Y. P. Udalov, J. Slovak, and Y. G. Morozov, "Liquid Immiscibility Phenomena in Melts of the ZrO_2-FeO-Fe_2O_3 System," *Glas. Phys. Chem.*, vol. 266, no. 3, pp. 139–146, 2002.

[37] S. V. Bechta, E. V. Krushinov, V. I. Almjashev, S. A. Vitol, L. P. Mezentseva, Y. B. Petrov, D. B. Lopukh, V. B. Khabensky, M. Barrachin, S. Hellmann, K. Froment, M. Fischer, W. Tromm, D. Bottomley, F. Defoort, and V. V. Gusarov, "Phase diagram of the ZrO_2-FeO system," *J. Nucl. Mater.*, vol. 348, no. 1-2, pp. 114-121, 2006.

[38] D. F. Carroll, "The system PuO_2-ZrO_2," *J. Am. Ceram. Soc.*, vol. 46, no. 4, pp. 194–195, 1963.

[39] P. G. Mardon, D. J. Hodkin, and J. T. Dalton, "Some observation on the Pu-Zr-O system," *J. Nucl. Mater.*, vol. 32, pp. 126–134, 1969.

[40] T. Albiol, H. Serizawa, and A. Yasuo, "Studies in the PuO_2-ZrO_2 Pseudo-binary Phase Diagram," *J. Nucl. Sci. Technol.*, vol. sup3, pp. 834–837, 2002.

[41] C. Guéneau, N. Dupin, B. Sundman, C. Martial, J. C. Dumas, S. Gossé, S. Chatain, F. De Bruycker, D. Manara, and R. J. M. Konings, "Thermodynamic modelling of advanced oxide and carbide nuclear fuels: Description of the U-Pu-O-C systems," *J. Nucl. Mater.*, vol. 419, no. 1–3, pp. 145–167, 2011.

[42] D. Manara, R. Böhler, K. Boboridis, L. Capriotti, A. Quaini, L. Luzzi, F. De Bruycker, C. Guéneau, N. Dupin, and R. Konings, "The Melting Behaviour of Oxide Nuclear Fuels: Effects of the Oxygen Potential Studied by Laser Heating," *Procedia Chem.*, vol. 7, pp. 505–512, 2012.

[43] P. Hofmann, S. Hagen, G. Schanz, and A. Skokan, "Chemical interaction of reactor core materials up to very high temperature," Kernforschungszentrum Karlsruhe, Report no. KfK 4485, 1984.

[44] V. I. Almjashev, M. Barrachin, S. Bechta, D. Bottomley, F. Defoort, M. Fischer, and E. Al., "Eutectic crystallization in the $FeO_{1.5}$-UO_{2+x}-ZrO_2 system," *J. Nucl. Mater.*, vol. 389, pp. 52-56, 2009.

[45] V. I. Almjashev, M. Barrachin, S. Bechta, D. Bottomley, F. Defoort, M. Fischer, and E. Al., "Phase equilibria in the FeO_{1+x}-UO_2-ZrO_2 system in the FeO_{1+x} enriched domain," *J. Nucl. Mater.*, vol. 400, pp. 119–126, 2010.

[46] V. I. Almjashev, M. Barrachin, S. V. Bechta, D. Bottomley, S. A. Vitol, V. V. Gusarov, F. Defoort, E. V. Krushinov, D. B. Lopukh, A. V. Lysenko, A. P. Martynov, L. P. Mezentseva, A. Miassoedov, Y. B. Petrov, M. Fischer, V. B. Khabensky, and S. Hellmann, "Ternary eutectics in the systems FeO-UO_2-ZrO_2 and Fe_2O_3-U_3O_8-ZrO_2," *Radiochemistry*, vol. 53, no. 1, pp. 13-18, 2011.

[47] T. Uchida, S. Hirooka, H. Sugata, K. Shibata, D. Sato, M. Kato, and K. Morimoto, "Melting Temperature of the ZrO_2-MOX System," *GLOBAL 2013, Salt Lake City, Utah, Sept. 29-October 3, 2013*, pp. 1549–1553, 2013.

[48] K. Minato, W. Hering, and S. Hagen, "Zircaloy Oxidation and Cladding Deformation in PWR-Specific CORA Experiments", Kernforschungszentrum Karlsruhe, Report no. KfK 4827, 1991.

[49] S. V. Bechta, V. B. Khabensky, S. A. Vitol, E. V. Krushinov, D. B. Lopukh, Y. B. Petrov, A. Y. Petchenkov, I. V. Kulagin, V. S. Granovsky, S. V. Kovtunova, V. V. Martinov, and V. V. Gusarov, "Experimental studies of oxidic molten corium-vessel steel interaction," *Nucl. Eng. Des.*, vol. 210, no. 1-3, pp. 193-224, 2001.

[50] B. R. Sehgal and B. W. Spencer, "ACE Program Phase D: Melt Attack and Coolability Experiments (MACE) Program," in *Second OECD (NEA) Specialist Meeting on Molten Core Debris-Concrete Interaction*, 1992, pp. 345–356.

[51] B. W. Spencer, M. T. Farmer, D. R. Armstrong, D. J. Kilsdonk, and E. Al., "Results of MACE test M0 and M1," in *Second OECD (NEA) Specialist Meeting on Molten Core Debris-Concrete Interaction*, 1992, pp. 357–373.

[52] I. Huhtiniemi, D. Magallon, and H. Hohmann, "Results of recent KROTOS FCI tests: alumina versus corium melts," *Nucl. Eng. Des.*, vol. 189, no. 1-3, pp. 379-389, 1999.

[53] W. Steinwarz and M. Sappok, "Large-scale experiments on ex-vessel core melt behavior," *Nucl. Technol.*, vol. 125, pp. 363–370, 1999.

[54] M. T. Farmer, S. Lomperski, D. J. Kilsdonk, and R. W. Aeschlimann, "OECD MCCI Project 2D Core Concrete Interaction (CCI) Tests: Final Report," 2006.

[55] T. Sevon, T. Kinnunen, J. Virta, S. Holmstrom, T. Kekki, and I. Lindholm, "HECLA experiments on interaction between metallic melt and hematite-containing concrete," *Nucl. Eng. Des.*, vol. 240, pp. 3586–3593, 2010.

[56] C. Journeau, F. Sudreau, S. Magne, and G. Cognet, "Physico-chemical analyses and solidification path reconstruction of multi-component oxidic spread melts," *Mater. Sci. Eng. A*, vol. 299, pp. 249–266, 2001.

[57] C. Journeau, J.-F. Piluso, P.Haquet, S. Saretta, E. Boccaccio, and J.-M. Bonnet, "Oxide-Metal Corium-Concrete Interaction Test in the VULCANO Facility," in *Proceeding of ICAAP 2007*, 2007, paper 7328.

[58] C. Journeau, P. Piluso, P. Correggio, L. Ferry, G. Fritz, J.-F. Haquet et al.., "Contribution of the VULCANO experimental programme to the understanding of the MCCI phenomena," *Nucl. Eng. Des.*, vol. 44, no. 3, pp. 261–272, 2012.

Chapter 3 – Thermodynamics of the in-vessel corium: experimental study

During a severe accident the molten core can easily overcome 2300 K leading to the formation of a mixture of solid and liquid phases called in-vessel corium. In the first two chapters, the importance of thermodynamics of the in-vessel corium and a lack of experimental data has been highlighted.

In this chapter the investigation of the prototypic U-Pu-Zr-Fe-O in-vessel corium system is presented.

The methodology applied during the thesis is first presented. It is based on the CALPHAD method that allows deriving the thermodynamic functions of a given system starting from a critical selection of significant experimental data.

The second part of the chapter is dedicated to the experimental results obtained on the O-U-Zr, Fe-O-Zr, Fe-O-U-Zr and PuO_2-UO_2-ZrO_2 sub-systems.

The thermodynamic modelling on the aforementioned prototypic in-vessel corium system and the thermodynamic calculations for interpreting the experimental results will be presented in the next Chapter.

3.1 Methodology

As already introduced in Chapter 1, the objective of this thesis is contributing to the amelioration of the thermodynamic description of the in-vessel and ex-vessel corium systems.

During the present study the CALPHAD approach has been used to investigate the in-vessel corium system.

Kaufman and Bernstein [1] in the 1970s summarized the features of the calculation of phase diagrams leading to the foundation of the CALPHAD method [2] [3].

CALPHAD, which stands for **Cal**culation of **pha**se **d**iagrams, is a method of deriving the thermodynamic functions of a system using critically evaluated and selected experimental data from literature. If these data are not sufficient, new experimental results should be obtained.

Figure 1 shows schematically the concept behind the CALPHAD method. In thermodynamics, the configuration of any system that possesses a lower Gibbs energy is more stable than the one with higher energy. Therefore, the knowledge of the Gibbs energy expressions of all phases as a function of the composition in the system as function of temperature, composition and pressure is necessary to calculate the equilibrium of the system in a given stable state (for a given number of moles of constituents, temperature and pressure) and its phase diagram. This is done by minimisation of the total Gibbs energy of the system. The Gibbs energy functions of the phases are assessed by optimising the adjustable model parameters in order to achieve the best possible fit between the calculation and the experimental results (phase diagram and thermodynamic data).

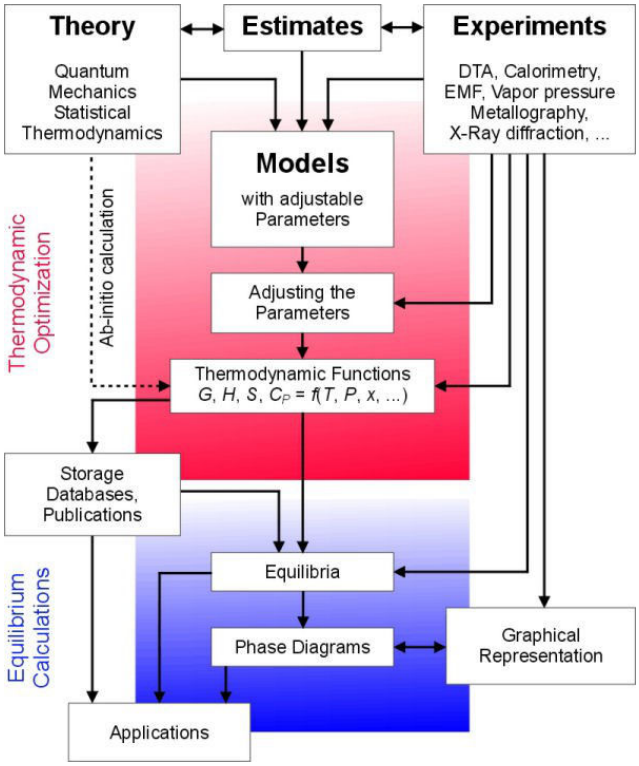

Figure 1: Graphical representation of the CALPHAD approach.

The thermodynamic assessment and the thermodynamic calculation presented in this work have been performed using the Thermo-Calc software [4].

The strength of the CALPHAD method lies in allowing the prediction of higher order system behaviour by extrapolation from lower order systems, namely its sub-systems (mainly binary and ternary systems).

After a critical analysis of the existent literature data, an experimental campaign was started on significant in-vessel corium sub-systems. Significant literature data together with the novel experimental results obtained in this work have been used for thermodynamic modelling of the in-vessel corium system.

3.2 Experimental study

The critical review of the literature data presented in Chapter 2 allowed the identification of the in-vessel corium sub-systems for which new experimental data were necessary. In Table 1, a summary of the experiments performed on the in-vessel systems during this thesis is presented.

Investigated system	Experimental technique	Results
O-U-Zr	Heat treatments	Equilibrium phases
	Laser heating	Transition temperatures
Fe-O-Zr	Laser heating	Transition temperatures
Fe-O-U-Zr	Arc furnace fabrication	Equilibrium phases
PuO_2-UO_2-ZrO_2	Laser heating	Transition temperatures

Table 1: Summary of the experiments performed during the present work

3.2.1 O-U-Zr system

The high temperature behaviour of the O-U-Zr system is crucial for the comprehension of the phenomena occurring during a severe accident as a result of the UO_2-Zircaloy interaction. As already shown in Chapter 2, numerous studies have been published on the subject. However, some experimental and modelling discrepancies still exist, especially concerning the extension of the miscibility gap in the liquid phase and the position of the solubility limit of oxygen in the metallic liquid phase. In this framework, two sets of experiments were performed during the present work:

- Heat treatments on four O-U-Zr samples in order to obtain tielines data in the miscibility gap in the liquid phase;
- Laser heating experiments to measure solid/liquid transition temperature of the Zr-rich side of the ternary phase diagram. These experiments have been performed in collaboration with the JRC-ITU (Institute for Transuranium Elements), Germany in the framework of the European Talisman project [5].

3.2.1.1 Heat treatments

Sample preparation

The initial atomic composition of the investigated samples is reported in Figure 2 and Table 2.

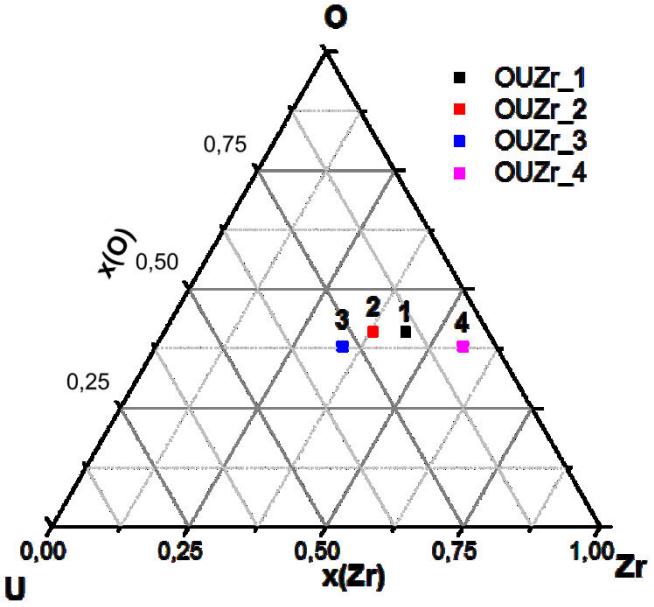

Figure 2: Initial composition of the O-U-Zr samples in the ternary phase diagram

The four samples were prepared starting from metallic U (CEA supply), metallic Zr (Goodfellow, purity 99.8 %) and ZrO_2 powder (Goodfellow, purity 99.9 %). M. Tabarant at the LISL (Laboratoire d'Ingénierie des Surfaces et Lasers), CEA Saclay performed a chemical analysis on the starting materials in order to check the impurities content by inductively coupled plasma mass spectrometry (ICP-MS). The results are reported in Table 1 in Appendix E.

Sample	at% O	at% U	at% Zr	total mass / g
OUZr_1	41	15	44	2.2447
OUZr_2	41	21	38	2.9771
OUZr_3	38	28	34	3.6675
OUZr_4	38	6	56	3.0928

Table 2: Initial composition of the five heat-treated O-U-Zr samples

Heat treatment conditions

The heat treatments were performed in a W-resistor heated furnace (Figure 3). This furnace is employed for high temperature mass spectrometer measurements [7].

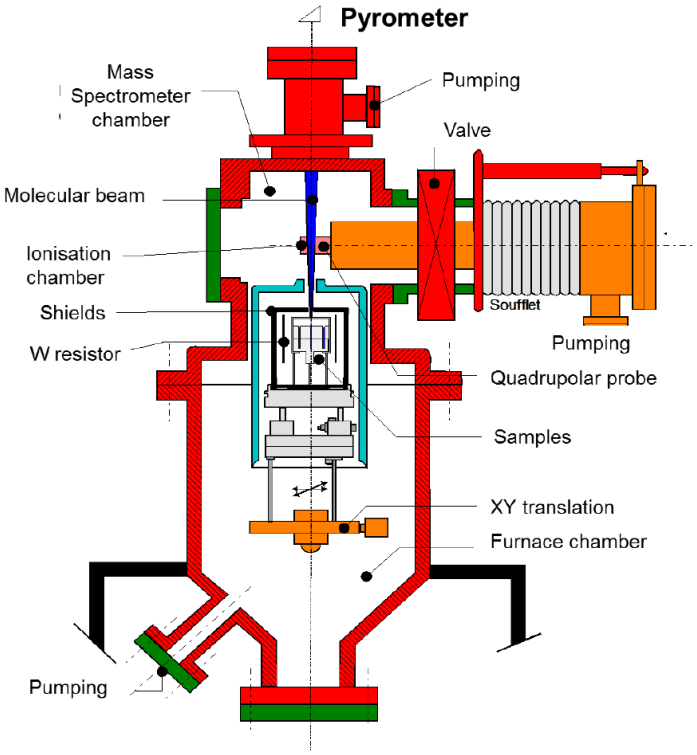

Figure 3: Scheme of the furnace employed for the heat treatments

The heat treatments were performed under secondary vacuum ($p = 10^{-7}$ Pa). The samples were prepared in W-Knudsen cells lodged in a Ta cells holder. A schematic view of the Ta holder and of the W effusion cells is reported in Figure 4.

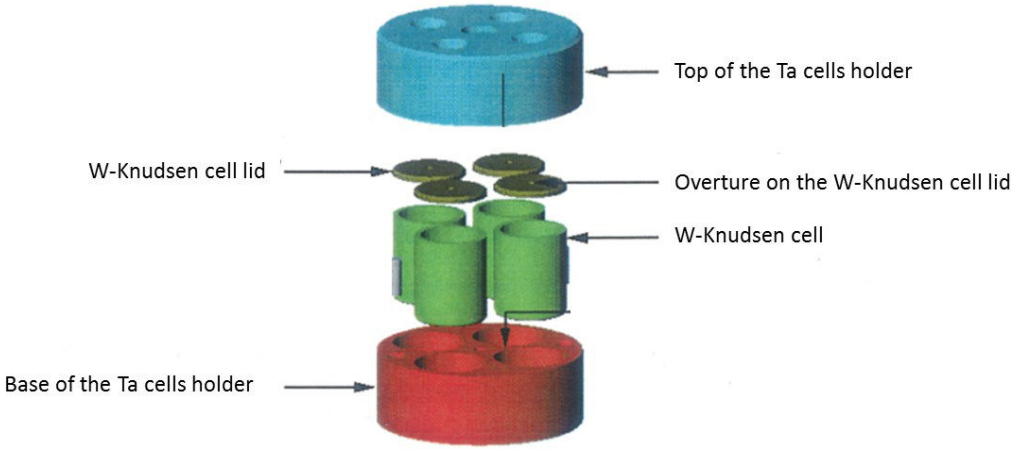

Figure 4: Exploded view of the Ta cells holder and the W cells and lids [7]

The ratio between the height of the cell and the overture on the lid of the Knudsen cells is greater than 10: the Knudsen cells can be then considered as black bodies (see Appendix A).

The temperature was monitored by a calibrated two-channel pyrometer (IMPAC ISR-900). The active area measured by the pyrometer is bigger than the Knudsen cell overture. In fact, the pyrometer looks only partially at the Ta cells holder. A further calibration of the pyrometer was performed to correct the changes with temperature of the Ta holder emissivity. The melting temperatures of Ag (1234.93 K) and Fe (1811 K) as well as the eutectic temperature of the C-Ru system (2226 K) have been measured. The resulting calibration line is reported in Figure 5.

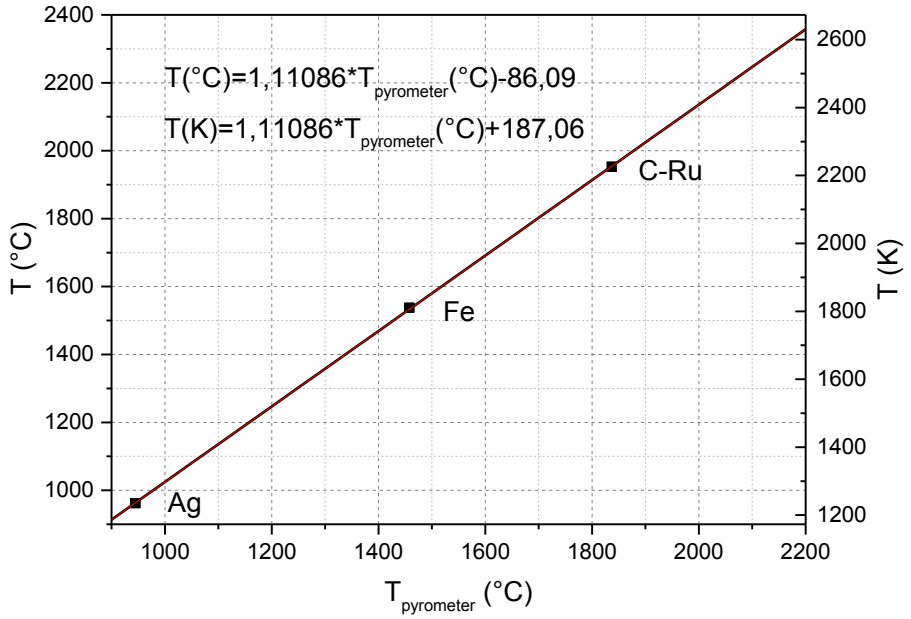

Figure 5: Calibration curve of the pyrometer used for the measurement of furnace temperature

The emissivity of Ta is function of the wavelength and of the temperature. A two-channel pyrometer measures in reality the ratio between the signals corresponding to the radiances at the two selected wavelengths. If the ratio between the emissivity at the two wavelengths is not equal to unity, a correcting factor must be selected and entered in the pyrometer controlling software. The calibration obtained during the present work is a rigorous procedure of correction for the emissivity ratio without passing through a manual software correction. **It must be pointed out that the present calibration is valid only for Ta cells holders**: if another material is employed, a corresponding calibration must be performed.

The heat treatments performed on the O-U-Zr samples are reported in Table 3.

Samples	Temperature / K	Duration / minutes
OUZr_1,2,3,4	2567±26	45

Table 3: Scheduled heat treatment performed on O-U-Zr samples. The reported uncertainties on the heat treatment temperatures are given by the pyrometer constructor (1% above 2273 K)

After the heat treatment conditions, the samples were cooled at 3 K/s. This cooling rate is the fastest that can be attained with the present experimental setup. Due to the high temperatures reached during the heat treatments, an interaction between the sample and the W-crucible was inevitable. Politis [8] and Baichi [7] showed that above 2273 , W in contact with a (O,U,Zr) liquid forms the W_2Zr compound. This phenomenon will be discussed in the following Sections.

Sample characterisation

After the heat treatments, the samples were analysed at the LMAC (Laboratoire Métallographie et Analyse Chimique), CEA Marcoule. For the characterisation a Carl Zeiss Merlin scanning electron microscope equipped with a Field Emission Gun (SEM-FEG) was used. It is coupled with energy dispersion spectroscopy (EDS, Oxford Instruments X-MAX 80 mm^2) and a wavelength-dispersive X-ray spectroscope (WDS, SX 100 CAMECA). The standards used for the analyses were:

- UO_2 for uranium and oxygen;
- Metallic Zr for zirconium.

The choice to use UO_2 as standard for both metallic and oxidised U may lead to significant errors on the estimation of U-content metallic phases. The overall compositions of the annealed samples as well as the local compositions of the observed phases were measured.

Concerning the samples investigated by laser heating, the post-experiment analyses were performed at ITU using a Philips XL40 SEM.

The mass fraction of the observed phases will be estimated by using ImageJ, image-processing software. Starting from the surface occupation of a back-scattering electrons image, the volumetric fraction of the phase is derived. The mass fraction can be then directly obtained knowing the density of the observed phases.

Sample OUZr_1

A back scattering electrons (BSE) image of the cross section of the solidified sample OUZr_1 is reported in Figure 6.

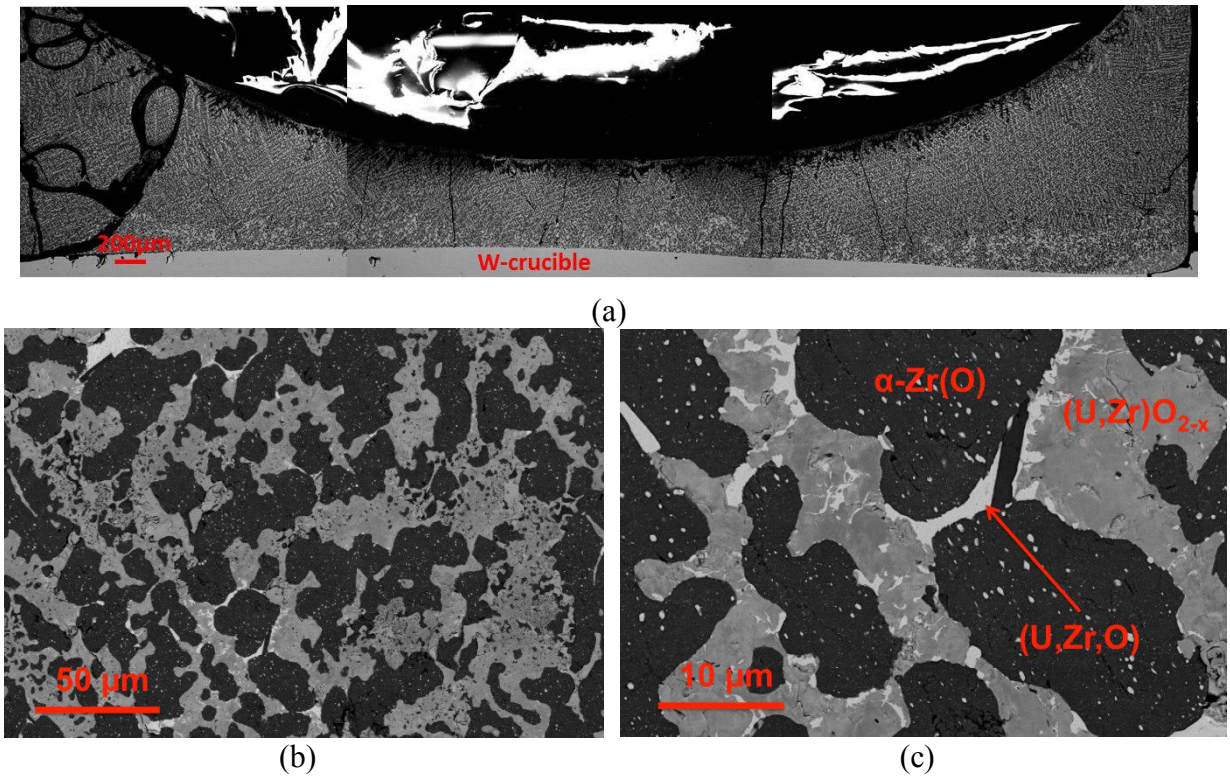

Figure 6: (a) Back-scattering electrons image of the cross section of sample OUZr_1; (b) Magnification of the dendritic structure; (c) Particular on the three identified phases, $(U,Zr)O_{2-x}$, α-(Zr,U)(O) and solidified ternary (U,Zr,O) liquid

A homogeneous dendritic microstructure (black phase) is observed. This microstructure is typical of a rapidly cooled single-phase liquid. Due to the extreme temperature conditions reached during the heat treatment, the liquid alloy penetrated within the grain boundaries of the W-crucible. This phenomenon leads to mechanical constraints which in turn lead to the detachment of some W grains at liquid/crucible interface. Figure 7 shows a magnification of the cross section close to the sample/crucible interface. EDS and WDS analyses revealed that the detached W particle has partially reacted with the liquid alloy leading to the formation of a W_2Zr ring that surrounds the intact W sphere.

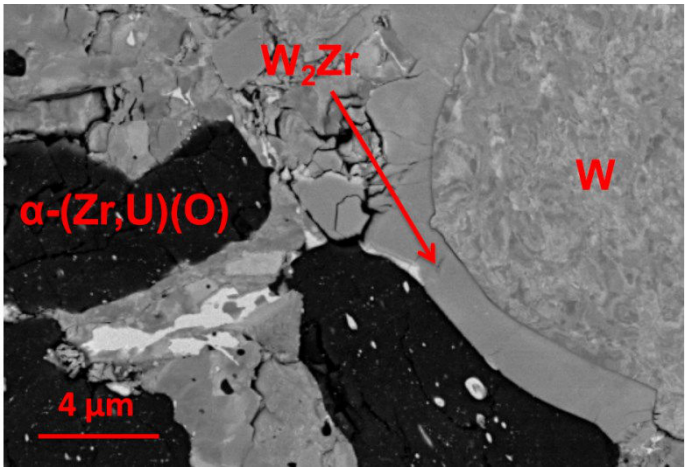

Figure 7: Magnification of the sample OUZr_1 close to the sample-crucible interface. The phases reported in the figure were identified by EDS analysis

Maurizi [9] argued that at high temperature, the solid W can be partially dissolved by the liquid (O,U,Zr) sample. The fact that the melting temperature of W_2Zr compound (T=2428 K) is lower than the experimental annealing temperature (T=2567±26 K) allows to conclude that the formation of W_2Zr at W/liquid interface occurs during cooling of the sample by peritectic reaction at 2428 K: $[W+(Zr)_{liq}] \rightarrow W_2Zr$. This reaction leads to the formation of a W_2Zr ring that surrounds the W particle. The formation of the W_2Zr compound removes part of the Zr from the O-U-Zr ternary equilibrium. Therefore, a correction was applied to the measured EDS composition to exclude the W contribution as well as the contribution coming from the Zr reacted to form the W_2Zr precipitates. It is considered that only a fraction of the W reacted with the Zr forming W_2Zr. The mass fraction of Zr is corrected as follows:

$$w(Zr)_{corr} = w(Zr) - \left(f \cdot w(W) \cdot \frac{M(Zr)}{2\,M(W)} \right) \quad (1)$$

where *w(Zr)* and *w(W)* are the measured mass fraction of Zr and W respectively, *M(Zr)* and *M(W)* stand for the molar mass of Zr and W, and *f* is the estimated fraction of W forming W_2Zr using image processing software ImageJ®.EDS analyses on the rest of the sample revealed negligible amount of W.

EDS analysis showed that the final global composition of OUZr_1 sample (i.e., the composition of the solidified sample measured after the heat treatment) moved within the ternary phase diagram (Figure 8). The evolution of the concentration can be explained by the formation of volatile species $UO_{(g)}$. The calculation of the gas composition in equilibrium with the liquid at the annealing temperature (T=2567±26 K) revealed that the major component was the volatile specie $UO_{(g)}$. After the heat treatment a mass loss of 0.41 g was measured. The comparison between the initial and the final elemental masses of components of the sample (measured by EDS) is reported in Table 4.

	Initial	Final	Δ		$UO_{(g)}$	
Mass / g	2.2447	1.8347	0.4100		Mass / g	0.4100
m(O) / g	0.1787	0.1500	0.0290		m(O) / g	0.0260
m(U) / g	0.9650	0.5850	0.3800		m(U) / g	0.3840
m(Zr) / g	1.1000	1.1000	0.0000			

Table 4: Comparison between the mass loss of the sample after the heat treatment and the elemental mass of UO specie. The elemental mass losses are comparable, meaning that $UO_{(g)}$ is the major cause of composition shift. The mass of U, Zr and O after the heat treatment (column "Final") is calculated starting from mass fractions measured by EDS

The elemental mass composition of the $UO_{(g)}$ species is in good agreement with the calculated U and O mass losses from the sample. The mass of Zr did not change.

It may be noted in Figure 8 that a practically straight line can be drawn to indicate the evolution of liquid phase composition starting from the UO species on the binary O-U side of the ternary phase diagram and passing by the initial composition and the final composition of the sample.

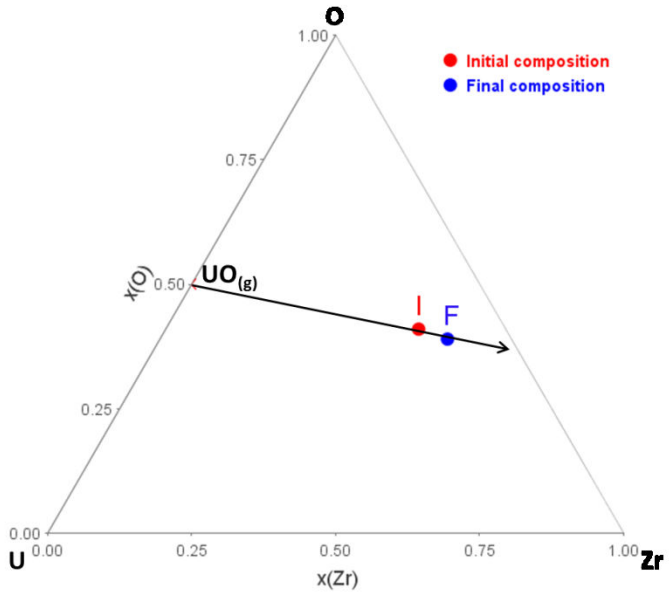

Figure 8: Schematic representation of the effect of the $UO_{(g)}$ species volatilisation during the heat treatment. "I" stays for the initial composition of the sample, while "F" stays for the measured composition of the solidified sample, representative of the final liquid composition

It can be concluded that the main actor for non-negligible mass losses was the $UO_{(g)}$ volatile specie.

Figure 9a shows a magnification of the microstructure of sample OUZr_1, corresponding to the regions of the sample not affected by the presence of W. Three main phases can be observed, and EDS and WDS analyses allowed indexing them as:

- Light grey phase: a mixed oxide $(U_{85.7}Zr_{14.3})O_{1.81}$;
- Dark grey phase: α-(Zr,U)(O), which is an oxygen saturated Zr phase containing a small amount of U;
- White phase: solidified ternary (U,Zr,O) liquid enriched in U.

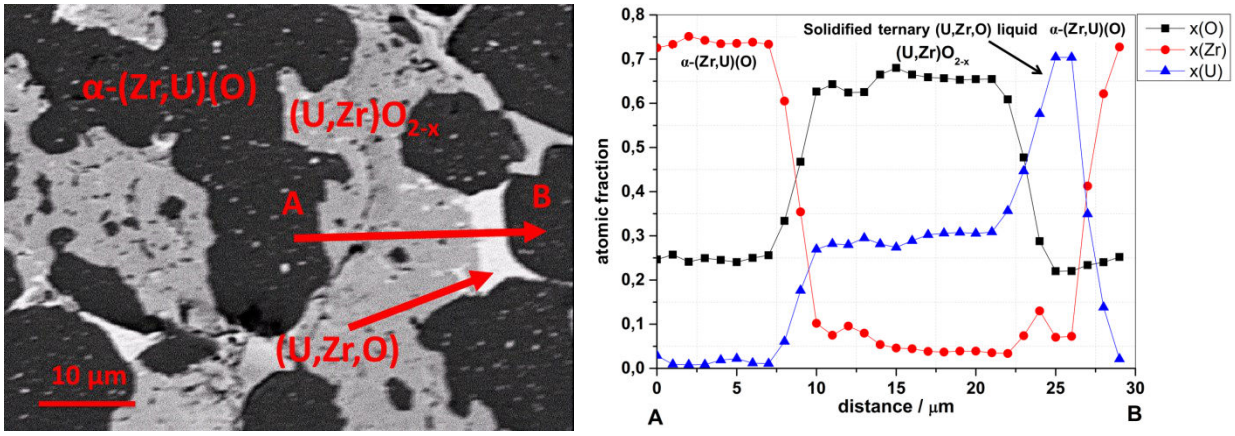

a) b)

Figure 9: BSE-SEM image of sample OUZr_1. The red arrow represents the line analysed by WDS analysis reported in Figure 5b (black squares=at% O; red circles=at% Zr; blue triangles=at% U). Three phases can be identified: a mixed oxide $(U,Zr)O_{2-x}$ (light grey phase), α-Zr(O) (dark grey phase) and a solidified ternary (U,Zr,O) liquid phase

The initial and final composition of sample OUZr_1 as well as the composition of the phases described above is reported in Table 5.

	Initial OUZr_1	**Final OUZr_1**	**$(U,Zr)O_{2-x}$**	**α-(Zr,U)(O)**	**(U,Zr,O) liquid**
at% O	41.0	39.1±1.4	64.4±0.8	25.1±1.7	33.1±2.6
at% U	15.0	10.2±0.3	30.5±0.1	2.0±0.2	63.9±0.1
at% Zr	44.0	50.7±0.8	5.1±2.1	72.9±0.5	2.6±1.0

Table 5: Initial and final composition of sample OUZr_1. The measured composition of the three phases observed in Figure 5 representative of the equilibrium phases at the heat treatment temperature are also reported. The data are reported in atomic fraction of O, U and Zr. A cover factor k=2 was applied to the uncertainties

The oxygen content in the fcc mixed oxide seems to be underestimated (O/(U+Zr)=1.81). The oxygen content in the ternary solidified (U,Zr,O) liquid is overestimated. Surface contamination and the presence of O-rich phases in the surroundings may have affected the WDS results. Furthermore, the composition of this phase was measured using UO_2 as a standard for U and O. This may also lead to errors in the O-content and U-content estimation. Considering the chemical contrast and the position of the final composition of the sample in the O-U-Zr ternary phase diagram, it can be concluded that the latter phase is a (U,Zr) alloy enriched in U. This point will be discussed in details in Chapter 4.

Sample OUZr_2

The microstructure observed on the cross-section of the solidified OUZr_2 sample is reported in Figure 10.

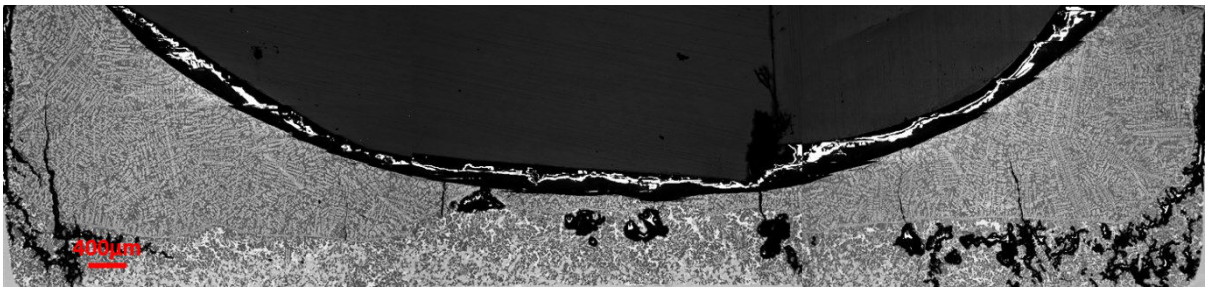

Figure 10: BSE-SEM image of the cross section of sample OUZr_2

The presence of a sharp separation between two regions of the sample can be seen more clearly in Figure 11.

EDS analysis revealed that the upper region was enriched in oxygen (oxide region), whilst the lower zone was enriched in metallic component (metallic region). **This particular configuration is typical of two cooled immiscible liquids, one oxide and one metallic: the existence of a miscibility gap at the liquid state at 2567 K was then inferred**. The two liquids are stratified because of the difference in their densities. This result confirm the experimental finds of Juenke & White [10], Politis [8] and Guéneau et al. [11], already reported in Chapter 2. The sharp separation between the two regions suggests that the two immiscible liquids cooled separately. This was possible because the cooling rate was fast enough to allow an independent solidification between the two liquids.

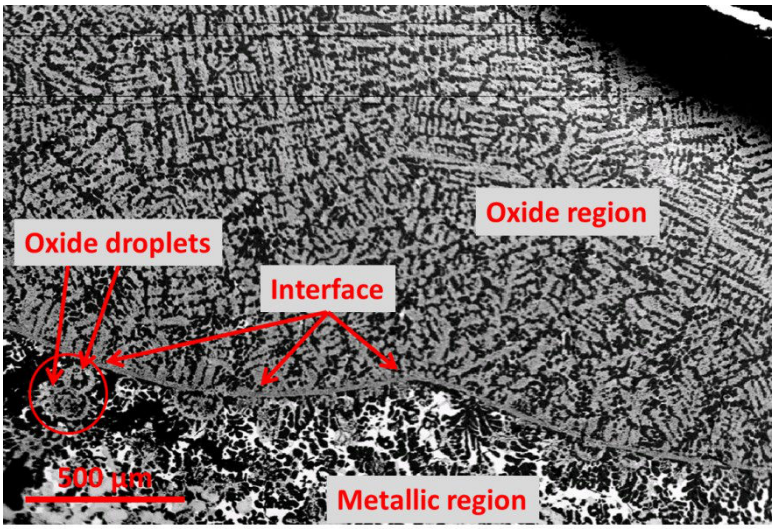

Figure 11: BSE image of sample OUZr_2. Two regions may be distinguished in the solidified sample: the upper region being an oxygen-richer zone (named insofar oxide or oxidic region), the lower region being an oxygen-poorer zone (named insofar metallic region). The red arrows highlight the interface between the oxide and the metallic region

Here also, as for sample OUZr_1, due to the high temperature reached during the annealing, W from the crucible was transported away. The interaction between the sample and W was limited at the metallic region: negligible traces of W were found in the oxidic zone (less than 0.5 at% W). The same consideration made for sample OUZr_1 may be used for the present case. A correction to the EDS analyses was applied in order to neglect the contribution coming from W and from the reacted Zr forming the W_2Zr compound. The composition of the sample after the annealing moved away from the initial one, which is due to the same effect of $UO_{(g)}$ evaporation described above. The global composition of the two quenched liquids is reported in Table 6.

	Initial OUZr_2	**Oxide liquid**	**Metallic liquid**
at% O	41.0	46.0±1.8	30.2±1.2
at% U	21.0	13.9±0.4	16.2±0.4
at% Zr	38.0	40.1±0.8	53.6±0.8

Table 6: Initial composition of sample OUZr_2 and EDS analyses on the oxide and metallic liquids. A cover factor k=2 was applied to the reported uncertainties

The final composition of sample OUZr_2 can be estimated as being on the tie-line between the oxide liquid and the metallic liquid compositions, and imposing that the mass loss during

the experiment was only caused by the departure of the $UO_{(g)}$ volatile species (see discussion for sample OUZr_1).

The measured compositions of the immiscible liquids are fundamental data for the thermodynamic modelling of the O-U-Zr ternary system. As already introduced in Chapter 2, the miscibility gap in the liquid phase of the O-U-Zr system was observed by several authors. However, large uncertainties still exist on its extension in temperature and in composition. Guéneau et al. [11] and Bechta et al. [12] were the only authors reporting the composition of the liquids in equilibrium. In addition, the temperature of co-existence of two immiscible liquids reported by Guéneau et al. is affected by an estimated uncertainty u(T)= ±100 K. In order to confirm previous results and better shape the extension of the miscibility gap across the O-U-Zr ternary phase diagram, the present data will be used in the second part of this Chapter for the thermodynamic modelling.

Figure 12 reports a magnification of the microstructure of the solidified oxide liquid. WDS analysis revealed that during the solidification of the oxide liquid two main phases were formed:

- Light grey phase: mixed oxide $(U_{77.6}Zr_{22.5})O_{1.81}$;
- Dark grey phase: α-(Zr,U)(O) containing a small amount of U.

- White phase: WDS results (atomic composition $U_{60}O_{40}$) are affected by surface oxygen contamination and by the surrounding oxidised phases. It can be concluded that this phase is metallic U with small oxygen content.

Small white precipitates within α-(Zr,U)(O) may be noted in Figure 12. The measured composition is affected by a significant uncertainty because of the small amount and the reduced dimensions of this phase. Furthermore the white precipitates are completely surrounded by a strongly oxidised phase: WDS analyses overestimated the oxygen content of the white phase. However, the chemical contrast suggests that the precipitates should be a uranium-based metallic phase.

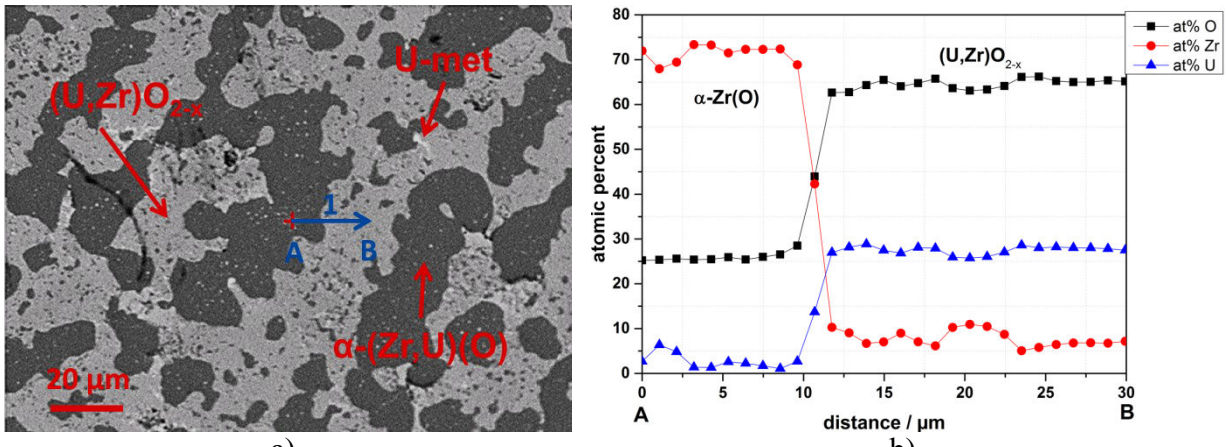

Figure 12: a) BSE-SEM image of the solidified oxide liquid in sample OUZr_2. b) WDS results on the blue arrow (black squares=at% O; red circles=at% Zr; blue triangles=at% U). Two phases were identified: a mixed oxide $(U,Zr)O_{2-x}$ (light grey) and α-(Zr,U)(O) (dark grey)

Within the microstructure of the solidified metallic liquid phase some oxide droplets can be observed (Figure 11). This can be due to the high annealing temperature that causes convective movements in the liquid phases. Local instabilities close to the liquid-liquid interface can drive small amount of the oxide liquid moving to the metallic liquid. Therefore, during solidification the oxide droplets got stuck within the metallic liquid. The U/Zr ratio of

the droplets ($U/Zr_{droplet}$=0.35) is comparable with the U/Zr ratio measured in the solidified oxide liquid ($U/Zr_{oxide\ liquid}$=0.347), confirming the previous interpretation.

Figure 13 reports some maps of a solidified oxide droplet obtained using EDS.The phases observed in the solidified bulk oxide liquid can be also identified within the oxide droplets (i.e., a mixed oxide $(U,Zr)O_{2-x}$, a α-(Zr,U)(O) phase and small precipitated of metallic U). It may be noted that inside the droplet a W_2Zr phase can be also identified. The compositions of the phases formed during cooling of the metallic liquid, the bulk oxide liquid and the oxide droplets are reported in Table 7.

	Oxide liquid			**Metallic liquid**			**Oxide droplets**		
	$(U,Zr)O_{2-x}$	α-(Zr,U)(O)	U-met *	$(U,Zr)O_{2-x}$	α-(Zr,U)(O)	U-met	$(U,Zr)O_{2-x}$	α-(Zr,U)(O)	U-met *
at% O	64.4±1.4	26.0±1.0	38	66.9	26.8±1.0	24	65.6±1.4	26.8±1.0	36
at% U	27.5±0.4	2.7±0.2	62	30.3	2.1±0.2	69	30.5±0.4	2.1±0.2	64
at% Zr	8.0±0.6	71.3±0.8	/	2.8	71.1±0.6	7	3.9±0.6	71.1±0.6	/

Table 7: Composition of the phases formed during solidification of the metallic liquid, the oxide liquid and the oxide droplets. A cover factor k=2 is applied to the reported uncertainties. * U-met represents the white phase that precipitates within the $(U,Zr)O_{2-x}$ and the α-(Zr,U)(O) phases. The reported values have to be treated carefully, since the large amount of oxide phase surrounding the white precipitates (U metallic) could affect the measured oxygen content

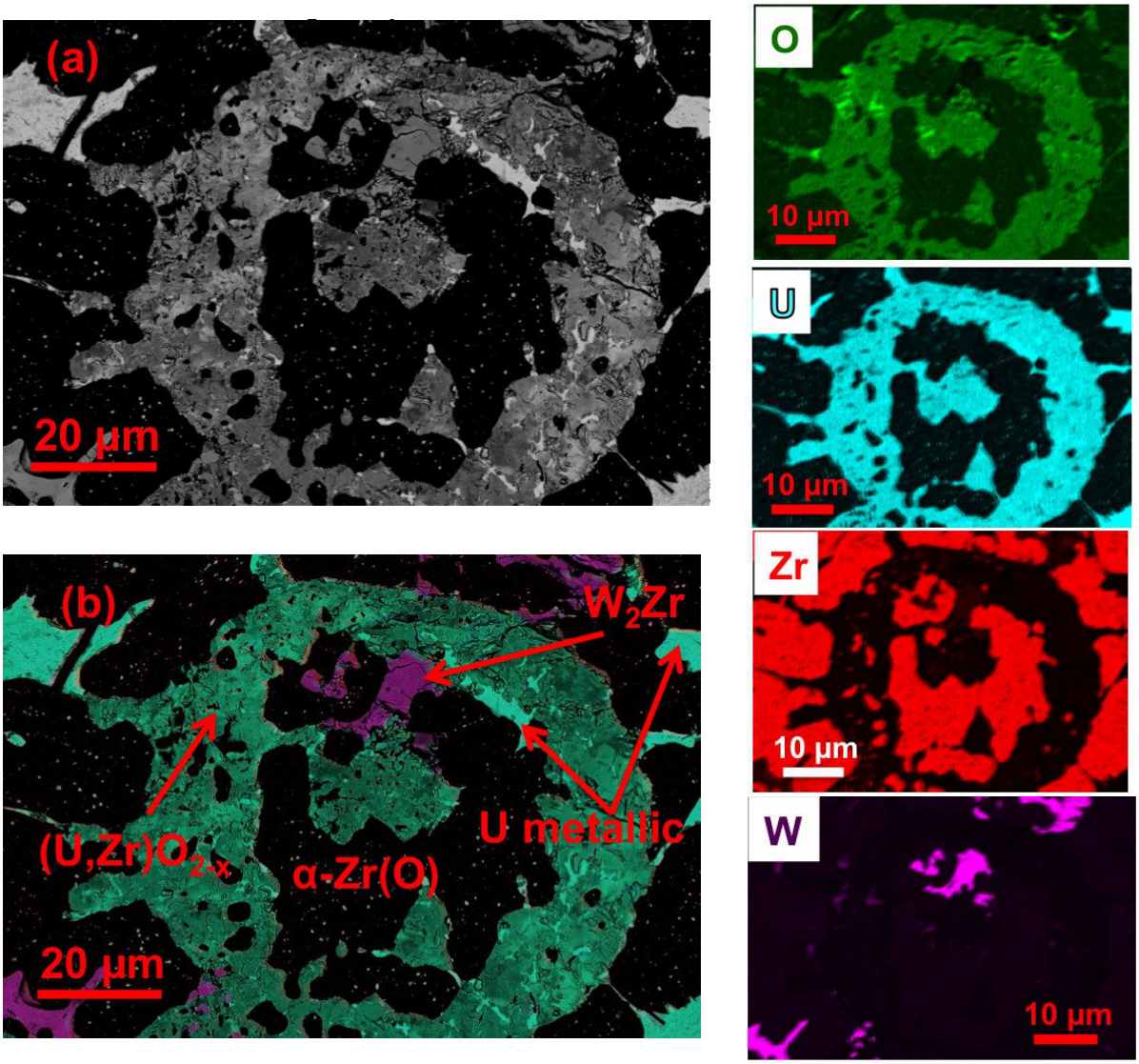

Figure 13: (a) SEM image of a solidified oxide droplet; (b) coloured image obtained superposing the four elemental analyses on the right side of the Figure

Sample OUZr_3

The microstructure of the solidified sample OUZr_3 is shown in Figure 14.

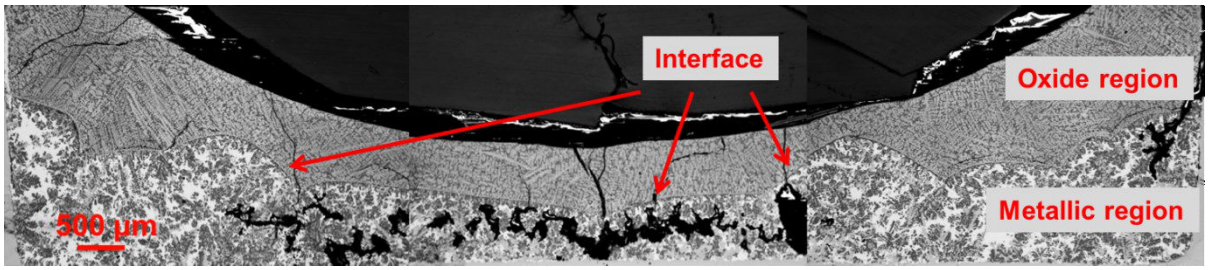

Figure 14: BSE-SEM image of the cross section of the solidified sample OUZr_3

A sharp separation between an upper and a lower microstructure can be observed. EDS allowed identifying the nature of the two structures as for sample OUZr_2. **A miscibility gap between two liquids, one oxide (upper region) and one metallic (lower region) was observed**. It can be noted that the difference in the chemical contrast between the oxide and the metallic solidified liquids in sample OUZr_3 is more evident compared to the one observed in sample OUZr_2.

The composition of the two solidified liquids in reported in Table 8.

	Initial OUZr_3	Oxide liquid	Metallic liquid
at% O	38.0	50.7±1.8	23.6±1.2
at% U	28.0	17.3±0.4	28.0±0.4
at% Zr	34.0	32.0±0.8	48.4±0.8

Table 8: Initial composition of sample OUZr_3 and EDS analyses on the oxide and metallic liquids. A cover factor k=2 was applied to the reported uncertainties

Within the metallic region, some solidified oxide droplets are identified. As for sample OUZr_2, convective movements drove a small fraction of the lighter oxide liquid to move towards the metallic liquid. During solidification the oxide liquid droplets remained trapped within the metallic liquid, forming the observed spherical structures (Figure 15 and Table 9).

A fraction of W was transported away from the crucible. The W contamination is evident in the solidified metallic liquid (about 5 at% W), whilst it can be considered negligible for the oxide liquid (less than 0.5 at% W). The same correction applied previously is applied for the present sample.

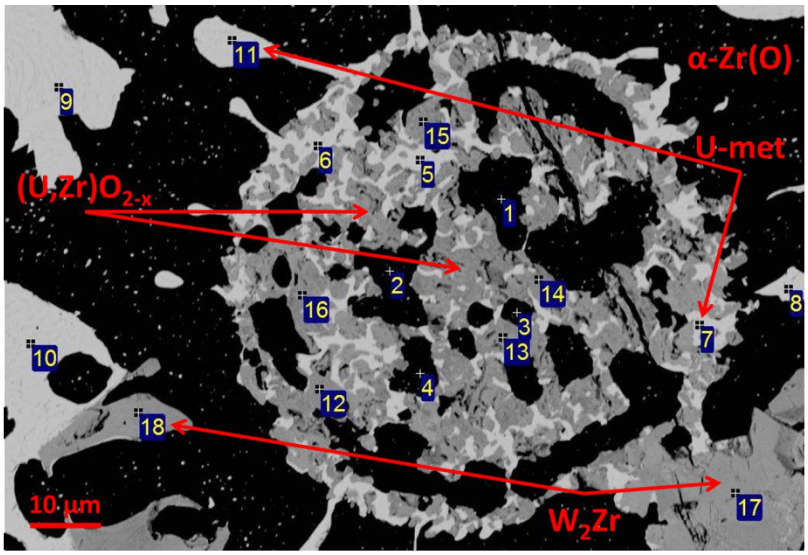

Figure 15: Oxide droplet solidified within the quenched metallic liquid. The EDS results on the reported spectra (1-18) are presented in Table 9.

Spectrum	1	2	3	4	5	6	7	8	9
at% O	25.9	26.9	26.6	26.2	21.5	21.5	21.7	21.7	20.4
at% U	3.4	1.5	2.5	0.8	78.5	78.5	78.3	78.3	74.8
at% Zr	70.7	71.6	70.9	73.0	/	/	/	/	4.8
at% W	/	/	/	/	/	/	/	/	/
Phase	α-(Zr,U)(O)	α-(Zr,U)(O)	α-(Zr,U)(O)	α-(Zr,U)(O)	U-met	U-met	U-met	U-met	U-met

Spectrum	10	11	12	13	14	15	16	17	18
at% O	18.8	21.2	/	65.3	66.2	65.5	66.0	/	/
at% U	81.2	78.8	/	30.6	31.1	30.1	30.7	/	/
at% Zr	/	/	34.8	4.1	2.7	4.4	3.3	34.6	34.5
at% W	/	/	65.2	/	/	/	/	34.8	65.2
Phase	U-met	U-met	W_2Zr	$(U,Zr)O_{2-x}$	$(U,Zr)O_{2-x}$	$(U,Zr)O_{2-x}$	$(U,Zr)O_{2-x}$	W_2Zr	W_2Zr

Table 9: EDS results on the solidified oxide droplet in Figure 12

EDS and WDS analyses showed that within the solidified oxide liquid, three phases might be identified (see Figure 16a):

- Light grey phase: mixed oxide $(U_{87}Zr_{13})O_{1.95}$;
- Dark grey phase: α-(Zr,U)(O).
- White precipitates: metallic U.

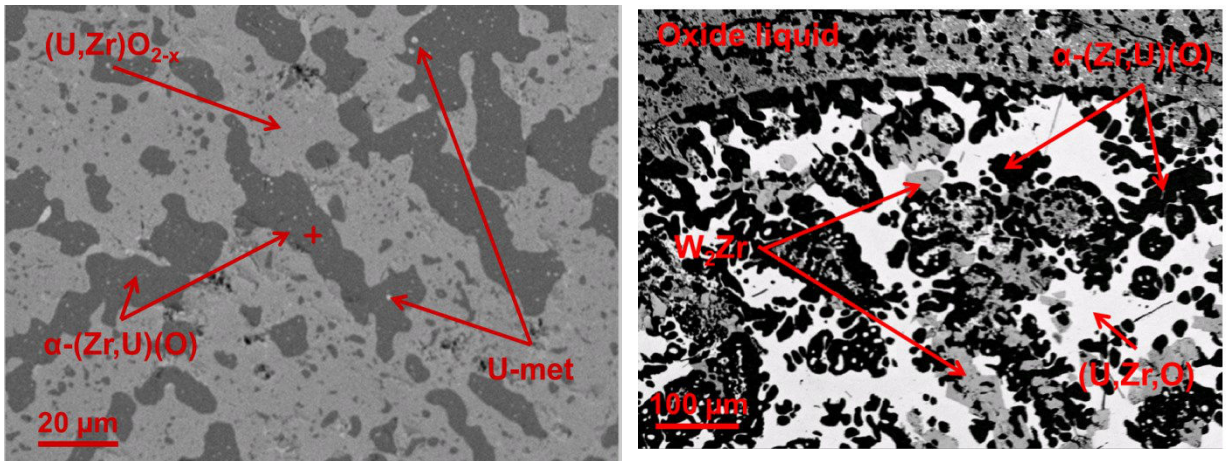

(a) (b)

Figure 16: SEM images of sample OUZr_3. (a) Solidified oxide liquid; (b) solidified metallic liquid

In Figure 16b the microstructure of the solidified metallic liquid is shown. A large amount a U-enriched metallic phase can be seen (i.e., the white phase). The black phase is the α-(Zr,U)(O). It may be also noted that W_2Zr (grey phase in Figure 16b) was found in the solidified metallic liquid.

The compositions of different phases detected in solidified oxide liquid, metallic liquid and oxide droplets are reported in Table 10.

	Oxide liquid			**Metallic liquid**			**Oxide droplets**		
	$(U,Zr)O_{2-x}$	α-(Zr,U)(O)	U-met	$(U,Zr)O_{2-x}$	α-(Zr,U)(O)	(U,Zr,O)	$(U,Zr)O_{2-x}$	α-(Zr,U)(O)	U-met
at% O	66.0±1.6	26.1±1.4	20±2	66.4	26.8±1.0	11±2	65.8±1.4	26.4±1.2	21±2
at% U	29.6±0.4	2.9±0.2	80±2	30.3	2.1±0.2	84±2	30.6±0.4	2.1±0.2	78±2
at% Zr	4.4±0.6	71.0±0.8	/	3.3	71.1±0.6	5±2	3.6±0.6	71.5±1.0	1±1

Table 10: Composition of the phases formed during solidification of the metallic liquid, the oxide liquid and the oxide droplets. A cover factor k=2 is applied to the reported uncertainties. An estimated uncertainties of ±2 is applied to the U-met and (U,Zr,O) results.

The fact that WDS analyses revealed the existence of a metallic phase with composition of about $U_{80}O_{20}$ is in contradiction with the U-O phase diagram (see Figure 12 in Appendix B) in which no such compound is calculated. This is a further confirmation that the choice of the standards for WDS analysis is crucial for the good estimation of phase composition. It can be concluded that this metallic phase is metallic U, with a small solubility of Zr (less than 5 at%).

Sample OUZr_4

The solidified microstructure of sample OUZr_4 is shown in Figure 17.

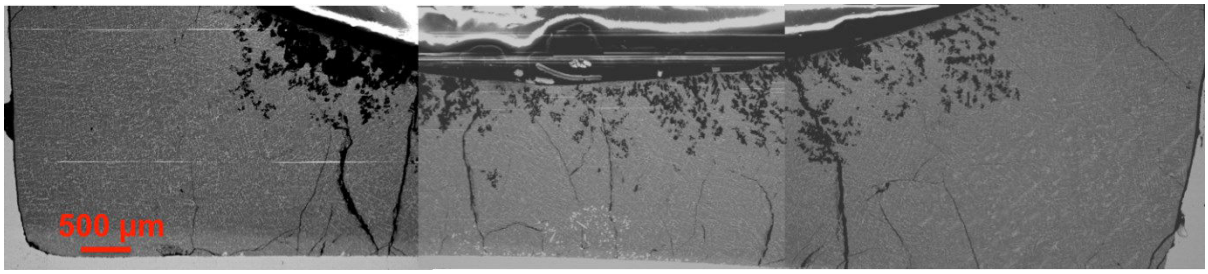

Figure 17: BSE-SEM image of the cross section of the solidified sample OUZr_4

The homogenous dendritic structure suggests that the sample, at the annealing temperature, was a single liquid phase. Only a negligible amount of W was transported away from the W effusion cell. Since the present sample had the lowest amount of U, the effect of the evaporation of $UO_{(g)}$ on the solidified composition is limited.

In Figure 18, a magnification of the microstructure of sample OUZr_4 is reported.

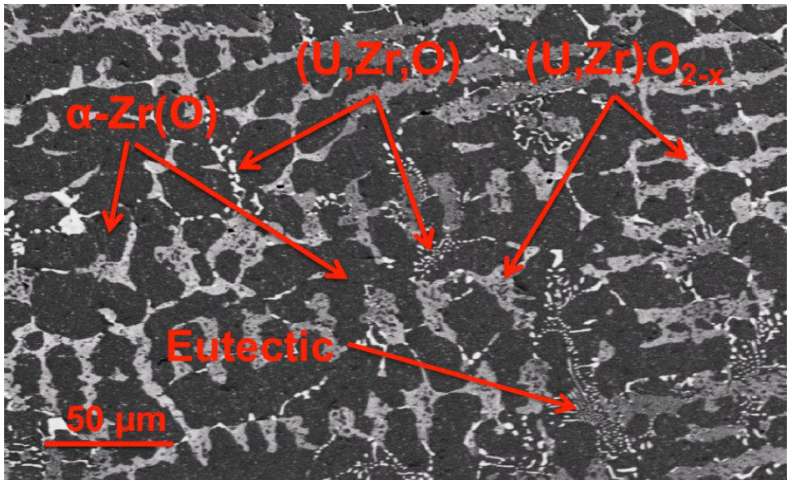

Figure 18: Magnification of the microstructure of sample OUZr_4

Thanks to EDS and WDS analyses, three phases can be detected:

- Light grey phase: a mixed oxide $(U_{44.6}Zr_{55.4})O_{1.8}$;
- Dark grey phase: α-Zr(O);
- White phase: solidified ternary (U,Zr,O) liquid.

Post annealing analyses did not reveal the presence of W_2Zr. However, an eutectic structure with a global composition of $U_{1.6}Zr_{58.2}W_{5.8}O_{34.4}$ can be seen.

EDS results on sample OUZr_4 are reported in Table 11.

	Initial OUZr_4	**Final OUZr_4**	**$(U,Zr)O_{2-x}$**	**α-Zr(O)**
at% O	38.0	35.7±1.2	64.2±1.2	26.9±1.4
at% U	6.0	4.8±1.8	16.0±0.4	2.3±0.2
at% Zr	56.0	59.5±0.8	19.8±1.0	70.7±0.2

Table 11: EDS results on sample OUZr_4. A cover factor k=2 was applied to the uncertainties

Summary

The first set of experiments performed on the O-U-Zr system allowed to confirm the existence of a miscibility gap in the liquid phase. Post-experiment examinations on three of the four investigated compositions showed the presence of two liquids, one oxide the other metallic.

Observations on the remaining two samples showed a solidified structure typical of a rapidly cooled monophasic liquid.

The compositions of the two liquids in equilibrium found in the solidified OUZr_2 and OUZr_3 samples were measured by EDS and WDS. These data are fundamental for the thermodynamic modelling of the ternary O-U-Zr system. In fact, the extension in temperature and in composition of the miscibility gap in the liquid phase in the O-U-Zr system is still ambiguous, especially at high temperature.

Experiments performed at temperature above 2000 K are affected by relevant source of uncertainty. Pyrometry is the best option in the present case, because it avoids direct contact between the investigated sample and the instrumentation. However, temperature measurement is normally affected by a relative error of 1 %. The interaction between the sample and the crucible is the other major source of uncertainty. W was the best available solution for the present study. However, more effective solutions exist to minimise the sample/crucible chemical interaction. ThO_2-crucibles are highly refractive and chemically resistant, but their utilisation is not allowed at the CEA Saclay. Another solution might be UO_2-crucible: recently the LM2T was equipped with a set of this type of crucible. Preliminary tests with these crucibles will be performed to verify the validity of this solution.

The observed microstructure and the effect of W will be interpreted using thermodynamic calculation in Section 3.4.1.

3.2.1.2 Laser heating experiments

The second part of the experimental investigation on the O-U-Zr system was performed at the Institute for Transuranium Elements (ITU), Germany in the framework of the TalismAn European project [5]. The laser heating setup installed in the Material Research Unit was used to study the melting behaviour of three O-U-Zr samples in the oxygen-poor region of the phase diagram. This experimental apparatus allows very high temperature studies on a wide set of materials (e.g., carbides [13,14], nitrides [15] and oxides [16,17]) under different atmospheres.

Sample fabrication

The starting materials, Zr Van Arkel (supplied by the LTMEx, CEA Saclay), U metallic (CEA supply) and ZrO_2 powder (see Appendix E), were arc melted using a Edmund Bühler GmbH Compact Arc Melter MAM-1. The advantages of arc melting are the rapidity of the fabrication process and the chemical homogeneity of the melted samples. The fusions were performed under an inert atmosphere (Ar, Messer purity 99.9999%) in order to limit parasitic oxidation. Before the arc melting, three purges were performed to minimise the residual oxygen inside the melting chamber. Before each fusion, an oxygen getter (Zr Van Arkel shavings) was melted. These precautions limited the amount of free oxygen inside the melting chamber. This was verified by measuring the oxygen content of Zr Van Arkel before and after arc-melting. The measure was performed by P.F. Giroux at the LTMEx, CEA Saclay using an HORIBA EMGA-820 oxygen/nitrogen analyser. The results are reported in Table 12.

	O content (ppm)
Zr Van Arkel – before arc melting	32±20
Zr Van Arkel – after arc melting	126±33

Table 12: Parasitic oxidation during arc melting

The oxygen content in the Zr Van Arkel increased by about 100 ppm after the arc-melting. It can then be estimated that during the preparation of the O-U-Zr samples, a maximum gain of 100 ppm of oxygen did affect the final compositions. For each sample, the arc melting was repeated three times in order to ensure the highest level of homogeneity.

The initial compositions of the investigated samples is reported in Table 13 and Figure 19.

Sample	at% O	at% U	at% Zr	mass / g	Δm /g	Δm/m %
OUZr_6	8.2	5.5	86.3	1.2196	0.000 2	0.016
OUZr_7	12.6	10.6	76.8	1.0384	0.0017	0.164
OUZr_8	19.2	15.3	65.5	0.9636	0.0013	0.135

Table 13: Initial composition of the three O-U-Zr samples. Δm stays for the mass loss after the arc-melting. In the three cases the mass loss can be considered negligible

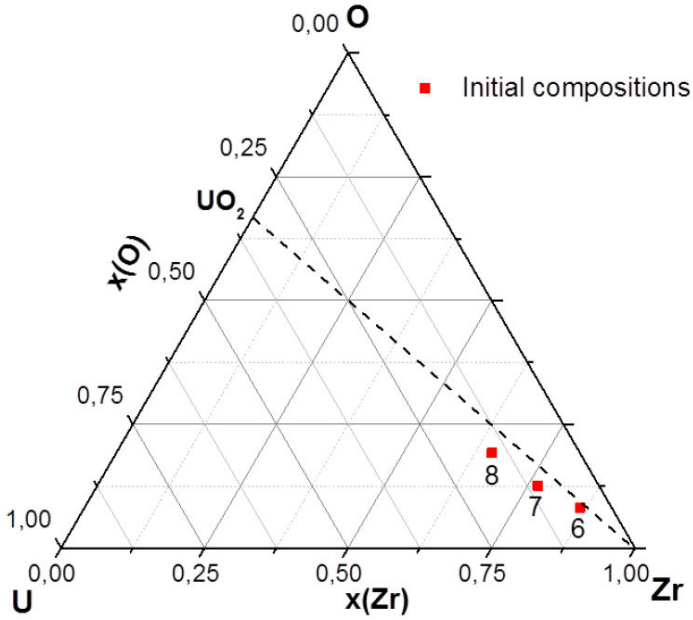

Figure 19: Initial composition of the O-U-Zr samples investigated by laser heating. The samples sit near the UO_2-Zr section

The obtained samples were then cut in two parts.

Laser heating setup

A schematic view of the laser heating experimental setup at ITU is reported in Figure 20.

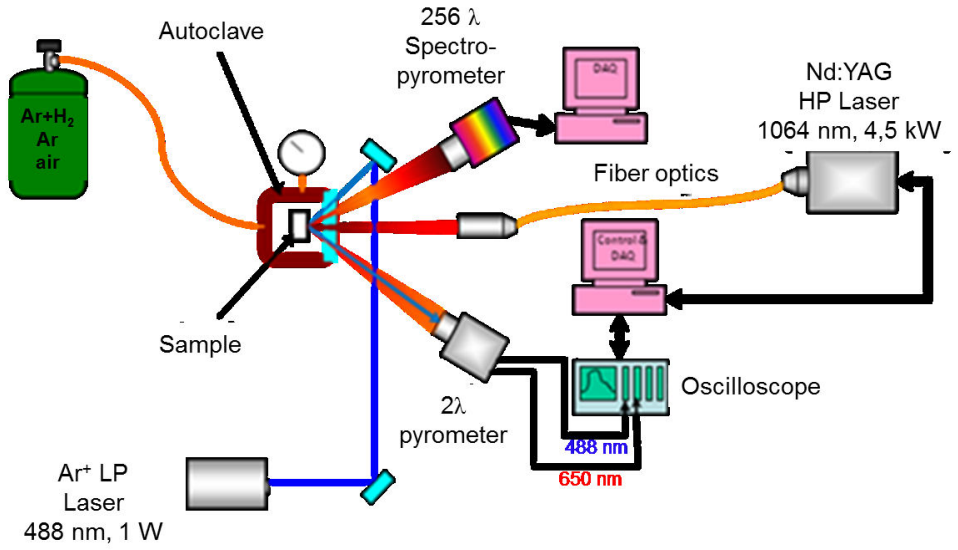

Figure 20: Laser heating apparatus at ITU. The Nd:YAG power laser, the Ar^+-laser and the optical instrumentation look at the surface of the sample through a BK7 window

The sample was held in a pressurised steel vessel under controlled atmosphere. The buffer gas (pressurised at 0.25 MPa) was chosen in order to maintain its composition as close as possible to the initial one during the heating-cooling cycles.

The heating source was a TRUMPF® Nd:YAG continuous-wave laser emitting at 1064.5 nm with a maximum power of 4.5 kW. The power vs. time profile is programmable allowing pulses of different duration and different maximal power.

The temperature at the centre of the heated area was measured with the 650 nm-channel of the fast pyrometer. The pyrometer was calibrated between 1800 and 2500 K using a standard tungsten ribbon lamp, as detailed in [18]. At the same time, a 256-channel spectrometer (integration time of 4 ms), operating in the range 488-1011 nm, was focused on the same spot. The channel operating at 649 nm was calibrated with the same procedure as for the fast pyrometer. The remaining channels were calibrated against a graphite tubular blackbody operating up to 3300 K. The radiance spectra obtained with the spectrometer were then used to calculate the Normal Spectral Emissivity (NSE), $\varepsilon(\lambda,T)$. A detailed description of the optical instrumentation for the temperature monitoring is reported in Appendix A.

The melting transition on the heating stage was detected using the Reflected Light Signal (RLS) method [18]. The reflected light of a continuous wave Ar^+ probe laser emitting at 488 nm aimed at the sample centre is detected by the 488 nm-channel of the fast two-channel pyrometer. The intensity of the reflected light is dependent on the angular reflectivity. The first appearance of the liquid during the heating of the sample leads to a rapid change in the reflectivity, and thus to a sharp variation in the recorded signal (Appendix A).

Laser heating results

The laser power and the duration of the laser pulses were optimised in order to obtain a freezing plateau long enough to clearly observe the solidification temperature. Furthermore, the dwelling time in the liquid state had to be as short as possible in order to limit incongruent vaporisation, which could affect the global composition of the samples. The pressure and the quality of the buffer experimental gas are also relevant. If the total pressure of the vapour phase in equilibrium with the liquid sample is lower than the pressure inside the autoclave, the vapours remain confined. In other words, the evaporation is kinetically limited.

A pre-heating level was set on the laser power to limit thermal stresses due to the extreme power density impinging on the surface of the sample. This procedure consists of heating the sample above 1000 K and limiting the temperature gradients during the laser pulse sequences. Four laser pulses with different power vs time shapes composed each laser sequence. A good set of data was thus obtained and it was possible to verify the effect of the cooling rate on the measured solidification temperature. Between two subsequent laser pulses within the same sequence, the laser power was set back to the pre-heating value and the laser beam delivered to a graphite beam shutter. The time interval between the pulses was optimised to reduce the 4-pulse sequence duration and to maintain the temperature of the sample above the limit of detection of the fast pyrometer (radiance temperature of 1500 K). The spectro-pyrometer was triggered manually on one pulse within each sequence. The selection of the spectro-pyrometer time resolution is related to the signal-to-noise ratio expected during the experiments. In the present case, since the temperature of interest were below 2500 K and the emissivity of metal is relatively low (at least lower than the oxide investigated in the past with the same setup [17]), an integration time of 6 ms was chosen.

Figure 21 shows sample OUZr_7 before and after a sequence of laser pulses.

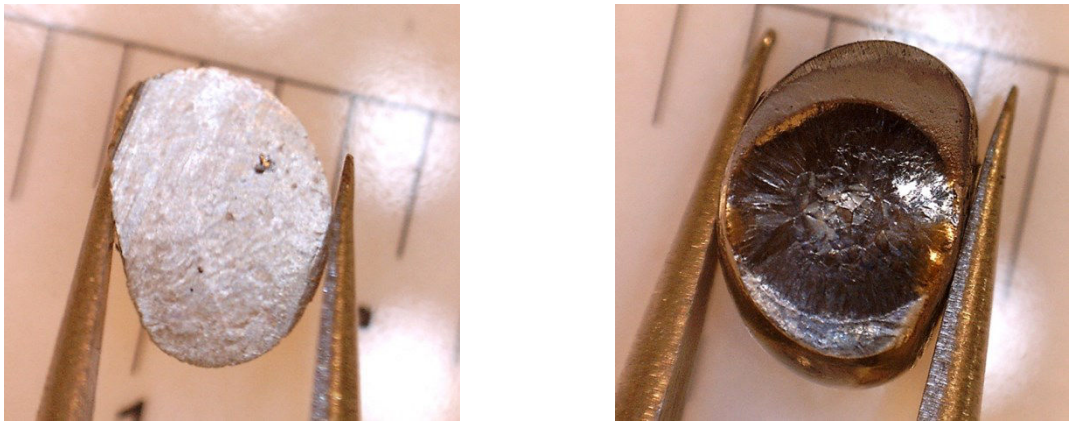

(a) (b)

Figure 21: Sample OUZr_7 before and after a laser pulse sequence. In figure (b) the circular trace of laser spot can be clearly seen

Figure 22 shows a sequence of thermograms obtained on sample OUZr_6 under Ar. In this section, radiance temperature will be reported. Only the correction for the window transmittance is applied (τ=0.86).

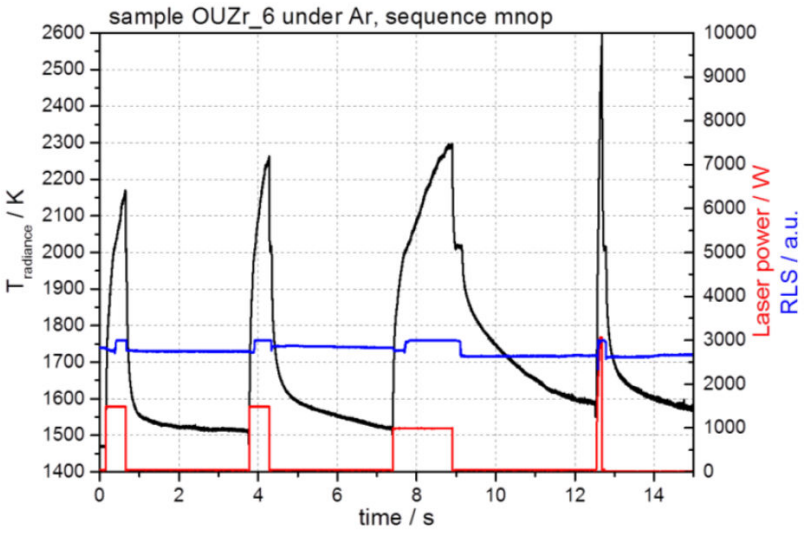

Figure 22: Radiance temperature measured during a sequence of laser pulses performed on sample OUZr_6 under Ar. Depending on the laser pulse duration and on the maximum laser power level, the solidification arrest is more or less visible. It may be noted that the third shot led to the formation of a large amount of liquid, which during cooling released its latent heat of solidification resulting in a pronounced thermal arrest

The black line represents the radiance temperature measured by the fast pyrometer working at 652 nm. The red line is the laser power sequence, whilst the blue line is the reflected light signal (RLS) from the second channel of the fast pyrometer.

The investigated samples have metallic properties. In particular, their thermal conductivity is relatively high. This required high-power laser pulses, especially considering the small size of the arc-melted samples (about 1 g and less than 1 cm in diameter). The laser pulse shape influenced the behaviour of the sample during cooling. Depending on the amount of liquid material formed during heating, the resulting thermal arrest on the cooling flank is more or less pronounced. However, the measured solidification temperatures are reproducible, within a single sequence and along all the sequences. This implies that the cooling rate did not affect the solidification results. Furthermore, the fact that the thermal arrests are reproducible shows that incongruent evaporation induced negligible composition changes in the samples during the laser shots.

The RLS method permits to identify a phase transformation when it is not evident in the thermogram. Figure 23 shows the application of the RLS technique on sample OUZr_6.

The melting point can be identified in correspondence of the sudden variation on the RLS. It may be noted that the RLS presents the same variation when the surface of the sample solidifies. Thanks to the RLS technique it is also possible to estimate the dwelling time in the liquid phase and thus to optimise the laser pulses sequence.

Looking at the thermogram obtained on sample OUZr_8 under Ar reported in Figure 24, a second thermal arrest on the cooling flank can be noted. The fast pyrometer permits to detect the formation of the first liquid and the complete solidification of the sample during cooling, at the condition that the observed phenomena are sufficiently energetic.

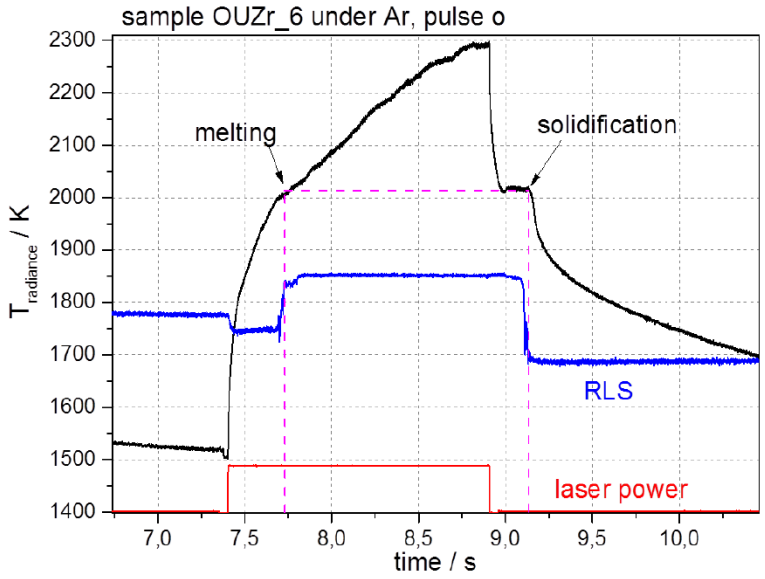

Figure 23: Application of the RLS method to identify the melting transition of the heating flank of the thermogram. The abrupt variation of the signal from the 488 nm-channel of the fast pyrometer during heating helps to identify the melting point. A good correspondence exists between the RLS estimation of the melting temperature and the solidification thermal arrest on the cooling flank of the thermogram

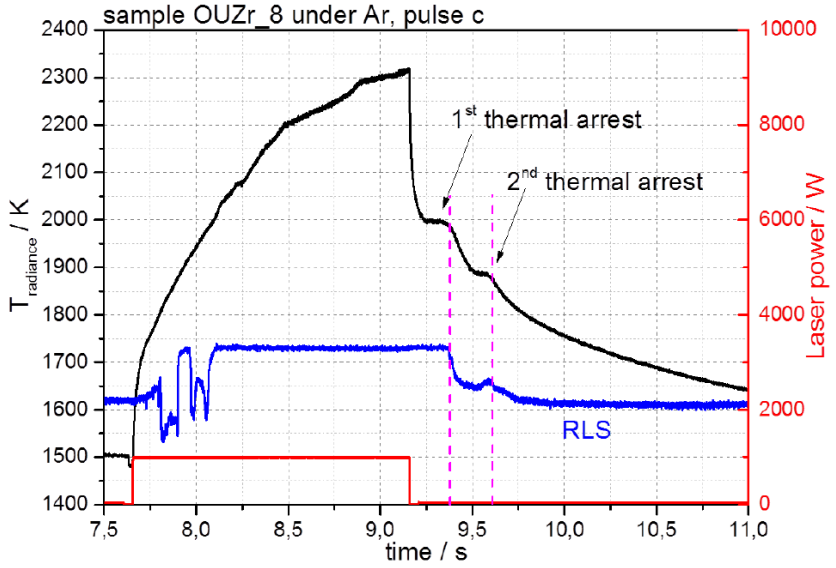

Figure 24: Thermogram obtained under Ar on sample OUZr_8. On the cooling flank, two distinct thermal arrests can be noted. In correspondence of the inflections, the RLS shows some features as well

The laser pulse c on sample OUZr_8 showed in Figure 25 allowed us to melt a large amount of sample. Evident thermal arrests can be observed during cooling. In agreement to the first thermal arrest, the RLS shows a sudden change. It can be noted that RLS changed also at the second thermal arrest on the thermogram. Between the two thermal arrests, the surface of the sample experienced significant changes. This means that the first thermal arrest corresponds to the formation and growth of the primary solid phase, whilst the second thermal arrest corresponds to the complete solidification of the surface of the sample. In the second part of this chapter, thermodynamic calculation will help interpreting this feature.

The same effect was also visible on the cooling flank of the thermograms obtained on sample OUZr_7. However, the second thermal arrest was less evident.

A summary of the experimental results obtained on the three O-U-Zr samples is shown in Figure 25. For each laser pulse the measured radiance temperature is reported. Samples OUZr_7 and OUZr_8 exhibit a second inflection.

A test under air was also performed on sample OUZr_8. The radiance temperature results are less regular than those obtained under Ar. The temperature detection resulted to be challenging. The buffer gas strongly interacts with the sample. No evident thermal arrests are visible on the cooling flank. Since the experimental conditions were not fully under control, this test cannot be considered for the thermodynamic modelling. However, it gives useful information on the paramount effect of the experimental atmosphere on the high temperature behaviour of the investigated samples.

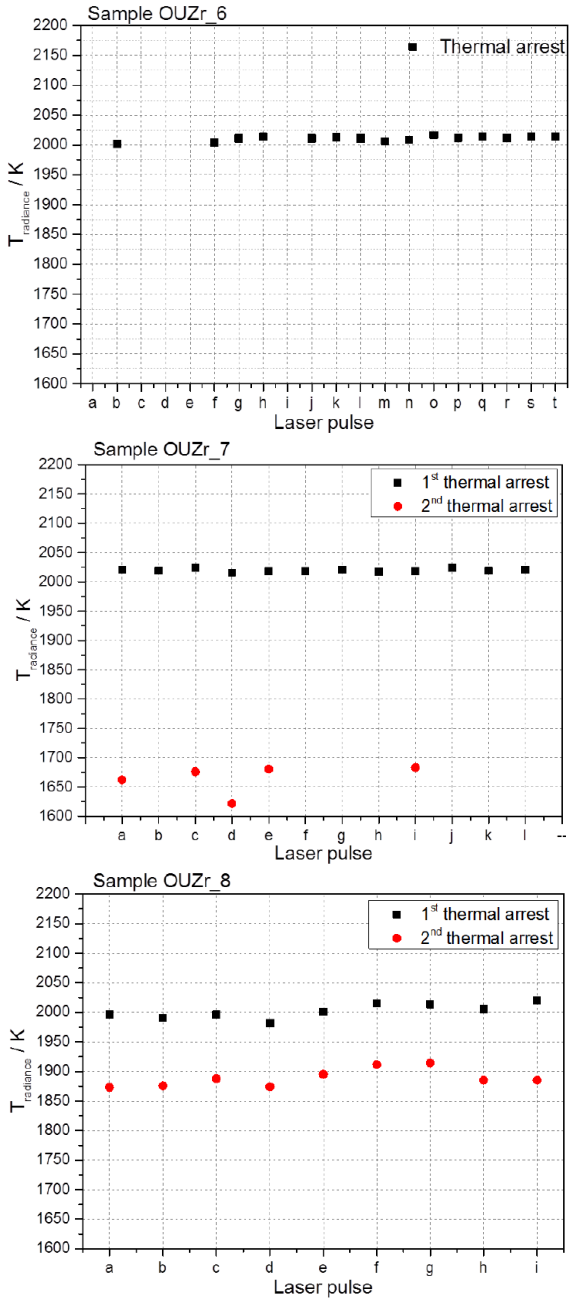

Figure 25: Summary of the experimental results obtained on samples OUZr_6, OUZr_7 and OUZr_8. The reported values are corrected only with the transmittance of the window. The reduced data dispersion in the three cases shows the excellent repeatability obtained during this experimental campaign

Emissivity analysis

In order to convert the radiance temperature into true temperature, the emissivity of the samples must be known. In the open literature no emissivity data are available for the present compositions. **The current emissivity estimation is the only available way to obtain true temperature values and represents the main source of uncertainty**.

The O-U-Zr samples studied by laser heating are lacated in the Zr-rich corner of the phase diagram (see Figure 19), with different amounts of oxygen. As mentioned above, because of the very low oxygen content, they display metallic properties. The optical properties of metals are normally dependent on wavelength and temperature. Furthermore, depending on the electronic configuration, the functional relation linking optical properties to wavelength and temperature is complex. Cagran et al. [19,20] showed that phase transitions (e.g., from solid to liquid state) may also drive abrupt changes in the emissivity.

Krishnan et al. [21] proved that the emissivity of liquid metals can be considered constant in a wide range of temperature above melting. The emissivity of liquid U and liquid Zr at 632.8 nm was measured by Krishnan et al. [22]. One can suppose that the optical behaviour of the investigated samples might be derived from the combination of the metallic components (e.g., it can be considered that the emissivity at 650 nm of the samples is the linear combination of the emissivity of liquid U and Zr). This approach works well for dielectrics materials as oxides [23]. In case of metals, it must be applied prudently. In fact, Krishnan et al. [21] showed that the emissivity of Zr-Ni alloys cannot be directly related to the optical behaviour of Zr and Ni. Furthermore, the non-negligible amount of oxygen in the investigated samples can induce radical changes in their electronic properties, leading the samples becoming dielectrics.

In the absence of any experimental data on the normal spectral emissivity, the samples were considered as grey bodies even if this assumption ($\varepsilon(\lambda)$=constant at least in the spectral range of interest) must be applied to metals very carefully. This approach follows the recommendation of Neuer et al. [24].

The extrapolation to zero wavelength (Appendix A) method applied to a spectrum recorded by the spectro-pyrometer during the thermal arrest detected on sample OUZr_8 is shown in Figure 26.

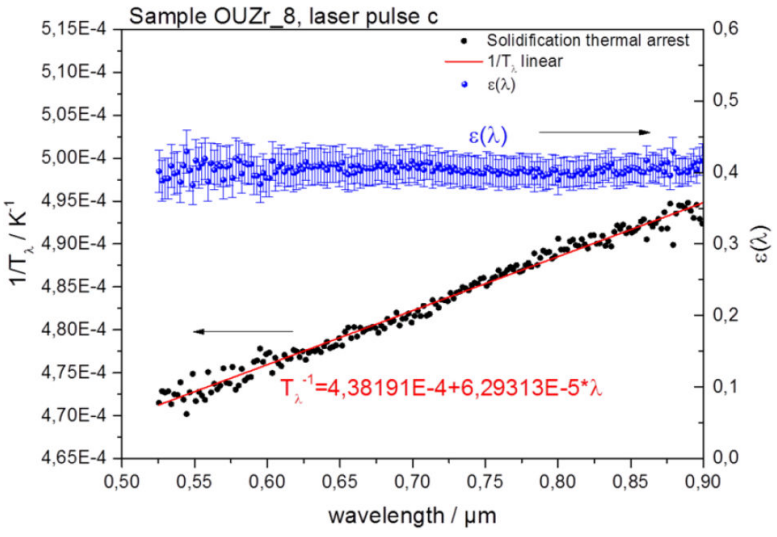

Figure 26: The extrapolation to zero wavelength method applied to the laser pulse c performed on sample OUZr_8. The black circles represent the radiance temperature spectrum recorded by the spectro-pyrometer ($t_{integration}$=6 ms) during the first thermal arrest. The spectrum is fitted using Equation (8) (red line) considering a constant normal spectral emissivity in the spectral range. The resulting emissivity $\varepsilon(\lambda)$ (blue circles) is 0.40

The normal spectral emissivity obtained with the same procedure on sample OUZr_6 and OUZr_7 is respectively 0.243 and 0.264. The difference between the emissivity of sample OUZr_8 (ε=0.40) and the other two samples is evident. This can be related to the amount of oxygen in the samples. Krishnan et al. [22] showed that the presence of an oxide layer (even 50 nm thick) on the sample's surface induces significant changes in the measured normal spectral emissivity.

The emissivity correction can lead to significant variations on the final result. For example, considering a measured radiance temperature of 2000 K, an emissivity of 0.3 or 0.4 give true temperatures of 2244 K and 2180 K respectively (ΔT=64 K).

Post-experiment characterisation

Post-experiment examinations were performed on the cross section of the laser-melted samples. The heated surface and the region underneath were observed by means of a scanning electron microscope (SEM) coupled with a energy dispersion spectrometer (EDS). The global composition of the sample was measured. However, due to the metallic nature of the sample, the oxygen content measure is challenging. Surface contamination and the low atomic weight make the uncertainty rise considerably. For this reason, the U/Zr ratio is taken as comparative parameter.

The microstructure of the post-melted samples OUZr_6 and OUZr_7 are similar. A thin lamellar structure is homogenously observed in the samples (Sample OUZr_6 in Figure 27). Two phases are visible. Considering the position of the sample in the ternary phase diagram, a α-Zr(O) phase (dark grey phase in the BSE image) and a metallic phase enriched in Zr (light grey phase) can be distinguished. EDS analysis on sample OUZr_6 and sample OUZr_7 confirmed qualitatively this argument. Using ImageJ® software the mass fraction of the observed phases was also estimated. These results are reported in Table 14.

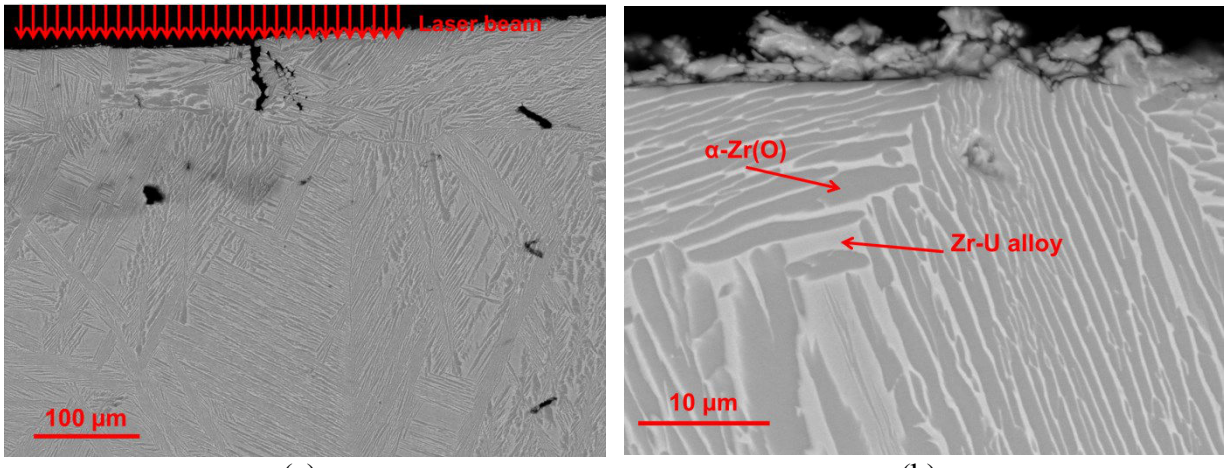

(a) (b)

Figure 27: BSE image of the microstructure of sample OUZr_7. (a) Laser-heated surface of the sample; (b) magnification close to the laser-heated surface

	Sample OUZr_6		Sample OUZr_7	
Phase	α-Zr(O)	Zr-U alloy	α-Zr(O)	Zr-U alloy
at% O	21	//	ND	//
at% U	1	8	ND	4
at% Zr	78	92	ND	96
Mass percentage	62	38	70	30

Table 14: EDS results on sample OUZr_6 and OUZr_7. The estimated mass percentage of the observed phases is also reported. ND=not detected

Table 15 summarises the EDS results obtained on the three samples in terms of U/Zr ratios.

Sample	**U/Zr before laser melting**	**U/Zr after laser melting**
OUZr_6	0.065	0.060±0.005
OUZr_7	0.138	0.135±0.005
OUZr_8	0.234	0.222±0.005

Table 15: Comparison between the U/Zr ratio in the investigated samples before and after the laser heating experiments

The U/Zr ratio for samples OUZr_6 and OUZr_7 did not changed after the laser heating, at least within the error bars. However, the composition of sample OUZr_8 slightly moved towards the Zr corner of the phase diagram.

The microstructure of sample OUZr_8 after laser melting is shown in Figure 28.

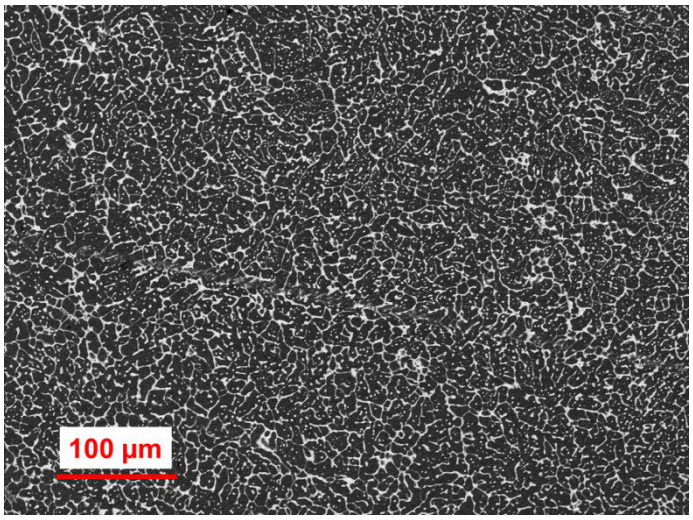

Figure 28. BSE image of the microstructure of sample OUZr_8. EDS analysis revealed that the white phase corresponds to a $(U,Zr)O_2$ mixed oxide, whilst the black phase is a α-(Zr,U)(O) phase

It may be noted that it is radically different compared to those of samples OUZr_6 and OUZr_7. Sample OUZr_8 has the highest oxygen content. Therefore, the presence of a cubic $(U,Zr)O_{2-x}$ phase is likely (white phase in Figure 28). Furthermore, the last laser sequence before the EDS analysis was performed under air. Therefore, the resulting microstructure is affected by the interaction between the sample and the oxidising atmosphere.

Discussion

The current laser heating results exhibit an excellent repeatability. The radiance temperatures measured during the solidification plateau of the three samples is affected by a relative error of about 0.5 %. This indicates that the experimental conditions used during the experiments allowed to limit incongruent evaporation. EDS analyses confirm this assumption. The

recorded radiance temperatures under Ar, for the three samples, are comparable. The temperature of the first inflection is about 2000 K for all compositions. This can be related to the solidification of a common phase in the three samples. However, these temperatures should be transformed into real temperatures through Equation (15) in Appendix A.

The emissivity of samples OUZr_6 and OUZr_7 is lower (about 30 %) than that of OUZr_8. This could be related to the different amount of oxygen dissolved in the samples. This can lead to the presence of an oxide layer affecting the emissivity estimation. **The validity of this approach should, however, be confirmed with further emissivity measurements**.

The uncertainties on the radiance temperature at 650 nm are the combination of the statistical dispersion of the experimental data and the systematic error of the pyrometric technique. The measured radiance temperatures lay within the calibration range of the fast pyrometer (1800-2500 K): the uncertainty contribution from the radiance temperature is thus minimised.

The second inflection measured on the cooling flank of sample OUZr_7 and OUZr_8 is less reproducible. The same emissivity correction used for the first inflections was applied for the second inflection recorded for sample OUZr_7 and OUZr_8. The low signal-to-noise ratio at the temperature of the second inflection did not allow us to obtain exploitable data from the extrapolation to zero wavelength method.

Table 16 summarises the laser heating experimental results on the three O-U-Zr samples.

Sample	**Radiance temperature / K**			**True Temperature / K**	
	1st inflection	**2nd inflection**	**ε(650 nm)**	**1st inflection**	**2nd inflection**
OUZr_6	2011±11	//	0.243±0.05	2307±101	//
OUZr_7	2020±10	1665±26	0.264±0.05	2299±94	1850±70
OUZr_8	2002±16	1889±18	0.40±0.08	2183±94	2049±61

Table 16: Summary of the laser heating experiments on the three O-U-Zr samples. In the table are reported both the radiance and the true temperatures. The expanded uncertainties on the true temperatures are corrected with a coverage factor k=2

Since the uncertainty on the emissivity estimation affects the final values of the true temperatures, Table 16 reports both radiance and true temperatures, corrected using the calculated emissivity at 650 nm. A conservative value of 20 % is selected for the uncertainty on the emissivity. The large error bars on the true temperature are due to the propagation of emissivity uncertainty. For sample OUZr_8, the uncertainty on emissivity contributes for 90 % on the overall error bar on true temperature.

3.2.2 O-Fe-Zr system

The same experimental setup described in Section 3.2.1.2 was used for the study of six O-Fe-Zr samples. This system is of great interest in the framework of severe accident investigation.

In the past, the O-Fe-Zr system has been studied especially in the oxygen-rich side of the phase diagram.

The experimental results on the O-Fe-Zr samples are reported in Table 17.

Sample	Radiance temperature / K			True Temperature / K	
	1st inflection	2nd inflection	ε(652 nm)	1st inflection	2nd inflection
OFeZr_1	1989±18	1660±4	0.56±0.11	2098±86	1735±54
OFeZr_2	1883±29	//	0.56±0.11	1980±94	//
OFeZr_5	1847±11	1572±15	0.55±0.11	1943±72	1642±58

Table 17: Summary of the laser heating experiments on the three O-Fe-Zr samples. In the table are reported both the radiance and the true temperatures. The expanded uncertainties on the true temperatures are corrected with a coverage factor k=2

As for O-U-Zr samples, both radiance and true temperature are presented. The emissivity constitutes once more the main source of uncertainty. The reported values are calculated using the extrapolation to zero wavelength method (Appendix A). A conservative 20 % uncertainty is selected for the calculated emissivity. A more detailed description of the laser heating experimental results on O-Fe-Zr samples is in Appendix A.

3.2.3 PuO_2-UO_2-ZrO_2 system

A large number of the PWR based nuclear power plants, are loaded with MOX fuel, a mixture of UO_2 and PuO_2. In order to be able to add plutonium to the thermodynamic description of the corium/concrete interaction, experimental data involving Pu-containing-subsystems are paramount. However, very few experimental investigations have been carried out on Pu-containing corium subsystems, due to the high radiotoxicity and limited availability of plutonium [25]. Furthermore, the high oxygen potential of actinide dioxides (AnO_2, where An represents a generic actinide) plays a crucial role in the high temperature behaviour of these compounds [26]. The oxygen potential is defined as:

$$\overline{\mu(O_2)} = RT \ln p(O_2) \qquad (2)$$

Where R is the ideal gas constant, T the absolute temperature and $p(O_2)$, the oxygen partial pressure, is specific to the reference atmospheric pressure (101325 Pa).

This parameter defines the tendency of a given compound to exchange oxygen with its environment. In the system under investigation, the oxygen potential of uranium dioxide is of most importance. Uranium can exist in the oxidation states +3, +4, +5 and +6 in its dioxide form. This particular feature, related to the $[Rn]5f^3 6d^1 7s^2$ electronic configuration of U, allows the occurrence, besides stoichiometric $UO_{2.00}$ (mostly U^{4+}), of both hypo-stoichiometric (down to $UO_{1.66}$, with mostly U^{3+} and U^{4+}) and hyper-stoichiometric dioxides (up to $UO_{2.25}$, with mostly U^{4+}, U^{5+}, and U^{6+}). In contrast, Pu and Zr are known to exist only in the oxidation states +3 and +4 (+2 and +4 for Zr) in their oxide forms (at least in the absence of humidity [27]). Therefore, it is generally sufficient to keep zirconium and plutonium dioxides in an oxidising atmosphere to ensure that they are stable at a composition very close to stoichiometry ($ZrO_{2.00}$ and $PuO_{2.00}$). The behaviour of uranium dioxide is atmosphere-dependent and therefore more complex. It was shown [18] that an inert or slightly reducing atmosphere stabilises nearly-stoichiometric $UO_{2.00}$, as a consequence of the very slow kinetics of the reduction to UO_{2-x}. An oxidising atmosphere will, however, result in the oxidation of uranium dioxide to UO_{2+x} or even to higher oxides, ultimately U_3O_8.

During experiments carried out at a temperature close to melting, as in standard furnace treatments, the oxygen chemical potential triggers an overwhelming oxidation reaction both towards the experimental atmosphere and the metallic containment (see Kato et al.'s work [29]). Guéneau et al. [28] argued that the atmosphere used during the experiment was a

crucial parameter for maintaining the composition of the samples as close as possible to their initial stoichiometries [26].

In this framework, collaboration with the JRC-ITU (Germany) allowed to explore the high temperature behaviour of the PuO_2-UO_2-ZrO_2 system. Uchida et al. [25] published the only experimental data on the melting behaviour of this system. The author performed melting experiments using W-capsules. Kato et al. [29] showed that employing W-capsules during high temperature experiments induces relevant errors in the temperature measurements. Therefore, these data must be treated carefully.

3.2.3.1 Sample preparation and characterisation

In this work six compositions within the pseudo-ternary system were studied. The compositions of the samples are reported in Table 18 and Figure 29. In the following, the composition of a PuO_2-UO_2-ZrO_2 mixture containing x mol % UO_2, y mol % PuO_2 and v mol % ZrO_2 will be noted $U_xP_yZ_v$. The samples were in the form of cylindrical pellets 3 mm high x 8 mm dia.

Sample	mol% UO_2	mol% PuO_2	mol% ZrO_2	mass / g
U48P3Z49	48	3	49	1.050
U45P10Z45	45	10	45	1.052
U33P33Z33	33	33	33	1.210
U20P40Z40	20	40	40	0.759
U10P45Z45	10	45	45	0.946
P50Z50	0	50	50	1.081

Table 18: Molar composition and mass of the six investigated PuO_2-UO_2-ZrO_2 samples

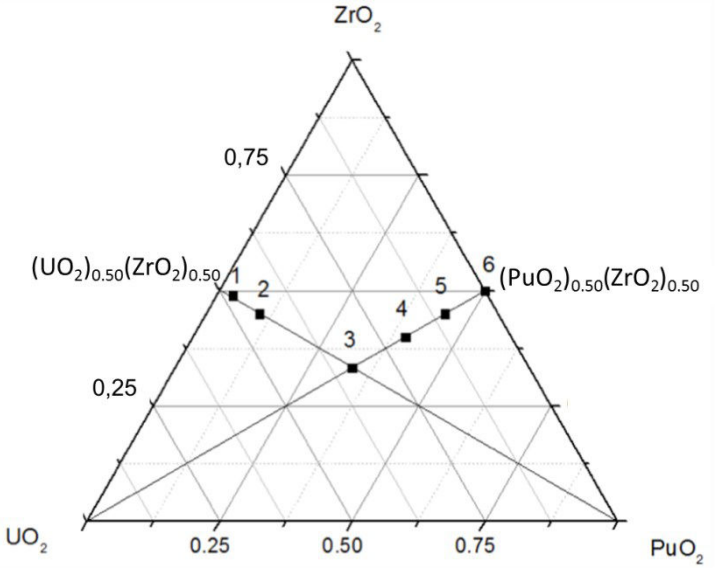

Figure 29: Compositions of the six samples investigated in the UO_2-PuO_2-ZrO_2 phase diagram

As described in an earlier JRC report [30] the samples were prepared in the JRC-ITU Nuclear Fuel Laboratories by mixing ZrO_2 (Alfa Aesar, 99.7 % purity with hafnium content less than 75 ppm), UO_2 and PuO_2 (JRC-ITU supplies). The mixed powders were then pressed into pellets at an operating pressure ranging from 500 to 800 MPa and placed on a Mo tray. Sintering was subsequently performed in a metallic furnace at 1873 K for 6 hours under Ar/6.5%H_2 atmosphere with 1500 ppm H_2O in order to maintain the oxygen-to-metal ratio as close as possible to O/M=2.

These compositions were specifically chosen to study the melting behaviour of the central part of the phase diagram. Furthermore, this choice allows to investigate the influence of the addition of UO_2 and PuO_2 when moving across the $(PuO_2)_{0.50}(ZrO_2)_{0.50}$-$UO_2$ and $(UO_2)_{0.50}(ZrO_2)_{0.50}$-$PuO_2$ sections, respectively, as well as the effect on the measured solidification temperature of the experimental buffer gas inside the autoclave.

The characterisation of the samples before and after the laser treatment is essential for understanding the phenomena occurring during the experiments. In this work, Secondary Electron (SE) images were recorded on a Philips XL40 scanning electron microscope operated at 25kV installed in a glove-box.

The crystal structures of the synthesised and laser-melted samples were determined at room temperature by X-ray diffraction (XRD) at ITU [31].

The XDR results before and after the laser heating experiments are presented in Chapter 4 and interpreted by using thermodynamic calculations.

3.2.3.2 Laser heating results

The experimental setup reported in Section 3.2.1.2 was slightly modified to face the high radiotoxicity of Pu. In particular the autoclave was enclosed in an alpha-tight glove box to enable the handling of PuO_2 samples and shield against β radiation.

The samples were pre-heated with a 30 s long low power (40 W) laser pulse to reduce thermal stresses and cracking phenomena. After this treatment, the temperature at the surface of the sample reaches a steady state between 1500 K and 2000 K. The sample was then brought to the liquid state with shorter (100 to 1000 ms) and more powerful (up to 700 W) pulses. A BSE image of the molten sample is reported in Figure 30.

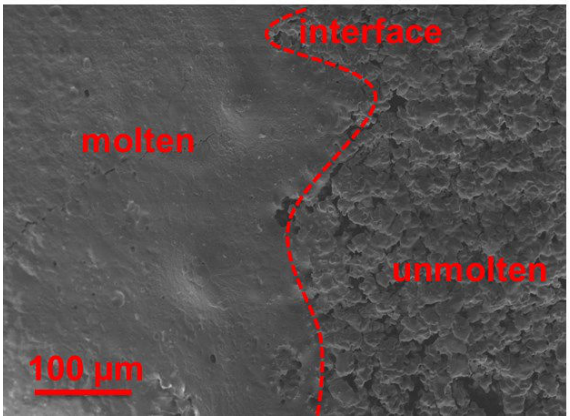

Figure 30: BSE image of the interface (highlighted by the red dashed line) between the molten and non-melted sample P50Z50

Each laser pulse sequence was composed of four low power/high power cycles in order to verify the repeatability and obtain a significant set of data. With this precaution, different heating and solidification rates were applied to the samples. The observed cooling rates were of the order of 10^5-10^6 K/s. A typical sequence of laser shots is reported in Figure 31.

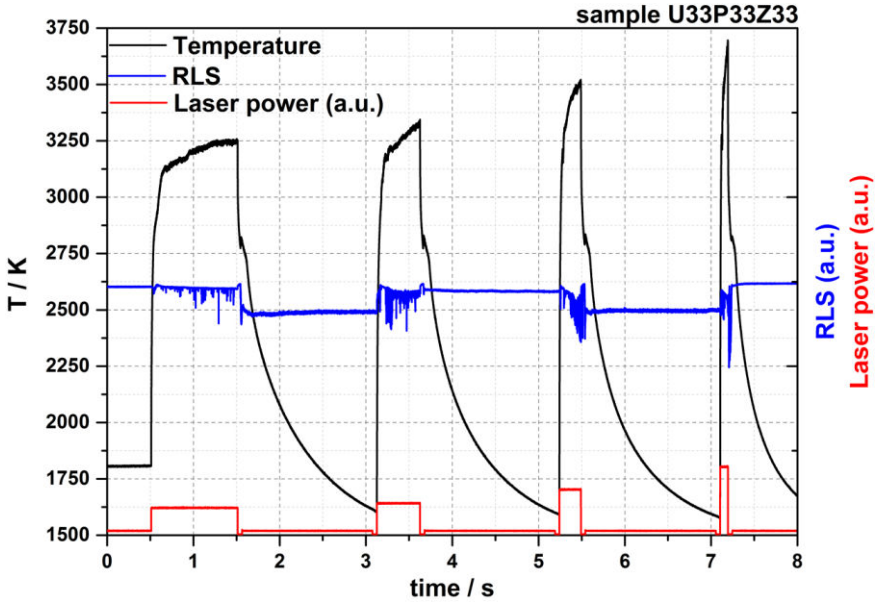

Figure 31: Sequence of laser shots on sample U33P33Z33 under Ar atmosphere (p=0.25 MPa)

The black line is the thermogram showing the true temperature of the sample versus time recorded with the 650 nm-channel of the fast pyrometer, whilst the red line is the power vs. time profile of the laser beam impinging on the sample. It may be noted that the shape of the laser pulse strongly influences the heating and cooling rates of the sample. The blue line shows the signal from the 488 nm-channel of the fast pyrometer used for the RLS technique. Figure 32 shows a melting/solidification cycle on sample U33P33Z33 sample. The reported thermogram was obtained under inert gas (0.25 MPa of Ar). This atmosphere can actually have reducing effects on the sample, as it provides no compensation for oxygen losses at high temperatures. No transitions are visible on the heating stage of the thermogram. However, thanks to the RLS (blue line) it is possible to identify the temperature where the surface of the sample became liquid.

On the cooling stage of the thermogram (black line), a clear thermal arrest can be observed. It corresponds to the solidification of the sample's surface. It can be noted that at the same time the oscillations on the RLS disappear due to the vanishing of the movements of the surface of the molten pool.

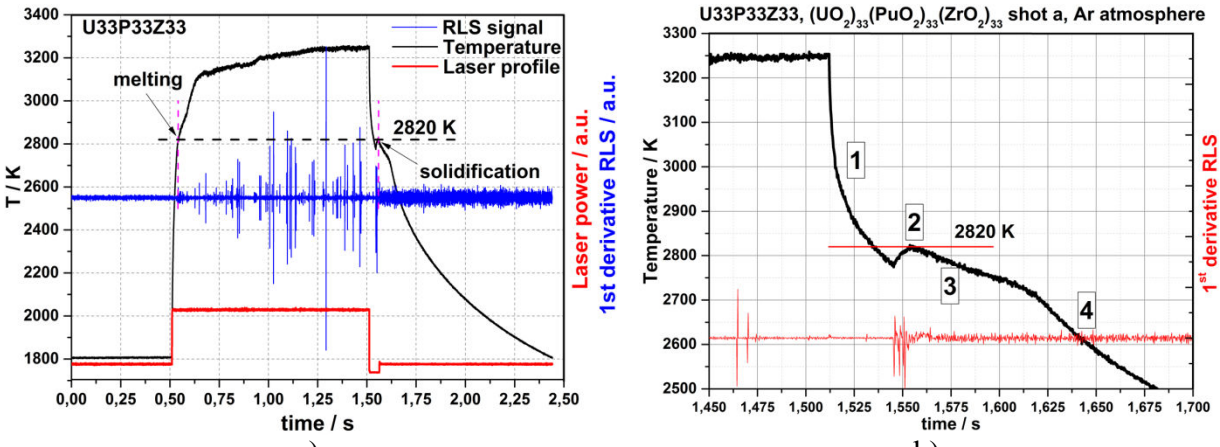

Figure 32: a) Melting/solidification cycle on sample U33P33Z33. The reported thermogram was obtained under reducing conditions (Ar atmosphere); b) magnification of the solidification process

The process of solidification under these experimental conditions was recently described by Böhler et al. [16] based on a multi-physical approach [32]. Figure 32b shows a magnification

of the cooling flank of the thermogram reported in Figure 32a. After the power laser is brought to the "lower level", the temperature of the molten material rapidly decreases reaching undercooling conditions (1). Meanwhile, the molten material starts to solidify at the bottom, on the sides and on the surface of the liquid pool. As long as the crust on the surface of the sample keeps growing, the latent heat of solidification contributes to the raise of the temperature up to a local maximum, which correspond to the formation of a completely re-solidified layer at the surface of the sample (2). The release of the latent heat of solidification from the remaining enclosed molten material counteracts the process of cooling of solid surface, itself driven by radiation and convection/conduction (3). The inflection after the local maximum is ascribable to the complete solidification of the molten pool (4). After the last inflection the solidified sample continues cooling to ambient temperature.

The radiance temperature obtained by the pyrometer has been converted in true temperature applying Equation (15) in Appendix A. Bober [33] reported an emissivity of 0.83 for UO_2 at the melting temperature, showing that the assumption of greybody is valid. The result on the emissivity of PuO_2 (0.83±0.05) reported by De Bruycker [23] is in good agreement with ab-initio calculations performed by Shy et al. [34]. De Bruycker used the same method described above to obtain the normal spectral emissivity at 652 nm. The emissivity of ZrO_2 can be estimated as ε(652 nm)=0.85 as reported by Avdoshenko & Strachan [35]. As a first approximation the emissivity at 652 nm for the mixed $U_xP_yZ_v$ is:

$$\varepsilon(650nm) = x \cdot \varepsilon(UO_2) + y \cdot \varepsilon(PuO_2) + v \cdot \varepsilon(ZrO_2) \qquad (3)$$

Figure 33 shows the calculated normal spectral emissivity (NSE) with the extrapolation to zero wavelength method (see Appendix A).

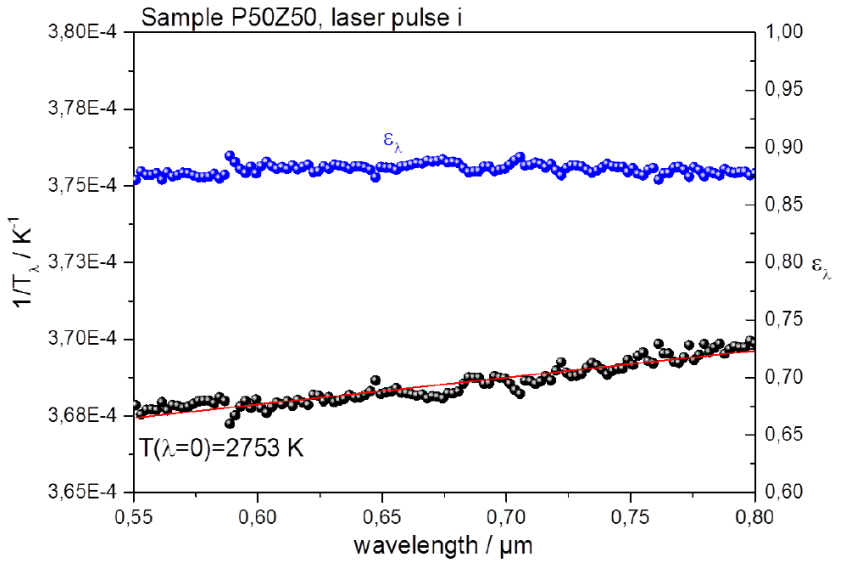

Figure 33: Normal spectral emissivity calculated with the extrapolation to zero wavelength method

The validity of the grey body approximation is confirmed for these compounds by the good linear fit plotted in Figure 33, at least in the spectral range of interest (550-800 nm). Moreover, good agreement exists between the emissivity calculated with Equation (13) and the extrapolation to zero wavelength method.

3.2.3.3 Discussion

The experimental atmosphere plays a crucial role in the melting behaviour of these samples. In fact, the high temperature fcc allotropic form of UO_2, PuO_2 and ZrO_2 is not stoichiometric. For UO_2, the cubic fcc phase is stable both in the presence of oxygen vacancies (hypo-stoichiometric domain) and oxygen interstitials (hyper-stoichiometric domain). For PuO_2 and ZrO_2, only a hypo-stoichiometric domain in the cubic fcc phase exists (Figure 34a-c).

The heating treatment in oxidising or reducing conditions could result in a departure from the stoichiometric plane (i.e., x(O)=.66667, where x(O) is the molar fraction of oxygen) toward regions richer or poorer in oxygen.

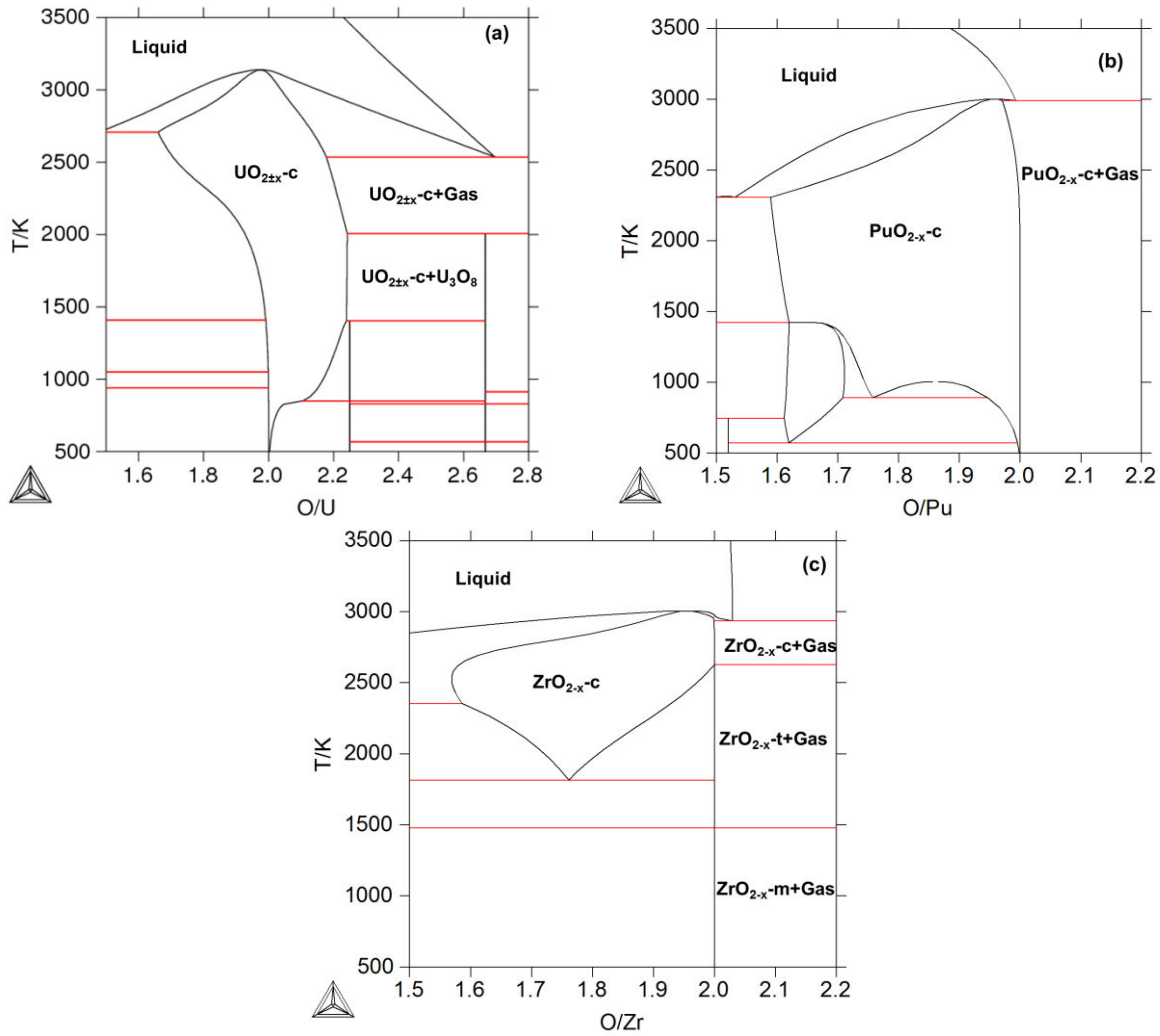

Figure 34: Calculated phase diagrams of: (a) U-O system [28]; (b) Pu-O system [28]; (c) Zr-O system (this work). The reported diagrams are a magnification of the high oxygen content regions of the respective systems

The calculated oxygen partial pressure as a function of the oxygen-to-metal ratio (O/M) for the three oxides at a temperature near to the melting/solidification points recorded in this work is reported in Figure 35.

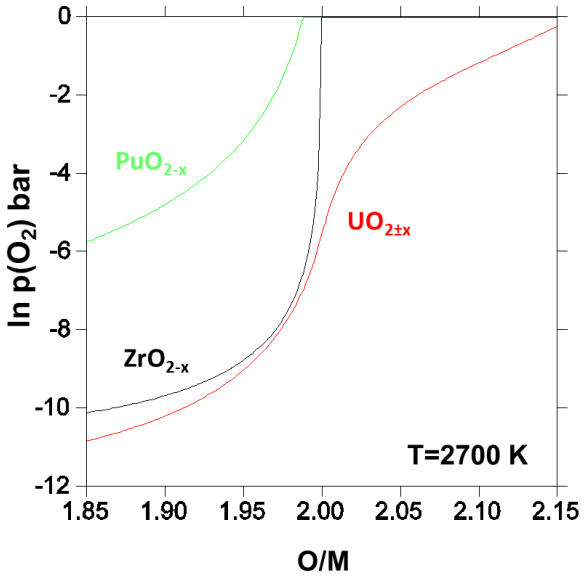

Figure 35: Calculated oxygen partial pressure in the cubic $UO_{2\pm x}$ (red line), ZrO_{2-x} (black line) and PuO_{2-x} (green line) oxide phases at T=2700 K and p=0.1 MPa. Concerning PuO_2 and ZrO_2 beyond O/M=2, it must be pointed out that the solid+gas equilibrium imposes a constant oxygen potential equal to zero, that is an oxygen partial pressure equal to 0.1 MPa

Knowledge of the oxygen partial pressure over the three oxides permits to estimate the behaviour of the samples under the different experimental gaseous conditions. Furthermore, it can be concluded that UO_2 and ZrO_2 are more stable than PuO_2. During the laser heating investigation, the melting/solidification behaviour of the whole set of samples was tested under different atmospheric conditions. In particular, reducing (i.e., Ar or Ar + 6.5 % H_2 mixture) and oxidising (i.e. air) conditions were used.

Figure 36 shows the comparison between two laser pulses performed on sample U48P3Z49 and U10P45Z45 under Ar and air respectively. The black line represents the temperature measured under Ar, whilst the blue line is the thermogram recorded under air.

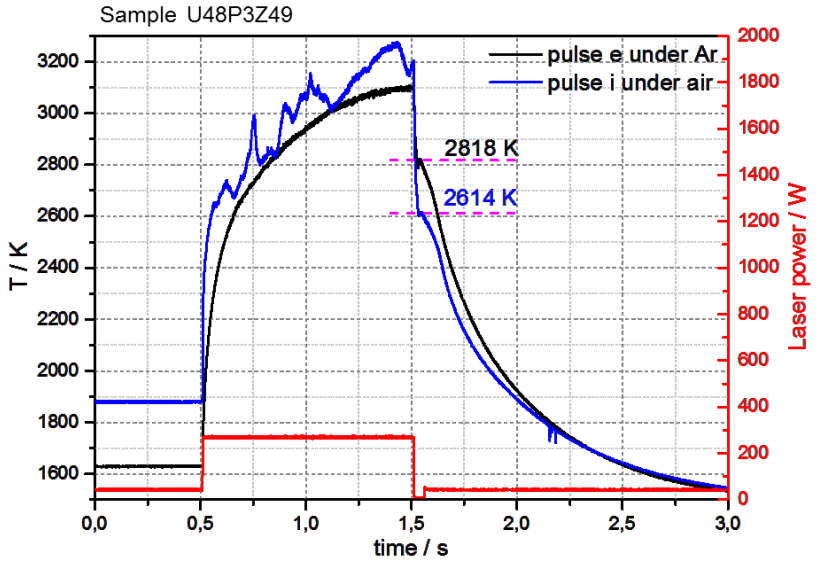

(a)

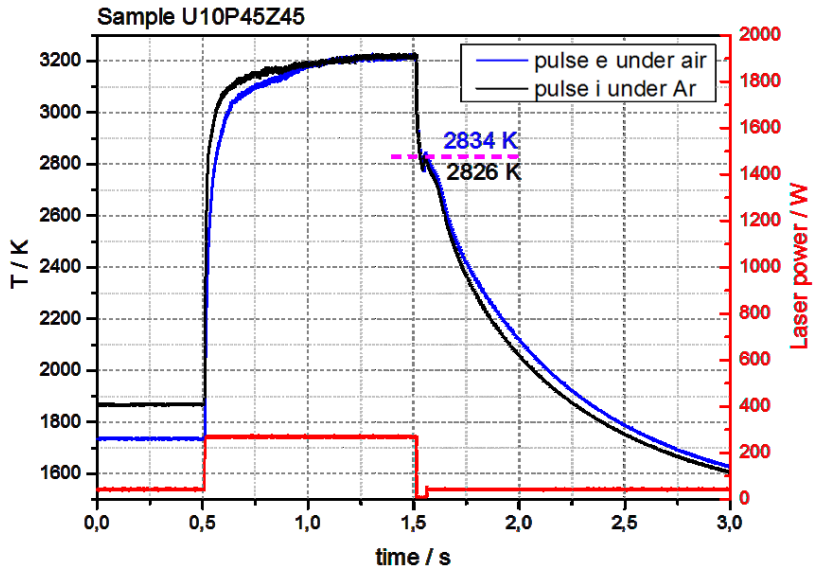

(b)

Figure 36: Effect of the atmosphere on the melting/solidification behaviour of samples U48P3Z49 and U10P45Z45. (a) Sample U48P3Z49; (b) sample U10P45Z45

Due to the high temperature chemical reactivity, in presence of an oxidising atmosphere the liquid sample must have dissolved part of the oxygen present in the buffer gas. Therefore, for high UO_2-content samples as U48P3Z49, the composition of the molten pool can move toward more oxidised regions, to a different extent depending on the experimental conditions (dwelling time beyond melting, purity of the atmosphere). During heating, the thermograms in Figure 36a resulted less smooth than the ones obtained under reducing conditions, confirming that a strong interaction between the liquid sample and the buffer gas was present. During the cooling stage under air, the prevailing effect of UO_2 oxidation leads the sample crossing the projection of the U-O hyper-stoichiometric liquidus line (Figure 34a). Agreementingly, the measured solidification temperatures obtained under oxidising conditions are significantly lower than those measured under Ar (by about 200 K). This effect is clearly visible comparing the solidification results obtained on sample U48P3ZR49 under oxidising and reducing conditions (Figure 36a).

The described liquid oxidation cannot be controlled accurately in the present experiments under air. Furthermore, the control of the oxygen potential was not possible, leading to a

limited repeatability of the observed solidification arrests. The thermodynamic calculation presented in Section 3.4.3 will help the comprehension of the complex phenomena occurring during the laser heating experiments. The solidification temperatures obtained under reducing conditions are more reproducible, confirming the observation of Manara et al. [18].

When a sample with a lower UO_2-content is considered, ZrO_2 and PuO_2 play the main role in the melting/solidification behaviour results. Looking at sample U10P45Z45when oxidising conditions were used, a smooth thermogram was obtained (blue line in Figure 36b). The molar fraction of UO_2 in the U10P45Z45 was not high enough to ensure accommodation of oxygen interstitials in the lattice. The solidification temperature measured under conditions is comparable to that under air.

Figure 37 and Figure 38 report the solidification results of three sequences of laser cycles performed on sample U45P10Z45 and four sequences on sample U10P45Z45 respectively.

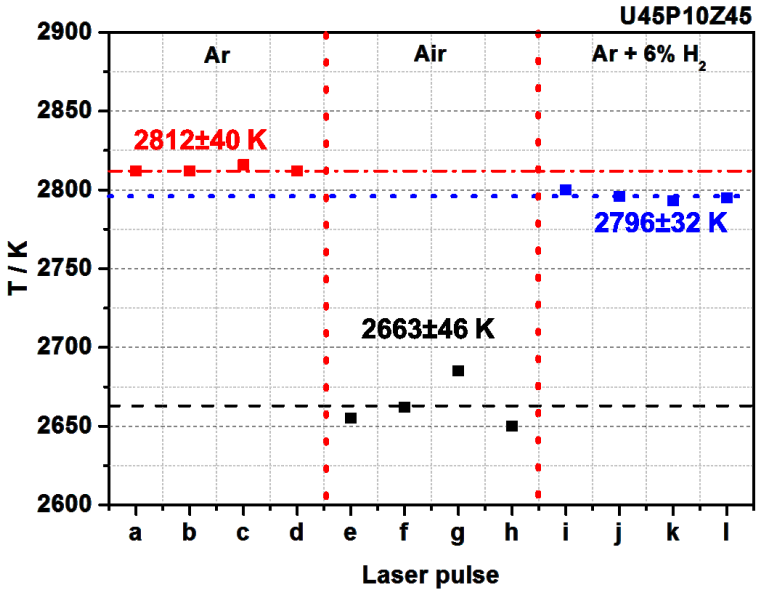

Figure 37: Sequence of experiments performed on sample U45P10Z45. The lines correspond to the overall mean values for the solidification temperature under Ar (2812±40 K), Ar-6.5 % H_2 (2796±32 K) and under air (2663±46 K). Solidification temperature obtained under (■) reducing conditions (i.e., under 0.25 MPa of Ar); (■) oxidising conditions (i.e., under 0.25 MPa of air); (■) reducing conditions (i.e., under 0.25 MPa of Ar-6.5 % H_2). It may be noted that the solidification temperatures obtained under oxidising conditions are significantly lower than the results under reducing atmosphere.

In Figure 37, the red squares represent the solidification temperatures measured under Ar, the blue squares the results under Ar-6.5 % H_2, whilst the black squares the results under oxidising conditions. Four laser pulses were performed under Ar-6.5 % H_2 atmosphere after the sequence under air. The observed solidification temperatures are slightly lower than those observed under Ar. However, the spread between the two sets of data is within the error bars. The difference between the sets of data under Ar (or Ar-6.5 % H_2) and under air is remarkable. Passing from reducing to oxidising conditions during experiments on sample U45P10Z45 resulted in a significant drop in the observed thermal arrest temperature (200 K). The Ar-6.5 % H_2 sequence performed after that under air drives the O/M ratio closer to 2, probably slightly lower than under Ar.

It can thus be concluded that the interaction kinetics between the molten sample and the buffer gas is extremely rapid, even taking into account the small dimension of the molten pool (approximately 5mm in diameter, 50 µm in depth [23]).

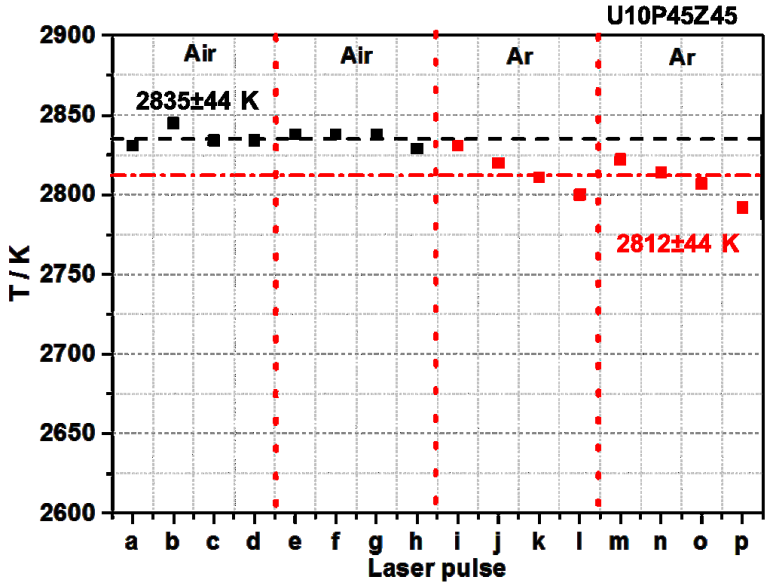

Figure 38: Sequence of experiments performed on sample U10P45Z45. The blue dotted lines correspond to the overall mean value calculated for the solidification temperature under Ar (2835±44 K) and under air (2812±44 K). (■) Solidification temperature obtained under reducing conditions; (■) Experimental results obtained under oxidising conditions (i.e., under 0.25 MPa of air).

Concerning sample U10P45Z45, the spread between the solidification temperature under Ar and under air is less evident. When oxidising conditions were used (i.e., sequences one and two in Figure 38), the measured solidification temperatures were rather consistent. During the cycles under reducing atmosphere, the detected solidification temperature progressively decreases. Since in the last two sequences the oxygen potential of the buffer gas was lower than that of the sample, a certain amount of oxygen passed from the molten sample to the atmospheric gas after each laser power cycle. The composition of the sample progressively moves towards the projection of the hypo-stoichiometric liquidus lines originating from the Pu-O and Zr-O phase diagrams (Figure 34b-c). This phenomenon is less strong than the oxidation observed for sample U48P3Z49: **UO_2 thermodynamics dominates the high temperature material behaviour in the current laser heating experiments, and in general is fundamental for the comprehension of the high temperature behaviour of U-containing mixed oxides**.

The selection of the atmospheric conditions that stabilise UO_2 the best during the experiments limits incongruent vaporisation and stabilise the oxygen-to-metal ratio O/M. The comparison between the experimental results obtained under reducing and oxidising conditions respectively on UO_2-rich and UO_2-poor samples corroborates this assumption: **as long as UO_2-rich samples are concerned, it is recommended employing reducing conditions during the laser melting experiments, whilst oxidising conditions are preferable when UO_2-poor samples are considered**.

The repeatability of the reported results indicates that segregation effects and incongruent evaporation were weak enough to not affect the experimental melting/freezing points.

3.2.3.4 Summary

The experimental results obtained during this work represent one of the rare sets of data investigating the high temperature behaviour of the UO_2-PuO_2-ZrO_2 system. It is nevertheless the first systematic study on the effect of the experimental gaseous atmosphere on the melting/solidification behaviour. In fact, it has been shown that the experimental atmosphere plays a crucial role on the measured solidification temperatures. Depending on the UO_2-

content of the samples, reducing or rather oxidising conditions tend to stabilise the O/M close to the stoichiometry (O/M=2). This is essentially related to the high temperature thermodynamics of the three actinide dioxides, UO_2, PuO_2 and ZrO_2.

A summary of the measured solidification temperatures under reducing and oxidising atmospheres for the six investigated samples is reported in Table 19. A cover factor k=2 has been applied to the reported uncertainties.

	Reducing atmosphere (Ar)		Oxidising atmosphere (air)	
Sample	**T solidification / K**	**Uncertainty / K**	**T solidification / K**	**Uncertainty / K**
U48P3Z49	2799	54	2620	39
U45P10Z45	2812	40	2663	46
U33P33Z33	2786	57	2772	150
U20P40Z40	2726	50	2731	58
U10P45Z45	2812	44	2835	44
P50Z50	2819	50	2848	43

Table 19. Experimental results obtained on the six analysed sample. A cover faction k=2 is applied to the reported uncertainties

Taking into account the very high temperature produced during the experiments, and the relative uncertainties, a good reproducibility has been shown, except for sample U33P33Z33 under air.

The evolution of the measured solidification temperatures gives an idea of the shape of the solid/liquid surface in the UO_2-PuO_2-ZrO_2 system. Across the UO_2-$(PuO_2)_{0.50}(ZrO_2)_{0.50}$ section, increasing the UO_2-content, the detected solidification temperature decreases showing a minimum at about $x(UO_2)$=0.20. In this region of the phase diagram, results obtained under Ar and under air are comparable, at least within the bars of incertitude. Starting from the UO_2-ZrO_2 side, the effect of adding PuO_2 is weak in the measured transition temperature under Ar, leading to the conclusion that the solidus curve is rather flat. On the other hand, results obtained under air show that adding PuO_2 increases the melting temperature. Across the latter section the differences between the results obtained under Ar and under air are significant.

In Chapter 4, the thermodynamic assessment of the UO_2-PuO_2-ZrO_2 system will be presented. Furthermore, the present set of results will be interpreted more thoroughly by means of thermodynamic calculations. XRD results obtained at JRC-ITU laboratories on sintered and melted samples will be also interpreted.

3.3 Conclusions

This chapter summarises the experimental results obtained on in-vessel corium key systems. The heat treatment performed on four O-U-Zr samples allowed to study the phase equilibria at 2567 K. Two of the four samples showed a stratified microstructure, meaning that at the annealing temperature two immiscible liquids were in equilibrium. **The compositions of the two liquids were measured obtaining two tie-lines in the miscibility gap in the ternary O-U-Zr liquid phase at 2567 K**. The laser heating experiments on three O-U-Zr samples give a good set of data. However, further investigations on the optical properties of the samples are needed to confirm the current results. The results obtained using the same technique on the O-Fe-Zr samples showed a more complex behaviour, probably due to Fe vaporisation.

The experimental results obtained on the UO_2-PuO_2-ZrO_2 samples represent the first systematic study on the effect of the atmosphere on their melting/solidification behaviour. The interaction with the buffer gas is more or less pronounced depending on the

nature of the gas and on the composition of the samples. The repeatability of the experimental thermal arrests means that incongruent vaporisation phenomena were minimised.
The present set of experimental data will be used in the next Chapter for the thermodynamic modelling of the prototypic in-vessel corium system.

3.4 References

[1] L. Kaufman and H. Bernstein, Book, *Computer calculation of the phase diagram: with special reference to refractory metals*. Academic Press Inc., 1970.

[2] N. Saunders and A. Miodokwin, Book, *CALPHAD - Calculation of Phase Diagrams, A Comprehensive Guide*. 1998.

[3] H. Lukas, S. Fries, and B. Sundman, Book, *Computational Thermodynamics - The Calphad Method*. 2007.

[4] B. Sundman, B. Jansson, and J.-O. Andersson, "The Thermo-Calc Databank System," *Calphad*, vol. 9, no. 2, pp. 153–190, 1985.

[5] TALISMAn, "TALISMAn project." [Online]. Available: http://www.talisman-project.eu/.

[6] M. Baichi, C. Chatillon, and C. Guéneau, "Mass spectrometer study of the UO_2-ZrO_2 pseudo-binary system," *J. Nucl. Mater.*, vol. 294, pp. 84–87, 2001.

[7] M. Baichi, "Contribution à l'étude du corium d'un réacteur nucléaire accidenté : aspects puissance résiduelle et thermodynamique des systèmes U-UO_2 et UO_2-ZrO_2,", PhD Thesis INP Grenoble, 2001.

[8] C. Politis, "Untersuchungen im Dreistoffsystem Uran-Zirkon-Sauerstoff," Kernforschungszentrum Karlsruhe, Report no. KfK 2167, 1976.

[9] A. Maurizi, "Réactivité chimique a haute température dans le système (U,Zr,Fe,O) - contribution a l'étude de la zircone comme récupérateur de 'corium,'" PhD Thesis, Univerisité Pierre et Marie Curie, 1996.

[10] E. F. Juenke and J. F. White, "Physico-chemical studies of clad UO_2 under reactor accident conditions," General Electric Company, Report no. GEMP-731, 1970.

[11] C. Guéneau, V. Dauvois, P. Pérodeaud, C. Gonella, and O. Dugne, "Liquid immiscibility in a (O,U,Zr) model corium," *J. Nucl. Mater.*, vol. 254, no. 2–3, pp. 158–174, Apr. 1998.

[12] S. V. Bechta, V. S. Granovsky, V. B. Khabensky, V. V. Gusarov, V. I. Almiashev, L. P. Mezentseva, E. V. Krushinov, S. Y. Kotova, R. A. Kosarevsky, M. Barrachin, D. Bottomley, F. Fichot, and M. Fischer, "Corium phase equilibria based on MASCA, METCOR and CORPHAD results," *Nucl. Eng. Des.*, vol. 238, pp. 2761-2771, 2008.

[13] D. Manara, F. De Bruycker, K. Boboridis, O. Tougait, R. Eloirdi, and M. Malki, "High temperature radiance spectroscopy measurements of solid and liquid uranium and plutonium carbides," *J. Nucl. Mater.*, vol. 426, no. 1–3, pp. 126–138, Jul. 2012.

[14] D. Manara, H. F. Jackson, C. Perinetti-Casoni, K. Boboridis, M. J. Welland, L. Luzzi, P. M. Ossi, and W. E. Lee, "The ZrC–C eutectic structure and melting behaviour: A high-temperature radiance spectroscopy study," *J. Eur. Ceram. Soc.*, vol. 33, no. 7, pp. 1349–1361, Jul. 2013.

[15] U. Carvajal Nunez, D. Prieur, R. Bohler, and D. Manara, "Melting point determination of uranium nitride and uranium plutonium nitride: A laser heating study," *J. Nucl. Mater.*, vol. 449, no. 1–3, pp. 1–8, Jun. 2014.

[16] R. Böhler, M. J. Welland, D. Prieur, P. Cakir, T. Vitova, T. Pruessmann, I. Pidchenko, C. Hennig, C. Guéneau, R. J. M. Konings, and D. Manara, "Recent advances in the study of the UO_2–PuO_2 phase diagram at high temperatures," *J. Nucl. Mater.*, vol. 448, pp. 330–339, 2014.

[17] R. Böhler, A. Quaini, L. Capriotti, P. Cakir, A. Guiot, K. Boboridis, L. Luzzi, R. J. M. Konings, and D. Manara, "The solidification behaviour of the UO_2-ThO_2 system in a laser heating study," *J. Alloys Compd.*, vol. 616, pp. 5–13, 2014.

[18] D. Manara, M. Sheindlin, W. Heinz, and C. Ronchi, "New techniques for high-temperature melting measurements in volatile refractory materials via laser surface heating," *Rev. Sci. Instrum.*, vol. 79, no. 2008, 2008.

[19] C. Cagran, C. Brunner, A. Seifter, and G. Pottlacher, "Liquid-phase behaviour of normal spectral emissivity at 684.5 nm of some selected metals," *High Temp. - High Press.*, vol. 34, no. 6, pp. 669–679, 2002.

[20] C. Cagran, B. Wilthan, and G. Pottlacher, "Optical properties (at 684.5 nm) and radiance temperatures at the melting point of group VIIIb transition metals cobalt, nickel, palladium, and platinum," *High Temp. - High Press.*, vol. 35/36, no. 6, pp. 667–675, 2007.

[21] S. Krishnan and P. C. Nordine, "Spectral emissivities in the visible and infrared of liquid Zr, Ni and nickel-based binary alloys," *J. Appl. Phys.*, vol. 80, no. 3, pp. 1735–1742, 1996.

[22] S. Krishnan, J. K. Richard Weber, C. D. Anderson, and P. C. Nordine, "Spectral emissivity and optical properties at l=632.8 nm for liquid uranium and zirconium at high temperatures," *J. Nucl. Mater.*, vol. 203, pp. 112–121, 1993.

[23] F. De Bruycker, "High Temperature Phase Transitions in Nuclear Fuels of the Fourth Generation,", PhD Thesis Universite d'Orleans, 2010.

[24] G. Neuer, L. Fiessler, M. Groll, and E. Schreuben, "Critical analysis of the different methods of multiwavelength pyrometry," in *Temperature: its measurement and control in science and industry. Vol 6*, J. F. Schooley, Ed. New York, 1996, pp. 787–789.

[25] T. Uchida, S. Hirooka, H. Sugata, K. Shibata, D. Sato, M. Kato, and K. Morimoto, "Melting Temperature of the ZrO_2-MOX System," *GLOBAL 2013, Salt Lake City, Utah, Sept. 29-October 3, 2013*, pp. 1549–1553, 2013.

[26] D. Manara, R. Böhler, K. Boboridis, L. Capriotti, A. Quaini, L. Luzzi, F. De Bruycker, C. Guéneau, N. Dupin, and R. Konings, "The Melting Behaviour of Oxide Nuclear Fuels: Effects of the Oxygen Potential Studied by Laser Heating," *Procedia Chem.*, vol. 7, pp. 505–512, 2012.

[27] J. M. Haschke, "Reaction of Plutonium Dioxide with Water: Formation and Properties of PuO_{2+x}," *Science (80-.).*, vol. 287, no. 5451, pp. 285–287, Jan. 2000.

[28] C. Guéneau, N. Dupin, B. Sundman, C. Martial, J. C. Dumas, S. Gossé, S. Chatain, F. De Bruycker, D. Manara, and R. J. M. Konings, "Thermodynamic modelling of advanced oxide and carbide nuclear fuels: Description of the U-Pu-O-C systems," *J. Nucl. Mater.*, vol. 419, no. 1–3, pp. 145–167, 2011.

[29] M. Kato, K. Morimoto, H. Sugata, K. Konashi, M. Kashimura, and T. Abe, "Solidus and liquidus temperatures in the UO_2-PuO_2 system," *J. Nucl. Mater.*, vol. 373, pp. 237–245, 2008.

[30] P. Lajarge and J. Somers, "Fabrication of ZrO_2 / UO_2 / PuO_2 pellets for phase diagram measurements in the Safety of Conventional Nuclear Fuel action," JRC-ITU 2008.

[31] A. Quaini, C. Guéneau, S. Gossé, B. Sundman, D. Manara, A. L. Smith, D. Bottomley, P. Lajarge, M. Ernstberger, and H. F, "High temperature investigation of the solid/liquid transition in the PuO_2-UO_2-ZrO_2 system," *J. Nucl. Mater.*, vol. 467, no.2, pp. 660-676, 2015.

[32] M. J. Welland, W. T. Thompson, B. J. Lewis, and D. Manara, "Computer simulations of non-congruent melting of hyperstoichiometric uranium dioxide," *J. Nucl. Mater.*, vol. 385, no. 2, pp. 358–363, 2009.

[33] M. Bober, "Spectral reflectivity and emissivity of solid and liquid UO_2 as a function of wavelength, angle of incidence and polarization," *High Temp. - High Press.*, vol. 12, no. 297–306, 1980.

[34] H. Shy, M. Chu, and P. Zhang, "Optical properties of UO_2 and PuO_2," *J. Nucl. Mater.*, vol. 400, pp. 151–156, 2010.

[35] S. M. Avdoshenko and A. Strachan, "High-temperature emissivity of silica, zirconia and samaria from ab-initio simulations: role of defects and disorder," *Model. Simul. Mater. Sci. Eng.*, vol. 22, pp. 075004–1, 2014.

Chapter 4 – Thermodynamics of the in-vessel corium: modelling and calculations

The prototypic in-vessel corium considered in this work is a "pentary" system. This implies the existence of 10 binary sub-systems and 10 ternary sub-systems. Figure 1 summarises the thermodynamic description of the binary systems selected for the present assessment.

Fe	Pu	U	Zr	O
Fe	Kurata 2010	Kurata 2010	Toffolon-Masclet 2008	Sundman 1991
	Pu	Kurata 1999	Kurata 2006	Guenéau 2011
		U	Kurata 1999	Guenéau 2011
			Zr	Liang 2001 (*)

Figure 1: Selected thermodynamic description for the 10 binary systems of the in-vessel corium system. These models can be found in the TAF-ID database. Kurata 1999 [1], Kurata 2006 [2], Kurata 2010 [3], Toffolon-Masclet 2008 [4], Sundman 1991 [5], Liang 2001 [6], Guéneau 2011 [7]. (*) means that the model was modified in this work

Table 1 summarises the origin of the thermodynamic description of the 10 ternary systems and the contribution of the present work to the thermodynamic model of the in-vessel corium system.

The mathematical models used to describe the Gibbs energy of the assessed phases are reported in Appendix C. The binary phase diagrams involved in the formation of the Pu-U-Zr-O-Fe in-vessel corium system are shown in Appendix B. In this chapter the assessed ternary systems are listed and the assessment procedure is described (the assessed thermodynamic parameter can be found in Appendix D).

The second part of the chapter is dedicated to the solidification path calculation, using this model, applied to the interpretation of the experimental results obtained during this work. It is shown that this kind of calculation helps the comprehension of the solidification behaviour of complex systems and might also be employed to estimate nature, composition and fraction of phases formed during a severe accident.

Ternary system	
Metallic systems	
Fe-Pu-U	Extrapolation from binary systems
Fe-Pu-Zr	Extrapolation from binary systems
Fe-U-Zr	Assessed by N. Dupin [8] (TAF-ID database)
Pu-U-Zr	Extrapolation from binary systems. A comparison with the experimental data was performed by N. Dupin showing a good agreement
Oxide systems	
O-Fe-Pu	Extrapolation from binary systems
O-Fe-U	**This work:** **UO_2-FeO_{1+x} section**
O-Fe-Zr	**This work:** **ZrO_2-FeO section** **ZrO_2-Fe_3O_4 section** **ZrO_2-FeO-Fe_2O_3 isothermal section at 1473 K**
O-Pu-U	Guéneau et al. [7]
O-Pu-Zr	**This work:** **PuO_2-ZrO_2 section**
O-U-Zr	UO_2-ZrO_2 section from Baichi [9] **This work:** **ternary phase diagram: UO_2-ZrO_2-U-Zr**

Table 1: Contribution of the present work to the thermodynamic model of the prototypic in-vessel corium system

4.1 Thermodynamic modelling

In the following, the thermodynamic assessment on the O-U-Zr, O-Fe-Zr and O-Fe-U ternary systems will be presented. The metallic Fe-U-Zr metallic system has been already assessed by Dupin [8].

4.1.1 O-U-Zr system

The present assessment on the O-U-Zr ternary system is based on the optimisation performed by Baichi [9] on the UO_2-ZrO_2 phase diagram and on the ternary experimental data reported in Table 2 of Chapter 2. Furthermore, the present experimental results obtained by thermal treatment at 2567 K and by laser heating given in Section 3.2.1 are used.

The addition of ternary interaction parameters in the liquid description and in the fcc mixed oxide model allows to better fit the solubility data of Maurizi [10] and to better shape the miscibility gap in the liquid phase.

In this section we will present successively the assessment of the UO_2-ZrO_2 system, of some isothermal section of O-U-Zr system at high temperature (2273 K, 2567 K and 3223 K) and at low temperature (1373 K and 1673 K). For each case, the calculated diagram will be compared to the existing experimental data found in literature.

4.1.1.1 UO_2-ZrO_2 system

The UO_2-ZrO_2 phase diagram has been widely studied in the past, as shown in Chapter 2. In the present work, the interaction parameters for this system have been taken from Baichi [9]. No solubility of UO_2 in monoclinic ZrO_2-m phase is considered. The calculated UO_2-ZrO_2 phase diagram is reported in Figure 2.

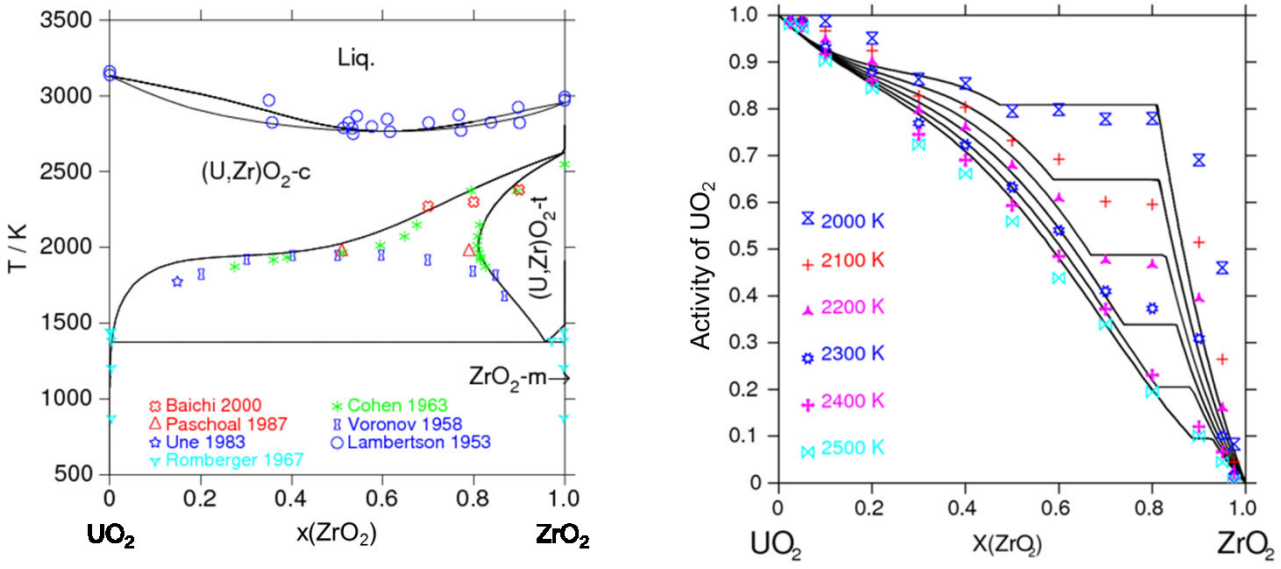

(a) (b)

Figure 2: (a) UO_2-ZrO_2 phase diagram calculated with the present thermodynamic model; (b) activity of UO_2 calculated at 2000 K, 2100 K, 2200 K, 2300 K, 2400 K and 2500 K compared to the experimental results of Baichi [11]

Baichi [11] based his thermodynamic assessment on the experimental data appended to the phase diagram in Figure 2a. The author assessed interaction parameters of 0^{th} and 1^{st} order in the fluoride (U,Zr)O_2-c phase between U^{4+} and Zr^{4+}. This permits to shape the solubility limit of ZrO_2 in cubic (U,Zr)O_2-c in equilibrium with (Zr,U)O_2-t. The calculated solubility limit well reproduces the selected experimental results. The author also added a 0^{th} order interaction parameter in the tetragonal (U,Zr)O_2-t phase in order to readdress the solubility of UO_2 in (Zr,U)O_2-t obtaining excellent agreement with the experimental data of Cohen & Shaner [12]. A 0^{th} and 1^{st} order interaction parameters were finally added in the liquid phase description to take into account the experimental data of Lambertson & Müller [13]. The liquidus/solidus lines present a minimum at about 52 mol % ZrO_2 in agreement with Lambertson & Mueller observation [13]. The calculated activity of UO_2 between 2000 K and 2500 K are in agreement with the activity data reported by Baichi et al. [11] (Figure 2b).

The fact that ZrO_2-c is hypo-stoichiometric at high temperature, leads to the presence of gas in equilibrium with the cubic (U,Zr)O_2-c phase. Therefore, the UO_2-ZrO_2 section cannot be considered a pseudo-binary system. The calculated phase diagram in Figure 2 is a simplified version, considering the cubic ZrO_2-c as perfectly stoichiometric.

4.1.1.2 O-U-Zr isothermal section at high temperatures (2273, 2567 and 3223 K)

a) *Optimised O-U-Zr isothermal sections*

- O-U-Zr isothermal section at *2273 K*

The isothermal section at 2273 K has been optimised to fit the data reported by Juenke & White [14], Politis [15], Skokan [16] and Maurizi [10]. The calculated 2273 K section is reported in Figure 3.

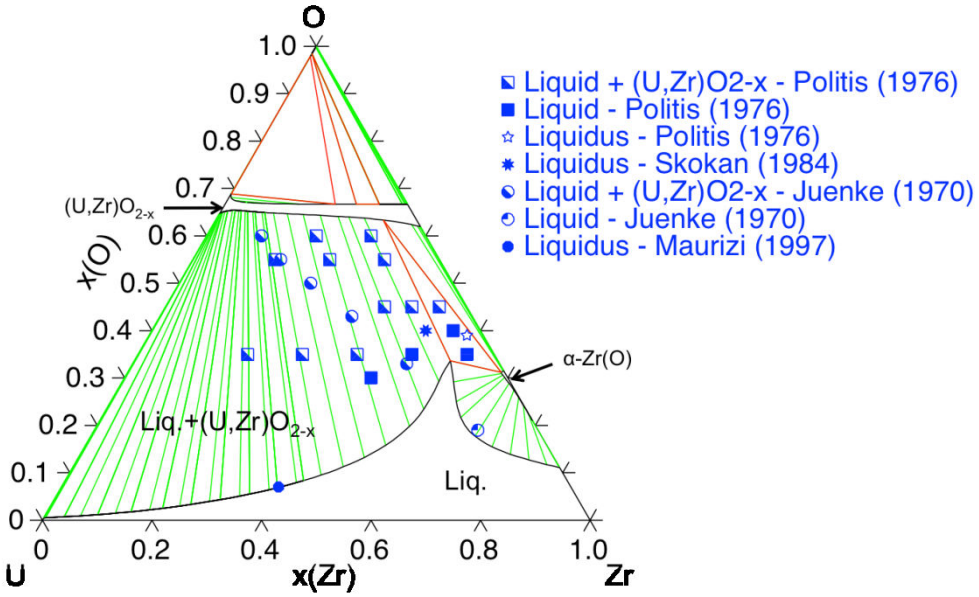

Figure 3: O-U-Zr isothermal section calculated at 2273 K. The reported experimental data are from Juenke & White [14], Politis [15], Skokan [16] and Maurizi [10]

The solubility limit of oxygen in metallic liquid was shaped using the 0th and 1st order interaction parameters $L^{liq}\left(U^{4+},Zr^{4+}:O^{2-},Va\right)$. The 0th order parameter has an entropic term in order to destabilise the liquid at higher temperature and allow the presence of the liquid miscibility gap. The 1st order parameter helps stabilise the liquid in the region close to the Zr-O side of the ternary phase diagram. The calculated solubility limit of *O* in metallic liquid (6.9 at % O) is in excellent agreement with the experimental data of Maurizi at U/Zr=1.5 (7 at % O). The tentative ternary liquidus line reported by Politis [15] (see also Figure 2b in Chapter 2) overestimates the oxygen solubility in the metallic liquid. In the present work, the experimental results obtained by Maurizi are considered the most reliable, since a detailed description of the experimental methods and the post-experiments analyses are given.

The calculated phase diagram reported in Figure 3 shows the presence of a [Liq.+α-(Zr,U)(O)] two-phase region. The tentative isothermal section reported by Politis [15] does not exhibit neither this feature nor the [$(U,Zr)O_{2-x}$+Liq.+α-(Zr,U)(O)] three-phase region.

The description of the cubic $(U,Zr)O_{2-x}$-c phase was also modified. The ternary interaction parameter $L^{cubic_oxide}\left(U^{4+},Zr^{2+}:O^{2-}:Va\right)$ was added to avoid a miscibility gap in the $(U,Zr)O_{2-x}$-c phase propagating across the ternary phase diagram. Furthermore, to better shape the stability region of the $(U,Zr)O_{2-x}$-c phase close to O/M=2, a ternary interaction parameter between U^{3+} and Zr^{4+}, $L^{cubic_oxide}\left(U^{3+},Zr^{4+}:O^{2-}:Va\right)$ was assessed.

In the present work an interaction parameter in the α-(Zr,U)(O) phase description was added to take into account the solubility of U.

It may be noted that close to the U-O binary section above O/M=2 a miscibility gap between two cubic $(U,Zr)O_{2+x}$-c phases is calculated. Barrachin et al. [17] reported a thermodynamic description of the hyper-stoichiometric region of the ternary phase diagram, obtaining the same feature. However, the lack of experimental data in this region and the large uncertainties on the few available experimental data [18] did not allow the authors to conclude on the validity of their description. In the present work, no interaction parameters were added to shape the hyper-stoichiometric region of the ternary phase diagram. **Nevertheless, it is recommended to obtain new experimental data to shed light on this region**.

- O-U-Zr isothermal section at *2567 K*

Using the experimental results obtained during heat treatment experiments (see Section 3.2.1), the isothermal section at 2567 K has been optimised (Figure 4).

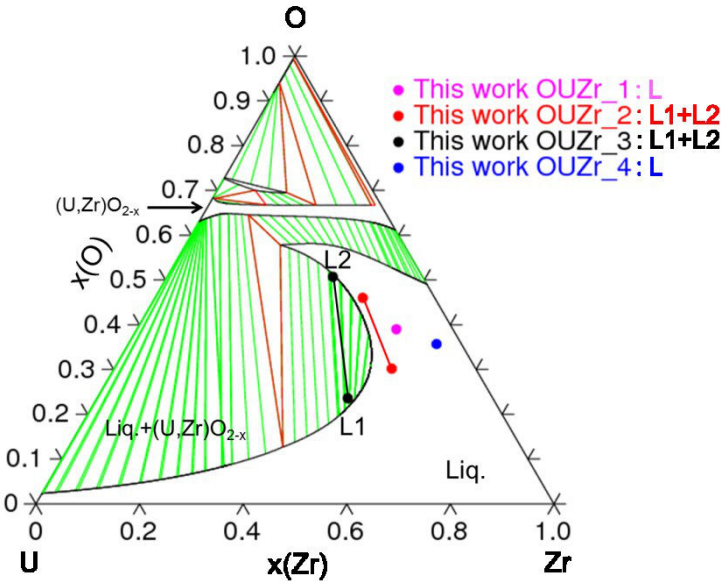

Figure 4: O-U-Zr isothermal section calculated at 2567 K. The present experimental tie-lines between metallic liquid L1 and oxide liquid L2 are appended on the ternary phase diagram

The miscibility gap in the liquid phase has been shaped considering the tie-lines of samples OUZr_2 and OUZr_3 by using the $L^{liq}\left(U^{4+},Zr^{4+}:O^{2-},Va\right)$ parameters described above. The calculated tie-line between the oxide and the metallic liquids in the case of a composition equal to that of sample OUZr_3 is in good agreement with the experiment. The calculation does not fit the experimental tie-line obtained on sample OUZr_2. This might be due to the stronger interaction between the sample and the W-crucible. The compositions of the two liquids detected in sample OUZr_2 are closer to each other compared to those measured in sample OUZr_3. This is consistent with the extension of the calculated miscibility gap: since the miscibility gap originates from the U-O binary section [19], moving towards composition richer in Zr leads to shorter tie-lines and then to closer liquid compositions. The remaining samples (OUZr_1 and OUZr_4) exhibited a microstructure typical of a solidified single liquid phase. **The calculated isothermal section is in agreement with the experimental observation.**

- O-U-Zr isothermal section at *3223 K*

The calculated isothermal section at 3223 K is reported in Figure 5.

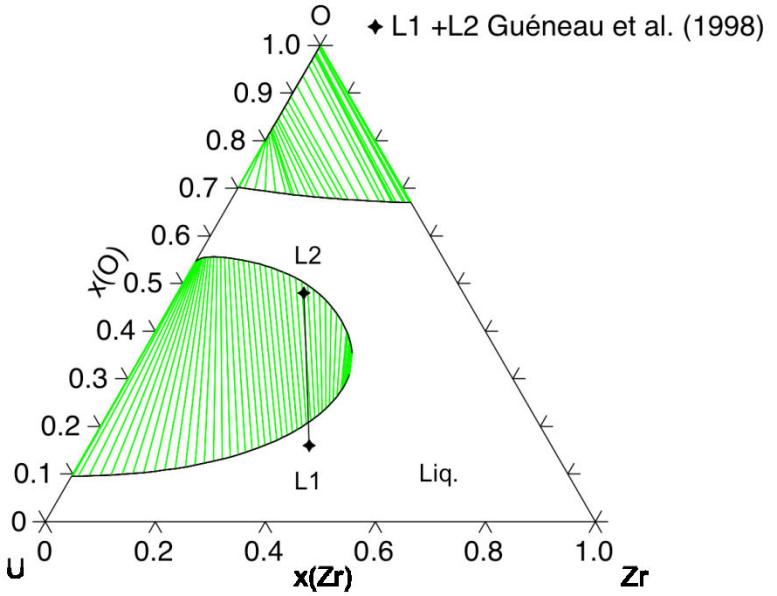

Figure 5: O-U-Zr isothermal section calculated at 3223K. The reported experimental tie-line between the metallic liquid L1 and the oxide liquid L2 is taken from Guéneau et al. [19]

The experimental tie-line between metallic and oxide liquids (L1 and L2 respectively) obtained by Guéneau et al. [19] was used to shape the miscibility gap at this temperature. Taking into account the large uncertainty on the temperature measurement (Guéneau et al. reported ±100 K at 3223 K) the tie-line at 3223 K is in good agreement with the calculated isothermal section.

b) *Comparison with the MASCA experimental data*

As introduced in Chapter 2, in the framework of the MASCA project [20], two tielines within the liquid miscibility gap were obtained at 2643 K and 2753 K (Table 1 in Chapter 2). These tie-lines are reported on two calculated section at 2643 K and 2753 K (Figures6a-b).

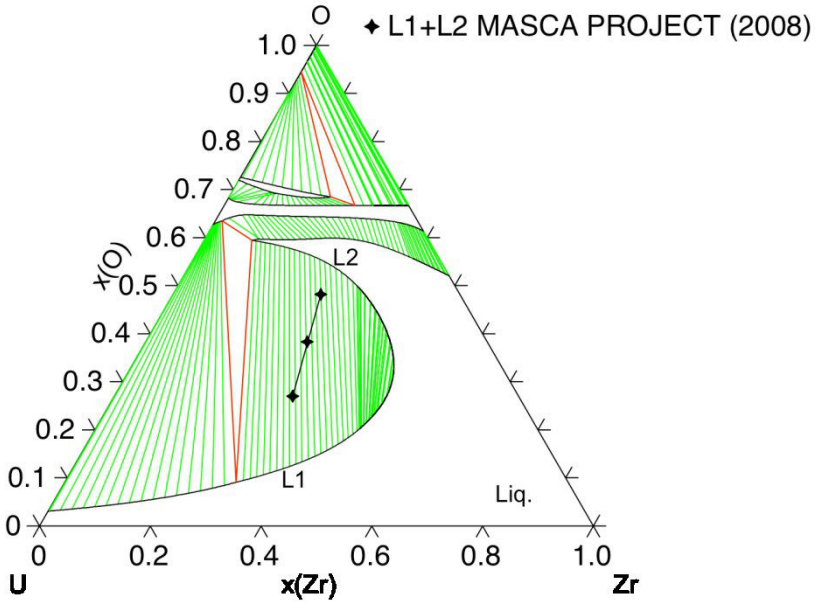

(a)

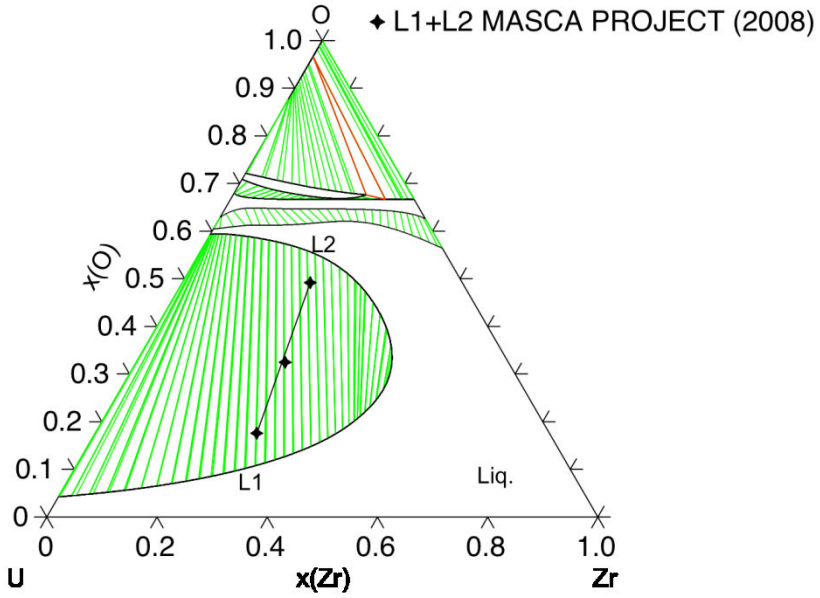

(b)

Figure 6: Comparison between the O-U-Zr calculated isothermal section at (a) 2643 K and (b) 2753 K and the experimental data reported by Bechta et al. [20]

It is clear that the orientation of the reported tie-lines are in disagreement with the present heat treatment results and with the data of Guéneau et al. [19]. The segregation argued by Bechta et al. [20] strongly affected the composition of the oxide and the metallic liquids. Furthermore, significant temperature gradients inside the samples are reported. In addition, no microstructures are presented in the publication. At 2643 K the calculated tie-line is significantly bigger than the experimental one. Nevertheless, these experimental results are still of great interest because they confirm the existence of a large miscibility gap in the ternary O-U-Zr liquid phase.

c) *Zr-UO_2 isopleth section*

In the past, a large number of research groups investigated the isopleth section Zr-UO_2. This section is extremely important during the normal functioning of a PWR as well as in the case of accidental scenario. The interaction between the UO_2-based fuel and the Zircaloy cladding, a Zr-based alloy, is crucial to understand the progression of a severe accident.

The calculated Zr-UO_2 isopleth section is shown in Figure 7. The experimental results of Juenke & White [14], and the present laser heating results are appended to the phase diagram.

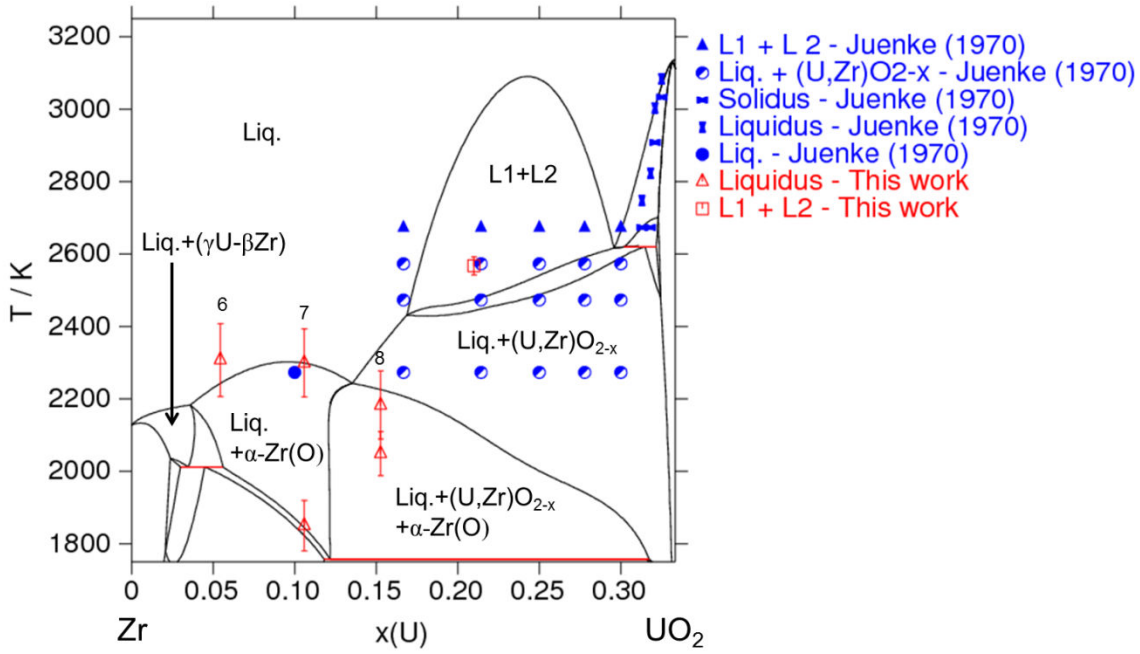

Figure 7: Calculated Zr-UO_2 isopleth section. The reported experimental data are from Juenke & White [14]. The L1+L2 reported for this work is referred to the heat treatment result obtained on sample OUZr_3

It must be pointed out that the Zr-UO_2 isopleth is not a pseudo-binary system, since tie-lines do not lie in the plane of this section. The extension of the liquid miscibility gap partially agree with the experimental data from Juenke & White [14]. The authors reported a tentative Zr-UO_2 section (Figure 1 in Chapter 2). It can be affirmed that their interpretation of the Zr-UO_2 is not fully accurate. In fact, they reported an isothermal ternary monotectic reaction, which is in contradiction with the Gibbs' rule. **The authors did not give neither a detailed chemical analysis on their samples nor the graphical results of the metallographic analysis**. The authors only argued the presence of a miscibility gap and of a [Liq.+$(U,Zr)O_{2-x}$] two-phase region. They also considered that the global composition of the samples did not change after the heat treatments. **However, as shown in Section 3.2.1.1, a certain mass is inevitably lost during a high temperature (T>2500 K) heat treatment**. The final composition of the sample investigated by Juenke & White probably moved across the O-U-Zr phase diagram. Juenke & White also affirmed that the post-test chemical analyses revealed a contamination with W, without giving any quantitative information. It has been shown in Section 3.2.1.1 that even a small fraction of W can drive the composition of the sample away from the initial one and affect the orientation of the tie-lines. Therefore, the discrepancies between the calculated diagram and the experimental results by Juenke & White could be related to the non-exhaustive interpretation of their results.

The laser heating results on sample OUZr_6, 7 and 8 are also reported on the calculated Zr-UO_2 section. It may be noted that especially for sample OUZr_7, the calculation is in good agreement with the experimental results. The first detected thermal arrest for sample OUZr_7 can be attributed to the formation of the α-(Zr,U)(O) phase, whilst the second inflection can be attributed to the complete solidification of the molten pool. The calculated liquidus underestimates the thermal arrest detected on sample OUZr_6. However, the calculation lies within the experimental error bar. The thermal arrest and the second inflection detected on sample OUZr_8 are significantly lower than the calculation transitions (Table 2).

Sample OUZr_8	Experimental result / K (ε=0.40)	Experimental result / K (ε=0.20)	Calculation / K
1st thermal arrest	2183	2343	2345
2nd thermal arrest	2049	2190	2220
Difference	134	153	125

Table 2: Comparison between the experimental results obtained on sample OUZr_8 and the calculation performed using the present thermodynamic model

However, the difference between the 1st and 2nd thermal arrest temperature, in the experiments and the calculation respectively, are similar. Therefore, the distance between the observed and calculated transitions is comparable. As introduced in Section 3.2.1.2, the emissivity correction can strongly influence the final result of a laser heating experiment. **In the present case it can be affirmed that the detected thermal arrests correspond to the calculated transitions [Liq.→Liq.+(U,Zr)O_{2-x}] and [Liq.+(U,Zr)O_{2-x}]→[Liq.+(U,Zr)O_{2-x}+α-Zr(O)]** respectively. Using an emissivity of 0.20 instead of the 0.40 as in Section 3.2.1.2, the resulting true temperatures would be 2343 K and 2190 K, which are significantly closer to the calculated value reported in Table 2. Furthermore, in principle, the emissivity correction applied to the radiance temperature is valid only for the first thermal arrest. However, emissivity estimation for the second thermal arrest was not possible, leading to the use of the same correction for the two temperature plateau.

4.1.1.3 O-U-Zr isothermal section at low temperatures (1373 and 1673 K)

a) *O-U-Zr isothermal section at 1373 K*

Once the high temperature ternary sections were optimised, the lower temperature sections were calculated to check their quality.

The calculated isothermal section at 1373 K is reported in Figure 8a. The calculated section presents a large [UO_2+(γU-βZr)+α-Zr(O)] three-phase region as inferred by Saller et al. [21]. Saller et al. proposed a tentative region between UO_2, ZrO_2 and α-Zr(O) starting from the data obtained by Lambertson & Müller on the UO_2-ZrO_2 phase diagram [13] (see Figure 8b). **However, Saller et al. did not confirm the shape of this zone of the phase diagram by experimental investigation**. Moreover, Saller et al. argued the existence of an equilibrium ZrO_2+α-Zr(O) (Figure 8b) but no experimental evident of this region has been reported. Politis [15] reported a tentative phase diagram at 1273 K very similar to that obtained by Saller et al.. **It can be concluded that a lack of experimental data exist in the [UO_2+ZrO_2-m+α-Zr(O)] region**. Therefore, no conclusion can be given on the quality of the calculated zone lying between UO_2, ZrO_2 and α-Zr(O).

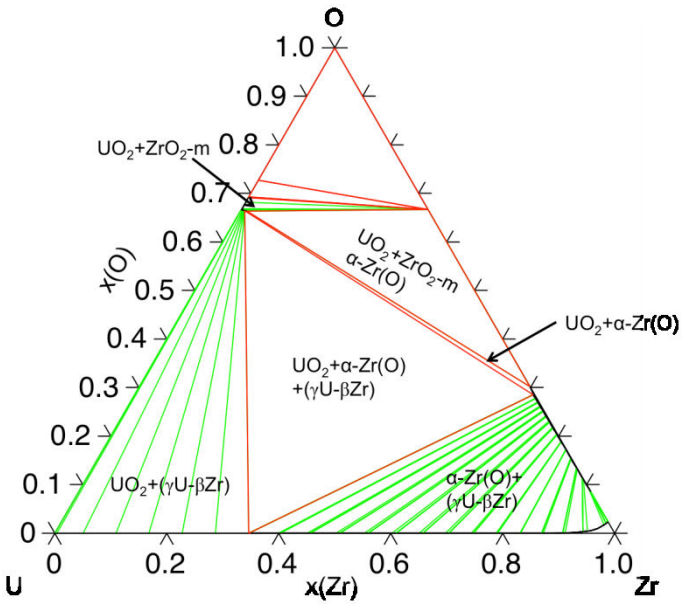

(a)

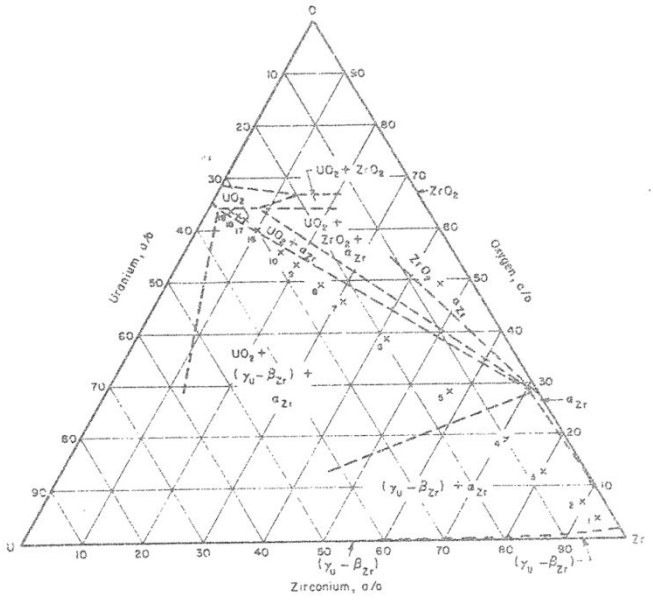

(b)

Figure 8: (a) Calculated O-U-Zr isothermal section calculated at 1373 K; (b) tentative O-U-Zr isothermal section reported by Saller et al. [21]

b) *O-U-Zr isothermal section at 1673 K*

The calculated section at 1673 K is reported in Figure 9a with the tentative isothermal section by Yamanaka et al. [22] (Figure 9b).

Significant differences exist between the calculated diagram and the experimental tentative isothermal section by Yamanaka et al. [22]. First of all, the calculated central three-phase region is an equilibrium [$(U,Zr)O_{2-x}$+α-(Zr,U)(O)+(γU-βZr)]. This implies that a biphasic equilibrium [$(U,Zr)O_{2-x}$+(γU-βZr)] is also calculated. At this temperature the UO_2-c solubilises a significant amount of ZrO_2-t, leading to an equilibrium with a $(U,Zr)O_{2-x}$-c mixed oxide. At the same time, the tetragonal ZrO_2-t solubilises a significant amount of UO_2-c. At 1673 K, the presence of equilibria involving mixed $(U,Zr)O_{2-x}$-c and $(Zr,U)O_2$-t is therefore expected. Yamanaka et al. did not report any chemical analysis on their O-rich samples; therefore no conclusion can be given on the validity of the extension of the UO_2 and ZrO_2-t domain of existence. Yamanaka et al. proposed a large central three-phase zone [UO_2+α-(Zr,U)(O)+Liq.]. The samples investigated to shape this region are on the UO_2-Zr

section, far from the inferred liquid corner. The authors did not use a systematic method to distinguish a solidified liquid from an (γU-βZr) alloy in equilibrium at the annealing temperature. They only inferred the existence of a liquid phase considering the U-Zr binary side of the ternary phase diagram. Furthermore, the authors affirmed that the composition of the liquid was not measured with precision.

Hofmann & Politis [23] performed diffusion couple experiments between 1173 K and 1773 K, showing that at 1673 K a U-rich liquid phase formed. They proposed a phase diagram similar to that of Yamanaka et al. on the bases of a tentative diffusion path. However, the authors chose only one of the possible diffusion paths available to interpret their results. In fact, considering the calculated diagram in Figure 9a, the diffusion layers reported by Hoffmann & Politis [23] could be also obtained. The region lying between UO_2, ZrO_2 and α-(Zr,U)(O) was also investigated by Yamanaka et al.. The study of this zone is challenging, because the solid/solid reaction kinetics is significantly slower those involving liquid. The authors performed heat treatments for 20 h. T**he authors reported the presence of four phases – UO_2, ZrO_2-t, ZrO_2-m and α-Zr(O) – in four investigated samples indicating that equilibrium conditions were not reached.** Therefore, the extension of this three-phase region in still uncertain at 1673 K.

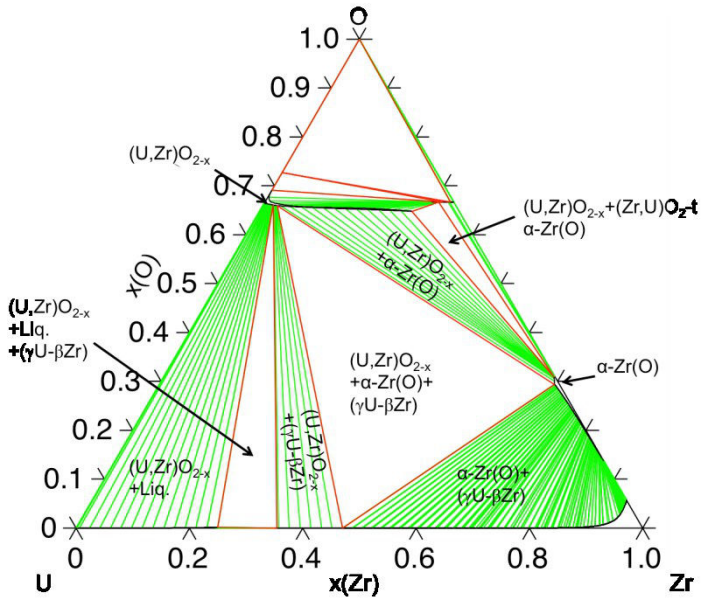

(a)

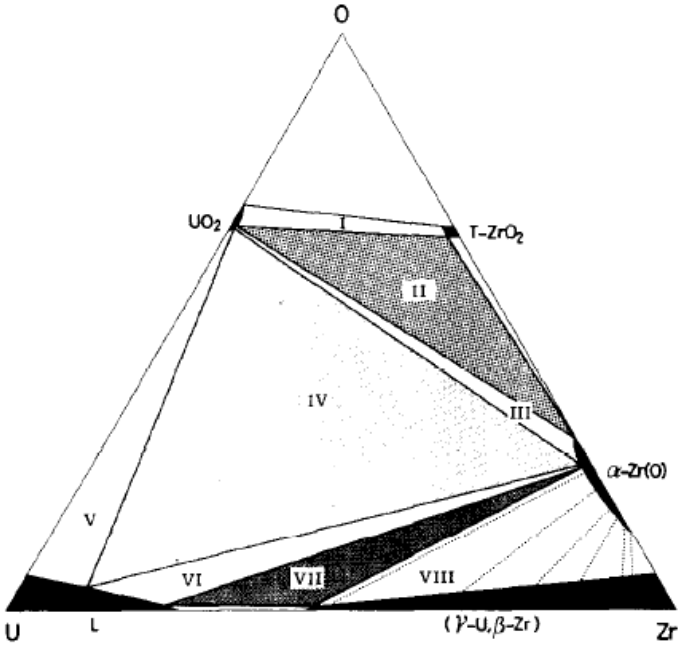

I	UO_2 + T-ZrO_2	V	UO_2 + L
II	UO_2 + T-ZrO_2 + α-Zr(O)	VI	α-Zr(O) + L
III	UO_2 + α-Zr(O)	VII	α-Zr(O) + L + (γ-U,β-Zr)
IV	UO_2 + α-Zr(O) + L	VIII	α-Zr(O) + (γ-U,β-Zr)

(b)

Figure 9: (a) O-U-Zr isothermal section calculated at 1673 K; (b) tentative O-U-Zr isothermal section at 1673 K proposed by Yamanaka et al. [22]

4.1.1.4 Summary

The O-U-Zr ternary system has been reassessed using significant experimental data and the present annealing results.

The calculated ternary phase diagram at 2567 K reproduces well the experimental tie-line observed during this work. **This new set of experimental data represents a precise investigation of the miscibility gap in the liquid phase**. These results can be considered more reliable than previous investigation by Juenke & White since the accurate temperature monitoring and the sound post-experiment analyses.

The present version of the thermodynamic model of the O-U-Zr ternary system is satisfactory, especially at high temperature (T>1800 K). However, the low temperature isothermal sections revealed that some inconsistencies exist with previous tentative diagrams. In particular, the presence of a large [UO_2+α-(Zr,U)(O)+Liq]. three-phase region at 1673 K must be confirmed experimentally investigating the U-rich corner of the O-U-Zr phase diagram. Furthermore, the region between UO_2, ZrO_2 and α-(Zr,U)(O) needs to be investigated between 1600 K and 2300 K to define the extension of the (U,Zr)O_2-ZrO_2-α-(Zr,U)(O) three-phase equilibrium.

A very small miscibility gap in the fcc (U,Zr)O_{2-x}-c phase is calculated between 1634 K and 1655 K. The presence of this miscibility gap is due to extrapolation of the parameters used to fit the high temperature experimental data. In the future, this feature should be removed by modifying the present assessment. Furthermore, new oxygen potential experimental data are needed to better model the region of existence of the (U,Zr)$O_{2\pm x}$-c phase in the ternary phase diagram.

4.1.2 O-Fe-Zr system

The experimental investigation of the O-Fe-Zr system is particularly challenging due to the strong affinity for oxygen for both Fe and Zr. The control of the oxygen potential and thus of the oxidation state of Fe are the main issues.

The limited number of available experimental data is concentrated in the O-rich region of the ternary phase diagram. Namely, equilibria involving ZrO_2 and iron oxides have been investigated.

The present assessment is essentially based on the experimental results reported by Bechta et al. [24], Kiminami et al. [25] and Katsura et al. [26]. The experimental results obtained by Jones et al. [27] will be also compared to the calculations but were not considered during the assessment.

The first step of the assessment was dedicated to the model of the ZrO_2-FeO section. Bechta et al. [24] reported a composition for the iron oxide of $FeO_{1.056}$. However, due to the large uncertainties on their measurements, the section ZrO_2-FeO is considered. The thermodynamic model by Fabrichnaya & Pavlyuchkov [28] has been used as a starting point for the present assessment. Their description was modified since the Zr-O model is different from the present one.

The second step of the modelling was dedicated to the assessment of the ZrO_2-Fe_3O_4 section. In this framework, the Fe^{3+} ion in (Zr,Fe)O_{2-x}-c, (Zr,Fe)O_2-t and (Zr,Fe)O_2-m phases plays the dominant role. Using the work of Fabrichnaya & Pavlyuchkov [28] as a start point, the spinel and the corundum phases have been also reassessed.

4.1.2.1 ZrO_2-FeO section

The interaction parameter ${}^0L^{oxide_cubic}_{(Fe^{2+},Zr^{4+})(O^{2-})(Va)}$ has been reassessed to better shape the domain of existence of the cubic (Zr,Fe)O_{2-x}-c phase. The parameter ${}^0L^{oxide_cubic}_{(Fe^{3+},Zr^{4+})(O^{2-})(Va)}$ has a weaker effect on the present section. The Gibbs energy of the end-members in the tetragonal (Zr,Fe)O_2-t phase reported by Fabrichnaya & Pavlyuchkov [28] have been modified to avoid the presence of a (Zr,Fe)O_2-t phase in the Fe-O phase diagram. The interaction parameter ${}^0L^{oxide_tetra}_{(Fe^{2+},Zr^{4+})(O^{2-})}$ has been reassessed to better fit the solubility data of Bechta et al. [24] and to increase the temperature of the reaction [T+L1+L2] → [C+L1+L2]. The description of the monoclinic (Zr,Fe)O_2-m phase has not been modified, maintaining the model reported by Fabrichnaya & Pavlyuchkov [28].

The ${}^0L^{liq}_{(Fe^{2+},Zr_{4+})(O^{2-})}$ interaction parameter in the liquid phase has been reassessed to better reproduce the experimental observation of Bechta et al. [24]. The 1st order interaction parameter reported by Fabrichnaya & Pavlyuchkov [28] has been maintained. The calculated ZrO_2-FeO section is shown in Figure 10.

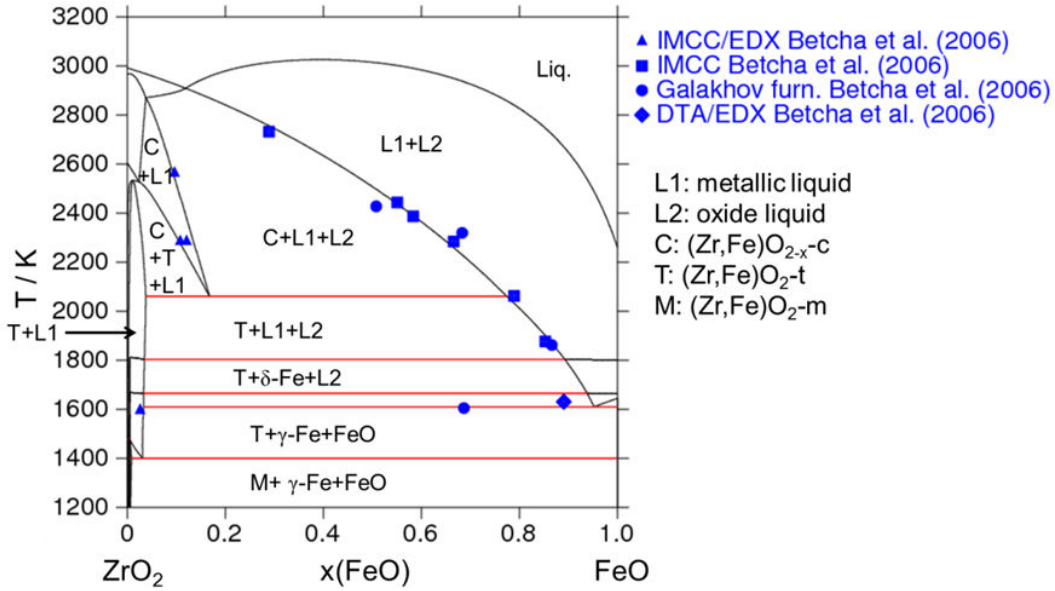

Figure 10: Calculated ZrO_2-FeO section, where the experimental data are from Bechta et al. [24]

A good agreement is obtained between calculation and experimental data. The calculated solubility of FeO in ZrO_2-t (3.3 mol % FeO) is in agreement with the experimental result (2.6 mol % FeO). The calculated eutectic composition, 5 mol % FeO, is lower than that reported by Bechta et al. (10.5 mol % FeO). The calculated liquidus curve is in excellent agreement with the experimental data of Bechta et al.. It may be noted that a miscibility gap in the liquid phase is calculated. The extension of the miscibility gap misses of experimental confirmations.

4.1.2.2 ZrO_2-Fe_3O_4 section

The solubility data obtained by Kiminami [25] and the oxygen partial pressure measurement of Katsura et al. [26] have been used to shape this section. The ZrO_2-Fe_3O_4 phase diagram calculated under a partial pressure of oxygen $p(O_2)$=0.21 atm is reported in Figure 11.

The temperature of transition [T+H] → [T+S] calculated in Figure 11 is 1674 K, consistent with the experimental observation of Kiminami [25] and Jones et al. [27] at about 1710 K. The calculated solubility of Fe_2O_3 in ZrO_2-t (1.3 mol % Fe_2O_3) is in fair agreement with Kiminami (3 mol % Fe_2O_3). However, the calculated solubility of ZrO_2-t in Fe_2O_3 is underestimated compared to the experimental results. The temperature of transition [T+S] → [T+L] is in agreement with Jones et al. data.

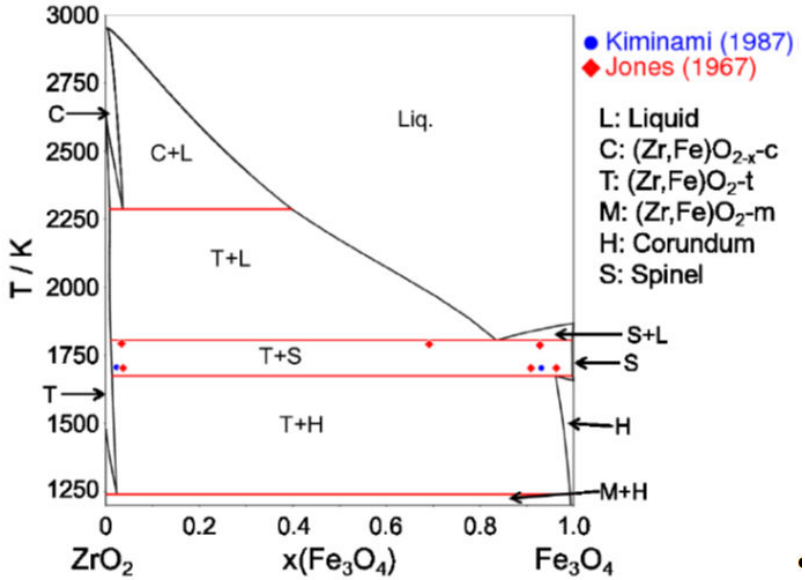

Figure 11: Calculated ZrO_2-Fe_3O_4 section under $p(O_2)$=0.21 atm. The reported experimental data are from Jones et al. [27] and Kiminami [25]

4.1.2.3 O-Fe-Zr isothermal section at 1473 K

Katsura et al. [26] determined phase equilibria and measured the oxygen partial pressure in the FeO-Fe_2O_3-ZrO_2 system at 1473 K. The calculated isothermal section of the FeO-Fe_2O_3-ZrO_2 system at 1473 K is presented in Figure 12.

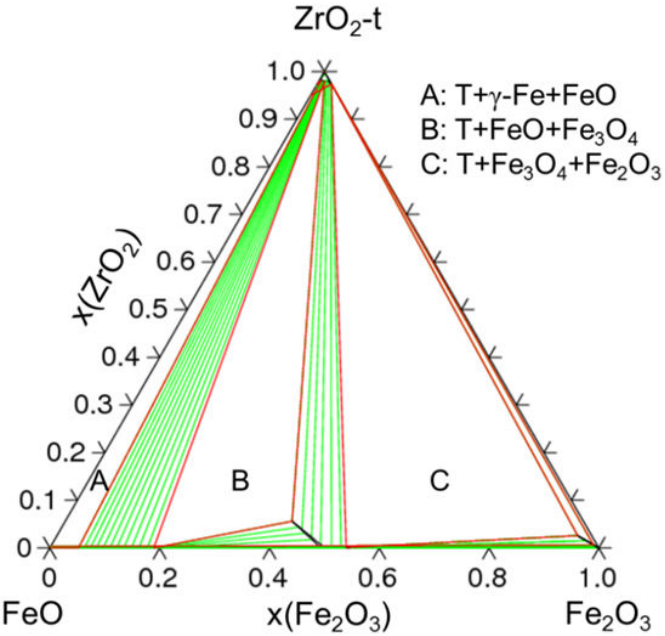

Figure 12: FeO-Fe_2O_3-ZrO_2 isothermal section calculated at 1473 K. The three-phase domains labelled A, B and C correspond to the equilibria reported in the legend. T stays for the ZrO_2-t

The calculated isothermal section in Figure 12 is in agreement with the experimental observation of Katsura et al. [26]. Katsura et al. also measured the variation of the oxygen partial pressure inside the two-phase regions separating the three phase regions A, B and C. The comparison between the calculated oxygen partial pressure in the three-phase regions and the experimental results is reported in Table 3.

	A		B		C	
	Exp.	Calc.	Exp.	Calc.	Exp.	Calc.
Log($p(O_2)$) / atm	< -11.82	-11.9	-9.21 ÷ -9.09	-9.45	> -3.76	-2.9

Table 3: Comparison between calculated and measured oxygen partial pressure in the three-phase regions (A, B and C) in Figure 12. The reported experimental values correspond to the results obtained in the two-phase regions separating A, B and C

Agreementing to the results of Katsura et al., the oxygen partial pressure P_{O2} inside the two-phase region between A and B varies from $10^{-11.82}$ to $10^{-9.21}$. The calculation of Po_2 in zone A is in good agreement with Katsura et al.. The calculated value of Po_2 in zone B is lower than the value suggested by Katsura et al. (i.e., between $10^{-9.21}$ and $10^{-9.09}$). The same discrepancy was obtained by Fabrichnaya & Pavlyuchkov [28]. The authors argued that a large solubility of ZrO_2 in Fe_3O_4 might induce a decrease in the oxygen partial pressure. The value of Po_2 calculated in zone C is consistent with the experimental observation.

4.1.2.4 Calculated O-Fe-Zr isothermal sections

Four calculated O-Fe-Zr isothermal sections are reported in Figure 13. The miscibility gapin the Fe-O system between liquid Fe and FeO (i.e., L1 and L2 respectively) propagates into the ternary phase diagram. The presence of this miscibility gap in the liquid phase is noticeable at 3073 K.

4.1.2.5 Summary

The O-Fe-Zr ternary system has been assessed using the limited number of significant experimental data found in literature. The optimisation is based on the recent reassessment published by Fabrichnaya & Pavlyuchkov [28]. Their model has been significantly modified mainly to be consistent with the mathematical description of the fcc mixed oxide phase used in this work.

It can be concluded that the available experimental data are not sufficient to perform an accurate thermodynamic modelling for the O-Fe-Zr ternary system. Furthermore, the limited amount of experimental data is concentrated in the O-rich part of the diagram. The region close to the Fe-Zr binary side is experimentally unknown.

In order to obtain a reliable description of the O-Fe-Zr system the O low-content region of the phase diagram must be investigated. Even if the experimental data on the ZrO_2-iron oxides equilibria cited above can be considered consistent, a new set of experimental data is needed to better shape the solubility limits of the ZrO_2 allotropic forms as well as those of iron oxides. Thermodynamic data such as oxygen potential measurements will be also extremely useful to define equilibria in the ternary phase diagram. Finally, the extension of the high temperature miscibility gap in the liquid phase is totally unknown. In the present work it is calculated by extrapolation from the binary systems and from the ternary interaction parameters assessed for the ZrO_2-iron oxides systems.

The presence of this miscibility gap is of great importance during a severe accident in a nuclear reactor. As for the O-U-Zr miscibility gap, it contributes to the stratification of the

molten corium into two immiscible liquid layers. The miscibility gap in the liquid phase has been investigated using the experimental setup developed during the present work. The results will be presented in Chapter 6 and represent an exploratory study. Therefore, they have not been used for the present assessment.

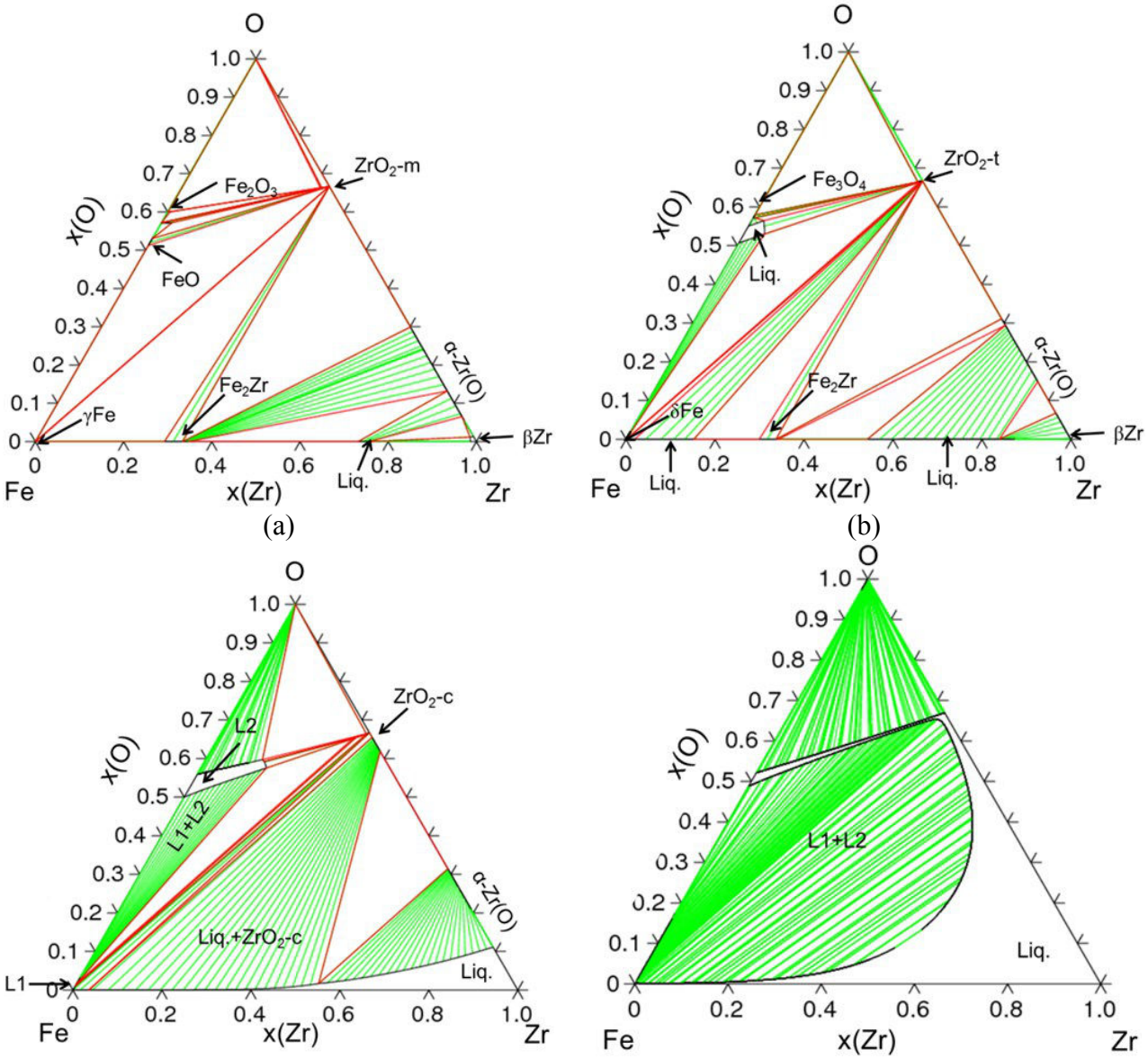

Figure 13: O-Fe-Zr isothermal sections calculated with the present model. (a) 1273 K; (b) 1773 K; (c) 2273 K; (d) 3073 K

4.1.3 O-Fe-U system

The experimental investigation of the O-Fe-U ternary system involves the same issues presented for the O-Fe-Zr system. Both Fe and U have several oxidation states depending on temperature, oxygen potential and total pressure during the experiments. The high temperature vaporisation tendency of Fe makes the control of the sample composition challenging.

In the present assessment, the experimental data of Bechta et al. [29] on the UO_2-FeO_{1+x} section were considered. As introduced in Chapter 2, significant uncertainties exist on the stoichiometry of the FeO_{1+x} phase. In this work, the section UO_2-$FeO_{1.1}$ has been modelled.

Three interaction parameters have been added in the fcc phase in order to model the solubility of Fe in UO_2. In the present work, only interaction parameters between U^{4+} and Fe^{2+} ions have been assessed. The Fe^{3+} ion certainty influences the equilibria between UO_2 and iron oxide. However, due to the lack of experimental data, it was preferred to keep the model as simple as possible.

The starting point of the assessment is the model of the UO_2-CaO system performed by N. Dupin [8].

4.1.3.1 UO_2-$FeO_{1.1}$ section

The calculated UO_2-$FeO_{1.1}$ section is reported in Figure 14.

The solubility of FeO in the (U,Fe)O_{2-x}-c phase has been initially shaped using the ${}^0L^{oxide_cubic}_{(Fe^{2+},U^{4+})(*)(*)}$ interaction parameter. However, this parameter stabilise the fcc cubic phase along the fictive UO_2-FeO_2 section. In order to stabilise the phase along the UO_2-FeO section, the 1st order parameter ${}^1L^{oxide_cubic}_{(Fe^{2+},U^{4+})(*)(*)}$ has been added. The calculated solubility of FeO in UO_2 at the eutectic temperature (1627 K) is 20 mol % FeO. This result is higher than the experimental observation by Bechta et al [29] (17±1 mol % FeO). The ternary parameter ${}^0L^{oxide_cubic}_{(Fe^{2+},U^{4+},U^{5+})(*)(*)}$ was added to the description of the (U,Fe)O_{2-x}-c phase in order to avoid the presence of a miscibility gap at high temperature (T>2000 K). However, the addition of this parameter was not sufficient to completely remove the miscibility gap from the UO_2-$FeO_{1.1}$ section. Below 1000 K, a miscibility gap in the (U,Fe)O_{2-x}-c phase is still calculated. Since no experimental studies are available, no conclusions can be drawn on the existence of this feature.

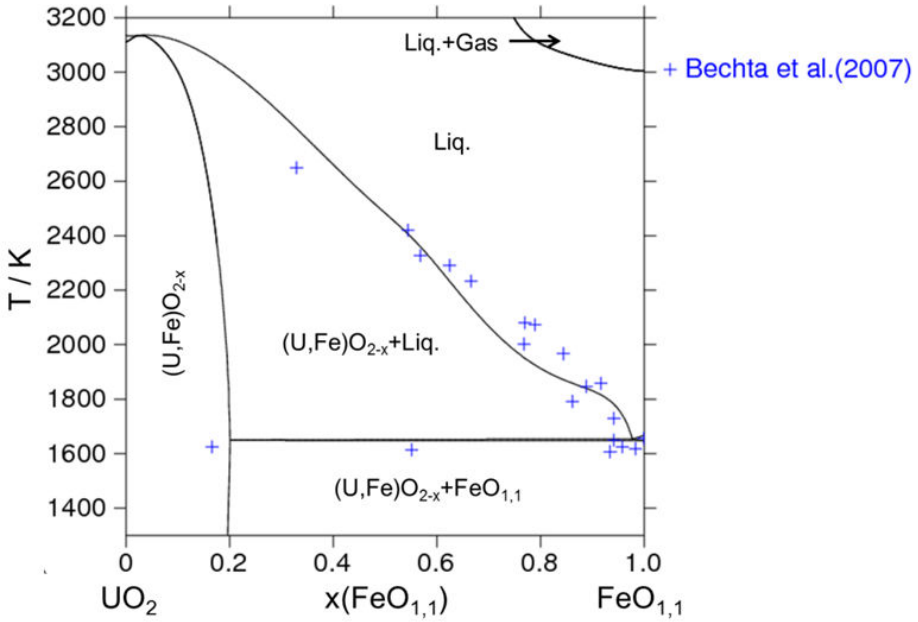

Figure 14: Calculated UO_2-$FeO_{1.1}$ section compared to Bechta et al [29] experimental data (b)

The calculated eutectic composition (3 mol % FeO) is in good agreement with the experiment (4 mol % FeO). The calculated eutectic temperature (1647 K) is overestimated compared to the value reported by Bechta et al. (1627±5 K). The liquidus line has been shaped by fitting the experimental data obtained by Bechta et al. [29]. Two interaction parameters, ${}^0L^{liq}_{(Fe^{2+},U^{4+})(O^{2-})}$ and ${}^1L^{liq}_{(Fe^{2+},U^{4+})(O^{2-})}$, have been assessed.

4.1.3.2 Calculated O-Fe-U isothermal sections

Four isothermal O-Fe-U sections calculated at 1273 K, 1773 K, 2273 K and 3073 K are reported in Figure 15. Both Fe-O and U-O binary systems exhibit a miscibility gap in the liquid phase (see Appendix B). At 3073 K the two binary miscibility gaps propagate into the ternary system, leading to the presence of a large immiscibility region.

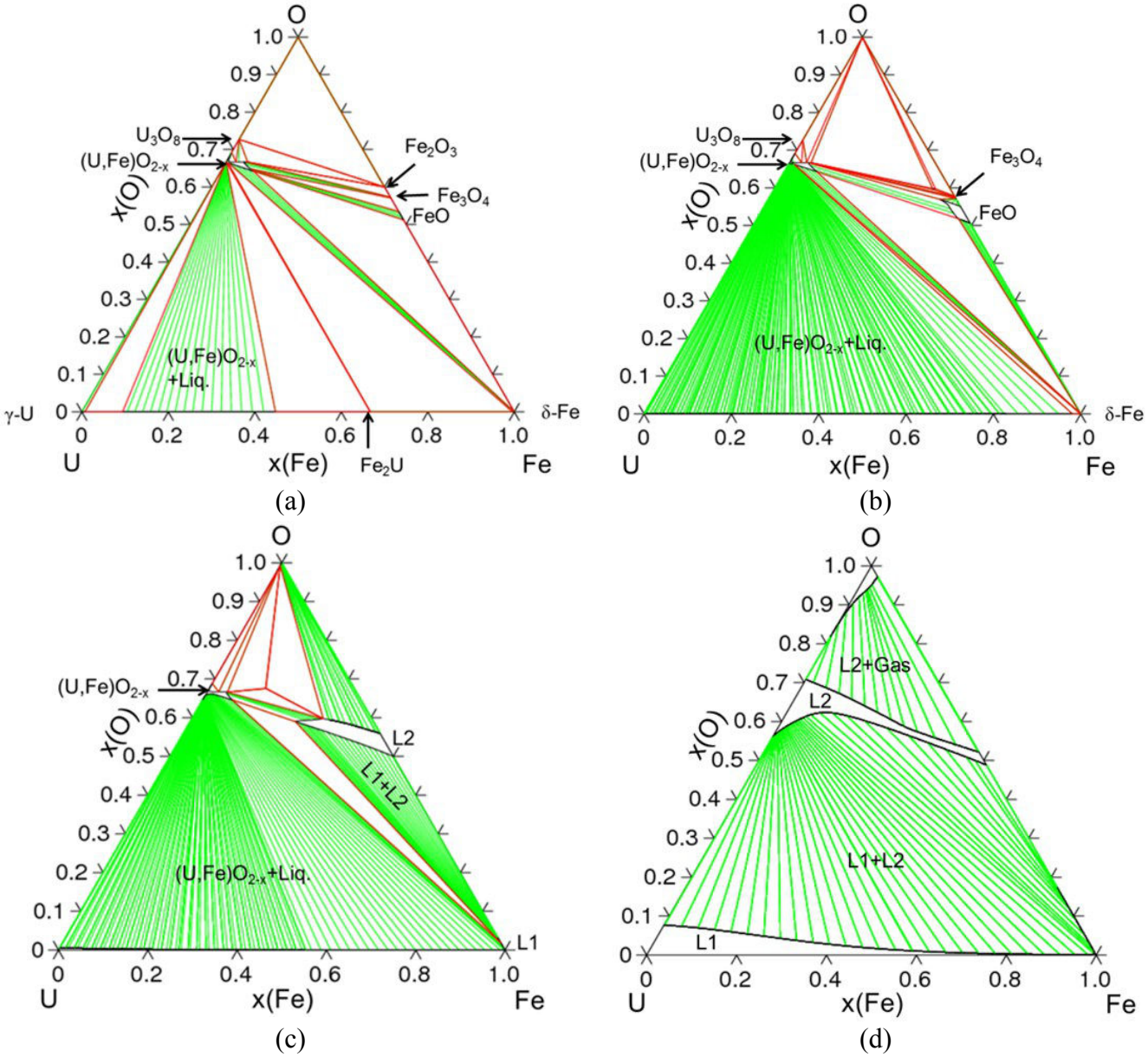

Figure 15: O-Fe-Zr isothermal section calculated with the present model. (a) 1273 K; (b) 1773 K; (c) 2273 K; (d) 3073 K

4.1.3.3 Summary

The UO_2-$FeO_{1.1}$ section has been optimised using the experimental data measured by Bechta et al. [29]. Taking into account the uncertainties on the exact stoichiometry of FeO_{1+x}, the present assessment can be considered satisfactory. However, the lack of experimental data in the ternary diagram does not allow to perform a sound modelling of the O-Fe-U system. As already affirmed for the O-Fe-Zr system, thermodynamic experimental data such as oxygen potential measurement are crucial for the thermodynamic assessment of a ternary system and

are missing for the present case. The metallic region of this ternary system is experimentally unknown, therefore the calculation in this zone are the result of extrapolation from the Fe-U binary system.

4.1.4 O-Pu-U-Zr system

In this work, only the PuO_2-ZrO_2 section has been optimised using the solubility data of Mardon et al. [30] and the HTXRD results by Albiol et al. [31]. The present laser heating results on sample P50Z50 has been also used to shape the liquidus/solidus transition. Since the lack of available experimental data, only two interaction parameters have been assessed. In particular, an interaction parameter in the liquid phase was added to fit the laser heating results obtained during this work. A second interaction parameter was added in the fcc $(Pu,Zr)O_2$-c phase to improve the agreement with the solubility data of Mardon et al. [30]. No interaction parameters were added to the description of the $(Pu,Zr)O_2$-m and $(Pu,Zr)O_2$-t phases, since the lack of available experimental data. Only the Gibbs energies of the end-members have been assessed. At the end of the section a calculated liquidus surface of the UO_2-PuO_2-ZrO_2 system will be also presented.

4.1.4.1 PuO_2-ZrO_2

The calculated PuO_2-ZrO_2 phase diagram is reported in Figure 16.

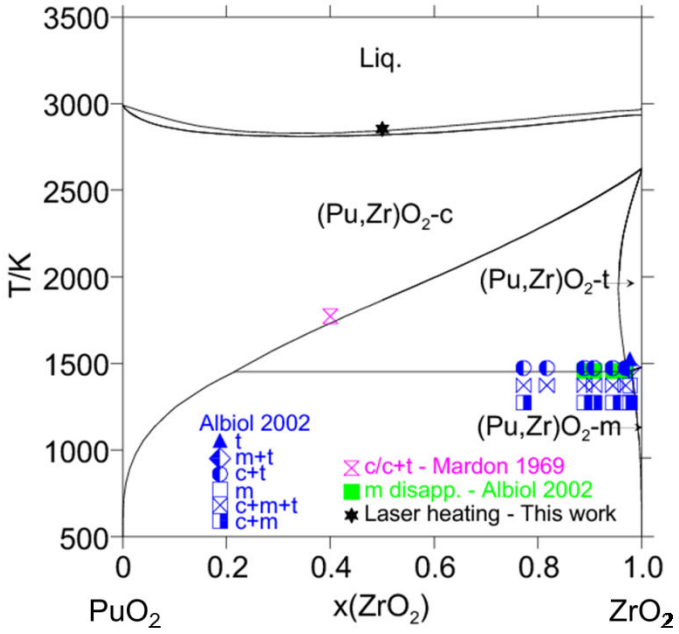

Figure 16: Calculated PuO_2-ZrO_2 phase diagram, where the experimental data are from Mardon et al. [30] and Albiol et al. [31]

A good agreement has been obtained with the selected experimental data. However, a need of new data is evident: The solubility limit of $(Pu,Zr)O_2$-t in cubic $(Pu,Zr)O_2$-c needs to be better investigated. The calculated liquidus/solidus lines are in excellent agreement with the experimental data obtained by laser heating during this work on sample P50Z50 ($(PuO_2)_{0.50}(ZrO_2)_{0.50}$).

The present calculated phase diagram is in general agreement with the calculated phase diagram reported by Kinoshita et al. [32–34], except for the selected melting temperature of PuO_2. Kinoshita et al. selected the experimental value by Kato et al. [35] (2843 K), whilst in

the present work, the value obtained by De Bruycker et al. [36] (3017±28 K) has been selected. As highlighted by Guéneau et al. [7] and Kato et al. [35], PuO_2-rich samples across the PuO_2-UO_2 system can be affected by uncontrolled reduction due to the contact with the metallic containment crucible. Indeed, De Bruycker et al. obtained the melting temperature of PuO_2 under containerless conditions, using the laser heating setup at ITU. This technique avoids the interaction of the sample interacting with the crucible, which is not the case in experiments performed by Kato et al. [35] who used a W and Re capsules that can interact with the liquid PuO_2. Furthermore, this choice allows to be consistent with the assessment of the UO_2-PuO_2 system by Guéneau et al. [7].

4.1.4.2 UO_2-PuO_2-ZrO_2 system

Starting from the thermodynamic assessment on the U-Pu-Zr-O systems it is possible to deduce the pseudo-ternary UO_2-PuO_2-ZrO_2 phase diagram. It must be pointed out that in the present work no quaternary interaction parameters were introduced. Therefore, the calculated UO_2-PuO_2-ZrO_2 phase diagram is a result of extrapolation from the UO_2-ZrO_2, UO_2-PuO_2 and PuO_2-ZrO_2 isopleth sections.

Figure 17 represents the extension of the liquidus lines into the UO_2-PuO_2-ZrO_2 pseudo-ternary system.

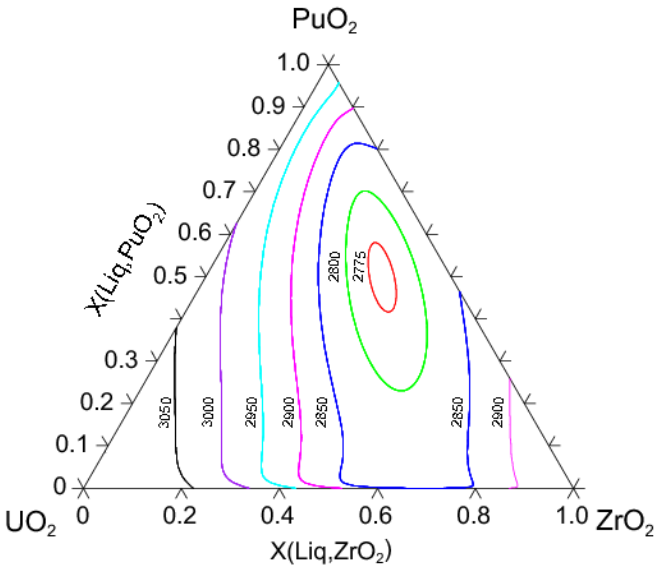

Figure 17: Calculated liquidus surface in the PuO_2-UO_2-ZrO_2 system showing the location of the minimum on this surface

This diagram allows to identify the minimum of the liquidus surface at the composition $(UO_2)_{0.15}(PuO_2)_{0.50}(ZrO_2)_{0.35}$ and temperature T=2770 K.
The reported liquidus surface has been calculated considering the system at the thermodynamic equilibrium. Note that the laser heating experiments described in Section 3.2.3 should be compared to this diagram with precaution.

In the following section dedicated to the thermodynamic calculation to interpret experimental results, it will be shown that the atmospheric conditions strongly influence the solidification behaviour of the UO_2-PuO_2-ZrO_2 samples.

4.2 Solidification path calculations

The experimental results reported in Chapter 3 on O-U-Zr and UO_2-PuO_2-ZrO_2 systems will be compared with calculation performed using the current thermodynamic model.

(i) The solidification path followed by the annealed samples OUZr_1 and OUZr_3 are calculated and the observed microstructures interpreted.
(ii) The laser heating experimental on the OUZr_7 sample will be also interpreted.
(iii) The effect of the experimental atmosphere on the UO_2-PuO_2-ZrO_2 laser heated samples can be taken into account during the calculations, showing that depending on the nature of the investigated samples, the buffer gas can play both minor and major role.
(iv) Solidification path calculations will be finally used to interpret the microstructure of an arc-melted U-Zr-Fe-O prototypic in-vessel corium.

4.2.1 O-U-Zr samples

The present annealing experimental results (Section 3.2.1) showed that the visual investigation of the microstructure of the solidified samples coupled with EDS and WSD analyses can help the identification of a prior single phase liquid or a two immiscible liquids structure respectively. However, to better understand the solidification sequence during cooling, it is useful to calculate the solidification path followed by the samples.

4.2.1.1 Sample OUZr_1

Using the global composition measured by WDS and corrected for W contamination ($O_{0.39}U_{0.103}Zr_{0.507}$), the solidification path of sample OUZr_1 has been calculated. The calculation has been performed considering the system at the thermodynamic equilibrium at each temperature step. The resulting path is reported in Figure 18.

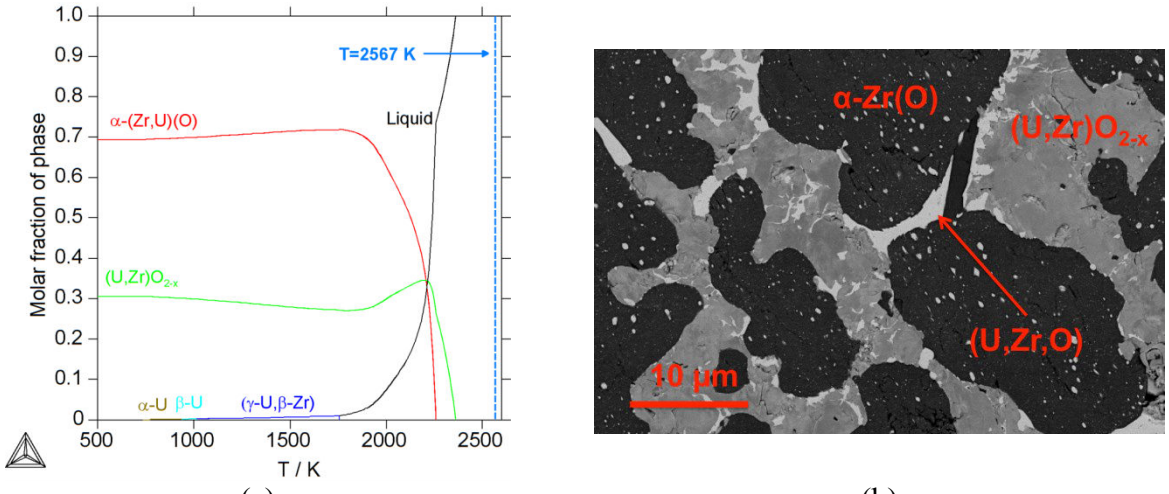

(a) (b)

Figure 18: (a) Solidification path of sample OUZr_1 annealed at 2567 K for 45 minutes. The calculation was performed considering the system at the thermodynamic equilibrium; (b) microstructure of the solidified sample OUZr_1

The different calculated phase transformations are:

T=2361 K: Liq. → Liq. + $(U,Zr)O_{2-x}$
T=2258 K: Liq. + $(U,Zr)O_{2-x}$ → Liq. + $(U,Zr)O_{2-x}$ + α-(Zr,U)(O)
T=1759 K: Liq. + $(U,Zr)O_{2-x}$ + α-Zr(O,U) → $(U,Zr)O_{2-x}$ + α-(Zr,U)(O) + (γU-βZr) alloy

At lower temperature, the allotropic transitions of U are also calculated.

The equilibrium calculation reveals that at the annealing temperature – T=2567 K – the sample consists in a single liquid phase. The calculations suggest that the first condensed phase formed during cooling is a fcc $(U,Zr)O_{2-x}$-c phase at 2361 K: by the reaction Liq. → [Liq. + $(U,Zr)O_{2-x}$-c]. This phase should grow in the form of dendrites. However, the observed microstructure (Figure 18b) shows that the dendritic phase is the α-(Zr,U)(O), meaning that it is this phase that firstly form during cooling. While oxide phases may experience large undercooling, metallic phases are normally characterised by small undercooling. The fact that the α-(Zr,U)(O) firstly formed, it can be explained by a metastable state of the system during cooling, which drove the liquid oxide in an undercooled condition, leading the α-(Zr,U)(O) phase solidifying first.

Following the solidification path, the composition of the liquid phase starts to change: the formation of an oxide phase leads to the decrease of the O atomic fraction and the simultaneous increase in the atomic fraction of U and Zr (Figure 19a). The mixed $(U,Zr)O_{2-x}$ oxide is initially enriched in Zr (Figure 19b). At 2252 K the liquid phase reacts with the mixed oxide leading to the formation of α-(Zr,U)(O). In correspondence of this transition, the atomic fraction of Zr and O in the liquid phase and in the mixed oxide decreases. It may be noted that a small solubility of U (2 at % U) is calculated in the α-(Zr,U)(O) (Figure 19c). Following the solidification path, the amount of liquid keeps decreasing whilst the α-(Zr,U)(O) experiences a rapid growing up to about a molar fraction of 0.7. At 1759 K, the solidus temperature, the remaining liquid solidifies into a (γU-βZr) alloy with a composition of $U_{0.52}Zr_{0.48}$. At this temperature, three condensed phases – $(U,Zr)O_{2-x}$, α-(Zr,U)(O) and (γU-βZr) alloy – are in equilibrium. The major phase is α-(Zr,U)(O) (molar fraction of 0.69). Considering the solidification path in the solid state (T<1759 K), the minor (γU-βZr) alloy progressively disappears. The room temperature configuration (T=300 K), is characterised by the presence of the two oxide phases, UO_2 and α-Zr(O). No metallic phase is calculated below 570 K. However, EDS and WDS analyses revealed the presence of a solidified metallic phase enriched in U within $(U,Zr)O_{2-x}$ and α-(Zr,U)(O) (see Table 5 of this Chapter 3).

It should be stressed that during the present experiment, thermodynamic equilibrium is reached when the sample is completely liquid that is at 2567 K. During the first part of cooling, the rapid decrease in temperature may lead to out-of-equilibrium conditions. However, the rapid kinetics reaction due to the high temperature and the presence of a liquid phase, counterbalanced temperatures effects. Therefore, the solidus temperature, 1759 K, is considered in this work, as the limit of validity of the solidification path calculations. Below the solidus temperature, solid/solid reactions take place. The kinetics of these reactions is slower that those involving liquid phase. This is also confirmed by the experimental observation: the presence of a mixed oxide $(U,Zr)O_{2-x}$ and of a metallic phase enriched in U is the sign that the sample did not completed the solidification path shown in Figure 19.

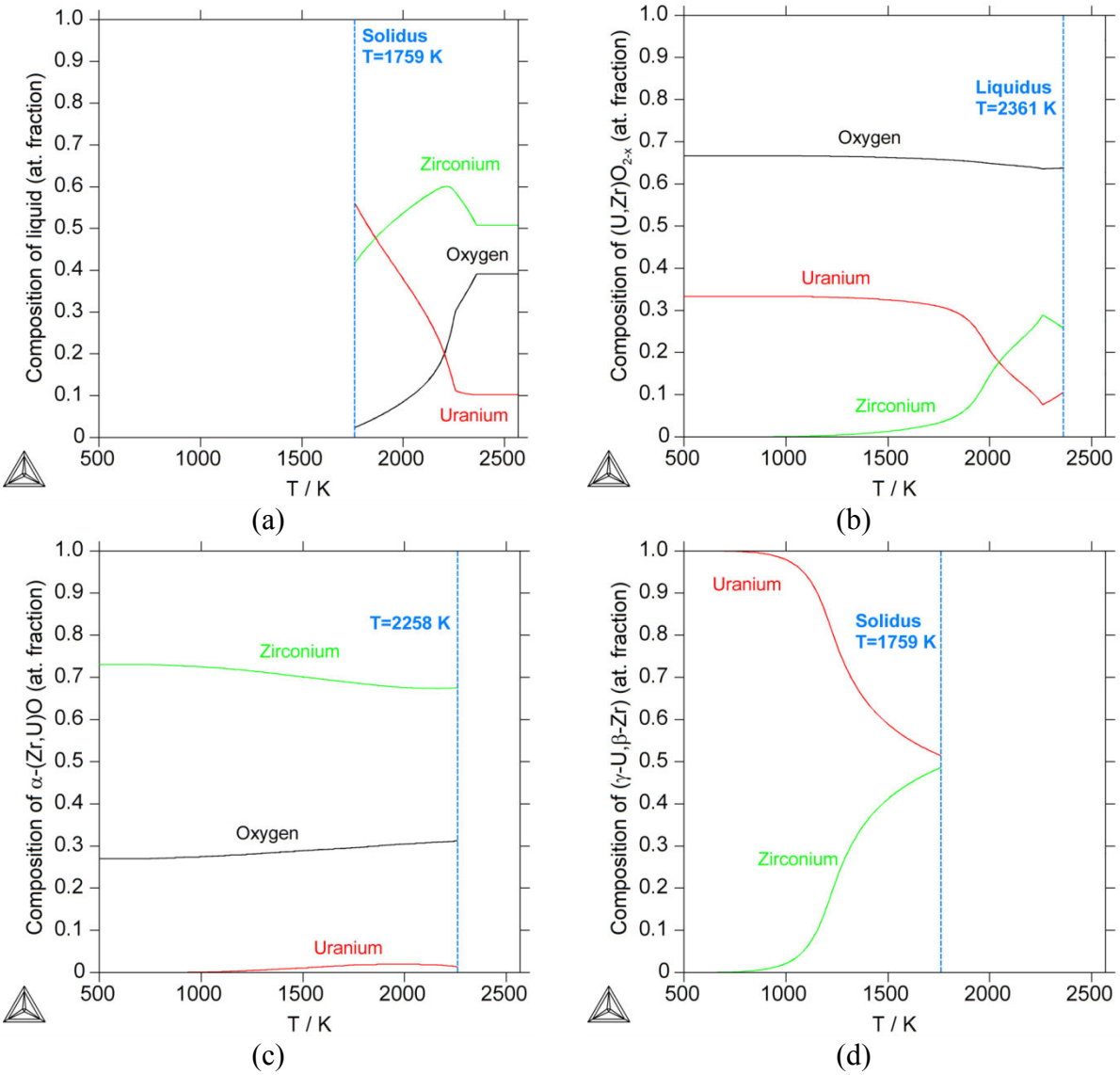

Figure 19: Composition of the phases appearing during the solidification of sample OUZr_1. (a) composition of the liquid; (b) composition of $(U,Zr)O_{2-x}$; (c) composition of α-Zr(O); (d) composition of (γU-βZr)

The composition of $(U,Zr)O_{2-x}$, α-(Zr,U)(O) and of liquid calculated at the solidus temperature (T=1759 K) is reported in Table 4 with the experimental observation.

	$(U,Zr)O_{2-x}$		**α-(Zr,U)(O)**		**Quenched liquid**	
	Calc.	**Exp.**	**Calc.**	**Exp.**	**Calc.**	**Exp.**
at % O	65.8	64.4±3	29.6	25.1±1	2.4	33.1±10
at % U	30.8	30.5±0.5	1.8	2.0±0.5	56.0	63.9±5
at % Zr	3.4	5.1±1	68.6	72.9±4	41.6	2.6±1
Molar fraction (%)	27	23*	72	76*	1	1*

Table 4: Comparison between calculated composition of different phases at equilibrium at 1759 K, the calculated solidus temperature, and experimental results. * Obtained using ImageJ® software

In general, a good agreement between experiment and calculation is obtained. The calculated U content in the fcc mixed oxide is in excellent agreement with the experiment. However, the calculated Zr content in the same phase is slightly underestimated compared to the experimental result. An exact comparison between the calculated and the experimentally observed O content in the $(U,Zr)O_{2-x}$-c phase cannot be done, since the significant

uncertainties in the experimental O detection. Nevertheless, it can be concluded that at the solidus temperature a hypo-stoichiometric mixed oxide is present. A general agreement is obtained on the α-(Zr,U)(O), except for the underestimated Zr content in the calculation. A significant discrepancy is observed between the calculated and the measured composition of the quenched liquid. The experimental O-content in the minor metallic phase is overestimated due to the presence of the surrounding major oxide phases. Furthermore, UO_2 has been used as a standard for the WDS analyses on both U and O. A metallic U standard should have been probably more adapted for WDS measurement on U-rich metallic phases.

The calculated mass fraction of each phase is in agreement with the results obtained using ImageJ® software.

A detailed calculation on the effect of W on the heat treatment experiment is given in Appendix C. Calculations confirm that W is not dissolved by the liquid. Therefore the only contribution of W is to bias the Zr fraction available for the O-U-Zr reaction.

4.2.1.2 Sample OUZr_3

The post-experiment analyses performed on sample OUZr_3 revealed the presence of two solidified immiscible liquids, one oxide and one metallic.

The final composition of the two liquids was measured by WDS at the LMAC, CEA Marcoule. However, a precise measurement of the final global composition of the sample was not possible. Applying the same procedure used for sample OUZr_1 (see Section 3.2.1.1) the final composition of sample OUZr_3 can be estimated. Considering that the mass loss was only due to the departure of the $UO_{(g)}$ volatile species, the estimated final composition is $O_{0.359}U_{0.243}Zr_{0.398}$ (Table 5).

Sample OUZr_3	**at % initial**	**w % initial**	**$m_{initial}$ / g**	**Δm / g ***	**m_{final} / g**	**w % final**	**at % final**
O	38	5.86	0.2149	0.0411	0.1738	5.74	35.9
U	28	64.20	2.3545	0.6000	1.7545	57.96	24.3
Zr	34	29.95	1.0990	/	1.0990	36.30	39.8
Total	100	100	3.6684	0.6411	3.0273	100	100

Table 5: Estimation of the final composition of sample OUZr_3 before cooling. * The mass loss is only due to the departure of the $UO_{(g)}$ volatile species

Starting from the estimated final composition, the calculated solidification path revealed the presence of two liquids in equilibrium at 2567 K (Figure 20).

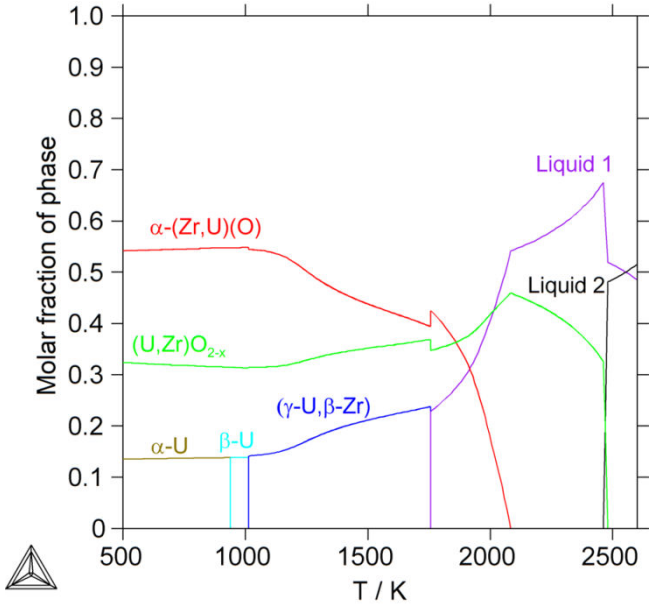

Figure 20: Solidification path calculated for sample OUZr_3, annealed at 2567 K for 45 minutes

The microstructure observed in Figure 14 of Chapter 3, shows two solidified liquids separated by a sharp interface. However, following the calculated solidification path down to 500 K, a three-phase equilibrium, [$(U,Zr)O_{2-x}$+α-(Zr,U)(O)+α-U] is obtained. Due to the rapid cooling of the sample, the two immiscible liquids solidified separately, following two parallel solidification paths.

The comparison between the calculated composition of the two liquids at 2567 K and the experimental results is reported in Table 6.

Sample OUZr_3	Estimated final composition	Metallic liquid L1		Oxide liquid L2	
		Calc.	Exp.	Calc.	Exp.
at % O	35.9	19.8	23.6±3	51.7	50.7±2
at % U	24.3	31.5	28.0±2	17.2	17.3±1
at % Zr	39.8	48.7	48.4±3	31.1	32.0±2
Mass fraction	/	0.6	~ 0.5	0.4	~ 0.5

Table 6: Comparison between calculation at 2567 K and experimental observation on the composition of the two immiscible liquids in sample OUZr_3. The experimental mass fractions are obtained using ImageJ® software

A good agreement is obtained between the calculation and experimental results. The comparison between the calculated and the measured liquid oxide composition reveals an excellent agreement. Concerning the composition of the metallic liquid, the calculated U and O contents are overestimated and underestimated, respectively.

In order to interpret the microstructure of the solidified liquids, metallic and oxide, two parallel solidification paths are calculated. The starting compositions of the liquids are those measured by WDS (see Table 6) on the oxide and metallic region in Figure 14 of Chapter 3.

The resulting solidification path for the metallic liquid is shown in Figure 21.

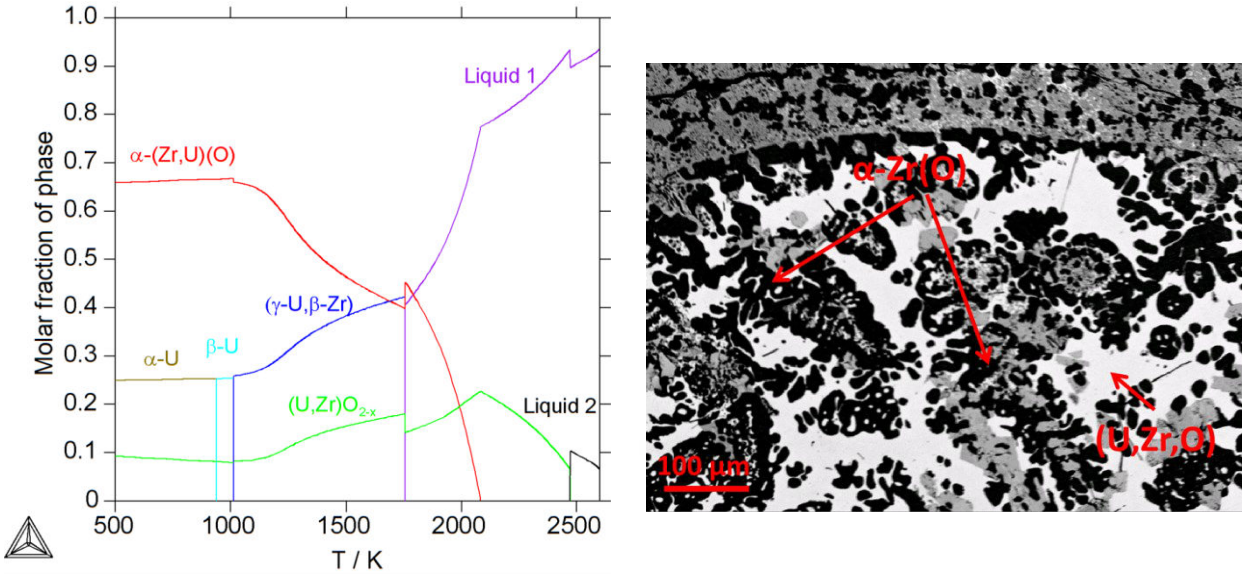

(a) (b)

Figure 21: (a) Solidification path calculated starting from the measured composition of the solidified metallic liquid; (b) SEM-BSE image of the solidified metallic liquid

At 2567 K the calculation reveals the presence of two liquids, one with a composition close to that of the initial liquid (Liquid 1), the other enriched in O (Liquid 2). Therefore, the formation of a secondary oxide liquid is due to the crossing of successive tie-lines in the miscibility gap. The starting composition of the metallic liquid lies within the miscibility gap. The amount of this secondary Liquid 2 phase increases down to 2470 K, where it is replaced by a $(U,Zr)O_{2-x}$-c cubic phase. Decreasing temperature, the miscibility gap becomes bigger until the ternary monotectic reaction [L1+L2] → [L1+$(U,Zr)O_{2-x}$] is reached. At 2083 K a α-(Zr,U)(O) phase is formed by the reaction [L1+$(U,Zr)O_{2-x}$] → [L1+$(U,Zr)O_{2-x}$+α-(Zr,U)(O)]. At the solidus temperature, T=1757 K, the remaining liquid transforms in a (γU,βZr) metallic phase. The composition of the phases calculated at this temperature is reported in Table 7 with the experimental results.

	$(U,Zr)O_{2-x}$		α-(Zr,U)(O)		Quenched liquid	
	Calc.	**Exp.**	**Calc.**	**Exp.**	**Calc.**	**Exp.**
at % O	65.8	66.4±3	29.6	26.8±1	2.3	11±10
at % U	30.8	30.3±1	1.8	2.1±1	56.2	84±5
at % Zr	3.4	3.3±1	68.6	71.1±4	41.6	5±3
Mass fraction	0.11	NA	0.28	NA	0.61	NA

Table 7: Comparison between calculation and experimental results on the solidified microstructure of the metallic liquid observed in sample OUZr_3. The calculation are performed at 1757 K. NA = Not Available

The measured amount of Zr in the quenched liquid is significantly lower than that calculated.

The calculated solidification path of the oxide liquid is reported in Figure 22.

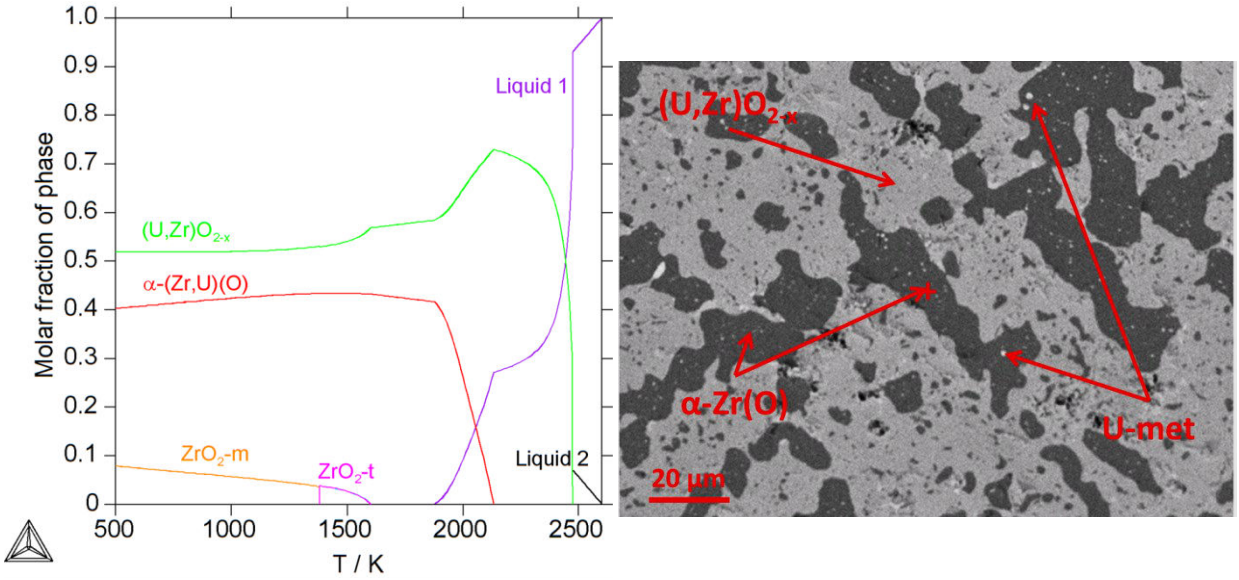

(a) (b)

Figure 22: Solidification path calculated starting from the measured composition of the solidified oxide liquid

A secondary metallic liquid is calculated between 2433 K and 2567 K. At 2475 K a $(U,Zr)O_{2-x}$-c phase is formed by the reaction [L1+L2] → [L1+$(U,Zr)O_{2-x}$]. The comparison between experimental and calculation results are reported in Table 8.

	$(U,Zr)O_{2-x}$		**α-(Zr,U)(O)**		**U-met**	
	Calc.	**Exp.**	**Calc.**	**Exp.**	**Calc.**	**Exp.**
at % O	65.4	66.0±3	30.0	26.1±1	/	20±10
at % U	28.3	29.6±1	1.9	2.9±1	/	80±5
at % Zr	6.3	4.4±1	68.1	71.0±4	/	/
Mass fraction	0.62	0.62*	0.38	0.38*	/	ND*

Table 8: Comparison between calculation and experimental results on the solidified microstructure of the oxide Liquid 2 observed in sample OUZr_3. The calculation are performed at 1757 K. * Obtained using ImageJ® software. ND= under the limit of detection of the employed technique

The calculation is in good agreement with the experimental results. The O-content calculated in the α-(Zr,U)(O) is underestimated compared to the experimental observation. From the calculation, at the solidus temperature, only two phases are in equilibrium: $(U,Zr)O_{2-x}$-c and α-(Zr,U)(O). A small quantity of a metallic phase was identified in the microstructure in Figure 16a of Chapter 3. However, this phase is present within the α-(Zr,U)(O) phase. During cooling, the solubility of U decreases leading to its rejection from the α-(Zr,U)(O) → [α-Zr(O)+U] phase in form of metallic precipitates. The calculated mass fraction is in excellent agreement with the results obtained with ImageJ®.

4.2.1.3 Sample OUZr_7

The solidification path, calculated at the equilibrium, of sample laser heated sample OUZr_7 (initial composition $O_{0.126}U_{0.106}Zr_{0.768}$) is reported in Figure 23.

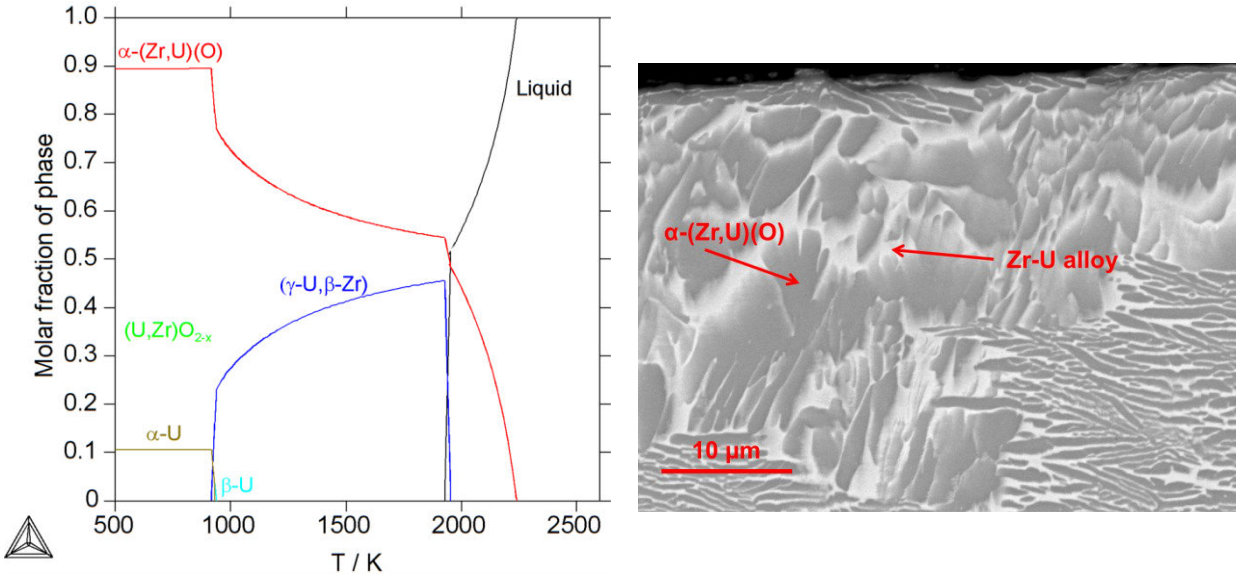

(a) (b)

Figure 23: (a) Solidification path of sample OUZr_7; (b) SEM-BSE image of the solidified OUZr_7 sample after a laser heating sequence under Ar

At the liquidus temperature, T=2239 K, the α-(Zr,U)(O) phase starts to form. In correspondence of the solidus temperature, T=1926 K a Zr-rich (γU,βZr) phase forms. There are only two solid phases at the end of the solidification. The comparison between the calculation at 1926 K and the experimental observation is reported in Table 9.

	α-Zr(O,U)		**(γU,βZr)**	
	Calc.	**Exp.**	**Calc.**	**Exp.**
at % O	23.1	21	Traces	//
at % U	0.7	1	22.4	28
at % Zr	76.2	78	77.6	72
Mass fraction	0.42	0.65*	0.58	0.35*

Table 9: Comparison of the calculated and experimental phase composition

The composition of the phases at 1926 K is in agreement with the EDS analyses. However, the calculated mass fraction is underestimated compared to the result obtained by image processing (ImageJ® software).

4.2.1.4 Summary

Solidification path calculations allowed to interpret the microstructure observed on O-U-Zr samples. The calculated equilibrium phases are in good agreement with the experimental observations. However, some systematic discrepancies have been highlighted between the calculated and the experimental composition of the quenched metallic liquid. Probably the hypothesis that no solid/solid reactions occur below solidus temperature is too strict. Figure 19d for example shows that the (γU,βZr) phase becomes richer in U with decreasing temperature, going towards a composition closer to that observed experimentally. Another explanation might come from the low temperature thermodynamic model of the O-U-Zr system. As already introduced in Section 4.1.2, the O-U-Zr phase diagram close to the U corner should be experimentally investigated to better shape the low temperature equilibria involving metallic liquid and (γU,βZr) with $(U,Zr)O_{2-x}$-c and α-(Zr,U)(O). Furthermore, the O-content measure by WDS is overestimated.

The effect of W on the solidification behaviour of the O-U-Zr samples can also be studied. Due to the low solubility of O in W, the liquid samples dissolve only a small quantity of W. During solidification, the formation of W_2Zr rings around pure W is explained by the independent cooling of the β-W(Zr,εU) phase (see Appendix C).

4.2.2 Laser heating results on the UO_2-PuO_2-ZrO_2 system

Using the thermodynamic model assessed during this work, calculation can be performed to better interpret experimental results as well as post-experiment analyses, such as X-ray diffraction results. Thermodynamic calculations can be used to investigate the solidification path followed by a laser-heated sample under Ar or air. This approach highlights the great importance of the atmospheric conditions during laser heating experiments performed on mixed oxides.

This approach requires assuming that the investigated system is at thermodynamic equilibrium. In the present case, the equilibrium between the sample and the whole volume of buffer gas cannot be completely achieved due to the small amount of molten material and due to the rapidity of the laser experiments. One can nevertheless assume that equilibrium conditions were established locally: at 3000 K, when the sample is in liquid state, diffusion kinetics are rapid, thus the molten sample can be considered in equilibrium with a small fraction of the buffer gas. However, the estimation of the amount of buffer gas in equilibrium with the sample is challenging. In the vicinity of the hot molten sample, the buffer gas exhibits density gradients, creating natural convective movements. Due to the small dimensions of the hot surface, only a laminar flow may take place [37]. The thickness of the boundary layer at the trailing edge of the molten area can be calculated to be about 3 mm [37]. Furthermore the sample tends to release a certain amount of vapour depending on the temperature and experimental pressure set in the autoclave.

In order to perform a calculation as close as possible to the real experimental conditions, the following assumptions were made:

- As previously shown by De Bruycker [38] the molten pool has a diameter that corresponds to the laser spot diameter (5 mm) and an average depth of 50 µm (volume equal to about 10-6 dm^3);
- An average density of 10 g/cm^3 was taken to calculate the mass of the molten pool;
- The molar mass of sample U48P3Z49 (M=182 g/mol) was taken to calculate the number of moles of the molten pool;
- The buffer gas was considered an ideal gas;

For the sample, the calculation was performed considering 2 moles of oxygen and 1 mole of metal atoms.

Only a small part of the gas volume inside the steel vessel reacted with the sample. The best estimation resulted in considering a number of moles of buffer gas equal to 1, which corresponds to a gas volume of 430 10^{-6} dm^3;

- A pressure of 0.25 MPa that is the initial pressure inside the autoclave.

The solidification path calculations performed on sample U48P3Z49 ($(UO_2)_{0.48}(PuO_2)_{0.03}(ZrO_2)_{0.49}$) and P50Z50 ($(PuO_2)_{0.50}(ZrO_2)_{0.50}$) will be presented. The calculations are performed considering both Ar and air as experimental buffer gas.

The solidus and liquidus surfaces in the UO_2-PuO_2-ZrO_2 system under both Ar and air will be shown.

X-ray diffraction results performed in ITU [39] on the sintered and laser melted samples will be also compared to calculations. Only three of the six samples were analysed by XRD after the laser heating experiments.

4.2.2.1 Solidification path of sample U48P3Z49

The solidification path calculated for sample U48P3Z49 is reported in Figure 24.

The calculations firstly show that liquidus/solidus transition temperatures are sensitive to the atmosphere, confirming the experimental observations. Figure 24a reveals that during cooling under Ar, the first phase formed is the $(Zr,U)O_2$-t at 2000 K. At lower temperatures, the equilibrium phases are $(Zr,U,Pu)O_{2-x}$-c and ZrO_2-m. Figure 24c shows the evolution of the composition of the $(Zr,U,Pu)O_{2\pm x}$-c phase during cooling under Ar. As the $(Zr,U)O_2$-t is formed, the amount of Zr in the fcc mixed oxide phase decreases, reaching negligible amounts below 1500 K. **The O/M ratio at the melting point is 1.96, and drifts towards 2 during cooling**.

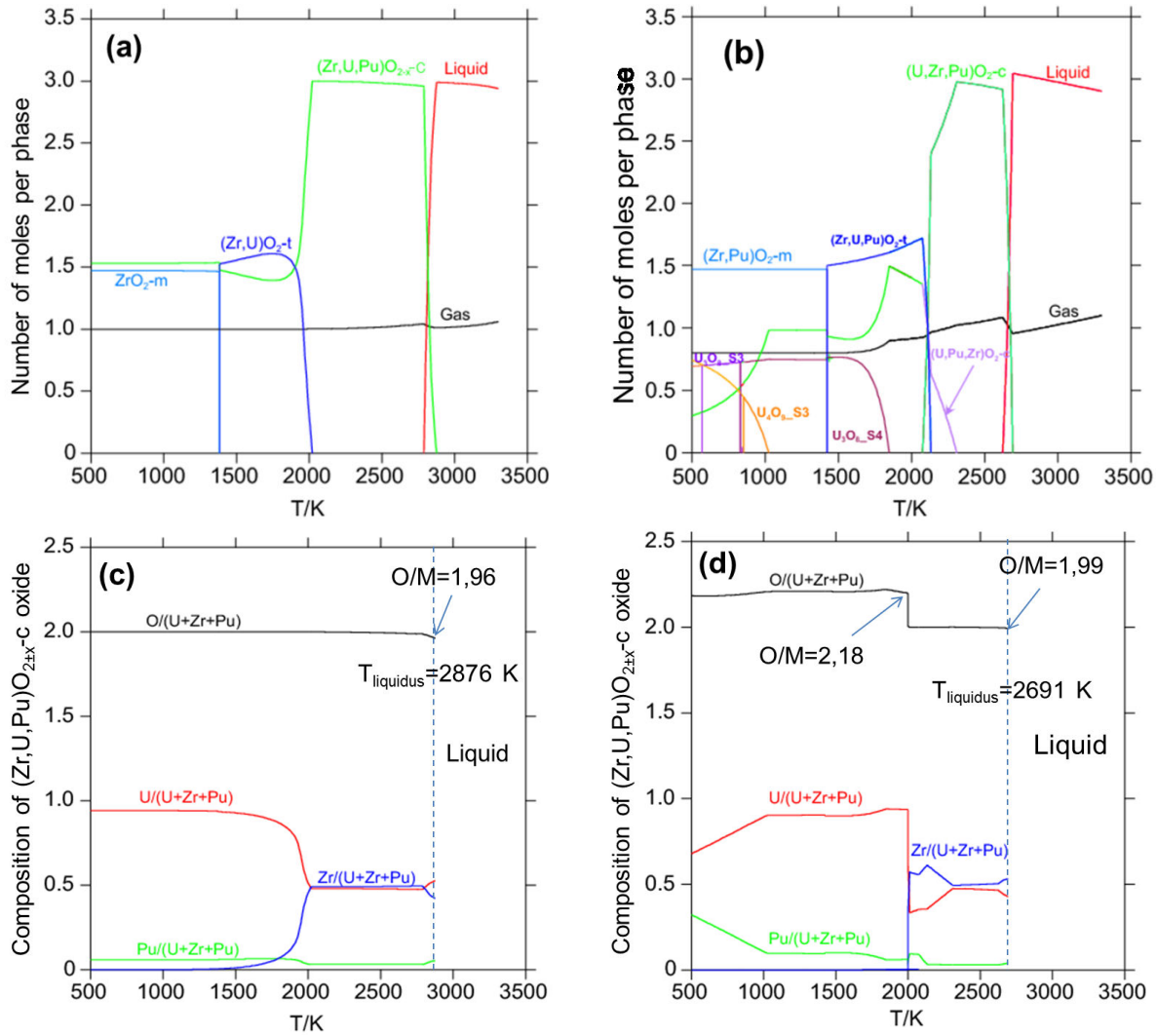

Figure 24: Calculated solidification paths on sample U48P3Z49. (a) Solidification path under Ar; (b) solidification path under air; (c) evolution of the composition of $(Pu,U,Zr)O_{2\pm x}$-c phase during cooling as a function of temperature under Ar; (d) same as in (c) but obtained under air

The solidification path calculated under air appears more complex, and involves some additional phases. The first phase solidifying is the $(U,Zr,Pu)O_{2-x}$-c oxide. During cooling, the O/M ratio of the cubic phase increases. At 2300 K a second cubic $(U,Pu,Zr)O_{2+x}$-c oxide enriched in U with a ratio O/M=2.18 forms. At about 2100 K a Zr-enriched $(Zr,U)O_2$-t oxide starts to replace the $(U,Zr,Pu)O_{2-x}$-c oxide first formed during cooling. At 1800 K, two phases are in equilibrium, $(U,Pu)O_{2+x}$-c (Figure 24d) and $(Zr,U)O_2$-t. Zr is preferentially incorporated

in $(Zr,U)O_2$-t rather than staying in an oxide phase with an O/M>2. Following the solidification path, the $(U,Pu)O_{2+x}$-c phase gradually transforms into U_3O_8 and U_4O_9. At the same time, Pu gradually moves into the $(Zr,Pu)O_2$-t and $(U,Pu)O_{2+x}$-c phases. At 500 K, the major phase $(Zr,Pu)O_2$-m is in equilibrium with U_3O_8 and the remaining $(U,Pu)O_{2+x}$-c phase. It must be pointed out that in the present thermodynamic assessment the Pu solubility in U_3O_8 and U_4O_9 was not taken into account

4.2.2.2 Solidification path of sample P50Z50

The same calculations were performed for sample P50Z50 (Figure 25). In this case, the effect of the experimental buffer gas on the solid/liquid transition is not as pronounced, confirming that the thermodynamics of UO_2 has the largest influence on the high temperature stoichiometry of the samples. **Under Ar, the tendency of the O/M ratio to move towards hypo-stoichiometric values (~1.96 at the melting temperature) is noticeable**. Even under air, the O/M ratio is found around 1.98 at melting. **The oxygen potential of the buffer gas (air at 0.25 MPa) is not high enough to keep the stoichiometry of the $(Pu,U,Zr)O_{2\pm x}$-c equal to 2**. The solidification paths calculated under Ar (Figure 25a) and under air (Figure 25b) are different.

During cooling under air, the formation of a fcc $(Pu,Zr)O_2$-c oxide is followed by the appearance a tetragonal $(Zr,Pu)O_2$-t phase. At this point, the amount of Zr in the fcc phase decreases (Figure 25c-d). The monoclinic phase stable at low temperatures contains a negligible amount of Pu: the resulting equilibrium phases are PuO_2-c and ZrO_2-m.

Under Ar, a pyrochlore phase forms below 2000 K, with the composition $Pu_2Zr_2O_{7.85}$ at 2000 K, $Pu_2Zr_2O_{7.99}$ at 1000 K, and $Pu_2Zr_2O_8$ at 500 K. This phase tends to O/M=2 during cooling.

Calculations performed using Ar-6 % H_2 as buffer gas were finally performed. The calculated O/M ratio in the $(Pu,Zr)O_{2-x}$-c at the liquidus is 1.955. This value is slightly lower than that calculated under Ar (O/M=1.96). The metal ratio in the $(Pu,Zr)O_{2-x}$-c is not affected by the presence of H_2. The calculated solidus temperature is 2860 K. The calculation overestimated the experimental observation T=2835 K. This result confirms that the effect of the atmosphere in this region of the UO_2-PuO_2-ZrO_2 phase diagram is limited.

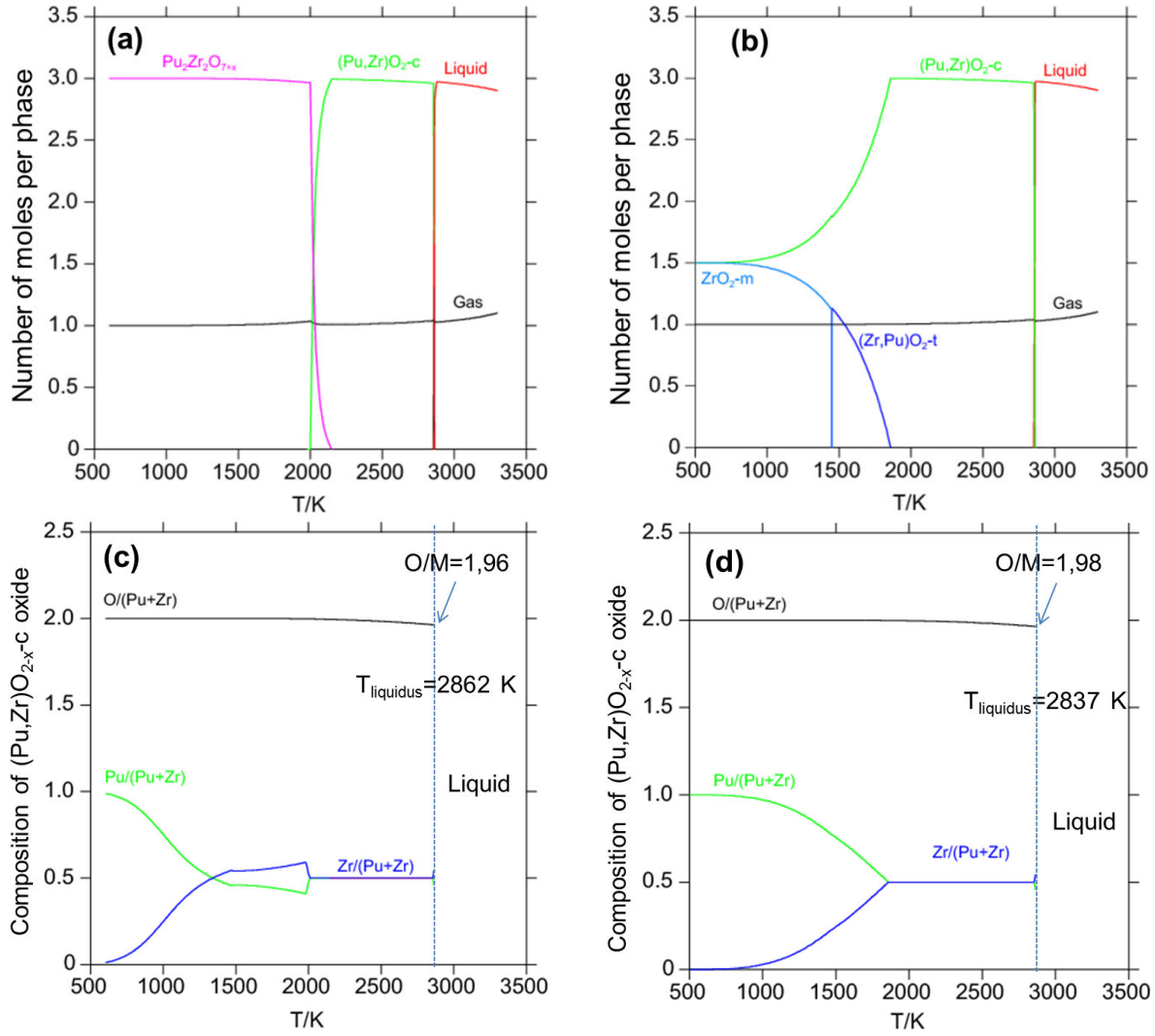

Figure 25: Calculated solidification paths on sample P50Z50. (a) Solidification path under Ar; (b) solidification path under air; (c) O/(Pu+Zr) ratio in the $(Pu,Zr)O_{2-x}$-c phase during solidification as a function of temperature under Ar; (d) same as in (c) but obtained under air.

4.2.2.3 Solidus and liquidus surfaces calculation

We recall that phase diagrams are calculated at thermodynamic equilibrium, while laser heating experimental results represent kinetics conditions. These results should therefore be compared with caution to the calculated phase diagram. In fact, at each temperature, the oxygen potential of the system changes along with the O/M ratio of the sample: placing an experimental point on a fixed isopleth with an oxygen-to-metal ratio equal to 2, could then be misleading. The present experimental results are then reported on the diagrams in Figure 26, showing the evolution of the liquidus/solidus lines of the system under the experimental conditions (reducing and oxidising).

The nature of the observed transition temperatures should be carefully considered. In the investigated region of the phase diagram, the solidus and the liquidus lines are close to each other. The large uncertainties on the experimental results cover the L+$(Pu,U,Zr)O_2$-c two-phase domain. Therefore, come to a sharp decision on whether the observed transitions correspond to liquidus or solidus is challenging. However, the interpretation of Böhler et al. [40] suggests that the first inflection after undercooling should be assigned to the solidus transition. The latter transition is of great interest for the design of the nuclear fuel because it corresponds to the temperature at which the fuel loses its mechanical strength.

A good agreement is generally obtained between the calculated solidus lines and the laser heating experimental results. A good agreement is obtained with the solidification temperature measured under Ar on sample U33P33Z33. However, the calculation performed under air largely underestimates the experimental observation. It must be reminded that the experimental result on sample U33P33Z33 obtained under air is affected by significant error bars.

The calculations reported in Figure 26a confirm that a minimum exists in the liquidus/solidus curves around $x(UO_2)$=0.15-0.20. An oxidising atmosphere affects the shape of the solidus curve when approaching the UO_2 corner. In Figure 26c the O/M ratio in the $(Pu,U,Zr)O_{2\pm x}$-c phase along the solidus and liquidus lines rises sharply after $x(UO_2)$=0.80 up to 2.05-2.10 at the UO_2 corner. The calculation performed under Ar (in Figures 26c-d) shows that the O/M ratio along the solidus and liquidus curves lies between 1.95 and 2, but never reaches stoichiometry. Figure 26b reports the calculated liquidus and solidus curves across the $(UO_2)_{0.50}(ZrO_2)_{0.50}$–$PuO_2$ section. The agreement between the calculation and the experimental results is excellent for samples U48P3Z49 and U45P10Z45.

Figure 26d shows the O/M ratio in the $(Pu,U,Zr)O_{2\pm x}$-c phase at the liquidus and solidus transitions as a function of $x(PuO_2)$ along the $(UO_2)_{0.50}(ZrO_2)_{0.50}$–$PuO_2$ section. The calculated O/M ratio at the PuO_2 corner remains lower than 2, and falls steadily from $(UO_2)_{0.50}(ZrO_2)_{0.50}$ towards PuO_2. Even using air at 0.25 MPa is not enough to keep PuO_2 at the stoichiometry O/M=2.

Although the calculated diagram was derived by direct extrapolation from the quaternary U-Pu-Zr-O system, without further optimisation, a good agreement between the calculated liquidus/solidus lines and the experimental results is already obtained.

4.2.2.4 Structural analysis on the as-synthetized samples

Using the present thermodynamic model, calculations were performed at the sintering conditions (T=1873 K, Ar/6.5 % H_2 with 1500 ppm H_2O). The calculations are compared in Table 10 to the X-ray diffraction data obtained in ITU [39]. The nature and the lattice parameters of the different phases are reported. However, the respective weight fractions could not be quantified accurately, which is mainly due to the rather poor quality of the X-ray diffraction patterns due to the limited amount powder available.

As listed in Table 10, the prepared samples showed several different phases except for sample P50Z50 (with the highest PuO_2 content) which showed only one phase.

The calculations performed at 1873 K yielded for samples U48P3Z49 and U45P10Z45 (with the lowest PuO_2 contents) fluorite $(U,Pu,Zr)O_{2-x}$-c as major phase with an oxygen-to-metal ratio of 1.98 and 1.96, respectively. A secondary tetragonal $(Zr,U)O_2$-t phase was also found. As the PuO_2 content increases in samples U33P33Z33, U20P40Z40, and U10P45Z45, a fluorite $(U,Pu,Zr)O_{2-x}$-c phase appears together with a disordered pyrochlore $Pu_2Zr_2O_{7+x}$ phase. Sample P50Z50, containing no UO_2, is a single disordered pyrochlore phase $Pu_2Zr_2O_{7+x}$. These results show that as the amount of plutonium increases, the pyrochlore fraction also grows. In contrast, the $(Zr,U)O_2$ oxide forms next to the fluorite in PuO_2 poor samples. In all cases, the reducing experimental conditions lead to the formation of a hypostoichiometric mixed oxide with an O/M ratio slightly lower than 2.

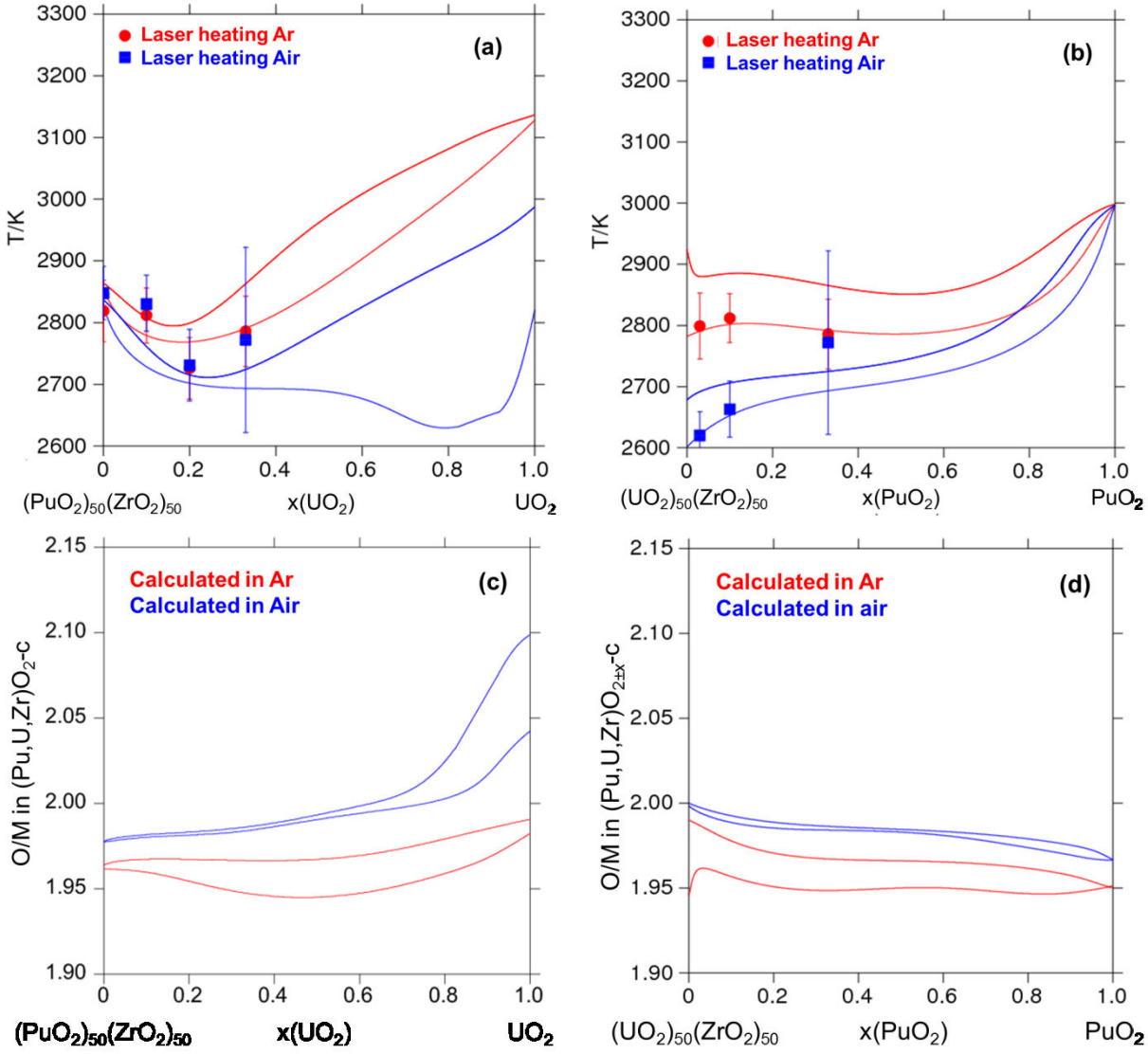

Figure 26. Calculated liquidus and solidus temperatures as a function of the experimental gaseous atmosphere (red lines for Ar, blue line for air). The red circles represent the laser heating experimental results obtained under Ar, whilst the blue squares are the experimental results obtained under compressed air. (a) Evolution of the liquidus/solidus lines along the $(PuO_2)_{0.50}(ZrO_2)_{0.50}$-$UO_2$ section; (b) evolution of the liquidus/solidus lines along the $(UO_2)_{0.50}(ZrO_2)_{0.50}$-$PuO_2$ section; (c) evolution of the O/M ratio in the $(Pu,U,Zr)O_{2\pm x}$-c phase at solidus and liquidus transitions along the $(PuO_2)_{0.50}(ZrO_2)_{0.50}$-$UO_2$ section; (d) the same as in (c) but along the $(UO_2)_{0.50}(ZrO_2)_{0.50}$-$PuO_2$ section

The cooling paths of the various samples were furthermore calculated using the present thermodynamic model. The calculated phase fractions at 500 K are compared with the X-ray diffraction results. For sample U45P10Z45 and sample U33P33Z33, calculations were performed at 1500 K and 800 K respectively, since at 500 K the phase pyrochlore was not present. The calculations are in rather good agreement with the structural analysis. Sample P50Z50 shows a single phase material that could be identified either as a fluorite $(Pu_{0.5}Zr_{0.5})O_{2-y}$ or a disordered pyrochlore $Pu_2Zr_2O_{7+x}$. The stoichiometric pyrochlore oxide $Pu^{3+}{}_2Zr^{4+}{}_2O_7$, where the transition metal Zr is tetravalent, and the plutonium cation is in a pure trivalent state, was reported to be cubic (space group Fd-3m) with a cell parameter as a=10.692 Å [41]. The pyrochlore $Pu_2Zr_2O_7$ shows a fluorite-type structure with a double unit cell and an ordered oxygen deficiency [42]. One oxygen atom is missing compared to a solid solution of the two fluorite cells ZrO_2 and PuO_2, while the oxygen-metal distances are also different to accommodate the plutonium cation in its Pu^{3+} oxidation state [41]. The trivalent Pu^{3+} cation is moreover eightfold coordinated, while the tetravalent Zr^{4+} cation is sixfold

coordinated. Upon oxidation, the plutonium cation adopts a mixed valence state (Pu^{3+},Pu^{4+}), and the corresponding disordered pyrochlore cell $Pu_2Zr_2O_{7+x}$ shows a smaller cell parameter. Upon a subsequent order-disorder transition, the fluorite solid solution $(Pu_{0.5}Zr_{0.5})O_{2-y}$ is obtained [41]. The cell parameter of this incompletely oxidized solid solution is larger than that of $(Pu_{0.5}Zr_{0.5})O_2$, expected as 5.265(5) Å [43], [44], due to the larger ionic radius of Pu^{3+} compared to Pu^{4+}. However, the discrimination between the disordered pyrochlore structure and that of a fluorite solid solution using X-ray diffraction is delicate. Our structural analysis revealed a cell parameter as 5.295(5) Å (fcc) or 10.59(1) Å (pyrochlore) for sample P50Z50, that could be either $(Pu_{0.5}Zr_{0.5})O_{2-y}$ or $Pu_2Zr_2O_{7+x}$. The same phase was also found in samples U20P40Z40 and U10P45Z45 with cell parameters as 5.315(5)/10.63(1) Å and 5.310(5)/10.62(1) Å, respectively. Interestingly, the parameter found for samples U45P10Z45 and U33P33Z33 (5.26(1) Å) suggests that the fcc phase is, in this case, fully oxidized, i.e. $(Pu_{0.5}Zr_{0.5})O_2$, which is probably related to the higher uranium content in those samples. Finally, when increasing the UO_2 content, a fluorite mixed oxide phase $(U,Pu,Zr)O_2$-c appeared with cell parameters between 5.320(5) Å (sample U10P45Z45) and 5.431(5) Å (sample U48P3Z49), as well as ZrO_2-m [45] and/or ZrO_2-t [46] (samples 1, 2, and 3).

The trends revealed by the X-ray diffraction results are consistent with the calculations at high temperatures and with the phase diagrams. The disordered pyrochlore fraction increases with the PuO_2 content of the samples, whereas the fluorite phase is stabilized for uranium rich samples. ZrO_2 (m or t) is moreover stabilized for the samples rich in UO_2 and ZrO_2.

Sample	Sample 1 U48P3Z49	Sample 2 U45P10Z45	Sample 3 U33P33Z33	Sample 4 U20P40Z40	Sample 5 U10P45Z45	Sample 6 P50Z50
Phases from XRD analysis	**fcc (U,Pu,Zr)O_2-c a=5.431(5) Å**	**fcc (U,Pu,Zr)O_2-c a=5.430(5) Å**	**fcc (U,Pu,Zr)O_2-c a=5.417(5) Å**	fcc (U,Pu,Zr)O_2-c a=5.325(5) Å	fcc (U,Pu,Zr)O_2-c a=5.320(5) Å	
		fcc ($Pu_{0.5}Zr_{0.5}$)O_2-c a=5.26(1) Å	fcc ($Pu_{0.5}Zr_{0.5}$)O_2-c a=5.26(1) Å	**fcc ($Pu_{0.5}Zr_{0.5}$)O_{2-y}-c a=5.315(5) Å or $Pu_2Zr_2O_{7+x}$ a=10.63(1) Å**	**fcc ($Pu_{0.5}Zr_{0.5}$)O_{2-y}-c a=5.310(5) Å or $Pu_2Zr_2O_{7+x}$ a=10.62(1) Å**	**fcc ($Pu_{0.5}Zr_{0.5}$)O_{2-y}-c a=5.295(5) Å or $Pu_2Zr_2O_{7+x}$ a=10.59(1) Å**
	ZrO_2-m	ZrO_2-m	ZrO_2-m			
	ZrO_2-t	ZrO_2-t				
Phases from calculations	T=500 K	T=1500 K	T=800 K	T=500 K	T=500 K	T=500 K
	70 w % fcc ($U_{0.94}Pu_{0.06}$)O_2-c a*=5.465 Å	65 w % fcc ($U_{0.83}Pu_{0.14}Zr_{0.03}$)$O_2$-c a*=5.449 Å	59 w % fcc ($U_{0.94}Pu_{0.06}$)O_2-c a*=5.465 Å	33 w % fcc ($U_{0.77}Pu_{0.23}$)O_2-c a*=5.453 Å	17 w % fcc ($U_{0.77}Pu_{0.23}$)O_2-c a*=5.453 Å	
		6 w % $Pu_2Zr_2O_{7.85}$	32 w % $Pu_2Zr_2O_{7.9}$	63 w % $Pu_2Zr_2O_{7.999}$	81 w % $Pu_2Zr_2O_{7.999}$	100 w % $Pu_2Zr_2O_{7.999}$
	30 w % ZrO_2-m	29 w % ZrO_2-t	8 w % ZrO_2-m	4 w % ZrO_2-m	2 w % ZrO_2-m	
	T=1873 K	T=1873 K	T=1873 K	T=1873 K	T=1873 K	T=1873 K
	80 w % ($U_{0.6}Pu_{0.04}Zr_{0.36}$)$O_{1.98}$-c	97 w % ($U_{0.46}Pu_{0.1}Zr_{0.43}$)$O_{1.96}$-c	56 w % ($U_{0.66}Pu_{0.17}Zr_{0.17}$)$O_{1.96}$-c	35 w % ($U_{0.66}Pu_{0.17}Zr_{0.17}$)$O_{1.96}$-c	18 w % ($U_{0.66}Pu_{0.17}Zr_{0.17}$)$O_{1.96}$-c	
	20 w % (Zr,U)O_2-t	3 w % (Zr,U)O_2-t	44 w % $Pu_2Zr_2O_{7.9}$	65 w % $Pu_2Zr_2O_{7.9}$	82 w % $Pu_2Zr_2O_{7.9}$	100 w % $Pu_2Zr_2O_{7.9}$

Table 10. Comparison between the X-ray diffraction results and the thermodynamic calculations on the as- synthesized samples. a* is the lattice parameter at 298.15 K of the fluorite phase calculated using Vegard's law assuming an oxygen-to-metal ratio equal to 2 and the same metallic composition as the one calculated at the specified temperature. [39] (The major phase is marked in bold)

4.2.2.5 Structural analysis after melting

The X-ray diffraction patterns collected after the melting experiments showed various phases depending on the initial composition of the investigated material and on the atmosphere of the laser heating tests (Table 11).

For sample 2 (U45P10Z45), after several shots under Ar, a major fcc (U,Pu,Zr)O_2-c phase (5.433(5) Å), a secondary fluorite $(Pu_{0.50}Zr_{0.50})O_{2-y}$ phase with a=5.310(5) Å (or disordered pyrochlore $Pu_2Zr_2O_{7+x}$), and a minor amount of ZrO_2-m, were found after the melting experiment, in good agreement with the results of thermodynamic calculations under Ar-6.5% H_2 for the as-synthesized samples in Table 10.

Sample 5 underwent two series of shots under air followed by two series of shots under Ar. The quenched sample was made mostly of the fluorite $(Pu_{0.5}Zr_{0.5})O_{2-y}$ or disordered pyrochlore $Pu_2Zr_2O_{7+x}$ with cell parameters as 5.275(5)/10.55(1) Å, and a small fraction of U_3O_8 and UO_3. The presence of U_3O_8 and UO_3 shows that the sample was oxidized during the series of experiments under air. The final tests under Ar were not sufficient to retrieve the initial stoichiometry close to 2. Moreover, the oxygen impurity contained in the argon used for the experiment can possibly contribute to the oxidation of the sample heated at very high temperatures. The disappearance of the secondary fcc phase (a=5.320(5) Å) found in the synthesized sample could be related to the oxidation of this phase into U_3O_8 and UO_3, and simultaneous segregation of the Pu and Zr into the pyrochlore structure.

Sample 6 was exposed to three series of shots under air, argon, and Ar-6.5%H_2 successively. The quenched sample was made mostly of the fluorite $(Pu_{0.5}Zr_{0.5})O_{2-y}$ or disordered pyrochlore $Pu_2Zr_2O_{7+x}$ with cell parameters as 5.280(5)/10.56(1) Å. A secondary cubic phase was also found with a structure that could be assigned to PuO_{2-x} . The formation of this reduced plutonium oxide phase was not predicted by the thermodynamic calculations. Nevertheless its presence is consistent with the reducing conditions of the last laser shots under Ar-H_2.

The cell parameters of the fluorite $(Pu_{0.5}Zr_{0.5})O_{2-y}$ or disordered pyrochlore $Pu_2Zr_2O_{7+x}$ phases in samples 5 and 6 are smaller than before melting, suggesting that the end materials contain a larger fraction of Pu^{4+} compared to the starting products, and are therefore slightly more oxidized.

Sample	Sample 2 U45P10Z45	Sample 5 U10P45Z45	Sample 6 P50Z50
Atmosphere	Argon	Air, Argon	Air, Argon, Ar-6.5%H_2
Phases from XRD analysis	**fcc (U,Pu,Zr)O_2 a=5.433(5) Å**		fcc PuO_{2-x} a=5.410(5) Å
	fcc $(Pu_{0.5}Zr_{0.5})O_{2-y}$ a=5.310(5) Å or $Pu_2Zr_2O_{7+x}$ a=10.62(1) Å	**fcc $(Pu_{0.5}Zr_{0.5})O_{2-y}$ a=5.275(5) Å or $Pu_2Zr_2O_{7+x}$ a=10.55(1) Å**	**fcc $(Pu_{0.5}Zr_{0.5})O_{2-y}$ a=5.280(5) Å or $Pu_2Zr_2O_{7+x}$ a=10.56(1) Å**
	ZrO_2-m	U_3O_8 , UO_3	

Table 11: X-ray diffraction results on melted samples. The major phases are marked in bold [39]

4.2.2.6 Summary

The present solidification path calculations well reproduce the experimental observation on the six UO_2-PuO_2-ZrO_2 samples. This set of calculations requires assumptions to be made with respect to the amount of reactive gas, and therefore cannot be fully representative of the laser heating experiments. Nevertheless they have appeared extremely useful to identify the general chemical behaviour of these systems.

The oxygen potential is a crucial parameter for the experimental conditions and it has been shown in the Section 3.2.3; that it is difficult to maintain the samples as close as possible to stoichiometry (O/M=2). This tendency is confirmed by the present set of solidification path calculations. **The O/M of the UO_2-PuO_2-ZrO_2 samples varies as a function of temperature and of the atmosphere.** The calculated solidus/liquidus curves exhibit different shapes depending on the atmospheric conditions considered during the calculations.

Thermodynamic calculations applied to X-ray diffraction results reported in [39] give satisfactory results. Even if the small amount of available materials did not allow a fully descriptive quantitative analysis, a general agreement is obtained between calculation and experimental observations.

For a complete understanding of the melting/solidification behaviour of the samples, a direct in-situ monitoring of the equilibrium conditions (i.e., direct measurement of the oxygen chemical potential) is needed. However, the rapidity of the experiments, as well as the limited volume of sample actually undergoing melting, makes technical solutions challenging.

4.2.3 In-vessel corium investigation

The high temperature behaviour of the quaternary O-Fe-U-Zr system is paramount for the comprehension of the first part of a severe accident in a nuclear reactor. As already introduced in Chapter 1, during a severe accident, the UO_2-based nuclear fuel reacts with the Zircaloy cladding and with metallic structures surrounding the fuel bundle (spacer grids, neutronic absorber cladding) leading to the formation of the so-called in-vessel corium. The aforementioned system contains the most abundant elements involved during the accident. Due to the complexity of the accidental phenomena, an exact in-vessel corium composition does not exist. In the present work, a representative sample of a possible European pressurised Reactor (EPR) in-vessel corium [47] has been fabricated by arc melting furnace. The starting composition of the sample is reported in Table 12.

All the components were placed inside the melting chamber. An inert atmosphere (Ar, Messer 99.9999 %) was set inside the chamber. In order to minimise the parasitic oxidation during elaboration, an oxygen getter (metallic shavings of Zr Van Arkel) was firstly melted. The arc melting was repeated three times for better homogenising the sample. The resulting marble was then cut and sent to the LMAC, CEA Marcoule for post-experiment analyses. The sample was analysed by means of the SEM-EDS and WDS already described in Section 3.2.1.

Component	wt %
UO_2	52.5
ZrO_2	6.0
Zr	18.4
Fe	23.1

(a)

	O	Fe	U	Zr
at%	36.2	30.8	14.5	18.5

(b)

Table 12: (a) Massic composition and (b) elemental atomic composition of the fabricated prototypic in-vessel corium sample

During the arc melting, monitoring of the temperature was not possible. The temperature of fabrication of the sample can be thus only estimated. A BSE image of the cross-section of the in-vessel sample is reported in Figure 27.

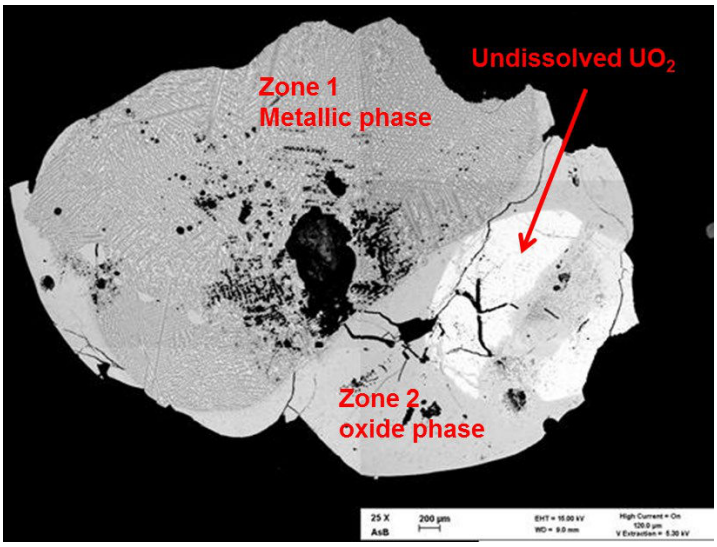

Figure 27: BSE image of the in-vessel corium sample cross-section

The chemical contrast visible in the BSE image allows identifying three zones. EDS analyses revealed:

- a metallic zone (named Zone 1);
- an oxide zone (named Zone 2);
- an undissolved piece of UO_2 (no traces of Zr and Fe were detected inside this zone of the sample).

Due to its high melting temperature (T=3120 K), the UO_2 disk was only partially dissolved. The fact that part of the UO_2 disk maintains its original shape suggests that the maximum temperature reached during the sample fabrication was lower than the UO_2 melting temperature.

Excluding the undissolved UO_2, the observed microstructure is typical of two solidified immiscible liquids. **The obtained composition lies within the miscibility gap in the quaternary (O,Fe,U,Zr) liquid phase**.

The fact that the two solidified liquids are separated by a sharp interface, as it was observed for sample OUZr_2 and OUZr_3, suggests that the cooling was fast enough to allow a separate quenching of the immiscible liquids.

In the following the two solidified liquids will be treated separately, considering that they experienced independent cooling.

4.2.3.1 Oxide liquid (Liquid 2)

WDS analysis performed on this region allows to determine the global composition of the oxide zone. The undissolved UO_2 was not taken into account in this measure. The WDS results are shown in Table 13.

	In-vessel corium sample / oxide liquid
at % O	61.4±3
at % U	14.9±1
at % Zr	21.8±2
at % Fe	1.9±1

Table 13: WDS analysis on the solidified oxide Liquid 2 (Zone 2 in Figure 27) of the in-vessel corium sample

The microstructure observed in the solidified oxide liquid is reported in Figure 28.

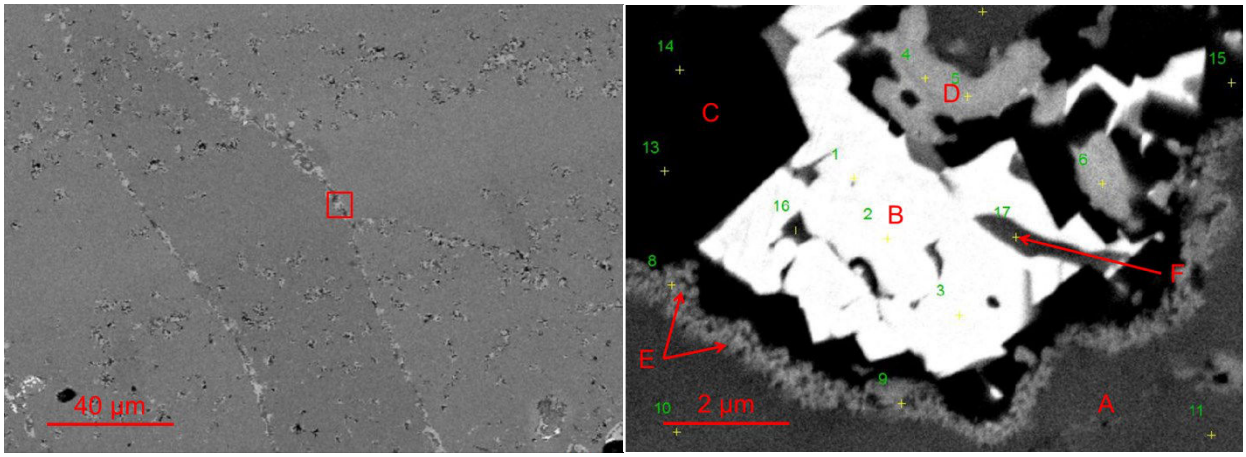

(a) (b)

Figure 28: (a) BSE image of the solidified oxide Liquid 2; (b) close up on the white precipitates along the mixed oxide $(U,Zr)O_{2-x}$ grain boundaries. Six phase are identified and analysed by WDS (A-F in the figure)

At the grain boundaries of a homogenous microstructure, white precipitates can be noted (Figure 28b). Actually, the zone along the grain boundaries is composed by several phases. WDS results on the detected phases are reported in Table 14.

	A	B	C	D	E	F
at % Fe	0.7	8.6	60.2	1.6	12.4	16.2
at % U	12.9	46.5	6.2	19.8	15.1	48.4
at % Zr	17.1	0.4	26.9	7.1	24.4	2.6
at % O	69.3	44.5	6.8	71.5	48.1	32.8
Fe/(Fe+U+Zr)	0.8	15.5	64.6	5.5	23.9	24.1
U/(Fe+U+Zr)	44.1	83.9	6.6	69.5	29.1	72.0
Zr/(Fe+U+Zr)	55.1	0.6	28.8	25.0	47.1	3.9

Table 14: WDS analyses on the zone along the mixed oxide grain boundaries. The first part of the table reports the raw data form the spectrometer. The second part reports the ratios between metals without taking into account oxygen contribution.

No X-ray analyses are available for these phases. In addition, the O-content is overestimated as shown in the previous section. The identification of the phases is then challenging. Solidification path calculation helps us in this task.

The solidification path of the oxide Liquid 2 ($O_{0.614}U_{0.149}Zr_{0.218}Fe_{0.019}$) is reported in Figure 29.

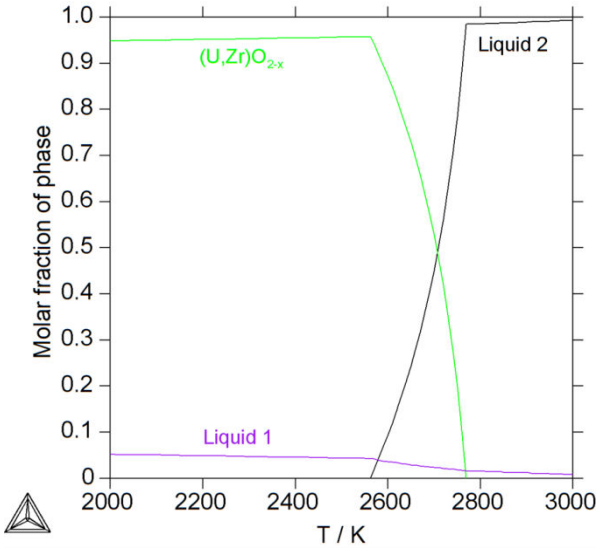

Figure 29: Solidification path of the oxide Liquid 2

At 3000 K, two liquids are in equilibrium: the major Liquid 2 has a composition $O_{0.618}Zr_{0.219}U_{0.15}Fe_{0.012}$, whilst the minor liquid phase Liquid 1 is essentially metallic, with a composition $Fe_{0.941}U_{0.03}Zr_{0.028}O_{0.001}$. From 2770 K, a $(U,Zr)O_{2-x}$-c phase starts to form by the reaction [L1+L2] → [L1+L2+$(U,Zr)O_{2-x}$]. At about 2560 K all the initial major Liquid 2 is replaced by the mixed oxide phase $(U,Zr)O_{2-x}$. The composition of the $(U,Zr)O_{2-x}$-c phase does not vary between 2560 K and 2000 K, leading to the conclusion that during cooling, the interaction between the remaining Liquid 1 and the solid mixed oxide phase is limited. The temperature interval between the complete transformation of the oxide Liquid 2 and the solidification of the metallic Liquid 1 is remarkable (~1200 K). Furthermore, the molar fraction of the Liquid 1 is small compared to the mixed oxide phase. At 2770 K during the reaction [L1+L2] → [L1+L2+$(U,Zr)O_{2-x}$] and/or during the transformation of Liquid 2 between 2770 K and 2560 K, Liquid 1 might have migrate in the free space between the grain boundaries of the already solidified $(U,Zr)O_{2-x}$. The solidification of Liquid 1 takes place along the grain boundaries of the mixed oxide. The white precipitates visible in Figure 28b are the results of the solidification process described above. The composition of the metallic Liquid 1 does not vary appreciably between 2560 K and 2000 K, and it corresponds to $Fe_{0.432}Zr_{0.306}U_{0.247}O_{0.015}$. The solidification path obtained starting from this composition is shown in Figure 30.

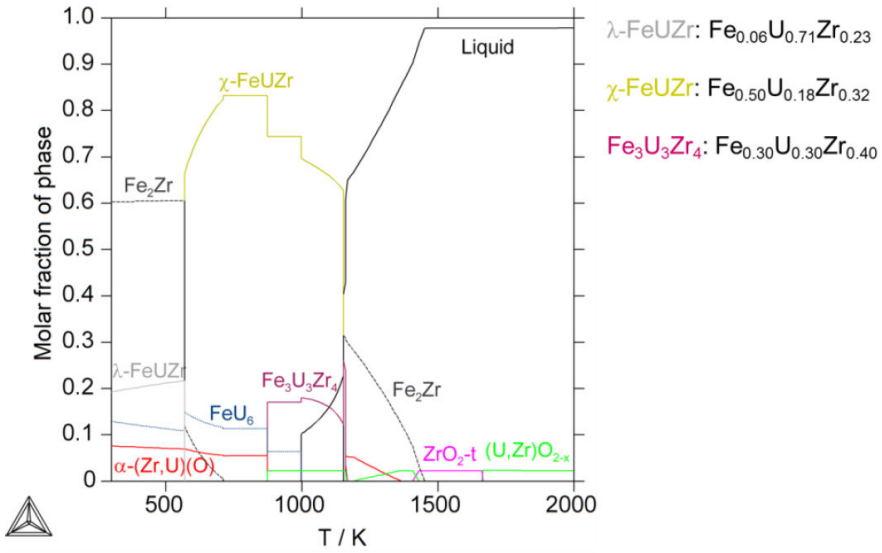

Figure 30: Independent calculated solidification path of metallic Liquid 1

At 300 K, four phases are calculated: Fe_2Zr + λ-FeUZr + FeU_6 + α-Zr(O).

Coupling calculation results with the WDS analyses in Table 14, it is possible to identify the phases formed during the solidification of Liquid 1. The reduced dimensions of the investigated phases, may affect the WDS results, especially the O content estimation. The comparison between WDS analyses on metals and the calculated phases is reported in Table 15 (see also Figure 31).

	A	B	C	D	E	F
Fe/(Fe+U+Zr)	0.8	15.5	64.6	5.5	23.9	24.1
U/(Fe+U+Zr)	44.1	83.9	6.6	69.5	29.1	72.0
Zr/(Fe+U+Zr)	55.1	0.6	28.8	25.0	47.1	3.9
Phase	$(U,Zr)O_{2-x}$	FeU_6	$Fe_2(Zr,U)$	λ-FeUZr	$Fe_3U_3Zr_4$	Undefined

Table 15: Comparison between WDS analysis and calculation on the solidification of Liquid 1. Zone A-F correspond to zones in Figure 31b. The proposed phases are chosen starting from the calculation on Liquid 1 (Figure 30)

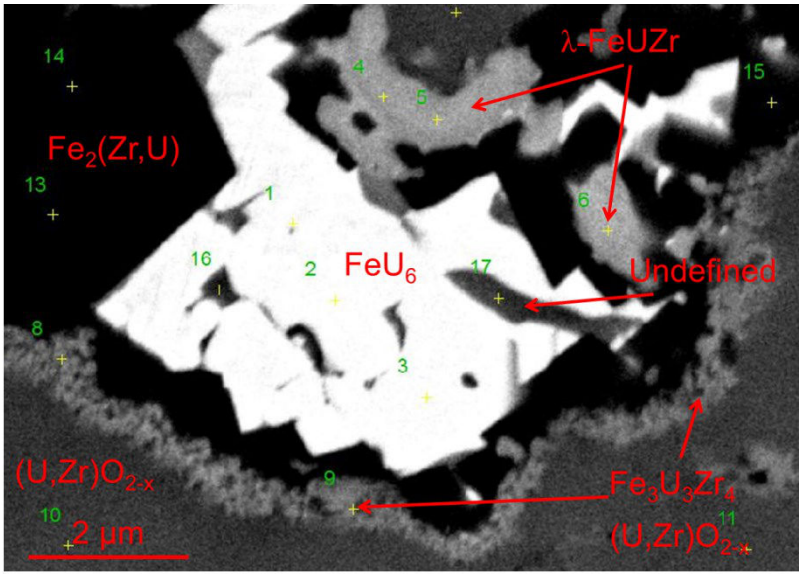

Figure 31: Results of solidification path calculation and WDS analysis coupling

The calculation are coherent with WDS observations. However, WDS analyses did not reveal the presence of α-(Zr,U)(O) that appears in the solidification path. Moreover, one of the phases detected by WDS could not be indexed (point F).

4.2.3.2 Metallic liquid (Liquid 1)

A WDS analysis on the quenched metallic liquid was performed from BSE image given in Figure 32 and is reported in Table 16. WDS analysis was also performed using higher magnification to estimate the composition of the solidified phases. The result of a WDS profile is shown in Figure 33.

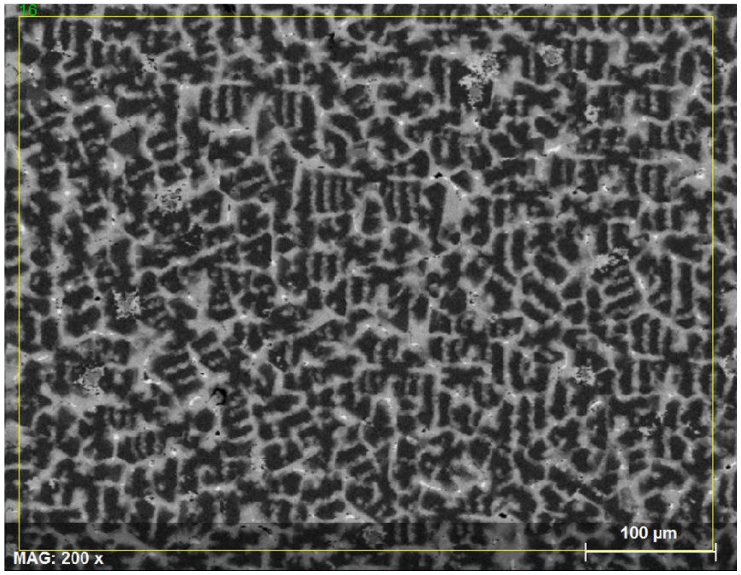

Figure 32: BSE image of the solidified metallic liquid.

	In-vessel corium sample / metallic liquid
at % O	1.8
at % U	6.3
at % Zr	13.8
at % Fe	78.1

Table 16: WDS analysis on the solidified metallic liquid of the in-vessel corium sample

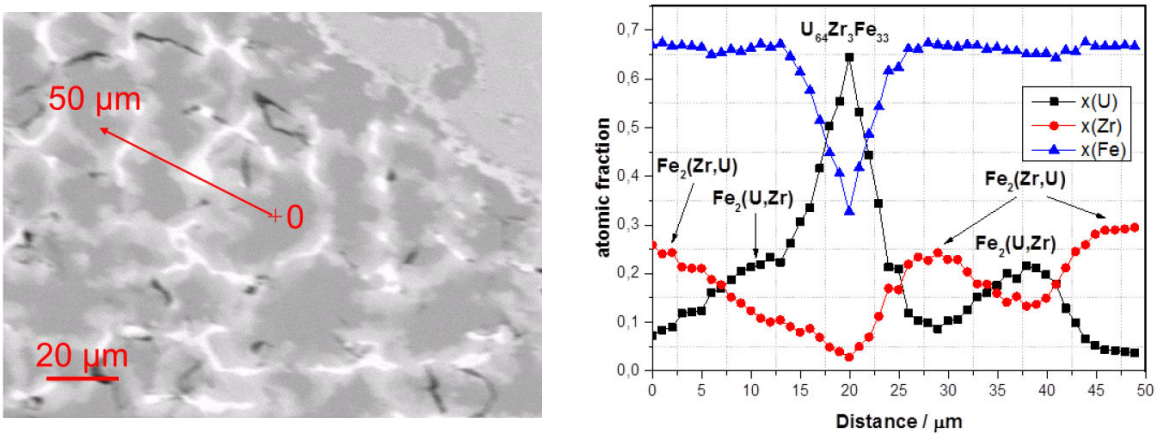

(a) (b)

Figure 33: WDS profiles obtained in the metallic solidified region

Two C15_Laves phases – $Fe_2(Zr,U)$ and $Fe_2(U,Zr)$ – are observed. A third U-enriched phase with a composition $Fe_{0.33}U_{0.64}Zr_{0.03}$ is also revealed. **The presence of two phases with the same structure means that the selected composition crosses a miscibility gap in the $Fe_2(U,Zr)$ phase during cooling.**

The solidification path calculated starting from the composition in Table 14, reveals the coexistence of a minor $(U,Zr)O_{2-x}$-c phase with an O depleted liquid between 2800 K and 1750 K. The composition of the liquid does not vary in this range of temperature, leading to the conclusion that, as observed for the oxide liquid, the mixed oxide and the coexisting metallic liquid cool separately. The composition of the liquid phase at 1750 K is $Fe_{80}U_6Zr_{14}$. The solidification path obtained starting from this composition is reported in Figure 34.

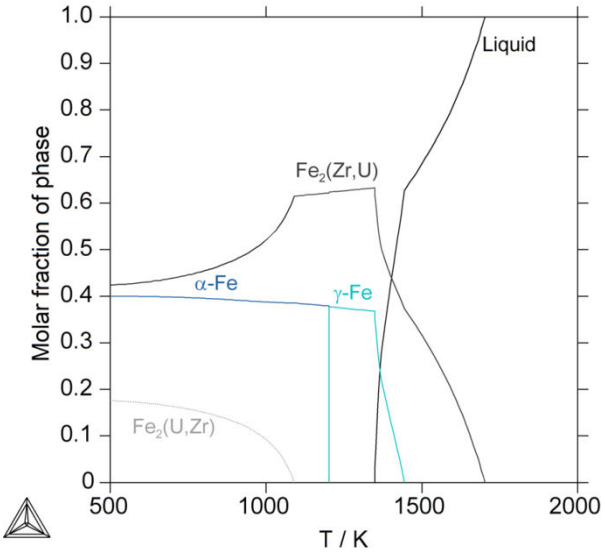

Figure 34: Independent solidification path of the metallic Liquid 1 $Fe_{80}U_6Zr_{14}$

The calculation confirms the presence of two C15_Laves phases. However, the U-enriched phase measured by WDS is not calculated.

Within the metallic matrix some spherical oxide droplets with an average diameter of 80 µm may be recognised (Figure 35). It can be noted that inside the oxide spheres a metallic phase could form. The U/Zr ratio in the oxide droplets (0.64) is comparable to the U/Zr ratio measured in the solidified oxide liquid (0.68). The presence of these droplets within the solidified metallic liquid is related to the convective movements during the fabrication. During cooling, the oxide liquid droplets solidified, partially surrounding a small amount of metallic liquid solidified into $Fe_2(Zr,U)$ and $Fe_2(U,Zr)$. WDS analyses on the metallic zone inside the solidified oxide droplet corroborate this interpretation.

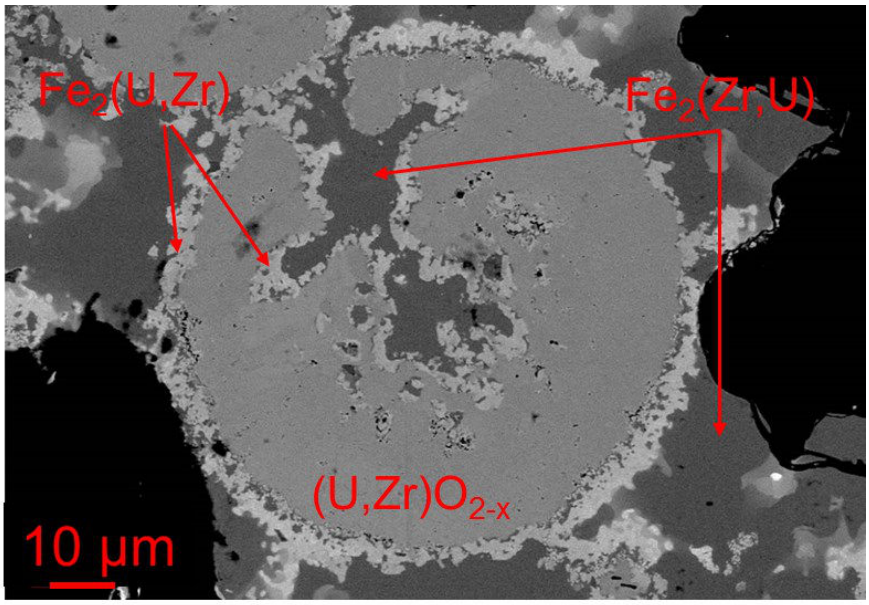

Figure 35: Magnification of a spherical oxide droplet within the solidified metallic liquid

4.2.2.3 Summary

Solidification path calculations performed on a prototypic U-Zr-O-Fe in-vessel corium sample allow interpreting the microstructure observed by SEM and the quantitative analyses by WDS. A good agreement is obtained between calculations and experimental observations. It must be pointed out that the calculations involve a quaternary system. In the present work, no quaternary interaction parameters have been assessed. Therefore, the solidification paths are the result of extrapolation from the thermodynamic models of lower order. Notwithstanding that, the calculations are predictive.

4.3 Conclusions

In this chapter we presented the thermodynamic assessment performed on the O-U-Zr, O-Fe-Zr, O-Fe-U and O-Pu-U ternary systems.

The critical selection of experimental data from the literature (Chapter 2) and current experimental results allowed to obtain a satisfactory model for the O-U-Zr. The miscibility gap in the liquid phase is now better described, especially at 2567 K, where the present annealing tests have been performed. However, new thermodynamic data, such as oxygen potential measurement will allow a better description of the cubic $(U,Zr)O_{2-x}$ phase.

Taking into account the lack of available experimental data on O-Fe-Zr and O-Fe-U systems, the present assessment on these systems can be considered satisfactory. It is however clear that large regions of these ternary systems are experimentally unknown. Oxygen potential measurement will help to better assess these systems.

Solidification path calculations are a useful tool to interpret experimental results. This kind of calculation can be also used to interpret complex microstructure of multi-component samples, such as the U-Zr-Fe-O in-vessel corium sample. **The coupling between experimental study and thermodynamic calculation is complete approach for the investigation of complex chemical systems**.

The laser heating results on the UO_2-PuO_2-ZrO_2 samples have been also interpreted using thermodynamic calculations. The high temperature behaviour of these samples is strongly dependent on the nature of the experimental buffer gas. The O/M of the cubic $(U,Pu,Zr)O_{2\pm x}$ phase can significantly vary in function of the oxygen potential, the temperature and the composition of the sample.

4.4 References

[1] M. Kurata, "Thermodynamic assessment of the Pu-U, Pu-Zr and Pu-U-Zr systems," *Calphad*, vol. 23, no. 3–4, pp. 305–337, 1999.

[2] M. Kurata, "Private communication," 2014.

[3] M. Kurata, "Thermodynamic database on U-Pu-Zr-Np-Am-Fe alloy system II - Evaluation of Np, Am, and Fe containing systems -," *IOP Conf. Ser. Mater. Sci. Eng.*, vol. 9, p. 012023, 2010.

[4] C. Toffolon-Masclet, J. C. Brachet, C. Servant, J. M. Joubert, P. Barberis, N. Dupin, and P. Zeller, "Contribution of Thermodynamic Calculation to Metallurgical Studies of Multi-Component Zirconium Based Alloys," *J. ASTM Int.*, vol. 5, no. 7, p. ID JAI101122, 2008.

[5] B. Sundman, "An assessment of the Fe-O System," *J. Phase Equilibria*, vol. 12, pp. 127–140, 1991.

[6] P. Liang, N. Dupin, S. Fries, H. J. Seifert, I. Ansara, H. Lukas, and A. F, "Thermodynamic Assessment of the Zr-O Binary System," *Zeitschrift fur Met.*, vol. 92, no. 7, pp. 747–756, 2001.

[7] C. Guéneau, N. Dupin, B. Sundman, C. Martial, J. C. Dumas, S. Gossé, S. Chatain, F. De Bruycker, D. Manara, and R. J. M. Konings, "Thermodynamic modelling of advanced oxide and carbide nuclear fuels: Description of the U-Pu-O-C systems," *J. Nucl. Mater.*, vol. 419, no. 1–3, pp. 145–167, 2011.

[8] N. Dupin, "Private communication," 2014.

[9] M. Baichi, "Contribution à l'étude du corium d'un réacteur nucléaire accidenté : aspects puissance résiduelle et thermodynamique des systèmes U-UO_2 et UO_2-ZrO_2,", PhD Thesis INP Grenoble, 2001.

[10] A. Maurizi, "Réactivité chimique à haute température dans le système (U,Zr,Fe,O) - contribution a l'étude de la zircone comme récupérateur de 'corium,'", PhD Thesis Univerisité Pierre et Marie Curie, 1996.

[11] M. Baichi, C. Chatillon, and C. Guéneau, "Mass spectrometer study of the UO_2-ZrO_2 pseudo-binary system," *J. Nucl. Mater.*, vol. 294, pp. 84–87, 2001.

[12] I. Cohen and B. Shaner, "A metallographic and X-ray study of the UO_2-ZrO_2 system," *J. Nucl. Mater.*, vol. 9, pp. 18–52, 1963.

[13] W. A. Lambertson and M. Mueller, "Uranium Oxide Phase Equilibria Systems: III, UO2-ZrO2," *J. Am. Ceram. Soc.*, vol. 36, pp. 365–368, 1953.

[14] E. F. Juenke and J. F. White, "Physico-chemical studies of clad UO_2 under reactor accident conditions," General Electric Company, Report no. GEMP-731, 1970.

[15] C. Politis, "Untersuchungen im Dreistoffsystem Uran-Zirkon-Sauerstoff," Kernforschungszentrum Karlsruhe, Report no. KfK 2167, 1976.

[16] A. Skokan, "A High Temperature Phase Relation in the U-Zr-O system," in *5th Internation Meeting on Thermal Nuclear Reactor Safety*, 1984, pp. 1035–1041.

[17] M. Barrachin, P. Y. Chevalier, B. Cheynet, and E. Fischer, "New modelling of the U-O-Zr phase diagram in the hyper-stoichiometric region and consequences for the fuel rod liquefaction in oxidising conditions," *J. Nucl. Mater.*, vol. 375, pp. 397–409, 2008.

[18] J. S. Punni and M. A. Mignanelli, "AEA-T Internal Report AEAT/R/NS/0428, Enthalpy Project Report," 2001.

[19] C. Guéneau, V. Dauvois, P. Pérodeaud, C. Gonella, and O. Dugne, "Liquid immiscibility in a (O,U,Zr) model corium," *J. Nucl. Mater.*, vol. 254, no. 2–3, pp. 158–174, Apr. 1998.

[20] S. V. Bechta, V. S. Granovsky, V. B. Khabensky, V. V. Gusarov, V. I. Almiashev, L. P. Mezentseva, E. V. Krushinov, S. Y. Kotova, R. A. Kosarevsky, M. Barrachin, D. Bottomley, F. Fichot, and M. Fischer, "Corium phase equilibria based on MASCA, METCOR and CORPHAD results," *Nucl. Eng. Des.*, vol. 238, pp. 2761-2771, 2008.

[21] H. A. Saller, A. F. Rough, J. M. Fackelmann, A. A. Bauer, and J. R. Doig, "Phase relations in the uranium-zirconium-oxygen systems involving zirconium and uranium dioxide,", Battelle Memorial Institute, Report no. BMI-1023, 1955.

[22] S. Yamanaka, M. Katsura, S. Imoto, and M. Miyaket, "Study of the U-Zr-O Ternary System" *Inorganica Chim. Acta*, vol. 140, pp. 127–131, 1987.

[23] P. Hofmann and C. Politis, "The kinetics of the uranium dioxide—Zircaloy reactions at high temperatures," *J. Nucl. Mater*., vol. 87, no. 2-3, pp. 375-397, 1979.

[24] S. V. Bechta, E. V. Krushinov, V. I. Almjashev, S. A. Vitol, L. P. Mezentseva, Y. B. Petrov, D. B. Lopukh, V. B. Khabensky, M. Barrachin, S. Hellmann, K. Froment, M. Fischer, W. Tromm, D. Bottomley, F. Defoort, and V. V. Gusarov, "Phase diagram of the ZrO_2-FeO system," *J. Nucl. Mater.*, vol. 348, no. 1-2, pp. 114-121, 2006.

[25] R. H. G. A. Kiminami, "Estudo do sistema ZrO_2-FeO-Fe_2O_3 através da termogravimetria à pressao parcial de oxygeno do ar e temperaturas de até 1500 ^oC," *Ceramica*, vol. 33, no. 213, pp. 207–210, 1987.

[26] T. Katsura, M. Wakihara, S.-I. Hara, and T. Sugihara, "Some Thermodynamic Properties in Spinel Solid Solutions with the Fe_3O_4 Component," *J. Solid State Chem.*, vol. 13, pp. 107–113, 1975.

[27] T. S. Jones, S. Kimura, and A. Muan, "Phase Relation in the System FeO-Fe_2O_3-ZrO_2-SiO_2," *J. Am. Ceram. Soc.*, vol. 50, pp. 137–142, 1967.

[28] O. Fabrichnaya and D. Pavlyuchkov, "Assessment of Experimental Data and Thermodynamic Modeling in the Zr-Fe-O System," *Metall. Mater. Trans. A*, 2015.

[29] S. V. Bechta, E. V. Krushinov, V. I. Almjashev, S. A. Vitol, L. P. Mezentseva, Y. B. Petrov, D. B. Lopukh, V. B. Khabensky, M. Barrachin, S. Hellmann, K. Froment, M. Fisher, W. Tromm, D. Bottomley, F. Defoort, and V. V. Gusarov, "Phase diagram of the UO_2-FeO_{1+x} system," *J. Nucl. Mater.*, vol. 362, no. 1, pp. 46-52 2007.

[30] P. G. Mardon, D. J. Hodkin, and J. T. Dalton, "Some observation on the Pu-Zr-O system," *J. Nucl. Mater.*, vol. 32, pp. 126–134, 1969.

[31] T. Albiol, H. Serizawa, and A. Yasuo, "Studies in the PuO_2-ZrO_2 Pseudo-binary Phase Diagram," *J. Nucl. Sci. Technol.*, vol. sup3, pp. 834–837, 2002.

[32] H. Kinoshita, M. Uno, and S. Yamanaka, “Phase relation assessment of the O-Pu-Zr system by thermodynamic modelling,” *J. Alloys Compd.*, vol. 354, pp. 129–137, 2003.

[33] H. Kinoshita, M. Uno, and S. Yamanaka, “Stability evaluation of fluorite structure phases in ZrO_2-MO_2 (M = Th, U, Pu, Ce) systems by thermodynamic modelling,” *J. Alloys Compd.*, vol. 370, pp. 25–30, 2004.

[34] S. Yamanaka, H. Kinoshita, and K. Kurosaki, “Phase relation assessment for O-Pu-U ternary system,” *J. Nucl. Mater.*, vol. 326, pp. 185–194, 2004.

[35] M. Kato, K. Morimoto, H. Sugata, K. Konashi, M. Kashimura, and T. Abe, “Solidus and liquidus temperatures in the UO_2-PuO_2 system,” *J. Nucl. Mater.*, vol. 373, pp. 237–245, 2008.

[36] F. De Bruycker, K. Boboridis, D. Manara, P. Poml, M. Rini, and R. J. M. Konings, “Reassessing the melting temperature of PuO_2,” *Mater. Today*, vol. 13, no. 11, pp. 52–55, 2010.

[37] P. Incropera, D. P. De Witt, T. L. Bergman, and A. S. Lavine, Book, *Fundamentals of Heat and Mass Transfer*, 6th ed. 2007.

[38] F. De Bruycker, “High Temperature Phase Transitions in Nuclear Fuels of the Fourth Generation,” PhD Thesis Universite d’Orleans, 2010.

[39] A. Quaini, C. Guéneau, S. Gossé, B. Sundman, D. Manara, A. L. Smith, D. Bottomley, P. Lajarge, M. Ernstberger, and H. F, “High temperature investigation of the solid/liquid transition in the PuO_2-UO_2-ZrO_2 system,” *J. Nucl. Mater.*, vol. 467, no. 2, pp. 660-676, 2015.

[40] R. Böhler, M. J. Welland, D. Prieur, P. Cakir, T. Vitova, T. Pruessmann, I. Pidchenko, C. Hennig, C. Guéneau, R. J. M. Konings, and D. Manara, “Recent advances in the study of the UO_2–PuO_2 phase diagram at high temperatures,” *J. Nucl. Mater.*, vol. 448, pp. 330–339, 2014.

[41] R. G. Haire, P. E. Raison, and Z. Assefa, “Systematics of the Fundamental Chemistry of the Pyrochlore oxides: $An_2Zr_2O_7$ [An=Pu, Am, Cm, Bk and Cf],” *J. Sci. Technol.*, vol. Supplement, pp. 616–619, 2002.

[42] P. Raison, R. G. Haire, and T. Ogawa, “Fundamental and technological aspects of actinide oxide pyrochlores: relevance for immobilization matrices,” *Mat. Res. Soc. Symp. Proc.*, vol. 556, 1999.

[43] D.-N. Wang, Y.-Q. Guo, K.-M. Liang, and K. Tao, “Crystal structure of zirconia by Rietveld refinement,” *Sci. China*, vol. 42, no. 1, pp. 80–86, 1999.

[44] T. Yamashita, N. Nitani, T. Tsuji, and H. Inagaki, *J. Nucl. Mater.*, vol. 245, pp. 72–78, 1997.

[45] A. Gualtieri, P. Norby, J. Hanson, and J. Hriljac, “Rietveld refinement using synchrotoron X-ray powder diffraction data collected in trasmission geometry using an imaging-plate detector: application to standard m-ZrO_2,” *J. Appl. Crystallogr.*, vol. 29, pp. 707–713, 1996.

[46] L. Lutterotti and P. Scardi, “Simultanous structure and size-strain refinement by a Rietveld method,” *J. Appl. Crystallogr.*, vol. 23, pp. 246–252, 1990.

[47] W. Steinwarz and M. Sappok, “Large-scale experiments on ex-vessel core melt behavior,” *Nucl. Technol.*, vol. 125, pp. 363–370, 1999.

Chapter 5 – Experimental and calculation results on ex-vessel corium

During a severe accident, the in-vessel corium (mainly U-Zr-Fe-O) made of a mixture of solid and liquid phases, may pierce the steel vessel and pour on the concrete slab at the bottom of the reactor. The phenomenology of the ex-vessel scenario has been widely studied (see Chapter 2). The coupling between physicochemical data with thermo-hydraulics allows to simulate the late events of a severe accident and to predict the medium and long-term behaviour of the ex-vessel mixture, permitting to find the most efficient mitigation action options. However, the thermodynamics of the in-vessel corium/concrete interaction is not well known.

The large-scale experiments dedicated to the MCCI (Molten Corium Concrete Interaction), investigated the dominant and macroscopic phenomena occurring during a severe accident. In these experimental conditions the significant thermal and composition gradients affects the rare thermochemical data [1].

In this framework, two ex-vessel corium samples have been investigated based on the prototypic U-Zr-Al-Ca-Si-O ex-vessel corium system (Fe is not taken into account). In this work, the accidental scenario consists of a fully oxidised in-vessel corium O-U-Zr (Fe is not taken into account) interacting with two concretes; one rich in CaO the other rich in SiO_2. This approach is important because the concrete used for the construction of a nuclear power plant is not standardised [2,3]. The quality and the nature of the employed concrete mainly depend on the geographic characteristic of the site. Since the very high temperatures reached during the MCCI, the contribution of CO_2 and H_2O are not taken into account, considering Al_2O_3-CaO-SiO_2 prototypic concretes. Thermodynamic calculations coupling the TAF-ID (Thermodynamics of Advanced Fuels – International Database Project) thermodynamic database and the present model for the prototypic in-vessel corium have been performed to interpret the current experimental results.

5.1 Experimental results

Two ex-vessel corium prototypic samples have been investigated. A. Boulin (LPMA, CEA Cadarache) calculated the initial compositions of the samples by using TOLBIAC-ICB severe accident code [4,5]. The calculation was performed assuming an oxidised in-vessel corium only composed of UO_2 (80 tons) and ZrO_2 (20 tons). The whole mass of molten corium at 2950 K pours on the concrete slab. Two types of concrete are considered: a limestone concrete (rich in CaO) and a siliceous concrete (rich in SiO_2). The composition of the liquid pools (CORIUM_1 for the interaction with limestone concrete, CORIUM_2 for the interaction with siliceous concrete) 24 h after the CCI (Corium Concrete Interaction) is obtained. The corresponding re-calculated massic compositions of the liquid pools are reported in Table 1.

w%	CORIUM_1	CORIUM_2
Al_2O_3	1.8	2.1
CaO	32.4	11.0
SiO_2	24.6	64.0
UO_2	30.8	15.4
ZrO_2	10.4	7.8

Table 1: Composition in mass percentage of the ex-vessel corium liquid pools 24 h after the Corium Concrete Interaction (CCI) (private communication by A. Boulin)

5.1.1 Samples preparation and characterisation

Two samples were prepared with the compositions reported in Table 1. The starting materials were Al_2O_3 powder (Alfa Aesar, 99.997 %), CaO powder (SCM, 99.9 %), SiO_2 spheres (SCM, 99.995 %), UO_2 powder (CEA supply) and ZrO_2 powder (Goodfellow, purity 99.9 %). ICP-MS (inductively coupled plasma mass spectrometry) analyses have been performed on Al_2O_3, CaO, SiO_2 and ZrO_2 to detect the impurities content. The results are reported in Appendix E. The starting materials were mixed in a W-crucible with screwed lid.

Samples underwent a heat treatment at 2500±25 K for 30 minutes in the same furnace already described in Section 3.2.1.1. After the annealing, the samples were cooled at 3 K/s.

After the heat treatment, the samples were analysed at the LMAC (Laboratoire Métallographie et Analyse Chimique), CEA Marcoule. For the characterisation a Carl Zeiss Merlin scanning electron microscope equipped with a Field Emission Gun (SEM-FEG) was used. It is coupled with energy dispersion spectroscopy (EDS, Oxford Instruments X-MAX 80 mm^2) and a wavelength-dispersive X-ray spectroscopy (WDS, SX 100 CAMECA). The standards used for the analyses are:

- UO_2 for uranium; $CaSiO_3$ for calcium and oxygen; SiO_2 for silicon; Zr for zirconium; W for tungsten; Al for aluminum.

5.1.2 CORIUM_1

A BSE image of the cross section of solidified sample CORIUM_1 after the heat treatment is reported in Figure 1.

Figure 1: Back-scattering electrons (BSE) image of the cross section of the solidified sample CORIUM_1

The solidified sample is homogeneous, with a dendritic structure, suggesting that a single liquid was present at 2500 K. EDS and WDS analyses did not reveal any significant amount of W dissolved in the sample (less than 0.5 at% W). Therefore, the interaction at the sample/crucible interface was limited in the present case.

A close up of the microstructure of sample CORIUM_1 is reported in Figure 2.

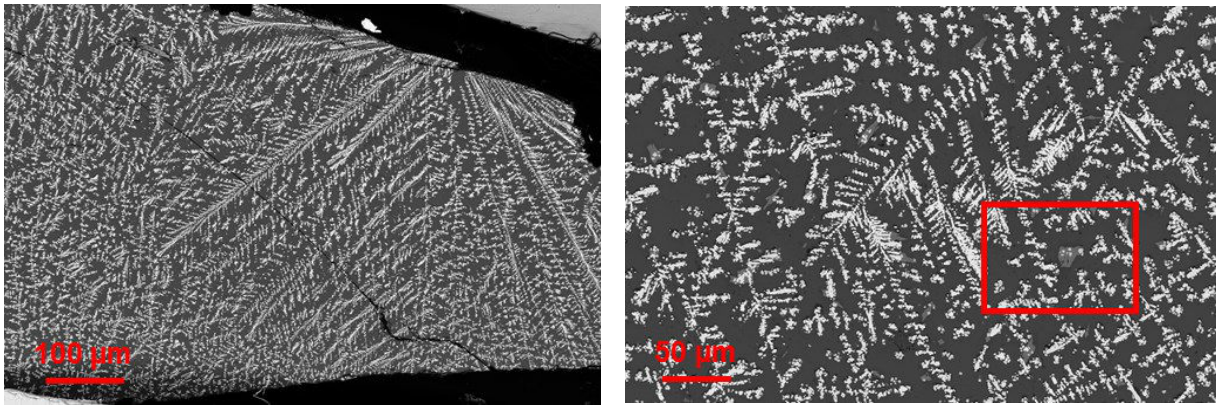

(a) (b)

Figure 2: (a) Magnification of the dendritic structure observed in sample CORIUM_1. Two main phases can be identified: white dendrites and a dark grey matrix. (b) The red square highlights the presence of a third minor light grey phase (see Figure 3)

Two main phases can be identified: the white dendrites and a dark grey phase (Figure 2a). However, looking at Figure 2b, a third minor phase can be also identified. Figure 3 shows a magnification of the red area in Figure 2b.

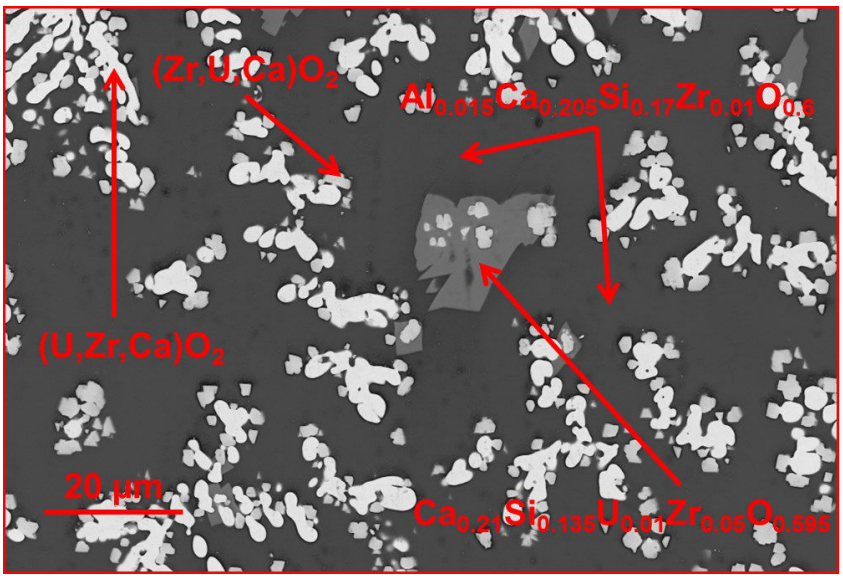

Figure 3: Larger view of the red square in Figure 2b. Three phases are identified: dendrites of $(U,Zr,Ca)O_2$, the light grey phase is a mixture (Ca,Si,Zr,εU,O) and the dark grey phase is a mixture of (Ca,Si,εAl,εZr,O), probably a quenched liquid

Thanks to EDS and WDS analyses, the white dendrites are identified as a fcc $(U,Zr,Ca)O_2$ phase. It may be noted that the dendrites are formed by two phases. The main difference between these phases is the U and Zr contents. In the whiter one, U is the major metallic element, while the other phase contains the same quantity of U and Zr. The dark grey phase is basically oxide, and it is enriched in Ca and Si. However, small amounts of Al and Zr have also been detected in this phase. The third minor light grey phase has a chemical composition close to that of the major dark grey phase. This phase contains less Si and a more significant amount of Zr. In addition, a small amount of U has been measured within this phase. It can be concluded that during cooling, the most stable oxide phase, $(U,Zr,Ca)O_2$, firstly appears in the form of dendrites. A small amount of the remaining liquid, precipitates in the minor light grey phase, which is mainly composed of Ca, Si and O. The rest of the liquid solidified, maintaining an amorphous structure. It can be noted that U is only present in the white precipitates and, in minor quantities, in the major dark grey phase. The identification of the

dark and light grey phases is difficult; the compositions of these phases measured by EDS are reported in Table 2.

	at % Al	at % Ca	at % Si	at % U	at % Zr	at % O	Phase
White phase 1	/	3.0±0.5	/	22.0±1	7.0±1	68.0±2	$(U,Zr,Ca)O_2$
White phase 2	/	5.0±1	/	11.5±2	16.6±2	67.4±3	$(Zr,U,Ca)O_2$
Dark phase	1.5±1.0	20.5±2	17.0±2	/	1.0±1	60.0±2	Not assigned
Light phase	/	21.0±2	13.5±2	1.0±1	5.0±1	59.5±2	Not assigned

Table 2: EDS analysis on the three phases identified in the solidified sample CORIUM_1. Only the white dendrites can be univocally indexed. The measured composition of the remaining two phases does not allow a reliable indexing

The oxygen content in the fcc mixed oxide phase seems to be overestimated. In fact, the presence of a hyper-stoichiometric fluorite phase $(U,Zr,Ca)O_{2.125}$ is unlikely.

5.1.3 CORIUM_2

The solidified sample CORIUM_2 presents a microstructure radically different to that of sample CORIUM_1. The BSE image of the cross section of the sample is reported in Figure 4.

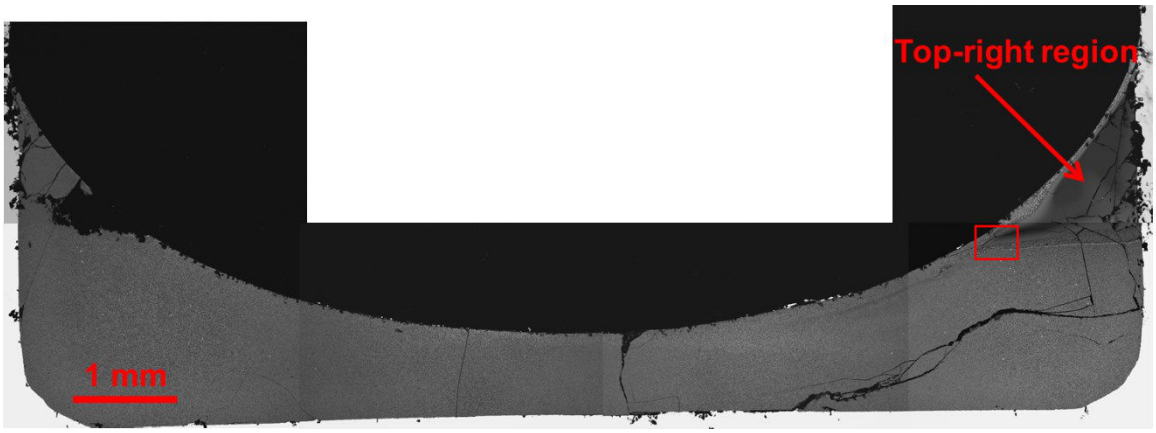

Figure 4: BSE image of the cross section of the solidified sample CORIUM_2

The observed microstructure is extremely fine. WDS analyisis detected a small amount of W coming from the crucible (about 1 at % W). On the top right of Figure 4, a region with a different chemical contrast is present.

Figure 5 shows the magnification of the interface between the two identified regions (red area in Figure 4).

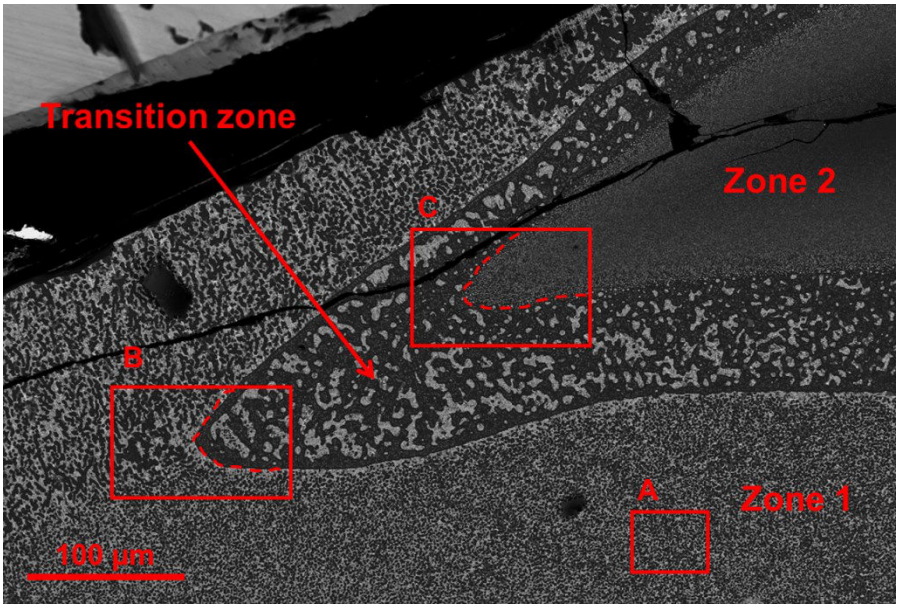

Figure 5: BSE image of the interface between the two regions. The major region "Zone 1" and the minor region "Zone 2" are separated by a third region named "Transition zone"

Figure 5 shows a third region at the interface between Zone 1 and Zone 2. This interface looks like a "Transition zone"; its thickness is about 50-100 µm, and its microstructure is a combination of those of Zone 1 and Zone 2.

The red areas in Figure 5 – A, B and C – highlight Zone 1 and the interfaces [Zone 1/Transition zone] and [Transition zone/Zone 2] respectively. The magnifications of these three zones are reported in Figure 6.

Figure 6a shows the microstructure of Zone 1. Black droplets (between 1 µm and 3 µm in diameter) are dispersed in a light structure. Within this structure, white structures are surrounded by a light grey phase. EDS analyses on this region are reported in Table 3.

	at % Al	at % Ca	at % Si	at % U	at % Zr	at % O
White region	1.3	4.4	20.8	4.3	3.7	65.5
Black region	0.4	0.8	31.5	0.2	0.4	66.7
Grey phase	2.2	7.7	24.6	0.2	1.1	64.2

Table 3: EDS analysis on Zone 1 of samples CORIUM_2

It can be concluded that the black region is mainly SiO_2, since the amount of Al, Ca, U and Zr is practically under the limit of detection of the spectrometer. The white region and the grey phases are rich in Si. The main difference between these phases is that in the white region a non-negligible amount of U is detected, whilst the amount of U measured in the grey phase is negligible. The analyses in Table 4 give only information on the overall composition of the observed regions. The phase within the black and the white regions are too small to be analysed.

The same characteristic structure can be seen in Figure 6b. Zone 1 and the Transition zone are separated by a sharp interface (red dashed line in Figure 6b). The Transition zone is formed by a black matrix with a fine dispersion of white droplets. The same light structure observed in Zone 1 is also present in the Transition zone.

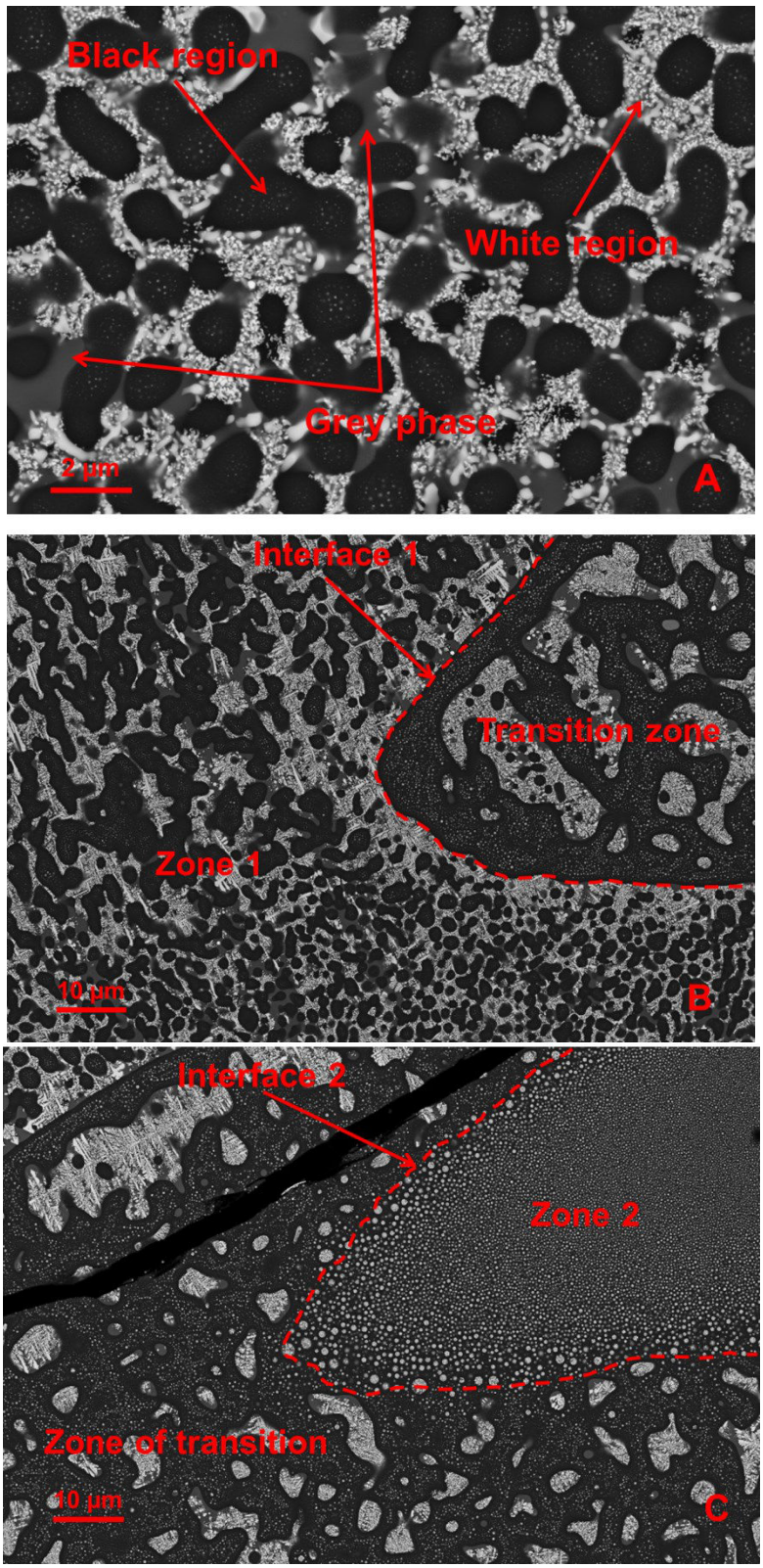

Figure 6: BSE images of the three identified regions of interest in the solidified sample CORIUM_2. (a) Zone 1; (b) interface Zone 1/Transition zone; (c) interface Transition zone/Zone 2

Figure 6c displays a detail of the interface between the Transition zone and Zone 2. The latter is formed by a dispersion of white droplets within a black matrix. The black structure corresponds to the black one observed in the Transition zone (the matrix) and in Zone 1 (the black droplets in Figure 6a). The white droplets in Zone 2 have the same composition of the white structure identified in both Zone 1 and Transition zone (Figures 6a and 6c, respectively), at least within the range of uncertainty of the current method of analysis.

Further magnification on Transition zone and Zone 2 reveals the inner structure of the white droplets (Figure 7).

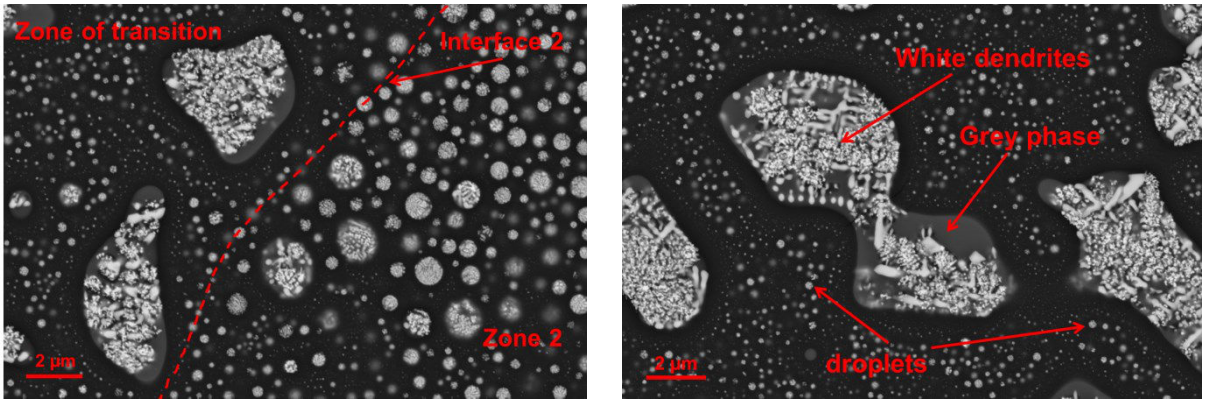

(a) (b)

Figure 7: (a) BSE image at the interface between Zone 2 and the Transition zone; (b) magnification of the white structure within the Transition zone.

The droplets and the white structure visible in Zone 1 and in Transition zone present the same features. Dendrites of a white phase are surrounded by an amorphous light grey phase, the same as that observed in Zone 1 (Figure 6a).

The drop-shaped solidified structure is a characteristic feature of the presence of two immiscible liquid in equilibrium at 2500 K. Remember that, the miscibility gap in the liquid phase observed in the OUZr_2 and OUZr_3 samples (see Chapter 3) is characterised by a stratification with the presence of small oxide droplets quenched inside the metallic liquid. **The peculiarity of this ex-vessel corium sample is that droplets are homogenously dispersed in the whole sample**. This feature can be related to the nature of the two immiscible liquids. In the O-U-Zr system, the tie-lines in the miscibility gap connect an oxide liquid and a metallic liquid. The different thermo-physical properties of the two liquid phases, such as density, viscosity and surface tension, are the main reason why a sharp stratification is observed. The presence of solidified oxide droplets within the metallic liquid is due to convective movements driven by the high temperature. CORIUM_2 sample has a global composition expressed in atomic fraction $Al_{0.01}Ca_{0.048}Si_{0.263}U_{0.014}Zr_{0.016}O_{0.649}$, therefore it can be considered essentially as an oxide. The two immiscible liquids at 2500 K are thus likely oxides. The physicochemical characteristics of the two liquids cannot be as different as in the case of the O-U-Zr system. The resulting separation is then less evident, with two liquids disposed to form a homogeneous emulsion. The cartographies of Transition zone reported in Figure 8 shows that the main difference between the two liquids is characterised by the U-content; the darker one does not contain U, whilst the lighter one does.

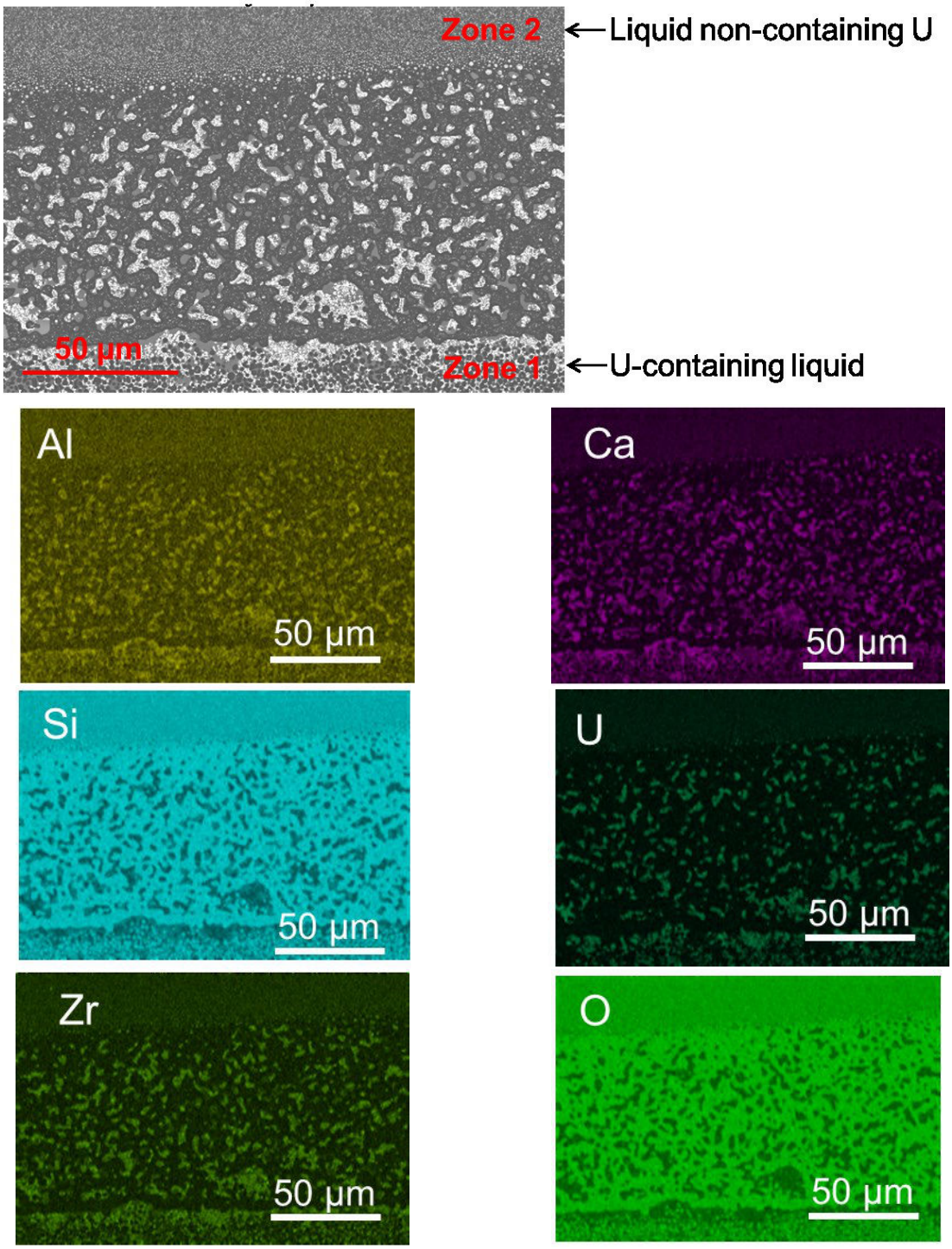

Figure 8: SEM-BSE image of the Transition zone. The elemental cartographies are reported in the lower part of the Figure

The dimension of the phases observed using the scanning electron microscope barely reaches 1 μm^2, making quantitative analysis challenging. Furthermore, the black phase is proved to fragile once confronted to the SEM electron beam, which produces a hole on the surface of the polished sample. Figure 7 also shows that the black phase is semi-transparent to the electron beam. In fact, the dispersed white droplets are visible on different planes below the sample cross section surface. These characteristics make quantitative analyses challenging. Using the WDS in a non-focalised configuration on a 200 μm^2 area, the average composition of Zone 1 has been measured. No WDS and EDS results are available for Zone 2.

The available analyses provided by LMAC, CEA Marcoule, are reported in Table 4.

	at % Al	at % Ca	at % Si	at % U	at % Zr	at % O
Zone 1	0.9	3.9	25.9	1.3	1.7	66.3

Table 4: WDS analysis in non-focalised configuration on Zone 1 of sample CORIUM_2

5.1.4 Summary

Heat treatment on two prototypic ex-vessel corium samples revealed that the type of concrete interacting with the in-vessel corium influences the high temperature configuration of the mixtures. The same in-vessel corium mixture (UO_2+ZrO_2) interacting at 2500 K with a prototypic limestone concrete (rich in CaO) results in a monophasic liquid phase, whilst the interaction with a prototypic siliceous concrete (rich in SiO_2) induces the formation of two immiscible liquids. This feature is a direct consequence of the interaction between SiO_2 and the other components of the investigated system. In fact, a miscibility gap in the liquid phase is present in the CaO-SiO_2 [6], ZrO_2-SiO_2 [7] and UO_2-SiO_2 [7] systems. In the present case, SEM-EDS and WDS analysis cannot give precise quantitative information of the composition of the two liquids due to their amorphous nature and reduced dimensions. However, qualitatively, U seems to be absent in one of the two liquid.

5.2 Solidification path calculations

Solidification path calculations can help to interpret the complex microstructures observed in the solidified ex-vessel corium samples. However, the thermodynamic model of U-Pu-Zr-Fe-O system assessed during this work does not contain the main components of the considered prototypic concretes, Al_2O_3, CaO and SiO_2. Therefore, the interaction between the in-vessel corium system and concrete (in this work, only composed by Al_2O_3-CaO-SiO_2) cannot be calculated.

Thus, in order to perform thermodynamic calculations, the missing chemical systems have been taken from the TAF-ID database [8].

5.2.1 TAF-ID database

Safety improvement and life extension for Generation II-III reactors, and the design of the Generation IV reactors are dependent on the available thermodynamic experimental data and modelling. These are needed to describe the complex phenomena occurring during the normal functioning as well as during accidental scenario of a nuclear power plant.

In 2013, in the framework of an OECD-NEA project (Organisation for Economic Co-operation and Development – Nuclear Energy Agency), several groups of research gather their calculation tools and thermodynamic database into the TAF-ID project. At the present stage Canada, France, Japan, The Netherlands, Republic of Korea and USA actively contribute to the development of the TAF-ID database.

The main objective of the TAF-ID project is to assure a comprehensive and reliable international thermodynamic database for the calculation of phase diagram and thermodynamic properties of advanced nuclear fuel, fission products and structural materials (steel, Zircaloy, concrete). The present work contributes to the development of the TAF-ID database with the assessment of the prototypic in-vessel corium system (U-Pu-Zr-Fe-O).
In order to perform calculation on the ex-vessel corium samples described above, the thermodynamic description of the complex U-Zr-Al-Ca-Si-O system is needed. The TAF-ID database contains the models describing all the 15 binary sub-systems of the prototypic ex-vessel corium, and the model for the 10 O-containing ternary systems: Al-Ca-O, Al-O-Si, Al-

O-U [9], Al-O-Zr, Ca-O-Si, Ca-O-U [9], Ca-O-Zr [9], O-Si-U [9], O-Si-Zr [9] and O-U-Zr (this work). No quaternary parameters are present in the current version of the TAF-ID database. Therefore, the model of the six-element ex-vessel corium system is extrapolated from the models of the ternary systems.

5.2.2 Results

The present set of calculations represents a tentative approach to better interpret the SEM-EDS and WDS analyses of samples CORIUM_1 and CORIUM_2 performed at LMAC, CEA Marcoule and presented in Section 5.2. Note however that these experimental results cannot be considered as fully descriptive. Indeed, significant difficulties have been reported during the analysis, especially for sample CORIUM_2, where its amorphous nature did not allow an accurate measurement of the global composition after the annealing at 2500 K.

5.2.2.1 CORIUM_1

At the present stage of the investigation, LMAC did not measure the global composition of solidified sample CORIUM_1 after the heat treatment. Therefore, the present calculations are performed considering the initial composition of the sample. The resulting solidification path is reported in Figure 9.

The solidification path reveals that at the annealing temperature (T=2500 K) two phases are in equilibrium: a liquid phase and a fcc (U,Zr,Ca)O_{2-x} phase. Only negligible amount of U and Zr are present in the liquid phase (less than 0.05 at %) according to the calculations. However, the dendritic form of the fcc phase identified on the microstructure of sample CORIUM_1 suggests that the formation of this phase was due to the rapid cooling of a liquid phase. Thus, the calculated solidification path is in disagreement with the experimental results (see interpretation given above).

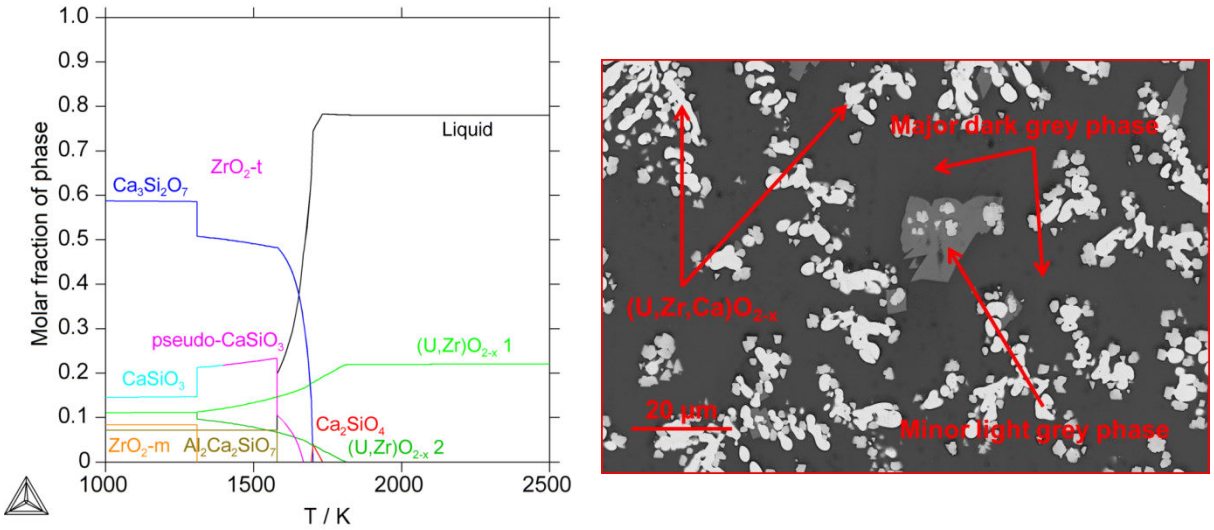

(a) (b)

Figure 9: Solidification path calculated for sample CORIUM_1, annealed at 2500 K for 30 minutes

This disagreement can be due either to the parameters used in the model or to the incorrect mixture composition used to perform the calculations. At about 1820 K a second fcc phase, (εCa,U,εZr)O_{2-x}, starts to form. The formation of a second mixed oxide cubic phase is coherent with the experimental observation. At 1732 K a small amount of Ca_2SiO_4 is formed: its content reached a maximum at 1700 K (about 4 mol%) and then disappears reacting with

the remaining liquid to form $Ca_3Si_2O_7$ (rankinite). At 1668 K the $CaSiO_3$ phase starts to precipitates. At the calculated solidus temperature, T=1579 K, the reaction L → [$CaSiO_3$+$Al_2Ca_2SiO_7$] takes place. At low temperature, below 1300 K, the solid phases in equilibrium are $Ca_3Si_2O_7$ (rankinite), $CaSiO_3$ (wollastonite), (U,εCa,εZr)O_{2-x}, ZrO_2-m and $Al_2Ca_2SiO_7$ (melilite).

The chemical compositions of liquid does not vary between 2500 K and 1732 K, suggesting that these phases follow independent cooling paths. The formation of the Ca,Si-based oxide phases in Figure 9 are essentially due to the liquid cooling. This is confirmed by the independent liquid solidification path in Figure 10. The liquid phase contains negligible amount of U and Zr, which rather stay in the fcc (U,Zr,Ca)O_{2-x}-c phase.

The calculated solidification path in Figure 9a can help the interpretation of the microstructure of sample CORIUM_1 (Figure 9b).

The first phase formed during the calculated solidification path is a (U,Zr,Ca)O_{2-x}-c phase. The calculated composition is consistent with the experimental results (Table 5). The calculation overestimates the Zr and Ca content, while underestimate the U content.

None of the calculated phase has a composition that corresponds to the minor light grey phase (Figure 9b). Considering the small amount of this phase it may however correspond to the calculated Ca_2SiO_4 phase. Due to the rapidity of the cooling, part of this phase could have not reacted with the liquid to form $Ca_3Si_2O_7$. The significant amount of Zr (and, in minor extent, the amount of U) measured inside this phase can be due to a small solubility of Zr and U in the Ca_2SiO_4. **The existence of a $(Ca,Zr,\varepsilon U)_2SiO_4$ phase can fit the current EDS and WDS results.**

The measured composition of the dark grey phase (Figure 9b) does not fit with any of the solid phases calculated in Figure 9a and Figure 10. However, the composition of the liquid calculated at T>1732 K seems to correspond to this phase. Due to the rapid cooling, the liquid phase did not have enough time to follow the solidification path in Figure 10, leading to the formation of the amorphous dark grey matrix visible in Figure 9b.

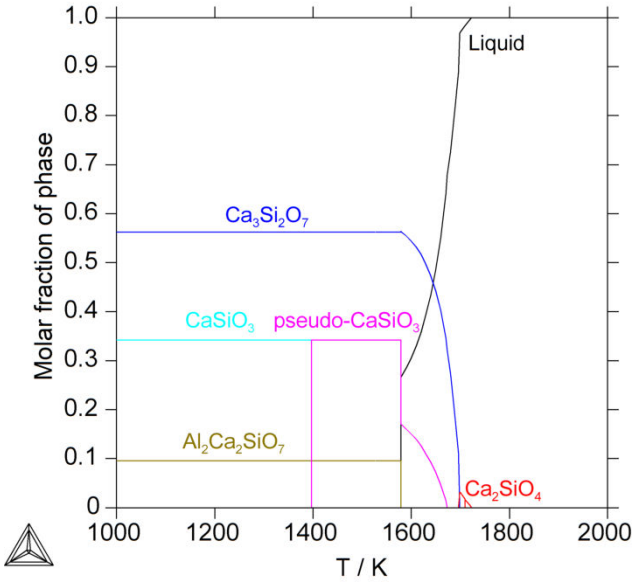

Figure 10: Independent solidification path of the liquid phase in Figure 9

The comparison between calculation and experimental results on sample CORIUM_1 is reported in Table 5.

		at % Al	at % Ca	at % Si	at % U	at % Zr	at % O	Phase
White dendrites	Exp.	/	3.0±1	/	22.0±1	7.0±1	68.0±2	$(U,Zr,Ca)O_{2-x}$
	Calc.	/	5.7	/	16.8	12.7	65.0	
Light grey	Exp.	/	21.0±2	13.5±2	1.0±1	5.0±1	59.5±2	$(Ca,Zr,\varepsilon U)_2SiO_4$
	Calc.	/	28.5	14.2	/	/	57	
Dark grey	Exp.	1.5±1.0	20.5±2	17.0±2	/	1.0±1	60.0±2	Quenched liquid
	Calc.	1.5	22.5	17.0	/	/	58.9	

Table 5: Comparison between the EDS results and calculations performed on CORIUM_1 sample. In order to confirm the existence of the $(Ca,Zr,\varepsilon U)_2SiO_4$ phase, further experimental investigation should be performed. At the present stage, its existence is only inferred to index the light grey phase observed by SEM-EDS

5.2.2.2 CORIUM_2

The amorphous nature of the solidified sample CORIUM_2 made the post-experiment analyses challenging. In order to calculate the solidification path of the sample, the initial composition given in Table 1 has been used.

The solidification path calculated for sample CORIUM_2 is reported in Figure 11.

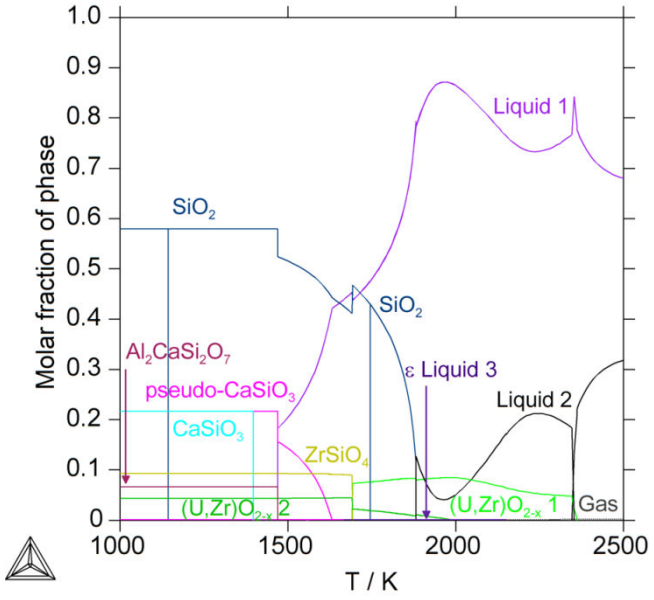

Figure 11: Solidification path calculated for sample CORIUM_2, annealed at 2500 K for 30 minutes

At 2500 K, two liquids are calculated, in agreement with the experimental observation in Section 5.2.3. The calculated composition of the two liquids indicates that they are basically oxide: Liquid 1=$Al_{0.013}Ca_{0.065}Si_{0.269}Zr_{0.010}O_{0.643}$ and
Liquid 2=$Al_{0.005}Ca_{0.011}Si_{0.249}U_{0.045}Zr_{0.028}O_{0.662}$. The composition of the calculated U-containing Liquid 2 is comparable with the measured composition of Zone 1 in Figure 5: $Al_{0.009}Ca_{0.039}Si_{0.259}U_{0.013}Zr_{0.017}O_{0.663}$. It may be noted that U is only present in Liquid 2. Furthermore, a very small amount (less than 0.2 mol%) of a gas phase with a composition $Si_{0.50}O_{0.50}$ is calculated between 2150 K and 2500 K. At 2360 K a $(U,Zr,Ca)O_{2-x}$ phase start to

form. The amount of $(U,Zr,Ca)O_{2-x}$ increases until 2000 K: at this temperature, there is no more Zr in Liquid 1, and Liquid 2 has a composition close to SiO_2. At 1878 K, the reaction [Liquid 1+Liquid 2+$(U,Zr,Ca)O_{2-x}$] → [Liquid 1+$(U,Zr,Ca)O_{2-x}$+SiO_2] (in the cristobalite allotropic form) takes place. The amount of solid SiO_2 increases until T=1687 K, where $ZrSiO_4$ (also named tchernobylite) forms via the reaction:

[Liquid 1+SiO_2+$(U,Zr,Ca)O_{2-x}$] → [Liquid 1+$(U,Zr,Ca)O_{2-x}$+SiO_2+$ZrSiO_4$]. It must be pointed out that tchernobylite exists also in the form $USiO_4$. However, in the present version of the thermodynamic model, this phase is not described yet. The reaction Liquid 1 → [SiO_2+$CaSiO_3$] starting at T=1635 K produces $CaSiO_3$. Below the solidus temperature, T=1470 K, the phases in equilibrium are SiO_2 (quartz), $CaSiO_3$, $ZrSiO_4$, $Al_2CaSi_2O_8$ (anorthite) and $(U,Zr,Ca)O_{2-x}$.

The microstructure of the solidified CORIUM_2 sample suggests that both liquids in equilibrium at 2500 K cooled separately. The independent solidification paths calculated considering the calculated compositions of the liquids are reported in Figure 12a-b.

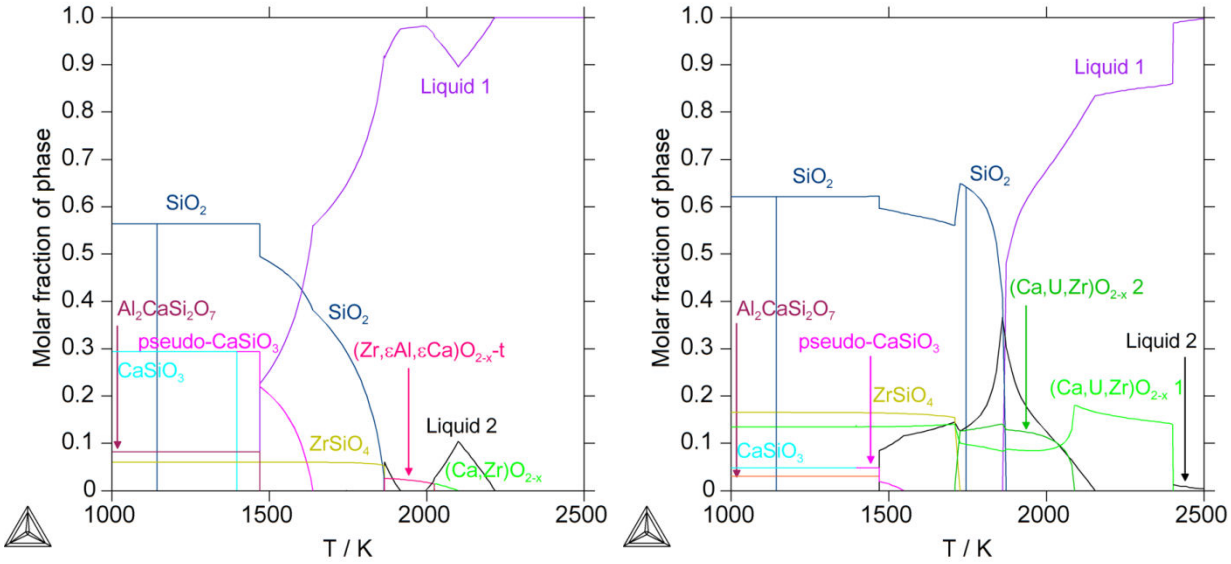

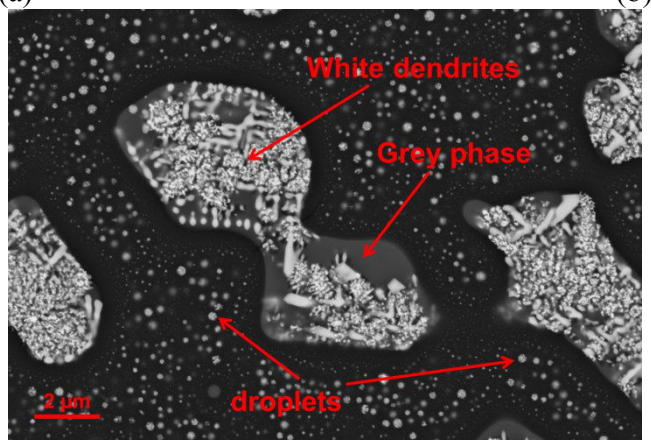

Figure 12: (a) Solidification path of Liquid 1=$Al_{0.013}Ca_{0.065}Si_{0.269}Zr_{0.010}O_{0.643}$; (b) solidification path of Liquid 2=$Al_{0.005}Ca_{0.011}Si_{0.249}U_{0.045}Zr_{0.028}O_{0.662}$; (c) microstructure observed in Transition zone

It may be noted that both the solidification path in Figure 12 show the presence of a major SiO_2 phase at low temperature. The solidification path followed by Liquid 2 shows the formation of a $(U,Zr,Ca)O_{2-x}$ phase at 2400 K. One may conclude that the white dendrites in

Figure 12c correspond to this fcc mixed oxide phase $(U,Zr,Ca)O_{2-x}$-c. The EDS analyses reported in Table 3 did not reveal the presence of a $(U,Zr,Ca)O_{2-x}$-c phase. However, the small dimension of the phases and the amorphous nature of the sample could have induced significant errors in the post-experiment analysis. The surrounding grey phase is the remaining liquid rapidly solidified around the dendrites. The light droplets dispersed within the black matrix seem to be of the same nature, suggesting that they result from the rapid solidification of Liquid 2. A direct measurement of the composition of the black matrix was not possible, since the fragility of this phase when faced to the electron beam. However, the chemical contrast suggests that it might be the result of the rapid cooling of Liquid 1.

5.3 Conclusions

In the past, the phenomenology of the severe accident has been widely studied, showing that complex phenomena occur. In this framework, thermochemical data were affected by large temperature and temperature gradients due to the large-scale dimensions of the investigated samples (up to hundreds of kilograms). Nevertheless, thermodynamic and thermochemical data are crucial for the comprehension of the accidental progress and for the severe accident simulation codes.

The present set of experiments is dedicated to the thermodynamics of the interaction between corium and concrete. **The experiments were performed under controlled experimental conditions, with an accurate temperature monitoring**. Unfortunately, the post-experiment examinations did not provide fully comprehensive results. The investigation of this type of samples is extremely challenging due to their very fine microstructure, their amorphous nature and the elevated number of constituents.

Nevertheless, post-test examination of the samples qualitatively revealed significant differences in solidified samples, depending on the type of prototypic concrete interacting with the oxidised UO_2-ZrO_2 in-vessel corium. Thermodynamic calculation performed with the TAF-ID database and the present prototypic in-vessel corium model helped in the interpretation of the microstructure of the solidified samples:

- the interaction with a CaO-rich concrete resulted in an homogenous dendritic microstructure. The $(U,Zr,Ca)O_{2-x}$-c dendrites formed within a dark grey phase, which might be the fast solidified liquid. The minor light grey phase might represent the first germs of a third phase formed during the rapid cooling.
- The interaction with a SiO_2-rich concrete resulted in the formation of two immiscible liquids. The two liquids formed an emulsion, without showing the stratification observed for samples OUZr_2 and OUZr_3. This may be related to the less pronounced difference in the thermophysical properties of the ex-vessel liquids (e.g., density, viscosity, surface tension).

This Chapter also allows to test the TAF-ID thermodynamic database coupled with the present in-vessel corium U-Pu-Zr-Fe-O model on two samples representative of the prototypic ex-vessel corium. The present calculations represent a supplementary tool for experiment interpretation. The calculations on the Al-Ca-Si-U-Zr-O system are the result of extrapolation from the thermodynamic model of the ternary sub-systems.

5.4 References

[1] C. Journeau and P. Piluso, "Core concrete interaction," in *Comprehensive Nuclear Materials*, vol. 2, pp. 635–654, 2012.

[2] "Tranches nucléaires REP 900 et 1300 MWe - Procedures U4 et U5," EDF internal report, 1985.

[3] M. Barrachin, "Assessment of Ablation Temperature of Concretes from Past MCCI and Thermodynamic Experiments,", IRSN, Report no. DPAM-SEMIC-2011-315, 2011.

[4] B. Spindler, B. Tourniaire, and J. M. Seiler, "Simulation of MCCI with the TOLBIAC-ICB code based on the phase segregation model," *Nucl. Eng. Des.*, vol. 236, pp. 2264-2270, 2006.

[5] B. Spindler, B. Tourniaire, and J. M. Seiler, "Simulation of MCCI with the TOLBIAC-ICB code based on the phase segregation model," *Nucl. Eng. Des.*, vol. 236, pp. 2264–2270, 2006.

[6] M. Hillert, B. Sundman, and X. Wang, "An assessment of the CaO-SiO_2," *Metall. Trans. B*, vol. 21B, pp. 303–312, 1990.

[7] R. G. J. Ball, M. A. Mignanelli, T. I. Barry, and J. A. Gisby, "The calculation of phase equilibria of oxide core-concrete systems," *J. Nucl. Mater.*, vol. 201, pp. 238–249, 1993.

[8] TAF-ID, "www.oecd-nea.org/science/taf-id." .

[9] N. Dupin, "Private communication," 2013.

Chapter 6 – ATTILHA experimental setup

The high temperature phenomena occurring during a severe accident (above 2300 K) impose to perform experiments under extreme conditions. However, when samples are in direct contact with the instrumentation (e.g., thermocouples) or with a crucible, an inevitable chemical interaction affects the experimental results. It has been showed in Chapter 3 that at 2567 K even the higher refractive metal, namely W, was not immune to the attack of the liquid samples.

In this framework a new experimental setup has been conceived and developed at LM2T, CEA Saclay. The ATTILHA (Advanced Temperature and Thermodynamic Investigation by Laser Heating Approach) setup is based on a laser heating technique coupled with contactless or containerless temperature monitoring. This setup has the final objective to study the high temperature thermodynamics and thermo-physical properties of corium and its sub-systems. At the present stage of the development, only non-radioactive materials can be investigated. At the time of the writing of this Chapter, safety authorisation process is on going at CEA Saclay to allow the handling and the study of U-containing samples.

6.1 Apparatus description

ATTILHA is a versatile experimental setup, which allows high temperature measurements on different kinds of materials; ceramic, metallic as well as oxide-metallic samples can be investigated. Furthermore, both aerodynamic levitation and quasi-containerless conditions can be used. In the following the aerodynamic levitation device will be described more in detail.

A picture of the ATTILHA setup is shown in Figure 1.

The sample is heated by means of a 250 W Coherent® CO_2 laser emitting at 10.6 μm (red line in Figure 1). The temperature is monitored by a bi-chromatic pyrometer (blue dotted line) and by a HgCdTe infrared detector (yellow line). Furthermore, a rapid infrared camera (green line) is employed for temperature monitoring and to get useful spatial data on the melting and solidification of the investigated samples. Temperature gradients and emissivity variation during the experiments can be also observed.

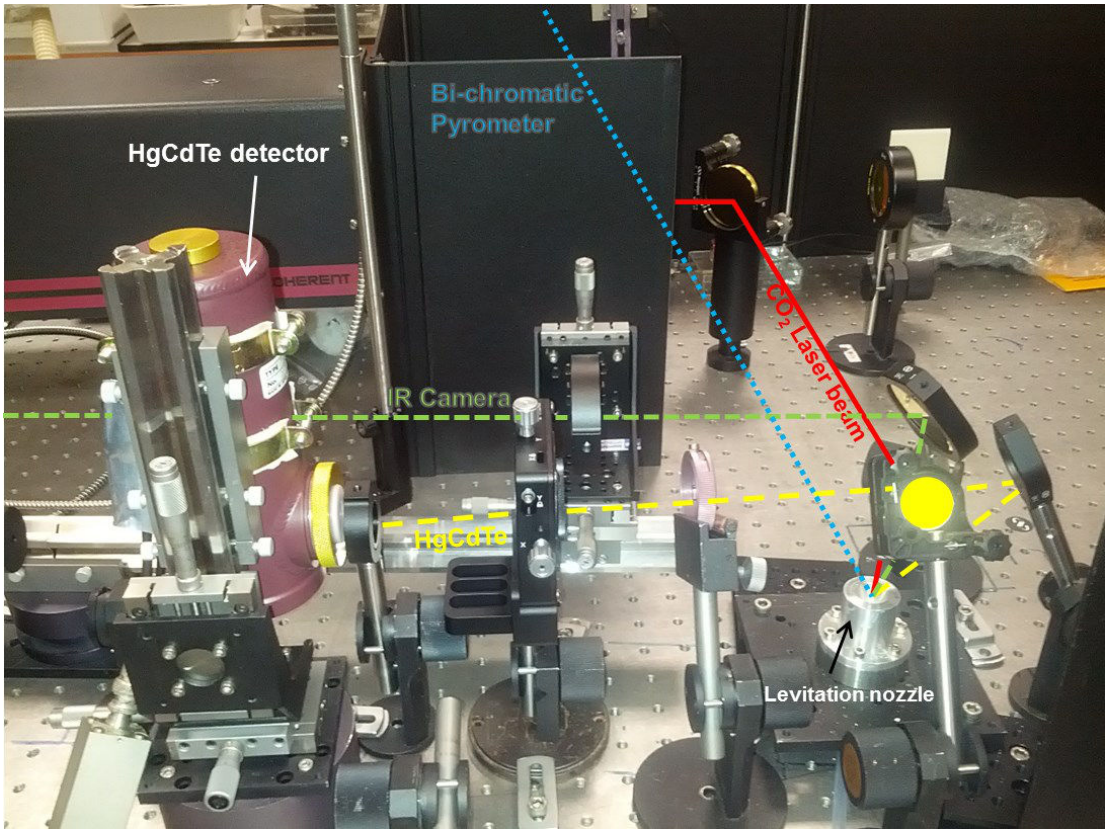

Figure 1: Picture of the ATTILHA setup in aerodynamic levitation configuration

The HgCdTe detector, the bi-chromatic pyrometer and the infrared camera acquisitions are synchronised by an external trigger. The sample levitates in a stream of gas out of an aluminium levitation nozzle (Figure 1).

It has been observed that levitation close to the output of the aluminium nozzle leads to a more controllable levitation. In principle, any gas can be used for the levitation. In the present work, compressed air, Ar (Messer purity 99.9999%) and Ar-20% O_2 (Messer) were used depending on the nature of the investigated sample. The pressure and the gas flow can be tuned. During experiments, as soon as the sample becomes liquid, its thermo-physical properties (density, surface tension, viscosity) change. The adjustable parameters allow re-establishing a stable levitation.

In the following a detailed description of the optical instrumentation for the temperature monitoring is given.

6.1.1 Bi-chromatic pyrometer

In the case of using a monochromatic pyrometer, as illustrated in Chapter 3, the knowledge of the transmission optical path between the sample and the pyrometer is needed to obtain the radiance temperature. Furthermore, the emissivity of the sample must be known to convert the radiance temperature into true temperature.

A bi-chromatic pyrometer is the combination of two detectors working at two different wavelengths. It indicates the ratio of the spectral radiances from a radiating object within two distinct but close wavelengths λ. The ratio R can be written, using Wien's law (see Appendix A) as [1]:

$$R = \frac{L_\lambda(\lambda_1, T)}{L_\lambda(\lambda_2, T)} = \frac{\varepsilon(\lambda_1)\lambda_1^{-5}\exp\left(-\frac{c_2}{\lambda_1 T}\right)}{\varepsilon(\lambda_2)\lambda_2^{-5}\exp\left(-\frac{c_2}{\lambda_2 T}\right)} = \frac{\varepsilon(\lambda_1)}{\varepsilon(\lambda_2)}\left(\frac{\lambda_1}{\lambda_2}\right)^{-5}\exp\left[\frac{c_2}{T}\left(\frac{1}{\lambda_1}-\frac{1}{\lambda_2}\right)\right] \quad (1)$$

where L_λ is the spectral radiance, $\varepsilon(\lambda)$ is the emissivity and c_2=14388 μm·K.

The pyrometer is calibrated by the constructor against a blackbody and measures the same value R when the blackbody temperature is T_r, the ratio temperature:

$$R = \left(\frac{\lambda_1}{\lambda_2}\right)^{-5}\exp\left[\frac{c_2}{T_r}\left(\frac{1}{\lambda_1}-\frac{1}{\lambda_2}\right)\right] \quad (2)$$

Since the ratios in Equations (1) and (2) have the same values, they can be rearranged as:

$$\frac{1}{T} = \frac{1}{T_r} + \frac{\ln\left(\frac{\varepsilon(\lambda_1)}{\varepsilon(\lambda_2)}\right)}{c_2\left(\frac{1}{\lambda_1}-\frac{1}{\lambda_2}\right)} \quad (3)$$

If the measured object is a perfect grey body ($\varepsilon(\lambda_1) = \varepsilon(\lambda_2)$), the temperature of the object is equal to the ratio temperature.

In practice, the observed objects are not perfect grey-bodies. The factor $\ln\left(\frac{\varepsilon(\lambda_1)}{\varepsilon(\lambda_2)}\right)$ must be known. The choice of the two wavelengths is the results of a compromise. The smaller the difference between the two wavelengths, the greater is the sensitivity of the pyrometer, but the precision on the temperature ratio will be less accurate. In fact, if the temperature is not sufficiently high (normally T must be higher than 773 K), the ratio results to be too small. On the other hand, if the two wavelengths are far apart, the ratio is well defined but the grey body assumption must be applied carefully.

Bi-chromatic pyrometers are insensitive to field of view conditions. If the observed sample is thermally heterogeneous, we can assume that the obtained temperature corresponds to the hottest spot of the sample that is the most radiant spot [2].

For the present application, a Lumasence IMPAC ISR 12-LO bi-chromatic pyrometer was used. The range of temperature of measurement is 1273 K-3273 K, and the two selected wavelengths are 0.8 μm and 1.05 μm (Silicon detector).

6.1.2 HgCdTe detector

The HgCdTe is a photoconductive detector whose electrical resistance lowers when exposed to infrared light. HgCdTe detectors are capable to detect infrared radiation in a wide range of wavelengths depending on the chemical composition of the significant semi-conductor. In the present case a Hamamatsu P5274-01 significant from 2 µm to 22 µm has been used. The response of the detector as a function of the wavelength is reported in Figure 2. In order to reduce the noise due to thermal induced currents, the detector must be cooled with liquid N_2 at about 77 K.

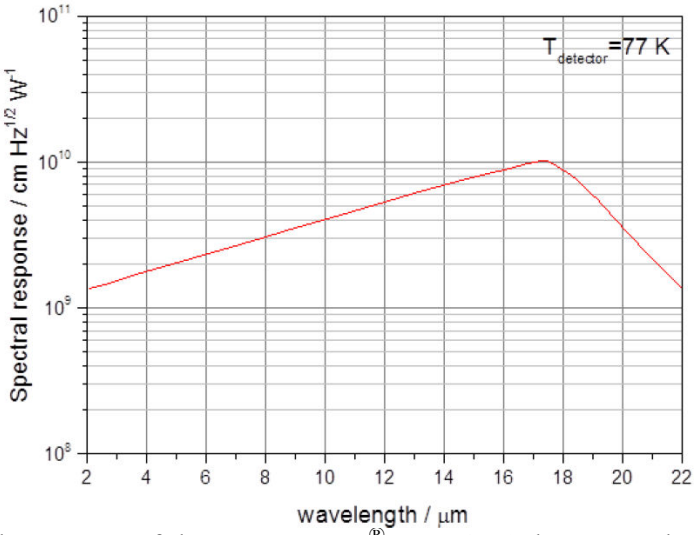

Figure 2: Spectral response of the Hamamatsu® P5274-01 detector. The reported curve is valid if the captor is kept at T=77 K

The drop in the detector resistance produces a current that is converted into a tension analogic signal (output in V) by a pre-amplifier. An optical chopper is placed between the HgCdTe detector and the sample in order to modulate the radiant signal from the hot source. The output signals from the HgCdTe detector and from the chopper are sent to a Stanford Research® SR530 lock-in amplifier to improve the signal/noise ratio. The synchronised output from the lock-in amplifier is finally sent to a National Instrument® NI cDAQ-9178 that allows the direct connection between the acquisition path and a LabView® application.

By interposing narrow interferential filters between the detector and the sample, it is possible to select specific wavelengths at which the HgCdTe detector would work. The filter must be placed as close as possible to the captor to limit parasitic contribution from the environment at different wavelengths. The interferential filters are provided by Northumbria Optical Coatings Ltd (Table 1).

	1 µm	2 µm	3 µm	4 µm	5 µm	6 µm	7 µm	8 µm	9 µm	10 µm	12 µm
λ (µm)	1	2	3	4	5	6	7	8	9	10	12.214
BW (nm)	<100	<100	<100	<100	<100	<100	<100	<100	<100	<100	<100

Table 1: Interferential filters. BW=Band width

The HgCdTe detector has been calibrated at 10 µm and 12.214 µm with the procedure described in Appendix F. The calibration curves obtained at 10 µm and 12.214 µm are reported in Figure 3 a-b.

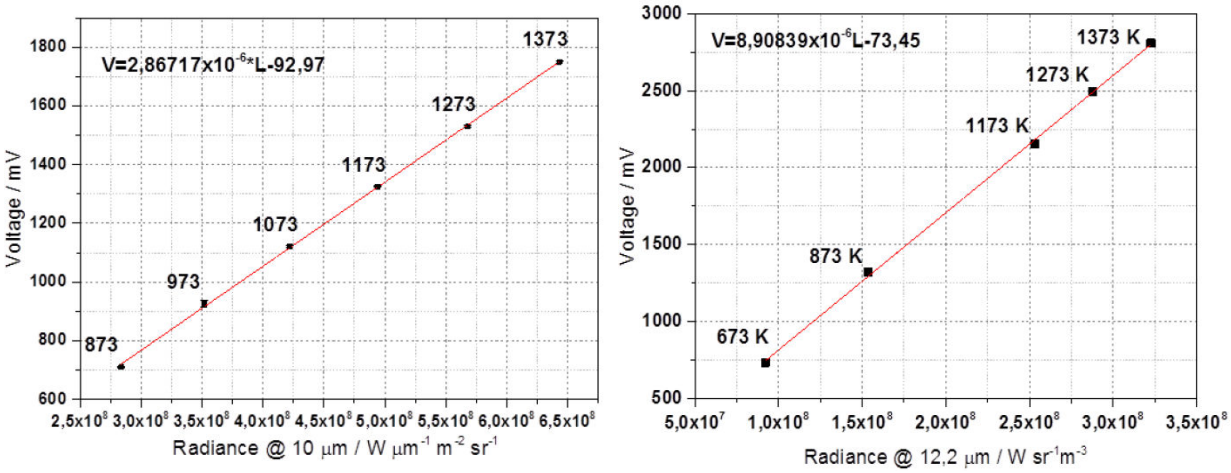

(a) (b)

Figure 3: Calibration curves for the HgCdTe detector. (a) 10 µm; (b) 12.2 µm

Using a quadratic approximation for the spectral radiance (Appendix F) and the definition of radiance temperature (Appendix A), the true temperature can be derived:

$$a+bT+cT^2=\frac{a+bT_\lambda+cT_\lambda^2}{\varepsilon(\lambda,T)}=L_{\lambda,b} \quad \Rightarrow \quad T=\frac{-b\pm\sqrt{b^2-4c(a-L_{\lambda,b})}}{2c} \tag{4}$$

where $\varepsilon(\lambda,T)$ is the emissivity of the observed object.

In order to quantify the propagation of the errors in the estimated true temperature, a rigorous error analysis has been performed in collaboration with F. Gamboa (IMT, Institut de Mathématiques de Toulouse). The detailed description of the mathematical formalism is given in Appendix F.

The main sources of error are the following:

- Bias due to the approximation of the Planck distribution between 1000 K and 3000 K with a quadratic function;
- Determination of the slope and the offset, A and B, in the linear relation between the HgCdTe output and the radiance (see Section 6.3);
- Estimation of the emissivity of the investigated sample.

Considering the most conservative case, with probability 0.95^2=0.9025, the true temperature lies within the range:

$$T\in\left[\hat{T}-\frac{K_2}{K_1}(e'+2\sigma)-2\frac{K_3}{K_1}\sigma_\varepsilon,\hat{T}+\frac{K_2}{K_1}(e'+2\sigma)+2\frac{K_3}{K_1}\sigma_\varepsilon\right]. \tag{5}$$

See Appendix F for the values of parameters in Equation 5.

For example, the true temperature of a sample with an estimated emissivity 0.9±0.045 and an estimated radiance temperature of 2000 K is 2158±98 K with a probability of 0.9025. It must be pointed out that 86 % of the reported error bar is due to the estimated emissivity.

6.1.3 Infrared Camera

An infrared camera is a device that converts an incoming infrared radiation coming from an infrared scene into a 2D image. The measure of temperature using this instrument is based on the same concepts used by optical pyrometry.

In this work a FLIR® SC7500 infrared camera has been used. The sensitivity of the InSb detector extends between 1.5 µm and 5.8 µm. The rectangular captor has dimensions 7.68x9.60 mm, which corresponds to a 2D image of 256x320 pixels (pitch=30 µm). Two types of objectives can be used. The technical details are reported in Table 2.

	MW50mm	MW G1 F/3.0
Spectral band / µm	3.5-5±0.25	3.7-5.15
Focal / mm	50±0.5	/
F/number	2±5 %	3±10 %
HFOV	10.97 (320x256 pixels, pitch 30 µm)	9.60 (320x256 pixels, pitch 30 µm)
VFOV	8.24 (320x256 pixels, pitch 30 µm)	7.68 (320x256 pixels, pitch 30 µm)
Transmission	>94 %	>70 %
Focus range	1.5 m to infinity	300±0.15 mm

Table 2: Technical specification of the two objectives. HFOV=Horizontal Field of View; VFOV=Vertical Field of View

The observed sample is considered as a grey body in the significant spectral range of the camera. As for the HgCdTe detector, the signal of the infrared camera *S(T)* is linear towards the measured spectral radiance *R(T)*:

$$S(T) = k \cdot R_{mesured}(T) \tag{6}$$

This signal is converted in a 14 bits digital value, named Digital Level (DL). In the processing of the signal, the final output is proportional to the measured spectral radiance *R(T)*.

In reality the camera response *S* is also a function of wavelength *S(λ)*. The sensibility of the InSb captor and the transmittance of the objective are dependent towards wavelength.

To avoid the saturation of the captor and optimise its dynamic range (i.e., the measurable range of temperature), a high-pass/low-pass filter centred at 3.99 µm is placed between the captor and the objective. This filter imposes a monochromatic measurement.

6.1.3.1 Calibration of the Infrared camera

The measured spectral radiance *R(T)*, the signal of the camera *S(T)* and finally the digital level *DL(T)* are function of temperature. A calibration is needed to express the response of the infrared camera as a function of the spectral radiance. The infrared camera is calibrated against a hot source of which the emissivity is known. The calibration curve allows to obtain a direct correspondence between the *DL(T)* and the temperature of the observed scene. The integration time of the camera can be adjusted to adapt the low value of the dynamic range and to avoid saturation.

The infrared camera was calibrated by the manufacturer (i.e., FLIR®) against different blackbodies to cover three ranges of temperature. The calibration certificates were delivered with the camera. Table 3 summarises the calibration curves performed by FLIR®.

Calibration file	Temperature range	Objective	Integration time
50mm_300-1500 °C	300-1500 °C	50 mm	15-300 µm
50mm_1500-2500 °C	1500-2500 °C	50 mm	15-300 µm
G1_300-1500 °C	300-1500 °C	G1	15-300 µm

Table 3: Calibration file delivered by FLIR.

Each calibration file contains different curves which link *DL(T)*, temperature and integration time. The smaller the integration time, the larger is the temperature range, but the poorer the sensitivity of the camera. An example of the calibration curve by FLIR *DL(T)* vs. *T* for different integration time is reported in Figure 4.

The linearity of the camera response is valid only in the region 20 % - 80 % of the maximum *DL(T)* ($DL_{max}=2^{14}=16384$).

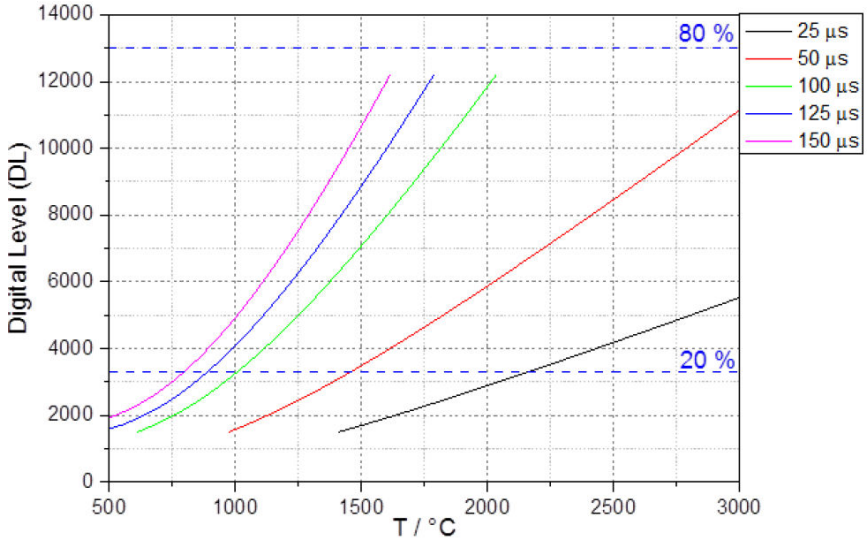

Figure 4: Response of the infrared camera expressed in Digital Level (DL) as a function of the blackbody temperature and for different integration time (25 µs, 50 µs, 100 µs, 125 µs and 150 µs). This calibration was delivered by FLIR®. The blue dotted lines represent the range of validity of the calibration, which corresponds to 20 % and 80 % of the maximum DL output of the infrared camera, respectively

The quality of the calibration curve has been checked at the laboratory using the HGH® RCN 1200 N1 blackbody (Appendix F). The camera was placed against the blackbody between 873 K and 1273 K. The camera outputs are consistent with the blackbody temperature (Table 4). The relative uncertainty on the temperature measured by the camera is ±1 % above 373 K.

Blackbody temperature / K	Camera output / K
873	872.28
973	974.12
1073	1074.73
1173	1175.43
1273	1274.87

Table 4: Acquisition performed with the thermal infrared camera on a qualified laboratory blackbody

6.1.3.2 Infrared images processing

The interest in using an infrared camera is the possibility to have simultaneously temperature monitoring and spatial information on the observed phenomena. Further information on the optical properties of the observed surface can be deduced by considering the temperature measurement of the HgCdTe detector. In particular, the emissivity at 3.99 µm can be obtained coupling the infrared camera images and the output of the HgCdTe detector.

The camera considers the observed sample as a grey body. By default, the controlling software of the camera is set on an emissivity value ε=1. This is equivalent to consider the object as a blackbody. However, a real object has an emissivity lower than unity. Therefore, the temperature measurement obtained with the infrared camera corresponds to the radiance temperature (Appendix A).

For each infrared image recorded by the infrared camera, a synchronised acquisition of the true temperature is available from the HgCdTe detector (or from the bi-chromatic pyrometer, depending on the nature of the investigated sample). Using the direct correlation between temperature, integration time and *DL(T)* (i.e., the calibration curves provided by FLIR®), the temperature measured by the HgCdTe (T_{HgCdTe}) detector can be used to obtain the $DL(T_{HgCdTe})$ (Figure 5).

For a fixed integration time t_{int}, the digital level output $DL(T_{HgCdTe})$ is univocally deduced knowing the temperature T_{HgCdTe}. This value corresponds to the digital level which would have been measured by the infrared camera if the investigated object was a perfect blackbody.

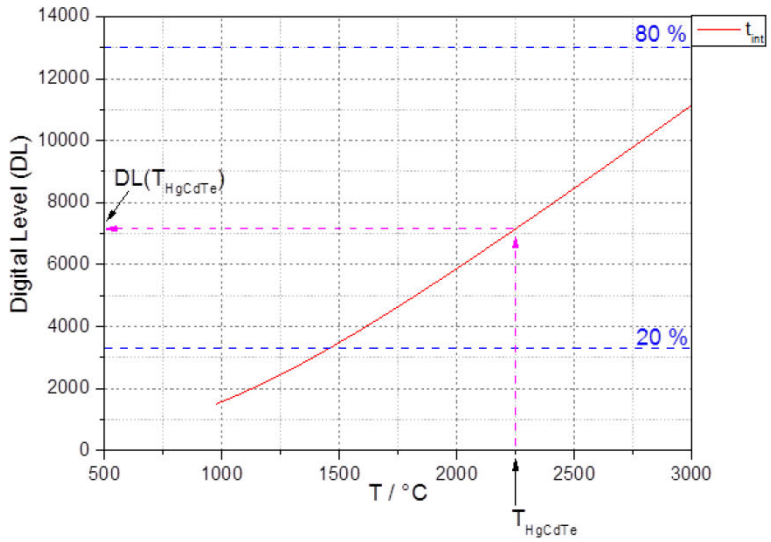

Figure 5: Derivation of the $DL(T_{HgCdTe})$ at a fixed integration time t_{int} and knowing T_{HgCdTe}

Considering the definition of radiance temperature, one can write:

$$L_{rs}(\lambda, T_\lambda) = \varepsilon(\lambda) L_b(\lambda, T) \tag{7}$$

where "rs" and "b" stay for "real surface" and "blackbody", respectively, T_λ is the radiance temperature and T the true temperature. In the same way, the digital level output of the camera can be expressed as:

$$DL_{measured} = \varepsilon(\lambda) DL(T_{HgCdTe}). \tag{8}$$

This expression allows to obtain the emissivity of the investigated sample at 3.99 µm:

$$\varepsilon(\lambda = 3.99\,\mu m) = \frac{DL_{measured}}{DL(T_{HgCdTe})} \tag{9}$$

This procedure is applied to all the infrared images recorded during a laser sequence. The automatic processing of the camera outputs is performed using a Python code developed during this thesis in collaboration with L. Risser and F. Gamboa (IMT). The main restriction for the use of the code is related to the available calibration curves provided by FLIR®. If true temperature measured by the HgCdTe detector (or the bi-chromatic pyrometer depending on the investigated sample) is outside the 20 %-80 % range of linearity of the calibration for all the available integration time the present method is not applicable (Figure 6). When using the G1 objective, the only available calibration file is defined up to 1500 °C, which is significantly lower than the expected melting temperature of the investigated mixture.

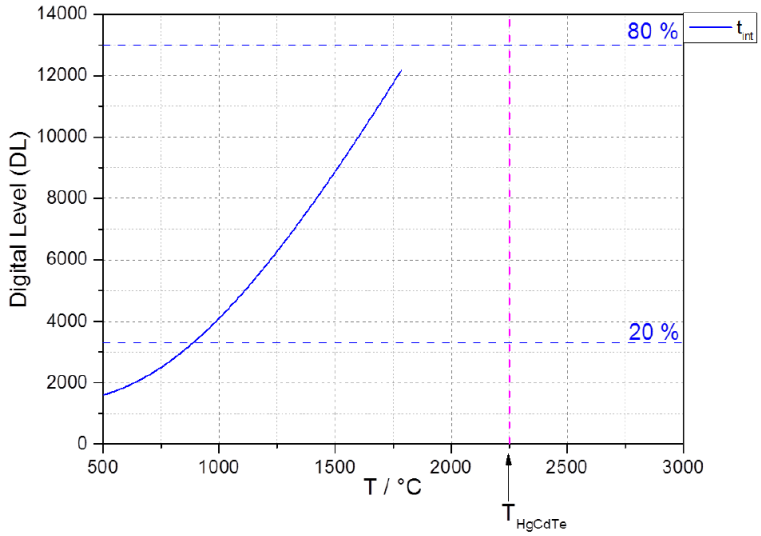

Figure 6: Practical case of non-applicability of the current image processing method. The blue line represent a calibration curve at t_{int}=25 µs valid for the G1 objective

6.2 Validation of the experimental setup

In the present work, the aerodynamic levitation configuration has been used to validate the experimental technique. In the future, the same procedure will be used for the containerless configuration.

A scheme of the experimental setup is reported in Figure 7.

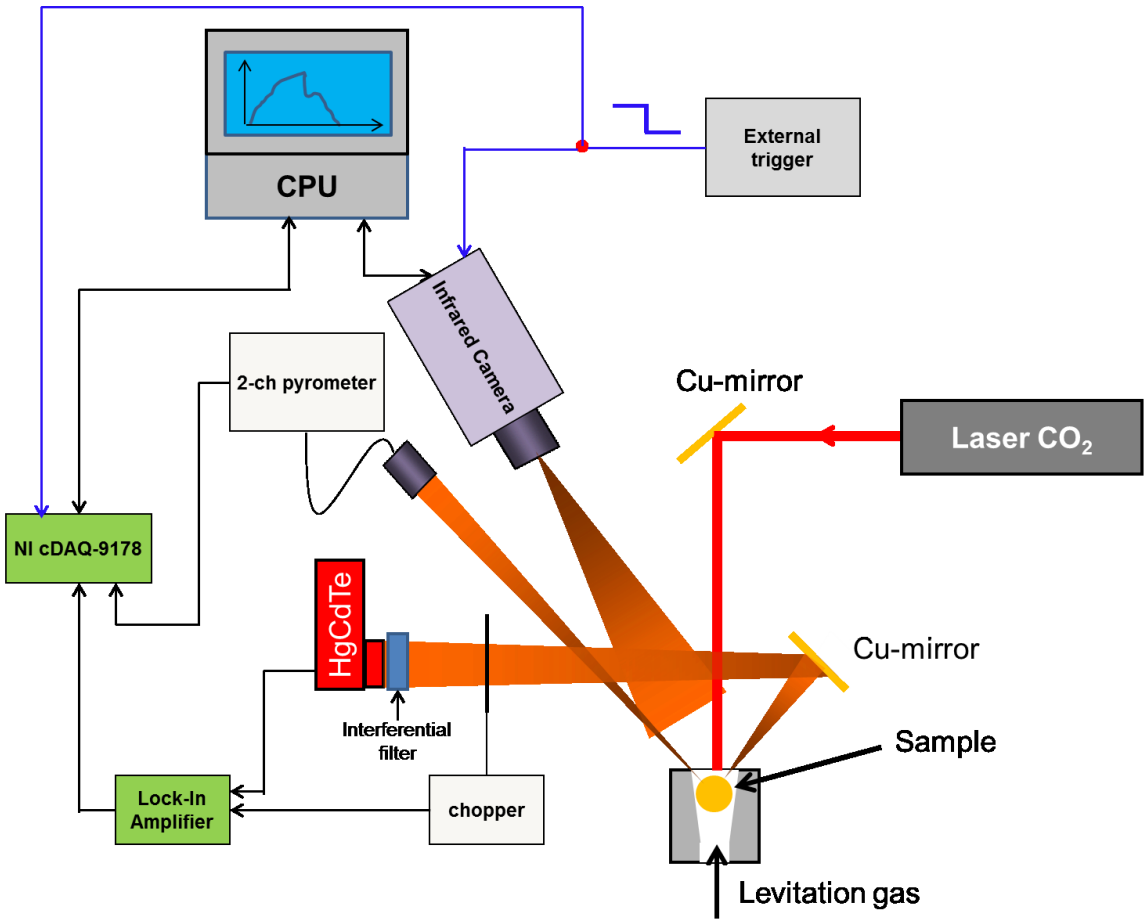

Figure 7: Schematic view of the ATTILHA setup in aerodynamic levitation configuration

The sample is placed inside the levitation nozzle. Once a stable levitation is obtained, the bi-chromatic pyrometer and the infrared camera are focused on the sample. The HgCdTe detector receives the radiative heat from the sample by means of a high-reflective mirror (reflectivity > 99.9 %). In order to focus the HgCdTe detector, the sample is heated using a low power laser pulse. The HgCdTe detector position is optimised using x-y-z stages to find the maximum of the output signal. The signal from the HgCdTe detector and the bi-chromatic pyrometer are collected by the NI cDAQ-9178 and sent to the computer. The infrared camera is directly connected with the computer. The acquisition is externally triggered by a square-wave generator.

The validity of the experimental setup has been tested on well-known chemical systems. In particular, Al_2O_3 and Al_2O_3-based oxide samples were used. Alumina is a refractory material. Its melting temperature as well as its optical properties has been widely studied in the past [3].

6.2.1 Al_2O_3

The melting temperature of alumina is 2328±5 K [3]. As reported in Appendix F, the Christiansen wavelength for alumina is around 10 µm. By interposing an interferential filter at 10 µm between the HgCdTe detector and the alumina samples, it is possible to obtain a direct measurement of the true temperature without passing through an emissivity correction.

The calibration curve in Figure 3 proves the linearity of the captor towards the radiance emitted by the blackbody. However, using that calibration for high temperature phenomena (T > 2000 K) can induce significant errors, since an extrapolation must be applied.

Using the aerodynamic levitation setup, a new calibration was performed measuring the temperature of a laser-heated sphere of Al_2O_3 levitating in air. During this calibration, the 10 µm interferential filter was placed between the HgCdTe detector and the levitating sample. Furthermore, an optical diaphragm was settled to avoid the saturation of the HgCdTe detector, and to stay in the same output range obtained with the low temperature calibration (Figure 3). In parallel, the bi-chromatic pyrometer was focused on the alumina sample. The laser heats the sample up to the liquid state. When the laser is switched off, the alumina sphere cooled down. The recorded signal output of the HgCdTe detector shows a thermal arrest; which corresponds to the solidification of the levitating sample. The synchronised output from the bi-chromatic pyrometer shows the same feature (Figure 8). The corresponding temperature of thermal arrest is 2323±25 K, confirming that the observed plateau reflects the solidification of the alumina sphere. Since the response of the HgCdTe detector is linear, a straight line can be drawn between the background signal and the value at the plateau signal.

As a consequence, a new calibration equation can be written. Considering the measured background of the output signal from the HgCdTe, U=0.026 V at 298 K, the new equation is:

$$U(L) = 1.04 \cdot 10^{-9} \cdot L(T) + 0.0168 \qquad (29)$$

where *U(L)* is the output HgCdTe detector and *L(T)* is the radiance at 10 µm.

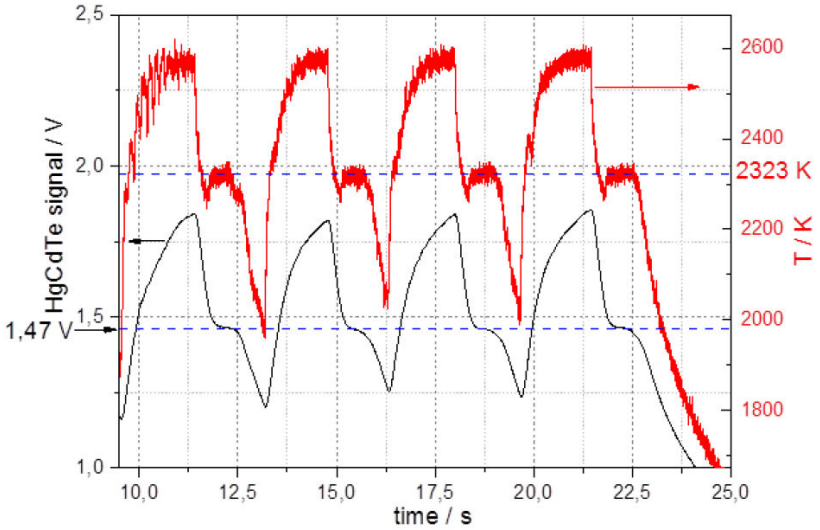

Figure 8: Sequence of four laser pulses on a levitating Al_2O_3 sample. The black line is the output signal from the HgCdTe (left layer), whilst the red line represents the temperature measured by the bi-chromatic pyrometer (right layer).

It must be pointed out that the calibration above is valid only using the present optical configuration. In order to minimise uncontrolled errors due to external phenomena, such as variations of the alignment or response of the HgCdTe detector and laboratory temperatures, this procedure is repeated at the beginning of each run.

Using the procedure described in Section 6.1.3.2 it is possible to estimate the variation of the emissivity of the levitating sample as a function of time and temperature at 3.99 µm. Figure 9 reports the evolution of the emissivity of an alumina sample during solidification.

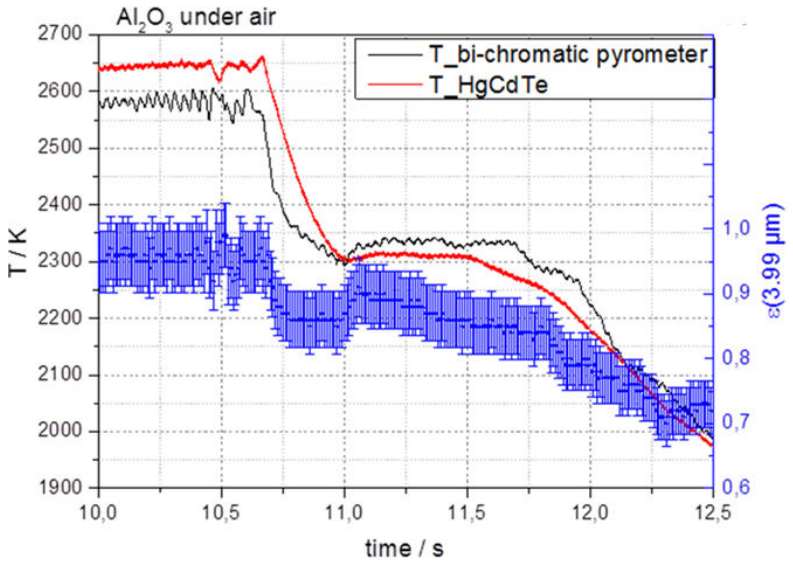

Figure 9: Evolution of the emissivity of an Al_2O_3 levitating sample during solidification (blue points, right layer). An estimated uncertainty of ±5 % has been reported. The black and red lines represent the bi-chromatic pyrometer and the HgCdTe signals, respectively (left layer)

The reported diagram has been obtained using the calibration file 50mm_1500-2500°C (Table 3). The emissivity seems to be constant when the sample is liquid. The calculated value of 0.95±0.05 is in good agreement with Sarou-Kanian et al [4]. In correspondence of the thermal arrest, both liquid and solid phases are present. In these conditions, Sarou-Kanian et al. recommended a constant emissivity of 0.75. In the present case, the emissivity varies from 0.9 to 0.85. This observation is in good agreement with Petrov & Vorobyev who reported a variation between 0.89 and 0.86 [5]. After the thermal arrest, the solid sample continues its natural cooling.

Figures 10-11 show that even if the objective G1 could not be used to estimate the emissivity of the sample, the melting and solidification processes can be clearly followed.

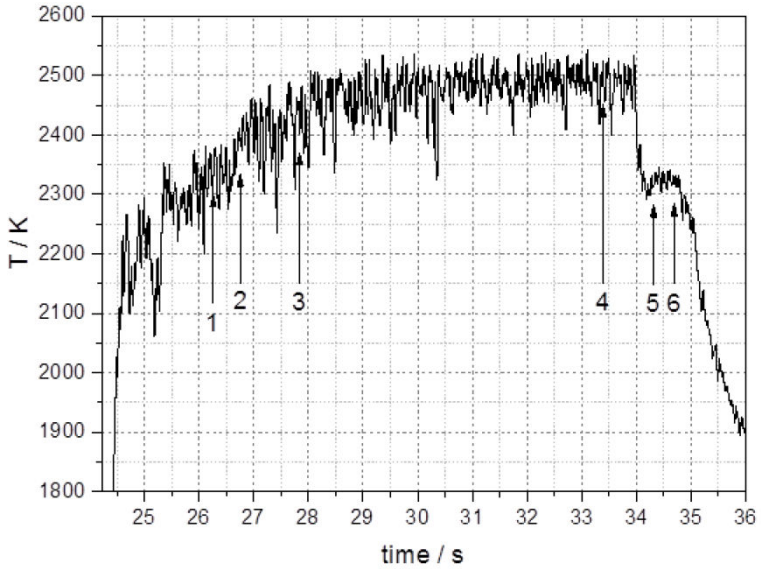

Figure 10: Thermogram obtained on an Al_2O_3 sample. The label on the diagram correspond to the synchronised infrared images in Figure 11

Figure 11 shows six frames recorded by the rapid infrared camera during the melting/solidification cycle in reported in Figure 10. The first liquid is formed in correspondence of the zone where the laser beam impinges on the sample surface (1). The

energy provided by the laser allows the liquid fraction rise (2-3) until the entire sample becomes liquid (4). When the laser is switched off, the levitated sample starts to cool, and at the thermal arrest temperature, the first germs of solid form (5). At the end of the thermal arrest, the latent heat of solidification has been entirely released, and the sample is now completely solid (6).

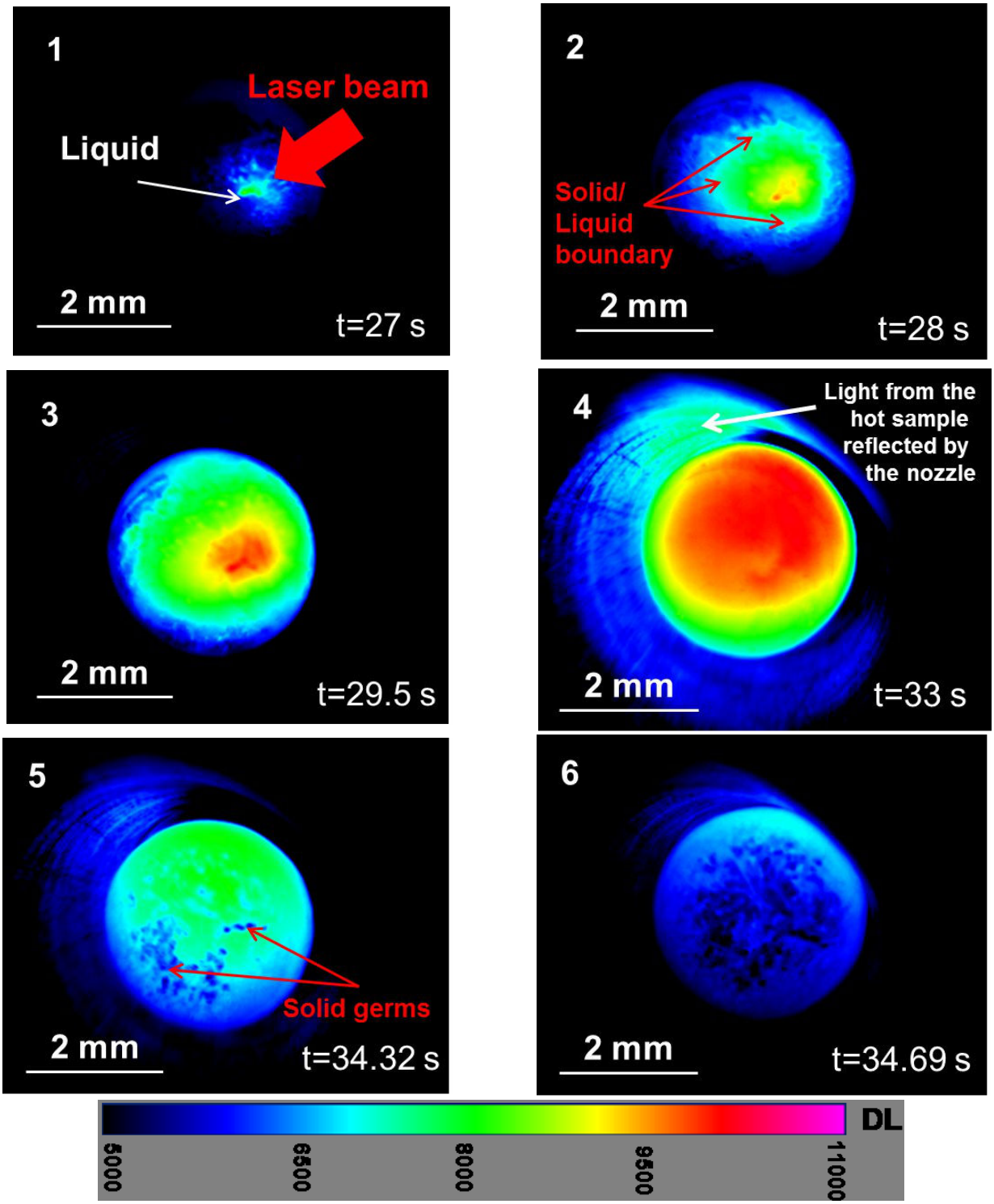

Figure 11: Synchronised infrared images recorded during the melting/solidification cycle in Figure 10 (integration time = 40 µs, acquisition rate = 200 Hz). (1) Liquid firstly forms where the laser beam impinges on the sample; (2) and (3) the liquid fraction grows; (4) the upper side of the sample is liquid; (5) the first germs of solid form at the thermal arrest; (6) the sample surface is almost completely solidified

6.2.2 Al_2O_3-ZrO_2

The calculated Al_2O_3-ZrO_2 pseudo-binary system (Figure 12) presents a eutectic temperature at 2165 K and a composition of 29 mol% ZrO_2.

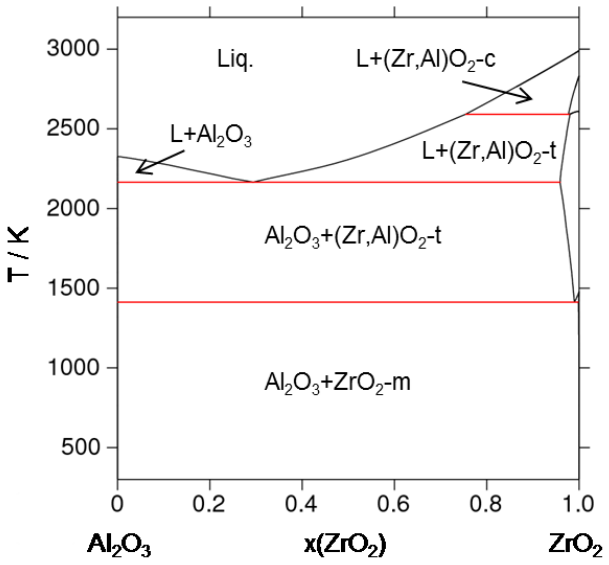

Figure 12: Calculated Al_2O_3-ZrO_2 phase diagram [6]

Two samples with 11 and 55 mol% ZrO_2 have been fabricated mixing pure Al_2O_3 and ZrO_2 (Table 5). The fabrication was performed placing the starting materials at the bottom of the levitation nozzle, with a reduced gas flow. The laser was then focused onto the pure oxides. When a spherical sample was obtained, a check on the mass loss was performed. To ensure the chemical homogeneity of the sample, this procedure was repeated at least three times after the formation of the drop-shaped sample.

Sample	mol% ZrO_2	Initial mass / g	Mass after laser experiments / g
Al_2O_3	0	0.1923	0.1919
A89Z11	11	0.2033	0.2033
A45Z55	55	0.1997	0.1994

Table 5: Molar composition of the Al_2O_3-ZrO_2 samples investigated using the ATTILHA setup in the aerodynamic levitation configuration. After the experiments, a negligible mass loss was observed

The drop-shaped sample is placed in the levitation nozzle in a stream of air. The sample is then heated by the CO_2-laser. Three to four consecutive laser pulses impinge on the sample. As for the laser heating experiments reported in Chapter 3, the solidification temperature of the sample is recorded on the cooling flank of the thermogram. The synchronised signal from the bi-chromatic pyrometer and the HgCdTe detector are collected and sent to the LabView® application. The interferential filter centred at 10 µm was settled between the HgCdTe detector and the sample. Results on sample A89Z11 are shown in Figure 13.

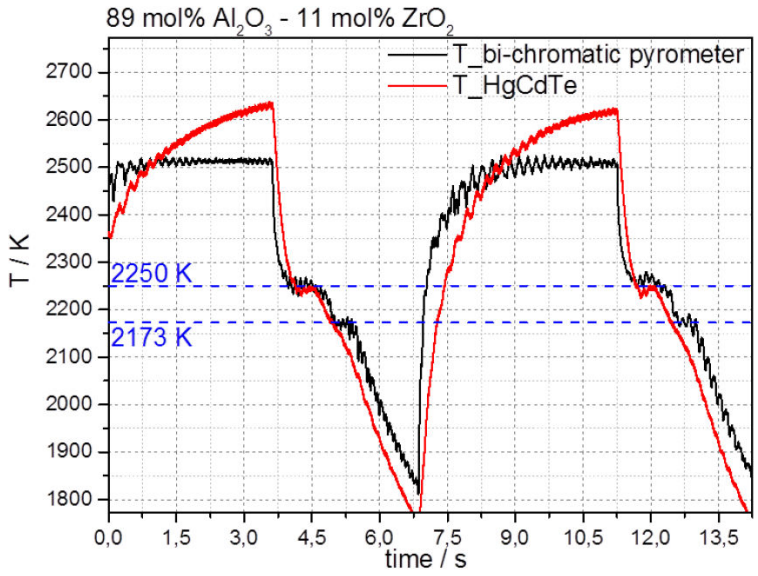

Figure 13: Comparison between bi-chromatic pyrometer and HgCdTe results on a sequence of two laser pulses

The HgCdTe signal was corrected to take into account the emissivity of the sample. In particular, a linear combination between the emissivity of Al_2O_3 (ε=1) and ZrO_2 (ε=0.95 [7]) at 10 µm is considered:

$$\varepsilon = 0.89\,\varepsilon(Al_2O_3) + 0.11\,\varepsilon(ZrO_2) = 0.995\,. \qquad (30)$$

Two thermal arrests are visible on the cooling flank recorded by the bi-chromatic pyrometer, whilst the HgCdTe detector recorded only one inflection (2250±96 K). The inflection at higher temperature corresponds to the liquidus transition. The measured value is in agreement with the literature data and the calculated phase diagram (Figure 12). The second inflection recorded by the bi-chromatic pyrometer is the eutectic transition, again in good agreement with the literature.

On the heating flank, the temperature measured by the HgCdTe detector and the pyrometer differs significantly. The pyrometer recorded a constant temperature. The HgCdTe detector measured rising temperature until the laser was switched off. The HgCdTe detector and the pyrometer look at the same phenomenon but at different wavelengths. Figure 14 shows the emissivity of Al_2O_3 as a function of wavelength for different temperature.

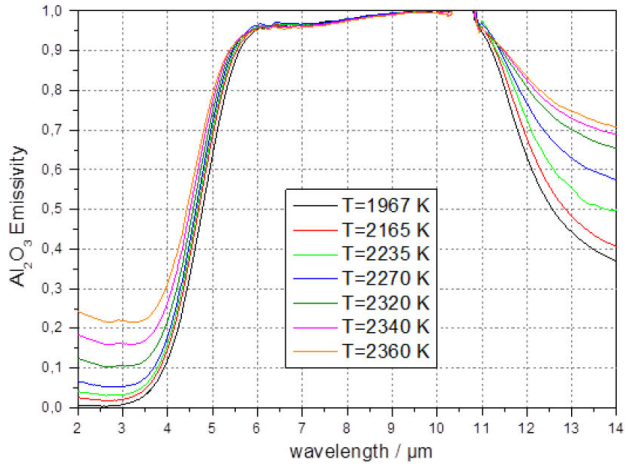

Figure 14: Normal spectral emissivity of Al_2O_3 (0.5 mm thick) as a function of wavelength [8]

At 10 µm, alumina and zirconia have an emissivity $\varepsilon > 0.97$. Therefore, the sample can be considered opaque. The HgCdTe detector, during the experiment, looks at the surface of the sample. The bi-chromatic pyrometer works between 0.8 and 1.05 µm. In this region, the sample is semi-transparent, that is its transmittance cannot be considered negligible. The optical properties of a semi-transparent material have a volumetric meaning [9]. Actually, the bi-chromatic pyrometer integrates the radiant flux coming from the surface as well as from a certain amount of the liquid sample underneath. In these conditions, the temperature measurement of the bi-chromatic pyrometer cannot be considered as only representative of the surface conditions, but as the combination of both surface and bulk contributions. In conclusion, the pyrometer measures also a colder zone inside the sample, which is not directly heated by the CO_2 laser beam. However, as soon as the laser is switched off, the sample cools and the first nuclei of solid phase start to appear at the liquidus temperature. The bi-chromatic pyrometer recorded a thermal arrest in correspondence of the liquidus transition as well as the eutectic transition, meaning that the semi-transparency of the sample did not affected the recording of these phenomena.

It may be noted that on the thermograms recorded on sample A45Z55 only one thermal arrest is visible (Figure 15).

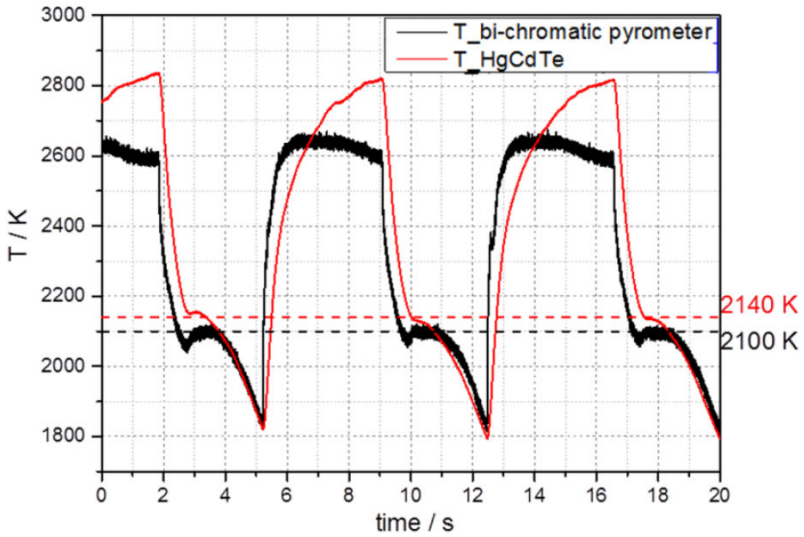

Figure 15: Sequence of three laser pulses on sample A45Z55. The red line is the temperature measured by the HgCdTe detector corrected with an emissivity of 0.972 (see Equation 30). The black line is the signal from the bi-chromatic pyrometer

The composition of the sample is close to the eutectic composition (Figure 12). Since the amount of the eutectic composition is larger than in sample A89Z11, the thermal arrest associated to the liquidus transition is less pronounced. Therefore, the thermal arrest associated to the liquidus transition is recorded only on the cooling flank of sample A89Z11. The temperatures of the thermal arrest recorded by the HgCdTe detector (2140±117 K) and the bi-chromatic pyrometer differ by 40 K. This deviation is observed in all the three reported cooling flanks. The repeatability of this phenomenon suggests that the bi-chromatic pyrometer deviation may be due to the combination of several factors:

- the high sensitivity of the estimated temperature towards the emissivity correction applied to the HgCdTe signal,
- the semi-transparent optical properties of the liquid sample in the spectral range of the bi-chromatic pyrometer,
- the possible misalignment of the optical path between the sample and the HgCdTe detector.

In parallel, the rapid infrared camera recorded the sample undergoing the same laser pulse sequence. The melting and solidification behaviour of the sample is observed. Thanks to the procedure described in Section 6.1.3.2 it is possible to follow the evolution of the emissivity of the sample. Figure 16 reports the evolution of the emissivity of sample A89Z11 during a melting/solidification cycle (first cycle in Figure 13).

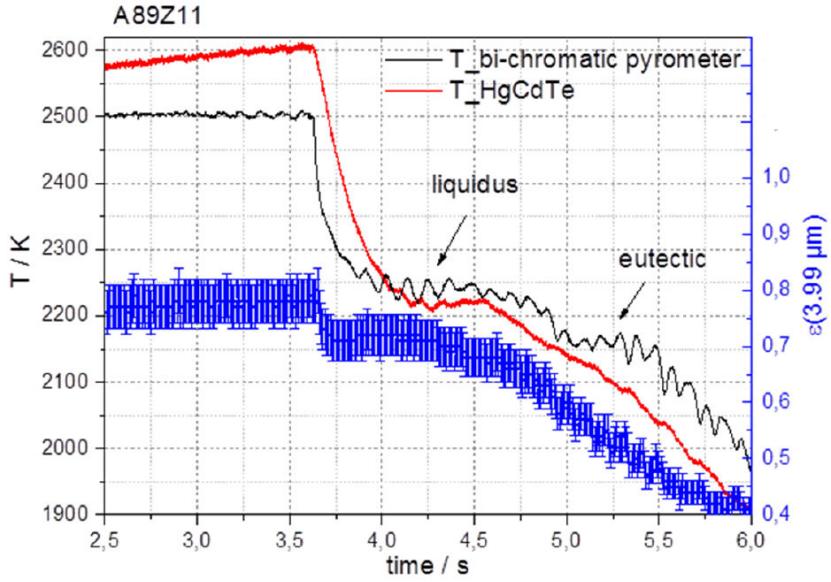

Figure 16: Evolution of the emissivity at 3.99 µm of sample A89Z11 during the first heating/cooling cycle in Figure 13 (blue points, right layer). The black and the red line are the thermograms recorded by the bi-chromatic pyrometer and the HgCdTe detector, respectively

The calculated emissivity of sample A89Z11 in the liquid state is constant, and equal to 0.78±0.04. When the laser is switched off, the temperature decreases (black and red line in Figure 13) as well as the emissivity (blue points). In correspondence of the first thermal arrest recorded by the bi-chromatic pyrometer and the HgCdTe detector, the emissivity stabilises at 0.72±0.04. However, as observed in Figure 9, the calculated emissivity tends to decrease during the thermal arrest. This is related to the rising quantity of solid present forming during the liquidus transition. At the second thermal arrest recorded by the bi-chromatic pyrometer, no evident variation of the emissivity can be noted. In general, the calculated emissivity for sample A89Z11 is lower than that calculated for pure Al_2O_3, meaning that the addition of ZrO_2 to the sample causes a decrease in the emissivity. This is also confirmed by the analysis performed on a melting/solidification cycle of sample A45Z55 (Figure 17).

Figure 17 shows that the addition of ZrO_2 leads to the decreases of the emissivity in the liquid state instead of staying constant as for pure Al_2O_3 and sample A89Z11. On the heating flank of the thermogram recorded by the pyrometer, the liquidus transition can be noted (T=2372±24 K). In its correspondence, the calculated emissivity displays a sharp variation. When the laser is switched off, the calculated emissivity sharply decreases reaching a minimum at 0.67 ± 0.03. Then the emissivity starts again to rise probably because of the presence of the undercooled liquid. During the eutectic thermal arrest, the emissivity initially stabilises at 0.62±0.03 and then decreases. Thank to this approach it is possible to follow the evolution of the emissivity of the investigated sample.

The next step of the development of the ATTILHA setup will be the extension of the calibration range of the objective G1 in order to have simultaneously emissivity estimation and a good spatial resolution as shown in Figure 11.

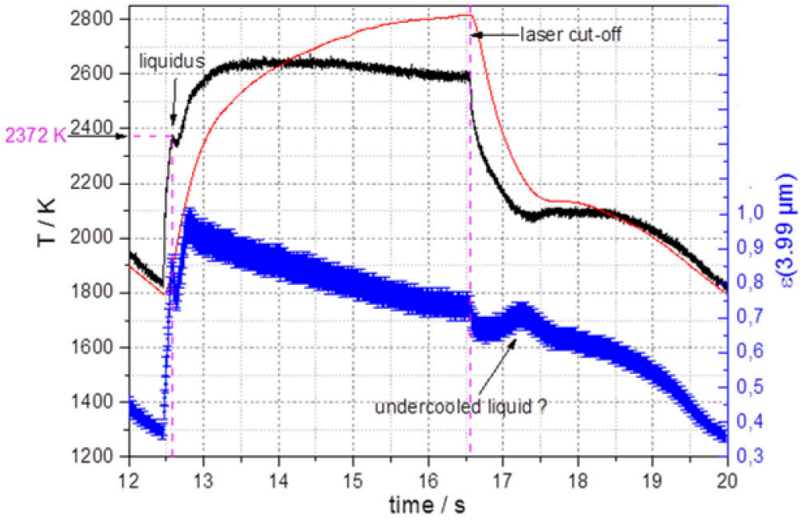

Figure 17: Evolution of the calculated emissivity of sample A45Z55 during the third heating/cooling cycle in Figure 15 (blue points). The black and the red lines represent the thermograms recorded by the bi-chromatic pyrometer and the HgCdTe detector, respectively (left layer)

Despite the good agreement between the thermal arrest recorded by the bi-chromatic pyrometer at 2372 K during the liquidus transition (Figure 17) and the calculated phase diagram in Figure 12, this measured temperature was not retained. The shape of pyrometer temperature profile for liquid samples does not follow the classical exponential rise; the more physical HgCdTe temperature profile was always preferred. The discrepancy between both infrared devices can be attributed to the distinct semi-transparent or opaque optical properties of the liquid in the spectral range of the bi-chromatic pyrometer (0.8 µm and 1.05 µm) and HgCdTe detector (10 µm), respectively.

After the laser heating experiments, the samples have been cut, polished and observed by SEM. The post-experiment analyses have been performed in collaboration with D. Bossu (cutting, polishing and preparation of the samples), and P. Bonnaillie and S. Poissonnet (SEM-EDS and WDS analyses). The comparison between the microstructure of samples A89Z11 and A45Z55 is reported in Figure 18.

The WDS results on the two samples are reported in Table 6.

	A89Z11		A45Z55	
	Eutectic	Dendrites	Eutectic	Dendrites
at% Al	31.0	40.0	30.0	2.0
at% Zr	7.0	/	7.0	34.0
at% O	62.0	60.0	63.0	64.0
Al/Zr	4.43	/	4.29	0.06

Table 6: WDS results on samples A89Z11 and A45Z55. Both the observed microstructure show a dendritic structure within a eutectic matrix

The dendrites observed in sample A89Z11 are pure Al_2O_3, confirming that alumina does not dissolve zirconia. The eutectic composition measured in the two samples is between 31 mol% ZrO_2 and 32 mol% ZrO_2, in good agreement with previous studies [6] and with the calculated Al_2O_3-ZrO_2 phase diagram (Figure 12). WDS results on the white dendrites observed in sample A45Z55 (Figure 18c-d) reveals a solubility of Al_2O_3 in ZrO_2 of about 3 mol% Al_2O_3.

The comparison between the current results and the calculated Al_2O_3-ZrO_2 phase diagram is reported in Figure 19.

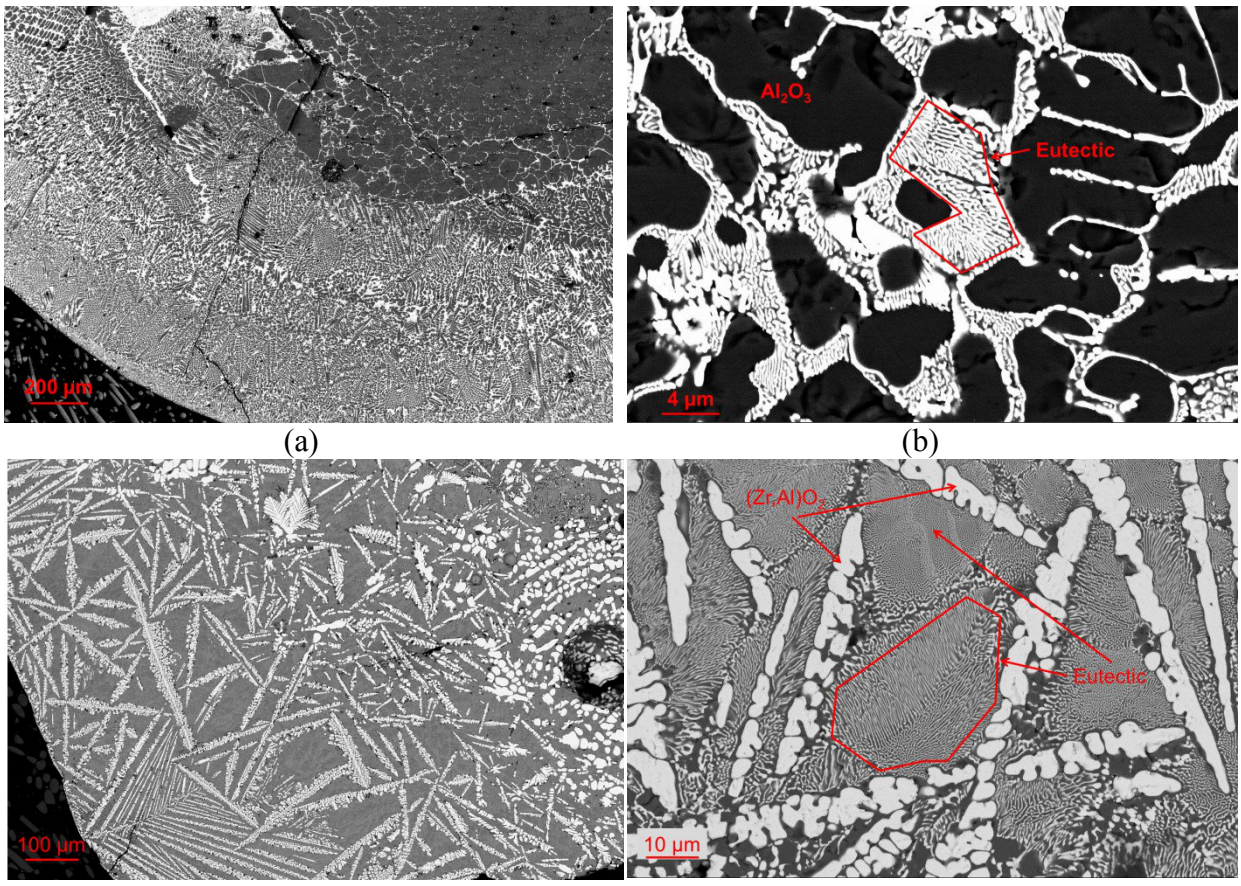

Figure 18: Comparison between the microstructure of sample A89Z11 (a-b) and sample A45Z55 (c-d)

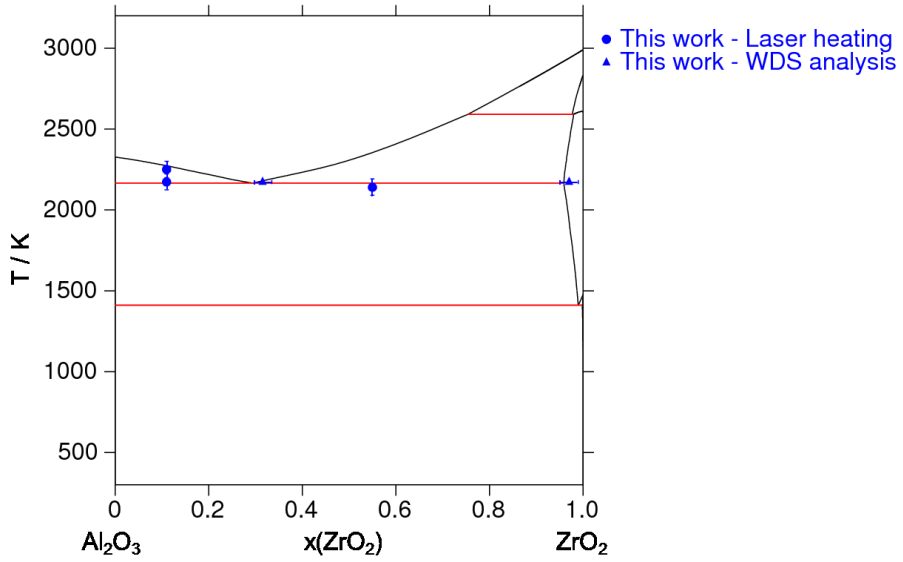

Figure 19: Comparison between current experimental results and calculated Al_2O_3-ZrO_2 phase diagram

6.2.3 Exploration of the miscibility gap in the liquid phase of the O-Fe-Zr system

The O-Fe-Zr ternary system exhibits a miscibility gap in the ternary liquid phase, as shown in Chapter 3. The extension of this immiscibility region is almost totally unknown. The ATTILHA setup allows to explore the extension of this miscibility gap. The starting material is an arc-melted Fe-Zr mixture. The initial composition of the investigated sample is reported in Table 7.

	w% Fe	w% Zr	at% Fe	at% Zr	m(Fe) / g	m(Zr) / g	m_{final} / g	Δm / g
FeZr_MG	81	19	87.6	12.4	0.1978	0.0457	0.2435	/

Table 7: Composition of the Fe-Zr sample

The sample was placed inside the levitation nozzle within a stream of Ar+20% O_2 to make it possible to oxidise the sample to enter into the high temperature liquid miscibility gap. The HgCdTe detector and the bi-chromatic pyrometer were focused on the levitated sample. However, since the emissivity of the sample is unknown at 10 µm, the output of the HgCdTe detector is the radiance temperature. The temperature provided by the bi-chromatic pyrometer is not fully representative since the factor $\ln\left(\frac{\varepsilon(\lambda_1)}{\varepsilon(\lambda_2)}\right)$ in Equation 3 can be considered neither equal to unity nor constant.

The sample underwent eight consecutive heating/cooling cycles. The thermograms recorded by the HgCdTe detector are reported in Figure 20.

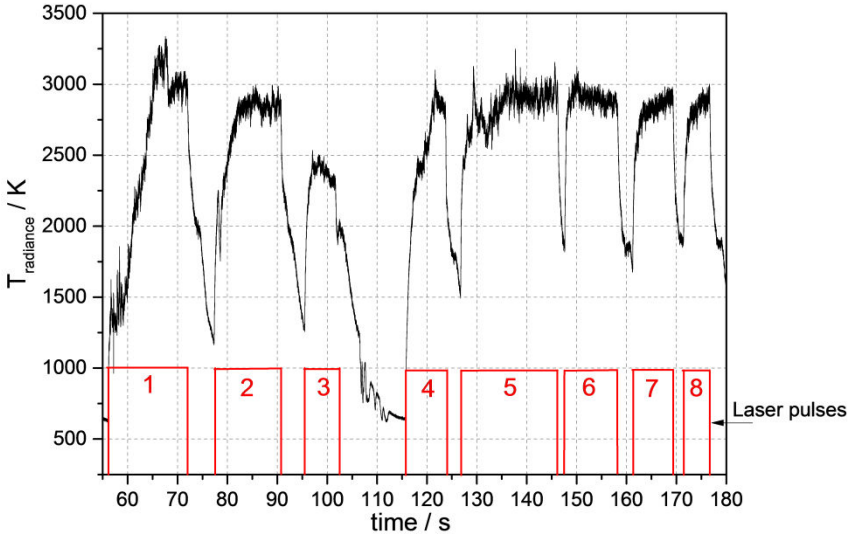

Figure 20: Eight-laser pulse sequence on sample FeZr_MG

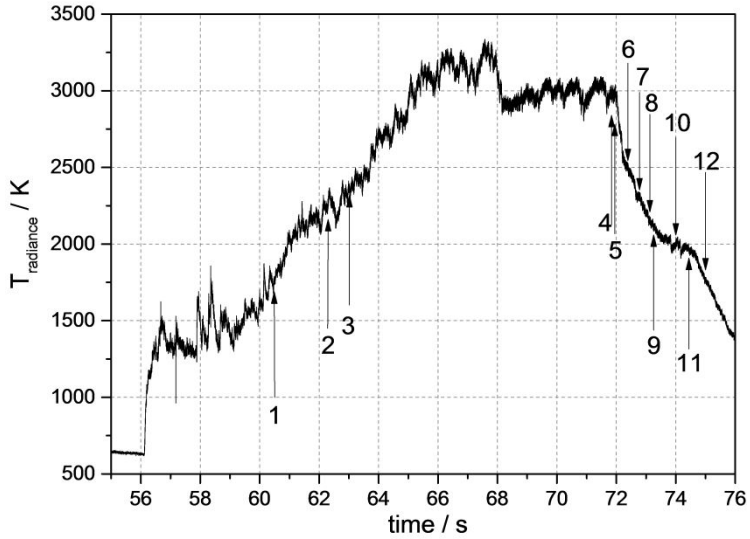

Figure 21: First laser pulse in Figure 20. The label on the thermograms correspond to the synchronised infrared images in Figure 22

Figure 21 and Figure 22 report the synchronised acquisition of the HgCdTe detector and the infrared camera during the first laser pulse in Figure 20.

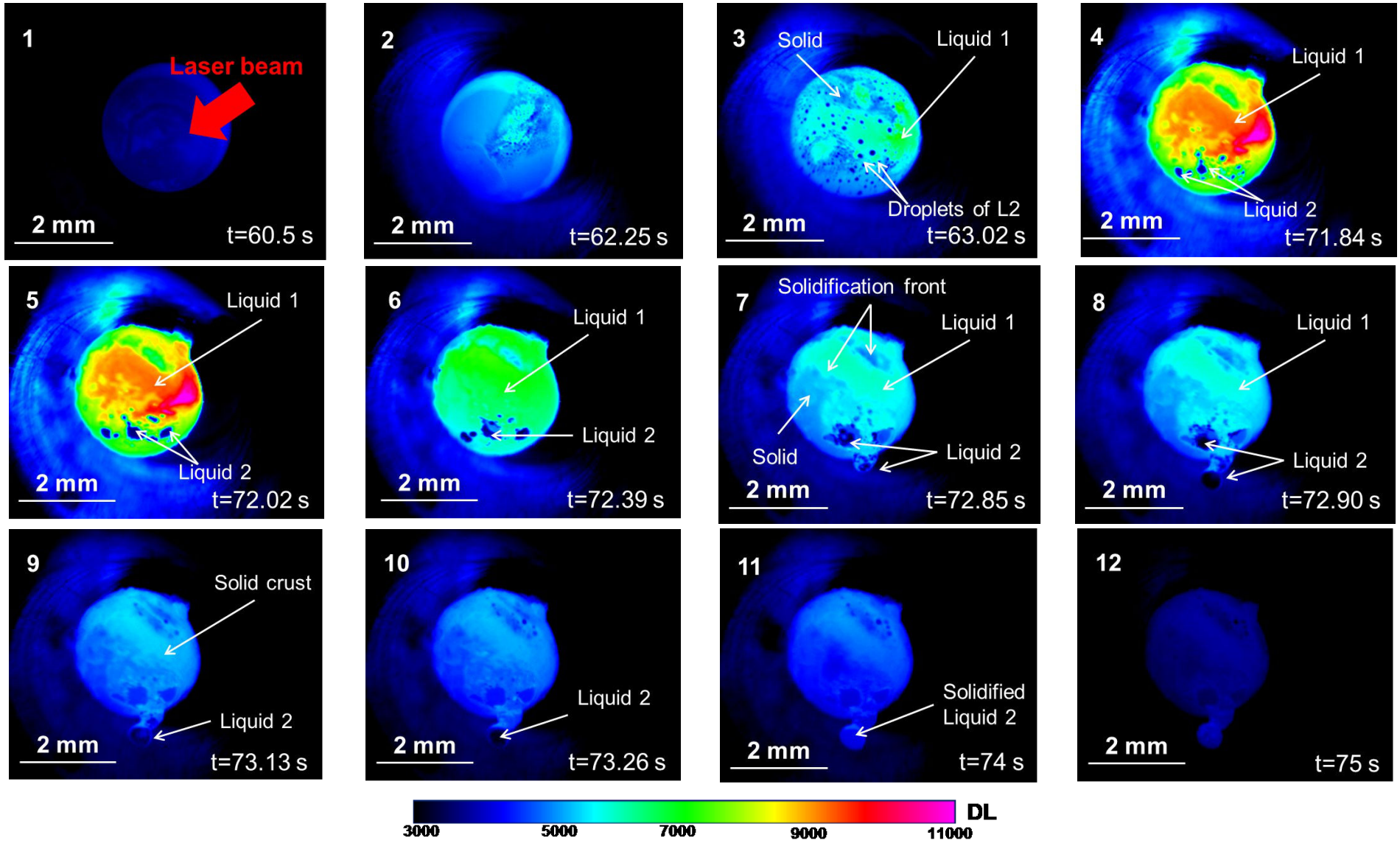

Figure 22: Infrared images of the levitating Fe-Zr sample. The twelve acquisitions corresponds to the labels in Figure 21

Images 1-5 in Figure 22 show the levitating sample during the heating stage of the cycle. Between 60 s and 62.25 s (1-2) the first trace of liquid phase appears. Starting from about 63 s (3), some droplets of a second liquid form: since no liquid immiscibility exist in the Fe-Zr binary phase diagram, **this means that during the laser pulses the sample interacted with the oxygen in the levitation gas, leading the composition moves from the Fe-Zr binary system towards the O-Fe-Zr ternary phase diagram**. Two immiscible liquids, one oxide and one metallic are highlighted during the fast infrared footage.

The infrared images allow distinguishing the two liquids, one blue the other green (3-6). The orange to pink zone represent the overheated liquid directly heated by the laser beam. It is assumed that the green and the blue liquids are at the same temperature (6), thus the difference in the colour is related to their different emissivity. In particular, the blue liquid emits less than the green. Therefore, the emissivity of the blue liquid is lower than that of the green liquid. It can be concluded that the green liquid is the oxide one (Liquid 1), whilst the blue liquid is the metallic one (Liquid 2). In correspondence of image 5, the laser is switched off. Image from 6 to 9 show the formation of a solid crust on the surface of the sample. At the same time, the metallic liquid seems to be ejected from the levitating sample, probably because of the significant difference in viscosity and surface tension between the two liquids. Images between 9 and 12, which correspond to the inflection on the thermogram in Figure 24, show the solidification of Liquid 2.

During the third heating/cooling cycle in Figure 20, the separation between the two immiscible liquid is even more pronounced (Figures 23-24).

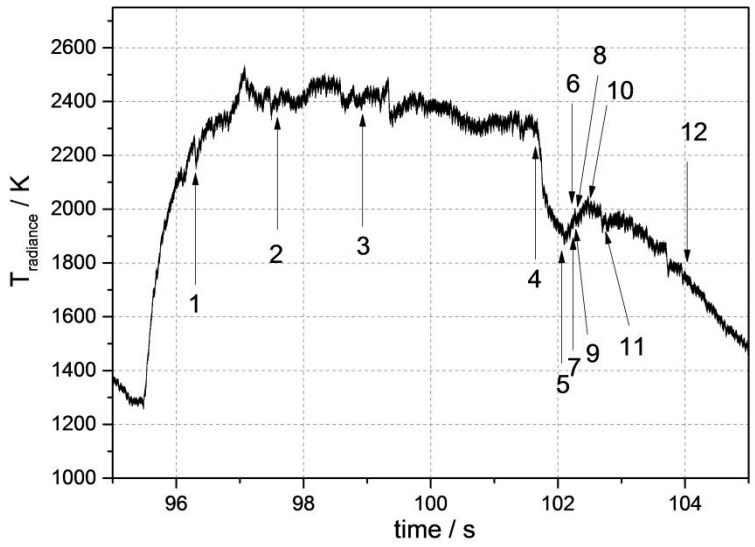

Figure 23: Thermogram recorded with the HgCdTe detector during the third heating/cooling cycle in Figure 20

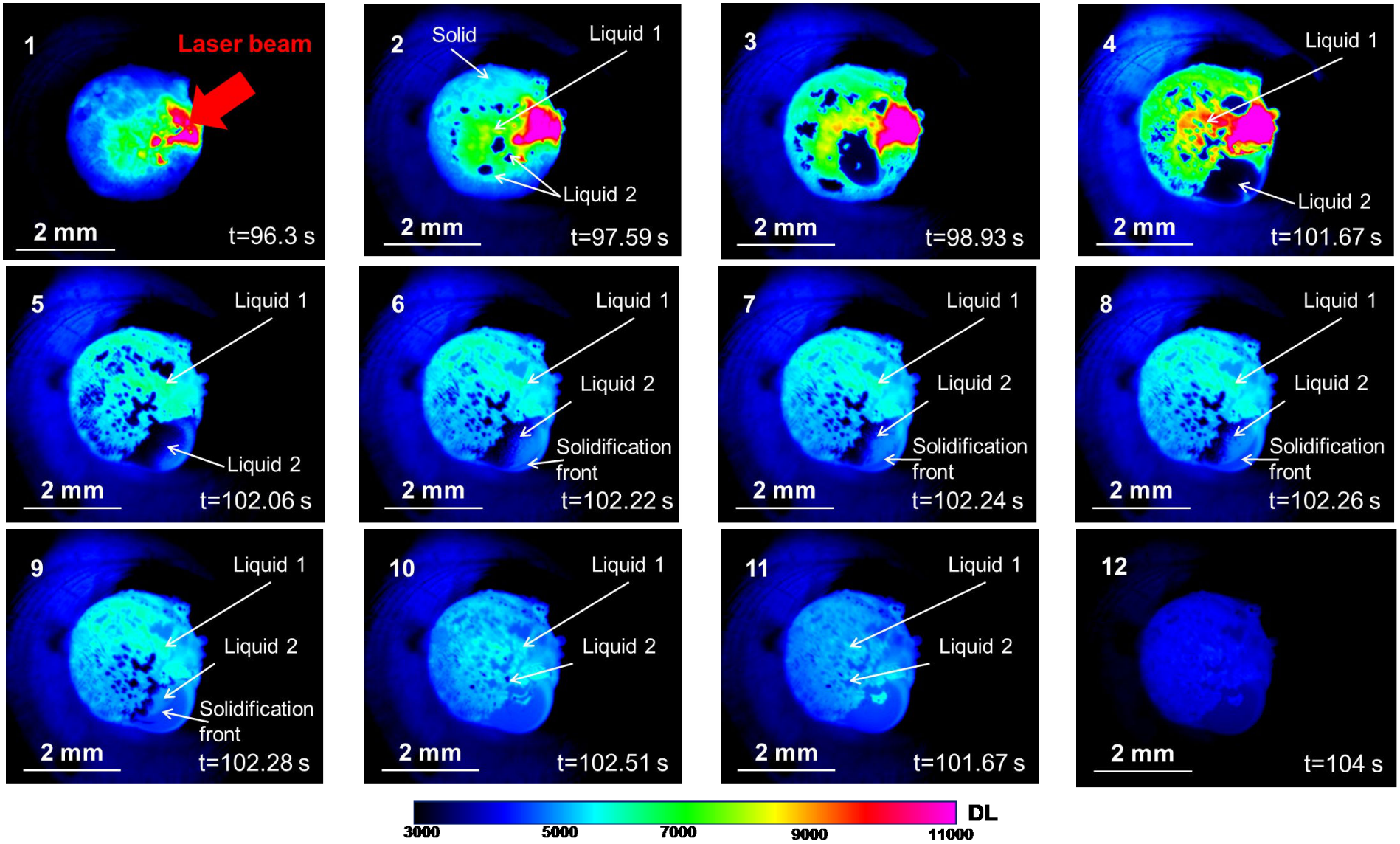

Figure 24:Infrared images synchronised with the labels in Figure 23

During the heating stage (1-4), the metallic liquid separated from the oxide liquid, forming a second droplet attached to the bigger one. A precise estimation of the emissivity of the two liquids is not possible with the present configuration (objective G1). **However, considering the Digital Level (DL) corresponding to the two liquids, it can be estimated that the emissivity of the oxide liquid is about twice the emissivity of the metallic liquid at 3.99 µm.** During solidification, the metallic droplet cooled separately, keeping its new configuration even in the solid state (12).

Post-experimental analyses are currently underway. Thanks to these analyses it will be possible to measure the chemical composition of both immiscible liquids.

6.3 Conclusions and perspectives

This Chapter summarises the current development of ATTILHA experimental setup performed during this thesis. This setup is dedicated to the investigation of the corium thermochemistry and thermophysical properties during nuclear severe accidents. The main advantage of this high temperature device is the possibility to perform fast measurements under aerodynamic levitation conditions. Furthermore, it allows to study high temperature dynamic phenomena observed in the infrared spectral range.

After having being developed, this setup was calibrated and validated on a well-known oxide (Al_2O_3); the calibration method was further extent to the more complex Al_2O_3-ZrO_2 system. These first results demonstrate the potentiality and the versatility of this smart experiment.
In parallel, an image processing routine was developed using Python language in collaboration with IMT-Toulouse in order to estimate the emissivity of the high temperature samples. This work was complemented by a rigorous analysis of the main errors affecting the final temperature results; this error formalism will be shortly implemented in the image processing code.

Because this setup does not allow uranium containing sample investigation, the first ATTILHA experiments were performed on the O-Fe-Zr key system; the authorization for nuclearization is underway.

The lack of data on the high temperature O-Fe-Zr liquid miscibility gap has motivated the present investigation. Preliminary fast infrared footages highlighted the coexistence of both a metallic and an oxide liquids. Even if the camera was not properly calibrated in the temperature range of interest, the emissivity ratio between these liquids could be estimated at 3.99 µm; this result is fundamental to evaluate the radiative contribution to heat transfer of corium pools during severe accident scenarios. Further experiments and analyses will be carried out to establish the temperature and composition dependence of this demixing phenomenon.

6.4 References

[1] D. P. DeWitt and G. D. Nutter, Book, *Theory and practice of radiation thermometry*. New York, 1988.

[2] F. Cabannes, “Techniques de l’Ingenieur - Pyrometrie optique,” 1990.

[3] J. F. Brun, “Mesure et analyse de l’émittance spectrale d'oxydes diélectriques à haute température - une approache des phénomenes préfusionnels,” PhD Thesis Univeristé d’Orléans, 2003.

[4] V. Sarou-Kanian, J. C. Rifflet, and F. Millot, “IR Radiative Properties of Solid and Liquid Alumina: Effects of Temperature and Gaseous Environment,” *Int. J. Thermophys.*, vol. 26, no. 4, pp. 1263–1275, 2005.

[5] V. A. Petrov and A. Y. Vorobyev, “Spectral emissity and radiance temperature plateau of self-supporting alumina melt at rapid solidification,” *High Temp. - High Press.*, vol. 35/36, pp. 677–689, 2007.

[6] TAF-ID, “www.oecd-nea.org/science/taf-id.” .

[7] K. Nakazawa and A. Ohnishi, “Simultaneous Measurement Method of Normal Spectral Emissivity and Optical Constants of Solid at High Temperature in Vacuum,” *Int. J. Thermophys.*, vol. 31, pp. 2010–2018, 2010.

[8] J. F. Brun, D. De Sousa Meneses, and P. Echegut, “Spectral Emissivity of Dielectric Oxides, Below and Above the Melting Point,” in *Fiftheenth Symposium on Thermophysical Properties*, 2003.

[9] L. Robin Carillon, “Etude expérimentale et théorique de l’émission infrarouge de ceramiques à haute température. Application aux barrieres thermiques,” PhD Thesis Institut National des Sciences Appliques de Lyon, 2007.

Conclusions and perspectives

The main objective of the present PhD thesis has been the investigation of the prototypic U-Pu-Zr-Fe-Al-Ca-Si-O corium system in the framework of severe accident study on PWR. The comprehension of the high temperature physico-chemistry of this system is crucial for the reactor design and the mitigation action management in accidental scenarios.

The methodology adopted in this thesis is based on the CALPHAD method, which allows to assess the thermodynamic model of complex systems starting from reliable experimental data. The strength of this approach relies on the possibility of obtaining information on high-order chemical systems (e.g., 8 elements in the present case) starting from low-order thermodynamic descriptions (i.e., binaries and ternaries).

In this framework, the thesis has developed along three main axes:

- Experimental campaign on key ternary and quaternary sub-systems of the prototypic corium. In particular, the O-U-Zr, O-Fe-Zr, O-Pu-U-Zr and O-Pu-U-Zr systems have been investigated using heat treatments, laser heating and arc-melting. An additional set of experimental results has been obtained on two complex U-Zr-Al-Ca-Si-O corium samples;
- Thermodynamic modelling of the O-U-Zr, O-Fe-Zr, O-Fe-U and O-Pu-Zr ternary systems using significant experimental data and the current experimental results. Solidification path calculations have been also performed to validate the present model and interpret current experimental results;
- Development of a novel experimental setup, ATTILHA (Advanced Temperature and Thermodynamic Investigation by Laser Heating Approach), for the high temperature investigation of metallic, ceramic and oxide/metallic samples.

The general conclusions and perspectives of this work are summarised in the following sections.

Corium thermodynamics

The current approach has allowed combining experimental and calculation results for a better understanding of the high temperature behaviour of the corium mixture. The experimental campaign has been tailored to meet the needs of the thermodynamic modelling lack of data. Different experimental techniques have been employed to investigate the aforementioned ternary systems, depending on the chemical system specification and on the desired type of results.

The O-U-Zr ternary system has been investigated by heat treatments and laser heating. The heat treatment results revealed that the miscibility gap in the liquid phase exists at 2567±26 K. Two of the four annealed samples show a stratified microstructure, typical of two quenched immiscible liquids. **The composition of the two liquids has been measured for the first time at this temperature, allowing to shape the extension of the immiscibility region in the ternary phase diagram. The present study can be considered more reliable than previous investigations, thanks to the precise temperature monitoring and post-experiment analyses**.

The Zr-rich corner of the ternary phase diagram has been investigated by laser heating in collaboration with the Materials Research Unit of the JRC-ITU. The measured radiance temperatures of transition are highly reproducible thanks to the optimised experimental conditions. However, the significant uncertainty in the emissivity estimation is propagated in the estimated real temperature. Further investigation on the optical properties of the samples may improve the quality of the present set of laser heating data.

The thermodynamic model of the O-U-Zr system has been evaluated agreementing to the present experimental results and significant literature data. **The resulting model reproduces well the selected experimental data and allows to interpret the microstructures observed in the annealed and laser-heated samples**. The present model can be considered satisfactory, especially for T > 1800 K. Oxygen potential data in the $(U,Zr)O_{2-x}$ are missing. These data will allow a better description of the cubic mixed oxide phase. Some discrepancies with low temperature experimental data may lead to a future effort to improve the current version of the O-U-Zr model.

Laser heating experiments on O-Fe-Zr samples were more challenging. The control of the incongruent evaporation was not completely achieved due to the high volatility of iron and iron oxides. Therefore, current results have not been used for the thermodynamic modelling of the O-Fe-Zr system. These experiments revealed that during the solid/liquid and liquid/solid transitions, the samples experienced a sharp emissivity change that affected the recorded thermograms. This phenomenon can be attributed both to the formation of a ZrO_2 oxide layer on the laser-heated surface and to electronic transitions in the metallic sample.

The present thermodynamic assessment of the O-Fe-Zr and O-Fe-U ternary systems has been based on experimental data in the oxide region of the ternary phase diagrams. Rare thermodynamic data, such as oxygen potential measurements, were obtained only in the fully oxide section ZrO_2-FeO-Fe_2O_3 of the O-Fe-Zr ternary phase diagram. In order to obtain a satisfactory model for the O-Fe-Zr and O-Fe-U systems new phase diagram data are needed in the metallic region of these ternary phase diagrams. Furthermore, a fundamental contribution to the modelling should be given by oxygen potential measurements.

During this work, the UO_2-PuO_2-ZrO_2 system was also investigated using the laser heating setup at the Materials Research Unit in JRC-ITU. It represents the first systematic study on the effect of experimental atmosphere on the melting/solidification behaviour of this system. These results are extremely instructive and provide important information on the thermo-chemistry of nuclear fuel under different atmospheres. The following considerations are proposed:

- The repeatability of the recorded thermal arrest temperatures confirms that the experimental conditions, such as laser power profile, dwelling time, pressure inside the autoclave and quality of the buffer gas, limited incongruent vaporisation and maintained the composition of the sample as close as possible to the initial one;
- The melting behaviour of the six investigated samples is strongly influenced by atmospheric conditions during the laser heating. Thermodynamic calculations confirmed that the O/M in the UO_2-PuO_2-ZrO_2 system varies as a function of temperature and atmosphere;
- The solid/liquid surface in the UO_2-PuO_2-ZrO_2 system can be estimated starting from the experimental results. Calculations revealed that the minimum corresponds to a composition $(UO_2)_{0.15}(PuO_2)_{0.50}(ZrO_2)_{0.35}$ and T=2770 K. These calculations results should be confirmed experimentally.

It must be pointed out that the current thermodynamic calculations on the UO_2-PuO_2-ZrO_2 system have been performed with the current in-vessel corium model, resulting from extrapolation of the UO_2-ZrO_2, UO_2-PuO_2 and PuO_2-ZrO_2 isopleth sections. The good consistency between experimental observations and calculations confirm the reliability and the quality of the present model. The experimental investigation of the UO_2-PuO_2-ZrO_2 system at the solid state and for O/M < 2 will be extremely useful for the thermodynamic modelling of this system, especially to better define the domain of existence of the pyrochlore phase.

The experimental investigation of the two corium samples in Chapter 4 has shown that depending on the nature of the concrete, the resulting mixture in-vessel corium+concrete may

exhibit radically different features. The interaction with a SiO_2-rich concrete may lead to the formation of two immiscible liquids, whilst the interaction with a CaO-rich concrete likely forms a single phase liquid. The present set of results motivates further investigation on ex-vessel corium samples, even considering Fe. The TAF-ID database can then be tested on further compositions. The measurement of liquidus temperatures is also of interest.

As a general conclusion, this work proved that the synergic contribution of experimental results and thermodynamic calculations leads to a powerful tool capable of predict experiments and interpret complex microstructures, as in the case of the U-Zr-Fe-O prototypic in-vessel corium sample. Furthermore, the experimental conditions can be tailored basing on thermodynamic calculation, limiting the uncontrolled parameters, which might affect the final result.

The current thermodynamic model can be also coupled with severe accident codes to predict the complex phenomena occurring in an accidental scenario. For example, the better description of the miscibility gap in the liquid phase of the O-U-Zr system will contribute to the understanding of the in-vessel corium configuration. The coupling between the current model and phase field code developed at the CEA Cadarache will allow to better describe the focusing effect phenomenon and therefore the process of mechanical loss of the steel vessel.

The effect of Pu on the in-vessel and ex-vessel accidental scenario will be investigated by thermodynamic calculation. The presence of Pu in one particular zone of the damaged reactor core (for example in one of the two stratified liquid in the in-vessel configuration) may lead to undesired re-criticality.

Current status, potential and perspectives of ATTILHA

The validity of ATTILHA (Advanced Temperature and Thermodynamic Investigation by Laser Heating Approach) as a novel experimental setup developed during this thesis has been proved on well-known systems. The melting temperature of Al_2O_3 has been measured, obtaining a value in excellent agreement with the literature. Two Al_2O_3-ZrO_2 samples have been also investigated, showing that the eutectic and the liquidus temperatures are well reproduced.

The main advantage of the present setup is the simultaneous acquisition of temperature measurement via three instruments. The HgCdTe detector and the bi-chromatic pyrometer monitor the temperature evolution, whilst the fast infrared camera provides useful spatial information on the melting/solidification behaviour of the sample. Thanks to this supplementary instrument, the miscibility gap in the liquid phase of the O-Fe-Zr system has been "physically" observed: the formation of the first droplets of a second immiscible liquid has been clearly displayed. The relative position of the two liquids has also been monitored. In collaboration with IMT Toulouse, a post-experiment processing of the infrared camera files permits to estimate the emissivity of the sample at 3.99 µm. The evolution of the emissivity can be then related to the temperature evolution during the experiment, and therefore to the presence of a liquid phase.

These results motivate further evolutions of the current setup. The implementation of an ultra-rapid camera (up to 5000 Hz) is planned. This instrument will allow an even more accurate study on the behaviour of two immiscible liquids in aerodynamic levitation. Important thermo-physical data, such as the viscosity and the surface tension, might be deduced.

The administrative authorisation for the investigation of U-containing samples has been validated in the first trimester of 2015. This further step will let to enlarge the range of chemical systems which can be studied with the present setup and it will allow to measure the melting/solidification temperature of U-containing corium mixtures.

Appendix A – Background on pyrometry and laser heating results

Optical pyrometry is practically the only temperature measurement technique available for the high temperatures, above 2500 K. Through this technique is in principle possible to measure the temperature of a specimen through the detection of radiant flux thermally emitted by it.

The main properties and definitions of thermal radiation processes are described in this section.

Spectral Radiance

Taking into account a surface element of area dA_1 and the emitted radiant power Φ from that surface element, spectral radiance is defined as the radiant power emitted at the wavelength λ in the (θ,ϕ) direction, per unit area of the emitting surface normal to this direction, per unit solid angle $d\omega$ around this direction and per unit wavelength $d\lambda$ around λ [1] (Figure 1).

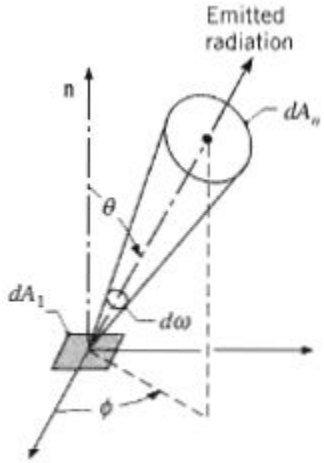

Figure 1: Emission of radiation from a differential area dA_1 [1]

$$L_\lambda(\lambda,\theta,\phi) = \frac{d^3\Phi}{dA_1 \cos\theta \, d\omega \, d\lambda} \tag{1}$$

In eq.(B.1) the area dA_n is the component of dA_1 perpendicular to the direction of the radiation so it is equal to $dA_1 \cos\theta$.

Blackbody

A blackbody is a surface that absorbs all incident radiation regardless of wavelength and direction. Furthermore, it is an isotropically diffuse emitter. Finally, for a prescribed temperature and wavelength no surface can emit more than it.

The concept of a blackbody serves as an ideal standard to which real surfaces are referred. There is no real surface that has these properties. However, a very good approximation is realised by the aperture of a cavity with internal isothermal walls (Figure 2).

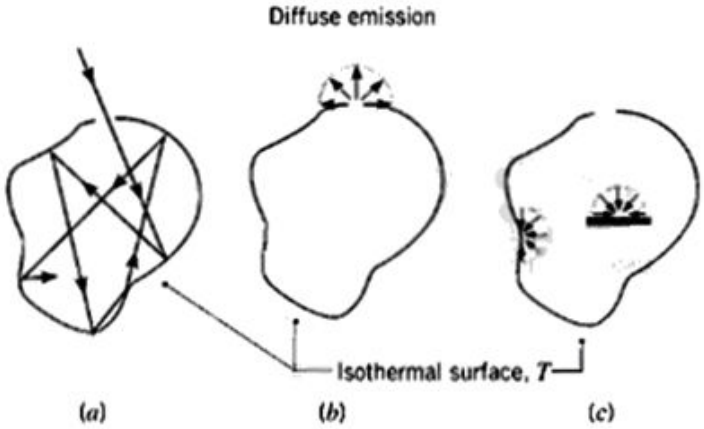

Figure 2: Characteristics of an isothermal blackbody cavity. (a) Complete absorption. (b) Diffuse emission from an aperture. (c) Diffuse irradiation of interior surfaces [2]

The Planck distribution

Planck's radiation law establishes a link between the spectral radiance $L_{\lambda,b}$ at "local" wavelength λ emitted by a blackbody and its temperature T:

$$L_{\lambda,b}(\lambda,T)=\frac{c_{1L}}{n^2\lambda^5}\left[\exp\left(\frac{c_2}{n\lambda T}\right)-1\right]^{-1} \tag{2}$$

where $c_{1L} = 2\,h\,c_0^2$ is the first radiation constant for spectral radiance and $c_2 = h\,c0\,k_B^{-1}$ is the second radiation constant. c_0 is the speed of light in vacuum, h is Planck's constant of action, k_B is the Boltzmann constant and n is the index of refraction of the non-attenuating medium in which the blackbody spectral radiance propagates. The blackbody distribution of different temperature is reported in Figure 3.

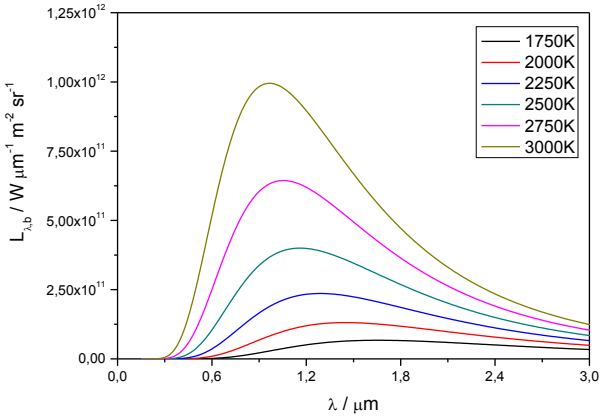

Figure 3: Planck's distribution for several temperatures

In the limit of the so-called $n\,\lambda\,T << c_2$ Wien´s approximation it is possible to approximate eq.(B.6) as

$$L_{\lambda,b}(\lambda,T)=\frac{c_{1L}}{n^2\lambda^5}\left[\exp\left(\frac{c_2}{n\lambda T}\right)-1\right]^{-1}\approx\frac{c_{1L}}{n^2\lambda^5}\left[\exp\left(\frac{c_2}{n\lambda T}\right)\right]^{-1} \quad (3)$$

This expression is accurate for short wavelengths and for low temperatures and is better than 1% if $n\,\lambda\,T\leq 3100$ μm K.

Within the measurement uncertainty reported in the present work, n can be approximated by unity, because the pyrometers (detecting radiance) were always located in air at ambient pressure and temperature.

Real surfaces optical properties

Emissivity

A real surface cannot emit more than a blackbody so the ratio of radiation emitted by the real surface to the radiation emitted by the ideal one is defined as emissivity.

As indicated in Figure 4, radiance may differ considerably from Planck shape for non-ideal radiator. Emissivity, in general, is a function of the temperature, direction and wavelength

$$\varepsilon(\lambda,\theta,\phi,T)=\frac{L_\lambda(\lambda,\theta,\phi,T)}{L_{\lambda,b}(\lambda,T)} \quad (4)$$

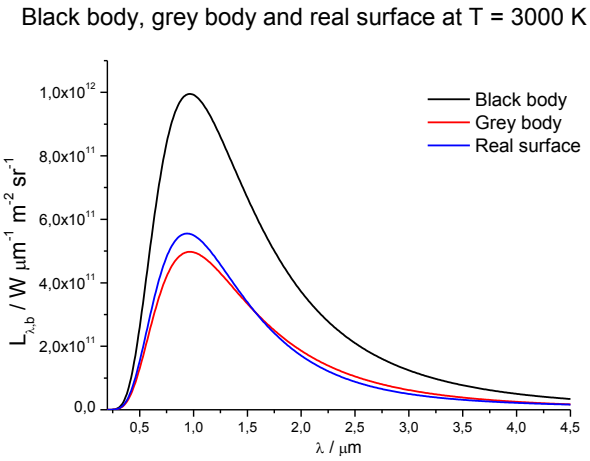

Figure 4: Comparison between black body, grey body and a real surface

The expression above refers to the spectral – directional emissivity. In the case the radiator is a gray body (Figure 4), the original shape of Planck´s curve is preserved but with lower emission: the spectral – directional emissivity is independent of wavelength.

Absorptivity, Transmissivity, Reflectivity

If we consider the interaction with a semitransparent medium (Figure 5) the radiation incident may be reflected, absorbed and transmitted. Evaluation of these components is difficult because the processes depend on the beam geometry, the incident wavelength, surfaces conditions, the composition and thickness of the medium. These processes are influenced by volumetric effects occurring within the medium.

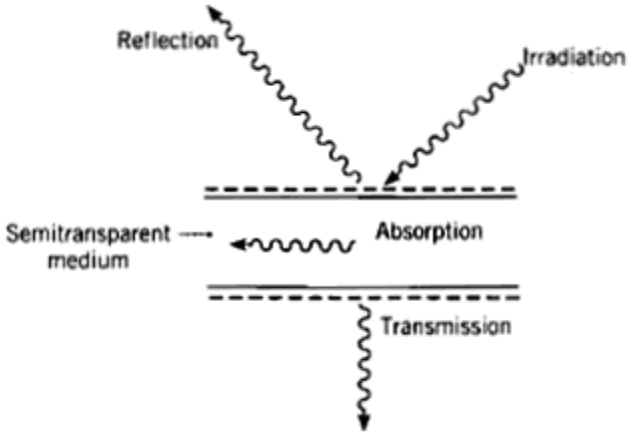

Figure 5: Absorption, reflection and transmission processes associated with a semitransparent medium [2]

When the radiation is incident on an opaque medium where the absorption process occurs at only a few wavelengths from the surface, the transmission process can be neglected and the other two processes may be considered as surface phenomena.

Radiation balance

From energy balance considerations it follows that the sum of the reflected, absorbed and transmitted radiant fluxes must equal the incident radiant flux.

$$\Phi_{\lambda,i} = \Phi_{\lambda,r} + \Phi_{\lambda,a} + \Phi_{\lambda,t} \tag{5}$$

Kirchhoff's law

Kirchhoff's law in its general form states that the spectral – directional emissivity is equal to the spectral – directional absorptivity for a surface

$$\varepsilon(\lambda,\theta',\phi',T) = \alpha(\lambda,\theta,\phi,T) \tag{6}$$

This expression is applicable without restrictions because the two properties are inherent of the surface, the only requirements are that the directions (θ', ϕ' of emission and θ, ϕ of absorption) and wavelength be the same and that the surface be at thermal equilibrium with the environment.

Radiation thermometry

This section describes how to apply the foregoing concepts in relation with the radiation thermometers, for measuring the temperature and how the instrument responds to the incident radiation.

First of all two important concepts will be introduced: the definition of the temperature scale and the spectral radiance temperature.

The International temperature scale of 1990 (ITS-90)

The International temperature scale of 1990 (ITS-90) defines the temperature T above the freezing point of silver (1234,93 K) as

$$\frac{L_{\lambda,b}(\lambda_0,T)}{L_{\lambda,b}(\lambda_0,T_0)}=\frac{\exp\left(\frac{c_2}{\lambda_0 T_0}\right)-1}{\exp\left(\frac{c_2}{\lambda_0 T}\right)-1} \tag{7}$$

where T_0 is a reference temperature (the freezing point of Ag, Au or Cu).

The right side of equation is the ratio between the blackbody spectral radiance at an unknown temperature T and the blackbody spectral radiance at the temperature of freezing point calculated at a specific wavelength (in vacuum) λ_0.

Equation 7 requires that the radiation thermometer be effectively monochromatic but in real cases it is not and for that reason in the next sections a more operational version of the above definition will be introduced.

Spectral radiance temperature

Considering a real surface (*rs*) and a blackbody (*b*) at the same temperature, they have different spectral radiance because the former has an emissivity less than one and they are related by

$$L_{\lambda,rs}(\lambda,\vartheta,\phi,T)=\varepsilon(\lambda,\vartheta,\phi,T)L_{\lambda,b}(\lambda,T) \tag{8}$$

Therefore, the concept of spectral radiance temperature T_λ is introduced. It is the temperature of a blackbody emitting the same spectral radiance at a given wavelength as the real surface

$$L_{\lambda,rs}(\lambda,T_\lambda)=\frac{c_{1L}}{n^2\lambda^5}\left[\exp\left(\frac{c_2}{n\lambda T_\lambda}\right)-1\right]^{-1} \tag{9}$$

For example, taking into account the spectral region where Wien's approximation is valid, comparing the latter definition with Equation 8 and Planck's equation it is easy to obtain an expression that links the real temperature and the spectral radiance temperature

$$\frac{1}{T}=\frac{1}{T_\lambda}+\frac{n\,\lambda}{c_2}\ln\varepsilon(\lambda,\vartheta,\phi,T) \tag{10}$$

The above relation is most used in pyrometry. The radiance temperature is always lower than the true temperature since the emissivity is less than one.

Fast two-channel pyrometer

Due to the rapidity of the observed phenomena, a fast two-channel pyrometer was used (approximate maximal time resolution of 10 μs). During the experiments, only the channel at 652 nm (bandwidth 27 nm) was used for radiance temperature measurements. The pyrometer's 652 nm - channel was calibrated in the range 1800-2500 K with W-ribbon lamps [3]. A linear relationship can be derived, between the lamp's radiance temperature and the pyrometer output signal, combining the linear response of the pyrometer with Wien's expression for blackbody spectral radiance:

$$V_{out}(T) = A + \frac{B}{T_\lambda} = 1.35817 + \frac{3568.6706}{T_\lambda} \qquad (11)$$

Where T_λ stays for radiance temperature. The true temperature can be then derived using the fundamental equation of pyrometry in Equation 10.

The second channel of the pyrometer at 488 nm was used to detect the reflected light of a continuous wave Ar^+ probe laser emitting at 488 nm (maximum power 1 W) to determine the instant at which melting or freezing occurred at the sample's surface (Figure 6).

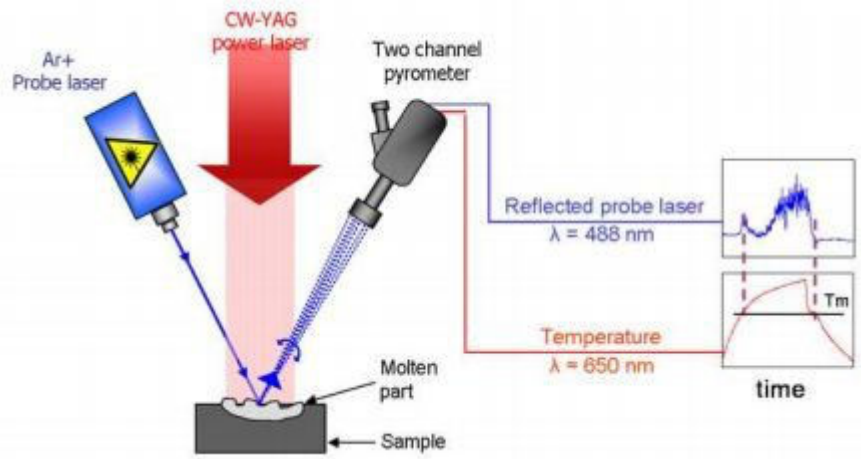

Figure 6: Principle of functioning of the Reflected Light Signal (RLS) technique for the detection of the melting and solidification transitions (3)

This technique named Reflected Light Signal (RLS) was developed to identify phase transitions even during the heat-up of the sample. The intensity of the reflected light is dependent from the angular reflectivity [4]. The first appearance of the liquid during the heating of the sample leads to a rapid change in the reflectivity. A sharp variation in the recorded signal is produced. Because of the movements of the liquid surface, the recorded signal oscillates. Solidification of the sample surface during the cooling stage leads to disappearance of the oscillations, permitting the identification of the phase transition.

Spectro-pyrometer

The current spectro-pyrometer is based on a linear array of 256 Si photodiodes. It is used to record the sample thermal radiance in the range 488 nm – 1011nm. This instrument allows a complete spectral analysis, whereby its main disadvantage is in the poorer time resolution (1 ms at best). Furthermore, due to the low signal-to-noise ratio, only the output signals in the range 550 – 850 nm were considered during the present work. The 649 nm – channel was calibrated against the W-ribbon lamps mentioned above. The rest of the channels were calibrated using a graphite tubular black body up to 2900 K [3]. The obtained transfer function K(λ) for the 488-1011 nm spectral range is:

$$K(\lambda) = \frac{\tau(\lambda)}{Counts(\lambda, T_{bb})} \frac{1}{\lambda^5 \left[\exp\left(\frac{c_2}{\lambda T_{bb}} \right) - 1 \right]} \tag{12}$$

In Equation 12 $\tau(\lambda)$ is the window transmittance at the generic wavelength λ, $Counts(\lambda, T_{BB})$ is the measured signal expressed in counts and T_{BB} is the blackbody temperature. The linearity of the output signal with respect to the integration time was checked. K(λ) permits to convert the output signal of the spectro-pyrometer into a function directly proportional to the emitted spectral radiance:

$$E_{\text{det}}(\lambda, T) = K(\lambda)\, Counts(\lambda, T) \tag{13}$$

In order to obtain the emissivity of the sample starting from the measured radiance spectra the measured radiance intensities form the spectro-pyrometer is converted into the inverse of the radiance temperature considering ε(λ,T)=1:

$$\frac{1}{T_\lambda(\lambda)} = \frac{\lambda}{c_2} \ln\left(\frac{1}{\lambda^5 E_{\text{det}}(\lambda)} + 1 \right) \tag{14}$$

The curves in Equation 14 can be fitted with:

$$\frac{1}{T_\lambda} = \frac{1}{T} - \frac{\lambda}{c_2} \ln \varepsilon(\lambda) \tag{15}$$

The emissivity can be approximated by polynomials as:

$$\varepsilon(\lambda) = \sum_{i=0}^{2} \alpha_i \lambda^i \tag{16}$$

Equation 16 is a simple Taylor expansion of the emissivity as a function of wavelength and constitutes the most general expression for it, although not the most physically accurate. More meaningful expression may be used if the optical properties of the investigated material are

known. The expression with *i=0* corresponds to the grey body assumption, that is ε=constant in the considered range of wavelengths.

Laser heating experimental result on the O-Fe-Zr system

The same experimental setup described in Section 3.2.1.2 was used for the study of six Fe-O-Zr samples. This system is of great interest in the framework of severe accident investigation.

In the past, the Fe-O-Zr system has been studied especially in the oxygen-rich side of the phase diagram.

Sample fabrication

Six samples have been fabricated by arc-melting starting from metallic Fe, Zr Van Arkel, ZrO_2 and Fe_2O_3 powders. The starting materials were firstly characterised by ICP-MS in order to detect metallic impurities. The results on the starting materials are reported in Appendix X. The initial composition of the sample is reported in Table 1 and in Figure 7.

Sample	at% O	at% Fe	at% Zr	mass / g	Δm / g	Δm/m %
OFeZr_1	21.0	14.0	65.0	0.7806	0.0020	0.156
OFeZr_2	13.2	12.7	74.1	0.7644	0.0140	1.832
OFeZr_3	21.9	29.1	49.0	0.5559	0.0063	1.133
OFeZr_4	3.9	34.1	62.0	0.5801	0.0006	0.103
OFeZr_5	11.7	23.8	64.5	0.6772	0.0030	0.443
OFeZr_6	22.6	11.1	66.3	0.5463	0.0069	1.263

Table 1: Initial composition of the six O-Fe-Zr samples investigated by laser heating

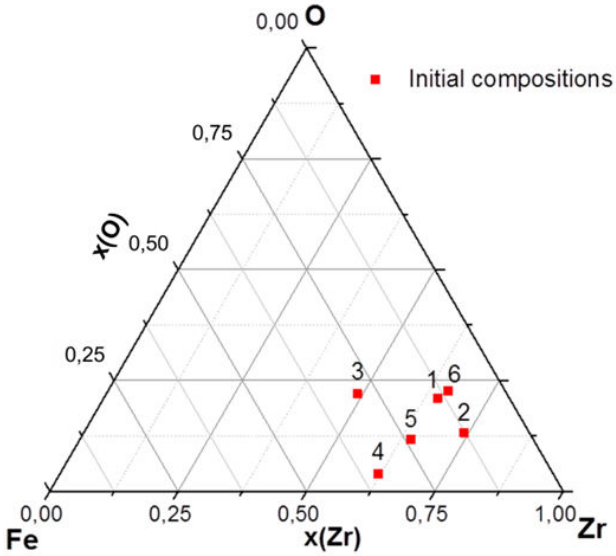

Figure 7: Initial composition of the O-Fe-Zr samples investigated by laser heating

The presence of Fe and Fe_2O_3 makes the samples less stable towards high temperature vaporisation.

Once the drop-shaped samples were ready, they were cut in two parts, one for the laser heating experiments and one for characterisation.

Laser heating results

Except for sample OFeZr_1, the samples underwent laser pulses cycles under both Ar and air.

These experiments were particularly challenging. Three of the six samples (OFeZr_3, OFeZr_4 and OFEZr_6) did not give any exploitable results.

Figure 8 shows the results of a sequence of laser pulses performed on sample OFeZr_1 under Ar. In this section are reported radiance temperatures corrected by the transmittance of the autoclave window (τ=0.86). No emissivity corrections are applied, so the plotted thermograms display the time dependence of the measured radiance temperature.

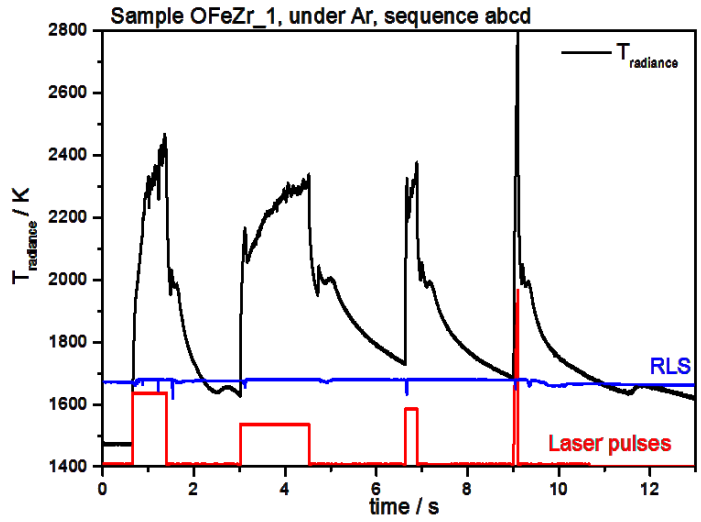

(a)

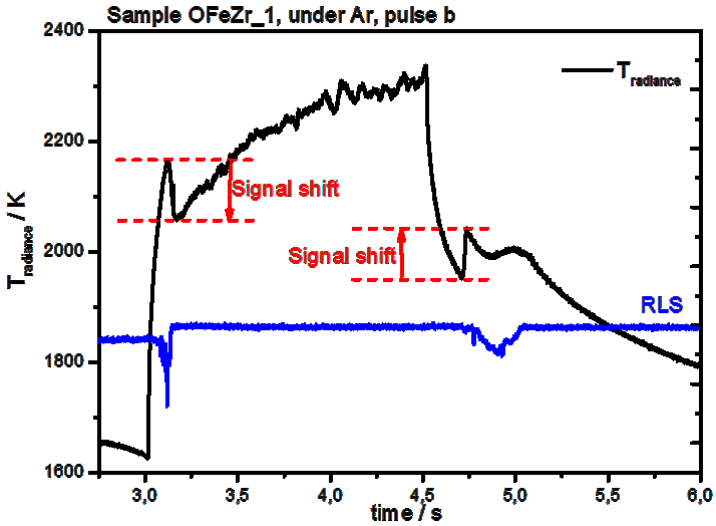

(b)

Figure 8: (a) Sequence of laser pulses performed on sample OFeZr_1 under Ar (p=0.25 MPa). The black line is the radiance temperature measured by the fast pyrometer at 650 nm, the red line is the sequence of laser pulses and the blue line is the RLS signal; (b) magnification on pulse b. The signal shift on the heating stage is also visible on the cooling stage, right before the thermal arrest

Looking at the laser pulse b (Figure 8b), during heating, the thermogram, as well as the RLS signal, exhibits a sharp variation. It can be concluded that the sample experienced phase transition. The same feature is present during cooling. These distinct variations in the recorded signal can be related to reflectivity (and, therefore, emissivity. See Kirchhoff's law) changes of the sample during phase transitions. Figure 9 reports the emissivity calculated

using the extrapolation to zero wavelength method for the whole set of spectra recorded by the spectro-pyrometer during pulse b.

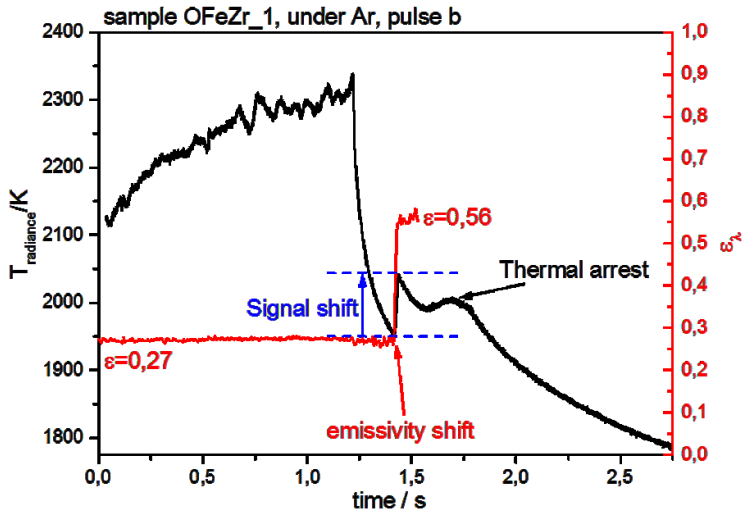

Figure 9: Solidification of sample OFeZr_1 after laser pulse b. The red curve shows a clear emissivity evolution passing from the liquid to the solid state

In correspondence to the sharp thermal arrest during cooling, the emissivity shows a noticeable variation. While in the liquid phase the calculated emissivity is 0.27, after the reported feature the emissivity is 0.56. This feature can be related to a formation of a highly emissivity material on the surface of the sample (e.g., an oxide layer). However, as shown by Cagran et al. [5], solid/liquid transition in metal can drive an evident change in the measured emissivity. In the present case it is not possible to choose one or the other interpretation. EDS analyses on the cross section of sample OFeZr_1 after melting (Figure 10) did not show any evidence of oxide layer on the laser-heated surface. However, Krishnan et al. [6] revealed that even a nanoscopic oxide layer can induce relevant change in the sample emissivity.

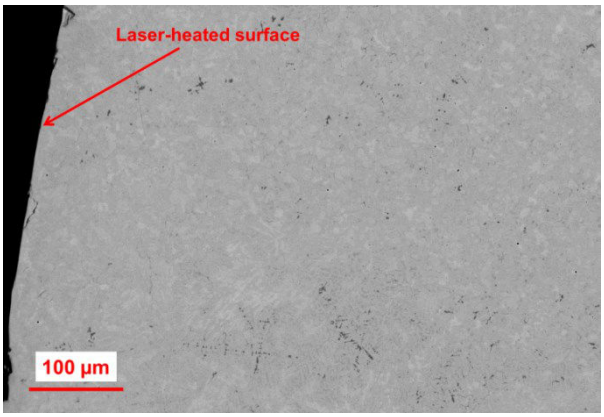

Figure 10: Back-scattering electrons image of laser-melted OFeZr_1 sample under Ar

The variation in the radiance temperature corresponds to higher recorded radiance intensity. The second inflection is the thermal arrest (Figure 9). The same feature was observed on sample OFeZr_2.

This emissivity transition observed in sample OFeZr_1 was also detected in sample OFeZr_5. The emissivity values before and after the shift are 0.25 and 0.55 respectively.

A lower temperature inflection was observed on the cooling flanks recorded during laser sequences on samples OFeZr_1 (Figure 9a) and OFeZr_5. These inflections are reproducible along all the laser pulse sequences. The thermograms recorded during laser pulses on sample OFeZr_2 did not reveal this inflection.

During laser pulses performed under air, a thick ZrO_2 layer (200 µm) was formed on the heated surface of the samples. Figure 11 shows a cross section of sample OFeZr_2 after a cycle under air.

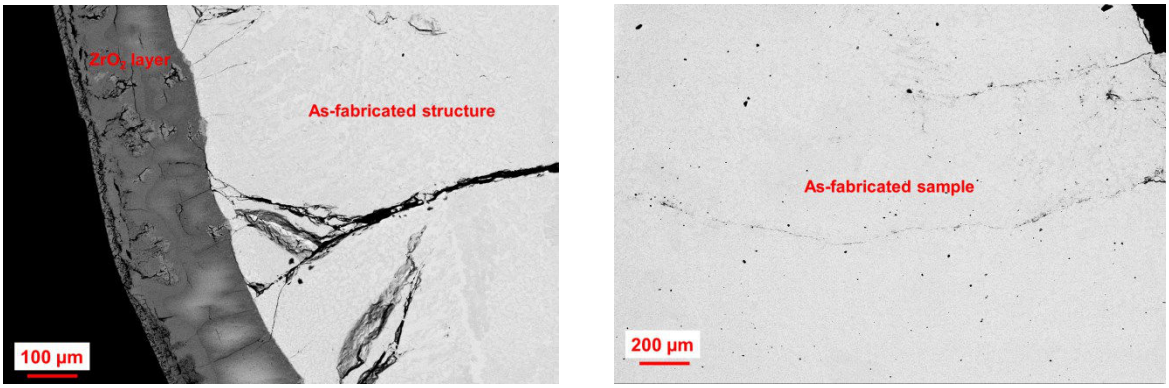

(a) (b)

Figure 11: (a) BSE image of the microstructure of sample OFeZr_2 after a laser pulse sequence under air. A 150 µm thick ZrO_2 layer formed on the surface of the laser heated sample; (b) BSE image of sample OFEZr_2 as-fabricated by arc-melting

WDS analyses confirmed that the external layer is pure ZrO_2. In the presence of the zirconia layer, the temperature detection becomes complex. The laser pulse sequences used during the present set of experiments are optimised for metallic samples. The ZrO_2 layer behaves as a thermal barrier, which prevents the complete fusion of the heated zone.

Discussion

The experimental results on the O-Fe-Zr samples are reported in Table 2.

Sample	**Radiance temperature / K**			**True Temperature / K**	
	1st inflection	**2nd inflection**	**ε(652 nm)**	**1st inflection**	**2nd inflection**
OFeZr_1	1989±18	1660±4	0.56±0.11	2098±86	1735±54
OFeZr_2	1883±29	//	0.56±0.11	1980±94	//
OFeZr_5	1847±11	1572±15	0.55±0.11	1943±72	1642±58

Table 2: Summary of the laser heating experiments on the three O-Fe-Zr samples. In the table are reported both the radiance and the true temperatures. The expanded uncertainties on the true temperatures are corrected with a coverage factor k=2

As for O-U-Zr samples, both radiance and true temperature are presented. The emissivity constitutes once more the main source of uncertainty. The reported values are calculated using the extrapolation to zero wavelength method. A conservative 20 % uncertainty is selected for the calculated emissivity.

References

[1] D. P. De Witt and G. D. Nutter, *Theory and practice of radiation thermometry*. Wiley, 1988.

[2] P. Incropera, D. P. De Witt, T. L. Bergman, and A. S. Lavine, *Fundamentals of Heat and Mass Transfer*, 6th ed. 2007.

[3] F. De Bruycker, "High Temperature Phase Transitions in Nuclear Fuels of the Fourth Generation," PhD Thesis Universite d'Orleans, 2010.

[4] D. Manara, M. Sheindlin, W. Heinz, and C. Ronchi, "New techniques for high-temperature melting measurements in volatile refractory materials via laser surface heating," *Rev. Sci. Instrum.*, vol. 79, no. 2008, 2008.

[5] C. Cagran, C. Brunner, A. Seifter, and G. Pottlacher, "Liquid-phase behaviour of normal spectral emissivity at 684.5 nm of some selected metals," *High Temp. - High Press.*, vol. 34, no. 6, pp. 669–679, 2002.

[6] S. Krishnan, J. K. Richard Weber, C. D. Anderson, and P. C. Nordine, "Spectral emissivity and optical properties at l=632.8 nm for liquid uranium and zirconium at high temperatures," *J. Nucl. Mater.*, vol. 203, pp. 112–121, 1993.

Appendix B – In-vessel corium binary phase diagrams

Binary systems

In the following the phase diagrams of the binary systems involved in the prototypic in-vessel corium formation (U-Pu-Zr-Fe-O) are reported. The thermodynamic models for these systems are taken form the TAF-ID [1] database.

Metallic systems

Binary systems containing Fe are characterised by the presence of intermetallic compounds. In particular, a C15_Laves phase $Fe_2(M)$, where M=U, Pu, Zr, is visible in the Fe-Pu, Fe-U and Fe-Zr phase diagram (Figures 1-5). An additional intermetallic compound, FeM_6, is also present in the Fe-U and Fe-Pu systems. This phase is replaced by $FeZr_3$ and the high temperature $FeZr_2$ compound in the Fe-Zr binary phase diagram. The presence of low temperature eutectics can be noted in the three system.

The Pu-U, Pu-Zr and U-Zr binary phase diagrams are characterised by the presence of intermediate phases with not well established large domain of existence. A continuous solid solution between the body centred cubic (bcc) phases ε-Pu, γ-U and β-Zr and a nearly ideal liquid can be also noticed.

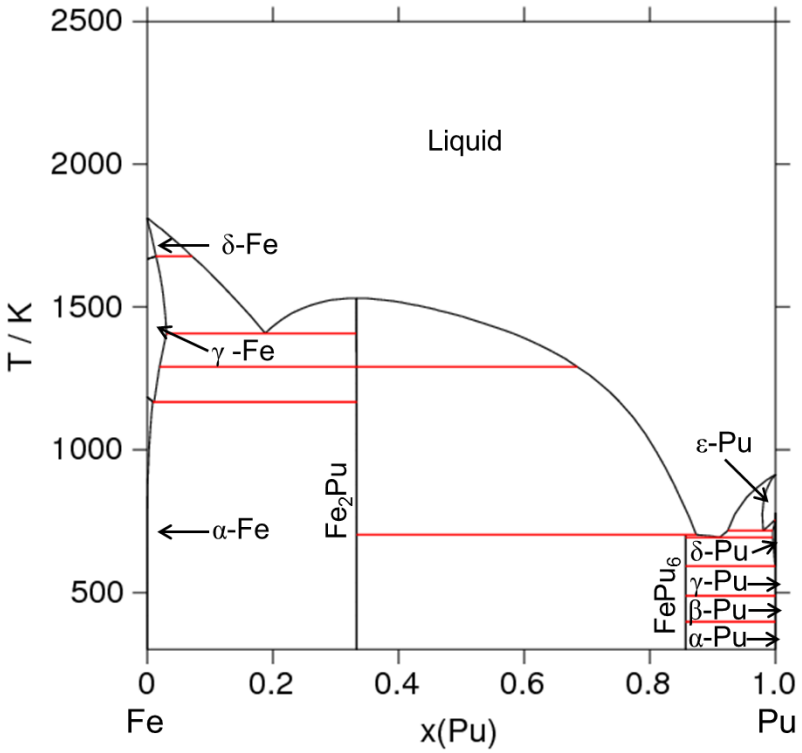

Figure 1: Fe-Pu phase diagram by Kurata [2]

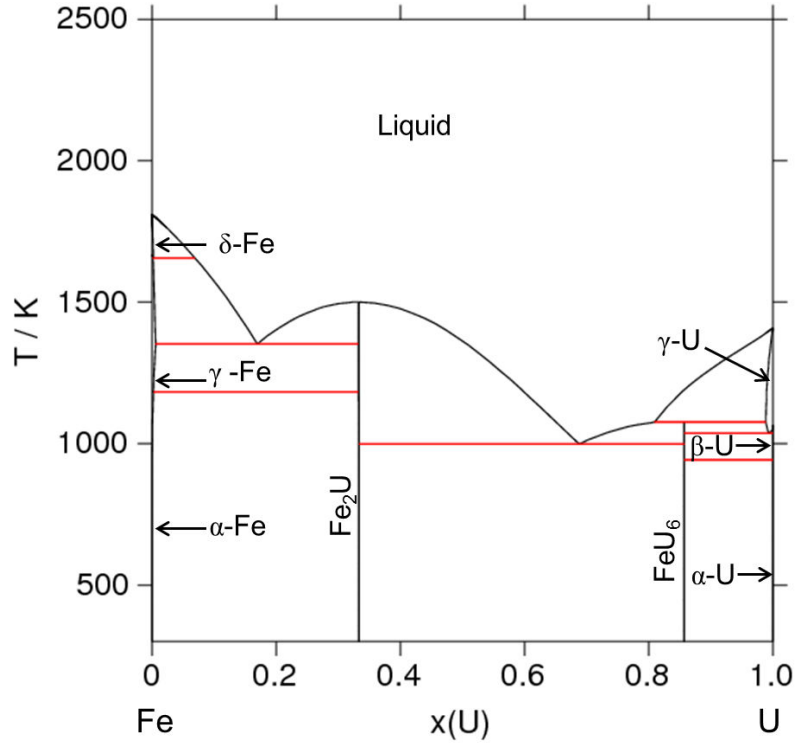

Figure 2: Fe-U phase diagram by Kurata [2]

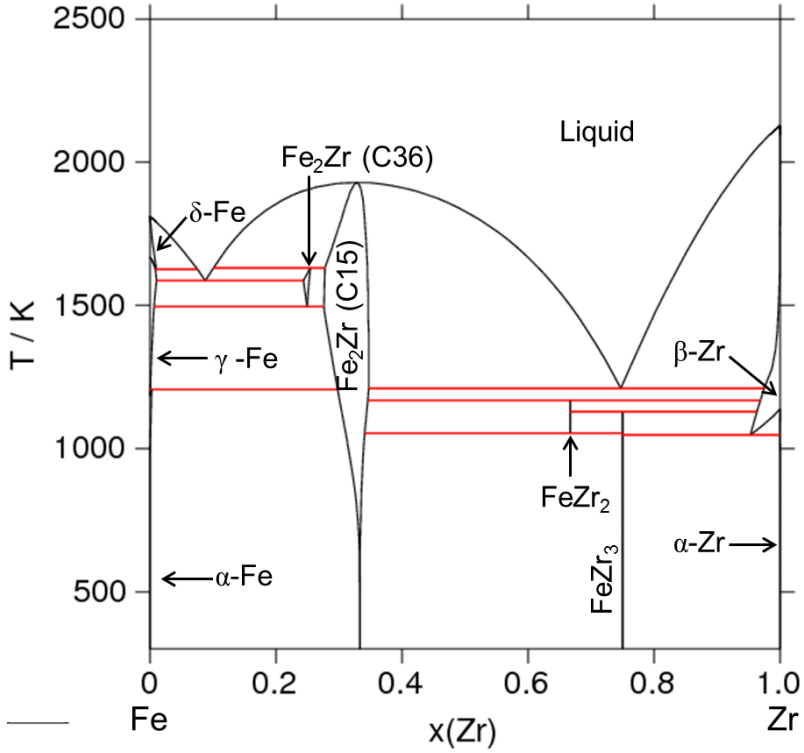

Figure 3: Fe-Zr phase diagram by Toffolon-Masclet et al. [3]

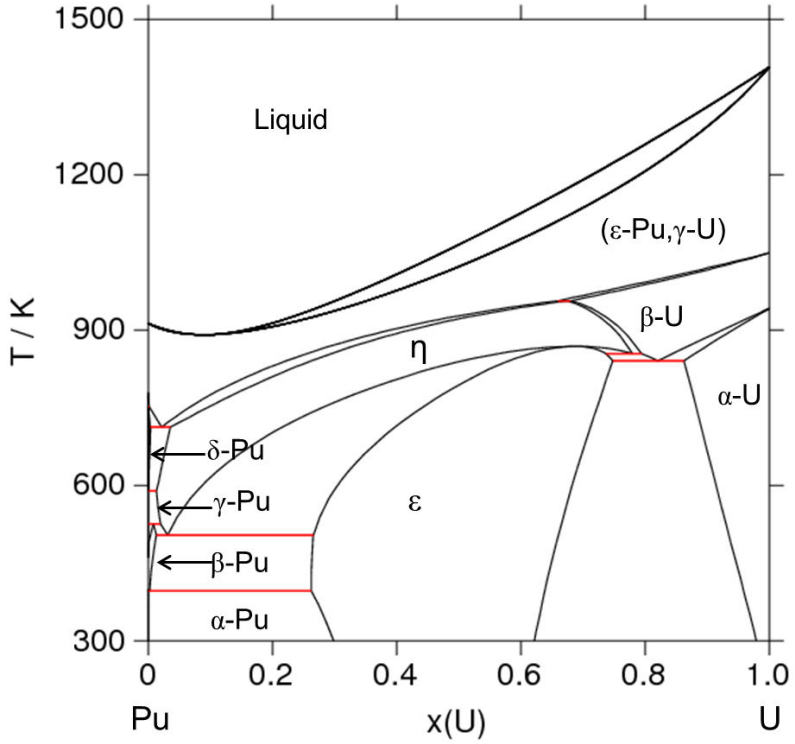

Figure 4: Pu-U phase diagram by Kurata [4]

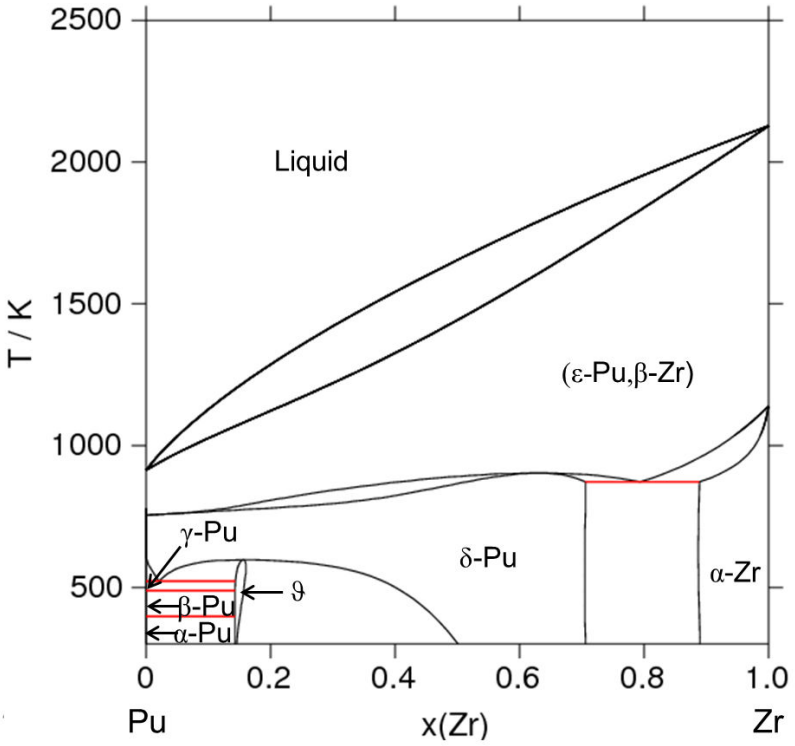

Figure 5 Pu-Zr phase diagram by Kurata [5]

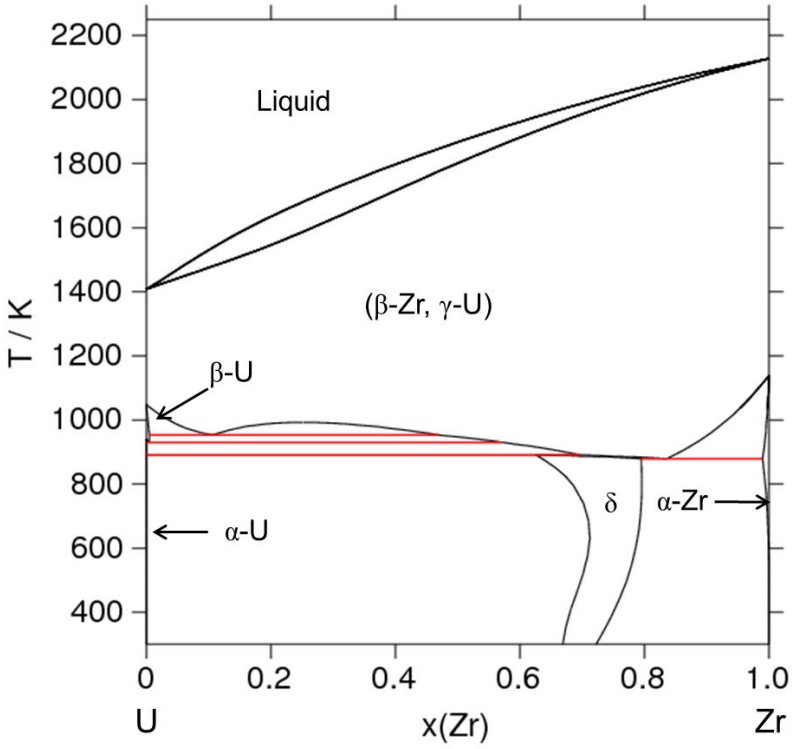

Figure 6: U-Zr phase diagram by Kurata [4], [6] and TAF-ID

Oxide systems

The Fe-O phase diagram exhibits three oxides phases: FeO, Fe_3O_4 and Fe_2O_3. Only Fe_2O_3 is a stoichiometric compound. A miscibility gap in the liquid phase can also be seen (Figure 7).

The Pu-O and U-O phase diagrams present a highly stable CaF_2-type phase, PuO_{2-x} and $UO_{2\pm x}$, respectively (Figure 8-9). At low temperature, a miscibility gap in the PuO_{2-x} phase is also observed. In the region O/Pu<2, three additional oxide phases, Pu_2O_3, $PuO_{1.52}$ and $PuO_{1.61}$ are present. The U-O phase diagram does not show stable oxide compounds for O/U<2. However, for O/U>2, U_4O_9, U_3O_8 and UO_3 compounds can be seen. Both Pu-O and U-O phase diagram exhibit a miscibility gap in the liquid phase between a metallic and an O-rich liquid. The solubility of O in liquid Pu is higher than in U, leading to a smaller miscibility gap in the liquid phase.

The Zr-O phase diagram presents the three allotropic form of ZrO_2 (Figure 10) The low temperature form is monoclinic ZrO_2-m, the intermediate temperature form is tetragonal ZrO_2-t and the high temperature form is face centred cubic ZrO_{2-x}-c. There is no miscibility gap in the liquid phase. The liquidus curve [Liq.+ZrO_{2-x}-c] is still not well established.

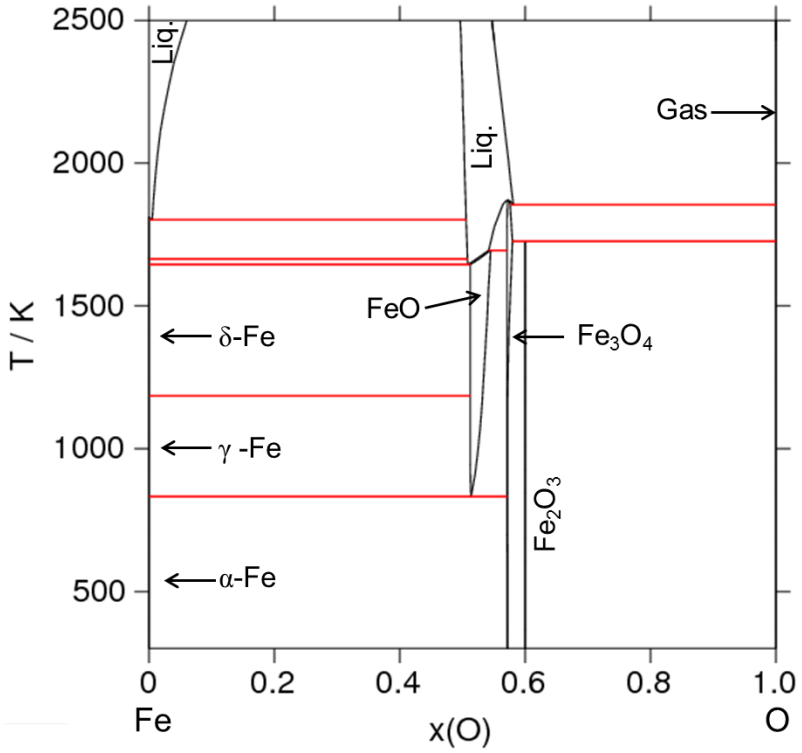

Figure 7: Fe-O phase diagram by Sundman [7]and Kjellqvist et al. [8]

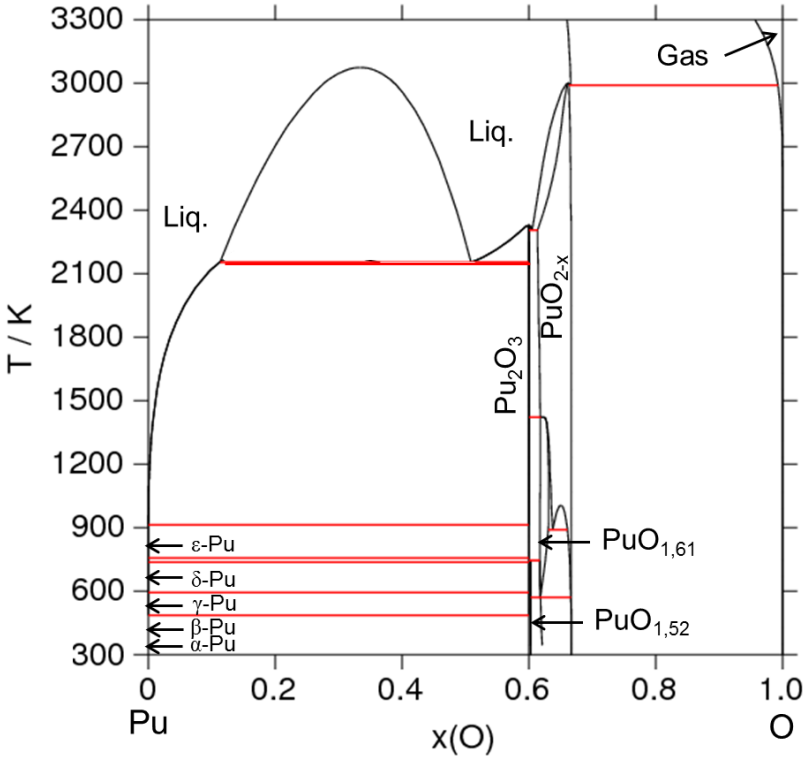

Figure 8: Pu-O phase diagram by Guéneau et al. [9]

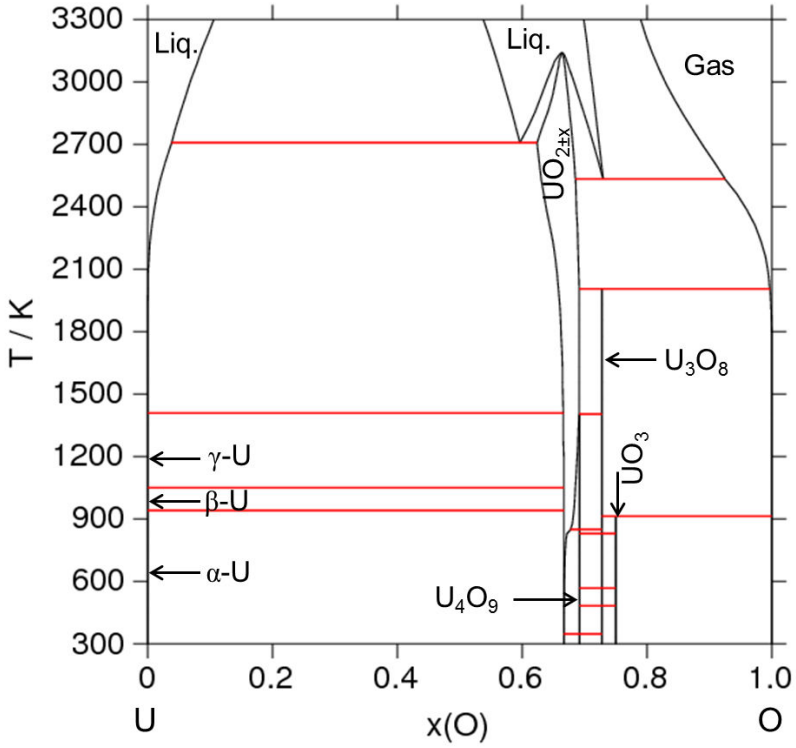

Figure 9: U-O phase diagram by Guéneau et al. [9]

Zr-O system

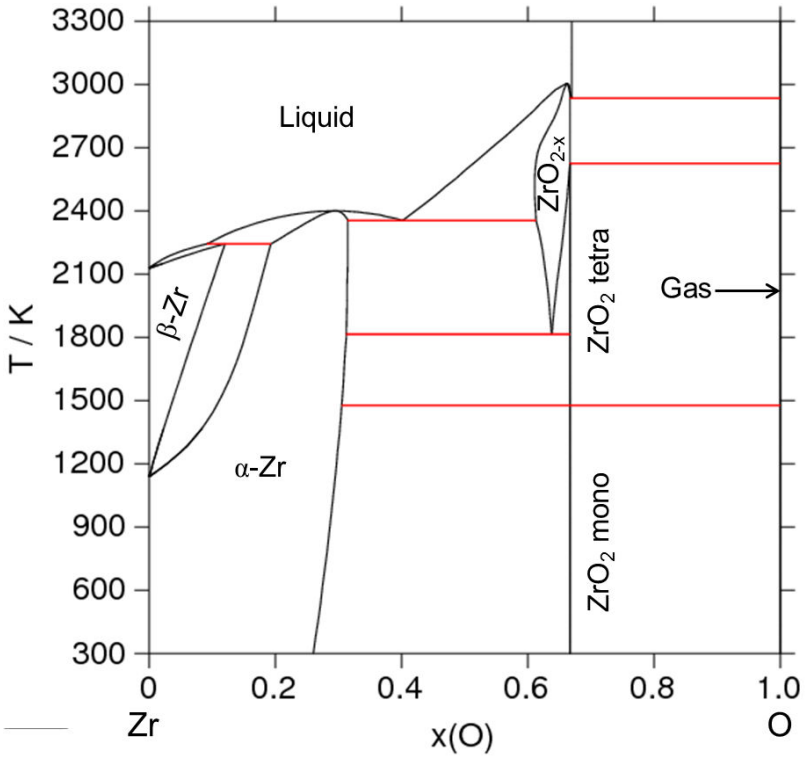

Figure 10: Zr-O phase diagram by Liang et al. [10] with the modified description of the fluorite ZrO_2-c phase of this work

The thermodynamic model retained for the Zr-O system has been published by Liang et al. [10]:

$$(Zr)(O,Va)_2$$

The thermodynamic parameters of the fluoride ZrO_2-c phase have been modified by introducing ionic species Zr^{2+} and Zr^{4+}, in collaboration with N. Dupin and B. Sundman, considering the available experimental data [11,12]. The resulting model is written as:

$$(Zr^{2+},Zr^{4+})(O^{2-},Va)_2$$

The main reason for this change is to be consistent with the model used by Guéneau et al. [9] to describe the $(U,Pu)O_{2\pm x}$-c mixed oxide. The resulting binary phase diagram is reported in Figure 10. The calculated phase diagram is very close to that of Liang et al. [10].

It must be pointed out that cubic ZrO_2-c is slightly hypo-stoichiometric. Between 2625 K and its melting temperature, the stoichiometric composition (O/Zr=2) is in reality a two-phase equilibrium between solid ZrO_{2-x}-c and O_2 (Figure 11).

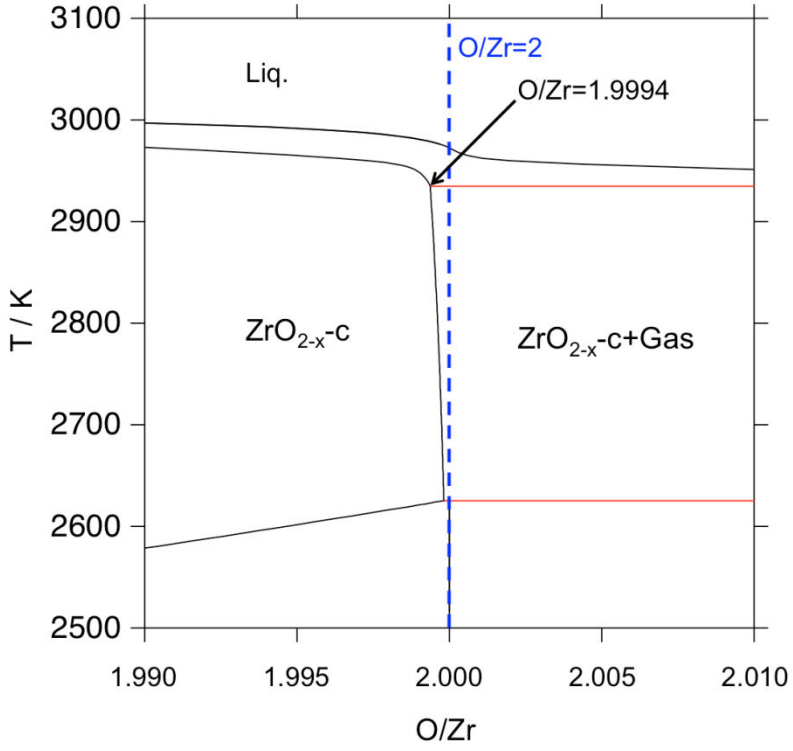

Figure 11: High temperature Zr-O phase diagram centred on O/Zr=2

References

[1] TAF-ID, “www.oecd-nea.org/science/taf-id.” .

[2] M. Kurata, “Thermodynamic database on U-Pu-Zr-Np-Am-Fe alloy system II - Evaluation of Np, Am, and Fe containing systems -,” *IOP Conf. Ser. Mater. Sci. Eng.*, vol. 9, p. 012023, 2010.

[3] C. Toffolon-Masclet, J. C. Brachet, C. Servant, J. M. Joubert, P. Barberis, N. Dupin, and P. Zeller, “Contribution of Thermodynamic Calculation to Metallurgical Studies of Multi-Component Zirconium Based Alloys,” *J. ASTM Int.*, vol. 5, no. 7, p. ID JAI101122, 2008.

[4] M. Kurata, “Thermodynamic assessment of the Pu-U, Pu-Zr and Pu-U-Zr systems,” *Calphad*, vol. 23, no. 3–4, pp. 305–337, 1999.

[5] M. Kurata, “Private communication,” 2006.

[6] M. Kurata, T. Ogata, M. Nakamura, and T. Ogawa, “Thermodynamic assessment of the Fe-U, U-Zr adn Fe-U-Zr systems,” *J. Alloys Compd.*, vol. 271–273, pp. 636–640, 1998.

[7] B. Sundman, “An assessment of the Fe-O System,” *J. Phase Equilibria*, vol. 12, pp. 127–140, 1991.

[8] L. Kjellqvist, M. Selleby, and B. Sundman, “Thermodynamic modelling of the Cr-Fe-Ni-O system,” *Comput. Coupling Phase Diagr. Thermochem.*, vol. 32, pp. 577–592, 2008.

[9] C. Guéneau, N. Dupin, B. Sundman, C. Martial, J. C. Dumas, S. Gossé, S. Chatain, F. De Bruycker, D. Manara, and R. J. M. Konings, “Thermodynamic modelling of advanced oxide and carbide nuclear fuels: Description of the U-Pu-O-C systems,” *J. Nucl. Mater.*, vol. 419, no. 1–3, pp. 145–167, 2011.

[10] P. Liang, N. Dupin, S. Fries, H. J. Seifert, I. Ansara, H. Lukas, and A. F, “Thermodynamic Assessment of the Zr-O Binary System,” *Zeitschrift fur Met.*, vol. 92, no. 7, pp. 747–756, 2001.

[11] R. J. Ackermann, S. P. Garg, and E. G. Rauh, “High-Temperature Phase Diagram for the System Zr-O,” *J. Am. Ceram. Soc.*, vol. 60, no. 7–8, pp. 341–345, 1977.

[12] E. G. Rauh and S. P. Garg, “The ZrO2-x (cubic)-ZrO2-x (cubic+tetragonal) Phase Boundary,” *J. Am. Ceram. Soc.*, vol. 63, no. 3–4, pp. 239–240, 1980.

Appendix C – Thermodynamic models and calculations

Thermodynamic Models

Only the models and the assessed parameters for the phases that have been added or modified during the present work are described. The remaining parameters can be found in literature, and they will not be detailed hereinafter.

Liquid

The liquid phase is described using the ionic two sublattice model [1]. This model can describe both metallic and oxide melts. The first sublattice contains the cations (C_i), whilst the second sublattice contains anions (A_j), neutral species (B_k) and charged vacancies (Va^{-Q}).

$$\left(Fe^{2+}, Pu^{3+}, U^{4+}, Zr^{4+}\right)_P\left(O^{2-}, Va^{-Q}, FeO_{3/2}, O, PuO_2\right)_Q$$

The charged vacancies are introduced to maintain electroneutrality of the liquid. The numbers of site on the sublattices, P and Q, vary with composition, and are defined as:

$$P = \sum_j v_j y_{A_j} + Q \cdot y_{Va} \tag{1}$$

$$Q = \sum_i v_i y_{C_i} \tag{2}$$

where v_i and y_i are the charge and the site fraction of the constituent i, respectively.

The Gibbs energy of the liquid phase is expressed as follows [2]:

$$G^{liq} = {}^{ref}G^{liq} + {}^{id}G^{liq} + {}^{ex}G^{liq} \tag{3}$$

$${}^{ref}G^{liq} = \sum_C \sum_A y_C y_A {}^{o}G^{liq}_{(C)(A)} + Q \cdot y_{Va} \sum_C y_C {}^{o}G^{liq}_{(C)} + Q \sum_B y_B {}^{o}G^{liq}_{(B)} \tag{4}$$

$${}^{id}G^{liq} = RT\left[P \sum_C y_C \ln y_C + Q\left(\sum_A y_A \ln y_A + y_{Va} \ln y_{Va} + \sum_B y_B \ln y_B\right)\right] \tag{5}$$

$$\begin{aligned} {}^{ex}G^{liq} = & \sum_{C_1}\sum_{C_2}\sum_A y_{C_1} y_{C_2} y_A L^{liq}_{(C_1,C_2)(A)} + \sum_{C_1}\sum_{C_2} y_{C_1} y_{C_2} y_{Va}^2 L^{liq}_{(C_1,C_2)(Va)} \\ & + \sum_C \sum_{A_1}\sum_{A_2} y_C y_{A_1} y_{A_2} L^{liq}_{(C)(A_1,A_2)} + \sum_C \sum_A y_C y_A y_{Va} L^{liq}_{(C)(A,Va)} \\ & + \sum_C \sum_A \sum_B y_C y_A y_B L^{liq}_{(C)(A,B)} + \sum_C \sum_B y_C y_B y_{Va} L^{liq}_{(C)(Va,B)} \\ & + \sum_{B_1}\sum_{B_2} y_{B_1} y_{B_2} L^{liq}_{(B_1,B2)} \end{aligned} \tag{6}$$

${}^{o}G^{liq}_{(C)(A)}$ is the Gibbs energy of $(v_C + v_A)$ moles of atoms of liquid $Cv_A Av_C$, ${}^{o}G^{liq}_{(C)}$ and ${}^{o}G^{liq}_{(B)}$ are the Gibbs energy of pure liquid *C* and neutral species *B*, respectively.

The ideal term in Equation (19) is the contribution of the random configurational entropy on each sublattice. The "*L*" parameters in Equation (20) represent the interaction between species in each sublattice.

The choice of the constituents to describe the liquid phase is based on the assumption that the most-stable solid compounds should be represented in the melt [3].

Cubic fcc (Fe,Pu,U,Zr)$O_{2\pm x}$-c

In the following, only the model for the face centred cubic (fcc) $UO_{2\pm x}$ is described in detail.

The ideal crystalline structure of UO_2 is of the type CaF_2 with two sublattice $(U^{4+})(O^{2-})_2$. Uranium atoms form an fcc lattice with oxygen atoms located in the tetrahedral sites (Figure 1).

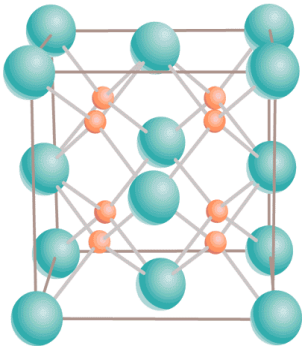

Figure 1: CaF_2 structure of ideal UO_2 from the perspective of uranium sublattice. Blue and red spheres are uranium and oxygen atoms, respectively

In reality the ideal fluorite structure contains interstitial sites and vacancy in the anionic sublattice. The hypo-stoichiometric UO_{2-x} is described introducing oxygen vacancies in the anionic sublattice. In order to maintain electroneutrality of the phase, U^{3+} ions are introduced in the cationic sublattice, leading to a modified sublattice model $(U^{3+},U^{4+})(O^{2-},Va)_2$. **The minimal composition in oxygen correspond to the neutral end-member $(U^{3+})(O^{-2}_{0.75},Va_{0.25})_2$ that is $UO_{1.5}$.**

In order to model the hyper-stoichiometric UO_{2+x} a third sublattice is added. This sublattice contains the oxygen interstitial outside the ideal sites of the CaF_2 structure. To maintain electroneutrality, the U^{5+} ion is added to the cation sublattice. In the present model, the U^{6+} ion is not taken into account [3]. The resulting complete sublattice model can be written as:

$$\left(U^{3+},U^{4+},U^{5+}\right)\left(O^{2-},Va\right)_2\left(O^{2-},Va\right)$$

The hyper-stoichiometric domain extends towards the maximum composition $(U^{5+})(O^{2-})_2(O^{-2}_{0.5},Va_{0.5})$. This corresponds to the neutral end-member $UO_{2.5}$.

The mathematic model for the fcc $UO_{2\pm x}$ phase can be represented graphically using the 3D prism in Figure 2.

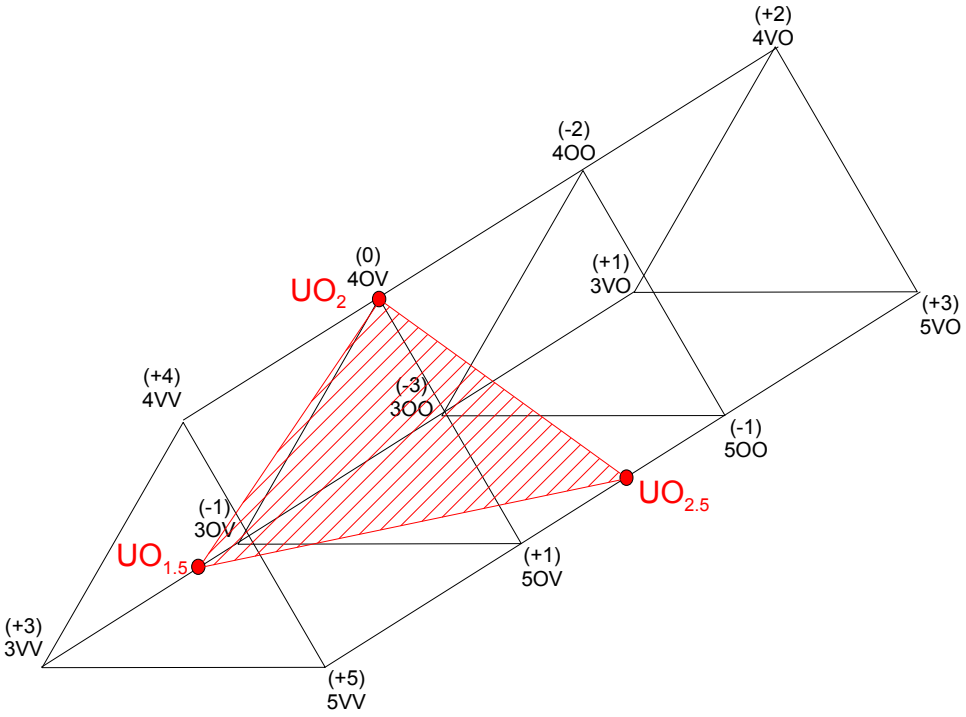

Figure 2: 3D representation of the three-sublattice model for the fcc $UO_{2\pm x}$ phase. The red surface is the domain of composition where the phase is neutral

The red surface in Figure 2 represents the domain of composition where the $UO_{2\pm x}$ phase is neutral and thermodynamically stable. It can be noted that the three corner of this surface are the three neutral end-members UO_2, $UO_{1.5}$ and $UO_{2.5}$. Most of the prism corners represent non-physical compounds. For example the corner 3VV stands for a compound with U^{3+} in the cationic sublattice, and vacancies Va in the second and third sublattice.

To decrease the number of Gibbs energy terms to assess for the end-members, very simple relations, based on mass balance equations, are fixed between these parameters, as reported in [3].

The model for the fcc mixed oxide is based on the $UO_{2\pm x}$ model described above. The additional cations are added to the first sublattice. The three sublattice model for the mixed oxide can be written as:

$$\left(Fe^{2+},Fe^{3+},Pu^{3+},Pu^{4+},U^{3+},U^{4+},U^{5+},Zr^{2+},Zr^{4+}\right)\left(O^{2-},Va\right)_2\left(O^{2-},Va\right)$$

The Gibbs energy of the mixed oxide can be written as follows:

$$G_m^{oxide_cubic} = \sum_i\sum_j\sum_k y_i y_j y_k^{'}\,{}^{o}G_{(i)(j)(k)}^{oxide_cubic} + RT\left(\sum_i y_i \ln y_i + 2\sum_j y_j \ln y_j + \sum_k y_k^{'} \ln y_k^{'}\right) + {}^{ex}G^{oxide_cubic} \quad (7)$$

The reference term is the sum of the product of the constituent fractions by the Gibbs energy of formation of the compounds. The Gibbs energy is defined considering a single constituent in each sublattice. Therefore, ${}^{o}G_{(i)(j)(k)}^{oxide_cubic}$ is the general expression for the Gibbs energy of all the end-members. As an example, the term ${}^{o}G_{(U^{4+})(O^{2-})(Va)}^{oxide_cubic}$ represents the standard Gibbs

energy of formation of the fcc phase with only U^{4+} species in the first sublattice, O^{2-} in the second sublattice and vacancies *Va* in the third sublattice, that is the UO_2 end-member.

The excess term is defined as follows:

$$
\begin{aligned}
&{}^{ex}G^{oxide_cubic} = y_{U^{3+}} y_{U^{4+}} y_{O^{2-}} y'_{Va} \left({}^{0}L^{oxide_cubic}_{(U^{3+},U^{4+})(O^{2-})(Va)} + (y_{U^{3+}} - y_{U^{4+}})\,{}^{1}L^{oxide_cubic}_{(U^{3+},U^{4+})(O^{2-})(Va)}\right) && \left.\vphantom{x}\right\} \rightarrow UO_{2\pm x}\\
&+ y_{U^{4+}} y_{U^{5+}} y_{O^{2-}} y'_{O^{2-}}\,{}^{0}L^{oxide_cubic}_{(U^{4+},U^{5+})(O^{2-})(O^{2-})} && \\
&+ y_{Pu^{3+}} y_{Pu^{4+}} y_{*} y'_{*} \left({}^{0}L^{oxide_cubic}_{(Pu^{3+},Pu^{4+})(*)(*)} + (y_{Pu^{3+}} - y_{Pu^{4+}})\,{}^{1}L^{oxide_cubic}_{(Pu^{3+},Pu^{4+})(*)(*)}\right) && \rightarrow PuO_{2-x}\\
&+ y_{Zr^{2+}} y_{Zr^{4+}} y_{*} y'_{*} \left({}^{0}L^{oxide_cubic}_{(Zr^{2+},Zr^{4+})(*)(*)} + (y_{Zr^{2+}} - y_{Zr^{4+}})\,{}^{1}L^{oxide_cubic}_{(Zr^{2+},Zr^{4+})(*)(*)}\right) && \rightarrow ZrO_{2-x}\\
&+ y_{U^{4+}} y_{Pu^{4+}} y_{O^{2-}} y'_{Va}\,{}^{0}L^{oxide_cubic}_{(U^{4+},Pu^{4+})(O^{2-})(Va)} && \left.\vphantom{x}\right.\\
&+ y_{U^{4+}} y_{Pu^{3+}} y_{O^{2-}} y'_{Va}\,{}^{0}L^{oxide_cubic}_{(U^{4+},Pu^{3+})(O^{2-})(Va)} && \left.\vphantom{x}\right\} (U,Pu)O_{2\pm x}\\
&+ y_{U^{4+}} y_{Pu^{3+}} y_{Va} y'_{Va}\,{}^{0}L^{oxide_cubic}_{(U^{4+},Pu^{3+})(Va)(Va)} && \left.\vphantom{x}\right.\\
&+ y_{U^{5+}} y_{Pu^{4+}} y_{O^{2-}} y'_{*}\,{}^{0}L^{oxide_cubic}_{(U^{5+},Pu^{4+})(O^{2-})(*)} && \left.\vphantom{x}\right.\\
&+ y_{U^{4+}} y_{Zr^{4+}} y_{O^{2-}} y'_{Va}\,{}^{0}L^{oxide_cubic}_{(U^{4+},Zr^{4+})(O^{2-})(Va)} && \left.\vphantom{x}\right.\\
&+ y_{U^{4+}} y_{Zr^{2+}} y_{O^{2-}} y'_{Va}\,{}^{0}L^{oxide_cubic}_{(U^{4+},Zr^{2+})(O^{2-})(Va)} && \left.\vphantom{x}\right\} (U,Zr)O_{2\pm x}\\
&+ y_{U^{3+}} y_{Zr^{4+}} y_{O^{2-}} y'_{Va}\,{}^{0}L^{oxide_cubic}_{(U^{4+},Zr^{4+})(O^{2-})(Va)} && \left.\vphantom{x}\right.\\
&+ y_{U^{4+}} y_{Zr^{4+}} y_{O^{2-}} y_{Va} y'_{Va}\,{}^{0}L^{oxide_cubic}_{(U^{4+},Zr^{4+})(O^{2-},Va)(Va)} && \left.\vphantom{x}\right.\\
&+ y_{Pu^{4+}} y_{Zr^{4+}} y_{O^{2-}} y'_{Va}\,{}^{0}L^{oxide_cubic}_{(Pu^{4+},Zr^{4+})(O^{2-})(Va)} && \rightarrow (Pu,Zr)O_{2-x}\\
&+ y_{U^{4+}} y_{Fe^{2+}} y_{*} y'_{*} \left({}^{0}L^{oxide_cubic}_{(U^{4+},Fe^{2+})(*)(*)} + (y_{U^{4+}} - y_{Fe^{2+}})\,{}^{1}L^{oxide_cubic}_{(U^{4+},Fe^{2+})(*)(*)}\right) && \left.\vphantom{x}\right\} (U,Fe)O_{2-x}\\
&+ y_{U^{4+}} y_{U^{5+}} y_{Fe^{2+}} y_{*} y'_{*}\,{}^{0}L^{oxide_cubic}_{(U^{4+},U^{5+},Fe^{2+})(*)(*)} && \left.\vphantom{x}\right.\\
&+ y_{Zr^{4+}} y_{Fe^{2+}} y_{O^{2-}} y'_{Va}\,{}^{0}L^{oxide_cubic}_{(Zr^{4+},Fe^{2+})(O^{2-})(Va)} && \left.\vphantom{x}\right\} (Zr,Fe)O_{2-x}\\
&++ y_{Zr^{4+}} y_{Fe^{3+}} y_{O^{2-}} y'_{Va}\,{}^{0}L^{oxide_cubic}_{(Zr^{4+},Fe^{3+})(O^{2-})(Va)} && \left.\vphantom{x}\right.
\end{aligned}
\qquad (8)
$$

The excess terms for the $UO_{2\pm x}$, PuO_{2-x} and $(Pu,U)O_{2\pm x}$ oxides are reported in [3]. The excess terms for ZrO_{2-x}-c, $(U,Zr)O_{2\pm x}$, $(Pu,Zr)O_{2-x}$-c, $(U,Fe)O_{2-x}$-c and $(Zr,Fe)O_{2-x}$-c have been assessed in this work, and are reported in Appendix D.

Monoclinic (Fe,Pu,Zr)O_2-m

The mathematical model describing the monoclinic phase is:

$$\left(Fe^{2+}, Fe^{3+}, Pu^{4+}, Zr^{4+}\right)\left(O^{2-}, Va\right)_2$$

Liang et al. [4] described the monoclinic allotropic form of ZrO_2 as a stoichiometric solid compound. To account the presence of U, Pu and Fe, the thermodynamic description of the phase has been modified. A two-sublattice model is used. The Gibbs energy of the monoclinic phase is written as:

$$G_m^{oxide_mono} = \sum_i \sum_j y_i y_j \, {}^o G_{(i)(j)}^{oxide_mono} + RT\left(\sum_i y_i \ln y_i + 2\sum_j y_j \ln y_j \right) \quad (9)$$

No interaction parameters have been assessed for this phase.

Tetragonal (Fe,Pu,U,Zr)O_2-t

As for the monoclinic phase, a two-sublattice model has been used to describe the tetragonal phase:

$$\left(Fe^{2+}, Fe^{3+}, Pu^{4+}, U^{4+}, Zr^{4+}\right)\left(O^{2-}, Va\right)_2$$

The model reported by Liang et al. [4] has been modified to take into account the addition of Fe^{2+}, Fe^{3+}, Pu^{4+} and U^{4+}.

The Gibbs energy of the tetragonal phase is written as:

$$G_m^{oxide_tetra} = \sum_i \sum_j y_i y_j \, {}^o G_{(i)(j)}^{oxide_tetra} + RT\left(\sum_i y_i \ln y_i + 2\sum_j y_j \ln y_j \right) + {}^{ex}G^{oxide_tetra} \quad (10)$$

The excess term of the tetragonal phase is defined as:

$${}^{ex}G^{oxide_tetra} = y_{U^{4+}} y_{Zr^{4+}} \, {}^0L_{(U^{4+},Zr^{4+})(O^{2-})}^{oxide_tetra} + y_{Zr^{4+}} y_{Fe^{2+}} \, {}^0L_{(Zr^{4+},Fe^{2+})(O^{2-})}^{oxide_tetra} + y_{Zr^{4+}} y_{Fe^{3+}} \, {}^0L_{(Zr^{4+},Fe^{3+})(O^{2-})}^{oxide_tetra} \quad (11)$$

Pyrochlore $Pu_2Zr_2O_{7+x}$

The sublattice model used for the pyrochlore phase is taken form Kurata (private communication) [5]:

$$(Zr^{4+})_2 (Pu^{3+}, Pu^{4+})_2 (O^{2-})_7 (O^{2-}, Va)$$

The phase has a composition ranging from $Pu_2Zr_2O_7$ to $Pu_2Zr_2O_8$. However, no evidence of the existence of pyrochlore phase was shown in the PuO_2-ZrO_2 section. The interaction parameters are also taken from Kurata (private communication) [5].

Spinel

The current model is based on the Fabrichnaya & Pavlyuchkov work [6]. Only Zr solubility in spinel phase is taken into account on the bases of Jones et al. [7] and Kiminami [8], [9] data. The sublattice model of the spinel phase is written as follow:

$$\left(Fe^{2+}, Fe^{3+}, Zr^{4+}\right)\left(Fe^{2+}, Fe^{3+}, Va\right)_2 \left(Fe^{2+}, Va\right)_2 \left(O^{2-}\right)_4$$

The Gibbs energy of one of the end-members ${}^o G_{(Zr^{4+})(Fe^{3+})(Va)(O^{2-})}^{spinel}$ defined by the authors has been modified. The enthalpic term has been modified in order to better fit the oxygen partial

pressure data of Katsura et al. [10] in the three-phase regions [ZrO_2-t+γ-Fe+FeO], [ZrO_2-t+FeO+Fe_2O_3] and [ZrO_2-t+Fe_2O_3+Fe_3O_4].

Corundum

The sublattice model adopted for corundum phase is written as follow:

$$\left(Fe^{2+},Fe^{3+},Zr^{4+}\right)_2\left(Fe^{2+},O^{2-},Va\right)\left(O^{2-}\right)_3$$

As for spinel phase, the model published by Fabrichnaya & Pavlyuchkov [6] has been used as a start point for the assessment. In the version reported in [6], the authors assessed the Gibbs energy of two end-members, ${}^{o}G^{corundum}_{(Zr^{4+})(O^{2-})(O^{2-})}$ and ${}^{o}G^{corundum}_{(Zr^{4+})(Va)(O^{2-})}$, and an interaction parameter ${}^{0}L^{corundum}_{(Fe^{3+},Zr^{4+})(O^{2-},Va)(O^{2-})}$. In the present work, the Gibbs energy of the end-members has been modified to fit the solubility data of Kiminami [8], [9]. Furthermore, the interaction parameter has not been considered.

Hcp α-(Zr,Fe,Pu,U)(O)

The sublattice model of the α-(Zr,Fe,Pu,U)(O) phase is written as follows:

$$\left(Fe,Pu,U,Zr\right)\left(O,Va\right)_{0.5}$$

In order to take into account the solubility of U in α-Zr(O), two end-members - ${}^{o}G^{hcp}_{(U)(O)}$ and ${}^{o}G^{hcp}_{(U)(Va)}$ - are introduced and the ternary interaction parameter ${}^{0}L^{hcp}_{(U,Zr)(O)}$ has been assessed.

Effect of W on the solidification path of sample OUZr_1

In Chapter 3, it was highlighted the effect of W on the annealed O-U-Zr samples. Due to the extreme temperature conditions, part of the W-crucible reacted with the samples, leading to the presence of a non-negligible amount of W dissolved in the solidified sample. Thanks to thermodynamic calculations, the effect of W on the solidification behaviour of the O-U-Zr samples can be investigated. The presence of a W_2Zr compound within the solidified sample can be explained by using solidification path calculations.

The U-W and Zr-W binary phase diagram are reported in Figure 3.

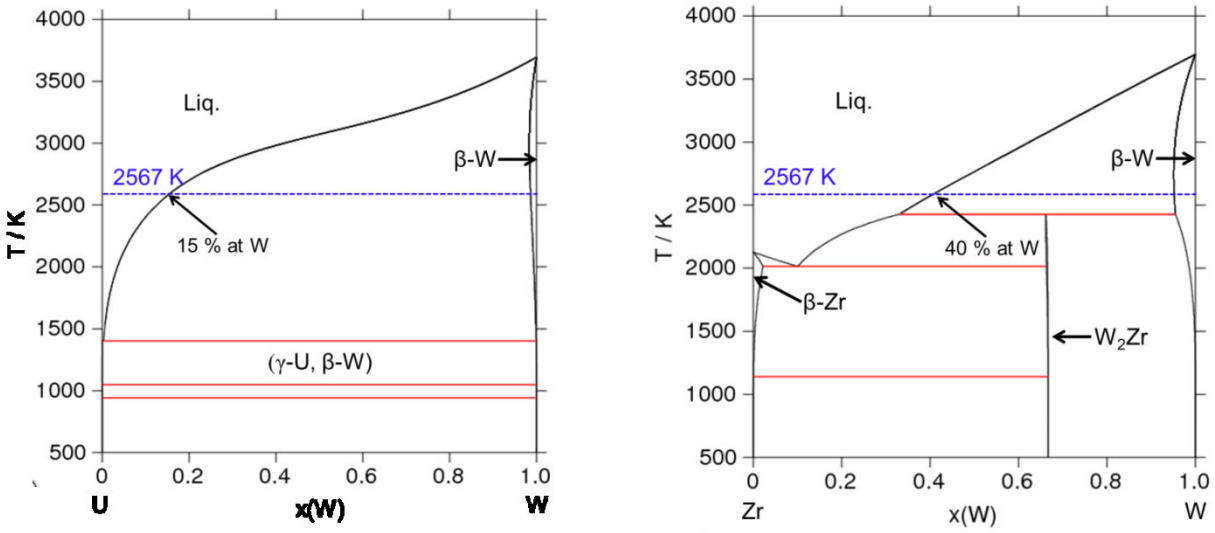

(a) (b)

Figure 3: (a) U-W binary phase diagram; (b) Zr-W binary phase diagram

At 2567 K, the solubility of W in liquid U and Zr is noticeable (15 at % and 40 % at, respectively).

The global composition measured by WDS of solidified sample OUZr_1 is $O_{0.385}U_{0.101}Zr_{0.500}W_{0.014}$. Considering the measured composition of sample OUZr_1 without taking into account the O contribution, a hypothetic metallic mixture $U_{0.164}W_{0.024}Zr_{0.812}$ is obtained. This composition on a ternary isothermal section of the U-W-Zr system at 2567 K is in the liquid region (Figure 4).

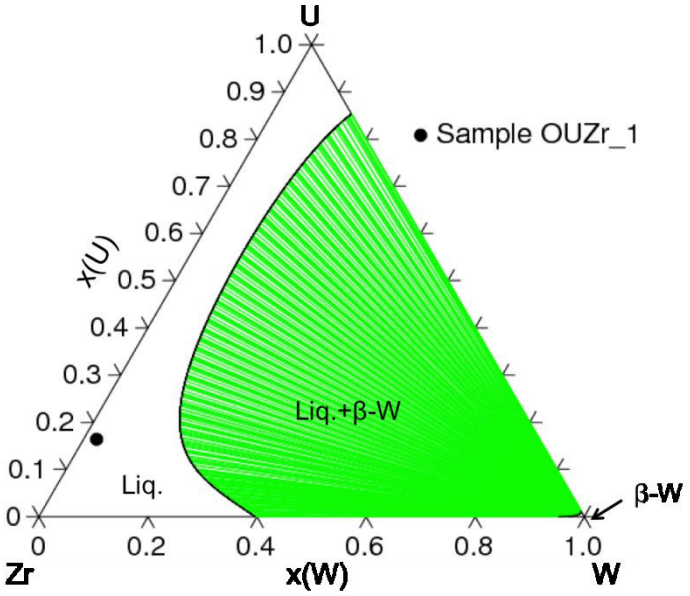

Figure 4: Isothermal U-W-Zr section calculated at 2567 K

However, the O is practically insoluble in W. Considering the global composition of sample OUZr_1 at 2567 K, a two-phase equilibrium is produced between an O-rich liquid phase and a β-W(Zr,εU) solid phase with a composition $W_{0.986}Zr_{0.013}U_{0.001}$ (εU means that U-content is negligible in this phase). The composition of the liquid phase, $O_{0.391}U_{0.102}Zr_{0.507}$, is the same as that used for the calculation on sample OUZr_1 after applying the correction for W. W preferentially stays in a solid solution in equilibrium with an O-containing liquid instead of forming a single liquid phase.

During cooling, the composition of the β-W(Zr,εU) phase does not vary significantly. The separated cooling path followed by the β-W(Zr,εU) phase is reported in Figure 5.

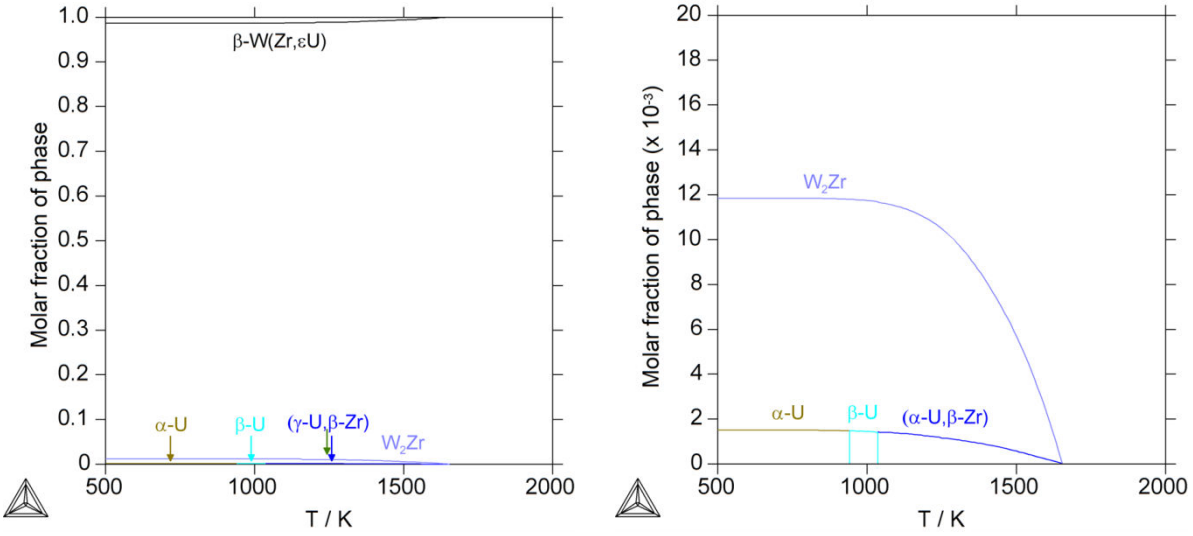

Figure 5: (a) Cooling path followed by the β-W(Zr,εU) phase; (b) close up on the ternary reaction β-W(Zr,εU) → β-W + (γU,βZr) + W_2Zr

At 1650 K, the ternary reaction β-W(Zr,εU) → [β-W + (γU,βZr) + W_2Zr] takes place (Figure 5b). This reaction corresponds to the formation of the W_2Zr rings surrounding the pure W shown in Figure 7 in Chapter 3. From the calculation, a negligible amount of (γU,βZr) phase should also precipitates. In Figure 5b, the (γU,βZr) phase represents only 0.16 mol%.

The detection of this phase is thus challenging. In fact, the analyses performed at the LMAC, CEA Marcoule, did not show a clear presence of this phase.

It can be concluded that the correction for W applied to O-U-Zr samples is satisfactory, leading to results in agreement with calculations performed taking into account the W contribution.

The cooling path calculation performed on the β-W(Zr,εU) allows to explain the presence of W_2Zr rings surrounding pure W precipitates.

References

[1] M. Hillert, B. Jansson, B. Sundman, and J. Agren, "A Two-Sublattice Model for Molten Solutions with Different Tendency for Ionization," *Metall. Trans.*, vol. 16A, pp. 261–266, 1985.

[2] N. Saunders and A. Miodokwin, Book, *CALPHAD - Calculation of Phase Diagrams, A Comprehensive Guide*. 1998.

[3] C. Guéneau, N. Dupin, B. Sundman, C. Martial, J. C. Dumas, S. Gossé, S. Chatain, F. De Bruycker, D. Manara, and R. J. M. Konings, "Thermodynamic modelling of advanced oxide and carbide nuclear fuels: Description of the U-Pu-O-C systems," *J. Nucl. Mater.*, vol. 419, no. 1–3, pp. 145–167, 2011.

[4] P. Liang, N. Dupin, S. Fries, H. J. Seifert, I. Ansara, H. Lukas, and A. F, "Thermodynamic Assessment of the Zr-O Binary System," *Zeitschrift fur Met.*, vol. 92, no. 7, pp. 747–756, 2001.

[5] M. Kurata, "Private communication," 2014.

[6] O. Fabrichnaya and D. Pavlyuchkov, "Assessment of Experimental Data and Thermodynamic Modeling in the Zr-Fe-O System," *Metall. Mater. Trans. A*, 2015.

[7] T. S. Jones, S. Kimura, and A. Muan, "Phase Relation in the System FeO-Fe_2O_3-ZrO_2-SiO_2," *J. Am. Ceram. Soc.*, vol. 50, pp. 137–142, 1967.

[8] R. H. G. A. Kiminami, "Estudo do sistema ZrO_2-FeO-Fe_2O_3 através da termogravimetria à pressao parcial de oxygeno do ar e temperaturas de até 1500 ^{o}C," *Ceramica*, vol. 33, no. 213, pp. 207–210, 1987.

[9] R. H. G. A. Kiminami, "Equiíbrio de fases do sistema ZrO_2-FeO-Fe_2O_3 à pO_2=2 10^{-3} atm," *Ceramica*, vol. 34, no. 223, pp. 121–123, 1988.

[10] T. Katsura, M. Wakihara, S.-I. Hara, and T. Sugihara, "Some Thermodynamic Properties in Spinel Solid Solutions with the Fe_3O_4 Component," *J. Solid State Chem.*, vol. 13, pp. 107–113, 1975.

Appendix D – prototypic in-vessel corium O-Fe-Pu-U-Zr assessed thermodynamic model

Thermodynamic parameters for the assessed phases (J mol.$^{-1}$)	Reference
Liquid : $\left(Fe^{2+},Pu^{4+},U^{4+},Zr^{4+}\right)_P\left(O^{-2},Va,FeO_{3/2},O,PuO_2\right)_Q$	
$G^{liq}_{(Fe^{2+})(O^{2-})}-2H^{SER}_{O}-2H^{SER}_{Fe}$	[1]
$G^{liq}_{(Fe^{2+})(O^{2-})}-H^{SER}_{O}$	[1]
$G^{liq}_{(Pu^{3+})(O^{2-})}-3H^{SER}_{O}-2H^{SER}_{Pu}$	[2]
$G^{liq}_{(Pu^{3+})(Va)}-H^{SER}_{Pu}$	[3]
$G^{liq}_{(U^{4+})(O^{2-})}-4H^{SER}_{O}-2H^{SER}_{U}$	[2]
$G^{liq}_{(U^{4+})(Va)}-H^{SER}_{U}$	[3]
$G^{liq}_{(Zr^{4+})(O^{2-})}-4H^{SER}_{O}-2H^{SER}_{Zr}$	[4]
$G^{liq}_{(Zr^{4+})(Va)}-H^{SER}_{Zr}$	[3]
$G^{liq}_{(FeO_{3/2})}-1.5H^{SER}_{O}-H^{SER}_{Fe}$	[1]
$G^{liq}_{(O)}-H^{SER}_{O}$	[3]
$G^{liq}_{(PuO_2)}-2H^{SER}_{O}-H^{SER}_{Pu}$	[2]
$L^{liq}_{(Fe^{2+})(O^{2-},Va)}$	[1]
$L^{liq}_{(Fe^{2+})(O^{2-},FeO_{3/2})}$	[1]
$L^{liq}_{(Fe^{2+})(Va,FeO_{3/2})}$	[1]
$L^{liq}_{(FeO_{3/2},O)}$	[1]
$L^{liq}_{(Fe^{2+},Pu^{3+})(Va)}$	[5]
$L^{liq}_{(Fe^{2+},U^{4+})(Va)}$	[5]
$L^{liq}_{(Fe^{2+},U^{4+})(O^{2-})}=-120000+100000(y_{Fe^{2+}}-y_{U^{4+}})$	This work
$L^{liq}_{(Fe^{2+},Zr^{4+})(O^{2-})}=-42000+3683(y_{Fe^{2+}}-y_{Zr^{4+}})$	This work
$L^{liq}_{(Fe^{2+},Zr^{4+})(Va)}$	[6,7]
$L^{liq}_{(Fe^{2+},U^{4+},Zr^{4+})(Va)}$	[8]
$L^{liq}_{(Pu^{3+})(O^{2-},Va)}$	[2]
$L^{liq}_{(Pu^{3+})(O^{2-},PuO_2)}$	[2]

$L^{liq}_{(Pu^{3+},U^{4+})(O^{2-})}$	[2]
$L^{liq}_{(Pu^{3+},U^{4+})(O^{2-},PuO_2)}$	[2]
$L^{liq}_{(U^{4+})(O^{2-},Va)}$	[2]
$L^{liq}_{(U^{4+})(O^{2-},O)}$	[2]
$L^{liq}_{(U^{4+})(O^{2-},PuO_2)}$	[2]
$L^{liq}_{(U^{4+},Zr^{4+})(O^{2-})} = -70000 + 40000(y_{U^{4+}} - y_{Zr^{4+}})$	[9]
$L^{liq}_{(Zr^{4+})(O^{2-},Va)}$	[4]
$L^{liq}_{(Zr^{4+})(O^{2-},O)}$	[4]
$L^{liq}_{(Zr^{4+})(O^{2-},FeO_{3/2})}$	[10]
$L^{liq}_{(Zr^{4+})(O^{2-},PuO_2)} = 50000$	This work
Cubic mixed oxide (Fe,Pu,U,Zr)$O_{2\pm x}$-c : $\left(Fe^{2+},Fe^{3+},Pu^{3+},Pu^{4+},U^{3+},U^{4+},U^{5+},Zr^{2+},Zr^{4+}\right)\left(O^{2-},Va\right)_2\left(O^{2-},Va\right)$	
$G^{oxide_cubic}_{(Fe^{2+})(O^{2-})(O^{2-})} - 3H^{SER}_O - H^{SER}_{Fe} = 500000 + 80T$	This work
$G^{oxide_cubic}_{(Fe^{3+})(O^{2-})(O^{2-})} - 3H^{SER}_O - H^{SER}_{Fe} = 80000 + 80T$	This work
$G^{oxide_cubic}_{(Fe^{2+})(Va)(O^{2-})} - H^{SER}_O - H^{SER}_{Fe} = 500000 + 80T$	This work
$G^{oxide_cubic}_{(Fe^{3+})(Va)(O^{2-})} - H^{SER}_O - H^{SER}_{Fe} = 80000 + 80T$	This work
$G^{oxide_cubic}_{(Fe^{2+})(O^{2-})(Va)} - 2H^{SER}_O - H^{SER}_{Fe}$	[10]
$G^{oxide_cubic}_{(Fe^{3+})(O^{2-})(Va)} - 2H^{SER}_O - H^{SER}_{Fe} = 0.5G^{oxide_mono}_{(Zr^{4+})(O^{2-})} + 0.5G^{SER}_O + 82734 + 7.35T$	This work
$G^{oxide_cubic}_{(Fe^{2+})(Va)(Va)} - H^{SER}_{Fe}$	[10]
$G^{oxide_cubic}_{(Fe^{3+})(Va)(Va)} - H^{SER}_{Fe} = -1.5G^{SER}_O + 0.5GFE2O3 + 150000 + 9.35T$	This work
$G^{oxide_cubic}_{(Pu^{3+})(O^{2-})(O^{2-})} - 3H^{SER}_O - H^{SER}_{Pu}$	[2]
$G^{oxide_cubic}_{(Pu^{4+})(O^{2-})(O^{2-})} - 3H^{SER}_O - H^{SER}_{Pu}$	[2]
$G^{oxide_cubic}_{(Pu^{3+})(Va)(O^{2-})} - H^{SER}_O - H^{SER}_{Pu}$	[2]
$G^{oxide_cubic}_{(Pu^{4+})(Va)(O^{2-})} - H^{SER}_O - H^{SER}_{Pu}$	[2]
$G^{oxide_cubic}_{(Pu^{3+})(O^{2-})(Va)} - 2H^{SER}_O - H^{SER}_{Pu}$	[2]
$G^{oxide_cubic}_{(Pu^{4+})(O^{2-})(Va)} - 2H^{SER}_O - H^{SER}_{Pu}$	[2]
$G^{oxide_cubic}_{(Pu^{3+})(Va)(Va)} - H^{SER}_{Pu}$	[2]
$G^{oxide_cubic}_{(Pu^{4+})(Va)(Va)} - H^{SER}_{Pu}$	[2]

$G^{oxide_cubic}_{(U^{3+})(O^{2-})(O^{2-})} - 3H^{SER}_{O} - H^{SER}_{U}$	[2]
$G^{oxide_cubic}_{(U^{4+})(O^{2-})(O^{2-})} - 3H^{SER}_{O} - H^{SER}_{U}$	[2]
$G^{oxide_cubic}_{(U^{5+})(O^{2-})(O^{2-})} - 3H^{SER}_{O} - H^{SER}_{U}$	[2]
$G^{oxide_cubic}_{(U^{3+})(Va)(O^{2-})} - H^{SER}_{O} - H^{SER}_{U}$	[2]
$G^{oxide_cubic}_{(U^{4+})(Va)(O^{2-})} - H^{SER}_{O} - H^{SER}_{U}$	[2]
$G^{oxide_cubic}_{(U^{5+})(Va)(O^{2-})} - H^{SER}_{O} - H^{SER}_{U}$	[2]
$G^{oxide_cubic}_{(U^{3+})(O^{2-})(Va)} - 2H^{SER}_{O} - H^{SER}_{U}$	[2]
$G^{oxide_cubic}_{(U^{4+})(O^{2-})(Va)} - 2H^{SER}_{O} - H^{SER}_{U}$	[2]
$G^{oxide_cubic}_{(U^{5+})(O^{2-})(Va)} - 2H^{SER}_{O} - H^{SER}_{U}$	[2]
$G^{oxide_cubic}_{(U^{3+})(Va)(Va)} - H^{SER}_{U}$	[2]
$G^{oxide_cubic}_{(U^{4+})(Va)(Va)} - H^{SER}_{U}$	[2]
$G^{oxide_cubic}_{(U^{5+})(Va)(Va)} - H^{SER}_{U}$	[2]
$G^{oxide_cubic}_{(Zr^{2+})(O^{2-})(O^{2-})} - 3H^{SER}_{O} - H^{SER}_{Zr} = -263000 + 28T + G^{SER}_{Zr} + 2G^{SER}_{O}$	This work
$G^{oxide_cubic}_{(Zr^{4+})(O^{2-})(O^{2-})} - 3H^{SER}_{O} - H^{SER}_{Zr} = \text{-}937342 \text{-} 49.9\text{T} + 29.65\text{T}\ln(\text{T}) \text{-} 0.01\text{T}^2 + G^{SER}_{Zr} + 2G^{SER}_{O}$	This work
$G^{oxide_cubic}_{(Zr^{2+})(Va)(O^{2-})} - H^{SER}_{O} - H^{SER}_{Zr} = -263000 + 28T + G^{SER}_{Zr}$	This work
$G^{oxide_cubic}_{(Zr^{4+})(Va)(O^{2-})} - H^{SER}_{O} - H^{SER}_{Zr} = \text{-}937342 \text{-} 49.9\text{T} + 29.65\text{T}\ln(\text{T}) \text{-} 0.01\text{T}^2 + G^{SER}_{Zr}$	This work
$G^{oxide_cubic}_{(Zr^{2+})(O^{2-})(Va)} - 2H^{SER}_{O} - H^{SER}_{Zr} = -363000 + 28T + 2G^{SER}_{O} + G^{SER}_{Zr}$	This work
$G^{oxide_cubic}_{(Zr^{4+})(O^{2-})(Va)} - 2H^{SER}_{O} - H^{SER}_{Zr} = \text{-}1037342 \text{-} 49.9\text{T} + 29.65\text{T}\ln(\text{T}) \text{-} 0.01\text{T}^2 + G^{SER}_{Zr} + 2G^{SER}_{O}$	This work
$G^{oxide_cubic}_{(Zr^{2+})(Va)(Va)} - H^{SER}_{Zr} = -363000 + 28T + G^{SER}_{Zr}$	This work
$G^{oxide_cubic}_{(Zr^{4+})(Va)(Va)} - H^{SER}_{Zr} = \text{-}1037342 \text{-} 49.9\text{T} + 29.65\text{T}\ln(\text{T}) \text{-} 0.01\text{T}^2 + G^{SER}_{Zr}$	This work
$L^{oxide_cubic}_{(Fe^{2+},U^{4+})(*)(*)} = -300000 + 20T + 210000(y_{Fe^{2+}} - y_{U^{4+}})$	This work
$L^{oxide_cubic}_{(Fe^{2+},U^{4+},U^{5+})(*)(*)} = -500000$	This work
$L^{oxide_cubic}_{(Fe^{2+},Zr^{4+})(O^{2-})(Va)} = -76667 + 28.9T$	This work
$L^{oxide_cubic}_{(Fe^{3+},Zr^{4+})(O^{2-})(Va)}$	[10]
$L^{oxide_cubic}_{(Pu^{3+},Pu^{4+})(O^{2-})(Va)}$	[2]
$L^{oxide_cubic}_{(Pu^{3+},Pu^{4+})(Va)(Va)}$	[2]

$L^{oxide_cubic}_{(Pu^{3+},U^{4+})(O^{2-})(Va)}$	[2]
$L^{oxide_cubic}_{(Pu^{4+},U^{4+})(O^{2-})(Va)}$	[2]
$L^{oxide_cubic}_{(Pu^{4+},U^{3+})(O^{2-})(Va)}$	[2]
$L^{oxide_cubic}_{(Pu^{3+},U^{5+})(O^{2-})(*)}$	[2]
$L^{oxide_cubic}_{(Pu^{3+},U^{4+})(Va)(Va)}$	[2]
$L^{oxide_cubic}_{(Pu^{4+},Zr^{4+})(O^{2-})(Va)} = +10000$	This work
$L^{oxide_cubic}_{(U^{3+},U^{4+})(O^{2-})(Va)}$	[2]
$L^{oxide_cubic}_{(U^{4+},U^{5+})(O^{2-})(O^{2-})}$	[2]
$L^{oxide_cubic}_{(U^{3+},Zr^{4+})(O^{2-})(Va)} = +200000$	This work
$L^{oxide_cubic}_{(U^{4+},Zr^{4+})(O^{2-})(Va)} = +86234 - 34.36\,\mathrm{T} + 12094\ (y_{U^{4+}} - y_{Zr^{4+}})$	[9]
$L^{oxide_cubic}_{(U^{4+},Zr^{4+})(O^{2-},Va)(Va)} = -430000$	This work
$L^{oxide_cubic}_{(U^{4+},Zr^{2+})(O^{2-})(Va)} = -300000$	This work
$L^{oxide_cubic}_{(Zr^{2+},Zr^{4+})(*)(*)} = -221948 + 96.44803T - 22085(y_{Zr^{2+}} - y_{Zr^{4+}})$	[8]
Tetragonal (Fe,Pu,U,Zr)O_2-t : $\left(Fe^{2+},Fe^{3+},Pu^{4+},U^{3+},U^{4+},Zr^{4+}\right)\left(O^{2-},Va\right)_2$	
$G^{oxide_tetr}_{(Fe^{2+})(O^{2-})} - 2H^{SER}_{O} - H^{SER}_{Fe}$	[10]
$G^{oxide_tetr}_{(Fe^{3+})(O^{2-})} - 2H^{SER}_{O} - H^{SER}_{Fe} = 0.5G^{oxide_cubic}_{(Zr^{4+})(O^{2-})(Va)} + G^{SER}_{O} + 150000 + 9.35T$	This work
$G^{oxide_tetr}_{(Fe^{2+})(Va)} - H^{SER}_{Fe} = GWUSTITE - G^{SER}_{O} + 120000 + 11.5263T$	This work
$G^{oxide_tetr}_{(Fe^{3+})(Va)} - H^{SER}_{Fe} = 0.5GGFE2O3 - 1.5G^{SER}_{O} + 150000 + 9.35T$	This work
$G^{oxide_tetr}_{(Pu^{4+})(O^{2-})} - 2H^{SER}_{O} - H^{SER}_{Pu} = G^{oxide_cubic}_{(Pu^{4+})(O^{2-})(Va)} + 40000$	This work
$G^{oxide_tetr}_{(Pu^{4+})(Va)} - H^{SER}_{Pu} = G^{oxide_cubic}_{(Pu^{4+})(O^{2-})(Va)} + 40000 - 2G^{SER}_{O}$	This work
$G^{oxide_tetr}_{(U^{4+})(O^{2-})} - 2H^{SER}_{O} - H^{SER}_{U} = G^{oxide_cubic}_{(U^{4+})(O^{2-})(Va)} + 40000$	[9]
$G^{oxide_tetr}_{(U^{4+})(Va)} - H^{SER}_{U} = G^{oxide_cubic}_{(U^{4+})(O^{2-})(Va)} - 2G^{SER}_{O}$	[13]
$G^{oxide_tetr}_{(Zr^{4+})(O^{2-})} - 2H^{SER}_{O} - H^{SER}_{Zr}$	[4]
$G^{oxide_tetr}_{(Zr^{4+})(Va)} - H^{SER}_{Zr} = G^{oxide_tetr}_{(Zr^{4+})(O^{2-})} - 2G^{SER}_{O}$	[13]
$L^{oxide_tetr}_{(Fe^{2+},Zr^{4+})(O^{2-})} = +30000$	This work
$L^{oxide_tetr}_{(Fe^{3+},Zr^{4+})(O^{2-})} = -40000$	This work
$L^{oxide_tetr}_{(U^{4+},Zr^{4+})(O^{2-})} = +41176 - 32.93\,\mathrm{T}$	[9]
Monoclinic (Fe,Pu,Zr)O_2-m : $\left(Fe^{2+},Fe^{3+},Pu^{4+},Zr^{4+}\right)\left(O^{2-},Va\right)_2$	
$G^{oxide_mono}_{(Fe^{2+})(O^{2-})} - 2H^{SER}_{O} - H^{SER}_{Fe}$	[10]
$G^{oxide_mono}_{(Fe^{3+})(O^{2-})} - 2H^{SER}_{O} - H^{SER}_{Fe} = 0.5G^{oxide_cubic}_{(Zr^{4+})(O^{2-})(Va)} + 0.5G^{SER}_{O} + 200000 + 9.35T$	This work

$G^{oxide_mono}_{(Fe^{2+})(Va)} - H^{SER}_{Fe}$	[10]
$G^{oxide_mono}_{(Fe^{3+})(Va)} - 2H^{SER}_{O} - H^{SER}_{Fe}$	[10]
$G^{oxide_mono}_{(Pu^{4+})(O^{2-})} - 2H^{SER}_{O} - H^{SER}_{Pu} = G^{oxide_cubic}_{(Pu^{4+})(O^{2-})(Va)} + 45000$	This work
$G^{oxide_mono}_{(Zr^{4+})(O^{2-})} - 2H^{SER}_{O} - H^{SER}_{Zr}$	[4]
$G^{oxide_mono}_{(Zr^{4+})(Va)} - H^{SER}_{Zr} = G^{oxide_mono}_{(Zr^{4+})(O^{2-})} - 2G^{SER}_{O}$	[13]
Pyrochlore $Zr_2Pu_2O_{7+x}$: $\left(Zr^{4+}\right)_2\left(Pu^{4+}\right)_2\left(O^{2-}\right)_7\left(O^{2-}\right)$	
$G^{pyrochlore}_{(Zr^{4+})(Pu^{3+})(O^{2-})(O^{2-})} - 8H^{SER}_{O} - 2H^{SER}_{Pu} - 2H^{SER}_{Zr}$	[11]
$G^{pyrochlore}_{(Zr^{4+})(Pu^{4+})(O^{2-})(O^{2-})} - 8H^{SER}_{O} - 2H^{SER}_{Pu} - 2H^{SER}_{Zr}$	[11]
$G^{pyrochlore}_{(Zr^{4+})(Pu^{3+})(O^{2-})(Va)} - 7H^{SER}_{O} - 2H^{SER}_{Pu} - 2H^{SER}_{Zr}$	[11]
$G^{pyrochlore}_{(Zr^{4+})(Pu^{4+})(O^{2-})(Va)} - 7H^{SER}_{O} - 2H^{SER}_{Pu} - 2H^{SER}_{Zr}$	[11]
Corundum : $\left(Fe^{2+},Fe^{3+},Zr^{4+}\right)_2\left(Fe^{3+},O^{2-},Va\right)\left(O^{2-}\right)_3$	[11]
$G^{corundum}_{(Fe^{2+})(Fe^{3+})(O^{2-})} - 3H^{SER}_{Fe} - 3H^{SER}_{O}$	[12]
$G^{corundum}_{(Fe^{2+})(O^{2-})(O^{2-})} - 2H^{SER}_{Fe} - 4H^{SER}_{O}$	[1]
$G^{corundum}_{(Fe^{2+})(Va)(O^{2-})} - H^{SER}_{Fe} - 3H^{SER}_{O}$	[1]
$G^{corundum}_{(Fe^{3+})(Fe^{3+})(O^{2-})} - 3H^{SER}_{Fe} - 3H^{SER}_{O}$	[12]
$G^{corundum}_{(Fe^{3+})(O^{2-})(O^{2-})} - 2H^{SER}_{Fe} - 4H^{SER}_{O}$	[1]
$G^{corundum}_{(Fe^{3+})(Va)(O^{2-})} - H^{SER}_{Fe} - 3H^{SER}_{O}$	[1]
$G^{corundum}_{(Zr^{4+})(O^{2-})(O^{2-})} - 2H^{SER}_{Zr} - 4H^{SER}_{O} = 2G^{oxide_mono}_{(Zr^{4+})(O^{2-})} + 255468 - 4T$	This work
$G^{corundum}_{(Zr^{4+})(Va)(O^{2-})} - 2H^{SER}_{Zr} - 4H^{SER}_{O} = 2G^{oxide_mono}_{(Zr^{4+})(O^{2-})} - G^{SER}_{O} + 255468 - 4T$	This work
Hcp α-(Fe,Pu,U,Zr)(O) : $\left(Fe,Pu,U,Zr\right)\left(O,Va\right)_{0.5}$	
$G^{hcp}_{(Fe)(O)} - H^{SER}_{Fe} - 0.5H^{SER}_{O}$	Not assessed
$G^{hcp}_{(Fe)(Va)} - H^{SER}_{Fe}$	Not assessed
$G^{hcp}_{(Pu)(O)} - H^{SER}_{Pu} - 0.5H^{SER}_{O}$	[13]
$G^{hcp}_{(Pu)(Va)} - H^{SER}_{Pu}$	[13]
$G^{hcp}_{(U)(O)} - H^{SER}_{U} - 0.5H^{SER}_{O}$	[13]
$G^{hcp}_{(U)(Va)} - H^{SER}_{U}$	[13]
$G^{hcp}_{(Zr)(O)} - H^{SER}_{Zr} - 0.5H^{SER}_{O}$	[13]
$G^{hcp}_{(Zr)(Va)} - H^{SER}_{Zr}$	[3]
$L^{hcp}_{(Fe,Pu)(Va)}$	[5]
$L^{hcp}_{(Fe,Zr)(Va)}$	[7]

$L^{hcp}_{(Pu,U)(Va)}$	[14]
$L^{hcp}_{(Pu,Zr)(Va)}$	[13]
$L^{hcp}_{(U,Zr)(O)} = -265000$	This work
$L^{hcp}_{(U,Zr)(Va)}$	[14]
$L^{hcp}_{(Zr)(O,Va)}$	[13]
Spinel : $\left(Fe^{2+},Fe^{3+},Zr^{4+}\right)\left(Fe^{2+},Fe^{3+},Va\right)_2\left(Fe^{2+},Va\right)_2\left(O^{2-}\right)_4$	
$G^{spinel}_{(Fe^{2+})(Fe^{2+})(Fe^{2+})(O^{2-})} - 5H^{SER}_{Fe} - 4H^{SER}_{O}$	[1]
$G^{spinel}_{(Fe^{2+})(Fe^{3+})(Fe^{2+})(O^{2-})} - 5H^{SER}_{Fe} - 4H^{SER}_{O}$	[1]
$G^{spinel}_{(Fe^{2+})(Va)(Fe^{2+})(O^{2-})} - 3H^{SER}_{Fe} - 4H^{SER}_{O}$	[1]
$G^{spinel}_{(Fe^{2+})(Fe^{2+})(Va)(O^{2-})} - 3H^{SER}_{Fe} - 4H^{SER}_{O}$	[1]
$G^{spinel}_{(Fe^{2+})(Fe^{3+})(Va)(O^{2-})} - 3H^{SER}_{Fe} - 4H^{SER}_{O}$	[1]
$G^{spinel}_{(Fe^{2+})(Va)(Va)(O^{2-})} - H^{SER}_{Fe} - 4H^{SER}_{O}$	[1]
$G^{spinel}_{(Fe^{3+})(Fe^{2+})(Fe^{2+})(O^{2-})} - 5H^{SER}_{Fe} - 4H^{SER}_{O}$	[1]
$G^{spinel}_{(Fe^{3+})(Fe^{3+})(Fe^{2+})(O^{2-})} - 5H^{SER}_{Fe} - 4H^{SER}_{O}$	[1]
$G^{spinel}_{(Fe^{3+})(Va)(Fe^{2+})(O^{2-})} - 3H^{SER}_{Fe} - 4H^{SER}_{O}$	[1]
$G^{spinel}_{(Fe^{3+})(Fe^{2+})(Va)(O^{2-})} - 3H^{SER}_{Fe} - 4H^{SER}_{O}$	[1]
$G^{spinel}_{(Fe^{3+})(Fe^{3+})(Va)(O^{2-})} - 3H^{SER}_{Fe} - 4H^{SER}_{O}$	[1]
$G^{spinel}_{(Fe^{3+})(Va)(Va)(O^{2-})} - H^{SER}_{Fe} - 4H^{SER}_{O}$	[1]
$G^{spinel}_{(Zr^{4+})(Fe^{2+})(Fe^{2+})(O^{2-})} - 4H^{SER}_{Fe} - 4H^{SER}_{O} - H^{SER}_{Zr}$	[10]
$G^{spinel}_{(Zr^{4+})(Fe^{3+})(Fe^{2+})(O^{2-})} - 4H^{SER}_{Fe} - 4H^{SER}_{O} - H^{SER}_{Zr}$	[10]
$G^{spinel}_{(Zr^{4+})(Va)(Fe^{2+})(O^{2-})} - 2H^{SER}_{Fe} - 4H^{SER}_{O} - H^{SER}_{Zr} = G^{oxide_mono}_{(Zr^{4+})(O^{2-})} + 2GWUSTUITE + 75468 - 4T$	This work
$G^{spinel}_{(Zr^{4+})(Fe^{2+})(Va)(O^{2-})} - 2H^{SER}_{Fe} - 4H^{SER}_{O} - H^{SER}_{Zr} = \vdots \quad G^{oxide_mono}_{(Zr^{4+})(O^{2-})} + 2GWUSTUITE + 65468 - 4T$	This work
$G^{spinel}_{(Zr^{4+})(Fe^{3+})(Va)(O^{2-})} - 2H^{SER}_{Fe} - 4H^{SER}_{O} - H^{SER}_{Zr} = G^{oxide_mono}_{(Zr^{4+})(O^{2-})} - G^{SER}_{O} + GFE2O3 + 2GWUSTUITE + 105468 + 11.8767T$	This work
$G^{spinel}_{(Zr^{4+})(Va)(Va)(O^{2-})} - 4H^{SER}_{O} - H^{SER}_{Zr} = G^{oxide_mono}_{(Zr^{4+})(O^{2-})} + 2G^{SER}_{O} + 5468 - 4T$	This work

The parameters GFE2O3 and GWUSTITE can be found in [12].

References

[1] B. Sundman, “An assessment of the Fe-O System,” *J. Phase Equilibria*, vol. 12, pp. 127–140, 1991.

[2] C. Guéneau, N. Dupin, B. Sundman, C. Martial, J. C. Dumas, S. Gossé, S. Chatain, F. De Bruycker, D. Manara, and R. J. M. Konings, “Thermodynamic modelling of advanced oxide and carbide nuclear fuels: Description of the U-Pu-O-C systems,” *J. Nucl. Mater.*, vol. 419, no. 1–3, pp. 145–167, 2011.

[3] A. T. Dinsdale, “SGTE data for pure elements,” *Calphad*, vol. 15, no. 4, pp. 317–425, Oct. 1991.

[4] P. Liang, N. Dupin, S. Fries, H. J. Seifert, I. Ansara, H. Lukas, and A. F, “Thermodynamic Assessment of the Zr-O Binary System,” *Zeitschrift fur Met.*, vol. 92, no. 7, pp. 747–756, 2001.

[5] M. Kurata, “Thermodynamic database on U-Pu-Zr-Np-Am-Fe alloy system II - Evaluation of Np, Am, and Fe containing systems -,” *IOP Conf. Ser. Mater. Sci. Eng.*, vol. 9, p. 012023, 2010.

[6] C. Toffolon-Masclet, J. C. Brachet, C. Servant, J. M. Joubert, P. Barberis, N. Dupin, and P. Zeller, “Contribution of Thermodynamic Calculation to Metallurgical Studies of Multi-Component Zirconium Based Alloys,” *J. ASTM Int.*, vol. 5, no. 7, p. ID JAI101122, 2008.

[7] C. Guéneau, S. Chatain, C. Toffolon-Masclet, P. Zeller, and N. Dupin, “Internal Report CEA,” 2005.

[8] N. Dupin, “Private communication,” 2014.

[9] M. Baichi, “Contribution à l’étude du corium d’un réacteur nucléaire accidenté : aspects puissance résiduelle et thermodynamique des systèmes U-UO_2 et UO_2-ZrO_2,” PhD Thesis INP Grenoble, 2001.

[10] O. Fabrichnaya and D. Pavlyuchkov, “Assessment of Experimental Data and Thermodynamic Modeling in the Zr-Fe-O System,” *Metall. Mater. Trans. A*, 2015.

[11] M. Kurata, “Private communication,” 2014.

[12] L. Kjellqvist, M. Selleby, and B. Sundman, “Thermodynamic modelling of the Cr-Fe-Ni-O system,” *Comput. Coupling Phase Diagr. Thermochem.*, vol. 32, pp. 577–592, 2008.

[13] TAF-ID, “www.oecd-nea.org/science/taf-id.” .

[14] M. Kurata, “Thermodynamic assessment of the Pu-U, Pu-Zr and Pu-U-Zr systems,” *Calphad*, vol. 23, no. 3–4, pp. 305–337, 1999.

Appendix E – ICP-MS results

Material	B	Na	Mg	Al	Si	Ca	K	Ti	V	Cr	Mn	Fe	Co	Ni	Cu	Zr	Mo	Sn	Hf	Pb	W	Tl	Bi
Al_2O_3	1.2	35	1.8	/	15	3	ND	0.15	<0.1	0.8	0.4	8	<0.1	0.2	2.5	<0.1	<0.1	ND	ND	<0.1	0.2	<0.1	<0.1
CaO	0.6	4.5	20	5	15	/	ND	<0.2	<0.2	0.9	0.6	10	<0.2	0.8	<0.2	<0.2	<0.2	ND	<1	<0.2	<0.2	<0.2	<0.2
SiO_2	12	40	1.1	20	/	0.5	ND	<0.2	<0.2	0.8	1.2	5.4	0.2	0.8	<0.2	0.4	<0.2	ND	<1	<0.2	<0.2	<0.2	<0.2
UO_2 *	<0.2	ND	<1	<1	<2	2	ND	<0.7	<1	5	<1	5	<1	8	<1	ND	<1	<1	ND	<2	<0.5	ND	<1
ZrO_2	0.4	ND	0.5	2	5	3	0.8	0.3	<0.1	0.2	<0.1	2	<0.1	0.1	0.2	/	<0.1	<0.1	10	<0.1	ND	ND	ND
Fe_2O_3	0.4	ND	0.3	3.5	10	8	4.5	1.5	0.3	3.5	0.4	//	1	2.4	1.7	<0.1	0.1	<0.1	<0.1	0.1	ND	ND	ND
Fe	0.3	ND	0.2	1.2	3.5	0.6	0.8	0.6	0.4	1.6	0.8	//	0.7	1.0	0.4	<0.1	<0.1	<0.1	<0.1	0.1	ND	ND	ND
U	<0.2	5	<0.2	15	20	0.5	ND	0.4	2.1	20	2.7	25	ND	2.5	10	<0.2	30	ND	<1	60	150	7	0.4
Zr	0.3	ND	0.5	0.8	10	2	1	0.5	0.5	35	3	150	1	35	4	//	<0.1	120	35	<0.1	ND	ND	ND
Zr VA	ND	ND	ND	ND	ND	ND	ND	ND	ND	<0.005	ND	0.008	ND	ND	ND	ND	ND	<0.005	ND	ND	ND	ND	ND

Table 1: ICP-MS results. The results are given in µg/g. ND = not detected. * = lot n° 428 measured by COGEMA Pierrelatte (Analyse TU2 n° 039)

Appendix F – HgCdTe detector calibration and error analysis

Calibration of the HgCdTe detector

Because the HgCdTe captors ar not linear, a calibration is needed to monitor the temperature. The raw signal from the HgCdTe is sent to a pre-amplifier, where the linearization is done electronically. The linearity is valid in a certain range of incident radiant flux. The linearity of the captor (output signal vs. spectral radiance) can be considered valid across all the sensibility range of the detector. A low temperature calibration (i.e., up to 1373 K) was performed to verify the validity of the linear response of the HgCdTe detector. It is interesting to perform calibrations at different wavelengths by interposing narrow high-pass/low-pass interferential filters. This reduces considerably the incident radiance flux, and therefore prevents the saturation of the captor. The acquisition setup used for the calibration is shown in Figure 1.

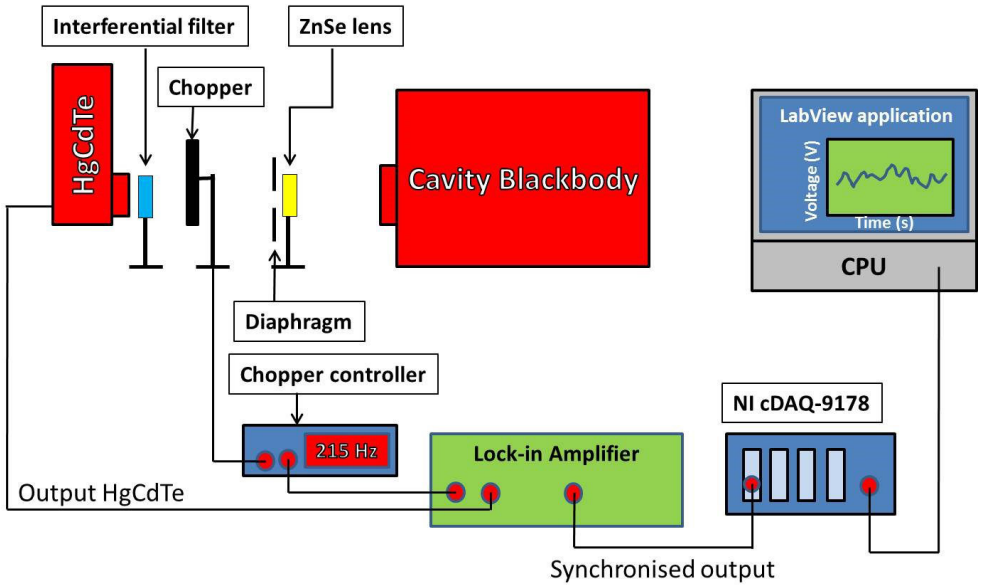

Figure 1: Schematic representation of the acquisition setup used for the HgCdTe calibration

The blackbody used for the calibration was a HGH® RCN 1200 N1 of which the main technical characteristics are reported in Table 1.

Model	Emissivity	T_{max} / K	Dimensions
HGH® RCN 1200 N1	>0.99	1473	∅ of the Cavity (mm): 25, 12.5, 6, 3, 1.5, 0.7

Table 1: Technical characteristics of the cavity black body used for the HgCdTe calibration

The black body was set at different temperatures. The saturation of the HgCdTe captor was avoided by settling an optical diaphragm between the HgCdTe and the black body. The calibration curves obtained at 10 µm and 12.214 µm are reported in Figure 2 a-b.

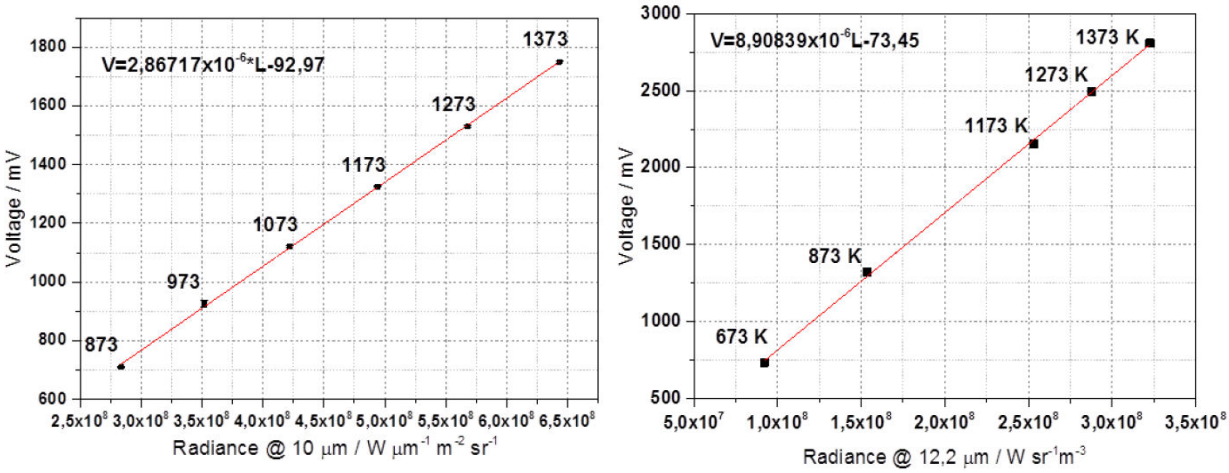

(a) (b)

Figure 2: Calibration curves for the HgCdTe detector. (a) 10 µm; (b) 12.2 µm

The validity of the linearity assumption is verified at both the reported wavelengths. Then, the HgCdTe detector can be used as a thermometer: the recorded analogic output and the radiance temperature of the observed object can be directly linked by resolving the system of equation reported below:

$$\begin{cases} U(L) = A + BL(\lambda, T_\lambda) \\ L(\lambda, T_\lambda) = \dfrac{c_1}{\lambda^5} \dfrac{1}{\exp\left(\dfrac{c_2}{\lambda T_\lambda}\right) - 1} \Rightarrow T_\lambda(U) = \dfrac{c_2}{\lambda} \dfrac{1}{\ln\left(1 + \dfrac{Bc_1}{\lambda^5 (U - A)}\right)} \end{cases} \quad (1)$$

where $U(L)$ is the analogic output showed on the LabView® application (i.e., an electrical tension in volt) and $L(\lambda,T_\lambda)$ is the spectral radiance. The resulting expression in Equation (4) permits to obtain the temperature of the observed sample directly from the output of the HgCdTe detector.

In the limit of the so-called Wien's approximation (see Appendix A) the Planck function can be simplified:

$$L_\lambda(\lambda, T_\lambda) = \frac{c_1}{\lambda^5} \frac{1}{\exp\left(\dfrac{c_2}{\lambda T_\lambda}\right) - 1} \approx \frac{c_1}{\lambda^5} \frac{1}{\exp\left(\dfrac{c_2}{\lambda T_\lambda}\right)} \quad (2)$$

This expression is accurate for short wavelengths and for low temperatures and is better than 1% if $\lambda T \leq 3100$ µm·K. Erminy [1] showed that the Planck function can be approximated with different equations, depending on the $\lambda \cdot T$ product. However, in the present case, none of the proposed expressions can be applied (Figure 3).

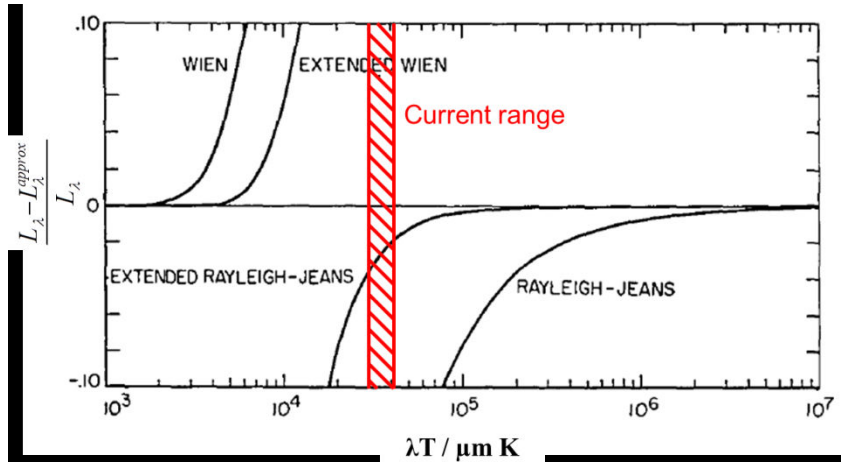

Figure 3: Accuracy with which four selected equation approximate the blackbody spectral radiance [1]. The current range of work is represent by the red region

Even using the Extended Rayleigh-Jeans approximation [1], a minimum error of 2 % affects the final result.

Alternatively, fixing the wavelength, the Planck function can be approximated with a polynomial expression. Figure 4 shows the accuracy with which a linear and a quadratic fit approximate the Planck function at 10 μm between 1000 K and 3200 K.

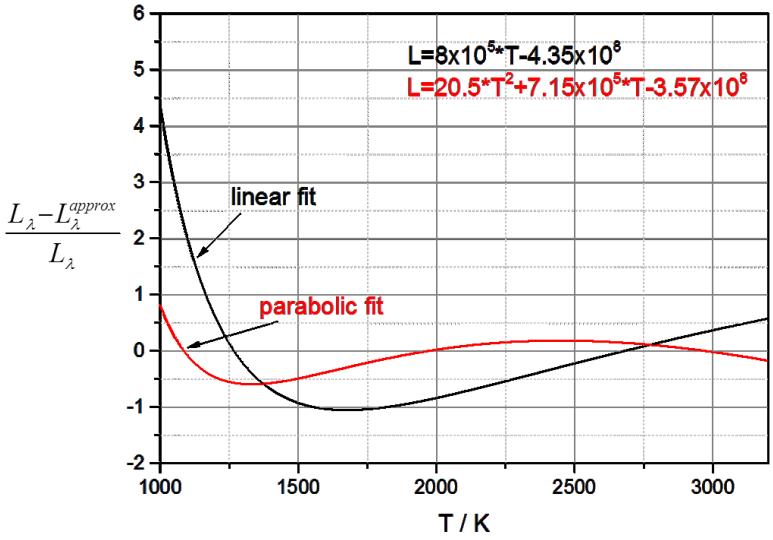

Figure 4: Relative accuracy (in %) of a linear and quadratic approximation at 10 μm between 1000 K and 3200 K

The parabolic fit replaces the Planck function in the system of equation (1):

$$\begin{cases} U(L) = A + BL(\lambda, T_\lambda) \\ L(10\,\mu m, T_\lambda) = a + bT_\lambda + cT_\lambda^{\,2} \end{cases} \Rightarrow T_\lambda = \frac{-bB \pm \sqrt{(bB)^2 - 4(cB)(A + aB - U(L)}}{2cB} \qquad (3)$$

where *a*, *b* and *c* are the coefficients of the parabolic fit in Figure 4. The solution with the physical meaning is retained as the measured radiance temperature. Using the definition of radiance temperature reported in Appendix A, one can deduce:

$$\frac{c_1}{\lambda^5}\frac{1}{\exp\left(\frac{c_2}{\lambda T_\lambda}\right)-1}=\varepsilon(\lambda,T)\frac{c_1}{\lambda^5}\frac{1}{\exp\left(\frac{c_2}{\lambda T}\right)-1}\ . \tag{4}$$

Using the quadratic approximation reported in Figure 4 and the radiance temperature calculated in Equation (3), the real temperature can be derived:

$$a+bT+cT^2=\frac{a+bT_\lambda+cT_\lambda^2}{\varepsilon(\lambda,T)}=L_{\lambda,b}\quad\Rightarrow\quad T=\frac{-b\pm\sqrt{b^2-4c(a-L_{\lambda,b})}}{2c} \tag{5}$$

where $\varepsilon(\lambda,T)$ is the emissivity of the observed object.

Error analysis

In order to quantify the propagation of the errors in the estimated true temperature, a rigorous error analysis has been performed in collaboration with F. Gamboa (IMT, Institut de Mathématiques de Toulouse).

The main sources of error are the following:

- Bias due to the approximation of the Planck distribution at 10 µm between 1000 K and 3000 K with a quadratic function;
- Determination of the slope and the offset, A and B, in the linear relation between the HgCdTe output and the radiance (see Section 6.3);
- Estimation of the emissivity of the investigated sample.

The quadratic approximation of the Planck function has been performed by a least square approximation on the considered range of temperatures. Roughly speaking, the quadratic function obtained may be considered as some rough second order Taylor approximation of the Planck function.

Using the parabolic fit in Figure 4, the maximum deterministic error on the approximation is observed at the temperature of 1000 K. This reminder of the rough Taylor expansion has been obtained numerically, and corresponds to the maximum deviation from the Planck distribution in the considered range of temperatures. In the present case, the maximum deterministic error can be written as:

$$\left\|L(T)-L^{approx}(T)\right\|_\infty\le e\quad\Rightarrow\quad\left\|L(1000\,K)-L^{approx}(1000\,K)\right\|_\infty\le 3.17\cdot10^6\ W\mu m^{-1}m^{-2}sr^{-1} \tag{6}$$

This bias propagates into the estimated radiance temperature $\hat{T}_\lambda$ by inverting the approximated Planck function. The maximum deterministic error on T_λ can be written as:

$$\left|\hat{T}_\lambda-T_\lambda\right|\le\frac{e}{2cT_{\min}+b}=e'=4.2\,K \tag{7}$$

where T_{min}=1000 K to consider the most conservative case.

In parallel, the estimation of the radiance temperature is affected by the stochastic contribution coming from coefficients A and B in Equation (1). The estimated radiance temperature can be expressed as:

$$\hat{T}_\lambda = \frac{-b\hat{B} \pm \sqrt{(b\hat{B})^2 - 4(c\hat{B})(\hat{A} + a\hat{B} - \hat{U})}}{2c\hat{B}} = \varphi\left(\hat{A}, \hat{B}, \hat{U}\right) \tag{8}$$

The vector $\left(\hat{A}, \hat{B}, \hat{U}\right)$ can be represented by a normal distribution of dimension 3, N_3:

$$\begin{pmatrix} \hat{A} \\ \hat{B} \\ \hat{U} \end{pmatrix} \approx N_3 \left(\begin{pmatrix} A \\ B \\ U \end{pmatrix}, \begin{pmatrix} \Gamma & 0 \\ 0 & \sigma_0^2 \end{pmatrix} \right) \tag{9}$$

where Γ is the covariance matrix of dimension 2 between $\hat{A}$ and $\hat{B}$, while σ_0^2 is the variance of the raw HgCdTe signal U. In the hypothesis of small σ_0 and small Γ (which means that the eingenvalues of Γ are small), the Δ-method [2] is applied to obtain the estimator of the variance of the estimated $\hat{T}_\lambda = \varphi\left(\hat{A}, \hat{B}, \hat{U}\right)$:

$$Var\,\hat{T}_\lambda = \left(\left.\frac{\partial \varphi}{\partial U}\right|_U \right)^2 \sigma_0^2 + \left(\left.\frac{\partial \varphi}{\partial A}\right|_A \right)^2 Var\,\hat{A} + \left(\left.\frac{\partial \varphi}{\partial B}\right|_B \right)^2 Var\,\hat{B} + \left.\frac{\partial \varphi}{\partial A}\right|_A \left.\frac{\partial \varphi}{\partial B}\right|_B Cov\left(\hat{A} - A, \hat{B} - B\right) + o(1) \tag{10}$$

where *o(1)* is a small remaining term.

The variance of $\hat{A}$, $\hat{B}$ and the covariance term can be expressed as:

$$Var(\hat{A}) = \sigma_0^2(U_1)\left(1 + \frac{L_1^2}{(L_2 - L_1)^2} - \frac{L_1}{(L_2 - L_1)^2}\right) - \frac{L_1\,\sigma_0^2(U_2)}{(L_2 - L_1)^2}(1 - L_1) \tag{11}$$

$$Var(\hat{B}) = \frac{1}{(L_2 - L_1)^2}(\sigma_0^2(U_1) + \sigma_0^2(U_1)) \tag{12}$$

$$Cov(\hat{A}, \hat{B}) = -\frac{L_1}{(L_2 - L_1)^2}(\sigma_0^2(U_1) + \sigma_0^2(U_1)) - \frac{\sigma_0^2(U_1)}{L_2 - L_1} \tag{13}$$

where L_1=*L(10 µm, 298 K)* and L_2=*L(10 µm, 2328 K)* (see Section 5.3) and U_1 and U_2 are the HgCdTe voltages used to estimate the unknown parameters A and B. The resulting estimated standard deviation is

$$\hat{\sigma}_{T_\lambda} = \sqrt{Var(\hat{T}_\lambda)}\,. \tag{14}$$

The estimator of the radiance temperature can be finally written as:

$$\hat{T}_\lambda = (T_\lambda + bias) + \hat{\sigma}_{T_\lambda}\ \xi \tag{15}$$

where *bias=e'* (Equation 7). If $\xi \sim N(0,1)$, with a probability of 95 %, the estimated standard deviation lies between $\pm 2\sigma$:

$$\hat{\sigma}_{T_\lambda}\ \xi \in \left[-2\sigma, 2\sigma\right]. \tag{16}$$

With a probability of 95 % and considering the most conservative case, the radiance temperature T_λ lies within

$$T_\lambda \in \left[\hat{T}_\lambda - e' - 2\sigma, \hat{T}_\lambda + e' + 2\sigma\right]. \tag{17}$$

The last step consists to propagate the previous error and the error on the emissivity estimation in the estimator of the true temperature $\hat{T}$:

$$\hat{T} - T = \frac{(b + c(\hat{T}_\lambda + T_\lambda))\left|\hat{T}_\lambda - T_\lambda\right| + (a + bT + cT^2)\left|\varepsilon - \hat{\varepsilon}\right|}{\hat{\varepsilon}\ (b + c(\hat{T} + T))} \tag{18}$$

Considering the most conservative case, it can be written:

$$\left|\hat{T} - T\right| \le \frac{K_2}{K_1}\left|\hat{T}_\lambda - T_\lambda\right| + \frac{K_3}{K_1}\left|\varepsilon - \hat{\varepsilon}\right| \tag{19}$$

$$\begin{cases} K_1 = \hat{\varepsilon}\,(b + 2cT_{\min}) \\ K_2 = b + 2cT_{\lambda,\max} \\ K_3 = a + bT_{\grave{u}ax} + cT_{\max}^2 \end{cases} \tag{20}$$

With probability 0.95^2=0.9025, the true temperature lies within the range:

$$T \in \left[\hat{T} - \frac{K_2}{K_1}(e' + 2\sigma) - 2\frac{K_3}{K_1}\sigma_\varepsilon, \hat{T} + \frac{K_2}{K_1}(e' + 2\sigma) + 2\frac{K_3}{K_1}\sigma_\varepsilon\right] \tag{21}$$

For example, the true temperature of a sample with an estimated emissivity 0.9±0.045 and an estimated radiance temperature of 2000 K is 2158±98 K with a probability of 0.9025. It must be pointed out that 86 % of the reported error bar is due to the estimated emissivity.

The Christiansen wavelength

For opaque materials, depending on their electronic configuration, the reflectivity becomes 0 at the Christiansen wavelength [3]. By definition, the Christiansen wavelength is the wavelength where the refractive index is unity and the extinction coefficient in very small. At

this wavelength, applying the Kirchhoff's law (see Appendix A), the emissivity is equal to 1. The material reaches a quasi-blackbody condition.

For oxides, the Christiansen wavelength is in the infrared range. Table 2 reports the wavelength range where the normal spectral emissivity $\varepsilon>0.99$ for Al_2O_3 and ZrO_2.

Material	Christiansen wavelength	Wavelength range where $\varepsilon>0.99$	Reference
Al_2O_3	9.5 µm	8.7-10.2	[4]
ZrO_2	12.8 µm	12.6-12.9	[4]

Table 2: Christiansen wavelength of Al_2O_3 and ZrO_2

The variation of the Christiansen wavelength towards temperature in oxides is limited [5]. This property can be used to obtain directly the true temperature by interposing an interferential filter between the HgCdTe detector and the sample. The selection of the wavelength depends on the nature of the sample.

References

[1] D. E. Erminy, “Some approximations to the Planck Function in the Intermediate Region with Applications in Optical Pyrometry,” *Appl. Opt.*, vol. 6, no. 1, pp. 107–117, 1967.

[2] V. der Vaart, Book, *Asymptotic statistics*, Cambridge. Cambridge, 2000.

[3] B. Rousseau, J. F. Brun, D. S. Meneses, and P. Echegut, “Temperature measurement: Christiansen wavelength and blackbody referenc,” *Int. J. Thermophys.*, vol. 26, pp. 1277–1286, 2005.

[4] L. Robin Carillon, “Etude expérimentale et théorique de l’émission infrarouge de ceramiques à haute température. Application aux barrieres thermiques,” PhD Thesis Institut National des Sciences Appliqués de Lyon, 2007.

[5] R. Gilblas, “Mesure de champs de températures vraies par thermoreflectometrie proche infrarouge,” PhD Thesis Université de Toulouse, 2012.

Étude thermodynamique du corium en cuve – Application à l'interaction corium/béton

Résumé en français

1 Introduction

Pendant le fonctionnement normal d'un réacteur à eau pressurisée (REP), les produits radioactifs (combustible nucléaire, produits de fission, éléments transuraniens) sont physiquement séparés de l'environnement par trois barrières de confinement (Figure 1) :

- la gaine du combustible en Zircaloy (1);
- le circuit de refroidissement primaire (2);
- le bâtiment contenant la cuve du réacteur (3).

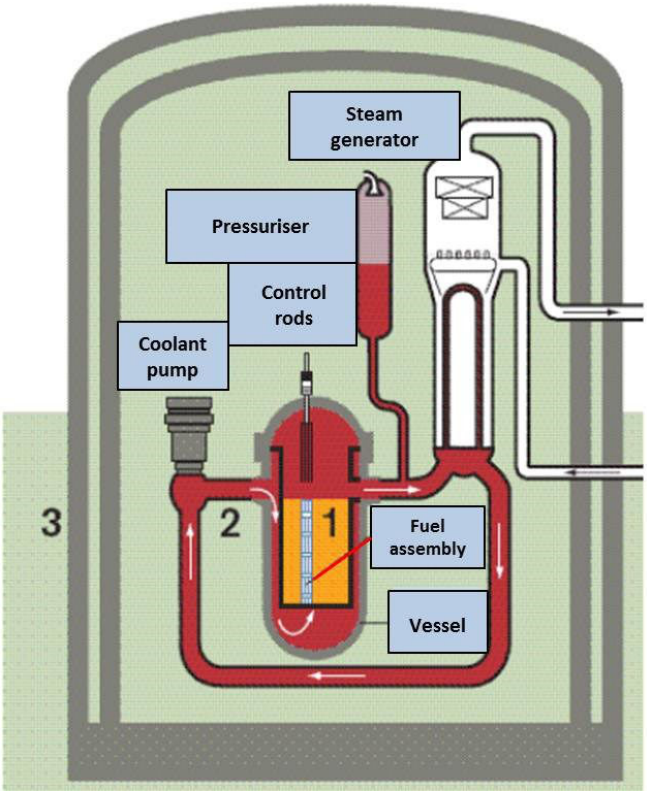

Figure 1 : Schéma d'un réacteur à eau pressurisée (REP)

Lors d'un accident, l'endommagement d'au moins une de ces barrières de confinement va conduire à la perte d'étanchéité du réacteur. Un accident peut évoluer vers un accident grave si le fonctionnement nominal du réacteur n'est pas rétabli. Si par exemple, le liquide

caloporteur n'évacue pas efficacement la puissance résiduelle, la température extérieure de la gaine de combustible peut monter en quelques secondes jusqu'à 1073 K. A cette température les absorbants neutroniques fondent en formant un mélange (Ag, In, Cd) qui peut alors interagit avec le Zircaloy et la gaine en Inconel des barres de commande. À 1473 K l'oxydation exothermique des gaines de Zircaloy entraine une augmentation incontrôlée de la température : le combustible nucléaire est alors progressivement dissout et réduit par le Zircaloy liquide. Par conséquent, déjà en-dessous de 2273 K, le cœur perd déjà sa tenue mécanique.

La formation d'un mélange oxyde-métal au fond de la cuve du réacteur, appelé ***corium en cuve***, est la conséquence directe des interactions chimiques à haute température entre les assemblages de combustible, les absorbants neutroniques et les éléments structuraux du réacteur. Dans les réacteurs REP de troisième génération, la rétention du corium « en cuve » est la stratégie choisie en cas d'accident grave. La rétention et le refroidissement de ce corium dans la cuve reposent sur le maintien de l'intégrité de celle-ci.

L'existence d'une lacune de miscibilité à l'état liquide dans le système « corium en cuve » [1] entraine une configuration de bain en fond de cuve menant à la stratification d'un liquide métallique et d'un liquide oxyde (Figure 2a).

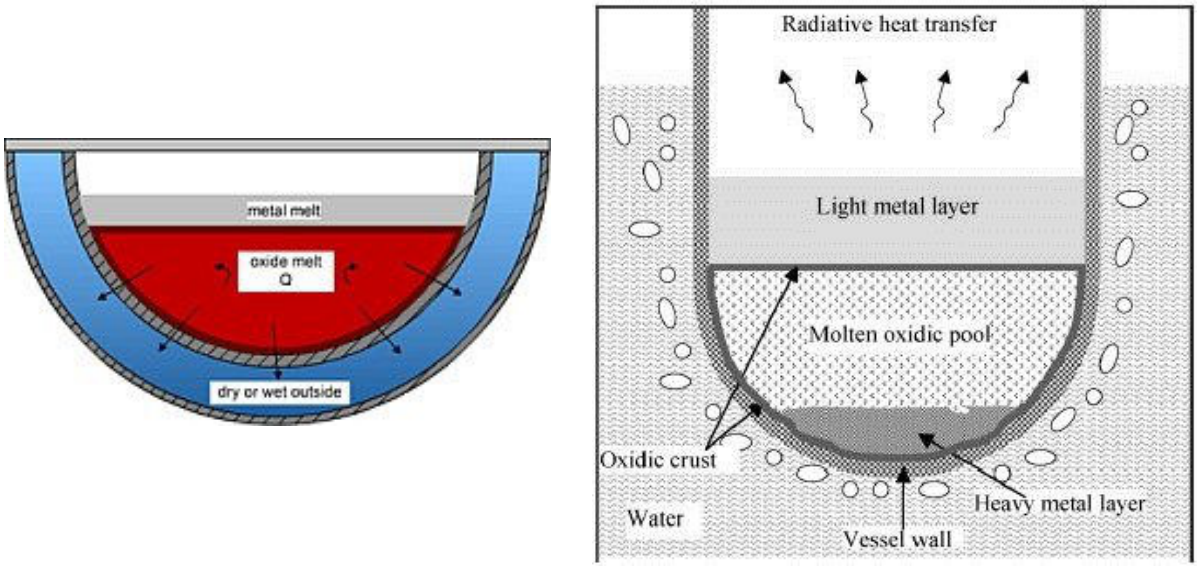

(a) (b)

Figure 2: Configuration stratifiée du corium en cuve. (a) Liquide oxyde en dessous du liquide métallique ; (b) formation d'un liquide riche en éléments lourds au fond de la cuve [1]

En fonction du degré d'oxydation du Zr, du rapport U/Zr et de la quantité d'acier dissout dans le mélange liquide, une troisième phase liquide métallique enrichie en uranium peut se former en dessous du liquide oxyde [1] (Figure 2b). Ce phénomène entraine la diminution de l'épaisseur de la couche métallique supérieure. Or, en l'absence d'eau à l'intérieur de la cuve, cette couche transmet environ 60 % de la puissance résiduelle vers l'interface entre la cuve et le liquide métallique [2]. Il s'en suit un phénomène de concentration de flux de chaleur, appelé ***focusing effect***, au niveau de cette couche métallique vers la surface intérieure de la cuve. L'intégralité de la cuve est alors assurée seulement si le flux transmis peut être extrait par l'eau à l'extérieur de la cuve. En général, le flux critique est autour d'une valeur de l'ordre de 1.5 MWm^{-2} [1,2]. Ces valeurs sont obtenues en couplant des données thermochimiques à des modèles thermo-hydrauliques. L'incertitude liée à la composition chimique des liquides métalliques et oxyde affecte ces résultats : **une meilleure description thermodynamique du**

système « corium en cuve », en première approximation U-Pu-Zr-Fe-O, est nécessaire pour améliorer la qualité des calculs et l'exactitude des simulations.

La rupture de la cuve mène à l'étape suivante de l'accident grave, l'interaction corium/béton (ICB), qui se traduit par une ablation progressive du béton par le corium. Au début, l'ICB est contrôlée par le corium surchauffé qui chauffe le béton. Le CO_2 et la vapeur d'eau relâchés du béton vont interagir avec le corium. Par la suite, la puissance résiduelle devient la source principale de chaleur.

Du point de vue chimique, les constituants du béton (Al_2O_3, CaO, MgO, SiO_2, H_2O et CO_2) doivent être ajoutés au système complexe « corium en cuve ». Le « corium hors cuve » peut être défini comme le mélange résultant de l'interaction entre le béton et le corium en cuve. Par conséquent, **en première approximation, le système U-Pu-Zr-Fe-O-Al-Ca-Si peut être considéré comme prototypique du cas réel**.

La conception de la cuve du réacteur ainsi que les études sur la gestion du scénario accidentel reposent sur la connaissance des propriétés physico-chimiques du corium en cuve et hors cuve. En effet, les données thermodynamiques sur le corium sont indispensables pour l'estimation de propriétés thermo-physiques du bain liquide en cuve et/ou hors cuve, comme par exemple, la viscosité et la tension de surface.

Dans ce cadre, l'objectif de cette thèse est de contribuer à l'amélioration du modèle thermodynamique du système prototypique corium en cuve, U-Pu-Zr-Fe-O. Après une analyse critique des données de la littérature, un programme expérimental a été mené pour obtenir de nouvelles données de diagramme de phase à haute température (T > 2000 K) dans les sous-systèmes U-Zr-O, Fe-Zr-O, Pu-Zr-O, U-Zr-Fe-O et U-Pu-Zr-O. Ces résultats, ainsi que les données sélectionnées dans la littérature ont été utilisés pour la réévaluation du modèle thermodynamique du corium en cuve prototypique par la méthode CALPHAD [3,4]. Ce modèle couplé à la base de données thermodynamiques TAF-ID [5] a été utilisé pour des calculs d'application sur des mélanges corium hors cuve. En parallèle, le montage expérimental ATTILHA (Advanced Temperature and Thermodynamic Investigation by Laser Heating Approach) a été conçu et développé pour disposer d'un moyen de mesure de températures de transition de phase à très haute température (T>2000°C). Il s'agit d'un banc de chauffage par laser couplé avec la technique de lévitation aérodynamique.

2 Etude bibliographique

Corium en cuve

Une partie importante de cette thèse a été dédiée à la revue critique des données de la littérature disponibles sur les systèmes chimiques du corium. Le système U-Zr-O a été largement étudié pour caractériser l'interaction entre le combustible nucléaire UO_2 et la gaine en Zircaloy. En particulier, à partir des années 1950, la section UO_2-Zr a fait l'objet de nombreuses études pour déterminer la température de formation de la phase liquide et la limite de solubilité de l'oxygène dans la phase liquide. L'extension du domaine d'existence de la phase liquide a été longtemps au centre du débat. En 1997, Maurizi [6] a déterminé la position du liquidus à 2273 K dans le diagramme de phase ternaire U-Zr-O. Cette étude a montré que la solubilité de l'oxygène dans le liquide est plus faible que ce qui était supposé dans les études précédentes [7]. A plus haute température, le système U-Zr-O est caractérisé par la présence d'une lacune de miscibilité à l'état liquide [8]. Cette lacune est une des causes principales de la stratification du corium en cuve. Néanmoins l'extension de la lacune n'est pas bien connue. La plupart des auteurs ne reporte pas les compositions chimiques des deux

liquides à l'équilibre. La seule conode disponible en littérature a été obtenue en 1998 par Guéneau et al. [9] à 3223±100 K. En conclusion, de nouvelles mesures de données sur la lacune de miscibilité sont nécessaires pour améliorer le modèle de la phase liquide. Le sous-système UO_2-ZrO_2 a été aussi largement étudié, car il est caractéristique d'un corium complètement oxydé. Le modèle thermodynamique de Baichi [10] est satisfaisant et en accord avec un très grand nombre de données expérimentales.

Le mélange U-Zr-O formé pendant l'accident peut ensuite interagir avec les structures métalliques du réacteur. Si on considère le cas simplifié d'un corium en cuve prototypique, U-Zr-Fe-O, les systèmes ternaires U-Fe-O et Fe-Zr-O sont les systèmes les plus importants. En ce que concerne le système U-Fe-O, les études expérimentales sont rares. Le contrôle de la composition des échantillons est difficile à cause des nombreux états d'oxydation du Fe et de l'U. Le peu de données disponibles sur ce système sont se situent dans la région oxyde du diagramme ternaire. La partie du diagramme ternaire près du binaire Fe-U (donc avec une basse teneur en oxygène) est inconnue. Les mêmes considérations peuvent être faites sur le système Fe-Zr-O. Très peu d'études expérimentales sont disponibles dans la littérature. La partie oxyde du diagramme ternaire a été la plus étudiée. Des données thermodynamiques, en particulier des pressions partielles d'oxygène dans la région FeO-Fe_3O_4-ZrO_2, ont été mesurées [11]. La modélisation thermodynamique de ces systèmes s'appuie donc sur très peu des données expérimentales. En conclusion, la nécessité de mesurer de nouvelles données expérimentales est évidente. En particulier, le manque de données thermodynamiques et de diagramme de phase dans la partie pauvre en oxygène limite la qualité de la modélisation thermodynamique associée aux systèmes ternaires U-Fe-O et Fe-Zr-O.

Si l'on considère un combustible nucléaire MOx (mélange UO_2-PuO_2), le Pu doit être également ajouté au système représentatif du corium en cuve. Néanmoins les systèmes contenant du Pu sont difficiles à étudier, principalement à cause de la radiotoxicité du Pu. Il existe un nombre réduit d'études sur le système Pu-Zr-O. La section PuO_2-ZrO_2 a été étudiée surtout dans les années 1960. Le diagramme de phase reste assez incertain. En fonction de la composition exacte de l'oxyde de plutonium (plus ou moins réduit) – PuO_2-ZrO_2 ou $PuO_{1.6}$-ZrO_{2-x} – le diagramme de phase correspondant est très différent [12]. Plus récemment, Albiol et al. (albiol) ont étudié la partie riche en ZrO_2 de la section PuO_2-ZrO_2 entre 1273 K et 1513 K et ont montré que du PuO_2 peut être solubilisé dans les trois formes allotropiques du ZrO_2 (monoclinique, tétragonale et cubique).

Corium hors cuve

Lors de l'ICB, de nombreux phénomènes se produisent : la décomposition du béton, le transfert de chaleur par mouvements convectifs, la formation de nombreuses phases, l'oxydation de métaux, etc. La dégradation du cœur du réacteur et l'interaction entre le corium en cuve et le béton ont été largement étudiés. Les phénomènes principaux qui ont été étudiés sont [13] :

- la dégradation du cœur du réacteur ;
- le relâchement des produits de fission (PF) ;
- l'interaction corium-eau (ICE) ;
- l'interaction corium-béton (ICB) ;
- l'étalement du mélange corium+béton sur le récupérateur de corium (configuration EPR).

Ces expériences ont permis de bien caractériser les phénomènes se produisant lors de l'accident. La plupart de ces études sont conduites dans une configuration « grande échelle »

pour pouvoir reproduire au mieux les conditions réelles de l'accident. Dans cette configuration, les rares données thermochimiques sont influencées par les gradients de température et de composition.

3 Thermodynamique du système prototypique corium en cuve

L'étude thermodynamique du système complexe U-Pu-Zr-Fe-O est basée sur la méthode CALPHAD [14]. Cette méthode permet de modéliser les fonctions thermodynamiques d'un système à partir d'une sélection de données expérimentales significatives. Dans ce cadre, de nouvelles données expérimentales ont été obtenues dans les systèmes U-Zr-O, Fe-Zr-O, U-Zr-Fe-O et U-Pu-Zr-O. La modélisation thermodynamique du système corium en cuve a été ensuite effectuée. Enfin des calculs de chemin de solidification à l'aide de ce modèle ont été effectués pour interpréter les microstructures observées pendant cette campagne expérimentale.

Méthodologie

La méthode CALPHAD (**Cal**culation of **Pha**se **D**iagrams) permet de développer un modèle thermodynamique d'un système chimique à partir de données expérimentales sélectionnées grâce à une analyse critique préliminaire des données de la littérature. Si ces données ne sont pas suffisantes, des mesures sont réalisées pour obtenir de nouvelles données (Figure 3).

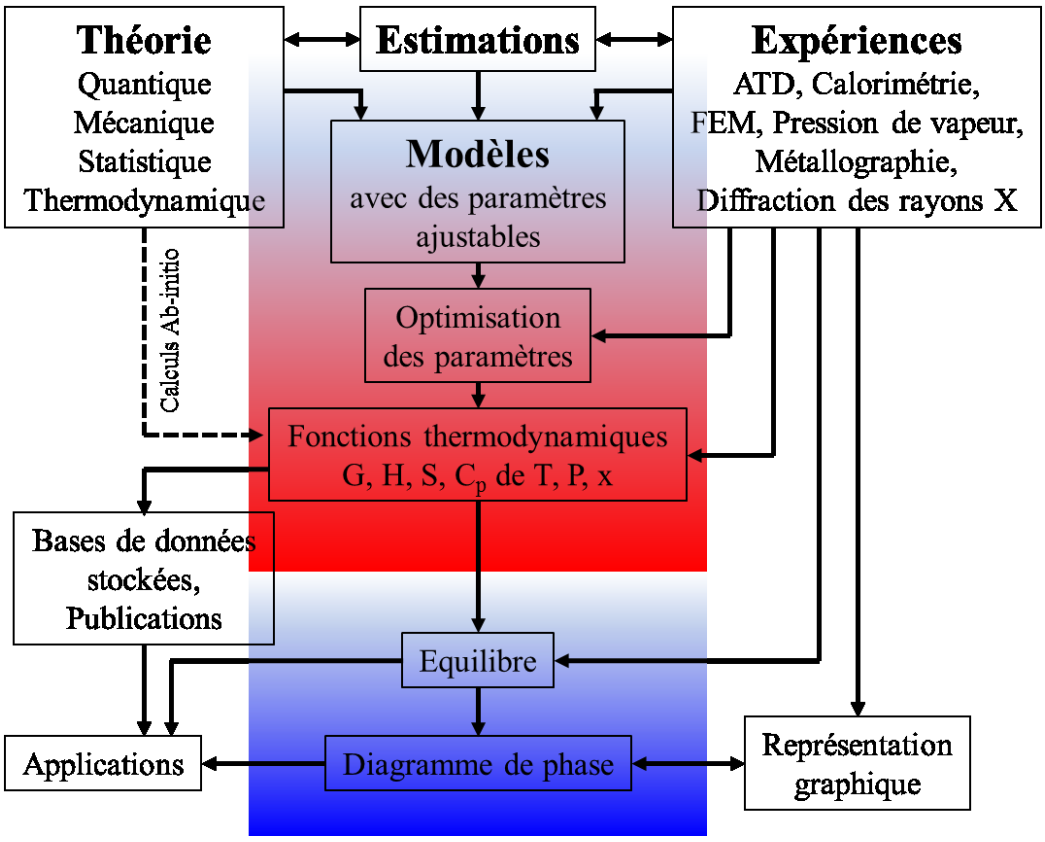

Figure 3 : Représentation graphique de la méthode CALPHAD

L'atout de cette méthode est la possibilité de prédire le comportement de systèmes multi-constitués par extrapolation de systèmes binaires et ternaires.

Etude expérimentale

Pendant cette thèse, de nouvelles expériences ont été effectuées, notamment :

- Des traitements thermiques à 2567 K sur 4 échantillons dans le système U-Zr-O pour obtenir des données d'équilibre de phases ;

- Des mesures de température de fusion, par chauffage laser, sur 3 échantillons dans le système U-Zr-O et sur 6 échantillons dans le système Fe-Zr-O en collaboration avec l'Institut des Transuraniens (ITU) en Allemagne dans le cadre du projet TALISMAN ;

- Des mesures de température de fusion par chauffage laser sur 6 échantillons dans le système UO_2-PuO_2-ZrO_2 en collaboration avec l'ITU en Allemagne ;

- L'élaboration par four à arc d'un échantillon de corium en cuve (UO_2-ZrO_2-Zr-Fe) ;

- Des traitements thermiques à 2500 K sur 2 échantillons de corium hors cuve (UO_2-ZrO_2-Al_2O_3-CaO-SiO_2) avec différentes teneurs en SiO_2.

Tous les échantillons ont été caractérisés au LMAC à Marcoule par microscopie électronique, EDS et microsonde électronique pour identifier les phases à l'équilibre.

Système U-Zr-O

Les compositions initiales des échantillons étudiés pendant la thèse sont reportées sur la Figure 4.

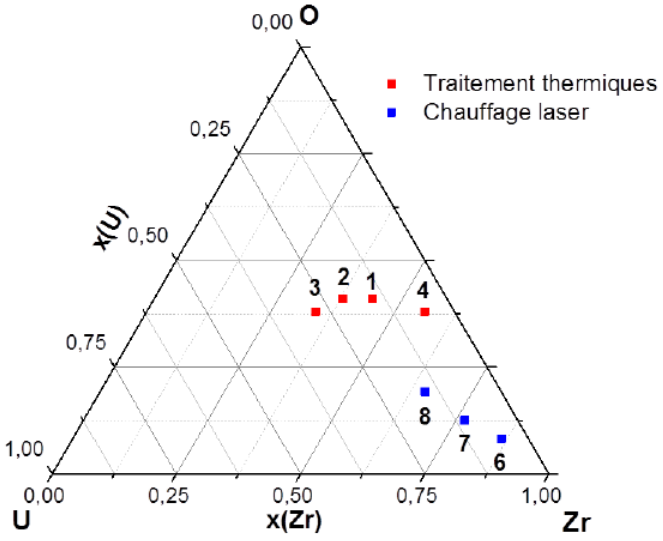

Figure 4 : Compositions initiales des échantillons U-Zr-O étudiés pendant la thèse

L'analyse de la microstructure des 4 échantillons trempés dans le système U-Zr-O a permis de déterminer les phases à l'équilibre à 2567 K. Deux échantillons (OUZr_1 et OUZr_4)

montrent une microstructure dendritique homogène, typique d'un liquide refroidi très rapidement (Figure 5). La présence de W dans les échantillons solidifiés est due à l'interaction entre le creuset en W et l'échantillon liquide.

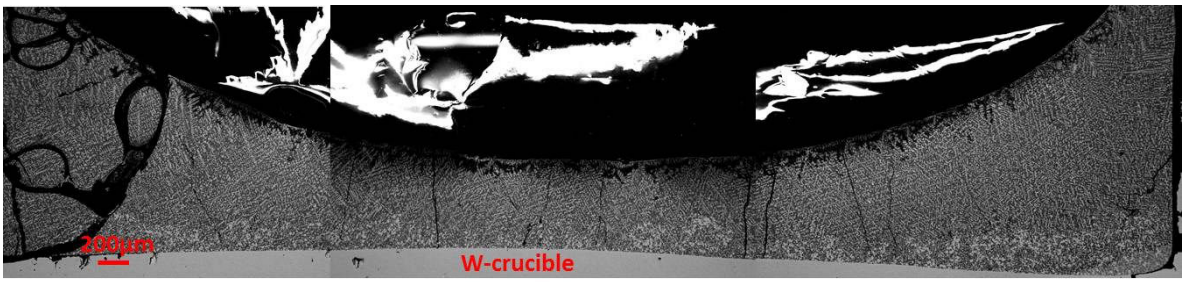

(a)

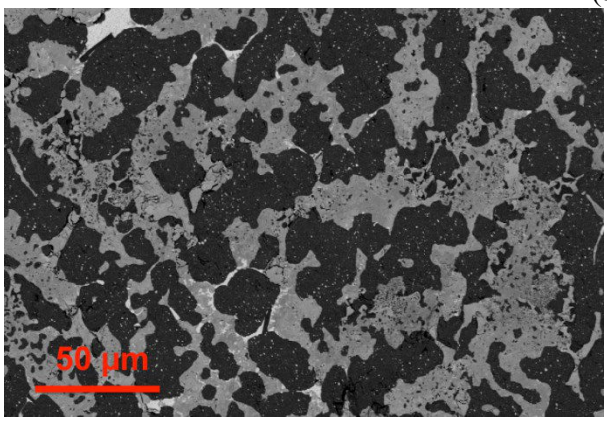

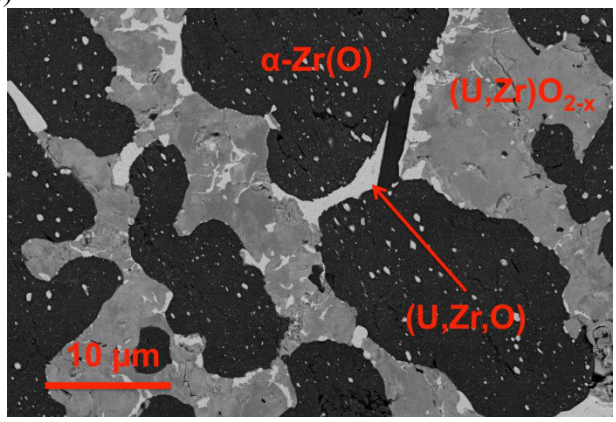

(b) (c)

Figure 5 : (a) Image MEB en électrons rétrodiffusés (BSD) de l'échantillon OUZr_1 ; (b) Agrandissement de la microstructure dendritique ; (c) les trois phases identifiées : $(U,Zr)O_{2-x}$, α-(Zr,U)(O) et une phase métallique enrichie en U

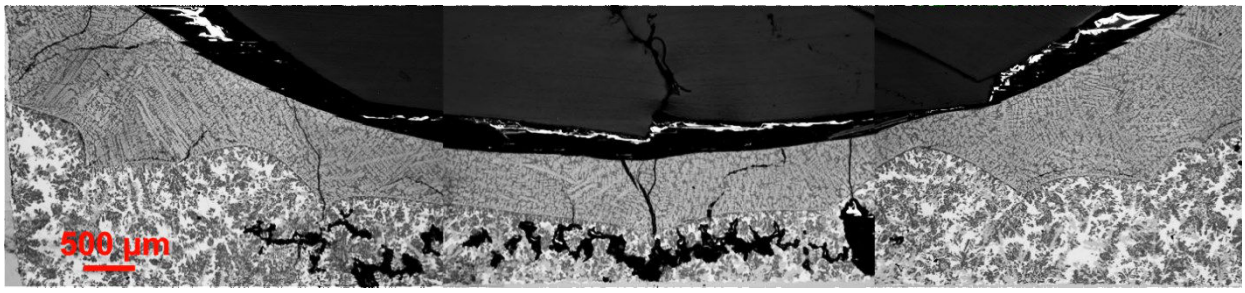

Figure 6: Image MEB en électrons rétrodiffusés (BSD) de la coupe transversale de l'échantillon OUZr_3 solidifié, montrant la séparation et la stratification entre le liquide oxyde (partie supérieure) et le liquide métallique (partie inférieure)

En revanche, les échantillons OUZr_2 et OUZr_3 présentent une microstructure avec deux couches distinctes stratifiées (Figure 6). Les analyses effectuées par microsonde électronique et par analyse dispersive en énergie (EDS) révèlent que la zone supérieure est enrichie en oxygène et la zone inférieure est enrichie en éléments métalliques. **Cette configuration est typique de la formation de deux liquides immiscibles refroidis très rapidement. La présence d'une lacune de miscibilité à l'état liquide a été ainsi confirmée**. Il s'agit d'un équilibre entre un liquide oxyde et un liquide métallique. L'étendue de cette lacune en composition et en température est un des paramètres clés qui détermine la présence de ces deux phases liquides dans le corium en cuve. Grâce à ces nouvelles données expérimentales, l'extension de la lacune de miscibilité à l'état liquide dans le système U-Zr-O est maintenant

mieux connue à 2567 K. Les résultats obtenus par traitement thermique sont présentés dans le Tableau 1.

Les échantillons étudiés par chauffage laser en collaboration avec l'ITU se situent dans la section UO_2-Zr, du côté riche en Zr. Une description détaillée de la technique de chauffage par laser est publiée dans [15]. Les résultats obtenus (en température de luminance) présentent une excellente reproductibilité. De ce fait, on peut conclure que les conditions expérimentales utilisées pendant les essais ont permis de ne pas évoluer en composition, tout en gardant l'intégrité mécanique des échantillons. Pour deux échantillons (OUZr_7 et OUZr_8), le pyromètre a mesuré deux arrêts thermiques (Figure 7). La source majeure d'incertitude est l'estimation de l'émissivité des échantillons. Les résultats de chauffage laser sur le trois échantillons U-Zr-O sont reportés dans le Tableau 2.

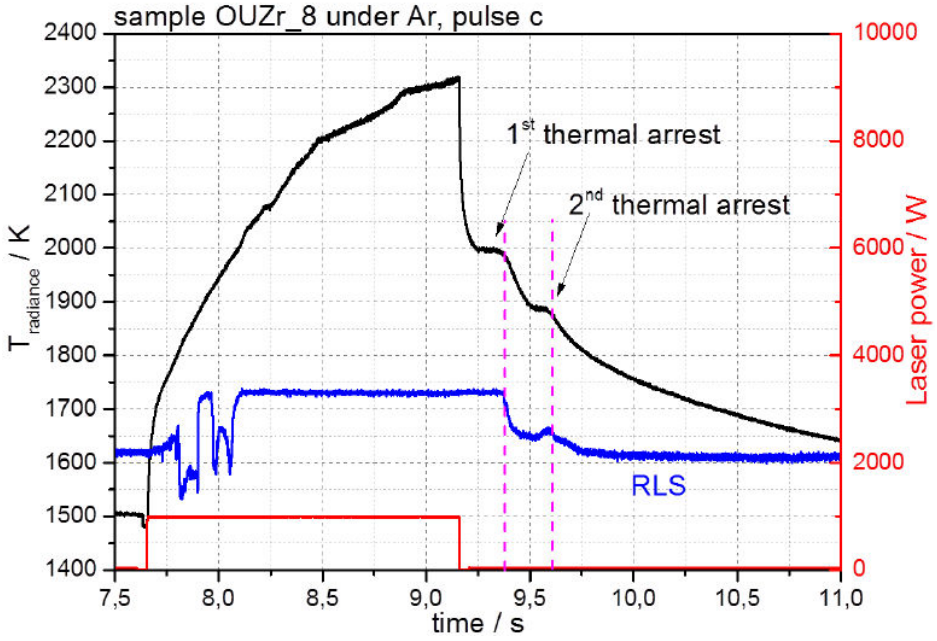

Figure 7: Thermogramme obtenu sous argon sur l'échantillon OUZr_8. Pendant le refroidissement deux arrêts thermiques sont bien visibles

OUZr_1					
	Initiale	**Finale**	**$(U,Zr)O_{2-x}$**	**α-(Zr,U)(O)**	**(U,Zr,O)**
at % O	41.0	39.1	64.4	25.1	33.1
at % U	15.0	10.2	30.5	2.0	63.9
at % Zr	44.0	50.7	5.1	72.9	2.6

OUZr_2							
	Initiale	**Liquide oxyde : $O_{0.46}U_{0.139}Zr_{0.401}$**			**Liquide métallique : $O_{0.302}U_{0.162}Zr_{0.536}$**		
		$(U,Zr)O_{2-x}$	**α-(Zr,U)(O)**	**(U,Zr,O)**	**$(U,Zr)O_{2-x}$**	**α-(Zr,U)(O)**	**(U,Zr,O)**
at % O	41.0	64.4	26.0	38	66.9	26.8	24
at % U	21.0	27.5	2.7	62	30.3	2.1	69
at % Zr	38.0	8.0	71.3	/	2.8	71.1	7

OUZr_3							
	Initiale	**Liquide oxyde : $O_{0.507}U_{0.173}Zr_{0.32}$**			**Liquide métallique : $O_{0.236}U_{0.28}Zr_{0.484}$**		
		$(U,Zr)O_{2-x}$	**α-(Zr,U)(O)**	**(U,Zr,O)**	**$(U,Zr)O_{2-x}$**	**α-(Zr,U)(O)**	**(U,Zr,O)**
at % O	38.0	66.0	26.1	20	66.4	26.8	11
at % U	28.0	29.6	2.9	80	30.3	2.1	84
at % Zr	34.0	4.4	71.0	/	3.3	71.1	5

OUZr_4					
	Initiale	**Finale**	**$(U,Zr)O_{2-x}$**	**α-(Zr,U)(O)**	**(U,Zr,O)**
at % O	38.0	35.7	64.2	26.9	
at % U	6.0	4.8	16.0	2.3	
at % Zr	56.0	59.5	19.8	70.7	

Tableau 2 : Résumé des résultats obtenus par traitement thermique sur les 4 échantillons U-Zr-O

Echantillon	Température de luminance / K			Température vraie / K	
	1er arrêt thermique	2ème arrêt thermique	ε(652 nm)	1er arrêt thermique	2ème arrêt thermique
OUZr_6	2011±11	//	0.243±0.05	2307±101	//
OUZr_7	2020±10	1665±26	0.264±0.05	2299±94	1850±70
OUZr_8	2002±16	1889±18	0.40±0.08	2183±94	2049±61

Tableau 2: Résultats des essais de chauffage laser sous argon sur les trois échantillons U-Zr-O. Les températures de luminance et les vraies températures sont reportées. L'incertitude sur les vraies températures est corrigée d'un facteur d'élargissement k=2

Il faut souligner que 86 % de l'incertitude sur les températures vraies est lié à l'estimation de l'émissivité.

Système Fe-Zr-O

En utilisant le même montage expérimental de chauffage par laser, le système Fe-Zr-O a été étudié. Les résultats sur le système Fe-Zr-O sont résumés dans le Tableau 3.

Echantillon	Température de luminance / K			Température vraie / K	
	1er arrêt thermique	2ème arrêt thermique	ε(652 nm)	1er arrêt thermique	2ème arrêt thermique
OFeZr_1	1989±18	1660±4	0.56±0.11	2098±86	1735±54
OFeZr_2	1883±29	//	0.56±0.11	1980±94	//
OFeZr_5	1847±11	1572±15	0.55±0.11	1943±72	1642±58

Tableau 3 : Résumé des résultats obtenus sur trois échantillons dans le système Fe-Zr-O. Les températures de luminance et les vraies températures sont reportées. L'incertitude sur les vraies températures est corrigée d'un facteur d'élargissement k=2

UO_2-PuO_2-ZrO_2

Si on considère un combustible nucléaire MOx (oxyde mixte UO_2-PuO_2), le Pu doit être ajouté à la description thermodynamique du corium en cuve. Six échantillons dans le système UO_2-PuO_2-ZrO_2 ont été étudiés par chauffage laser en collaboration avec l'ITU. La composition initiale des échantillons est présentée dans le Tableau 4.

Échantillon	mol% UO_2	mol% PuO_2	mol% ZrO_2
U48P3Z49	48	3	49
U45P10Z45	45	10	45
U33P33Z33	33	33	33
U20P40Z40	20	40	40
U10P45Z45	10	45	45
P50Z50	0	50	50

Tableau 4 : Composition initiale des échantillons UO_2-PuO_2-ZrO_2

Pour la première fois, une étude systématique de l'effet de l'atmosphère expérimentale (plus ou moins oxydante ou réductrice) sur le comportement pendant la solidification et la fusion du système UO_2-PuO_2-ZrO_2 a été menée (Tableau 5). En fonction de la teneur en UO_2 dans l'échantillon, une atmosphère oxydante ou plutôt réductrice peut stabiliser le rapport O/(U+Pu+Zr) près de la stœchiométrie (O/(Pu+U+Zr)=2). La température de solidification mesurée sur l'échantillon U48P3Z49 sous air est environ 200 K plus basse de celle mesurée sous Ar. En plus, pendant le chauffage, le thermogramme obtenu sou air est moins régulier que celui mesuré sous argon (Figure 8a). En effet, à cause de la réactivité chimique à haute température de l'échantillon avec l'atmosphère, le liquide s'oxyde et dissout une partie de l'oxygène présent dans le gaz. Le rapport O/(U+Pu+Zr) de l'échantillon évolue donc vers un rapport oxygène/métal supérieur à 2. En revanche, pour l'échantillon U10P45Z45, les thermogrammes obtenus sous air et sous Ar sont similaires (Figure 8b). Dans ce cas, la fraction molaire d'UO_2 dans l'échantillon n'était pas suffisante pour qu'une oxydation significative se produise.

	Atmosphère réductrice	**Atmosphère oxydante**
Echantillon	**T solidification / K**	**T solidification / K**
U48P3Z49	2799±54	2620±39
U45P10Z45	2812±40	2663±46
U33P33Z33	2786±57	2772±150
U20P40Z40	2726±50	2731±58
U10P45Z45	2812±44	2835±44
P50Z50	2819±50	2848±43

Tableau 5: Résultats expérimentaux sur les six échantillons UO_2-PuO_2-ZrO_2. L'incertitude sur les varies températures est corrigée par un facteur d'élargissement k=2

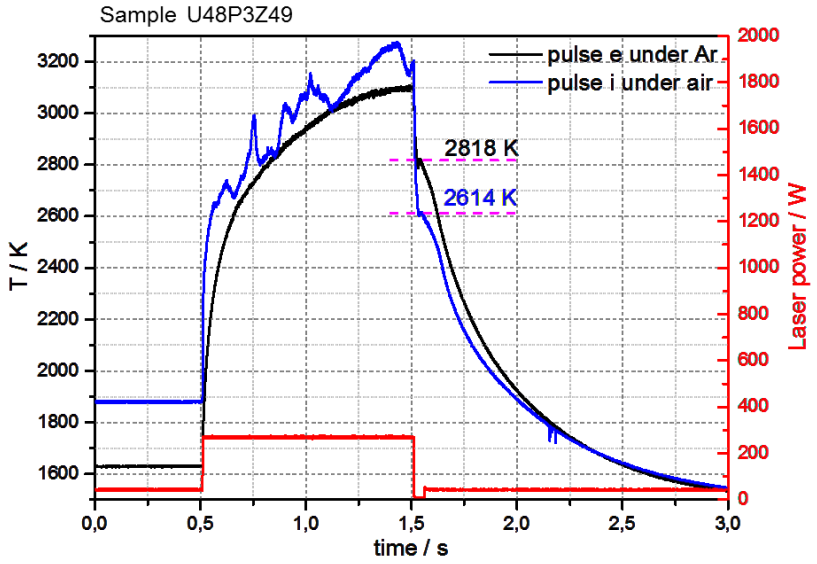

(a)

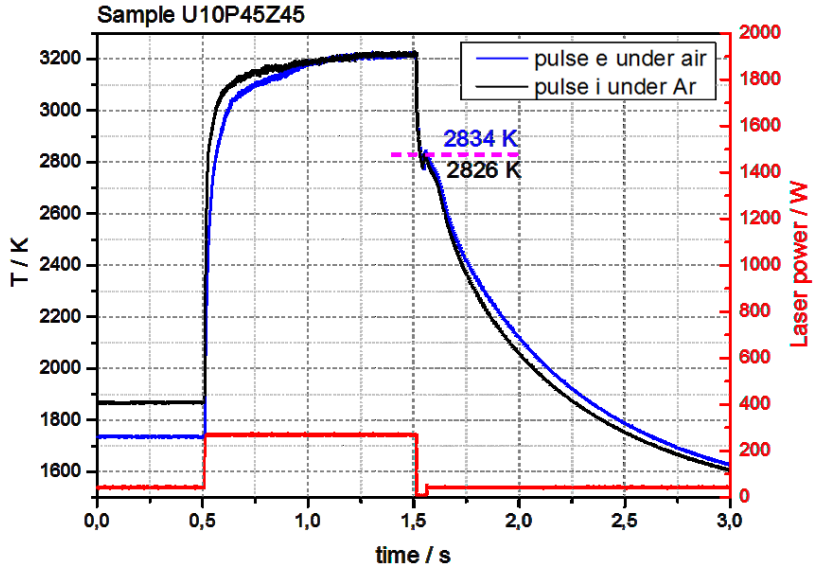

(b)

Figure 8 : Effet de l'atmosphère expérimentale sur le comportement pendant la fusion/solidification. (a) Echantillon U48P3Z49 ; (b) échantillon U10P45Z45

Modélisation thermodynamique

Système U-Zr-O

La modélisation thermodynamique du système U-Zr-O a été effectuée en prenant en compte les données expérimentales sélectionnées de la littérature ainsi que les résultats expérimentaux obtenues pendant la thèse (traitement thermique à 2567 K et chauffage laser).

Les diagrammes de phase calculés sont en accord avec les données expérimentales. A 2273 K la solubilité d'oxygène calculée dans la phase liquide est en très bon accord avec celle obtenue par Maurizi [6]. A 2567 K, les données sur la lacune de miscibilité à l'état liquide ont permis de mieux décrire son domaine d'extension. La coupe isotherme calculée à 2567 K est présentée sur la Figure 9.

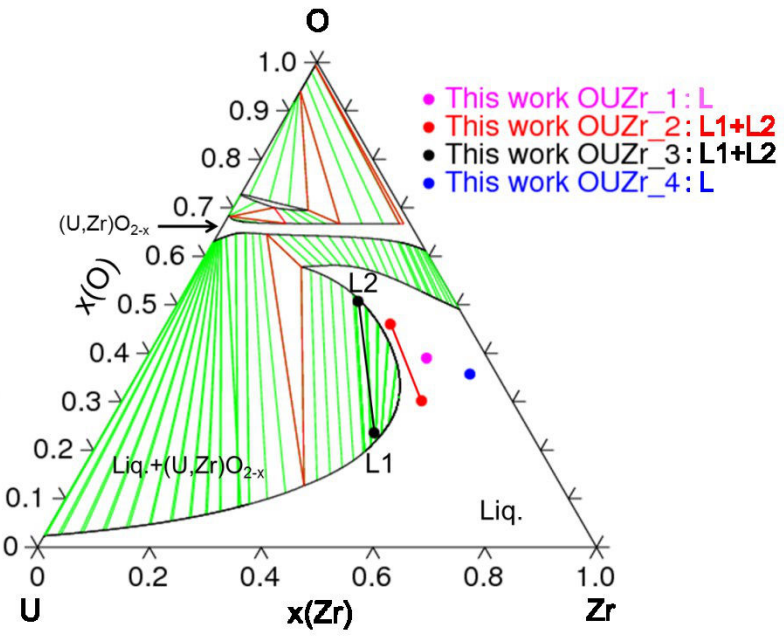

Figure 9 : Section isotherme calculée à 2567 K

La section isoplèthe Zr-UO_2 a été également été optimisée en utilisant les données de Juenke & White [8] et les résultats de chauffage laser obtenus pendant la thèse. La coupe calculée est sur la Figure 10.

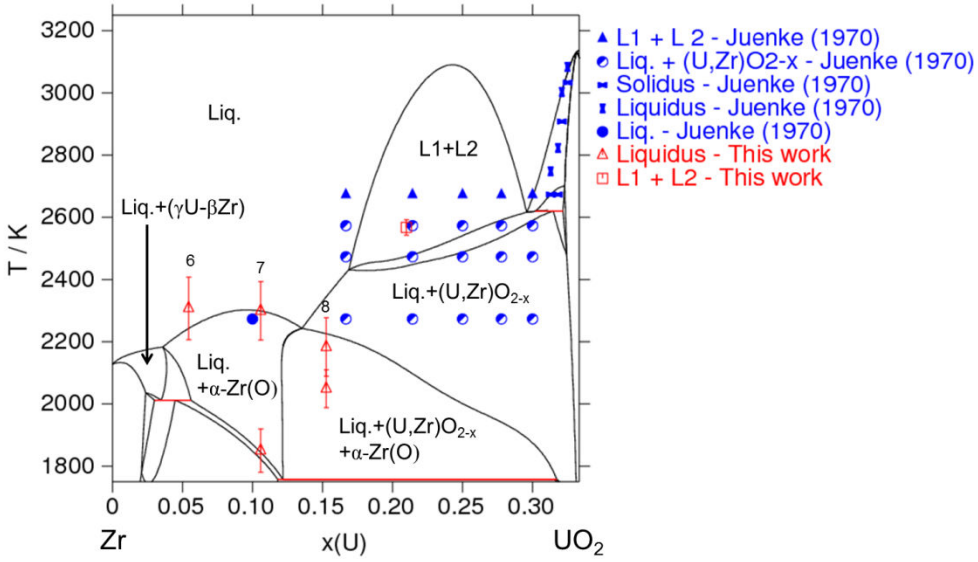

Figure 10 : Section Zr-UO_2 calculée

Le domaine d'extension calculé de la lacune de miscibilité n'est que partiellement en accord avec les données de Juenke & White [8]. Cependant, les auteurs n'ont pas donné d'informations précises sur la composition chimique des échantillons et sur leur microstructure. Les résultats de chauffage par laser sur les échantillons OUZr_6, OUZr_7 et OUZr_8 ont été également utilisés pour modéliser la section Zr-UO_2. Un bon accord est obtenu entre les calculs et les données expérimentales sur les échantillons OUZr_6 et OUZr_7. Pour l'échantillon OUZr_8, la différence entre le calcul et les résultats expérimentaux peut être liée à une mauvaise estimation de l'émissivité, qui entraine une

baisse de la température vraie. Ces résultats montrent qu'une analyse plus approfondie des propriétés optiques de ces échantillons est nécessaire.

La version actuelle du modèle thermodynamique pour le système ternaire U-Zr-O est satisfaisante, en particulier pour T > 1800 K. Néanmoins, des mesures de potentiel d'oxygène sont nécessaires pour mieux décrire la phase cubique $(U,Zr)O_{2-x}$-c.

Système Fe-Zr-O

Pour ce système, peu de données sont disponibles dans la littérature. Les équilibres entre ZrO_2 et les oxydes de fer FeO_{1+x} ont été les plus étudiés. Un modèle thermodynamique pour le système Fe-Zr-O a été publié en 2015 par Fabrichnaya & Pavlyuchkov [16]. Ce modèle a été pris comme point de départ pour cette étude. Néanmoins, leur modèle pour la phase ZrO_2-c est différent de celui que nous utilisons. Les données de solubilité du FeO dans ZrO_2 et de liquidus obtenues par Bechta et al. [17] ont été utilisées pour modéliser la section ZrO_2-FeO (Figure 11). En plus, la section ZrO_2-Fe_3O_4 a été modélisée en utilisant les données de Kiminami [18,19].

Notre modèle dans la région oxyde ZrO_2-FeO-Fe_3O_4 reproduit bien les données de pression partielle d'oxygène obtenues par Katsura [11] à 1473 K.

Le reste du diagramme ternaire est obtenu par extrapolation des diagrammes binaires Fe-Zr, Fe-O et Zr-O. De nouvelles données de potentiel d'oxygène pourraient aider à mieux décrire les équilibres ternaires.

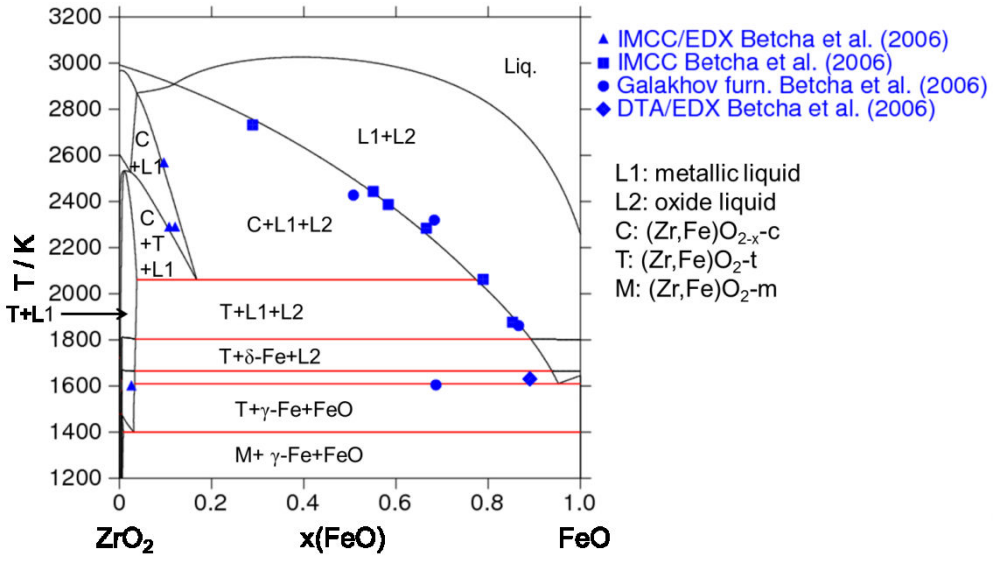

Figure 11 : Section ZrO_2-FeO calculée avec notre modèle. Comparaison avec les points expérimentaux de Bechta et al [17]

Système U-Fe-O

L'étude expérimentale du système U-Fe-O pose les mêmes difficultés que pour le système Fe-Zr-O. De plus, le Fe et l'U ont de nombreux états d'oxydation en fonction de la température, du potentiel d'oxygène et de la pression totale. Dans ce travail, la section UO_2-FeO_{1+x} a été modélisée (Figure 12). Pour cela, les données de Bechta et al. [20] ont été utilisées.

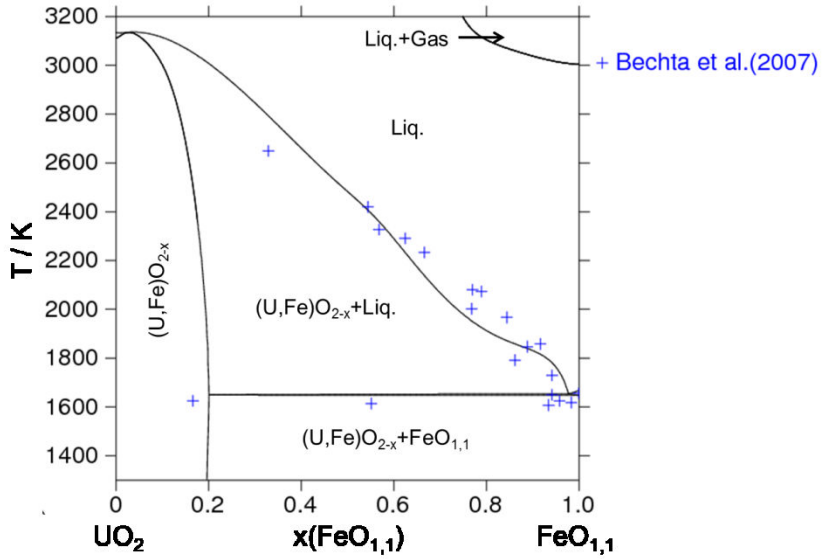

Figure 12 : Section UO_2-$FeO_{1.1}$ calculée avec le modèle développé pendant la thèse. Comparaison avec les points expérimentaux de Bechta et al. [20]

La solubilité calculée de $FeO_{1.1}$ dans UO_2 est surestimée par rapport aux données expérimentales de Bechta et al. [20].

Système U-Pu-Zr-O

La section PuO_2-ZrO_2 a été modélisée. Les données de Mardon et al. [12] et Albiol et al. [21] ainsi que le résultat de chauffage laser sur l'échantillon P50Z50 ($(PuO_2)_{0.50}(ZrO_2)_{0.50}$) ont été utilisés. La section calculée est présentée sur la Figure 13.

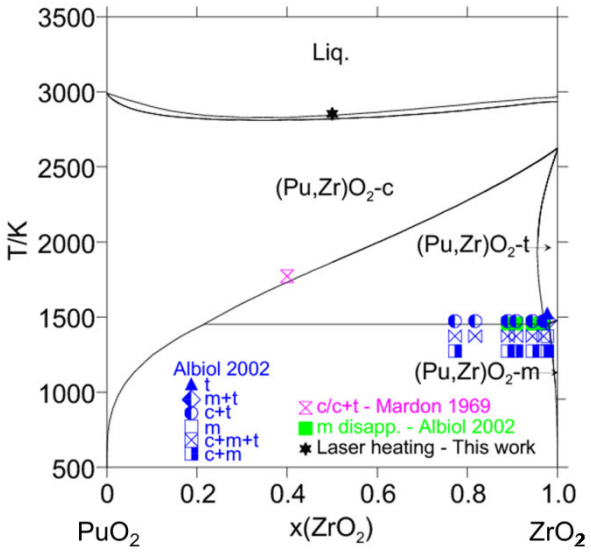

Figure 13 : Section PuO_2-ZrO_2, où les points expérimentaux de Mardon et al. [12] et Albiol et al. [21] ont été reportés

Le diagramme de phase calculé est en bon accord avec les données expérimentales. Néanmoins, très peu de résultats expérimentaux existent sur ce système. De nouvelles études sont nécessaires pour confirmer notre modélisation.

Calculs de chemins de solidification

Le modèle thermodynamique du système corium en cuve prototypique U-Pu-Zr-Fe-O développé dans le cadre de cette thèse, a été utilisé pour interpréter la microstructure d'un échantillon quaternaire U-Zr-Fe-O fabriqué par fusion à arc. L'échantillon refroidi a une structure similaire à celle observée pour les échantillons ternaires OUZr_2 et OUZr_3, avec une zone enrichie en oxygène et une autre enrichie en éléments métalliques. La composition étudiée se situe donc dans la lacune de miscibilité à l'état liquide. La partie oxyde est formée d'un phase majoritaire $(U,Zr)O_{2-x}$ et de précipités métalliques au bord de grains de la phase oxyde. Le couplage entre l'analyse par microsonde électronique et les calculs de chemin de solidifications ont permis d'identifier les phases observées au MEB (Figure 14).

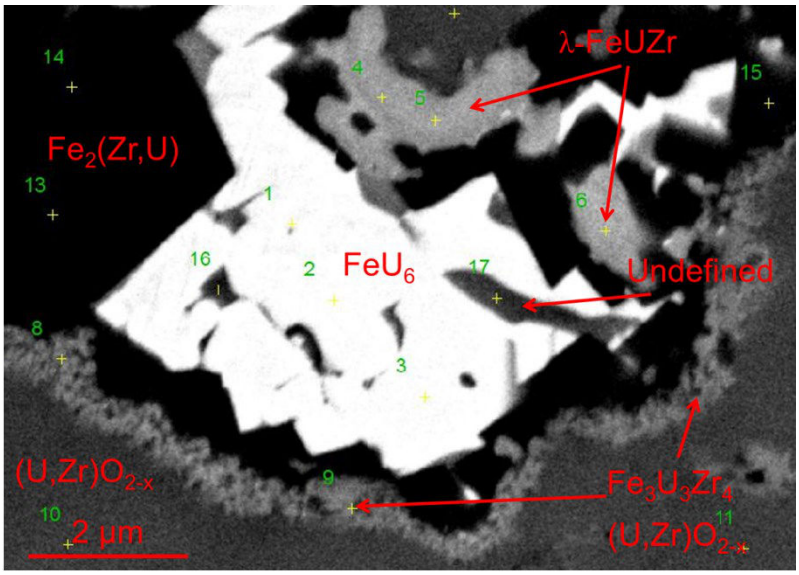

Figure 14 : Microstructure observée au bord des grains de la phase $(U,Zr)O_{2-x}$ dans la région oxyde de l'échantillon U-Zr-Fe-O. Les phases indexées sont le résultat du couplage calculs de chemin de solidification/analyse par microsonde

4 Calcul d'application sur le système corium hors cuve prototypique

La base de données thermodynamique TAF-ID a été développée dans le cadre d'un projet international de l'OCDE. L'objectif principal de ce projet est d'obtenir une base thermodynamique pour calculer les diagrammes de phase et les propriétés thermodynamiques du combustible nucléaire contenant des produits de fission et sur l'interaction de ce combustible avec les matériaux structuraux (acier, Zircaloy, béton).

Cette base couplée avec le modèle développé pendant la thèse sur le corium en cuve prototypique U-Pu-Zr-Fe-O a été testée sur deux compositions de corium hors cuve Al-Ca-Si-U-Zr-O. Ces compostions représentent deux scenarii d'ICB entre un corium en cuve oxydé (UO_2-ZrO_2) et deux type de béton, un calcaire (riche en CaO) et un siliceux (riche en SiO_2). Cette approche est importante car le béton utilisé dans les installations nucléaires dans le monde n'est pas standardisé [22,23].

Les deux échantillons ont subi un traitement thermique à 2500 K. Une trempe a ensuite permis de déterminer les phases présentes à la température du recuit (Figure 15).

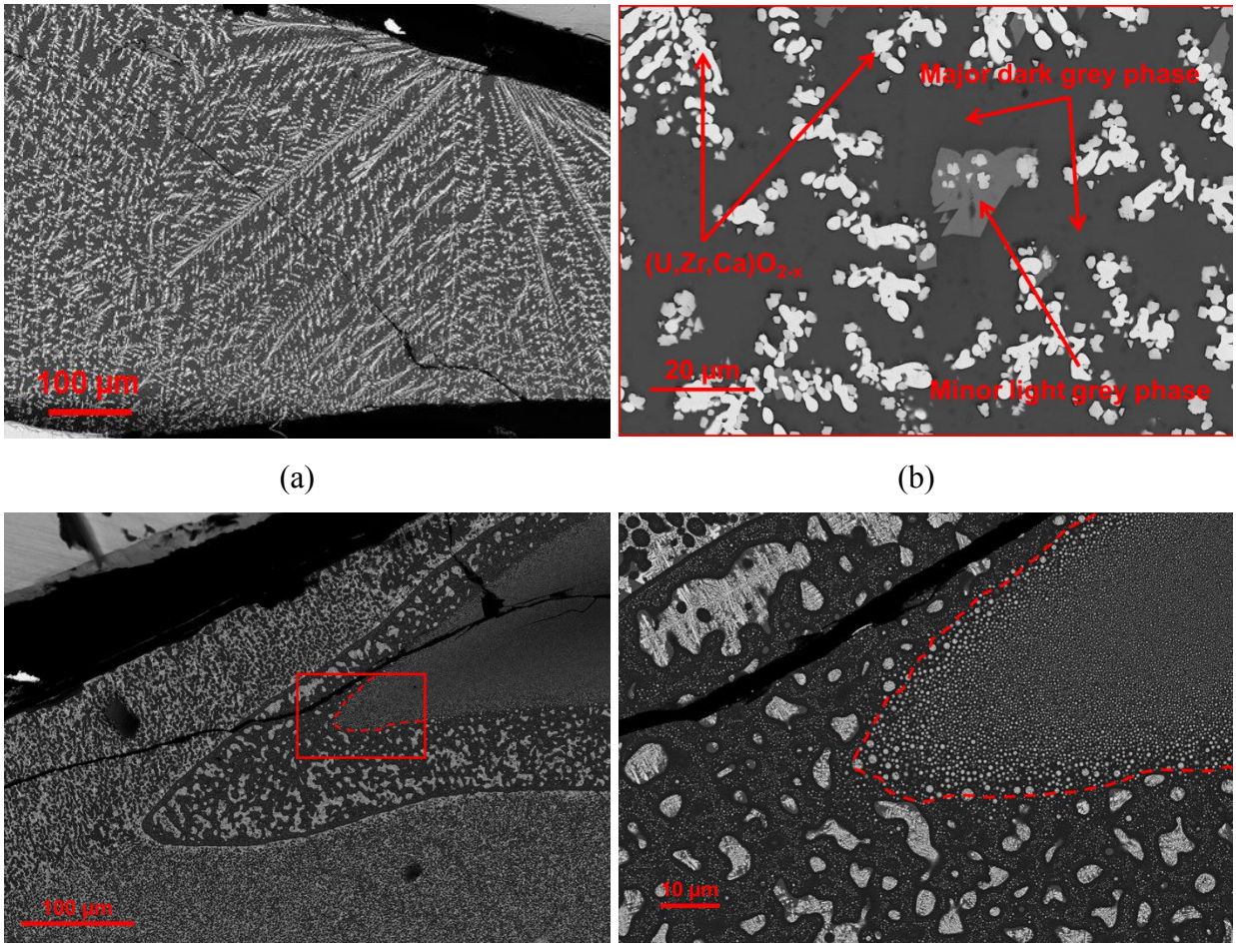

Figure 15 : Comparaison entre la microstructure de l'échantillon riche en CaO (a-b) et l'échantillon riche en SiO_2 (c-d)

L'échantillon riche en CaO a une structure dendritique, typique d'un seul liquide refroidi tandis que l'échantillon riche en SiO_2 présente une structure caractérisée par une matrice

amorphe avec une dispersion de microgouttelettes. Cette dernière microstructure indique qu'à 2500 K deux liquides immiscibles étaient à l'équilibre. Des difficultés ont été rencontrées lors des analyses sur ces échantillons solidifiés à cause de la présence de phases amorphes et des dimensions très petites de ces phases.

Les calculs de chemin de solidification ont permis d'identifier que partiellement les phases observées par MEB-EDS et par microsonde électronique. Des analyses supplémentaires pourront aider à mieux interpréter les microstructures.

5 Développement du montage expérimental ATTILHA

Le montage expérimental ATTILHA (Advanced Temperature and Thermodynamic Investigation by Laser Heating Approach) a été développé dans cette thèse pour pouvoir étudier le comportement à haute température de matériaux céramiques, métalliques et mélanges oxyde/métal. Il s'agit d'un couplage entre la technique de chauffage par laser et de lévitation aérodynamique. Un schéma de principe du dispositif expérimental ATTILHA est montré la Figure 16. Les échantillons sphériques lévitent dans un écoulement gazeux (air, Ar ou Ar+20 % O_2). Le lévitateur est une buse en Al constituée d'un convergent et d'un divergent. La bille initialement placée au fond de la buse est expulsée grâce à l'injection du gaz de lévitation. Le réglage de la pression et du débit de gaz permet de stabiliser l'échantillon en lévitation à l'intérieur du col divergent.

L'échantillon est chauffé par un laser CO_2 (Coherent®, P_{max}=250 W) qui émet à la longueur d'onde λ=10.6 µm. A ce stade, le réglage de la puissance laser est manuel.La mesure de température est effectuée par un pyromètre bi-chromatique et par un détecteur MCT. Le pyromètre bi-chromatique est du type *Lumasence IMPAC ISR 12-LO* (λ_1=0.8 µm, λ_2=1.05 µm). La plage de température mesurée est 1273-3273 K. Ce pyromètre a été livré avec un certificat d'étalonnage par le constructeur. La validité de ce certificat a été testée sur le point de fusion de l'alumine pure.

Le détecteur MCT utilisé est un *Hamamatsu P5274-01* sensible entre 2 µm et 22 µm. Un « chopper » optique a été placé entre le détecteur et l'échantillon pour moduler le flux radiatif provenant de la source chaude (l'échantillon chauffé par le laser). La sortie analogique du détecteur MCT est du chopper ont été envoyés à vers une détection synchrone Stanford Research® SR530 pour augmenter le rapport signal/bruit. Puis le signal synchronisé a été envoyé vers un incrustateur de données National Instrument® NI cDAQ-9178 directement connecté à l'unité centrale via une application LabView®. Le détecteur MCT a été étalonné à plusieurs longueurs d'onde pour vérifier la linéarité de sa réponse en sortie en fonction de la luminance reçue par la source chaude. Deux filtres interférentiels centrés sur 10 µm et 12.214 µm ont été interposés entre le détecteur et la source chaude.

En parallèle, une caméra infrarouge rapide FLIR® SC7500 a été utilisée pour observer et enregistrer le comportement de l'échantillon pendant la fusion et la solidification. Grâce à une collaboration avec l'Institut de Mathématiques de Toulouse (IMT), l'émissivité de l'échantillon à 3.99 µm peut être obtenue.

L'acquisition synchrone du pyromètre bi-chromatique, du détecteur MCT et de la caméra infrarouge est assurée par un trigger externe.

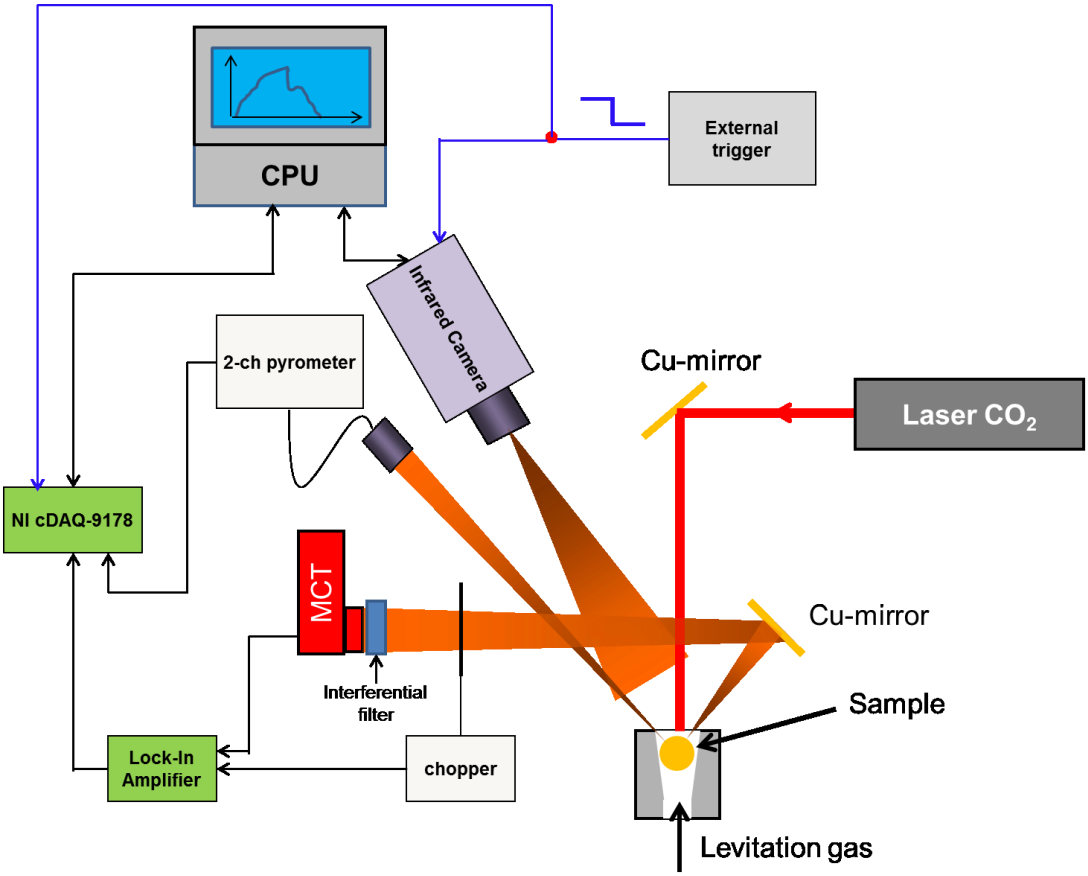

Figure 16 : Schéma du dispositif expérimental ATTILHA

La validité du montage expérimental a été testée sur l'alumine, dont les propriétés optiquse et thermiques sont bien connues. Ensuite, deux échantillons dans le système Al_2O_3-ZrO_2 ont été étudiés. Grâce aux signaux synchronisés du détecteur MCT et de la caméra infrarouge, il est possible d'obtenir l'évolution de l'émissivité de l'échantillon pendant un cycle de chauffage/refroidissement. Le résultat obtenu sur l'échantillon A89Z11 (89 mol% Al_2O_3 – 11 mol% ZrO_2) est présenté sur la Figure 17.

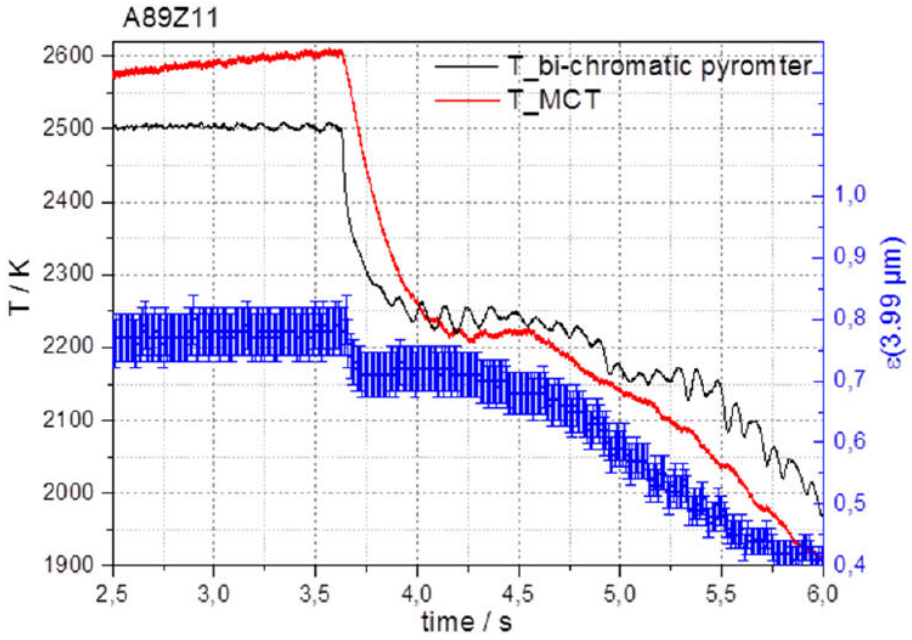

Figure 16 : Résultat obtenu sur l'échantillon A89Z11. La ligne rouge représente la température enregistrée par le détecteur MCT, la ligne noire représente la température enregistrée par le pyromètre bi-chromatique. Les points bleus montrent la variation de l'émissivité à 3.99 µm de l'échantillon au cours du cycle chauffage/refroidissement

Les deux arrêts thermiques enregistrés par le pyromètre bi-chromatique correspondent respectivement à la température de liquidus et à la transition eutectique. En revanche, le détecteur MCT n'a enregistré qu'un seul arrêt thermique correspondant à la transition eutectique. En effet, l'émissivité de l'échantillon à 3.99 µm varie au cours du cycle chauffage/refroidissement. La valeur maximale est atteinte à l'état liquide.

Grâce au montage expérimental ATTILHA il est également possible d'obtenir des informations spatiales sur le comportement d'un échantillon en lévitation pendant la fusion et la solidification. En particulier, on a montré qu'il est possible de suivre la formation d'une lacune de miscibilité à l'état liquide dans le système ternaire Fe-Zr-O. L'échantillon de départ – un échantillon métallique Fe-Zr – a été fondu sous une atmosphère d'Ar + 20 % O_2. Pendant plusieurs cycles de chauffage/refroidissement, la présence d'une lacune de miscibilité a été mise en évidence (Figure 17). L'échantillon initialement métallique, a interagi avec l'oxygène présent dans le gaz de lévitation : la composition globale a alors évolué dans le système ternaire Fe-Zr-O.

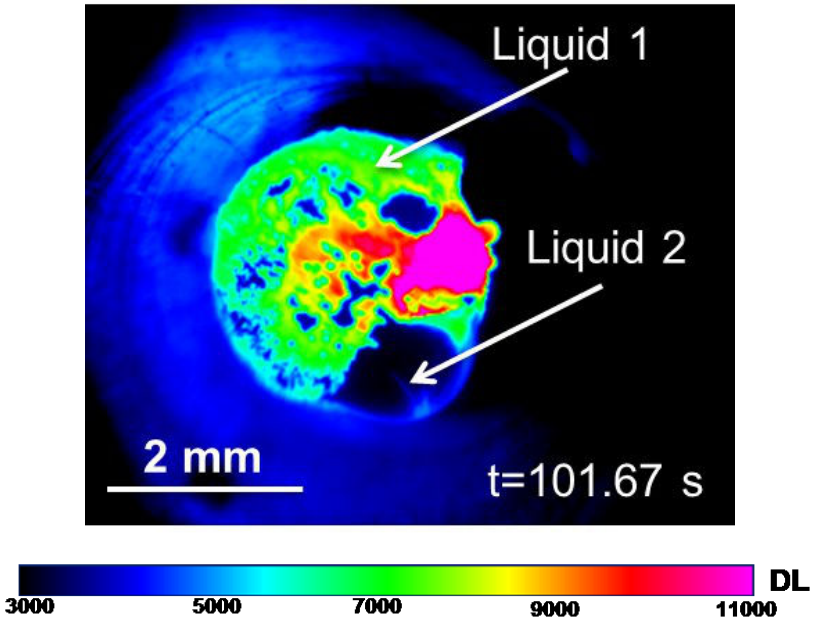

Figure 17 : Mise en évidence de la présence d'une lacune de miscibilité à l'état liquide dans le système ternaire Fe-Zr-O

Le deuxième liquide a la forme d'un lobe qui se déplace à la surface de l'échantillon. La différence de couleur dépend du niveau numérique (Digital Level DL) mesuré par la caméra infrarouge : le violet correspond à un niveau de signal élevé, le bleu correspond à un niveau de signal faible. Cette différence a une signification physique. Si on fait l'hypothèse que le Liquide 1 et le Liquide 2 sont à la même température, la différence de couleur correspond alors à une différence d'émissivité des liquides. Le Liquide 2 est donc moins émissif que le Liquide 1.

6 Conclusions et perspectives

Cette thèse entre dans le cadre des études sur les accidents graves dans les réacteurs nucléaires de 2ème et 3ème génération. L'objectif était d'étudier le système complexe U-Pu-Zr-Fe-Al-Ca-Si-O, qui peut être considéré comme le système prototypique du corium hors cuve.

La méthodologie adoptée est basée sur la méthode CALPHAD, qui permet de développer un modèle thermodynamique sur des systèmes complexes à partir d'une sélection de données de la littérature. Si les résultats de la littérature ne sont pas suffisants pour l'étape de modélisation, de nouvelles données peuvent être obtenues. Dans ce cadre, après une revue critique de la littérature existante sur les sous-systèmes chimiques du corium, une campagne expérimentale a été effectuée pour obtenir des données supplémentaires, notamment sur les systèmes U-Zr-O, Fe-Zr-O, Pu-Zr-O, U-Zr-Fe-O et U-Pu-Zr-O. De plus, un traitement thermique sur deux échantillons prototypiques du corium hors cuve a été effectué pour étudier les phases à l'équilibre dans ce système complexe.

Grâce à la campagne expérimentale effectuée pendant cette thèse, la lacune de miscibilité à l'état liquide dans le système ternaire U-Zr-O a été mise en évidence et caractérisée à 2567 K. Deux conodes ont été mesurées est ont permis d'améliorer le modèle thermodynamique de la phase liquide. Les essais de chauffage laser ont également permis d'améliorer le modèle du système U-Zr-O. Les résultats de chauffage laser sur les échantillons Fe-Zr-O ne sont pas utilisés pour la modélisation à cause des incertitudes sur la composition finale après les essais.

Les résultats sur les échantillons UO_2-PuO_2-ZrO_2 ont permis d'étudier le comportement de ce matériau pendant la fusion et la solidification en fonction de l'atmosphère expérimentale. On a montré que pour ce type d'échantillons, il est très difficile de garder un rapport O/M=2. Le rapport O/M de l'échantillon varie en fonction de la température mais aussi de l'atmosphère expérimentale utilisée. Des calculs thermodynamiques ont confirmé ce comportement.

Le modèle thermodynamique du système corium en cuve prototypique (U-Pu-Zr-Fe-O) a été développé avec succès. Cependant, de nouvelles données thermodynamiques telles que des potentiels d'oxygène sont nécessaires pour pouvoir mieux décrire les équilibres de phases.

L'analyse post-trempe sur deux échantillons de corium hors cuve a montré qu'en fonction de la teneur en SiO_2, une ou deux phase liquides sont à l'équilibre à 2500 K. Le modèle évalué pendant la thèse a été couplé avec la base thermodynamique TAF-ID et testé sur les deux échantillons. Les calculs sont cohérents avec les résultats expérimentaux. Néanmoins, des différences ont été mises en évidence, surtout pour ce qui concerne la composition chimique des phases observées dans ces échantillons complexes.

Le dispositif expérimental ATTILHA a été conçu et développé pendant la thèse. Il s'agit d'un montage de chauffage par laser couplé à de la lévitation aérodynamique. Cette technique permet d'étudier le comportement à haute température d'une large gamme de matériaux sans un contact direct entre l'échantillon et un support solide. Des résultats préliminaires sur de l'alumine et sur des échantillons Al_2O_3-ZrO_2 ont démontré la validité de la technique. On a aussi montré que l'étude d'une lacune de miscibilité à l'état liquide est possible. La prochaine étape du développement consiste à tester le dispositif sur des matériaux contentant de l'U.

Bibliographie

[1] J.M. Seiler, B. Tourniaire, F. Defoort, K. Froment, Nucl. Eng. Des. 237 (2007) 1752.

[2] IRSN, CEA, EDF, R&D Relative Aux Accidents Graves Dans Les Réacteur à Eau Pressurisée : Bilan et Perspectives, 2006.

[3] N. Saunders, A. Miodokwin, CALPHAD - Calculation of Phase Diagrams, A Comprehensive Guide, 1998.

[4] H. Lukas, S. Fries, B. Sundman, Computational Thermodynamics - The Calphad Method, 2007.

[5] TAF-ID, "www.oecd-nea.org/sceince/taf-id".

[6] A. Maurizi, Réactivité Chimique a Haute Température Dans Le Système (U,Zr,Fe,O) - Contribution a l'Etude de La Zircone Comme Récuperateur de Corium", PhD Thesis Univerisite Pierre et Marie Curie, 1996.

[7] C. Politis, Untersuchungen Im Dreistoffsystem Uran-Zirkon-Sauerstoff, Kernforschungszentrum Karlsruhe, Report no. KfK 2167, 1976.

[8] E.F. Juenke, J.F. White, Physico-Chemical Studies of Clad UO_2 under Reactor Accident Conditions, General Electric Company, Report GEMP-731, 1970.

[9] C. Guéneau, V. Dauvois, P. Pérodeaud, C. Gonella, O. Dugne, J. Nucl. Mater. 254 (1998) 158.

[10] M. Baichi, Contribution à L'Étude Du Corium D'un Réacteur Nucléaire Accidenté : Aspects Puissance Résiduelle et Thermodynamique Des Systèmes U-UO2 et UO2-ZrO2, PhD Thesis INP Grenoble, 2001.

[11] T. Katsura, M. Wakihara, S.-I. Hara, T. Sugihara, J. Solid State Chem. 13 (1975) 107.

[12] P.G. Mardon, D.J. Hodkin, J.T. Dalton, J. Nucl. Mater. 32 (1969) 126.

[13] C. Journeau, Contribution Des Essais En Matériaux Prototypiques Sur La Plate-Forme PLINIUS à l'Etude Des Accidents Graves de Réacteurs Nucléaires, HDR Thesis 2008.

[14] L. Kaufman, H. Bernstein, Computer Calculation of the Phase Diagram: With Special Reference to Refractory Metals, Academic Press Inc., 1970.

[15] F. De Bruycker, High Temperature Phase Transitions in Nuclear Fuels of the Fourth Generation, PhD Thesis Universite d'Orleans, 2010.

[16] O. Fabrichnaya, D. Pavlyuchkov, Metall. Mater. Trans. A (2015).

[17] S. V. Bechta, E. V. Krushinov, V.I. Almjashev, S.A. Vitol, L.P. Mezentseva, Y.B. Petrov, D.B. Lopukh, V.B. Khabensky, M. Barrachin, S. Hellmann, K. Froment, M. Fischer, W. Tromm, D. Bottomley, F. Defoort, V. V. Gusarov, J. Nucl. Mater. 348 (2006) 114.

[18] R.H.G.A. Kiminami, Ceramica 34 (1988) 121.

[19] R.H.G.A. Kiminami, Ceramica 33 (1987) 207.

[20] S. Bechta, E. V. Krushinov, V.I. Almyashev, S.A. Vitol, L. Mezentseva, Y.B. Petrov, E. Al., J. Nucl. Mater. 362 (2007) 46.

[21] T. Albiol, H. Serizawa, A. Yasuo, J. Nucl. Sci. Technol. sup3 (2002) 834.

[22] M. Barrachin, Assessment of Ablation Temperature of Concretes from Past MCCI and Thermodynamic Experiments, 2011.

[23] Tranches Nucléaires REP 900 et 1300 MWe - Procedures U4 et U5, 1985.